Numerics of photonic and plasmonic nanostructures with advanced material models

Dissertation

zur Erlangung des akademischen Grades

doctor rerum naturalium

(Dr. rer. nat.)

im Fach Physik

Spezialisierung: Theoretische Physik

eingereicht an der

Mathematisch-Naturwissenschaftlichen Fakultät

der Humboldt-Universität zu Berlin

von

M.Sc. Thomas Kiel

Präsidentin der Humboldt-Universität zu Berlin

Prof. Dr.-Ing. Dr. Sabine Kunst

Dekan der Mathematisch-Naturwissenschaftlichen Fakultät

Prof. Dr. Elmar Kulke

Gutachter: 1. Prof. Dr. Kurt Busch

2. Prof. Dr. Alejandro Saenz

3. Prof. Dr. Andrei Laurynenka

Tag der mündlichen Prüfung: 23.06.2021

Mathematisch-Naturwissenschaftliche Fakultät
Institut für Physik
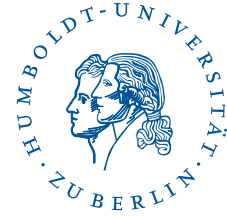
Numerics of photonic and plasmonic nanostructures with advanced material models

Application of selected material models within the discontinuous Galerkin time-domain and Fourier modal method

Ph.D. thesis
by Thomas Kiel

Supervisor: Prof. Dr. Kurt Busch

To my family

Zusammenfassung

In dieser Arbeit untersuchen wir mehrere Anwendungen von photonischen und plasmonischen Nanostrukturen unter Verwendung zweier verschiedener numerischer Methoden: die Fourier-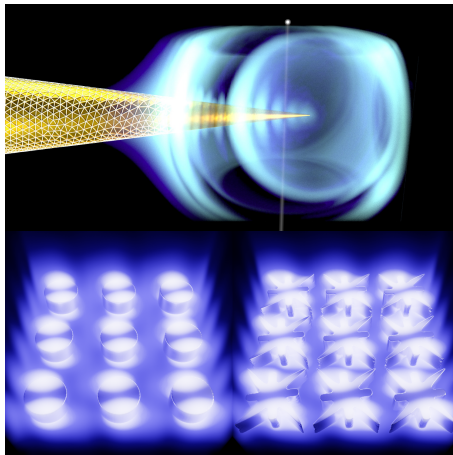Moden-Methode (FMM) und ein unstetiges Galerkin-Zeitraumverfahren (discontinuous Galerkin time-domain method, DGTD method). Die Methoden werden für vier verschiedene Anwendungen eingesetzt, die alle eine Materialmodellerweiterung in der Implementierung der Methoden erfordern. Diese Anwendungen beinhalten die Untersuchung von dünnen, freistehenden, periodisch perforierten Goldfilmen. Wir charakterisieren die auftretenden Oberflächenplasmonenpolaritonen durch die Berechnung von Transmissions- und Elektronenenergieverlustspektren, die mit experimentellen Messungen verglichen werden. Dazu stellen wir eine Erweiterung der DGTD-Methode zur Verfügung, die sowohl absorbierende, impedanzangepasste Randschichten als auch Anregung mit geglätteter Ladungsverteilung für materialdurchdringende Elektronenstrahlen beinhaltet. Darüber hinaus wird eine Erweiterung auf nicht-dispersive anisotrope Materialien für eine Formoptimierung einer volldielektrischen magneto-optischen Metaoberfläche verwendet. Diese Optimierung ermöglicht eine verstärkte Faraday-Rotation zusammen mit einer hohen Transmission. Zusätzlich untersuchen wir abstimmbare hyperbolische Metamaterialresonatoren im nahen Infrarot mit Hilfe der FMM. Wir berechnen deren Resonanzen und vergleichen sie mit dem Experiment. Zum Schluss wird die Implementierung eines nichtlinearen Vier-Niveau-System-Materialmodells in der DGTD-Methode verwendet, um die Laserschwellen eines Mikroresonators mit Bragg-Spiegeln zu berechnen. Bei Einführung eines Silbergitters mit variablen Spaltgrößen wird eine defektinduzierte Kontrolle der Laserschwellen ermöglicht. Die Berechnung der vollständigen, zeitaufgelösten Felddynamik innerhalb des Resonator gibt dabei Aufschluss über die beteiligten Lasermoden.

Abstract

In this thesis, we study several applications of photonic and plasmonic nanostructures by employing two different numerical methods: the Fourier modal method (FMM) and discontinuous Galerkin time-domain (DGTD) method. The methods are used for four different applications, all of which require a material model extension for the implementation of the methods. These applications include the investigation of thin, free-standing periodically perforated gold films. We characterize the emerging surface plasmon polaritons by computing both transmittance and electron energy loss spectra, which are compared to experimental measurements. To this end, we provide an extension of the DGTD method, including absorbing stretched coordinate perfectly matched layers as well as excitations with smoothed charge distribution for material-penetrating electron beams. Furthermore, an extension to non-dispersive anisotropic materials is used for shape optimization of an all-dielectric magneto-optic metasurface. This optimization enables an enhanced Faraday rotation along with high transmittance. Additionally, we study tuneable near-infrared hyperbolic metamaterial cavities with the help of the FMM. We compute the cavity resonances and compare them to the experiment. Finally, the implementation of a non-linear four-level system material model in the DGTD method is used to compute lasing thresholds of a distributed Bragg reflector microcavity. Introducing a silver grating with variable gap sizes allows for a defect-induced lasing threshold control. The computation of the full time-resolved field dynamics of the cavity provides information on the involved lasing modes.

Contents

Introduction

Advances in the fabrication of nanometer-sized optical and optoelectronic systems and the fascination for light-matter interaction therein are the driving force for the investigation of a huge variety of such systems. Whether one is interested in photonic crystals, waveguides, light-emitting diodes, lasers, solar cells, or just plasmonic systems, all must be properly designed to exploit one or another effect in their response to the electromagnetic field. This requires careful material selection and the determination of a suitable geometrical layout. When designing a specific experiment, numerical computations are an indispensable tool to determine the system parameters a priori or optimize already fabricated structures. Furthermore, numerical computations help with the interpretation of the experimental results.

This thesis discusses a few exemplary systems, for which we perform numerical computations. These computations are used either to obtain an understanding of the internal electromagnetic fields, the scattering, and emission behavior or to even propose optimized geometries to enhance resonant effects. For these specific systems, we employ two different numerical methods, which are extended by and tested for the required material models in order to predict the systems' behavior and explain the experimental findings.

1.1 Different applications and material models

For the first exemplary structure, the focus lies on the mapping of surface plasmon polariton (SPP) [1–3] resonances of a periodically perforated gold film using electron energy loss spectroscopy (EELS) [4–6]. This experimental method is one possibility to investigate both localized as well as propagating SPP resonances [7]. Examples include the characterization of localized SPPs of nanometer-sized metallic spheres given by the corresponding Mie resonances [8, 9], metallic tapers, which depending on the opening angle exhibit slow light [10–12, K1], and a strong field enhancement and localization at the apex. This can be, e.g., used for tip-enhanced Rama spectroscopy (TERS) [13] and apatureless scanning near-field optical microscopy (SNOM) [14–16]. Micrometer-long metallic nanowires [17–19], as well as indented metallic cones [K2], allow for a continuous transition between localized and propagating SPP modes. Moreover, SPPs, as well as Djakonov surface waves [20] and plasmons, can be investigated at anisotropic thin-film boundaries, see e.g., [21]. Here, the investigated periodically perforated gold films (see Fig. 1.1) exhibit the effect of extraordinary optical transmission (EOT) [22], as the SPPs carry a significant amount of radiation through the holes of the gold film. Both the EELS measurement and computation allow a characterization of the SPPs modes contributing to the transmittance spectra and also show the dark SPP modes, i.e., modes inaccessible under optical excitation from far-field for free-standing metal films [23]. The computation of both the transmittance and EELS

spectra enables a controlled design of the film parameters important for possible applications like spectral filters [24, 25], plasmonic printing [26], and chemical sensing applications [27, 28].
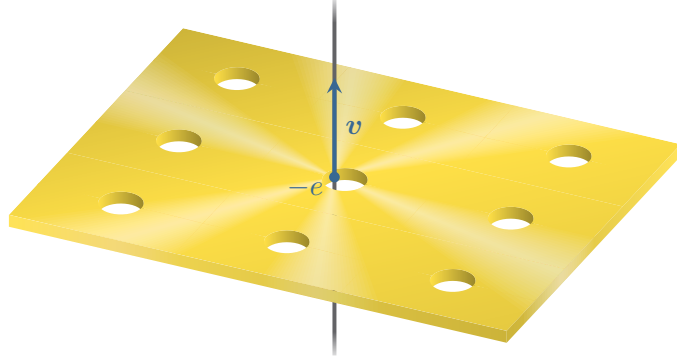
Figure 1.1: Sketch of an electron beam passing a periodically perforated gold film. EELS with relativistically moving electrons ($v \approx 0.7c_0$) is used to map the SPP resonances of the gold film.

Secondly, we investigate a complementary system, consisting of a metasurface based on shaped-modified magneto-optic (MO) nano-disk scatterers. While MO materials provide several rare opportunities to control light at the nanoscale, here we concentrate on the Faraday effect [29] only. An enhanced Faraday effect is important for photonic applications in non-reciprocal devices but is challenging to achieve due to the relatively weak MO material response within the optical domain. For our structure, we demonstrate an enhanced Faraday rotation accompanied by near-unity transmittance in the near-infrared (NIR). There exists a wide variety of plasmonic systems with different geometries, like metallic nanoparticles [30–33], core-shell systems [34–36], multilayer structures [37–39] as well as perforated metallic films [40–42]. However, all these systems suffer from the absorptive losses of the involved metallic MO materials, which might lead to a strong Faraday rotation but lack sufficient field transmittance. Based on a recently measured MO response in high permittivity nanoantennas [43], it was shown that an all-dielectric MO metasurface can lead to a simultaneously high Faraday rotation along with a near-unity transmittance [44]. In this Huygens' metasurface, high transmittance is achieved by the spectral overlap of both the electric and magnetic dipole resonances in the systems [45]. The frequencies of these two modes are controlled by a careful choice of the scatterer geometry within the meta-surface. Here, as an extension to the work presented in [44], we show how to even further improve the Faraday rotation angle of an all-dielectric MO metasurface by optimization of the scatterer geometry, while simultaneously fulfilling the high transmittance constraint. Fig. 1.2 sketches the basic idea for improving the Faraday rotation of a metasurface by replacing cylindrical nano-disk scatterers [44] with scatterers found in basic random search optimization.

As a third system, we investigate hyperbolic metamaterial (HMM) cavities consisting of alternating dielectric and metallic layers. HMMs have been in the spotlight of photonic research for the past decade [46–48]. They enable a wide variety of applications, such as super-resolution imaging [49–51], spontaneous emission engineering [52, 53] with an enhanced Purcell effect [54] and reach as far as an increase in fluctuation induced phenomena like, e.g., quantum friction [55]. Here, we compute resonance frequencies of the field and its distribution to explain the NIR reflectance spectra for an HMM cavity based on the tunable, highly doped transparent conducting

oxide ZnO:Ga [56, K3]. This simple, effectively one-dimensional, layered system of dielectric and metallic layers leads to a hyperbolic dispersion relation. It supports a high photonic local density of states (LDOS) as well as short-wavelength modes at finite frequencies due to the coupling of the SPPs between the individual metallic layers [57].

(a)

(b)

E_{inc}

k_{inc}

E_{inc}

k_{inc}

θ

k_{trans} E_{trans}

θ

k_{trans} E_{trans}
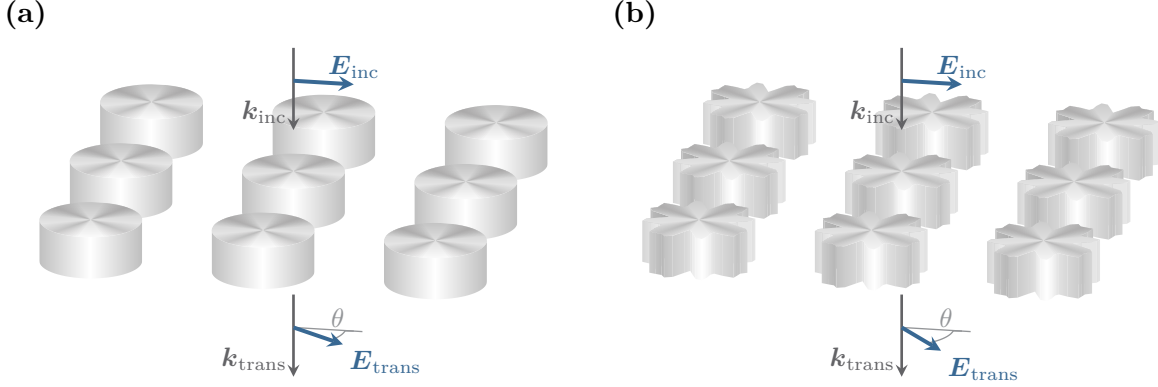
Figure 1.2: Sketch of a metasurface with a lattice of magneto-optic nano-disk scatterers. The **(a)** cylindrical and **(b)** shape-modified nano-disks are optimized to provide a zero-order diffraction resonance with near-unity transmittance and high Faraday rotation angle θ between the incident E_{inc} and transmitted field E_{trans} polarization.

As the fourth and final system, we investigate an optical microlaser cavity. It consists of a dye material layer [58, 59] which is embedded into two distributed Bragg reflectors (DBRs) constituting the cavity [60, K4]. Additionally, a thin metal layer is introduced into the cavity on one of the DBRs, which gives rise to Tamm plasmon polaritons [61] within the cavity. While a subwavelength patterning of the metal layer in the lateral direction leads to the formation of spoof SPPs [62], which, e.g., can be used to design simple terahertz beamsplitters [K5], here a several wavelengths wide patterning is introduced [K4]. Adjusting the width of the single metal layer bars allows for direct control of the cavity lasing threshold upon a focused pump beam excitation. Despite the absorptive losses in the metal, the introduction of a single defect on the order of the pump beam focal width remarkably leads to the lowest lasing threshold onset in the experiment [K4]. To explain the basic lasing and field dynamics and the plasmonic confinement in the cavity, we solve Maxwell's equations in conjunction with a four-level system (4LS) material model [63, 64] for the dye. We compare the experimental and numerically obtained lasing thresholds.

1.2 Outline of the thesis

To compute the relevant quantities for the analysis of the systems listed in Section 1.1, we use two different numerical methods in this thesis.

The first method is the Fourier modal method (FMM) [65–71]. It works in the frequency domain. As it concentrates on periodic layered systems like the aforementioned DBR or the HMM cavities, it makes use of the scattering matrix (S-matrix) algorithm [72].

The second method is the discontinuous Galerkin time-domain (DGTD) method [73–76]. It is used to compute the space and time dependence of the fully vectorial electromagnetic field. As a finite element method, the DGTD is particularly advantageous for setups involving complicated geometries. Moreover, a time-dependent method easily allows to also incorporate non-linear material models, e.g., the lasing material model.

The goals of this thesis are to present the basic theory needed for an understanding of the presented systems and the underlying material models. Furthermore, it shall be shown how the corresponding equations of motion can be implemented in either the DGTD or FMM and S-matrix method. Finally, we compute the different quantities of interest and also assess the computation accuracy for newly implemented material models in the DGTD method.

This thesis is therefore structured in the following way: In Chapter 2 we review the basic electrodynamics and introduce Maxwell's equations as well as the basic observables, like scattering cross sections or transmittance and reflectance spectra. In the following Chapter 3, we discuss the different material models used either in the DGTD or the modal method. This includes dispersive and non-dispersive iso- and anisotropic material models and also the non-linear 4LS material model used to describe the lasing system.

Next, we review the numerical methods themselves. In Chapter 4 we present the working principle of the S-matrix algorithm used in modal methods. Afterward, we discuss the basics of the DGTD method in Chapter 5.

As already outlined in the preceding Section 1.1, we investigate different applications. For the numerical computations of the electron energy loss probability (EELP) spectra of the perforated gold films with the DGTD method, we use a novel implementation including a smoothed charge distribution (see Appendix A) to compute the required Green's tensor components for electron beams passing through the gold material. Both thorough tests comparing the DGTD EELS computations to Mie calculations [8, 9] as well as the final gold film characterization are presented in Chapter 6.

In the following Chapter 7, we analyze the shape-optimized MO metasurfaces and compute both transmittance and Faraday rotation spectra. These rely on the implementation of the non-dispersive anisotropic materials within the DGTD method [77]. Here, a full convergence study of the DGTD computations compared to Mie calculation results [78, 79] is presented. After the metasurface setup, Chapter 7 focuses on the investigation of the uniaxial HMM cavities, the characterization of their emerging resonances, and outlines potential use cases.

We close the set of applications with the lasing cavity setup in Chapter 8. This brings together the characterization of plasmonic systems with the computation of the single cavity modes and the introduced non-linear 4LS material model for the DGTD method to compute the lasing threshold characteristics observed in the experiment [K4].

Finally, we conclude the thesis with Chapter 9 in which, we provide a brief outlook on further applications for the presented methods and material models and discuss how to address open questions in the future.

Basic electrodynamics

Any investigation of light-matter interaction and the propagation of light is deeply rooted in the theory of electrodynamics. Therefore, we start by recapitulating the required concepts of electrodynamics required for the numerical methods and experimental setups presented in the introduction Chapter 1.

In this chapter, we present the macroscopic Maxwell equations in Section 2.1 and mention the basic assumptions on the material models used within this thesis (see Section 2.2). The actual details on the specific materials and material models are then presented in Chapter 3. Next, we show which internal unit system is used for all the numeric computations and give the conversion to the SI unit system in Section 2.3. In the following, all equations explicitly relying on the SI unit system are marked with a tag (SI), while all others rely on the introduced "dimensionless" units.

In Section 2.5 we discuss the boundary conditions of the electromagnetic fields, which are important for both the Fourier modal method (FMM) as well as the discontinuous Galerkin time-domain (DGTD) method. Furthermore, we show which simplifications in Maxwell's equations arise by reducing the effective system dimensions from three to two- and one-dimensional space. Next, we present the plane wave solution of the wave equation for linear, homogeneous, isotropic materials in Section 2.7. Finally, we discuss energy conservation and how to compute scattering and absorption cross sections as well as transmittance, reflectance, and absorbance spectra in Section 2.8. Please note that this chapter loosely follows the presentation within my (German) master thesis [80] with a similar notation used in the formulas.

2.1 Macroscopic Maxwell's equations

The equations of motion in differential form for the electromagnetic fields in classical electrodynamics read

$$\text{(SI)} \qquad \nabla \cdot \boldsymbol{D}(\boldsymbol{r},t) = \rho_{\mathrm{f}}(\boldsymbol{r},t)\,, \tag{2.1a}$$

$$\text{(SI)} \qquad \nabla \cdot \boldsymbol{B}(\boldsymbol{r},t) = 0\,, \tag{2.1b}$$

$$\text{(SI)} \qquad \nabla \times \boldsymbol{E}(\boldsymbol{r},t) = -\frac{\partial}{\partial t}\boldsymbol{B}(\boldsymbol{r},t)\,, \tag{2.1c}$$

$$\text{(SI)} \qquad \nabla \times \boldsymbol{H}(\boldsymbol{r},t) = \frac{\partial}{\partial t}\boldsymbol{D}(\boldsymbol{r},t) + \boldsymbol{j}_{\mathrm{f}}(\boldsymbol{r},t)\,, \tag{2.1d}$$

as can be found in practically every textbook on electrodynamics (see e.g., [81–84]). In these equations, $\boldsymbol{E}(\boldsymbol{r},t)$ is the electric and $\boldsymbol{H}(\boldsymbol{r},t)$ is the magnetic field, $\boldsymbol{D}(\boldsymbol{r},t)$ is the dielectric displacement, and $\boldsymbol{B}(\boldsymbol{r},t)$ is the magnetic induction. These four equations are also commonly referred to individually by their name. Gauss's law, Eq. (2.1a), states that free charge carrier density ρ_{f} is the source of the dielectric displacement $\boldsymbol{D}$. Here, we define free charges as all the charge carriers which are not considered part of a modeled macroscopic material. These bound charges are instead accounted for by the constitutive relations of the specific material in question, which are presented in the following Section 2.2. The magnetic counterpart to Gauss's law, Eq. (2.1b), states that there are no magnetic charges. Faraday's induction law, Eq. (2.1c), states that the electric field $\boldsymbol{E}$ is induced by a time-varying magnetic induction $\boldsymbol{B}$. Finally, Eq. (2.1d) states, that besides a free current density $\boldsymbol{j}_{\mathrm{f}}$ (Ampère's law), also a time-varying dielectric displacement $\boldsymbol{D}$ (Maxwell's addition) induces the magnetic field $\boldsymbol{H}$.

With Maxwell's addition one also directly obtains charge conservation by the continuity equation

$$\text{(SI)} \qquad \frac{\partial}{\partial t}\rho_{\mathrm{f}}(\boldsymbol{r},t) = \nabla \cdot \frac{\partial}{\partial t}\boldsymbol{D}(\boldsymbol{r},t) \overset{(2.1\mathrm{d})}{=} \nabla \cdot \left(\nabla \times \boldsymbol{H}(\boldsymbol{r},t) - \boldsymbol{j}_{\mathrm{f}}(\boldsymbol{r},t) \right) = -\nabla \cdot \boldsymbol{j}_{\mathrm{f}}(\boldsymbol{r},t)\,. \qquad (2.2)$$

2.2 Constitutive relations

In the way we presented Maxwell's equations (2.1), they are still underdetermined. Besides the information on the boundary and initial conditions, we still need the information on how to compute the $\boldsymbol{D}$- and $\boldsymbol{B}$-fields, given the $\boldsymbol{E}$- and $\boldsymbol{H}$-fields. In the most general case, the fields might have a complicated functional dependence

$$\boldsymbol{D} = \boldsymbol{D}\left(\boldsymbol{E},\boldsymbol{H}\right) \quad \text{and} \quad \boldsymbol{B} = \boldsymbol{B}\left(\boldsymbol{E},\boldsymbol{H}\right)\,. \qquad (2.3)$$

This actual functional dependence itself is determined by the material model in question (see Chapter 3). In vacuum, the material equations simplify to

$$\text{(SI)} \qquad \boldsymbol{D} = \varepsilon_0\boldsymbol{E} \quad \text{and} \quad \boldsymbol{B} = \mu_0\boldsymbol{H}\,. \qquad (2.4)$$

Here ε_0 is the permittivity and μ_0 the permeability of the vacuum. The latter is defined (cf. [85]) to have the value

$$\text{(SI)} \qquad \mu_0 = 4\pi \times 10^{-7}\,\mathrm{N\,A^{-2}}\,. \qquad (2.5)$$

With the fixed value of the speed of light

$$\text{(SI)} \qquad c_0 = 299\,792\,458\,\mathrm{m\,s^{-1}}\,, \qquad (2.6)$$

also the vacuum permittivity is fixed to

$$\text{(SI)} \qquad \varepsilon_0 = \frac{1}{\mu_0 c_0^2} \approx 8.854\,187\,817 \times 10^{-12}\,\mathrm{A\,s\,V^{-1}\,m}\,. \qquad (2.7)$$

Hence $\boldsymbol{D}$ and $\boldsymbol{E}$, as well as $\boldsymbol{B}$ and $\boldsymbol{H}$ are proportional. The scaling factor is absorbed in the change of units following in Section 2.3.

In the most general case, the material's constitutive relations are both non-local and non-linear. Yet in most optical cases, it is sufficient to only deal with local and linear field relations. All material models considered in this thesis are local materials models. Except for the non-linear four-level system (4LS) material model described in Section 3.5, also all other material models are linear. This normally is the case as long as the involved field strengths are not too high. We assume the materials models to be of the form

$$(\text{SI}) \qquad \boldsymbol{D}(\boldsymbol{r},t) = \varepsilon_0 \int_0^\infty \mathrm{d}\tau \, \underline{\underline{\boldsymbol{\varepsilon}}}\left(\boldsymbol{r},\tau\right) \cdot \boldsymbol{E}\left(\boldsymbol{r},t-\tau\right) \qquad (2.8\mathrm{a})$$

$$(\text{SI}) \qquad \text{and} \quad \boldsymbol{B}(\boldsymbol{r},t) = \mu_0 \int_0^\infty \mathrm{d}\tau \, \underline{\underline{\boldsymbol{\mu}}}\left(\boldsymbol{r},\tau\right) \cdot \boldsymbol{H}\left(\boldsymbol{r},t-\tau\right) \, . \qquad (2.8\mathrm{b})$$

Here, $\underline{\underline{\boldsymbol{\varepsilon}}}(\boldsymbol{r},t)$ and $\underline{\underline{\boldsymbol{\mu}}}(\boldsymbol{r},t)$ are the response kernels of the $\boldsymbol{E}$- and $\boldsymbol{H}$-field, respectively. This allows for dispersive material models. Here, we assume no mixing of electric and magnetic fields, as it is present, e.g., in bi-isotropic and chiral materials [86]. Yet, we consider anisotropic material tensors $\underline{\underline{\boldsymbol{\varepsilon}}}$ and $\underline{\underline{\boldsymbol{\mu}}}$. Note that causality is preserved in the given time convolutions by the restriction to positive times τ. For instantaneous field generation, e.g., in vacuum, we have

$$\underline{\underline{\boldsymbol{\varepsilon}}}\left(\boldsymbol{r},\tau\right) = \underline{\underline{\boldsymbol{\varepsilon}}}\left(\boldsymbol{r}\right)\delta\left(\tau\right) \quad \text{and} \quad \underline{\underline{\boldsymbol{\mu}}}\left(\boldsymbol{r},\tau\right) = \underline{\underline{\boldsymbol{\mu}}}\left(\boldsymbol{r}\right)\delta\left(\tau\right) \, . \qquad (2.9)$$

Also notice, that commonly one separates the vacuum part, such that

$$(\text{SI}) \qquad \boldsymbol{D}(\boldsymbol{r},t) = \varepsilon_0 \boldsymbol{E}(\boldsymbol{r},t) + \boldsymbol{P}(\boldsymbol{r},t) \, , \qquad (2.10\mathrm{a})$$

$$(\text{SI}) \qquad \boldsymbol{B}(\boldsymbol{r},t) = \mu_0 \boldsymbol{H}(\boldsymbol{r},t) + \boldsymbol{M}(\boldsymbol{r},t) \, , \qquad (2.10\mathrm{b})$$

with the macroscopic polarization $\boldsymbol{P}$ and magnetization $\boldsymbol{M}$.

2.3 Unit system conversion

Before proceeding, we want to introduce the unit system used throughout this thesis. While we so far have used the SI unit system, we change into a "unit-less" set of equations in order to perform numeric computations. This is done by fixing some characteristic scales of the system, i.e., effectively setting some physical constants like the speed of light to one. Normally the main goal of the unit system choice is to achieve numerical rounding errors as small as possible. Therefore, one tries to guarantee that all the magnitudes of quantities to be computed are relatively close to one.

First, we consider the units of space and time. We, therefore, consider the dynamics of the $\boldsymbol{E}$- and $\boldsymbol{H}$-field, which are governed by the curl-equations (2.1c) and (2.1d). We start with the wave equation in vacuum, which can be derived by double application of the curl-operator on

the fields:

(SI) $$\nabla \times \nabla \times \boldsymbol{E} + \varepsilon_0\mu_0 \frac{\partial^2}{\partial t^2}\boldsymbol{E} = \boldsymbol{0} \qquad \text{and} \qquad \nabla \times \nabla \times \boldsymbol{H} + \varepsilon_0\mu_0 \frac{\partial^2}{\partial t^2}\boldsymbol{H} = \boldsymbol{0}\,. \tag{2.11}$$

Using $\varepsilon_0\mu_0 = c_0^{-2}$, we can motivate the transformation of the time derivative operator

(SI) $$\frac{1}{c_0}\frac{\partial}{\partial t} = \frac{\partial}{\partial t'}\,, \tag{2.12}$$

in order to eliminate the explicit appearance of the speed of light in the wave equation. Consequently, we could set $c_0 \to 1$ by introducing a scaled time

(SI) $$t' = c_0 t\,. \tag{2.13}$$

However, this time still has a physical length dimension. Here, we can exploit the scale-invariance of Maxwell's equations (2.1), i.e., the invariance under the transformation

(SI) $$\boldsymbol{r}' = \frac{\boldsymbol{r}}{\lambda_0} \quad \text{and} \quad t' = \frac{c_0 t}{\lambda_0}\,, \tag{2.14}$$

where λ_0 can be an arbitrary length. Since the characteristic length scales of the optical systems we are concerned with, lie between several nanometers to a few microns (see Section 1.1), we conveniently set

(SI) $$\lambda_0 = 1\,\text{nm}\,. \tag{2.15}$$

Inserting the rescaled time and space coordinates into the source-free curl-equations (2.1c) and (2.1d), we get

(SI) $$\frac{\partial}{\partial t'}\int_0^\infty \mathrm{d}\tau\, \underline{\underline{\boldsymbol{\varepsilon}}}\left(\boldsymbol{r}',\tau\right)\boldsymbol{E}\left(\boldsymbol{r}',t'-\tau\right) = \underbrace{\frac{1}{c_0\varepsilon_0}}_{Z_0}\nabla' \times \boldsymbol{H}\left(\boldsymbol{r}',t'\right)\,, \tag{2.16}$$

(SI) $$\frac{\partial}{\partial t'}\int_0^\infty \mathrm{d}\tau\, \underline{\underline{\boldsymbol{\mu}}}\left(\boldsymbol{r}',\tau\right)\underbrace{c_0\mu_0}_{Z_0}\boldsymbol{H}\left(\boldsymbol{r}',t'-\tau\right) = \nabla' \times \boldsymbol{E}\left(\boldsymbol{r}',t'\right)\,, \tag{2.17}$$

substituting the vacuum impedance

(SI) $$Z_0 = \mu_0 c_0 = \frac{1}{\varepsilon_0 c_0} = \sqrt{\frac{\mu_0}{\varepsilon_0}} \approx 119.9\pi\,\Omega\,. \tag{2.18}$$

Here, we can either scale the $\boldsymbol{E}$- or the $\boldsymbol{H}$-field. In this thesis, we do the latter and thus set

(SI) $$\boldsymbol{H}' = Z_0\boldsymbol{H}\,. \tag{2.19}$$

The only thing that remains for the wave equation is how the $\boldsymbol{E}$-field's amplitude is set:

(SI) $$\boldsymbol{E}' = \boldsymbol{E}/E_0\,. \tag{2.20}$$

For all linear material models, we are completely free to choose the scale E_0 of said amplitude. It only becomes important as soon as one deals with non-linear systems, such as the 4LS described in Section 3.5. There, we use the $\boldsymbol{E}$-fields amplitude to fix the unit of energy. For now, we only present its value. The derivation based on setting $\hbar \to 1$ is presented in Section 2.8.1. Subsequently, we use the following unit system within this thesis:

(SI)	length:	$[\boldsymbol{r}] = 1\lambda_0$	$=$	$1\,\mathrm{nm}$,	(2.21)
(SI)	time:	$[t] = 1\lambda_0 c_0^{-1}$	$\approx$	$3.335\,641 \times 10^{-3}\,\mathrm{fs}$,	(2.22)
(SI)	frequency:	$[\nu] = [t^{-1}] = 1\lambda_0^{-1} c_0$	$=$	$299\,792.458\,\mathrm{THz}$,	(2.23)
(SI)	$\boldsymbol{E}$-field:	$[\boldsymbol{E}] = 1 E_0$	$\overset{(2.99)}{\approx}$	$59.75\,\mathrm{GV\,m^{-1}}$,	(2.24)
(SI)	$\boldsymbol{H}$-field:	$[\boldsymbol{H}] = 1 E_0 Z_0^{-1}$	$\overset{(2.99)}{\approx}$	$1.586 \times 10^8\,\mathrm{A\,m^{-1}}$,	(2.25)
(SI)	$\boldsymbol{D}$-field:	$[\boldsymbol{D}] = 1\varepsilon_0 E_0$	$\overset{(2.99)}{\approx}$	$0.529\,\mathrm{A\,s\,m^{-2}}$,	(2.26)
(SI)	$\boldsymbol{B}$-field:	$[\boldsymbol{B}] = 1\mu_0 E_0 Z_0^{-1}$	$\overset{(2.99)}{\approx}$	$199.3\,\mathrm{T}$,	(2.27)
(SI)	charge density:	$[\rho_{\mathrm{f}}] = 1\varepsilon_0 E_0 \lambda_0^{-1}$	$\overset{(2.99)}{\approx}$	$5.291 \times 10^8\,\mathrm{C\,m^{-3}}$,	(2.28)
(SI)	current density:	$[\boldsymbol{j}_{\mathrm{f}}] = 1 E_0 Z_0^{-1} \lambda_0^{-1}$	$\overset{(2.99)}{\approx}$	$1.586 \times 10^{17}\,\mathrm{A\,m^{-2}}$.	(2.29)

Hereafter, all equations marked with an (SI)-tag explicitly take into account the SI unit system [85], while all the others assume the unit conventions above. From now on we do not distinguish between those quantities and drop the notation including the apostrophes. If necessary, we present the unit change for newly introduced quantities, e.g., the Poynting vector in Section 2.8.1.

2.4 Frequency domain Maxwell's equations

Since we not only solve Maxwell's equations in the time but also in the frequency domain, we have to specify the convention for the Fourier transform used in this thesis. We define

$$\boldsymbol{E}\left(\boldsymbol{r}, t\right) = \frac{1}{2\pi} \int_{-\infty}^{\infty} \boldsymbol{E}\left(\boldsymbol{r}, \omega\right) \mathrm{e}^{-\mathrm{i}\omega t}\, \mathrm{d}\omega \quad \text{and} \quad \boldsymbol{E}\left(\boldsymbol{r}, \omega\right) = \int_{-\infty}^{\infty} \boldsymbol{E}\left(\boldsymbol{r}, t\right) \mathrm{e}^{\mathrm{i}\omega t}\, \mathrm{d}t, \tag{2.30}$$

where $\omega = 2\pi\nu$ is the angular frequency. If we insert the Fourier transformed fields into Maxwell's equations, we arrive at

$$\nabla \cdot \boldsymbol{D}(\boldsymbol{r}, \omega) = \rho_{\mathrm{f}}(\boldsymbol{r}, \omega), \tag{2.31a}$$
$$\nabla \cdot \boldsymbol{B}(\boldsymbol{r}, \omega) = 0, \tag{2.31b}$$
$$\nabla \times \boldsymbol{E}(\boldsymbol{r}, \omega) = \mathrm{i}\omega \boldsymbol{B}(\boldsymbol{r}, \omega), \tag{2.31c}$$
$$\nabla \times \boldsymbol{H}(\boldsymbol{r}, \omega) = -\mathrm{i}\omega \boldsymbol{D}(\boldsymbol{r}, \omega) + \boldsymbol{j}_{\mathrm{f}}(\boldsymbol{r}, \omega). \tag{2.31d}$$

Please note, that when solving the Maxwell equations with linear material equations it suffices to only take into account positive frequencies $\omega \geq 0$, since the fields are in general real-valued, i.e.,

$$\boldsymbol{E}^*\left(\omega\right) = \boldsymbol{E}\left(-\omega\right) . \tag{2.32}$$

Furthermore, we can solve the equations for a given frequency one after the other. Due to the linearity, it is often useful to use complex-valued fields and take the real part after the computation. We do not assign a new set of letters to the complex-valued amplitudes and only specify the real part when necessary. Also notice, what happens to the time derivative operators when inserting the Fourier transformed fields: it is technically a replacement of type

$$\partial_t \overset{\text{FT}}{\longleftrightarrow} -\mathrm{i}\omega . \tag{2.33}$$

This substitution under Fourier transform is used a lot for the derivation of auxiliary differential equations (ADEs) (see Section 5.5) used for dispersive material models in the DGTD method presented in Chapter 5. The convolution for the linear material models of Eq. (2.8) turns into a simple product in frequency domain:

$$\boldsymbol{D}\left(\boldsymbol{r},\omega\right) = \underline{\underline{\boldsymbol{\epsilon}}}\left(\boldsymbol{r},\omega\right) \cdot \boldsymbol{E}\left(\boldsymbol{r},\omega\right) , \tag{2.34a}$$

$$\boldsymbol{B}\left(\boldsymbol{r},\omega\right) = \underline{\underline{\boldsymbol{\mu}}}\left(\boldsymbol{r},\omega\right) \cdot \boldsymbol{H}\left(\boldsymbol{r},\omega\right) . \tag{2.34b}$$

All the linear material models of this thesis are initially parameterized in frequency domain, so the need to transform them back into time domain arises for the DGTD method discussed in Chapter 5.

Another important fact from the frequency domain Maxwell's equations is, that from the curl-equations (2.31c) and (2.31d) and the charge conservation

$$\mathrm{i}\omega\rho_{\mathrm{f}}(\boldsymbol{r},\omega) = \nabla \cdot \boldsymbol{j}_{\mathrm{f}}(\boldsymbol{r},\omega) \tag{2.35}$$

it follows that

$$\nabla \cdot \boldsymbol{B}(\boldsymbol{r},\omega) \overset{(2.31c)}{=} \frac{\mathrm{i}}{\omega} \underbrace{\nabla \cdot \nabla \times \boldsymbol{E}(\boldsymbol{r},\omega)}_{=0} = 0 \tag{2.36}$$

$$\text{and} \quad \nabla \cdot \boldsymbol{D}(\boldsymbol{r},\omega) \overset{(2.31d)}{=} \frac{\mathrm{i}}{\omega} \underbrace{\nabla \cdot \nabla \times \boldsymbol{H}(\boldsymbol{r},\omega)}_{=0} - \frac{\mathrm{i}}{\omega}\nabla \cdot \boldsymbol{j}_{\mathrm{f}}(\boldsymbol{r},\omega) \overset{(2.35)}{=} \rho_{\mathrm{f}}(\boldsymbol{r},\omega) . \tag{2.37}$$

This means that for all frequencies $\omega \neq 0$ the divergence conditions are automatically fulfilled. Hence, for (numerically) solving Maxwell's equations in frequency domain for non-static fields, it suffices to look at the curl-equations only. At the same time, this observation transforms into the statement, that if the divergence conditions in time domain are fulfilled for an arbitrary time t_0, they are also fulfilled for any time thereafter. It is important to note that in case the charge conservation is violated, as it is slightly by construction in the electron energy loss spectroscopy (EELS) computations presented in Chapter 6, we expect static fields remaining in the system of interest for sufficiently long computation times. This can lead to potential systematic errors

(see Section 6.3.1) for low- frequency field components and derived quantities.

2.4.1 Causality

Due to the integration being constrained to positive times τ, i.e., causal behavior, in the convolution in the integrals Eqs. (2.8), it immediately follows, from the reality of the fields and response functions, that both

$$\underline{\underline{\epsilon}}(\omega) = \underline{\underline{1}} + \underline{\underline{\chi}}_{\epsilon}(\omega) \quad \text{and} \quad \underline{\underline{\mu}}(\omega) = \underline{\underline{1}} + \underline{\underline{\chi}}_{\mu}(\omega) \,, \tag{2.38}$$

are analytic functions for $\mathrm{Im}\,(\omega) > 0$ (see [81], Chapter 7). Hence, the real and imaginary parts of the permittivity and permeability can be related using Cauchy's integral formula [81] via

$$\mathrm{Re}\left(\underline{\underline{\epsilon}}(\omega)\right) = \underline{\underline{1}} + \frac{2}{\pi}\mathrm{P}\int_0^\infty \frac{\omega'\,\mathrm{Im}\left(\underline{\underline{\epsilon}}(\omega')\right)}{\omega'^2 - \omega^2}\mathrm{d}\omega' \,, \tag{2.39}$$

$$\mathrm{Im}\left(\underline{\underline{\epsilon}}(\omega)\right) = -\frac{2\omega}{\pi}\mathrm{P}\int_0^\infty \frac{\mathrm{Re}\left(\underline{\underline{\epsilon}}(\omega')\right) - \underline{\underline{1}}}{\omega'^2 - \omega^2}\mathrm{d}\omega' \,, \tag{2.40}$$

and analogous for $\underline{\underline{\mu}}$. Here $\mathrm{P}\int$ denotes Cauchy's principal value

$$\mathrm{P}\int_{-\infty}^\infty f(x)\,\mathrm{d}x := \lim_{\epsilon \to 0^+}\left[\int_{-\infty}^{x_0-\epsilon} f(x)\,\mathrm{d}x + \int_{x_0-\epsilon}^\infty f(x)\,\mathrm{d}x\right] \,, \tag{2.41}$$

if $f(x)$ has a singularity at x_0. These Kramers-Kronig relations have the consequence that for explicitly ω-dependent, i.e., dispersive permittivities $\mathrm{Re}\left(\underline{\underline{\epsilon}}\right) = \mathrm{Re}\left(\underline{\underline{\epsilon}}(\omega)\right)$, there automatically needs to be a dissipative contribution $\mathrm{Im}\left(\underline{\underline{\epsilon}}(\omega)\right) \neq \underline{\underline{0}}$. So vacuum $\underline{\underline{\epsilon}} \equiv \underline{\underline{1}}$, should be the only material for which there is no dissipative part, i.e., $\mathrm{Im}\left(\underline{\underline{\epsilon}}(\omega)\right) = \underline{\underline{0}}$. Though not causal, we also use permittivities in this thesis with real-valued and hermitian material tensors constant for all frequencies ω. This is possible as long as one is interested only in an interval of frequencies for which the dissipative term is negligible. It turns out that causality is a sufficient but not necessary criterion for the stability of the DGTD method in Chapter 5.

2.5 Field boundary conditions on interfaces

Whether we want to solve Maxwell's equations either in time or frequency domain, in both cases we have to deal with different regions of material and their interfaces. It is important to both the FMM and DGTD method to know how the fields change at such an interface and how to enforce their boundary condition. To derive the boundary conditions of the fields, one casts Maxwell's equations (2.1) into the integral form using Gauss' and Stokes' theorem (see e.g., [81,

83]). Consequently, the Maxwell equations in integral form read

$$\oint_{\partial V} \boldsymbol{D} \cdot \mathrm{d}\boldsymbol{f} = \int_V \rho_\mathrm{f} \, \mathrm{d}V \, , \tag{2.42a}$$

$$\oint_{\partial V} \boldsymbol{B} \cdot \mathrm{d}\boldsymbol{f} = 0 \, , \tag{2.42b}$$

$$\oint_{\partial A} \boldsymbol{E} \cdot \mathrm{d}\boldsymbol{r} = -\int_A \frac{\partial}{\partial t} \boldsymbol{B} \cdot \mathrm{d}\boldsymbol{f} \, , \tag{2.42c}$$

$$\oint_{\partial A} \boldsymbol{H} \cdot \mathrm{d}\boldsymbol{r} = \int_A \left[\boldsymbol{j}_\mathrm{f} + \frac{\partial}{\partial t} \boldsymbol{D} \right] \cdot \mathrm{d}\boldsymbol{f} \, . \tag{2.42d}$$

Applying Gauss's theorem for the divergence equations, we integrated over a given closed volume V containing the material interface S (see Figure 2.1). With Stokes' theorem applied on the curl equations, we integrate over a given closed surface A intersecting said interface.
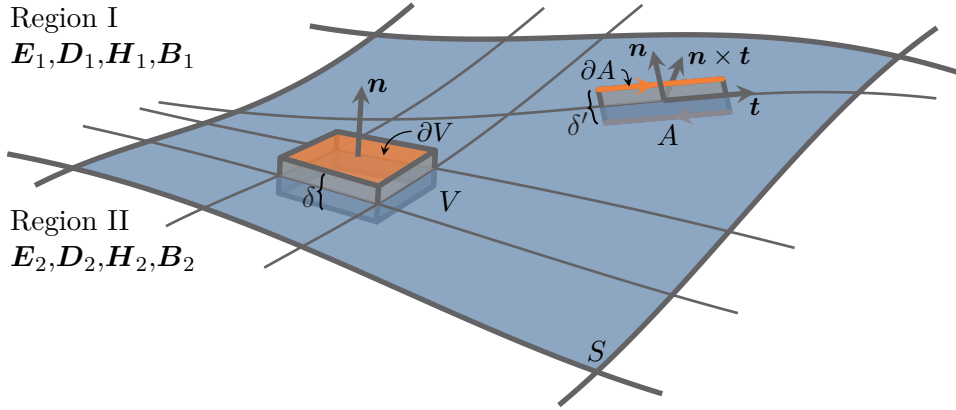
Figure 2.1: Sketch how to compute the electromagnetic field boundary conditions using a Gaussian pillbox and Stokes plane.

From the two Eqs. (2.42a) and (2.42b) we can extract the normal components of the $\boldsymbol{D}$- and $\boldsymbol{B}$-fields. We, therefore, choose the integration volume V and its surface element $\mathrm{d}\boldsymbol{f} \parallel \boldsymbol{n}$ as depicted in Fig. 2.1. Choosing the thickness $\delta \to 0$ of the Gaussian pillbox, only the two faces parallel to the interface contribute to the integral. At the same time, the volume integral over the charge density ρ vanishes, as long as the charge density is not divergent on the interface. In the latter case, this might lead to a finite surface charge density σ_surf. Hence, we find the condition for the normal components to be

$$\left(\boldsymbol{D}_1 - \boldsymbol{D}_2 \right) \cdot \boldsymbol{n} = \sigma_\mathrm{surf} \, , \tag{2.43a}$$

$$\left(\boldsymbol{B}_1 - \boldsymbol{B}_2 \right) \cdot \boldsymbol{n} = 0 \, . \tag{2.43b}$$

Following the other two Equations (2.42c) and (2.42d) we obtain the condition for the tangential field components. We, therefore, integrate along a Stokes' surface A as shown in Fig. 2.1. Using an infinitesimal thickness $\delta' \to 0$, again only the contour lines parallel, i.e., tangential to the interface, give a finite contribution. Furthermore, the surface integral over the current density only contributes for divergent current densities, which lead to a corresponding surface current

density $\boldsymbol{j}_{\mathrm{surf}}$. This only contributes if it is binormal to the surface, i.e., $\mathrm{d}\boldsymbol{f} \parallel \boldsymbol{n} \times \boldsymbol{t}$. Hence, we find

$$\left(\boldsymbol{E}_1 - \boldsymbol{E}_2\right) \cdot \boldsymbol{t} = 0\,, \tag{2.44a}$$

$$\left(\boldsymbol{H}_1 - \boldsymbol{H}_2\right) \cdot \boldsymbol{t} = \boldsymbol{j}_{\mathrm{surf}} \cdot \left(\boldsymbol{n} \times \boldsymbol{t}\right)\,, \tag{2.44b}$$

for any freely chosen vector $\boldsymbol{t}$ tangential to the interface. Although, we see different free source terms applied with the DGTD method in Chapter 5 and the potential surface currents can appear in the form of current sheets in that method (see [87]), in the remainder of this thesis we only use systems that do not contain free surface charges or currents. Hence, we summarize the field boundary conditions as follows: The divergence equations imply the continuity of normal components

$$\nabla \cdot \boldsymbol{D} = 0 \quad \Rightarrow \quad \Delta D_\perp = 0 \quad \text{and} \quad \nabla \cdot \boldsymbol{B} = 0 \quad \Rightarrow \quad \Delta B_\perp = 0\,, \tag{2.45}$$

while the curl-equations imply the continuity of the tangential field components

$$\mathrm{rot}\,\boldsymbol{E} = -\partial_t \boldsymbol{B} \quad \Rightarrow \quad \Delta E_{\parallel} = 0 \quad \text{and} \quad \nabla \cdot \boldsymbol{H} = \partial_t \boldsymbol{D} \quad \Rightarrow \quad \Delta H_{\parallel} = 0\,. \tag{2.46}$$

2.6 Symmetries and lower-dimensional systems

In this section, we show how to exploit system symmetries to simplify the solution of Maxwell's equations, as it is relevant for the hyperbolic metamaterial (HMM) and lasing system applications in Chapter 7 and Chapter 8, respectively. First, we consider two-dimensional systems in which the material configuration is assumed to be constant along one spatial dimension. In the next step, we discuss what happens, if a system of stacked material layers, i.e., constant material distributions in two spatial dimensions or an effectively one-dimensional system is considered. Especially in the latter case, one can exploit the inner symmetry of the source-free Maxwell's equations, which remain invariant under the transformation

$$\boldsymbol{E} \to \boldsymbol{H} \quad \text{and} \quad \boldsymbol{H} \to -\boldsymbol{E} \quad \text{and} \quad \underline{\underline{\boldsymbol{\epsilon}}} \to \underline{\underline{\boldsymbol{\mu}}} \quad \text{and} \quad \underline{\underline{\boldsymbol{\mu}}} \to \underline{\underline{\boldsymbol{\epsilon}}}\,. \tag{2.47}$$

2.6.1 Two-dimensional systems

In the case of an effectively two-dimensional system, both material tensors $\underline{\underline{\boldsymbol{\epsilon}}}$ and $\underline{\underline{\boldsymbol{\mu}}}$ are invariant under the change in one of the spatial coordinates. Without loss of generality, we assume this to be the coordinate varying along the y-axis. If one further assumes that also the electromagnetic fields vary slowly compared to their frequencies (and therefore also characteristic wavelengths) in the same direction, we approximate the fields as constant in this direction. This means

$$\frac{\partial}{\partial y} \boldsymbol{E}(\boldsymbol{r}, \omega) = \boldsymbol{0} \quad \text{and} \quad \frac{\partial}{\partial y} \boldsymbol{H}(\boldsymbol{r}, \omega) = \boldsymbol{0}\,. \tag{2.48}$$

Consequently, Maxwell's equations simplify to

$$\underbrace{\partial_y E_z}_{=0} - \partial_z E_y = \mathrm{i}\omega \sum_i \mu_{xi} H_i \,, \tag{2.49a}$$

$$\partial_z E_x - \partial_x E_z = \mathrm{i}\omega \sum_i \mu_{yi} H_i \,, \tag{2.49b}$$

$$\partial_x E_y - \underbrace{\partial_y E_x}_{=0} = \mathrm{i}\omega \sum_i \mu_{zi} H_i \,, \tag{2.49c}$$

$$\underbrace{\partial_y H_z}_{=0} - \partial_z H_y = -\mathrm{i}\omega \sum_i \epsilon_{xi} E_i \,, \tag{2.49d}$$

$$\partial_z H_x - \partial_x H_z = -\mathrm{i}\omega \sum_i \epsilon_{yi} E_i \,, \tag{2.49e}$$

$$\partial_x H_y - \underbrace{\partial_y H_x}_{=0} = -\mathrm{i}\omega \sum_i \epsilon_{zi} E_i \,, \tag{2.49f}$$

where we sum over $i = x, y, z$. Although, we here present the frequency domain equations the same holds for the time-domain as well. It only involves the more unpleasant convolution terms Eqs. (2.8). In the case, in which we have diagonal material tensors

$$\underline{\underline{\epsilon}} = \begin{pmatrix} \epsilon_{xx} & 0 & 0 \\ 0 & \epsilon_{yy} & 0 \\ 0 & 0 & \epsilon_{zz} \end{pmatrix} \quad \text{and} \quad \underline{\underline{\mu}} = \begin{pmatrix} \mu_{xx} & 0 & 0 \\ 0 & \mu_{yy} & 0 \\ 0 & 0 & \mu_{zz} \end{pmatrix} \,, \tag{2.50}$$

we find a decoupling of Maxwell's equations into two sets of equations with three fields each, namely

$$\text{H-polarization:} \quad E_x, H_y, E_z \,, \tag{2.51a}$$

$$\text{E-polarization:} \quad H_x, E_y, H_z \,. \tag{2.51b}$$

For this thesis, we use different nomenclature for the two sets depending on the fields' polarization (also see Section 2.7.1). The first one is named after the field component perpendicular to the x-z-coordinate plane, as listed above. For the DGTD method transverse magnetic (TM) polarization refers to the **E**-field components being in-plane and transverse electric (TE) polarization to the **H**-field components being in-plane. However, this convention changes depending on the potential experimental setup and the interpretation to what geometrical setup, which field component is tangential to. For typical scattering setups, one also finds the convention s- and p-polarization in the literature.

2.6.2 One-dimensional systems

Assuming the system has yet another spatial invariance, which without loss of generality shall lie in x-direction, also the partial derivatives in that direction vanish

$$\frac{\partial}{\partial x} \boldsymbol{E}(\boldsymbol{r}, \omega) = \boldsymbol{0} \quad \text{and} \quad \frac{\partial}{\partial x} \boldsymbol{H}(\boldsymbol{r}, \omega) = \boldsymbol{0} \,. \tag{2.52}$$

As a consequence, we arrive at the one-dimensional Maxwell's equations (in frequency domain) reading

$$0 - \partial_z E_y = \mathrm{i}\omega \sum_i \mu_{xi} H_i \,, \tag{2.53a}$$

$$\partial_z E_x - \underbrace{\partial_x E_z}_{=0} = \mathrm{i}\omega \sum_i \mu_{yi} H_i \,, \tag{2.53b}$$

$$\underbrace{\partial_x E_y}_{=0} - 0 = \mathrm{i}\omega \sum_i \mu_{zi} H_i \,, \tag{2.53c}$$

$$0 - \partial_z H_y = -\mathrm{i}\omega \sum_i \epsilon_{xi} E_i \,, \tag{2.53d}$$

$$\partial_z H_x - \underbrace{\partial_x H_z}_{=0} = -\mathrm{i}\omega \sum_i \epsilon_{yi} E_i \,, \tag{2.53e}$$

$$\underbrace{\partial_x H_y}_{=0} - 0 = -\mathrm{i}\omega \sum_i \epsilon_{zi} E_i \,. \tag{2.53f}$$

For the case of diagonal material tensors, we find that the fields' z-components for each polarization are

$$E_z = 0 \quad \text{and} \quad H_z = 0 \,. \tag{2.54}$$

2.7 Wave equations in homogeneous materials

Though the main point of this thesis is to numerically solve Maxwell's equations for the setups provided in the introduction Section 1.1, we require different basic solutions for either constructing the numerical methods (cf. FMM in Chapter 4), introducing source terms, or having analytic benchmarks to assess the methods' convergence behavior. To this end, we consider the plane wave solution of the wave-equations within homogeneous and isotropic media. The wave equation, or here Helmholtz equation (frequency domain) is obtained by double application of the curl-operator on Maxwell's equations (2.31d) and (2.31c), such that

$$\nabla \times \left[\underline{\underline{\boldsymbol{\mu}}}^{-1}(\boldsymbol{r}, \omega) \nabla \times \boldsymbol{E}(\boldsymbol{r}, \omega) \right] = \omega^2 \underline{\underline{\boldsymbol{\epsilon}}}(\boldsymbol{r}, \omega) \boldsymbol{E}(\boldsymbol{r}, \omega) \,, \tag{2.55a}$$

$$\nabla \times \left[\underline{\underline{\boldsymbol{\epsilon}}}^{-1}(\boldsymbol{r}, \omega) \nabla \times \boldsymbol{H}(\boldsymbol{r}, \omega) \right] = \omega^2 \underline{\underline{\boldsymbol{\mu}}}(\boldsymbol{r}, \omega) \boldsymbol{H}(\boldsymbol{r}, \omega) \,. \tag{2.55b}$$

With the restriction to homogeneous and isotropic media, we have

$$\underline{\boldsymbol{\epsilon}}(\boldsymbol{r},\omega) = \epsilon(\omega)\underline{\underline{\mathbf{1}}} \quad \text{and} \quad \underline{\boldsymbol{\mu}}(\boldsymbol{r},\omega) = \mu(\omega)\underline{\underline{\mathbf{1}}}\,. \tag{2.56}$$

We additionally apply the Fourier transform to the fields from real into reciprocal $\boldsymbol{k}$-space, i.e.,

$$\boldsymbol{E}(\boldsymbol{r},\omega) = \frac{1}{(2\pi)^3}\int_{\mathbb{R}^3}\mathrm{d}^3k\,\boldsymbol{E}(\boldsymbol{k},\omega)\,\mathrm{e}^{\mathrm{i}\boldsymbol{k}\cdot\boldsymbol{r}} \quad \text{and} \quad \boldsymbol{H}(\boldsymbol{r},\omega) = \frac{1}{(2\pi)^3}\int_{\mathbb{R}^3}\mathrm{d}^3k\,\boldsymbol{H}(\boldsymbol{k},\omega)\,\mathrm{e}^{\mathrm{i}\boldsymbol{k}\cdot\boldsymbol{r}}\,. \tag{2.57}$$

Since the fields are real-valued, the field amplitudes fulfill

$$\boldsymbol{E}^*\left(k_i,\omega\right) = \boldsymbol{E}\left(-k_i,\omega\right) \quad \text{and} \quad \boldsymbol{H}^*\left(k_i,\omega\right) = \boldsymbol{H}\left(-k_i,\omega\right)\,, \tag{2.58}$$

for each component k_i of the $\boldsymbol{k}$-vector. Inserting the transformed fields into the Helmholtz equation (2.55), we get

$$-\boldsymbol{k}\times\left(\boldsymbol{k}\times\boldsymbol{E}(\boldsymbol{k},\omega)\right) = \left(\boldsymbol{k}\cdot\boldsymbol{k}\right)\boldsymbol{E}(\boldsymbol{k},\omega) - \left(\boldsymbol{E}(\boldsymbol{k},\omega)\cdot\boldsymbol{k}\right)\boldsymbol{k} = \epsilon(\omega)\mu(\omega)\omega^2\boldsymbol{E}(\boldsymbol{k},\omega)\,, \tag{2.59a}$$

$$-\boldsymbol{k}\times\left(\boldsymbol{k}\times\boldsymbol{H}(\boldsymbol{k},\omega)\right) = \left(\boldsymbol{k}\cdot\boldsymbol{k}\right)\boldsymbol{H}(\boldsymbol{k},\omega) - \left(\boldsymbol{H}(\boldsymbol{k},\omega)\cdot\boldsymbol{k}\right)\boldsymbol{k} = \epsilon(\omega)\mu(\omega)\omega^2\boldsymbol{H}(\boldsymbol{k},\omega)\,. \tag{2.59b}$$

This now poses some restrictions on the plane wave solutions, i.e., field amplitude vectors and the $\boldsymbol{k}$-vector. Since the solutions should also satisfy the (here source-free) divergence equations (2.31a) and (2.31b), this leads to the conditions

$$\epsilon(\omega)\boldsymbol{k}\cdot\boldsymbol{E}(\boldsymbol{k},\omega) = \mathbf{0} \quad \text{and} \quad \mu(\omega)\boldsymbol{k}\cdot\boldsymbol{H}(\boldsymbol{k},\omega) = \mathbf{0}\,. \tag{2.60}$$

Furthermore, the curl-equations themselves must be satisfied, i.e.,

$$\boldsymbol{k}\times\boldsymbol{E}(\boldsymbol{k},\omega) = \omega\mu(\omega)\boldsymbol{H}(\boldsymbol{k},\omega)\,. \tag{2.61}$$

Hence, for each permissible $\boldsymbol{k}$-vector, there are two linear independent (complex-valued) polarizations

$$\boldsymbol{E}(\boldsymbol{r},\omega)\,||\,\boldsymbol{p}_1 \quad \text{or} \quad \boldsymbol{E}(\boldsymbol{r},\omega)\,||\,\boldsymbol{p}_2\,, \tag{2.62}$$

in which the fields can point (assuming $\epsilon(\omega)\neq 0$ and $\mu(\omega)\neq 0$). From Eqs. (2.60) it follows, that these polarization vectors are perpendicular

$$\boldsymbol{k}\cdot\boldsymbol{p}_1 = 0 \quad \text{and} \quad \boldsymbol{k}\cdot\boldsymbol{p}_2 = 0\,, \tag{2.63}$$

to the $\boldsymbol{k}$-vector and according to Eq. (2.61) also form a pairwise right-hand system

$$\boldsymbol{k}\times\boldsymbol{p}_1\propto\boldsymbol{p}_2\,, \quad \text{and thus} \quad \boldsymbol{p}_1\cdot\boldsymbol{p}_2 = 0\,. \tag{2.64}$$

The last restriction on the degrees of freedom of the plane wave solutions arises from the Eqs. (2.59), i.e., the dispersion relation fixing the amplitude

$$\left|\boldsymbol{k}\right| = \omega\sqrt{\epsilon(\omega)\mu(\omega)} = \omega\,n(\omega)\,. \tag{2.65}$$

Here $n(\omega)$ is the refractive index for the plane wave determined by the underlying material model.

As the effective dimension of the system in question is reduced (cf. the preceding Section 2.6), we find further restrictions to the plane wave solutions Eq. (2.57). For two-dimensional Maxwell's equations, we find

$$\partial_y \boldsymbol{E}(\boldsymbol{r}, \omega) = \partial_y \boldsymbol{H}(\boldsymbol{r}, \omega) = \boldsymbol{0}\,, \quad \text{such that} \quad k_y = 0\,. \tag{2.66}$$

So one of the two potential polarizations points in the y-direction. That is the reason for the E- and H-polarization nomenclature introduced before, which assumes linear polarization. In the case of one-dimensional Maxwell's equations, we also have

$$\partial_x \boldsymbol{E}(\boldsymbol{r}, \omega) = \partial_x \boldsymbol{H}(\boldsymbol{r}, \omega) = \boldsymbol{0} \quad \text{and therefore} \quad k_x = 0\,. \tag{2.67}$$

That means the polarization vectors lie in the x-y plane and the k_z-component of the wave-vector is completely fixed by the dispersion relation to be

$$k_z = \omega\, n(\omega)\,. \tag{2.68}$$

In all these cases, different polarization states for the single plane wave contributions to the fields are allowed. Besides the electric field strength $|\boldsymbol{E}|(\boldsymbol{k}, \omega)$ the polarization vectors $\boldsymbol{p}_1$ and $\boldsymbol{p}_2$ can be complex-valued and point in different directions. These polarizations are discussed in the following section.

2.7.1 Plane wave polarizations

The electric field has two potential polarization directions perpendicular to the $\boldsymbol{k}$-vector for single plane wave contributions. Assume, these two polarization vectors to point in $\boldsymbol{e}_{\boldsymbol{p}_1}$ and $\boldsymbol{e}_{\boldsymbol{p}_2}$ direction. Furthermore, we demand the vectors to form an orthonormal system, i.e.,

$$\boldsymbol{e}_{\boldsymbol{p}_i} \cdot \boldsymbol{e}_{\boldsymbol{p}_j} = \delta_{ij} \quad \text{and} \quad \boldsymbol{e}_{\boldsymbol{p}_i} \cdot \boldsymbol{e}_{\boldsymbol{k}} = 0 \quad \text{and} \quad \boldsymbol{e}_{\boldsymbol{p}_2} = \boldsymbol{e}_{\boldsymbol{k}} \times \boldsymbol{e}_{\boldsymbol{p}_1}\,. \tag{2.69}$$

Thus, we can decompose the $\boldsymbol{E}$-fields' amplitude vector into its linear polarization components

$$\boldsymbol{E}_0 = E_{01} \boldsymbol{e}_{\boldsymbol{p}_1} + E_{02} \boldsymbol{e}_{\boldsymbol{p}_2}\,. \tag{2.70}$$

Linear polarization

If both E_{01} and E_{02} have the same complex phase, we are in the case of linear polarization, i.e., the field only oscillates in a single given direction. In principle, it is also possible to rotate the polarization axis frame such that either E_{01} or E_{02} vanish identically to zero.

Elliptical polarization

In the most general case, the relative complex phase

$$\delta = \arg\left(\frac{E_{01}}{E_{02}}\right), \tag{2.71}$$

is not zero but takes a finite value. Therefore, in the most generic case, the plane wave is elliptically polarized, since the electric field

$$\boldsymbol{E}(t) = \mathrm{Re}\left(\boldsymbol{E}_0 \mathrm{e}^{-\mathrm{i}\omega t}\right), \tag{2.72}$$

scribes an ellipse in the $\boldsymbol{p}_1$-$\boldsymbol{p}_2$-plane (see Fig. 2.2), as the phase ωt evolves a whole period. While for the linear polarization only the field strength $|\boldsymbol{E}_0|$ is important, there are more characteristic quantities to specify elliptical polarization.
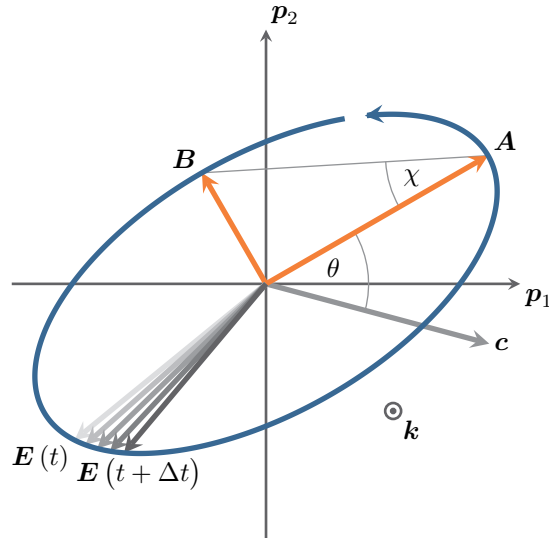
Figure 2.2: Polarization ellipse, including the main axes $\boldsymbol{A}$ and $\boldsymbol{B}$ (see Eq. (2.73)), the ellipticity angle χ and relative rotation angle θ against a given axis $\boldsymbol{c}$

One way is to characterize the elliptical polarization by the ellipse's real-valued and orthogonal main axes $\boldsymbol{A}$ and $\boldsymbol{B}$ [88, 89]. To compute these, we can decompose the complex-valued field amplitude into its real and imaginary parts $\boldsymbol{P}$ and $\boldsymbol{Q}$ and simultaneously into the main axes

$$\boldsymbol{E}_0 = \boldsymbol{P} + \mathrm{i}\boldsymbol{Q} \equiv \left(\boldsymbol{A} + \mathrm{i}\boldsymbol{B}\right)\mathrm{e}^{\mathrm{i}\epsilon}. \tag{2.73}$$

Here, ϵ is the phase shift the field has to evolve to point in the direction of the main axis $\boldsymbol{A}$ (at $t = 0$). To avoid ambiguities, we assume that, without loss of generality

$$|\boldsymbol{A}| \geq |\boldsymbol{B}| \quad \text{and} \quad \boldsymbol{A} \cdot \boldsymbol{e}_{\boldsymbol{p}_1} \geq 0. \tag{2.74}$$

We can extract the phase ϵ by multiplying

$$\boldsymbol{E}_0 \cdot \boldsymbol{E}_0 = \boldsymbol{P}^2 - \boldsymbol{Q}^2 + 2\mathrm{i}\boldsymbol{P} \cdot \boldsymbol{Q} = \left(\boldsymbol{A}^2 - \boldsymbol{B}^2\right)\mathrm{e}^{2\mathrm{i}\epsilon}\,. \tag{2.75}$$

Since all vectors $\boldsymbol{P}, \boldsymbol{Q}, \boldsymbol{A}$, and $\boldsymbol{B}$ are real-valued, we can extract the phase being

$$\epsilon = \frac{1}{2}\arg\left(\boldsymbol{P}^2 - \boldsymbol{Q}^2 + 2\mathrm{i}\boldsymbol{P}\cdot\boldsymbol{Q}\right) + n\pi \quad \text{with} \quad n \in \mathbb{Z}\,. \tag{2.76}$$

The second condition in Eq. (2.74) fixes whether n is even or odd. Furthermore, we can directly compute the main axes vectors as

$$\boldsymbol{A} = \mathrm{Re}\left(\boldsymbol{P}\mathrm{e}^{-\mathrm{i}\epsilon} + \mathrm{i}\boldsymbol{Q}\mathrm{e}^{-\mathrm{i}\epsilon}\right) \quad \text{and} \quad \boldsymbol{B} = \mathrm{Im}\left(\boldsymbol{P}\mathrm{e}^{-\mathrm{i}\epsilon} + \mathrm{i}\boldsymbol{Q}\mathrm{e}^{-\mathrm{i}\epsilon}\right)\,. \tag{2.77}$$

The two main vectors characterize the polarization state of a plane wave completely. However, often one is interested in derived quantities, such as the angle θ of the main axis $\boldsymbol{A}$ to a given axis $\boldsymbol{c}$, e.g., the direction of a polarization filter, and the ellipticity angle, i.e., the angle χ spanned from the axis $\boldsymbol{A}$ by the length of axis $\boldsymbol{B}$ (see Fig. 2.2). These angles can vary between

$$\theta = \arcsin\left[\frac{(\boldsymbol{c} \times \boldsymbol{A}) \cdot \boldsymbol{e}_k}{|\boldsymbol{c}||\boldsymbol{A}|}\right] \qquad \in \left[-\frac{\pi}{2}, \frac{\pi}{2}\right] \tag{2.78a}$$

$$\text{and} \quad \chi = \arctan\left[\frac{(\boldsymbol{A} \times \boldsymbol{B}) \cdot \boldsymbol{e}_k}{|\boldsymbol{A}|^2}\right] \qquad \in \left[-\frac{\pi}{4}, \frac{\pi}{4}\right]\,. \tag{2.78b}$$

Note that given the main axes decomposition the actual $\boldsymbol{E}$-field of the plane wave

$$\boldsymbol{E} = \mathrm{Re}\left(\left(\boldsymbol{A} + \mathrm{i}\boldsymbol{B}\right)\mathrm{e}^{\mathrm{i}(\boldsymbol{k}\cdot\boldsymbol{r}-\omega t+\epsilon)}\right)\,, \tag{2.79}$$

rotates "from $\boldsymbol{A}$ to $\boldsymbol{B}$", i.e., either to the right (clockwise) or the left (counter-clockwise). This is indicated by the arrow on the ellipse in Fig. 2.2. Here, one has to notice, that the $\boldsymbol{k}$-vector points out of plane and we are looking from a potential receiver to the source of the plane wave. For the case that $\boldsymbol{B} \equiv \boldsymbol{0}$ we are back to linear polarization 2.7.1.

Circular polarization

If the ellipticity angle equals

$$\chi = +\frac{\pi}{4} \quad \text{or} \quad \chi = -\frac{\pi}{4}\,, \tag{2.80}$$

we are in the special case of left circular polarization (LCP) or right circular polarization (RCP), respectively. In these cases, the main axis vectors are of equal length

$$|\boldsymbol{A}| = |\boldsymbol{B}| \tag{2.81}$$

and can thus be rotated arbitrarily in the e_{p_1}-e_{p_2}-frame. Also note that it is possible to write any elliptically polarized amplitude vector E_0 not only as the superposition of two linearly polarized waves, but also of two circularly counter-polarized waves, i.e.,

$$E_0^+ = c_+ \left(e_{p_1} + i e_{p_2} \right) \quad \text{and} \quad E_0^- = c_- \left(e_{p_1} - i e_{p_2} \right) . \tag{2.82}$$

If $E_0 = E_0^+ + E_0^-$, we find that

$$c_\pm = \frac{1}{2} \left(E_0 \cdot e_{p_1} \mp i E_0 \cdot e_{p_2} \right) . \tag{2.83}$$

All the presented polarization states are especially important for the characterization of the magneto-optic (MO) metasurface presented in the introductory Section 1.1 and discussed in Section 7.2.

2.8 Typical scattering quantities

For nearly all experimental setups presented in the introduction Chapter 1, the main observables are the field intensities, i.e., the time-averaged energy flux as measured within a specified detection area. In this section, we, therefore, discuss the underlying energy conservation of the electromagnetic field and introduce the derived quantities, like the scattering and absorption cross sections in Section 2.8.2, as well as transmittance, reflectance, and absorbance spectra in Section 2.8.3. These basics described here can be found in standard textbooks of electrodynamics, e.g., [81, 83].

2.8.1 Energy conservation and intensity

First, we consider the change of mechanical work per time, i.e., power, which is delivered by the field acting on charge carriers in a given volume V, e.g., a detector. The mechanical power in a given volume V, which can be deduced from the Lorentz force density, is given by

$$\frac{\mathrm{d}}{\mathrm{d}t} W_V = \int_V \mathrm{d}^3 r \, j_{\mathrm{f}}(r, t) \cdot E(r, t) . \tag{2.84}$$

Inserting Maxwell's curl-equations, one can directly deduce Poynting's theorem

$$j_{\mathrm{f}}(r, t) \cdot E(r, t) = -\frac{\partial}{\partial t} u(r, t) - \nabla \cdot S(r, t) . \tag{2.85}$$

It relates the mechanical power density $j_{\mathrm{f}} \cdot E$ and the change of the electromagnetic fields' energy density

$$\frac{\partial}{\partial t} u(r, t) = E(r, t) \cdot \frac{\partial}{\partial t} D(r, t) + H(r, t) \cdot \frac{\partial}{\partial t} B(r, t) \tag{2.86}$$

and the energy flow of the field through the boundary of the chosen volume V namely the divergence of the Poynting vector, which is

$$\boldsymbol{S}(\boldsymbol{r},t) = \boldsymbol{E}(\boldsymbol{r},t) \times \boldsymbol{H}(\boldsymbol{r},t) \,. \tag{2.87}$$

Here the term $\boldsymbol{j}_{\mathrm{f}} \cdot \boldsymbol{E}$ accounts for energy dissipating into Joule heating, or induced currents in conductive materials, i.e., movement of free charge carriers. The energy density u accounts for both the energy stored in the field as well as the dissipation of energy in the volume V, which is determined by the permittivity and permeability models and consequently the macroscopic electromagnetic fields. Lastly, the Poynting vector describes the energy flux of the field out or into the volume's boundary, as can be easily seen by applying Gauss' theorem to the energy conservation Eq. (2.85):

$$\frac{\mathrm{d}}{\mathrm{d}t}W_V = \int_V \mathrm{d}^3r \, \boldsymbol{j}_{\mathrm{f}}(\boldsymbol{r},t) \cdot \boldsymbol{E}(\boldsymbol{r},t) = -\frac{\partial}{\partial t} \int_V \mathrm{d}^3r \, u(\boldsymbol{r},t) - \int_{\partial V} \mathrm{d}\boldsymbol{f} \cdot \boldsymbol{S}(\boldsymbol{r},t) \,. \tag{2.88}$$

The following two subsections deal with typical scattering setups relevant for the experimental applications and their numerical predictions as well as convergence tests for the DGTD method implementation. For both finite-sized scatterers as well as layer structures, these setups are sketched in Figs. 2.3 and 2.4, respectively. These setups involve an electromagnetic field source that irradiates the system. These fields then scatter either on an arbitrarily shaped scatterer or a scattering layer, composed of potentially several different materials.

Here, the experimental or numerical quantity of interest is the intensity or power, which occurs on a given detection surface, i.e., a detector model. Note, that the surface chosen for the computations does not necessarily require to be the same as in the detector opening in the experiment. This is possible as long as the detector is placed in a (nearly) dissipation-free environment, e.g., vacuum or air ($\underline{\boldsymbol{\epsilon}} \approx \underline{\mathbf{1}}$). The intensity I or energy current density is defined by the time-averaged Poynting vector projected on the detection surface normal vector, i.e.,

$$I(\boldsymbol{r}) = \big\langle \boldsymbol{S}(\boldsymbol{r},t) \big\rangle_{\tau} \cdot \boldsymbol{n}_{\mathrm{f}}(\boldsymbol{r}) \,. \tag{2.89}$$

Here, the normal vector

$$\boldsymbol{n}_{\mathrm{f}} = \frac{\mathrm{d}\boldsymbol{f}}{\left|\mathrm{d}f\right|} \,, \tag{2.90}$$

is defined at a given point $\boldsymbol{r}$ of the infinitesimal detection surface element $\mathrm{d}\boldsymbol{f}$. Due to the fact that at optical frequencies detectors are not able to resolve the time dependence of the fields, we need to time-average over a time span τ much greater than the characteristic time period of the fields. Although the fields cannot be resolved in time, they can be decomposed into their frequency contributions using a spectrometer. This is the reason we only consider a single frequency ω to be detected at once. The time-averaged and frequency-dependent Poynting vector consequently reads

$$\big\langle \boldsymbol{S} \big\rangle_{\tau}(\boldsymbol{r},\omega) = \frac{1}{4} \Big\langle \Big(\boldsymbol{E}(\boldsymbol{r},\omega)\mathrm{e}^{-\mathrm{i}\omega t} + \boldsymbol{E}^*(\boldsymbol{r},\omega)\mathrm{e}^{\mathrm{i}\omega t} \Big) \times \Big(\boldsymbol{H}(\boldsymbol{r},\omega)\mathrm{e}^{-\mathrm{i}\omega t} + \boldsymbol{H}^*(\boldsymbol{r},\omega)\mathrm{e}^{\mathrm{i}\omega t} \Big) \Big\rangle_{\tau}$$

$$= \frac{1}{2}\text{Re}\left(\boldsymbol{E}(\boldsymbol{r},\omega) \times \boldsymbol{H}^*(\boldsymbol{r},\omega)\right) + \frac{1}{2}\text{Re}\left(\boldsymbol{E}(\boldsymbol{r},\omega) \times \boldsymbol{H}(\boldsymbol{r},\omega)\left\langle \text{e}^{-2\text{i}\omega t}\right\rangle_\tau\right). \tag{2.91}$$

Using the time-average with a time $\tau \gg 2\pi\omega^{-1}$ of the highly oscillatory ($\omega \neq 0$) term

$$\left\langle \text{e}^{-2\text{i}\omega t}\right\rangle_\tau \approx \lim_{\tau\to\infty}\frac{1}{\tau}\int_t^{t+\tau}\text{e}^{-2\text{i}\omega t'}\text{d}t' = \lim_{\tau\to\infty}\frac{\text{i}}{2\omega\tau}\text{e}^{-2\text{i}\omega t}\left(\text{e}^{-2\text{i}\omega\tau} - 1\right) = 0, \tag{2.92}$$

we get

$$\left\langle \boldsymbol{S}\right\rangle_\tau(\boldsymbol{r},\omega) = \frac{1}{2}\text{Re}\left(\boldsymbol{E}(\boldsymbol{r},\omega) \times \boldsymbol{H}^*(\boldsymbol{r},\omega)\right). \tag{2.93}$$

The change in total energy inside is changed by field energy flowing to a fixed volume V, e.g., the detector volume and is determined by

$$\Delta E_V \overset{(2.85)}{=} -\int_{-\infty}^{\infty}\text{d}t\int_{\partial V}\text{d}\boldsymbol{f}\cdot\boldsymbol{S}(\boldsymbol{r},t). \tag{2.94}$$

We can calculate it by spectral integration of the time-averaged Poynting vector, using

$$\Delta E_V \overset{(2.30)}{=} -\frac{1}{(2\pi)^2}\int_{-\infty}^{\infty}\text{d}\omega\int_{-\infty}^{\infty}\text{d}\omega'\int_{\partial V}\text{d}\boldsymbol{f}\cdot\left(\boldsymbol{E}(\boldsymbol{r},\omega)\times\boldsymbol{H}(\boldsymbol{r},\omega')\right)\underbrace{\int_{-\infty}^{\infty}\text{d}t\,\text{e}^{-\text{i}\omega t}\text{e}^{-\text{i}\omega' t}}_{2\pi\delta(\omega+\omega')},$$

$$= -\frac{1}{\pi}\int_0^{\infty}\text{d}\omega\int_{\partial V}\text{d}\boldsymbol{f}\cdot\text{Re}\left(\boldsymbol{E}(\boldsymbol{r},\omega)\times\boldsymbol{H}^*(\boldsymbol{r},\omega)\right),$$

$$\overset{(2.93)}{=} -\frac{2}{\pi}\int_0^{\infty}\text{d}\omega\int_{\partial V}\text{d}\boldsymbol{f}\cdot\left\langle \boldsymbol{S}\right\rangle_\tau(\boldsymbol{r},\omega). \tag{2.95}$$

This change in energy is used in Chapter 8 to compute the lasing thresholds by integration of a finite emission frequency window. For the used DGTD method, we also fix the units and scale of the fields. For both intensity and Poynting vector, we find, following the definitions made in Section 2.3, that

$$\text{(SI)} \qquad \text{intensity}: \qquad [\boldsymbol{S}] = [I] = 1\varepsilon_0 c_0 E_0^2 = E_0^2 Z_0^{-1} \qquad \overset{(2.99)}{\approx} \qquad 9.48\cdot10^{18}\text{W}\,\text{m}^{-2}. \tag{2.96}$$

At the same time, we can also set the $\boldsymbol{E}$-field amplitude fixing the unit of energy. As energies of the form $E = \hbar\omega$ appear in the 4LS material model (see Section 3.5), it is convenient to set $\hbar \to 1$. Hence, we demand that the energy is scaled as

$$\text{(SI)} \qquad\qquad E' = \frac{E}{\tilde{E}_0} \quad \text{with} \quad \tilde{E}_0 = \hbar\omega_0 \equiv \hbar c_0\lambda_0^{-1}. \tag{2.97}$$

From Eq. (2.94) it also follows that

$$\text{(SI)} \qquad\qquad \tilde{E}_0 = t_0\lambda_0^2[\boldsymbol{S}] = t_0\lambda_0^2 E_0^2 Z_0^{-1}, \tag{2.98}$$

such that the $\boldsymbol{E}$-field amplitude and energy are fixed as

$$(SI) \qquad \boldsymbol{E}\text{-field}: \qquad [\boldsymbol{E}] = 1\sqrt{\hbar Z_0} c_0 \lambda_0^{-2} \qquad \approx \qquad\qquad 59.75\,\text{GV}\,\text{m}^{-1}\,, \qquad (2.99)$$

$$(SI) \qquad \text{energy}: \qquad [E] = 1\hbar\omega_0 \qquad \approx \qquad 197.3\,\text{eV} \approx 3.162 \times 10^{-17}\,\text{J}\,. \qquad (2.100)$$

2.8.2 Scattering and absorption cross sections

We now consider a scattering setup as shown in Fig. 2.3. Here, we want to compare the power of an incident wave (package) to the power of the back-scattered electromagnetic waves and which amount of energy is absorbed by the scatterer. We therefore first perform a total field / scattered field (Tf/Sf) decomposition, in which the total field (Tf) is split into the incident field and scattered field (Sf), i.e.,

$$\boldsymbol{E}_{\text{tot}} = \boldsymbol{E}_{\text{inc}} + \boldsymbol{E}_{\text{scat}} \quad \text{and} \quad \boldsymbol{H}_{\text{tot}} = \boldsymbol{H}_{\text{inc}} + \boldsymbol{H}_{\text{scat}}\,. \qquad (2.101)$$

Then, the incident power

$$P_{\text{inc}}(\omega) = \int_{A_{\text{inc}}} I_{\text{inc}}(\boldsymbol{r}, \omega)\,\text{d}f\,, \qquad (2.102)$$

is defined by the irradiance (maximum intensity)

$$I_{\text{inc}}(\boldsymbol{r}, \omega) = \left|\langle \boldsymbol{S}_{\text{inc}}\rangle_\tau (\boldsymbol{r}, \omega)\right| = \left|\langle \boldsymbol{E}_{\text{inc}}(\boldsymbol{r}, \omega) \times \boldsymbol{H}_{\text{inc}}(\boldsymbol{r}, \omega)\rangle_\tau\right|\,, \qquad (2.103)$$

of the incident field, as recorded on the illuminated surface A_{inc}.
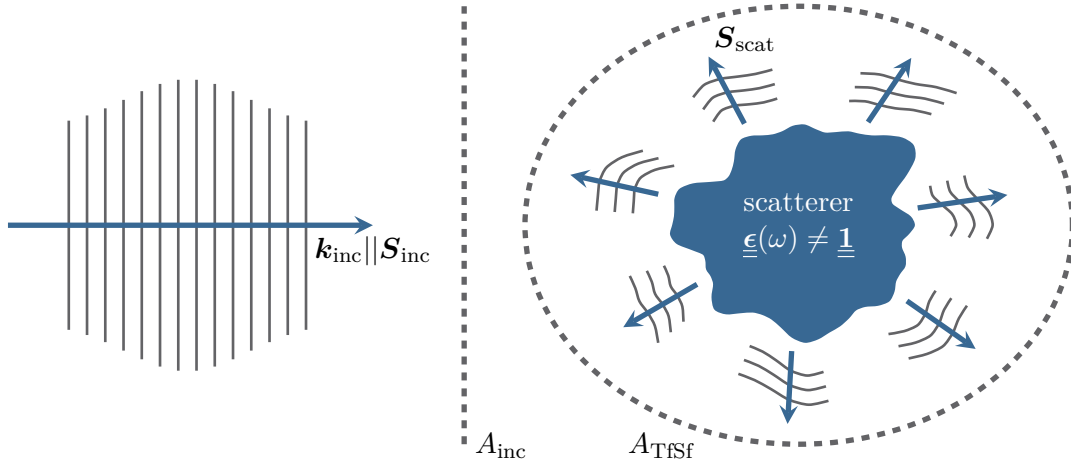
Figure 2.3: Sketch of a prototypical scattering setup containing a finite-size scatterer, used to compute the scattering and absorption cross section. An incident plane wave package passes the contours A_{inc} as well as $A_{\text{Tf/Sf}}$ and is scattered by the particle.

We then compute both the scattering cross section and the absorption cross section of the scatterer. To this end, we normalize the corresponding field power recorded on a Tf/Sf contour

$A_{\mathrm{Tf/Sf}}$ by the incident intensity. The scattering cross section is defined as

$$C_{\mathrm{scat}}(\omega) = -\frac{1}{\left|\left\langle \boldsymbol{S}_{\mathrm{inc}}\right\rangle_{\tau}(\omega)\right|} \int_{A_{\mathrm{Tf/Sf}}} \left\langle \boldsymbol{S}_{\mathrm{scat}}\right\rangle_{\tau}(\omega) \cdot \mathrm{d}\boldsymbol{f}\,, \qquad (2.104)$$

and provides an effective area measure of the scatterer's size (see e.g., [75, 90, 91]). It is determined by the induced Sf, such that $\boldsymbol{S}_{\mathrm{scat}} = \boldsymbol{E}_{\mathrm{scat}} \times \boldsymbol{H}_{\mathrm{scat}}$. The absorption cross section is consequently defined by

$$C_{\mathrm{abs}}(\omega) = \frac{1}{\left|\left\langle \boldsymbol{S}_{\mathrm{inc}}\right\rangle_{\tau}(\omega)\right|} \int_{A_{\mathrm{Tf/Sf}}} \left\langle \boldsymbol{S}_{\mathrm{tot}}\right\rangle_{\tau}(\omega) \cdot \mathrm{d}\boldsymbol{f}\,. \qquad (2.105)$$

Due to energy conservation, it accounts for the difference between incident and scattered energy. Thus, it measures the amount of energy lost in the enclosed volume of $A_{\mathrm{Tf/Sf}}$ and assigns an effective absorption area to the scatterer due to the normalization to the incidence irradiance. Assuming there are no free moving charges in said volume, the field energy is absorbed with a power loss given by

$$p_{\mathrm{loss}}(\boldsymbol{r},\omega) = \omega \boldsymbol{E}^*_{\mathrm{tot}}(\boldsymbol{r},\omega) \cdot \mathrm{Im}\left(\underline{\underline{\boldsymbol{\epsilon}}}(\boldsymbol{r},\omega)\right) \cdot \boldsymbol{E}_{\mathrm{tot}}(\boldsymbol{r},\omega)$$
$$+ \omega \boldsymbol{H}^*_{\mathrm{tot}}(\boldsymbol{r},\omega) \cdot \mathrm{Im}\left(\underline{\underline{\boldsymbol{\mu}}}(\boldsymbol{r},\omega)\right) \cdot \boldsymbol{H}_{\mathrm{tot}}(\boldsymbol{r},\omega)\,, \qquad (2.106)$$

which can be obtained from the time derivative of the energy density u (cf. Eq. (2.86)) assuming a monochromatic excitation of the scatterer. Finally, the extinction cross section is defined by

$$C_{\mathrm{ext}}(\omega) = C_{\mathrm{abs}}(\omega) + C_{\mathrm{scat}}(\omega)\,. \qquad (2.107)$$

Intuitively, the extinction cross section can be understood as the size of the scatterer in the limit of geometrical optics [91]. However, for nanophotonic scatterers, it can increase significantly on resonances, which depend on both the material and geometry of the scatterer. In this thesis, we especially use them for testing DGTD implementations and compare them to Mie calculations [91] of spherical scatterers.

2.8.3 Transmittance, reflectance and absorbance

We close with the characterization of scattering properties of a (potentially periodic) layered system of materials (see Fig. 2.4), which extend far in two (lateral) directions compared to the finite focus size of the incident light. For these structures, we compute the transmittance, reflectance, and absorbance spectra. In this thesis, we use the spectra to identify the resonances of the perforated gold films in Chapter 6, the MO metasurfaces and HMM cavities in Chapter 7 as well as the distributed Bragg reflector (DBR) cavities in Chapter 8 and compare them to the respective experimental spectra. They are defined completely analogous to the scattering coefficients in the previous section, however, the energy flux is integrated over different detection contours (see Fig. 2.4).
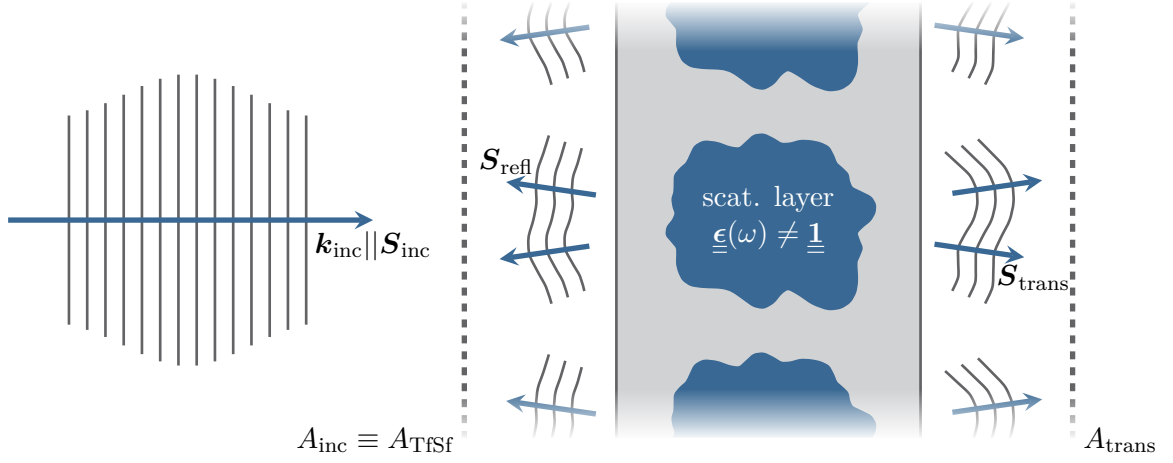
Figure 2.4: Sketch of scattering setup with a periodical material layer. The contours A_{inc} and A_{trans} suffused by the incident pulse are used to compute the transmittance and reflectance.

For the reflectance, we normalize the power of the back-scattered fields to the incident power, instead of the irradiance:

$$R(\omega) = \frac{1}{P_{\text{inc}}(\omega)} \int_{A_{\text{Tf/Sf}}} \langle \boldsymbol{S}_{\text{scat}} \rangle_\tau (\omega) \cdot \mathrm{d}\boldsymbol{f} \, . \tag{2.108}$$

In analogy, the transmittance is defined by normalizing the transmitted field to the incident power:

$$T(\omega) = \frac{1}{P_{\text{inc}}(\omega)} \int_{A_{\text{out}}} \langle \boldsymbol{S}_{\text{tot}} \rangle_\tau (\omega) \cdot \mathrm{d}\boldsymbol{f} \, . \tag{2.109}$$

By normalizing to the incident power instead of irradiance, we find a dimensionless coefficient instead of a cross section with the dimension of an area. For passive materials both the reflectance and transmittance lie between zero and one. Finally, we also define the absorbance

$$A(\omega) = \frac{1}{P_{\text{inc}}(\omega)} \int_{V_1} \mathrm{d}^3 r \, p_{\text{loss}}(\boldsymbol{r}, \omega) \, , \tag{2.110}$$

which is simply given by the energy loss in the volume V_1 enclosed by the surfaces A_{TfSf} and A_{trans}. From the energy conservation Eq. (2.85) it follows that

$$T(\omega) + R(\omega) + A(\omega) = 1 \, , \tag{2.111}$$

which can be used to compute the absorbance $A(\omega)$, given $R(\omega)$ and $T(\omega)$, without actually solving the integral Eq. (2.110).

Material models

Within this chapter, we provide a brief overview of the different (dispersive) material models used in this thesis. We present both the Lorentz model in Section 3.1 and Drude model in Section 3.2 to classically describe dielectrics and metals. This is followed by anisotropic materials. First, we present a model of magneto-optic (MO) materials in Section 3.3. Secondly, we introduce hyperbolic metamaterials (HMMs) with an example composition of alternating metal and dielectric layers. Finally, in Section 3.5 we introduce laser rate equations providing a semi-classical model for an effective four-level system (4LS) which can be used to model active materials like atoms and organic dyes [63, 64, 92, 93], quantum dots, or semiconductors [94].

The basic idea for a material model is to provide a model for the relative permittivity tensor $\underline{\underline{\epsilon}}$, which only needs a few parameters to describe the macroscopic response of a material to an external electric field $\boldsymbol{E}$. As the magnetic response is rather weak in the optical regime, we only consider materials with permeability $\underline{\underline{\boldsymbol{\mu}}} = \underline{\underline{\mathbf{1}}}$. In the following, material permittivities are introduced by a model for the microscopic response of either dielectrics or metals. Given a specific density of charge carriers n_0, i.e., electrons within the material, we can then introduce a macroscopic polarization

$$(\text{SI}) \qquad \boldsymbol{P}(\boldsymbol{r}, t) = \boldsymbol{D}(\boldsymbol{r}, t) - \epsilon_0 \boldsymbol{E}(\boldsymbol{r}, t) = n_0 \boldsymbol{p}(\boldsymbol{r}, t) \,, \qquad (3.1)$$

for a given microscopic polarization $\boldsymbol{p}$, like e.g., dipole moments for bound charges in the Lorentz model. Then the equation of motion for the microscopic polarization determines both the response and susceptibility of the macroscopic system. For metals, e.g., the Drude model, we can also introduce the polarization current

$$\boldsymbol{J}_p(\boldsymbol{r}, t) = \partial_t \boldsymbol{P} \left[\boldsymbol{E}(\boldsymbol{r}, t) \right] \,, \qquad (3.2)$$

which then couples back into Maxwell's curl equations

$$\nabla \times \boldsymbol{E}(\boldsymbol{r}, t) = -\partial_t \boldsymbol{B}(\boldsymbol{r}, t) \quad \text{and} \quad \nabla \times \boldsymbol{H}(\boldsymbol{r}, t) = \partial_t \boldsymbol{D}(\boldsymbol{r}, t) + \boldsymbol{J}_p(\boldsymbol{r}, t) + \boldsymbol{j}_{\mathrm{f}}(\boldsymbol{r}, t) \,, \qquad (3.3)$$

as additional, essentially relabeled current (see e.g., [81]).

3.1 Lorentz model

The basic idea of the Lorentz model is to describe bound charges in a material as a driven harmonic oscillator [81, 95]. The susceptibility of the Lorentz model can be derived both quantum-mechanically (see Section 3.5) as well as in the scope of classical equations of motion (see e.g.,

[96], Chapter 1). Therein, the external electric field induces fluctuations within the charge carrier density. Classically, this behavior can be modeled with a driven microscopic dipole moment $\boldsymbol{p} = p\,\boldsymbol{e_p}$, where p is the dipole strength and $\boldsymbol{e_p}$ the corresponding direction vector. As the Lorentz model describes bound oscillating charges q with mass m and resonance frequency ω_{L}, the charge displacement x is modeled by

$$(\text{SI}) \qquad \partial_t^2 x + \gamma_L \partial_t x + \omega_L^2 x = -\frac{q}{m}\boldsymbol{e_p} \cdot \boldsymbol{E}\left(\boldsymbol{r_p}, t\right). \qquad (3.4)$$

Here, the charge oscillates around the point $\boldsymbol{r_p}$, generating the microscopic dipole moment $\boldsymbol{p} = q\,x\,\boldsymbol{e_p}$. Within this driven harmonic oscillator model, the interaction with the background material is accounted for by the damping constant γ_{L} and the dipole is driven by the external $\boldsymbol{E}$-field with the electric part of the Lorentz force. Thus, in frequency domain, the dipole moment is

$$(\text{SI}) \qquad \boldsymbol{p}\left(\boldsymbol{r_p}, \omega\right) \overset{(2.33)}{=} \frac{q^2}{m}\frac{1}{\omega_L^2 - \mathrm{i}\gamma_L\omega - \omega^2}\boldsymbol{e_p}\left[\boldsymbol{e_p} \cdot \boldsymbol{E}\left(\boldsymbol{r_p}, \omega\right)\right]. \qquad (3.5)$$

Given a dipole density distribution $n_0(\boldsymbol{r_p})$, we can directly infer the polarization

$$(\text{SI}) \qquad \boldsymbol{P}(\boldsymbol{r}, \omega) = \epsilon_0 \underline{\underline{\chi}}(\omega) \cdot \boldsymbol{E}(\boldsymbol{r}, \omega) \overset{(3.1)}{=} n_0(\boldsymbol{r})\boldsymbol{p}(\boldsymbol{r}, \omega). \qquad (3.6)$$

Because of the linearity of the model, this results in an additive term to the relative permittivity tensor

$$(\text{SI}) \qquad \underline{\underline{\epsilon}}(\omega) = \underline{\underline{\epsilon}}_{\mathrm{bg}} + \underline{\underline{\chi}}(\omega) = \underline{\underline{\epsilon}}_{\mathrm{bg}} + \frac{\Delta_\epsilon \omega_{\mathrm{L}}^2}{\omega_L^2 - \mathrm{i}\gamma_L\omega - \omega^2}\boldsymbol{e_p}\boldsymbol{e_p}^{\mathrm{T}}, \qquad (3.7)$$

where

$$(\text{SI}) \qquad \Delta_\epsilon = \frac{n_0 e^2}{\epsilon_0 m_e}f_L \qquad (3.8)$$

defines the coupling strength of the dipole moments. Here, f_{L} is the corresponding oscillator strength (see e.g., [81]) of the corresponding electron ($q = -e$) transition within the material.

As a linear model, the Lorentz model is additive, such that one can account for several resonances within the material by adding several Lorentz functions to the background permittivity $\underline{\underline{\epsilon}}_{\mathrm{bg}}$. If there are no internal restrictions on allowed dipole transition directions $\boldsymbol{e_p}$, the material is isotropic and thus the induced dipole moments are aligned to the $\boldsymbol{E}$-field, i.e.,

$$\boldsymbol{e_p} || \boldsymbol{E}, \qquad (3.9)$$

such that

$$\boldsymbol{e_p}\boldsymbol{e_p}^{\mathrm{T}} = \underline{\underline{1}}, \qquad (3.10)$$

leads also to an isotropic permittivity tensor.

3.2 Drude model

Contrary to the Lorentz model the Drude model does not describe bound valence but moving conduction electrons as a free electron gas (see e.g., [81, 95]). Therefore, it is used to describe the permittivity of metals, in which the electrons can move freely on a positively charged background. This background is constituted by the positively charged, quasi-static atomic nuclei, which hardly move on the electron time scale (Born-Oppenheimer approximation [97]). Furthermore, the Drude model assumes a spatially constant electron charge density n_0. Then the response to an external $\boldsymbol{E}$-field is governed by the current density

(SI)
$$\boldsymbol{J}(\boldsymbol{r}, t) = -\frac{e}{m_e} n_0 \boldsymbol{p}_e(t) \,, \tag{3.11}$$

for which the equation of motion for the electron momentum

(SI)
$$\partial_t \boldsymbol{p}_e(t) - \gamma_{\mathrm{D}} \boldsymbol{p}_e(t) = -e\boldsymbol{E}(t) \,, \tag{3.12}$$

has to be accounted for. Here, the change in momentum is again just equal to Lorentz force and the phenomenological damping γ_{D} accounts for electron scattering with the background material. Consequently, the current density in frequency domain is

(SI)
$$\boldsymbol{J}(\omega) \overset{(2.33)}{=} -\frac{n_0 e^2}{m_e} \frac{1}{\mathrm{i}\omega - \gamma_{\mathrm{D}}} \boldsymbol{E}(\omega) = \sigma(\omega) \boldsymbol{E}(\omega) \,. \tag{3.13}$$

With the conductivity $\sigma(\omega)$, the resulting polarization current can also be attributed to the $\boldsymbol{D}$-field as

$$\boldsymbol{D}(\omega) = \underline{\underline{\boldsymbol{\epsilon}}}_{\mathrm{bg}} \cdot \boldsymbol{E}(\omega) + \frac{\mathrm{i}}{\omega} \boldsymbol{J}(\omega) = \underline{\underline{\boldsymbol{\epsilon}}}_{\mathrm{bg}} \cdot \boldsymbol{E}(\omega) + \frac{\mathrm{i}}{\omega} \sigma(\omega) \boldsymbol{E}(\omega) \,. \tag{3.14}$$

Thus, the isotropic dielectric tensor reads

$$\underline{\underline{\boldsymbol{\epsilon}}}(\omega) = \underline{\underline{\boldsymbol{\epsilon}}}_{\mathrm{bg}} + \frac{\mathrm{i}}{\omega} \sigma(\omega) \underline{\underline{\mathbf{1}}} = \underline{\underline{\boldsymbol{\epsilon}}}_{\mathrm{bg}} - \frac{\omega_{\mathrm{D}}^2}{\omega \left(\omega + \mathrm{i}\gamma_{\mathrm{D}}\right)} \underline{\underline{\mathbf{1}}} \,, \tag{3.15}$$

where $\omega_{\mathrm{D}} = \sqrt{\frac{n_0 e^2}{m_e}}$ is the plasma frequency of the metal.

3.3 Magneto-optic materials

For both preceding material models, we used only the electric part of the Lorentz force to describe the action of the external field to the material charges. While accurate modeling requires not only an external magnetic field but also a quantum mechanical derivation [29], we here merely add the magnetic interaction term [98, 99]. Hence, the equation of motion for the polarization within the (isotropic) Lorentz model changes to

$$\partial_t^2 \boldsymbol{P}(\boldsymbol{r}, t) + \gamma_L \partial_t \boldsymbol{P}(\boldsymbol{r}, t) + \omega_{\mathrm{L}}^2 \boldsymbol{P}(\boldsymbol{r}, t) \overset{(3.4)}{=} \Delta_\epsilon \omega_{\mathrm{L}}^2 \boldsymbol{E}(\boldsymbol{r}, t) + \boldsymbol{\Omega}(\boldsymbol{r}, t) \times \partial_t \boldsymbol{P}(\boldsymbol{r}, t) \,, \tag{3.16}$$

where one introduces the auxiliary field

$$\text{(SI)} \qquad \boldsymbol{\Omega}(\boldsymbol{r}, t) = \frac{e}{m_e} \boldsymbol{B}(\boldsymbol{r}, t)\,. \qquad (3.17)$$

Since the newly introduced term is a nonlinear combination of the polarization current $\boldsymbol{J_p} = \partial_t \boldsymbol{P}$ and the $\boldsymbol{B}$-field, we linearize the term (similar to [100, K6]), which yields

$$\boldsymbol{\Omega}(\boldsymbol{r}, t) \times \boldsymbol{J_p}(\boldsymbol{r}, t) \to \boldsymbol{\Omega}_0(\boldsymbol{r}) \times \boldsymbol{J_p}(\boldsymbol{r}, t) + \boldsymbol{\Omega}(\boldsymbol{r}, t) \times \boldsymbol{J_{p,0}}(\boldsymbol{r})\,. \qquad (3.18)$$

Here

$$\text{(SI)} \qquad \boldsymbol{\Omega}_0 = \frac{e}{m_e} \boldsymbol{B}_{\text{ext}}\,, \qquad (3.19)$$

where $\boldsymbol{B}_{\text{ext}}$ is a static and constant magnetic field, which for simulation purposes is accounted for as an external field. Note, that the term with constant polarization current vanishes, as the equilibrium polarization current of the unexcited system also vanishes $\boldsymbol{J_{p,0}} = \boldsymbol{0}$. The change into frequency domain gives

$$\left(\omega_{\text{L}}^2 - i\gamma_{\text{L}}\omega - \omega^2\right) \boldsymbol{P}(\boldsymbol{r}, \omega) + i\omega\boldsymbol{\Omega}_0 \times \boldsymbol{P}(\boldsymbol{r}, \omega) = \Delta_\epsilon \omega_{\text{L}}^2 \boldsymbol{E}(\boldsymbol{r}, \omega)\,. \qquad (3.20)$$

To obtain the permittivity tensor, we assume that without loss of generality $\boldsymbol{\Omega}_0 = \Omega \boldsymbol{e}_z$ and find

$$\boldsymbol{P}(\boldsymbol{r}, \omega) = \underline{\underline{\boldsymbol{\chi}}}(\omega) \cdot \boldsymbol{E}(\boldsymbol{r}, \omega) \qquad (3.21)$$

$$= \frac{\Delta_\epsilon \omega_{\text{L}}^2}{(\omega_{\text{L}}^2 - i\gamma_{\text{L}}\omega - \omega^2)^2 - \omega^2\Omega^2} \begin{pmatrix} \omega_{\text{L}}^2 - i\gamma_{\text{L}}\omega - \omega^2 & i\omega\Omega & 0 \\ -i\omega\Omega & \omega_{\text{L}}^2 - i\gamma_{\text{L}}\omega - \omega^2 & 0 \\ 0 & 0 & \frac{(\omega_{\text{L}}^2 - i\gamma_{\text{L}}\omega - \omega^2)^2 - \omega^2\Omega^2}{\omega_{\text{L}}^2 - i\gamma_{\text{L}}\omega - \omega^2} \end{pmatrix} \boldsymbol{E}(\boldsymbol{r}, \omega),$$

where Ω is the cyclotron frequency of the electrons with effective mass m_e and therefore another parameter to fit for specific experimentally realized materials. As the MO effects are typically rather weak, we can expand the susceptibility for $\Omega \ll \omega_{\text{L}}$, i.e.,

$$\underline{\underline{\boldsymbol{\chi}}}(\omega) \overset{\Omega \ll \omega_{\text{L}}}{=} \frac{\Delta_\epsilon \omega_{\text{L}}^2}{\omega_{\text{L}}^2 - i\gamma\omega - \omega^2} \begin{pmatrix} 1 & \frac{i\Omega\omega}{\omega_{\text{L}}^2 - i\gamma\omega - \omega^2} & 0 \\ -\frac{i\Omega\omega}{\omega_{\text{L}}^2 - i\gamma\omega - \omega^2} & 1 & 0 \\ 0 & 0 & 1 \end{pmatrix} + \mathcal{O}\left(\frac{\Omega^2}{\omega_{\text{L}}^2}\right)\,. \qquad (3.22)$$

Here, we recover the Lorentzian susceptibility for the diagonal elements, while the MO effect enters the off-diagonal elements, causing different refraction for light with left circular polarization (LCP) and right circular polarization (RCP). When investigating a material far from the resonance as done in Chapter 7, it is also sufficient to approximate the dielectric tensor as essentially non-dispersive for frequencies $\omega \approx \omega_0 \ll \omega_{\text{L}}$. When we also neglect the material damping

$(\gamma_{\mathrm{L}} < \Omega)$, this yields

$$\underline{\underline{\chi}}(\omega) \stackrel{\omega \ll \omega_{\mathrm{L}}}{=} \Delta_\epsilon \begin{pmatrix} 1 + \mathrm{i}\frac{\gamma_{\mathrm{L}}}{\omega_{\mathrm{L}}}\frac{\omega}{\omega_{\mathrm{L}}} & \mathrm{i}\frac{\Omega}{\omega_{\mathrm{L}}}\frac{\omega}{\omega_{\mathrm{L}}} & 0 \\ -\mathrm{i}\frac{\Omega}{\omega_{\mathrm{L}}}\frac{\omega}{\omega_{\mathrm{L}}} & 1 + \mathrm{i}\frac{\gamma_{\mathrm{L}}}{\omega_{\mathrm{L}}}\frac{\omega}{\omega_{\mathrm{L}}} & 0 \\ 0 & 0 & 1 + \mathrm{i}\frac{\gamma_{\mathrm{L}}}{\omega_{\mathrm{L}}}\frac{\omega}{\omega_{\mathrm{L}}} \end{pmatrix} + \mathcal{O}\left(\frac{\omega^2}{\omega_{\mathrm{L}}^2}\right) \stackrel{\omega \approx \omega_0}{\approx} \begin{pmatrix} \Delta_\epsilon & \mathrm{i}g & 0 \\ -\mathrm{i}g & \Delta_\epsilon & 0 \\ 0 & 0 & \Delta_\epsilon \end{pmatrix}, \tag{3.23}$$

such that the dielectric displacement $\boldsymbol{D}$ takes the form

$$\boldsymbol{D}(\boldsymbol{r}, \omega) = \epsilon_r \boldsymbol{E}(\boldsymbol{r}, \omega) + \boldsymbol{g} \times \boldsymbol{E}(\boldsymbol{r}, \omega). \tag{3.24}$$

Here, $\epsilon_r \equiv \Delta_\epsilon$ and $\boldsymbol{g} \propto \boldsymbol{B}_{\mathrm{ext}}$ is the gyration vector [29].

The same derivation can also be performed for the Drude model, such that (3.14) can be resolved for the polarization and turns into

$$(-\mathrm{i}\omega + \gamma)\boldsymbol{P}(\boldsymbol{r}, \omega) - \Omega \boldsymbol{e}_z \times \boldsymbol{P}(\boldsymbol{r}, \omega) = \mathrm{i}\frac{\omega_{\mathrm{D}}^2}{\omega}\boldsymbol{E}(\boldsymbol{r}, \omega). \tag{3.25}$$

Consequently, the susceptibility reads

$$\underline{\underline{\chi}}(\omega) = -\frac{\omega_{\mathrm{D}}^2}{\omega}\frac{1}{(\omega + \mathrm{i}\gamma_{\mathrm{D}})^2 - \Omega^2} \begin{pmatrix} \omega + \mathrm{i}\gamma_{\mathrm{D}} & -\mathrm{i}\Omega & 0 \\ \mathrm{i}\Omega & \omega + \mathrm{i}\gamma_{\mathrm{D}} & 0 \\ 0 & 0 & \frac{(\omega+\mathrm{i}\gamma_{\mathrm{D}})^2 - \Omega^2}{\omega + \mathrm{i}\gamma_{\mathrm{D}}} \end{pmatrix}, \tag{3.26}$$

which in the regime of small Ω resembles the same form as for the dielectric case Eq. (3.22), while maintaining the typical ω^{-2} dependency for metals:

$$\underline{\underline{\chi}}(\omega) \stackrel{\Omega \ll \omega_{\mathrm{D}}}{=} -\frac{\omega_{\mathrm{D}}^2}{\omega(\omega + \mathrm{i}\gamma_{\mathrm{D}})} \begin{pmatrix} 1 & -\frac{\mathrm{i}\Omega}{\omega + \mathrm{i}\gamma_{\mathrm{D}}} & 0 \\ \frac{\mathrm{i}\Omega}{\omega + \mathrm{i}\gamma_{\mathrm{D}}} & 1 & 0 \\ 0 & 0 & 1 \end{pmatrix} + \mathcal{O}\left(\frac{\Omega^2}{\omega_{\mathrm{D}}^2}\right). \tag{3.27}$$

While, this model can be well used to describe metals with strong MO effects, like Nickel [99], we use the dielectric model Eq. (3.23) to describe an all-dielectric bismuth iron garnet (BIG) [101] material here.

3.4 Hyperbolic metamaterials

In contrast to the previously described materials, metamaterials are artificially engineered sub-wavelength structured media with an unusual optical response [46, 102]. While the field of metamaterial research originated from left-handed materials with negative refraction [102–104] ($\epsilon < 0$ and $\mu < 0$), we here introduce HMMs, which provide the eponymous hyperbolic dispersion

[46, 47, 105]. Considering an effective medium relative permittivity tensor

$$\underline{\underline{\epsilon}}(\omega) = \begin{pmatrix} \epsilon_{xx}(\omega) & 0 & 0 \\ 0 & \epsilon_{yy}(\omega) & 0 \\ 0 & 0 & \epsilon_{zz}(\omega) \end{pmatrix}, \tag{3.28}$$

the dispersion relation can be obtained similarly as in Section 2.7, leading to a fourth-order equation in $\boldsymbol{k}$ (see [82], Eq. (7.10)):

$$\epsilon_{xx}\epsilon_{yy}\epsilon_{zz} + \frac{k^2}{\omega^4\mu^2}\left(\epsilon_{xx}k_x^2 + \epsilon_{yy}k_y^2 + \epsilon_{zz}k_z^2\right)$$
$$- \frac{1}{\omega^2\mu}\left(k_x^2\epsilon_{xx}\left(\epsilon_{yy} + \epsilon_{zz}\right) + k_y^2\epsilon_{yy}\left(\epsilon_{xx} + \epsilon_{zz}\right) + k_z^2\epsilon_{zz}\left(\epsilon_{xx} + \epsilon_{yy}\right)\right) = 0. \tag{3.29}$$

Given an angular frequency ω, the dispersion relation defines an isofrequency contour (IFC) in $\boldsymbol{k}$-space, which determines all allowed $\boldsymbol{k}$-vectors of a plane wave propagating through the bulk anisotropic material. In the isotropic case ($\epsilon_{xx} = \epsilon_{yy} = \epsilon_{zz} = \epsilon$) this IFC is a two-fold degenerate sphere as shown in Fig. 3.1 (a). The degeneracy arises from the two allowed polarization (cf. Section 2.7) in the isotropic material. In the case of a biaxial anisotropic material $\epsilon_{xx} < \epsilon_{yy} < \epsilon_{zz}$ this degeneracy is lifted except for four singular points in the k_x-k_z-plane [82] of the IFC (see Fig. 3.1 (b)). However, for each direction $\boldsymbol{k}$ of a traveling wave, there are still two different polarizations allowed. For a uniaxial anisotropic material, with $\epsilon_\perp := \epsilon_{xx} = \epsilon_{yy}$ orthogonal and $\epsilon_{||} := \epsilon_{zz}$ parallel to the anisotropy axis, the IFCs turn into hyperboloids, if the permittivity entries differ in sign, i.e., $\epsilon_\perp\epsilon_{||} < 0$. As the dispersion relation (3.29) simplifies to

$$\left(\boldsymbol{k}^2 - \epsilon_\perp\omega^2\right)\left(\epsilon_{||}k_z^2 + \epsilon_{\epsilon_\perp}\left(k_x^2 + k_y^2\right) - \epsilon_\perp\epsilon_{||}\omega^2\right) = 0, \tag{3.30}$$

we recover two IFCs for an HMM type I, where

$$\epsilon_\perp = \epsilon_{xx} + \epsilon_{yy} > 0 \quad \text{and} \quad \epsilon_{||} = \epsilon_{zz} < 0. \tag{3.31}$$

The first is the sphere

$$\boldsymbol{k}^2 = \epsilon_\perp(\omega)\,\omega^2, \tag{3.32}$$

from the isotropic case, in which the polarization vector is orthogonal to the anisotropy axis, i.e., $\boldsymbol{E} \perp \boldsymbol{e}_z$. For the second polarization we find a hyperbolic dispersion (see Figure 3.1 (c)) with

$$\omega^2 = \frac{k_z^2}{\epsilon_\perp(\omega)} + \frac{k_x^2 + k_y^2}{\epsilon_{||}(\omega)}. \tag{3.33}$$

However, for an HMM type II with the opposite combination of permittivity tensor entries

$$\epsilon_\perp = \epsilon_{xx} + \epsilon_{yy} < 0 \quad \text{and} \quad \epsilon_{||} = \epsilon_{zz} > 0, \tag{3.34}$$

only one propagating polarization is recovered. The corresponding IFC is shown in Fig. 3.1 (d).
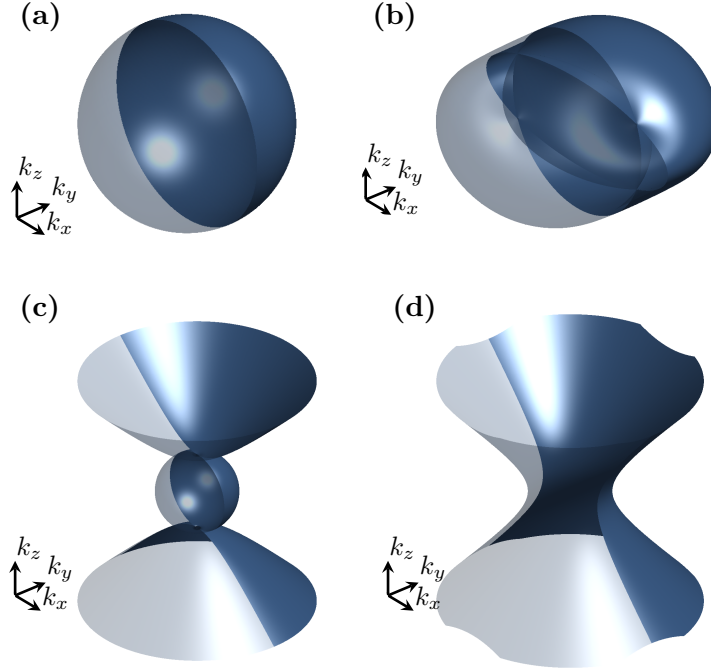
Figure 3.1: IFCs for a dispersion relation with different classes of relative diagonal anisotropic permittivity tensors $\underline{\underline{\epsilon}}$. **(a)** Isotropic case $\epsilon_{xx} = \epsilon_{yy} = \epsilon_{zz} = \epsilon$. **(b)** Biaxial anisotropy with $0 < \epsilon_{xx} < \epsilon_{yy} < \epsilon_{zz}$. **(c)** HMM type I with $\epsilon_{xx} = \epsilon_{yy} > 0$ and $\epsilon_{zz} < 0$. **(d)** HMM type II with $\epsilon_{xx} = \epsilon_{yy} < 0$ and $\epsilon_{zz} > 0$.

3.4.1 Periodically stacked metal-dielectric layers

Although there exists a wide variety of HMM realizations [46] including subwavelength-sized plasmonic nanowire arrays [106–108], we here concentrate on a simple realization of alternating metal and dielectric subwavelength-sized material layers. Therefore, we consider the dielectric layers to be modeled by a simple positive constant and the metal layers with the Drude model from Section 3.2, i.e.,

$$\epsilon_{\mathrm{d}}(\omega) = \epsilon_{\mathrm{d}} \quad \text{and} \quad \epsilon_{\mathrm{m}}(\omega) = \epsilon_{\mathrm{bg}} - \frac{\omega_{\mathrm{pl}}^2}{\omega(\omega + \mathrm{i}\gamma)}. \tag{3.35}$$

As the thickness d_{d} of the dielectric and d_{m} of the metallic layers are assumed to be much smaller than the operation (in-medium) wavelength, we can apply an effective medium approximation (EMA) [109]. Therefore, we average the fields over an entire HMM unit cell thickness $d = d_{\mathrm{d}} + d_{\mathrm{m}}$, such that the original field continuities across surfaces (see Section 2.5) are maintained for the effective (averaged) fields. We assume the material layers are stacked in z-direction. Due to the continuity of the normal component of the $\boldsymbol{D}$-field, we have

$$D_z^{(\mathrm{d})} \approx D_z^{(\mathrm{m})} \approx \langle D_z \rangle_d, \tag{3.36}$$

such that the E_z-component can be averaged as

$$\langle E_z \rangle_d(\boldsymbol{r}, \omega) = \frac{1}{d}\left[\frac{d_\mathrm{d}}{\epsilon_\mathrm{d}} D_z^{(\mathrm{d})}(\boldsymbol{r}, \omega) + \frac{d_\mathrm{m}}{\epsilon_\mathrm{m}(\omega)} D_z^{(\mathrm{m})}(\boldsymbol{r}, \omega) \right] \overset{!}{=} \frac{1}{\epsilon_{||}(\omega)} \langle D_z \rangle_d(\boldsymbol{r}, \omega). \qquad (3.37)$$

Consequently, we find a relative permittivity

$$\epsilon_{||}(\omega) = \frac{d\epsilon_\mathrm{d}\epsilon_\mathrm{m}(\omega)}{d_\mathrm{m}\epsilon_\mathrm{d} + d_\mathrm{d}\epsilon_\mathrm{m}(\omega)}. \qquad (3.38)$$

Analogously, the tangential $\boldsymbol{E}$-field components are continuous, such that

$$E_{x,y}^{(\mathrm{d})} \approx E_{x,y}^{(\mathrm{m})} \approx \langle E_{x,y} \rangle_d, \qquad (3.39)$$

and within the EMA we demand

$$\langle D_{x,y} \rangle_d(\boldsymbol{r}, \omega) = \frac{1}{d}\left[d_\mathrm{d}\epsilon_\mathrm{d} E_{x,y}^{(\mathrm{d})}(\boldsymbol{r}, \omega) + d_\mathrm{m}\epsilon_\mathrm{m}(\omega) E_{x,y}^{(\mathrm{m})}(\boldsymbol{r}, \omega) \right] \overset{!}{=} \epsilon_\perp(\omega) \langle E_{x,y} \rangle_d(\boldsymbol{r}, \omega). \qquad (3.40)$$

This defines the second entry of the EMA permittivity tensor as

$$\epsilon_\perp(\omega) = \frac{d_\mathrm{d}\epsilon_\mathrm{d} + d_\mathrm{m}\epsilon_\mathrm{m}(\omega)}{d}. \qquad (3.41)$$

Although this shows how to construct an effective anisotropic material, the actual material parameters of the constituting metal and dielectric layers determine the frequency regions, in which this effective material is hyperbolic. Therefore, we first introduce the fill factor of the HMM unit cell

$$f = \frac{d_\mathrm{d}}{d_\mathrm{d} + d_\mathrm{m}} = \frac{d_\mathrm{d}}{d} \quad \text{and} \quad 1 - f = \frac{d_\mathrm{m}}{d}, \quad \text{with} \quad f \in [0, 1], \qquad (3.42)$$

which determines the limiting cases of a pure dielectric ($f = 1$) and pure metallic ($f = 0$) material. Furthermore, we assume that the background dielectric constant for the metallic layers is the same as for the dielectric layer, i.e., $\epsilon_\mathrm{d} = \epsilon_\mathrm{bg}$. In Figure 3.2 (a-c), we show the different permittivity tensor entries for different metal damping γ as well as fill factors f. Here, we normalize both damping and frequency to the effective plasma-frequency

$$\bar{\omega}_\mathrm{pl} := \frac{\omega_\mathrm{pl}}{\sqrt{\epsilon_\mathrm{bg}}} \qquad (3.43)$$

of the Drude metal. While the $\epsilon_\perp$ permittivity smoothly varies between the two limiting cases of a pure dielectric and metallic layer, the permittivity $\epsilon_{||}$ has a pole, as the denominator in (3.38) vanishes. For non-zero damping γ, the pole is smoothed, as it shifts in the complex frequency plane. Nevertheless, the condition of different signs of the two permittivity components is met for two frequency regions. These both are determined by the pole and the change in sign inherent to the Drude model. Hence, we compute the frequencies at which $\mathrm{Re}(\epsilon_{||}(\omega))$ and $\mathrm{Re}(\varepsilon_\perp(\omega))$ change
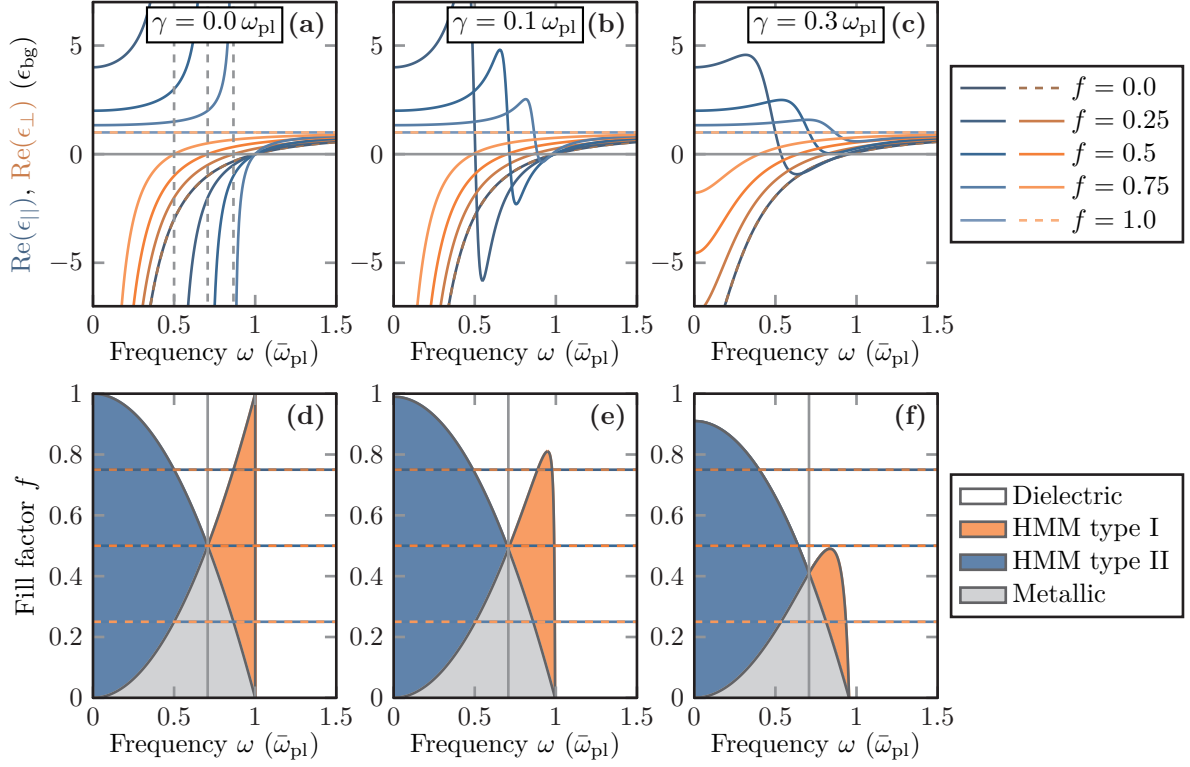
Figure 3.2: **(a-c)** Permittivities for an HMM in EMA consisting of alternating layers of a dielectric and Drude metal with effective plasma frequency $\bar{\omega}_{\text{pl}}$, damping γ, and different fill factors f of the HMM unit cell. **(a)** Poles in $\epsilon_{||}$ occur at $\omega = \sqrt{f}\,\bar{\omega}_{\text{pl}}$. **(d-f)** Fill factor and frequency map of the dispersion behavior of the resulting anisotropic material in EMA for same dampings as in the panels above. The intersection point between HMM type I and type II lies at $\omega = \frac{\bar{\omega}_{\text{pl}}}{\sqrt{2}}$ as the dielectric constant and metallic dielectric background are assumed equal ($\epsilon_{\text{d}} = \epsilon_{\text{m}}$).

signs. We find

$$\text{Re}\left(\varepsilon_{\perp}(\omega)\right) = 0 \qquad \text{at} \quad \omega_{0,\perp} = \bar{\omega}_{\text{pl}}\sqrt{F - \bar{\gamma}^2}\,, \tag{3.44a}$$

$$\text{Re}\left(\varepsilon_{||}(\omega)\right) = 0 \qquad \text{at} \quad \omega_{0,||}^{\pm} = \frac{\bar{\omega}_{\text{pl}}}{\sqrt{2}}\sqrt{1 - \bar{\gamma}^2 + F \pm \sqrt{(1 - \bar{\gamma}^2 + F)^2 + 4F}}\,, \tag{3.44b}$$

where

$$F = \frac{1}{1 + \frac{1-f}{f}\frac{\epsilon_{\text{d}}}{\epsilon_{\text{bg}}}} \quad \text{and} \quad \bar{\gamma} = \frac{\gamma}{\bar{\omega}_{\text{pl}}}\,. \tag{3.44c}$$

The corresponding frequency boundaries are shown in Fig. 3.2 (d-f) and define the different dispersion types of the EMA material model. If both $\text{Re}(\epsilon_{\perp}) > 0$ and $\text{Re}(\epsilon_{||}) > 0$ it behaves as a damped anisotropic dielectric. If the tensor components have different signs, the material is an HMM type I for high frequencies $\omega > \frac{\bar{\omega}_{\text{pl}}}{\sqrt{2}}$ and a type II HMM for frequencies below. If both

entries have negative real parts, the material shows metallic behavior. Note, that for the assumed constituting material models the interchange frequency between the type I and type II HMM is solely determined by the ratio of $\epsilon_{\mathrm{d}}/\epsilon_{\mathrm{bg}}$ given the optimally chosen fill factor f. Furthermore, with increased damping, it is also possible that the EMA only supports a type II HMM.

3.5 Four-level system for modeling of lasing materials

Despite the Lorentz model being well suited to describe a single absorption transition, we need to further extend the material model in order to describe a lasing material, which requires at least a three-level system [93]. Therefore, we follow the modeling of a 4LS suitable for time-domain methods [64]. In general, this requires a fully quantum mechanical description of the involved material. This would include both a quantized electronic structure and electromagnetic field as well as a coupling to a bath of neighboring molecules or atoms, which results in dissipative open quantum system dynamics [110]. However, we here restrict ourselves to a semiclassical model. While the electronic structure of the molecules is described quantum-mechanically, the electromagnetic field is described classically. Yet, the required spontaneous emission rates are taken from a fully quantum mechanical derivation for a two-level system (see e.g., [84, 111]). Additionally, the electronic structure of the material, which for molecules is normally described with a Jablonski diagram [112–114] and for semiconductors with the corresponding band structure, is reduced to four states $|i\rangle$, such that the electronic Hamiltonian [63, 64, 92] reads:

(SI)
$$\hat{H}_{\mathrm{el}} = \sum_{i=0}^{3} \hbar\omega_i \hat{N}_i \,, \quad \text{with} \quad \hat{N}_i = |i\rangle\langle i| \,. \tag{3.45}$$

Furthermore, we assume a radiative coupling to the electric field in dipole approximation [96, 115], such that the interaction Hamiltonian is given as

$$\hat{H}_{\mathrm{I}} = -\left(\hat{\boldsymbol{\mu}}_{03} + \hat{\boldsymbol{\mu}}_{12}\right) \cdot \boldsymbol{E}\left(\boldsymbol{r}, t\right) \,, \tag{3.46}$$

with the dipole transition operator

$$\hat{\boldsymbol{\mu}}_{ij} = \boldsymbol{\mu}_{ij} \hat{V}_{ij}^{\dagger} + \boldsymbol{\mu}_{ij}^* \hat{V}_{ij} \,, \quad \text{where} \quad \hat{V}_{ij} = |i\rangle\langle j| \,, \tag{3.47}$$

coupling the two states $|i\rangle$ and $|j\rangle$. The coupling strength is defined by the dipole transition moment

(SI)
$$\boldsymbol{\mu}_{ij} = -\langle i|e\boldsymbol{r}|j\rangle \,. \tag{3.48}$$

In this model, we restrict the radiative coupling to a pairwise coupling of the energy states, which is sketched in Figure 3.3.

To obtain the equations of motion for both the occupation numbers $\langle \hat{N}_i \rangle(t)$ and dipole transition
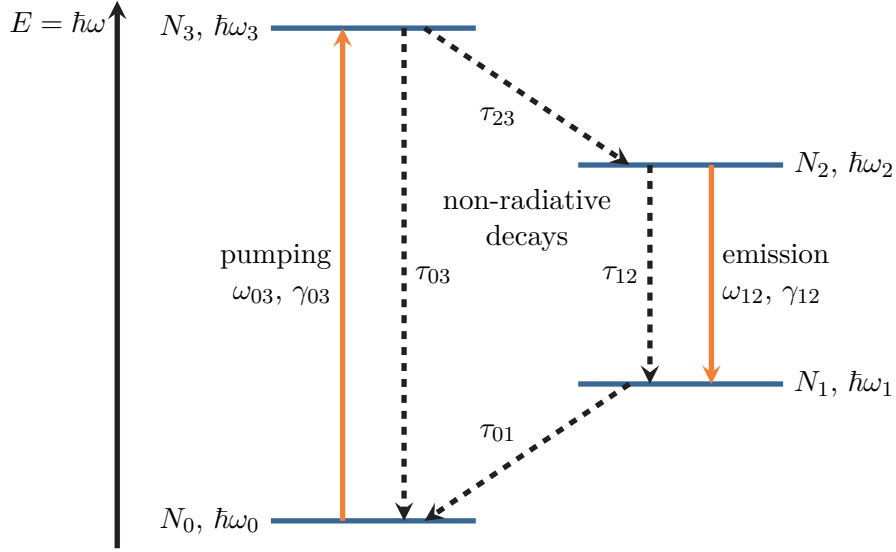
Figure 3.3: Energy level scheme of a material modeled by a 4LS. Level 0 and 1 are optically coupled to level 2 and 3, respectively, via dipole transitions with transition frequencies ω_{03}, ω_{12}, and dephasing rates γ_{03}, γ_{12}. Phenomenological non-radiative transition times τ_{ij} are introduced between particular states of the 4LS.

moments $\langle \hat{\boldsymbol{\mu}}_{ij} \rangle(t)$, we need to solve the Heisenberg equation of motion [116] for each operator $\hat{A}$:

$$\text{(SI)} \qquad \frac{\mathrm{d}}{\mathrm{d}t}\hat{A} = \frac{\mathrm{i}}{\hbar}\left[\hat{H}, \hat{A}\right]_{-}, \quad \text{with} \quad \hat{H} = \hat{H}_{\mathrm{el}} + \hat{H}_{\mathrm{I}}. \tag{3.49}$$

The involved commutators for the number operators are

$$\left[\hat{N}_i, \hat{N}_j\right]_{-} = 0 \quad \text{and} \quad \left[\hat{N}_i, \hat{V}_{jk}\right]_{-} = \delta_{ij}\hat{V}_{ik} - \delta_{ik}\hat{V}_{jk}. \tag{3.50}$$

Because of the pairwise coupling, the transition operators $\hat{V}_{ij}$ commute, i.e.,

$$\left[\hat{V}_{03}, \hat{V}_{12}\right]_{-} = \left[\hat{V}_{03}^{\dagger}, \hat{V}_{12}\right]_{-} = \left[\hat{V}_{03}, \hat{V}_{12}^{\dagger}\right]_{-} = \left[\hat{V}_{03}^{\dagger}, \hat{V}_{12}^{\dagger}\right]_{-} = 0. \tag{3.51}$$

Thus, only the commutators

$$\left[\hat{V}_{ij}, \hat{V}_{ij}^{\dagger}\right]_{-} = -\left[\hat{V}_{ij}^{\dagger}, \hat{V}_{ij}\right]_{-} = \hat{N}_i - \hat{N}_j, \tag{3.52}$$

result in a state population difference for the 0–3 and 1–2 transitions.

The equation of motion for the transition operators is

$$\text{(SI)} \qquad \frac{\mathrm{d}}{\mathrm{d}t}\hat{V}_{ij} = \frac{\mathrm{i}}{\hbar}\left[\hat{H}, \hat{V}_{ij}\right]_{-} \overset{(3.49)}{=} \mathrm{i}\sum_k \omega_k \left[\hat{N}_k, \hat{V}_{ij}\right]_{-} - \frac{\mathrm{i}}{\hbar}\boldsymbol{\mu}_{ij} \cdot \boldsymbol{E}(\boldsymbol{r}, t)\left[\hat{V}_{ij}^{\dagger}, \hat{V}_{ij}\right]_{-}. \tag{3.53}$$

Applying the commutators from before, we find

(SI) $$\frac{\mathrm{d}}{\mathrm{d}t}\hat{V}_{ij} = = \mathrm{i}\left(\omega_i - \omega_j\right)\hat{V}_{ij} - \frac{\mathrm{i}}{\hbar}\left(\hat{N}_j - \hat{N}_i\right)\boldsymbol{\mu}_{ij}\cdot\boldsymbol{E}(\boldsymbol{r},t)\,. \tag{3.54}$$

Thus the hermitian conjugate operator evolves by

(SI) $$\frac{\mathrm{d}}{\mathrm{d}t}\hat{V}_{ij}^\dagger = -\mathrm{i}\left(\omega_i - \omega_j\right)\hat{V}_{ij}^\dagger + \frac{\mathrm{i}}{\hbar}\left(\hat{N}_j - \hat{N}_i\right)\boldsymbol{\mu}_{ij}^*\cdot\boldsymbol{E}(\boldsymbol{r},t)\,. \tag{3.55}$$

Consequently, the first-order time-derivatives of the dipole operators are

$$\frac{\mathrm{d}}{\mathrm{d}t}\hat{\boldsymbol{\mu}}_{ij} = \boldsymbol{\mu}_{ij}\frac{\mathrm{d}}{\mathrm{d}t}\hat{V}_{ij}^\dagger + \boldsymbol{\mu}_{ij}^*\frac{\mathrm{d}}{\mathrm{d}t}\hat{V}_{ij} = \mathrm{i}\left(\omega_j - \omega_i\right)\left[\boldsymbol{\mu}_{ij}\hat{V}_{ij}^\dagger - \boldsymbol{\mu}_{ij}^*\hat{V}_{ij}\right] - \gamma^{(ij)}\hat{\boldsymbol{\mu}}_{ij}\,. \tag{3.56}$$

Here, we introduce an empirical dephasing with a damping constant $\gamma^{(ij)}$, which can be derived from an open quantum system master equation [110] with a coupling to one or several baths, e.g., the quantized electromagnetic field, or a coupling to surrounding molecules via phonon-interaction. As this equation does not directly map back to a function of dipole and number operators, we also consider the derivative of the resulting difference in transition operators, i.e.,

$$\frac{\mathrm{d}}{\mathrm{d}t}\left[\boldsymbol{\mu}_{ij}\hat{V}_{ij}^\dagger - \boldsymbol{\mu}_{ij}^*\hat{V}_{ij}\right] = \mathrm{i}\left(\omega_j - \omega_i\right)\underbrace{\left[\boldsymbol{\mu}_{ij}\hat{V}_{ij}^\dagger + \boldsymbol{\mu}_{ij}^*\hat{V}_{ij}\right]}_{=\hat{\boldsymbol{\mu}}_{ij}} + \frac{2\mathrm{i}}{\hbar}\left[\hat{N}_j - \hat{N}_i\right]|\boldsymbol{\mu}_{ij}|^2\boldsymbol{e}_{\boldsymbol{\mu}_{ij}}\boldsymbol{e}_{\boldsymbol{\mu}_{ij}}\cdot\boldsymbol{E}(\boldsymbol{r},t)\,, \tag{3.57}$$

where $\boldsymbol{e}_{\boldsymbol{\mu}_{ij}}$ is the direction of the transition dipole moment. When we apply the time derivative twice to the dipole operator, we obtain the equation of motion

$$\frac{\mathrm{d}^2}{\mathrm{d}t^2}\hat{\boldsymbol{\mu}}_{ij} + \gamma^{(ij)}\frac{\mathrm{d}}{\mathrm{d}t}\hat{\boldsymbol{\mu}}_{ij} + \left(\omega_j - \omega_i\right)^2\hat{\boldsymbol{\mu}}_{ij} = -\frac{2\left(\omega_j - \omega_i\right)|\boldsymbol{\mu}_{ij}|^2}{\hbar}\left[\hat{N}_j - \hat{N}_i\right]\boldsymbol{e}_{\boldsymbol{\mu}_{ij}}\boldsymbol{e}_{\boldsymbol{\mu}_{ij}}\cdot\boldsymbol{E}(\boldsymbol{r},t)\,, \tag{3.58}$$

which only depends on the dipole transition and number operators. Correspondingly, we also find that the number operators evolve as

(SI) $$\frac{\mathrm{d}}{\mathrm{d}t}\hat{N}_i = \frac{\mathrm{i}}{\hbar}\left[\hat{H},\hat{N}_i\right]_- = -\frac{\mathrm{i}}{\hbar}\sum_{k<l}\left[\boldsymbol{\mu}_{kl}\hat{V}_{kl}^\dagger + \boldsymbol{\mu}_{kl}^*\hat{V}_{kl},\hat{N}_i\right]_-\cdot\boldsymbol{E}(\boldsymbol{r},t)\,,$$

(SI) $$= \frac{\mathrm{i}}{\hbar}\sum_{k<i}\left(\boldsymbol{\mu}_{ki}\hat{V}_{ki}^\dagger - \boldsymbol{\mu}_{ki}^*\hat{V}_{ki}\right)\cdot\boldsymbol{E}(\boldsymbol{r},t) - \frac{\mathrm{i}}{\hbar}\sum_{i<k}\left(\boldsymbol{\mu}_{ik}\hat{V}_{ik}^\dagger - \boldsymbol{\mu}_{ki}^*\hat{V}_{ki}\right)\cdot\boldsymbol{E}(\boldsymbol{r},t)\,,$$

(SI) $$\overset{(3.56)}{=} \sum_{k<i}\frac{1}{\hbar\left(\omega_i - \omega_k\right)}\boldsymbol{E}(\boldsymbol{r},t)\cdot\frac{\mathrm{d}}{\mathrm{d}t}\hat{\boldsymbol{\mu}}_{ki} - \sum_{i<k}\frac{1}{\hbar\left(\omega_k - \omega_i\right)}\boldsymbol{E}(\boldsymbol{r},t)\cdot\frac{\mathrm{d}}{\mathrm{d}t}\hat{\boldsymbol{\mu}}_{ik}\,. \tag{3.59}$$

The dynamics are then described by classical fields, i.e., the operator expectations values, which are computed in a time-domain simulation. For the occupation numbers, we use

$$N_i(t) = \langle\hat{N}_i(t)\rangle \tag{3.60}$$

and introduce both the macroscopic polarization $\boldsymbol{P}_{ij}$ and microscopic polarization $\boldsymbol{p}_{ij}$:

$$\boldsymbol{P}_{ij} = N_{\text{dye}} \boldsymbol{p}_{ij} \quad \text{with} \quad \boldsymbol{p}_{ij} = \frac{1}{4\pi} \int d\Omega_{\boldsymbol{\mu}_{ij}} \langle \hat{\boldsymbol{\mu}}_{ij} \rangle . \tag{3.61}$$

Here, we not only take the expectation value for the dipole operator but also perform an angular averaging of the dipole directions, which are assumed to be isotropic for a sufficiently high densities N_{dye} of dipoles, e.g., molecules. Thus, the coupling term of the driving electric field and for the resulting microscopic polarization in Equation (3.58) turns to

$$\frac{1}{4\pi} \int d\Omega_{\boldsymbol{\mu}_{ij}} \, \boldsymbol{e}_{\boldsymbol{\mu}_{ij}} \boldsymbol{e}_{\boldsymbol{\mu}_{ij}}^{\mathrm{T}} = \frac{1}{3} \underline{\underline{\boldsymbol{1}}}, \tag{3.62}$$

which facilitates an isotropic coupling.

Consequently, we obtain a complete set of equations describing the 4LS material model: The dielectric displacement is given by

$$\boldsymbol{D}(\boldsymbol{r},t) = \epsilon_{\text{bg}}(\boldsymbol{r})\,\boldsymbol{E}(\boldsymbol{r},t) + N_{\text{dye}} \left(\boldsymbol{p}_{03}(\boldsymbol{r},t) + \boldsymbol{p}_{12}(\boldsymbol{r},t) \right) , \tag{3.63}$$

where

$$\partial_t \boldsymbol{p}_{03}(\boldsymbol{r},t) = \boldsymbol{j}_{03}(\boldsymbol{r},t) \quad \text{and} \quad \partial_t \boldsymbol{p}_{12}(\boldsymbol{r},t) = \boldsymbol{j}_{12}(\boldsymbol{r},t), \tag{3.64}$$

are the microscopic polarizations between the respective levels. The corresponding current densities

$$\partial_t \boldsymbol{j}_{03}(\boldsymbol{r},t) = -\gamma_{03}\boldsymbol{j}_{03}(\boldsymbol{r},t) + \omega_{03}^2\boldsymbol{p}_{03}(\boldsymbol{r},t) - \zeta_{03}(N_3(\boldsymbol{r},t) - N_0(\boldsymbol{r},t))\boldsymbol{E}(\boldsymbol{r},t), \tag{3.65a}$$

$$\text{and} \quad \partial_t \boldsymbol{j}_{12}(\boldsymbol{r},t) = -\gamma_{12}\boldsymbol{j}_{12}(\boldsymbol{r},t) + \omega_{12}^2\boldsymbol{p}_{12}(\boldsymbol{r},t) - \zeta_{12}(N_2(\boldsymbol{r},t) - N_1(\boldsymbol{r},t))\boldsymbol{E}(\boldsymbol{r},t), \tag{3.65b}$$

are damped harmonic oscillators with transition frequencies $\omega_{ij} := \omega_j - \omega_i$ and are driven by the $\boldsymbol{E}$-field, given the occupation differences $\Delta N_{ij} = N_j - N_i$. The level occupations follow the rate equations

$$\partial_t N_3(\boldsymbol{r},t) = -\frac{N_3(\boldsymbol{r},t)\left[1 - N_2(\boldsymbol{r},t)\right]}{\tau_{32}} - \frac{N_3(\boldsymbol{r},t)\left[1 - N_0(\boldsymbol{r},t)\right]}{\tau_{30}} + \frac{\boldsymbol{E}(\boldsymbol{r},t) \cdot \boldsymbol{j}_{03}(\boldsymbol{r},t)}{\hbar\omega_{03}}, \tag{3.66a}$$

$$\partial_t N_2(\boldsymbol{r},t) = +\frac{N_3(\boldsymbol{r},t)\left[1 - N_2(\boldsymbol{r},t)\right]}{\tau_{32}} - \frac{N_2(\boldsymbol{r},t)\left[1 - N_1(\boldsymbol{r},t)\right]}{\tau_{12}} + \frac{\boldsymbol{E}(\boldsymbol{r},t) \cdot \boldsymbol{j}_{12}(\boldsymbol{r},t)}{\hbar\omega_{12}}, \tag{3.66b}$$

$$\partial_t N_1(\boldsymbol{r},t) = +\frac{N_2(\boldsymbol{r},t)\left[1 - N_1(\boldsymbol{r},t)\right]}{\tau_{12}} - \frac{N_1(\boldsymbol{r},t)\left[1 - N_0(\boldsymbol{r},t)\right]}{\tau_{01}} - \frac{\boldsymbol{E}(\boldsymbol{r},t) \cdot \boldsymbol{j}_{12}(\boldsymbol{r},t)}{\hbar\omega_{12}}, \tag{3.66c}$$

$$\partial_t N_0(\boldsymbol{r},t) = +\frac{N_3(\boldsymbol{r},t)\left[1 - N_0(\boldsymbol{r},t)\right]}{\tau_{03}} + \frac{N_1(\boldsymbol{r},t)\left[1 - N_0(\boldsymbol{r},t)\right]}{\tau_{01}} - \frac{\boldsymbol{E}(\boldsymbol{r},t) \cdot \boldsymbol{j}_{03}(\boldsymbol{r},t)}{\hbar\omega_{03}}, \tag{3.66d}$$

and are restricted to

$$N_0, N_1, N_2, N_3 \in [0,1] . \tag{3.67}$$

Additionally, we introduce non-radiative decays between the levels, which can be realized by

coupling to a Markovian bath, e.g., phonon-coupling or spontaneous emission at much longer wavelengths than the optically active transitions. We set decay times τ_{ij} between the states shown in Figure 3.3 (see also [64]). However, we neglect the actual spontaneous emission into the electromagnetic field, as it normally occurs at much larger time scales than the lasing, i.e., the stimulated emission. Yet, the coupling constants to the electric field in Eqs. (3.65)

(SI)
$$\zeta_{ij} = \frac{1}{3} \frac{2\omega_{ij}}{\hbar} |\boldsymbol{\mu}_{ij}|^2 = \frac{1}{3} \frac{6\pi\epsilon_{\mathrm{bg}}\epsilon_0 c_0^2}{\omega_{ij}^2 \tilde{\tau}_{ij}} , \tag{3.68}$$

which includes the dipole-strength of the transition, can be expressed in terms of the spontaneous emission time $\tilde{\tau}_{ij}$ [84, 117]. Here, the factor 1/3 results from angular averaging over the dipole directions. Compared to aligned emitters, it reduces the effective coupling of the polarization in the homogeneous material to the driving electric field.

This material model enables us to simulate active optical materials, like the guest:host material with Tris(8-hydroxyquinoline)aluminum (Alq$_3$) as matrix and 4-(dicyanomethylene)-2-methyl-6-[p-(dimethylamino)-styryl]-4H-pyran (DCM) as emitter (Alq$_3$:DCM) material used for a lasing cavity in Chapter 8. There, the set of material parameters (cf. Fig. 3.3) is obtained from experimentally accessible quantities. The absorption and photoluminescence spectra can provide the dephasing rates γ_{03} and γ_{12}, the transition frequencies ω_{03} and ω_{12}, and the absorption coupling ζ_{03}. The spontaneous emission sets the radiative coupling strength ζ_{12} and the non-radiative decay times τ_{ij} in principle can be accessed by pump-probe experiments [118]. A more detailed explanation for the specific parameters is provided in Section 8.2.1.

Fourier modal method

In this chapter, we present the basic concepts of the Fourier modal method (FMM) [65, 67, 69, 119], also known as rigorous coupled-wave analysis (RCWA). This method is used to solve Maxwell's equations in the frequency domain for periodically layered systems, e.g., gratings. In Section 4.1 we present the basic assumptions of the FMM and introduce the staircase approximation used to transform any feasible setup into a layered grating system. In the following Section 4.2, we describe how to solve Maxwell's equations in a single layer using a plane-wave basis set, which leads to the use of the Fourier transform eponymous for the FMM. This is followed by the introduction of the scattering matrix (S-matrix) algorithm in Section 4.3, which couples the fields in the different layers. It provides the fields for typical scattering setups, which enables the computation of transmittance, reflectance, and absorbance spectra. We close with the computation of the S-matrix pole frequencies in Section 4.4. For a given material setup this determines the resonances [120], also known as quasinormal modes (QNMs) [121, 122] of the system.

4.1 Scattering setups and staircase approximation

The main purpose to use the FMM in this thesis is to numerically determine the resonances and scattering spectra of both the hyperbolic metamaterial (HMM) microcavities presented in Chapter 7.3 as well as the distributed Bragg reflector (DBR) lasing cavities from Chapter 8. While the first system is effectively one-dimensional with homogeneous layers in two directions, the second includes a silver stripe grating as was explained in the introduction Section 1.1.

The characterization of these systems requires solving Maxwell's equations (2.31) in the frequency domain for effectively two-dimensional systems. Therefore, the presentation of the FMM is reduced from a general and complete three-dimensional treatment, which can e.g., be found in Refs. [70, 71, 123]. We not only restrict ourselves to two-dimensional systems but also only consider diagonal anisotropic material tensors here, i.e.,

$$\underline{\underline{\epsilon}}(\omega) = \begin{pmatrix} \epsilon_{xx}(\omega) & 0 & 0 \\ 0 & \epsilon_{yy}(\omega) & 0 \\ 0 & 0 & \epsilon_{zz}(\omega) \end{pmatrix} \quad \text{and} \quad \underline{\underline{\mu}}(\omega) = \begin{pmatrix} \mu_{xx}(\omega) & 0 & 0 \\ 0 & \mu_{yy}(\omega) & 0 \\ 0 & 0 & \mu_{zz}(\omega) \end{pmatrix}. \quad (4.1)$$

Modal methods, like the FMM, are particularly well-suited to compute the fields, resonances, and scattering properties of layered structures. Throughout this thesis, we assume that the main layer direction points in z-direction.

The main idea of a modal method is to compute the electromagnetic field propagation through such a layered system. Each of the layers can be periodically patterned in the lateral direction, e.g., like the silver grating embedded in the DBR setup from Chapter 8. Within the modal method, gratings are approximated by piecewise constant material layers as shown in Fig. 4.1. This allows obtaining the field propagation in stacking direction by an expansion into single-layer modes, which propagate as plane waves through each layer and have a distinct lateral field distribution. These modes are computed using a plane-wave basis in the FMM. Finally, the fields are expanded into the specific layer's modes and matched by the field boundary conditions Eqs. (2.44) to compute the field distributions in the entire computational domain.
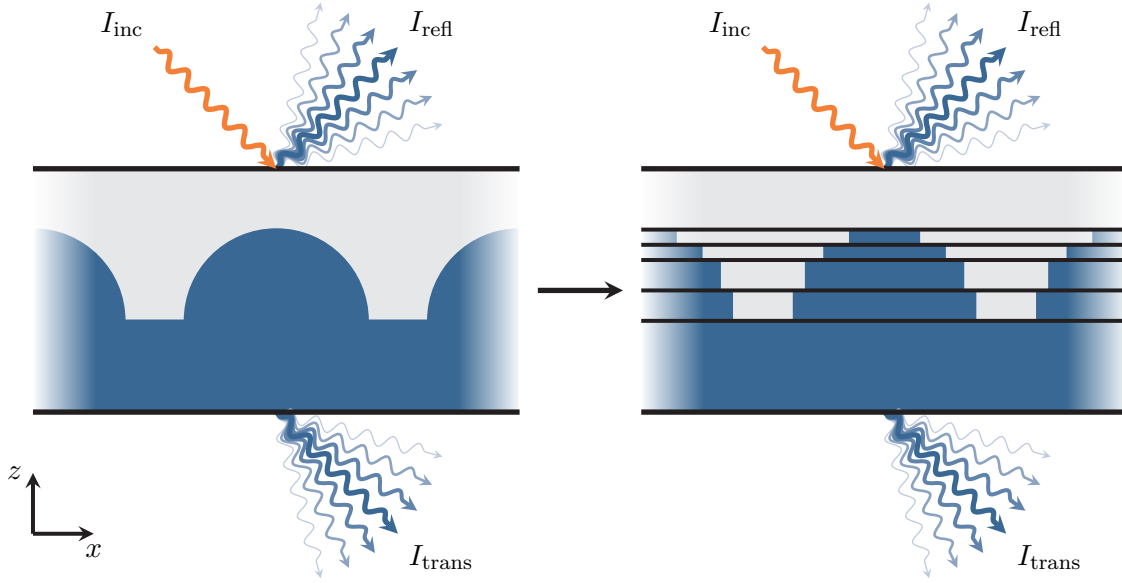
Figure 4.1: Staircase approximation of an effectively two-dimensional grating with smooth material distribution. Oblique incident light with field intensity I_{inc} is reflected (I_{refl}) and transmitted (I_{trans}) into different diffraction orders. The material distribution is approximated by homogeneous layers stacked in z-direction.

As the field propagation in stacking direction is the essential point of the modal method, we cast the two-dimensional Maxwell's equations into the form

$$-\frac{i}{\omega}\partial_z \boldsymbol{q}(x,z,\omega) = \hat{\boldsymbol{L}}(x,z,\omega) \cdot \boldsymbol{q}(x,z,\omega)\,, \tag{4.2}$$

for both transverse electric (TE) and transverse magnetic (TM) polarization. Here, the respective fields $\boldsymbol{q}$ contain only the transverse field components, i.e.,

$$\boldsymbol{q}_{\text{TE}}(x,z,\omega) = \begin{pmatrix} E_y(x,z,\omega) \\ H_x(x,z,\omega) \end{pmatrix} \quad \text{or} \quad \boldsymbol{q}_{\text{TM}}(x,z,\omega) = \begin{pmatrix} E_x(x,z,\omega) \\ H_y(x,z,\omega) \end{pmatrix}\,, \tag{4.3}$$

for the respective polarizations, into which the two-dimensional Maxwell's equations split (see

Section 2.6.1). The matrix operators are given by

$$\hat{\boldsymbol{L}}_{\mathrm{TE}}(x,z,\omega) = \begin{pmatrix} 0 & -\mu_{xx} \\ -\epsilon_{yy} - \frac{\partial_x}{\omega}\frac{1}{\mu_{zz}}\frac{\partial_x}{\omega} & 0 \end{pmatrix} \tag{4.4a}$$

$$\text{and} \quad \hat{\boldsymbol{L}}_{\mathrm{TM}}(x,z,\omega) = \begin{pmatrix} 0 & \mu_{yy} + \frac{\partial_x}{\omega}\frac{1}{\epsilon_{zz}}\frac{\partial_x}{\omega} \\ \epsilon_{xx} & 0 \end{pmatrix}, \tag{4.4b}$$

respectively, and depend on the lateral x-derivates as well as the spatially and frequency-dependent material tensors. Note, that the field components aligned to the stacking direction, i.e., the z-components are completely determined by

$$H_z(x,z,\omega) = \frac{\partial_x E_y(x,z,\omega)}{\mathrm{i}\omega\mu_{zz}(x,z,\omega)} \quad \text{and} \quad E_z(x,z,\omega) = -\frac{\partial_x H_y(x,z,\omega)}{\mathrm{i}\omega\epsilon_{zz}(x,z,\omega)}, \tag{4.5}$$

for TE and TM polarization, respectively.

The goal of the modal method is to compute the field propagation, for which Eq. (4.2) can be solved in closed-form provided an initial field distribution

$$\boldsymbol{q}_0(x,\omega) = \boldsymbol{q}(x, z=z_0, \omega), \tag{4.6}$$

by solving for the path-ordered matrix exponential [124]

$$\boldsymbol{q}(x, z=z_1, \omega) = \hat{\mathcal{P}}\exp\left[\mathrm{i}\omega\int_{z_0}^{z_1}\mathrm{d}z\,\hat{\boldsymbol{L}}(x,z,\omega)\right]\cdot\boldsymbol{q}_0(x,\omega). \tag{4.7}$$

This is highly non-trivial, especially if the underlying material tensors and therefore the matrix operator $\hat{\boldsymbol{L}}$ are explicitly z-dependent. Consequently, we decompose the problem by performing the aforementioned staircase approximation, which is sketched in Fig. 4.1. While there exist methods, which approximate the z-dependence of the matrix operator $\hat{\boldsymbol{L}}$ by polynomials using the Magnus expansion [125, 126, T1], we here use the simplest piecewise approximation. We introduce N layers, for which the permittivity and permeability are explicitly z-independent. In the l-th layer, we may then use the decomposition of the matrix operator

$$\hat{\boldsymbol{L}}^{(l)}(x,\omega) = \hat{\boldsymbol{L}}(x, z=z_l, \omega) \quad \text{for} z \in [z_l, z_{l+1} = z_l + d_l], \tag{4.8}$$

to solve the field propagation Eq. (4.2) in a single layer. Assume, we find the eigenmodes $\boldsymbol{q}_\lambda^{(l)}(x,\omega)$ of this operator, i.e.,

$$\hat{\boldsymbol{L}}^{(l)}(x,\omega)\cdot\boldsymbol{q}_\lambda^{(l)}(x,\omega) = \lambda\,\boldsymbol{q}_\lambda^{(l)}(x,\omega), \tag{4.9}$$

then the path-ordered matrix exponential Eq. (4.7) simplifies to

$$\boldsymbol{q}_\lambda^{(l)}(x, z=z_l + d_l, \omega) = \mathrm{e}^{\mathrm{i}\omega\lambda d_l}\boldsymbol{q}_\lambda^{(l)}(x, z=z_l, \omega). \tag{4.10}$$

Thus, the mode acquires a plane-wave phase when propagating through the layer of thickness d_l.

Hence, the field propagation inside a single layer can be easily described by a decomposition of the field into the modes of the respective operator $\hat{\boldsymbol{L}}^{(l)}$. In order to find such a mode decomposition, we employ a finite plane-wave basis expansion of the modes in lateral x-direction, which in detail is described in the following section.

4.2 Single layer field propagation

Since the mode propagation through a single layer of materials in the staircase approximation is simplified to a phase acquisition, we expand the fields in the l-th material layer into these modes by

$$\boldsymbol{q}^{(l)}\left(x, z, \omega\right) = \sum_{k_z} \boldsymbol{q}^{(l)}\left(x, k_z, \omega\right) e^{ik_z z}. \tag{4.11}$$

Here, every mode is characterized by the angular wavenumber

$$k_z \overset{(4.10)}{=} \omega \lambda, \tag{4.12}$$

which is directly related to the spectrum of the TE and TM propagation operators introduced in Eqs. (4.4). Due to their anti-diagonal form, the computation of the eigenmodes and -values is reduced to a single field component. Here, we choose the out-of-plane field components for both polarizations. Within the l-th layer, we recover the Helmholtz equation (2.55) for the respective polarization, i.e.,

$$\text{TE polarization:} \quad \frac{k_z^2}{\omega^2} E_y^{(l)}(x, k_z, \omega) = \underbrace{\left(\mu_{xx}^{(l)} \epsilon_{yy}^{(l)} + \mu_{xx}^{(l)} \frac{\partial_x}{\omega} \frac{1}{\mu_{zz}^{(l)}} \frac{\partial_x}{\omega} \right)}_{\hat{L}_{\text{TE}}} E_y^{(l)}(x, k_z, \omega), \tag{4.13a}$$

$$\text{TM polarization:} \quad \frac{k_z^2}{\omega^2} H_y^{(l)}(x, k_z, \omega) = \underbrace{\left(\epsilon_{xx}^{(l)} \mu_{yy}^{(l)} + \epsilon_{xx}^{(l)} \frac{\partial_x}{\omega} \frac{1}{\epsilon_{zz}^{(l)}} \frac{\partial_x}{\omega} \right)}_{\hat{L}_{\text{TM}}} H_y^{(l)}(x, k_z, \omega). \tag{4.13b}$$

The remaining field components are set by

$$\text{TE polarization:} \quad H_x^{(l)} = -\frac{k_z}{\omega \mu_{xx}^{(l)}} E_y^{(l)}, \tag{4.14a}$$

$$\text{TM polarization:} \quad E_x^{(l)} = \frac{k_z}{\omega \epsilon_{xx}^{(l)}} H_y^{(l)}. \tag{4.14b}$$

Here, the permittivity $\underline{\underline{\boldsymbol{\epsilon}}}^{(l)} = \underline{\underline{\boldsymbol{\epsilon}}}^{(l)}(x, \omega)$ and permeability $\underline{\underline{\boldsymbol{\mu}}}^{(l)} = \underline{\underline{\boldsymbol{\mu}}}^{(l)}(x, \omega)$ are explicitly x-dependent, to facilitate the modeling of gratings. Additionally, we assume the material distributions to be periodic as we want to compute the reflectance and transmittance spectra for

gratings or supercell gratings in this thesis. Due to the periodicity of the modes, the field distributions turn into Bloch periodic functions, which is shown in the following section.

4.2.1 Bloch periodic fields

The periodicity in the lateral direction of the material tensors

$$\underline{\underline{\boldsymbol{\epsilon}}}^{(l)}\left(x + x_{\mathrm{shift}}\right) = \underline{\underline{\boldsymbol{\epsilon}}}^{(l)}\left(x\right) \quad \text{and} \quad \underline{\underline{\boldsymbol{\mu}}}^{(l)}\left(x + x_{\mathrm{shift}}\right) = \underline{\underline{\boldsymbol{\mu}}}^{(l)}\left(x\right) \tag{4.15}$$

shall hold for any shift

$$x_{\mathrm{shift}} = Na \quad \text{with} \quad N \in \mathbb{Z}\,. \tag{4.16}$$

Here a is the unit cell period of the considered grating. The invariance under translation has a direct impact on the fields. Let

$$\hat{T}_{x_{\mathrm{shift}}} f(x) := f(x + x_{\mathrm{shift}}) \tag{4.17}$$

be the shift generating translation operator. Then the invariance of the material tensors implies that the layer mode propagation operator and the lateral shift operator commute, i.e.,

$$\left[\hat{\boldsymbol{L}}^{(l)}, \hat{T}_{x_{\mathrm{shift}}}\right]_{-} = 0\,. \tag{4.18}$$

Hence, both operators share a common set of eigenmodes. According to the Bloch-Floquet theorem [95, 127], the field eigenvectors are Bloch functions, i.e.,

$$\boldsymbol{q}_{\lambda}^{(l)}\left(x\right) = \mathrm{e}^{\mathrm{i}\kappa x}\boldsymbol{q}_{\kappa,\lambda}^{(l)}\left(x\right)\,, \tag{4.19}$$

where

$$\boldsymbol{q}_{\kappa,\lambda}^{(l)}\left(x + x_{\mathrm{shift}}\right) = \boldsymbol{q}_{\kappa,\lambda}^{(l)}\left(x\right) \tag{4.20}$$

is a grid-periodic function. The corresponding eigenvalues Φ_{κ} of the translation operator

$$\hat{T}_{x_{\mathrm{shift}}}\boldsymbol{q}_{\lambda}^{(l)}\left(x\right) = \mathrm{e}^{\mathrm{i}\kappa x_{\mathrm{shift}}}\boldsymbol{q}_{\lambda}^{(l)}\left(x\right) := \Phi_{\kappa}\boldsymbol{q}_{\lambda}^{(l)}\left(x\right)\,, \tag{4.21}$$

are the Bloch phases. They are characterized by the Bloch scalar κ (cf. Bloch vector in [95, 127]), which in the most general case can be a complex-valued number. This means that in general the fields inside a single layer are a linear combination of several Bloch modes. Thus, the eigenvalue problem Eq. (4.13) has to be solved for any contributing κ. In Section 4.3.1, we show that for transmittance and reflectance computations relying on the excitation of an external plane wave only a single real-valued κ has to be considered, which is directly related to the plane wave's transverse $\boldsymbol{k}$-vector component and therefore to the incident angle. The reduction to Bloch modes is a significant simplification. The eigenvalues and modes in Eq. (4.13) only need to be solved for a single unit cell of the grating. To achieve this, we expand the fields into a plane-wave basis.

4.2.2 Plane-wave basis discretization

To compute the eigenmodes within a unit cell with period a in x-direction, we expand all the fields in the reciprocal lattice using the Fourier transform, i.e.,

$$q(x) = \sum_G \tilde{q}_G \mathrm{e}^{\mathrm{i}(G+\kappa)x} = \sum_{N=-\infty}^{\infty} \tilde{q}_N T_N(x) \,. \tag{4.22}$$

Within this expansion for a general field component q,

$$T_N(x) = \mathrm{e}^{\mathrm{i}\left(\frac{2\pi}{a}N+\kappa\right)x} \,, \tag{4.23}$$

are the plane-wave expansion basis functions and $G = \frac{2\pi}{a}N$ are the points in the reciprocal lattice [95, 127]. By adding κ into the exponent the Bloch-Floquet theorem is automatically fulfilled for every basis function

$$T_N(x+a) = \mathrm{e}^{\mathrm{i}\kappa a} T_N(x) \,, \tag{4.24}$$

and therefore for the entire solution. For the actual numerical computations, we restrict ourselves to a finite number N of basis functions and only approximate the field expansion. To compute the expansion coefficients $\tilde{q}_i$, we exploit the plane waves' orthonormality with respect to the inner product

$$\frac{1}{a} \int_0^a \mathrm{d}x \, T_i^*(x) \, T_j(x) = \delta_{ij} \,. \tag{4.25}$$

The expansion coefficients are given by the inverse Fourier transform

$$\tilde{q}_i = \tilde{q}(k_i) = \frac{1}{a} \int_0^a \mathrm{d}x \, q(x) \, T_i^*(x) \,. \tag{4.26}$$

With the numerical implementation of the modal method, we restrict the basis size to a finite number of plane waves and perform the underlying Fourier transform with help of the fast Fourier transform (FFT) [128, 129]. For this, we sample the unit cell $[0, a]$ with an equidistant grid

$$x_k = \Delta_x \, k \quad \text{with} \quad \Delta_x = \frac{a}{N_{\mathrm{FFT}}} \quad \text{and} \quad k \in \left[1, N_{\mathrm{FFT}}\right] \tag{4.27}$$

with N_{FFT} grid points. The field coefficients are then approximated by a finite sum

$$\tilde{q}_i = \frac{1}{a} \int_0^a \mathrm{d}x \, q(x) \, T_i^*(x) \approx \frac{1}{N_{\mathrm{FFT}}} \sum_{k=1}^{N_{\mathrm{FFT}}} q(x_k) \mathrm{e}^{\mathrm{i}\frac{2\pi}{N_{\mathrm{FFT}}} ik} \,. \tag{4.28}$$

According to the sampling theorem [130, 131] the approximation of the Fourier coefficients in the discrete FFT is sufficiently good, as long as the full Fourier transformation of the field $q(x)$ is bandwidth limited. This means that all frequency components beyond the Nyquist frequency

should vanish, i.e.,

$$\tilde{q}\left(k_i\right) = 0\,, \quad \forall \left|k_i\right| > \frac{1}{2\Delta_x}\,. \tag{4.29}$$

Correspondingly, only the N_{FFT} smallest frequency components $\tilde{q}_i$ are computed in the discrete Fourier transform in Eq. (4.28).

Here, a potential problem arises, if the eigenmodes contain a discontinuity in either the field or its spatial derivative. These discontinuities occur at material interfaces in the x-direction lying within a unit cell due to the continuity conditions of the normal $\boldsymbol{D}$- and $\boldsymbol{B}$-field components, as introduced in Eqs. (2.43). In this case, the field is not bandwidth limited, which leads to field oscillations due to the Gibbs phenomenon [132]. In order to avoid such oscillations, the number N_{FFT} of Fourier components has to be increased significantly. Although this problem can be circumvented by using a different piecewise basis set, e.g., piecewise polynomials with a B-spline basis [80, 133, 134, T2], the coupling of the modes at the single-layer interfaces (cf. Section 4.3) becomes more challenging in that case. As we use the FFT for the discrete Fourier transform in Eq. (4.28), the numerical effort increases not quadratically with $\mathcal{O}\left(N_{\text{FFT}}^2\right)$ but with $\mathcal{O}\left(N_{\text{FFT}}\log_2 N_{\text{FFT}}\right)$ (see [129]). This reduction in computational effort and a simplified implementation of the method leads us to resort to the FMM, instead of relying on a different set of basis functions. Despite the larger basis sets a sufficient numerical accuracy can be achieved by computing all the modes, as long as a high enough number of Fourier components is used.

To numerically determine both the eigenmodes and eigenvalues defined by Eq. (4.13), we need to discretize the underlying differential operator $\hat{L}$ for the respective polarization. Given these eigenvalue equations of the form

$$\lambda^2 q_{\kappa,\lambda}^{(l)}(x,\omega) = \frac{k_z^2}{\omega^2} q_{\kappa,\lambda}^{(l)}(x,\omega) = \hat{L}_{\text{TE/ TM}}\, q_{\kappa,\lambda}^{(l)}(x,\omega)\,, \tag{4.30}$$

we insert the plane-wave expansion of the modes according to Eq. (4.22). If we furthermore project the mode expansion onto the same basis function set of plane waves, i.e., we perform a Galerkin choice, we obtain algebraic eigenvalue equations for the field expansion coefficients $\tilde{q}_i$, which read

$$\lambda^2 \sum_i \underbrace{\frac{1}{a}\int_0^a \mathrm{d}x\, T_j^*(x)\, T_i(x)}_{\delta_{ij}} \tilde{q}_i = \sum_i \underbrace{\frac{1}{a}\int_0^a \mathrm{d}x\, T_j^*(x)\, \hat{L}_{\text{TE/ TM}}\, T_i(x)}_{\hat{\mathbf{L}}_{ij}^{(\text{TE/ TM})}} \tilde{q}_i\,, \tag{4.31a}$$

$$\lambda^2 \tilde{\boldsymbol{q}} = \hat{\mathbf{L}}^{(\text{TE/ TM})} \cdot \tilde{\boldsymbol{q}}\,. \tag{4.31b}$$

In order to numerically compute the eigenvalues λ, i.e., the propagation constants k_z as well as the Fourier coefficients determining the associated eigenmodes, we need to determine the matrix elements

$$\hat{\mathbf{L}}_{ij}^{(\text{TE/ TM})} = \int_0^a \mathrm{d}x\, T_j^*(x)\, \hat{L}_{\text{TE/ TM}}\, T_i(x)\,. \tag{4.32}$$

As the underlying operators $\hat{L}_{\text{TE/TM}}$ contain scalar functions as well as derivatives in the coordinate x, we can exploit the completeness relation of the plane-wave basis functions to simplify the matrix element computation.

Assume, we want to compute the matrix elements

$$\hat{\mathbf{A}}_{ij} = \frac{1}{a} \int_0^a \mathrm{d}x \, T_i^*(x) \, \hat{A} \, T_j(x) \,, \tag{4.33}$$

of an operator

$$\hat{A} = \hat{B} \, \hat{C} \,, \tag{4.34}$$

which splits into (at least) two single operators $\hat{B}$ and $\hat{C}$. As the full plane-wave basis fulfills the completeness relation (see e.g., [83])

$$\delta(x) = \frac{1}{a} \sum_{n=-\infty}^{\infty} \mathrm{e}^{\mathrm{i}k_n x} = \frac{1}{a} \sum_{n=-\infty}^{\infty} T_n(x) \, \mathrm{e}^{-\mathrm{i}\kappa x} \quad \text{with} \quad k_n = \frac{2\pi}{a} n \,, \tag{4.35}$$

we can split the computation of the elements of matrix $\hat{\mathbf{A}}$ into that of single matrices $\hat{\mathbf{B}}$ and $\hat{\mathbf{C}}$. We insert the completeness relation from Eq. (4.35) and obtain

$$
\begin{aligned}
\hat{\mathbf{A}}_{ij} &= \frac{1}{a} \int_0^a \mathrm{d}x \, T_i^*(x) \hat{B} \, \hat{C} \, T_j(x) \,, \\
&= \frac{1}{a} \int_0^a \mathrm{d}x \, T_i^*(x) \hat{B}_x \int_0^a \delta\left(x - x'\right) \mathrm{e}^{\mathrm{i}\kappa(x-x')} \hat{C}_{x'} T_j(x) \,, \\
&= \sum_{n=-\infty}^{\infty} \hat{\mathbf{B}}_{in} \hat{\mathbf{C}}_{nj} = \left(\hat{\mathbf{B}} \cdot \hat{\mathbf{C}}\right)_{ij} \,.
\end{aligned} \tag{4.36}
$$

Thus, the operator product in Eq. (4.34) induces the matrix product

$$\hat{\mathbf{A}} = \hat{\mathbf{B}} \cdot \hat{\mathbf{C}} \,, \tag{4.37}$$

for the chosen basis. With this operator splitting, we can compute the entire operator matrix $\hat{L}_{\text{TE/TM}}$ of the eigenvalue problem Eq. (4.32) by the computation of only two generic types of operators.

The first type of operators are scalar functions. For the matrix elements of a scalar kernel $\epsilon(x)$, e.g., the permittivity entries in Eq. (4.13), we find that

$$\hat{\mathbf{E}}_{ij} = \frac{1}{a} \int_0^a \mathrm{d}x \, T_n^*(x) \, \epsilon(x) \, T_j(x) = \frac{1}{a} \int_0^a \mathrm{d}x \, \epsilon(x) \, \mathrm{e}^{\mathrm{i}\frac{2\pi}{a}(j-i)x} = \hat{\mathbf{E}}_{i-j} \,. \tag{4.38}$$

Here, we obtain a Toeplitz matrix [129] of the corresponding Fourier transformed function, like the permittivity $\epsilon(x)$ supposed here. In cases in which two scalar functions with canceling discontinuities shall be multiplied, there is a sophisticated method to Fourier transform the inverted function and then additionally multiply it with the inverse Toeplitz matrix. These

Fourier factorization rules [71, 135] can avoid convergence problems arising from the Gibbs phenomenon and are used in the FMM implementation of this thesis.

The second type of operators are the spatial derivatives. For these, the matrix in Fourier space is diagonal, i.e.,

$$\hat{\mathbf{K}}_{ij} = \frac{1}{a} \int_0^a \mathrm{d}x \, T_n^*(x) \, \partial_x \, T_j(x) = \frac{1}{a} \int_0^a \mathrm{d}x \, \left(k_j + \kappa \right) \, \mathrm{e}^{\mathrm{i}\frac{2\pi}{a}(j-i)x} = \left(k_j + \kappa \right) \delta_{ij} \, . \tag{4.39}$$

With these matrices, we compute the mode propagation matrices and spectral decomposition

$$\hat{\mathbf{L}}^{(\mathrm{TE})} = \hat{\hat{\boldsymbol{e}}}_y \cdot \hat{\boldsymbol{\lambda}}^2 \cdot \hat{\hat{\boldsymbol{e}}}_y^{-1} \quad \text{and} \quad \hat{\mathbf{L}}^{(\mathrm{TM})} = \hat{\hat{\boldsymbol{h}}}_y \cdot \hat{\boldsymbol{\lambda}}^2 \cdot \hat{\hat{\boldsymbol{h}}}_y^{-1} \, . \tag{4.40}$$

Here, the matrices $\hat{\hat{\boldsymbol{e}}}_y$ and $\hat{\hat{\boldsymbol{h}}}_y$ contain the respective eigenvectors of Fourier coefficients, which define the modes. The modes then propagate with

$$k_z^{\pm} = \pm \omega \lambda \, , \tag{4.41}$$

in two opposite directions. Consequently, we obtain $2N_{\mathrm{FFT}}$ modes from the $N_{\mathrm{FFT}} \times N_{\mathrm{FFT}}$ matrices $\hat{\mathbf{L}}^{(\mathrm{TE/TM})}$. This means for each Fourier amplitude eigenvectors of the out-of-plane fields, there exist two k_z-values as well as two associated Fourier amplitude vectors for the in-plane field components. Based on Eqs. (4.14), we can directly compute the associated $\hat{\hat{\boldsymbol{h}}}_x$ and $\hat{\hat{\boldsymbol{e}}}_x$ Fourier amplitudes of the specific modes for the respective polarization. This allows for a complete expansion of the transverse field components in the l-th material layer, given by

$$\boldsymbol{q}^{(l)}(x,z,\omega) = \sum_{i,j=1}^{N_{\mathrm{FFT}}} \boldsymbol{u}_j^{(l)}(z) \, T_i(x) \begin{pmatrix} \hat{\mathrm{e}}_{x/y,ij}^{(l)} \\ \hat{\mathrm{h}}_{y/x,ij}^{(l)} \end{pmatrix} + \sum_{i,j=1}^{N_{\mathrm{FFT}}} \boldsymbol{d}_j^{(l)}(z) \, T_i(x) \begin{pmatrix} \hat{\mathrm{e}}_{x/y,ij}^{(l)} \\ -\hat{\mathrm{h}}_{y/x,ij}^{(l)} \end{pmatrix} \, . \tag{4.42}$$

Besides the plane-wave basis functions T_i and Fourier components $\hat{\hat{\boldsymbol{e}}}_{ij}$ and $\hat{\hat{\boldsymbol{h}}}_{ij}$ of the j-th mode for the respective polarization, we also introduce the z-dependent amplitudes

$$\boldsymbol{u}_j^{(l)}(z) = \mathrm{e}^{\mathrm{i}k_{z,j}^{(l)}(z-z_l)} \boldsymbol{u}_j^{(l)}(z_l) \quad \text{and} \quad \boldsymbol{d}_j^{(l)}(z) = \mathrm{e}^{\mathrm{i}k_{z,j}^{(l)}(z_{l+1}-z)} \boldsymbol{d}_j^{(l)}(z_{l+1}) \, . \tag{4.43}$$

These amplitudes contain the propagation constant $k_{z,j}^{(l)}$ of the associated j-th mode and include the phase propagation in opposite z-directions. Therefore, they are referred to as up- and downwards propagating amplitudes.

As the $k_{z,j}^{(l)}$-values in the most general case are complex-valued, this also includes a damping or exponential growth of the amplitudes with increasing position z. For a numerically stable evaluation of the amplitudes in a single layer, it is important to avoid exponential growth. Hence, the modes are classified according to Fig. 4.2 into upward damped $\mathrm{Im}(k_{z,j}^{(l)}) > 0$ (white area) and downward damped $\mathrm{Im}(k_{z,j}^{(l)}) < 0$ modes. In the case of non-dispersive real-valued permittivity materials, e.g., vacuum with $\epsilon = \mu = 1$, the modes have either purely real or purely imaginary k_z values. This corresponds to propagating waves or evanescent fields, respectively. To correctly

classify the modes, we introduce a small tolerance value $k_{z,\text{tol}}$ to include the positive real-axis as upwards-propagating $\text{Re}(k_{z,j}^{(l)}) > 0$ modes with a positive phase velocity. The opposite holds for the negative real axis.

For the actual computation of the amplitude phases in Eq. (4.43), it is only necessary to store one of the two opposite k_z-values. Therefore, we only compute the positive branch in Eq. (4.41) of the square root from the eigenvalues defined in Eqs. (4.30). We exchange the sign of the resulting k_z-values as indicated by the blue arrow in Fig. 4.2 to only store the upward k_z-values. Additionally, we shift the k_z-values to slightly damped values if $\left|k_z\right|_\infty < k_{z,\text{tol}}$, which stabilizes the numerical field evaluation for else spatially constant modes. Note, that for stability reasons, we also defined the amplitude propagation for the up-amplitudes from the layer's lower boundary z_l such that they are potentially damped with increasing z-values. For the down-amplitudes, the reference point lies at the upper boundary z_{l+1} of the l-th layer and is damped downwards with increasing z-values.
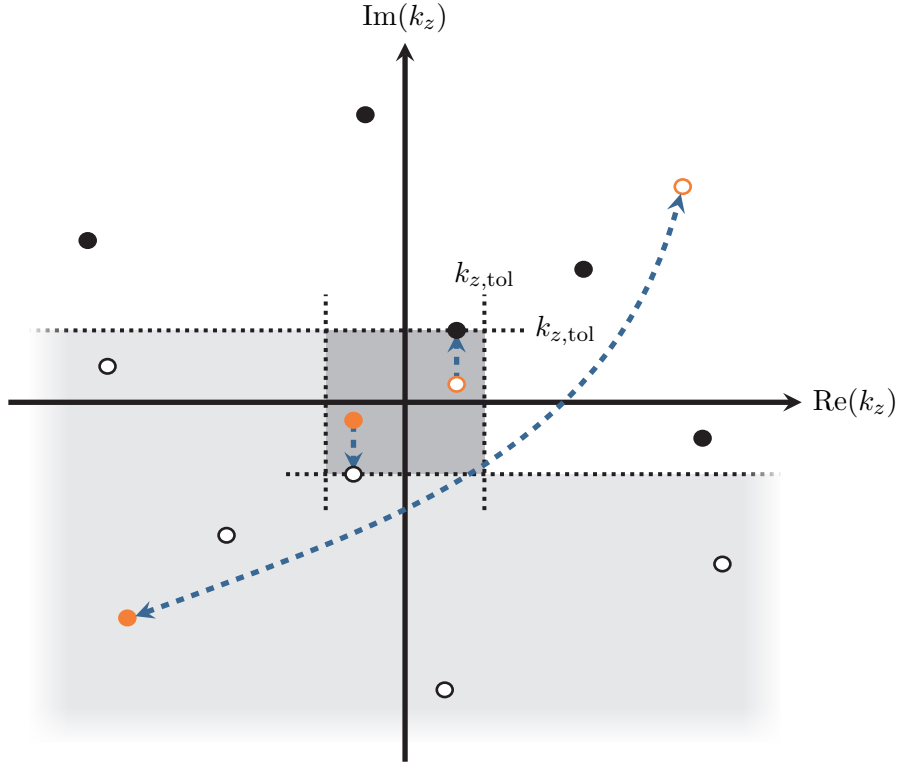
Figure 4.2: Classification of mode propagation constants k_z from Eq. (4.41) into upwards (white area) and downwards (grey area) propagating modes in a single grating layer. Blue arrows indicate the exchange of incorrectly classified k_z-values or the shift to the tolerance value $ik_{z,\text{tol}}$ if they are too close to zero, to stabilize the numerical computations.

Based on the field expansion of a single layer, one can compute the field in the entire layer structure obtained from the staircase approximation. For this, we need to match the fields of two adjacent layers on their interface. This relies on the mode matching of the layers, for which it is convenient to introduce the complete eigenvectors of the $2N_{FFT}$ modes in a single eigenvector

matrix for the two polarizations in the l-th layer, i.e.,

$$\text{TE polarization:}\quad \hat{\mathbf{Q}}^{(l)} := \begin{pmatrix} \hat{\tilde{\boldsymbol{e}}}_y^{(l)} & \hat{\tilde{\boldsymbol{e}}}_y^{(l)} \\ \hat{\tilde{\boldsymbol{h}}}_x^{(l)} & -\hat{\tilde{\boldsymbol{h}}}_x^{(l)} \end{pmatrix}, \tag{4.44a}$$

$$\text{TM polarization:}\quad \hat{\mathbf{Q}}^{(l)} := \begin{pmatrix} \hat{\tilde{\boldsymbol{e}}}_x^{(l)} & \hat{\tilde{\boldsymbol{e}}}_x^{(l)} \\ \hat{\tilde{\boldsymbol{h}}}_y^{(l)} & -\hat{\tilde{\boldsymbol{h}}}_y^{(l)} \end{pmatrix}. \tag{4.44b}$$

With this, the field expansion Eq. (4.42) simplifies to

$$\boldsymbol{q}^{(l)}(x,z,\omega) = \sum_{i=1}^{N_{\mathrm{FFT}}} T_i(x)\,\boldsymbol{e}_i \cdot \hat{\mathbf{Q}}^{(l)} \cdot \begin{pmatrix} \boldsymbol{u}^{(l)}(z) \\ \boldsymbol{d}^{(l)}(z) \end{pmatrix}. \tag{4.45}$$

Here, we additionally introduced a vector of all up- and down-amplitudes for all modes in the layer. Note that all components are implicitly dependent on the frequency ω as well as the Bloch value κ. Provided this expansion, we discuss the mode matching and field propagation with both transfer and S-matrices in the following section.
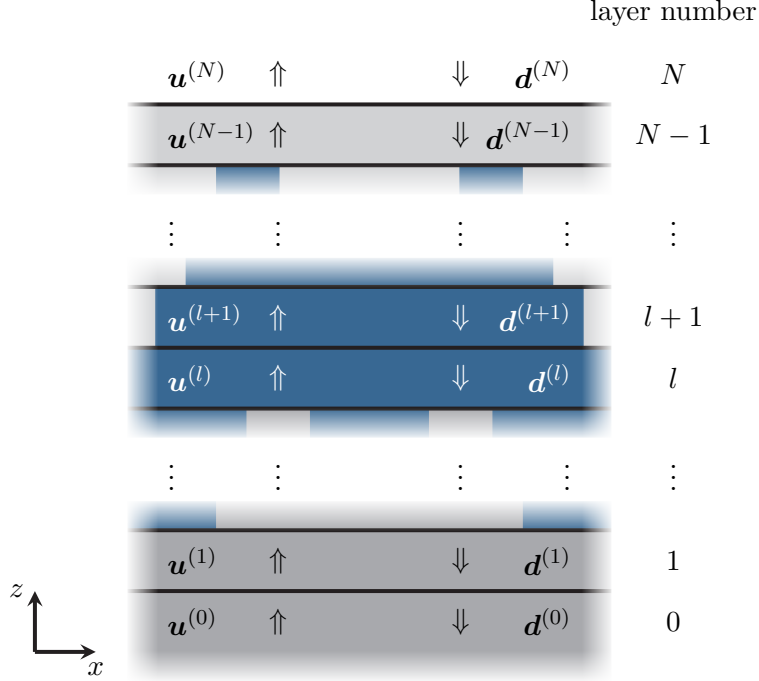
4.3 Transfer and scattering matrix algorithm

We introduce both the transfer and S-matrix algorithms to compute the up- and down-amplitudes for all layers, as they are required to determine the field in every single layer and therefore everywhere in the computational domain. The computation of the scattered fields then allows computing scattering quantities like the transmittance and reflectance spectra, which we discuss in detail in Section 4.3.1.

Before discussing the more elaborate S-matrix algorithm, we introduce the transfer matrix, which is simpler to implement and provides the basic ingredients for the S-matrix algorithm. However, it is in comparison to the S-matrix only conditionally stable in numerical computations [119]. For both algorithms, we want to determine the amplitude vectors in an $N+1$ layer system as sketched in Fig. 4.3. For the computation of reflectance and transmittance spectra the amplitudes in the lower, 0-th layer and upper, N-th layer, which both have to be understood as infinite half-spaces, are of main importance. Within the transfer matrix scheme [119] these are related by a matrix $\hat{\mathbf{T}}_{\mathrm{tot}}$. It couples the lower to the upper amplitudes by

$$\begin{pmatrix} \boldsymbol{u}^{(N)}(z_N) \\ \boldsymbol{d}^{(N)}(z_N) \end{pmatrix} = \hat{\mathbf{T}}_{\mathrm{tot}} \cdot \begin{pmatrix} \boldsymbol{u}^{(0)}(z_0) \\ \boldsymbol{d}^{(0)}(z_0) \end{pmatrix}. \tag{4.46}$$

This transfer matrix can be decomposed into propagation matrices $\hat{\mathbf{T}}^{(l)}$ and mode matching interface matrices $\hat{\mathbf{I}}(l, l+1)$ by simple matrix multiplication, i.e.,

$$\hat{\mathbf{T}}_{\mathrm{tot}} = \hat{\mathbf{I}}(N, N-1) \cdot \hat{\mathbf{T}}(d_{N-1}) \cdot \ldots \cdot \hat{\mathbf{T}}(d_{l+1}) \cdot \hat{\mathbf{I}}(l, l+1) \cdot \ldots \cdot \hat{\mathbf{T}}(d_1) \cdot \hat{\mathbf{I}}(0, 1). \tag{4.47}$$

layer number

Figure 4.3: Schematic representation of the layer system and the field amplitudes used in the S-matrix algorithm. The $N-1$ layer structure is contained in two half-spaces with layer numbers $l = 0$ and $l = N$. Each layer contains the up- and down-amplitude vectors $\boldsymbol{u}^{(l)}$ and $\boldsymbol{d}^{(l)}$ completely determining the electromagnetic field inside each layer.

The propagation matrices couple the amplitudes at the lower and upper boundary of a single layer l by

$$
\begin{pmatrix} \boldsymbol{u}^{(l)}(z_l + d_l) \\ \boldsymbol{d}^{(l)}(z_l + d_l) \end{pmatrix} = \hat{\mathbf{T}}^{(l)}(d_l) \cdot \begin{pmatrix} \boldsymbol{u}^{(l)}(z_l) \\ \boldsymbol{d}^{(l)}(z_l) \end{pmatrix} .
\tag{4.48}
$$

The entries of this diagonal matrix are determined by the acquired phases of the single-mode amplitudes according to Eq. (4.43). Given the thickness d_l of the l-th layer, the entries are determined by

$$
\hat{\mathbf{T}}^{(l)}_{\boldsymbol{uu},ij} = \mathrm{e}^{\mathrm{i}k^{(l)}_{z,i}d_l}\delta_{ij}, \quad \hat{\mathbf{T}}^{(l)}_{\boldsymbol{dd},ij} = \mathrm{e}^{-\mathrm{i}k^{(l)}_{z,i}d_l}\delta_{ij}, \quad \text{and} \quad \hat{\mathbf{T}}_{\boldsymbol{ud}} = \hat{\mathbf{T}}_{\boldsymbol{du}} = \hat{\mathbf{0}} .
\tag{4.49}
$$

Here, the conditional stability of the transfer matrix method becomes evident. For the down-amplitude entries, the phases turn into an exponential growth with increasing layer thickness d_l as soon as any $\mathrm{Im}(k^{(l)}_{z,i}) \gg d_l^{-1}$. This problem is remedied in the S-matrix algorithm, in which the amplitudes do not propagate into the same but opposite directions.

The second matrix required for both the transfer as well as the S-matrix algorithm is the interface matrix $I(l, l+1)$. It relates the amplitudes infinitesimally below the interface to that

infinitesimally above the interface in adjacent layers, i.e.,

$$\begin{pmatrix} \boldsymbol{u}^{(l+1)}(z_{l+1}) \\ \boldsymbol{d}^{(l+1)}(z_{l+1}) \end{pmatrix} = \hat{\mathbf{I}}(l, l+1) \cdot \begin{pmatrix} \boldsymbol{u}^{(l)}(z_l + d_l) \\ \boldsymbol{d}^{(l)}(z_l + d_l) \end{pmatrix} . \tag{4.50}$$

To determine its entries, we require that the tangential field boundary condition at the interface

$$\boldsymbol{q}^{(l)}(x, z_l + d_l, \omega) \overset{!}{=} \boldsymbol{q}^{(l+1)}(x, z_{l+1}, \omega), \tag{4.51}$$

is fulfilled in accordance with Eq. (2.44). The easiest way is to apply the Fourier transform Eq. (4.28) for both layers and match the Fourier components of the modes in layers l and $l + 1$. With the introduction of the mode's Fourier coefficient matrices from Eq. (4.44), we find that

$$\hat{\mathbf{I}}(l, l+1) \overset{(4.45)}{=} \left[\hat{\mathbf{Q}}^{(l+1)} \right]^{-1} \cdot \hat{\mathbf{Q}}^{(l)} . \tag{4.52}$$

Provided both the propagation matrix $\hat{\mathbf{T}}^{(l)}$ and interface matrix $\hat{\mathbf{I}}(l, l+1)$ for each layer, we can in principle reconstruct all amplitudes and therefore the electromagnetic fields in the computational domain.

Besides the potential stability problem of the transfer propagation matrix, the reflectance and transmission spectra are computed from the scattered field. For these two reasons, we introduce the S-matrix, which relates the out-going amplitudes determining the scattered field to the in-going amplitudes. This in detail means that the S-matrix couples the up-amplitudes of the lowest layer and down-amplitudes of the topmost layer to the up-amplitudes of the topmost and down-amplitudes of the lowest layer, respectively. Thus, a system's S-matrix [72] is given by

$$\begin{pmatrix} \boldsymbol{u}^{(N)}(z_N) \\ \boldsymbol{d}^{(0)}(z_0) \end{pmatrix} = \hat{\mathbf{S}}_{\text{tot}} \cdot \begin{pmatrix} \boldsymbol{u}^{(0)}(z_0) \\ \boldsymbol{d}^{(N)}(z_N) \end{pmatrix} . \tag{4.53}$$

Here, the block entries of the S-matrix can be directly related to that of the associated transfer matrix by

$$\hat{\mathbf{S}}_{\boldsymbol{uu}} = \hat{\mathbf{T}}_{\boldsymbol{uu}} - \hat{\mathbf{T}}_{\boldsymbol{ud}} \cdot \hat{\mathbf{T}}_{\boldsymbol{dd}}^{-1} \cdot \hat{\mathbf{T}}_{\boldsymbol{du}} , \tag{4.54a}$$

$$\hat{\mathbf{S}}_{\boldsymbol{ud}} = \hat{\mathbf{T}}_{\boldsymbol{ud}} \cdot \hat{\mathbf{T}}_{\boldsymbol{dd}}^{-1} , \tag{4.54b}$$

$$\hat{\mathbf{S}}_{\boldsymbol{du}} = -\hat{\mathbf{T}}_{\boldsymbol{dd}}^{-1} \cdot \hat{\mathbf{T}}_{\boldsymbol{du}} , \tag{4.54c}$$

$$\hat{\mathbf{S}}_{\boldsymbol{du}} = \hat{\mathbf{T}}_{\boldsymbol{dd}}^{-1} . \tag{4.54d}$$

Because the total transfer matrix is only conditionally stable, so would be the directly computed S-matrix. To prevent an unstable S-matrix scheme, one also splits the total system S-matrix into single sub-matrices both for the propagation and interface mode matching.

The propagation S-matrix couples the in- and out-going amplitudes from the top and bottom of

a single layer l as

$$\begin{pmatrix} \boldsymbol{u}^{(l)}(z_l + d_l) \\ \boldsymbol{d}^{(l)}(z_l) \end{pmatrix} = \hat{\mathbf{S}}^{(l)}(d_l) \cdot \begin{pmatrix} \boldsymbol{u}^{(l)}(z_l) \\ \boldsymbol{d}^{(l)}(z_l + d_l) \end{pmatrix}, \tag{4.55}$$

where the block entries of the matrix are given by

$$\hat{\mathbf{S}}^{(l)}_{\boldsymbol{uu},ij} = \mathrm{e}^{\mathrm{i}k^{(l)}_{z,i}d_l}\delta_{ij}, \quad \hat{\mathbf{S}}^{(l)}_{\boldsymbol{dd},ij} = \mathrm{e}^{\mathrm{i}k^{(l)}_{z,i}d_l}\delta_{ij}, \quad \text{and} \quad \hat{\mathbf{S}}_{\boldsymbol{ud}} = \hat{\mathbf{S}}_{\boldsymbol{du}} = \hat{\mathbf{0}}. \tag{4.56}$$

Because the down-amplitudes propagate downwards from the top boundary of the layer, the acquired phase switches sign for the $\hat{\mathbf{S}}^{(l)}_{\boldsymbol{dd}}$ entries compared to these of the transfer matrix in Eq. (4.49). Therefore, the S-matrix algorithm becomes unconditionally stable. Any mode amplitude that grows exponentially in the transfer matrix is damped here and set to zero as soon as it falls below the machine accuracy level.

The S-matrix interface matrix is defined similarly to the interface matrix in Eq. (4.50) as

$$\begin{pmatrix} \boldsymbol{u}^{(l+1)}(z_{l+1}) \\ \boldsymbol{d}^{(l)}(z_{l+1}) \end{pmatrix} = \hat{\mathbf{S}}(l, l+1) \cdot \begin{pmatrix} \boldsymbol{u}^{(l)}(z_{l+1}) \\ \boldsymbol{d}^{(l+1)}(z_{l+1}) \end{pmatrix}. \tag{4.57}$$

As the interface matrix $\hat{\mathbf{I}}(l, l+1)$ does not include divergent terms, we transform it into the entries of its S-matrix pendant using Eqs. (4.54).

The unconditionally stable S-matrix of the system, given by

$$\hat{\mathbf{S}}_{\mathrm{tot}} = \hat{\mathbf{S}}(0,1) * \hat{\mathbf{S}}(d_0) * \ldots * \hat{\mathbf{S}}(l, l+1) * \hat{\mathbf{S}}(d_{l+1}) * \ldots * \hat{\mathbf{S}}(N-1, N), \tag{4.58}$$

entails the disadvantage of a newly introduced S-matrix product [72]

$$\hat{\mathbf{S}} = \hat{\mathbf{S}}^{(1)} * \hat{\mathbf{S}}^{(2)}. \tag{4.59}$$

This product couples the up- and down-amplitude blocks as

$$\hat{\mathbf{S}}_{\boldsymbol{uu}} = \hat{\mathbf{S}}^{(2)}_{\boldsymbol{uu}} \cdot \left[\hat{\mathbf{1}} - \hat{\mathbf{S}}^{(1)}_{\boldsymbol{ud}} \cdot \hat{\mathbf{S}}^{(2)}_{\boldsymbol{du}} \right]^{-1} \cdot \hat{\mathbf{S}}^{(1)}_{\boldsymbol{uu}}, \tag{4.60a}$$

$$\hat{\mathbf{S}}_{\boldsymbol{ud}} = \hat{\mathbf{S}}^{(2)}_{\boldsymbol{uu}} \cdot \left[\hat{\mathbf{1}} - \hat{\mathbf{S}}^{(1)}_{\boldsymbol{ud}} \cdot \hat{\mathbf{S}}^{(2)}_{\boldsymbol{du}} \right]^{-1} \cdot \hat{\mathbf{S}}^{(1)}_{\boldsymbol{uu}} \cdot \hat{\mathbf{S}}^{(2)}_{\boldsymbol{dd}} + \hat{\mathbf{S}}^{(2)}_{\boldsymbol{ud}}, \tag{4.60b}$$

$$\hat{\mathbf{S}}_{\boldsymbol{du}} = \hat{\mathbf{S}}^{(1)}_{\boldsymbol{du}} + \hat{\mathbf{S}}^{(1)}_{\boldsymbol{dd}} \cdot \hat{\mathbf{S}}^{(2)}_{\boldsymbol{du}} \cdot \left[\hat{\mathbf{1}} - \hat{\mathbf{S}}^{(1)}_{\boldsymbol{ud}} \cdot \hat{\mathbf{S}}^{(2)}_{\boldsymbol{du}} \right]^{-1} \cdot \hat{\mathbf{S}}^{(1)}_{\boldsymbol{uu}}, \tag{4.60c}$$

$$\hat{\mathbf{S}}_{\boldsymbol{dd}} = \hat{\mathbf{S}}^{(1)}_{\boldsymbol{dd}} \cdot \left[\hat{\mathbf{S}}^{(2)}_{\boldsymbol{du}} \cdot \left[\hat{\mathbf{1}} - \hat{\mathbf{S}}^{(1)}_{\boldsymbol{ud}} \cdot \hat{\mathbf{S}}^{(2)}_{\boldsymbol{du}} \right]^{-1} \cdot \hat{\mathbf{S}}^{(1)}_{\boldsymbol{uu}} + \hat{\mathbf{1}} \right] \cdot \hat{\mathbf{S}}^{(2)}_{\boldsymbol{dd}}. \tag{4.60d}$$

In contrast to the simple matrix product for the transfer matrix in Eq. (4.47) it involves the block matrix inverse $\left[\hat{\mathbf{1}} - \hat{\mathbf{S}}^{(1)}_{\boldsymbol{ud}} \cdot \hat{\mathbf{S}}^{(2)}_{\boldsymbol{du}} \right]^{-1}$, which needs to be computed for every consecutive S-

matrix product for the total system S-matrix in Eq. (4.58). Especially for the computation of the interface matrices $\hat{\mathbf{S}}(l, l+1)$, this involves both the S-matrix product as well as the conversion between the transfer matrix from Eq. (4.52) to the S-matrix using Eq. (4.54). As this overall requires two numerically expensive matrix inversions, one defines a third product

$$\hat{\mathbf{S}}' = \hat{\mathbf{S}} \odot \hat{\mathbf{T}} \quad \Leftrightarrow \quad \hat{\mathbf{S}}' = \hat{\mathbf{S}} * \hat{\mathbf{S}}^{(2)}(\hat{\mathbf{T}}) \,. \tag{4.61}$$

It completes the transfer matrix conversion and S-matrix product in a single step using only one instead of two inversions, such that the resulting S-matrix blocks are given by

$$\hat{\mathbf{S}}'_{uu} = \hat{\mathbf{T}}_{uu} \cdot \hat{\mathbf{S}}_{uu} - \left(\hat{\mathbf{T}}_{uu} \cdot \hat{\mathbf{S}}_{ud} + \hat{\mathbf{T}}_{ud} \right) \cdot \left(\hat{\mathbf{T}}_{dd} + \hat{\mathbf{T}}_{du} \cdot \hat{\mathbf{S}}_{ud} \right)^{-1} \cdot \hat{\mathbf{T}}_{du} \cdot \hat{\mathbf{S}}_{uu} \,, \tag{4.62a}$$

$$\hat{\mathbf{S}}'_{ud} = \left(\hat{\mathbf{T}}_{uu} \cdot \hat{\mathbf{S}}_{ud} + \hat{\mathbf{T}}_{ud} \right) \cdot \left(\hat{\mathbf{T}}_{dd} + \hat{\mathbf{T}}_{du} \cdot \hat{\mathbf{S}}_{ud} \right)^{-1} \,, \tag{4.62b}$$

$$\hat{\mathbf{S}}'_{du} = \hat{\mathbf{S}}_{du} - \hat{\mathbf{S}}_{dd} \cdot \left(\hat{\mathbf{T}}_{dd} + \hat{\mathbf{T}}_{du} \cdot \hat{\mathbf{S}}_{ud} \right)^{-1} \cdot \hat{\mathbf{T}}_{du} \cdot \hat{\mathbf{S}}_{uu} \,, \tag{4.62c}$$

$$\hat{\mathbf{S}}'_{dd} = \hat{\mathbf{S}}_{dd} \cdot \left(\hat{\mathbf{T}}_{dd} + \hat{\mathbf{T}}_{du} \cdot \hat{\mathbf{S}}_{ud} \right)^{-1} \,. \tag{4.62d}$$

A full derivation can be, e.g., found in [80]. Provided the full system S-matrix and the single steps on how to compute it, we can apply the S-matrix algorithm to different problems. We start with the computation of transmittance and reflectance spectra, which is followed by the reconstruction scheme to compute the complete fields inside a grating structure. Finally, the system's resonances defined both by the geometry and used materials are analyzed by the computation of the S-matrix poles.

4.3.1 Transmittance and reflectance spectra

First, we discuss how to compute the reflectance and transmittance spectra of a layered (grating) structure for excitation with an oblique incident plane wave, which is used both for the HMM setup in Chapter 7 as well as the DBR microcavities in Chapter 8. As explained in Section 2.8.3 the reflectance and transmittance spectra require to compute the transmitted and reflected power from the scattered field Poynting vector. To determine the underlying scattered fields, we employ the S-matrix algorithm to obtain the out-going amplitudes from the in-going amplitudes of the exciting plane wave, given by

$$\boldsymbol{E}^{(0)}_{\text{inc}}(x, z, \omega) = \boldsymbol{E}_0(\omega) \mathrm{e}^{\mathrm{i}\boldsymbol{k}\cdot\boldsymbol{r}} \quad \text{with} \quad \boldsymbol{k} = \left(k_x, 0, k_z\right)^{\mathrm{T}} \quad \text{and} \quad k_z > 0 \,. \tag{4.63}$$

Here, we consider the incident field being inside the lower half-plane, which for the scattering setups is assumed to be air with $\epsilon = \mu = 1$. Setting the associated incident $\boldsymbol{H}$-field as

$$\boldsymbol{H}^{(0)}_{\text{inc}}(x, z, \omega) = \frac{1}{\omega} \boldsymbol{k} \times \boldsymbol{E}_0(\omega) \mathrm{e}^{\mathrm{i}\boldsymbol{k}\cdot\boldsymbol{r}} \,, \tag{4.64}$$

the plane wave propagates upwards to the layered system. The incident angle θ is defined by the $\boldsymbol{k}$-vector, such that

$$k_x = \omega \sin \theta \, . \tag{4.65}$$

To apply the S-matrix algorithm, we need to compute the input amplitudes for the incident field. For this, we can first split the field into both TE and TM polarization contributions and then apply the Fourier transform of the incident field like in Eq. (4.28) to obtain the corresponding Fourier components at the fixed position $z_0 = 0$, such that

$$\boldsymbol{E}_{x/y,\text{inc}}(k_i, z = 0, \omega) = \tilde{E}_{x/y,\text{inc},i} \overset{!}{=} \sum_j \boldsymbol{u}_j^{(0)} \underbrace{e^{ik_{z,j}^{(0)}z}}_{\overset{z=0}{\equiv} 1} \hat{\boldsymbol{e}}_{x/y,ij}^{(0)} \, . \tag{4.66}$$

Here, we choose $\kappa = k_x$ for the Bloch phase implicitly contained in the plane-wave basis $T_i(x)$. Due to the continuity of the fields over all system layers, the Bloch phase is the same in each layer. The incident field's up-amplitudes are then computed by inversion of the mode eigenvectors $\hat{\boldsymbol{e}}$, such that

$$\boldsymbol{u}^{(0)} = \left[\hat{\boldsymbol{e}}^{(0)}\right]^{-1} \cdot \tilde{\boldsymbol{E}}_{\text{inc}} \, . \tag{4.67}$$

As we assume that no field impinges from above into the layered system, the corresponding down-amplitudes of the N-th layer are

$$\boldsymbol{d}^{(N)} = \boldsymbol{0} \, . \tag{4.68}$$

Given all the in-going amplitudes, we apply the S-matrix algorithm as described before to compute the out-going amplitudes $\boldsymbol{u}^{(N)}$ and $\boldsymbol{d}^{(0)}$. Here, the first describes the transmitted, while the latter describes the reflected field. The fields can be obtained in the corresponding upper or lower half-space by the respective field expansion according to Eq. (4.42).

With the incident and the two scattered fields, we can compute the time-averaged Poynting vector. For the respective incident, transmitted and reflected power as e.g., in Eq. (2.102), we integrate over boundary surfaces parallel to the layers both on top and at the bottom of the structure (cf. Fig. 2.4). As the corresponding face-normal vectors point in z-direction, we only require the z-component of the time-averaged Poynting vector, i.e.,

$$P_{\text{inc/scat}}\left(z_{0/N}, \omega\right) = \int_0^a \mathrm{d}x \, \left\langle S_{z,\text{inc/scat}} \right\rangle_\tau \left(z_{0/N}, \omega\right) , \tag{4.69}$$

$$= \frac{1}{2} \int_0^a \mathrm{d}x \, \mathrm{Re} \left[E_x(x, z_{0/N}, \omega) H_y^*(x, z_{0/N}, \omega) - E_y(x, z_{0/N}, \omega) H_x^*(x, z_{0/N}, \omega) \right] .$$

We insert the field expansion Eq. (4.45), which results in the following incident, transmitted and reflected powers

$$P_{\text{inc,TE}}(\omega) = -\frac{a}{2} \mathrm{Re} \left[\boldsymbol{u}^{(0)*} \cdot \hat{\boldsymbol{h}}_x^{(0)\dagger} \cdot \hat{\boldsymbol{e}}_y^{(0)} \cdot \boldsymbol{u}^{(0)} \right] , \tag{4.70a}$$

$$P_{\text{inc,TM}}(\omega) = \frac{a}{2}\text{Re}\left[\boldsymbol{u}^{(0)*} \cdot \hat{\boldsymbol{e}}_x^{(0)\dagger} \cdot \hat{\hat{\boldsymbol{h}}}_y^{(0)} \cdot \boldsymbol{u}^{(0)}\right], \tag{4.70b}$$

$$P_{\text{refl,TE}}(\omega) = \frac{a}{2}\text{Re}\left[\boldsymbol{d}^{(0)*} \cdot \hat{\hat{\boldsymbol{h}}}_x^{(0)\dagger} \cdot \hat{\boldsymbol{e}}_y^{(0)} \cdot \boldsymbol{d}^{(0)}\right], \tag{4.70c}$$

$$P_{\text{refl,TM}}(\omega) = -\frac{a}{2}\text{Re}\left[\boldsymbol{d}^{(0)*} \cdot \hat{\boldsymbol{e}}_x^{(0)\dagger} \cdot \hat{\hat{\boldsymbol{h}}}_y^{(0)} \cdot \boldsymbol{d}^{(0)}\right], \tag{4.70d}$$

$$P_{\text{trans,TE}}(\omega) = -\frac{a}{2}\text{Re}\left[\boldsymbol{u}^{(N)*} \cdot \hat{\hat{\boldsymbol{h}}}_x^{(N)\dagger} \cdot \hat{\boldsymbol{e}}_y^{(N)} \cdot \boldsymbol{u}^{(N)}\right], \tag{4.70e}$$

$$P_{\text{trans,TM}}(\omega) = \frac{a}{2}\text{Re}\left[\boldsymbol{u}^{(N)*} \cdot \hat{\boldsymbol{e}}_x^{(N)\dagger} \cdot \hat{\hat{\boldsymbol{h}}}_y^{(N)} \cdot \boldsymbol{u}^{(N)}\right], \tag{4.70f}$$

for the two respective polarizations. Note, that the integration along the unit cell reduces the problem to the amplitudes and mode eigenvectors $\hat{\boldsymbol{e}}_{x,y}$ and $\hat{\hat{\boldsymbol{h}}}_{y,x}$ of the respective layers.

Given the power values, we can directly compute both the reflectance and transmittance spectra as outlined in Section 2.8.3 by

$$R(\omega) = \frac{P_{\text{refl}}(\omega)}{P_{\text{inc}}(\omega)} \quad \text{and} \quad T(\omega) = \frac{P_{\text{trans}}(\omega)}{P_{\text{inc}}(\omega)}. \tag{4.71}$$

Finally, the absorbance spectra are computed by

$$A(\omega) = 1 - R(\omega) - T(\omega). \tag{4.72}$$

With the computation of the spectra, we are able to analyze the layered system's resonances as they cause peaks in the spectra. To gain a deeper insight, we also want to examine the field distributions inside the investigated cavities, especially for resonance frequencies. Therefore, we explain how to obtain these fields in every layer.

4.3.2 Field reconstruction

To determine the fields throughout the layered system, we need to evaluate the field expansion Eq. (4.42) for every query point (x, z). Here, the z-coordinate determines the layer number l. For this evaluation of the field distribution, we require both the up- and down-amplitudes in the specific layer.

For the computation of the scattering spectra, we have so far only discussed how to obtain the amplitudes in the lowest and top-most layer. To obtain all other amplitudes, we can apply the S-matrix algorithm recursively, as sketched in Fig. 4.4. In this three-step process, we reduce the effective structure for the S-matrix evaluation one layer after the other. In each iteration of the recursion algorithm, we determine the amplitudes in the lowest layer and restart with the amplitude computation in the layer above. To guarantee a stable field evaluation, we require the up-amplitudes to be at the bottom and the down-amplitudes to be at the top of each single

layer l. These are propagated by multiplying the phase-difference to reach the query position z according to Eq. (4.43).
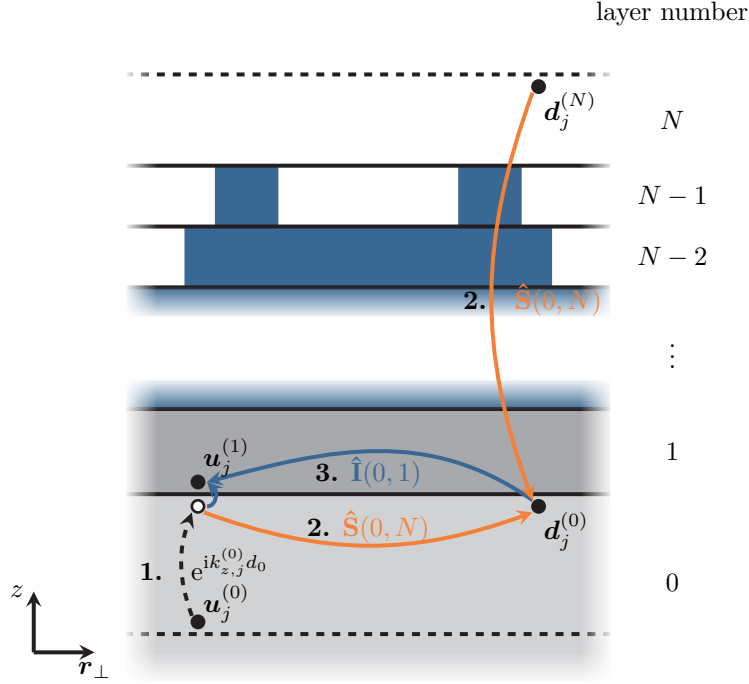
Figure 4.4: Recursive three-step process to determine all amplitude vectors $\boldsymbol{u}$ and $\boldsymbol{d}$ inside all layers. **Initially**, the outer in-going amplitudes are provided. **First**, the lower up-amplitudes are propagated. **Second**, the down-amplitudes in the lower layer are computed by the S-matrix. **Third**, the up-amplitudes in the layer above are computed with the help of the interface matrix $\hat{\mathbf{I}}$. Then the process is repeated.

The three-step recursion works as follows. Initially, we assume that the up- and down-amplitudes of the outermost layers are known, e.g., by the incident field defined in Eq. (4.66). In the first step, we propagate the up-amplitudes of the lowest layer by multiplying it with the phases of the single modes according to Eq. (4.43). As these up-amplitudes are only propagated upwards numerical stability is guaranteed. In the second step, we compute the complete S-matrix as in Eq. (4.58) between the outermost layers and then apply it to determine the down-amplitudes $\boldsymbol{d}^{(0)}$ at the top boundary of the lowest layer. In the third and final step, we apply the interface transfer matrix $\hat{\mathbf{I}}(0,1)$ to determine the up-amplitudes $\boldsymbol{u}^{(1)}$ at the layer above. Thus, we have determined both the up- and down-amplitudes in the bottom layer and restored the initial assumption in which the first layer now replaces the zeroth one. This recursion is then applied until all amplitudes and therefore all fields are determined.

4.4 Resonances and quasi-normal modes

The reflectance and transmittance spectra allow for a general characterization of the resonances supported in a given cavity, which cause peaks in the spectra [122]. Moreover, one can investigate the field distributions at the excitation frequency, which corresponds to that of the excited QNM if the peak is narrow enough. In the case of the degeneracy of the QNMs the field distribution is a superposition.

A full analysis of the QNMs requires solving Maxwell's equations in frequency domain with radiation conditions [136–138]. Within the S-matrix algorithm, this is equivalent to computing the complex resonance frequencies of the S-matrix [120–122]. As it couples in-going to out-going amplitudes as

$$\boldsymbol{A}_{\text{out}} = \hat{\mathbf{S}}(\omega) \cdot \boldsymbol{A}_{\text{in}} \,, \tag{4.73}$$

and at a resonance frequency $\tilde{\omega} \in \mathbb{C}$ the S-matrix has a pole, i.e.,

$$\lim_{\omega \to \tilde{\omega}} \hat{\mathbf{S}}(\omega) \to \infty \,, \tag{4.74}$$

the out-going kernel vectors $\boldsymbol{A}_{\text{out}}(\tilde{\omega})$ defined by

$$\hat{\mathbf{S}}^{-1}(\tilde{\omega}) \cdot \boldsymbol{A}_{\text{out}}(\tilde{\omega}) = \mathbf{0} \,, \tag{4.75}$$

determine the QNM field distributions of the cavity. There are no in-going amplitudes at the resonance frequency and as the amplitudes $\boldsymbol{A}_{\text{out}}(\tilde{\omega}) \neq \mathbf{0}$ lie in the kernel of the inverse S-matrix the radiation conditions are automatically fulfilled.

The computation of the QNMs requires the analytic continuation of the S-matrix in the frequency domain. Hence, also the material tensors $\underline{\underline{\boldsymbol{\epsilon}}}(\omega)$ and $\underline{\underline{\boldsymbol{\mu}}}$ need to be continued to the complex frequency plane. To this end, we use the material models from Chapter 3 which are fitted to experimentally obtained permittivities and can be easily evaluated at any complex frequency. Although the criterion

$$\det \hat{\mathbf{S}}^{-1}(\tilde{\omega}) = 0 \,, \tag{4.76}$$

is sufficient to find the QNM resonance frequencies, we discuss the example of surface plasmon polaritons (SPPs) in the following section, for which the S-matrix has a pole but its determinant is one. Instead of the determinant, we compute the full singular value decomposition of the S-matrix [129], i.e.,

$$\hat{\mathbf{S}}(\omega) = \hat{\mathbf{U}}(\omega) \cdot \hat{\boldsymbol{\Sigma}}(\omega) \cdot \hat{\mathbf{V}}^{\dagger}(\omega) \,. \tag{4.77}$$

Here, the matrix $\hat{\boldsymbol{\Sigma}}$ is diagonal

$$\hat{\boldsymbol{\Sigma}}(\omega) = \text{diag}\left(\sigma_1(\omega), \ldots, \sigma_N(\omega)\right) \,, \tag{4.78}$$

and contains the singular values $\sigma_i(\omega)$ of the S-matrix. As several singular values can diverge at

the same resonance frequency $\tilde{\omega}$ also the QNMs can be degenerate. To numerically determine the poles of the S-matrix, we have to compute

$$\lim_{\omega \to \tilde{\omega}} \underbrace{\left[\max_{\forall i} \sigma_i(\omega) \right]^{-1}}_{:= \bar{\sigma}^{-1}(\omega)} = 0 \quad \text{with} \quad \tilde{\omega} \in \mathbb{C} \,. \tag{4.79}$$

As the singular values are strictly positive in the standard singular value decomposition algorithm [129], we replace the search for roots to that of the minimization of the logarithm

$$\min_{\omega \in \Omega \subset \mathbb{C}} \log_{10} \bar{\sigma}^{-1}(\omega) \,, \tag{4.80}$$

in a predefined region Ω of the complex frequency plane. In the numerical minimization one sets a tolerance value, for which we assume to have found a numerically approximated resonance frequency $\tilde{\omega}_{\text{num}}$ once it is undershot.

The reconstruction of the QNM field distributions requires the out-going amplitudes implicitly defined in Eq. (4.75). Given the singular value decomposition of $\hat{\mathbf{S}}$ in Eq. (4.77), the singular value decomposition of the required inverse is

$$\hat{\mathbf{S}}^{-1} = \hat{\mathbf{V}} \cdot \hat{\mathbf{\Sigma}}^{-1} \cdot \hat{\mathbf{U}}^{\dagger} \,. \tag{4.81}$$

Therefore, the entries of $\boldsymbol{A}_{\text{out}}(\tilde{\omega}_{\text{num}})$ are defined by the j-th row of the hermitian matrix $\hat{\mathbf{U}}$ for each inverse singular value σ_j in $\hat{\mathbf{\Sigma}}^{-1}$ tending towards zero, i.e.,

$$\boldsymbol{A}_{i,\text{out}}(\tilde{\omega}_{\text{num}}) = \hat{\mathbf{U}}_{ij} \quad \text{for} \quad \sigma^{-1}(\tilde{\omega}_{\text{num}}) \approx 0 \,. \tag{4.82}$$

If the resonance frequency would be perfectly matched, one could use the field reconstruction from the previous Section 4.3.2 to directly determine the fields. However, the frequency is only approximated in the numerical minimization, which leads to residual in-going amplitudes

$$\boldsymbol{A}_{\text{in}}(\tilde{\omega}_{\text{num}}) = \hat{\mathbf{S}}^{-1}(\tilde{\omega}_{\text{num}}) \cdot \hat{\mathbf{A}}_{\text{out}}(\tilde{\omega}_{\text{num}}) = \hat{\mathbf{V}}(\tilde{\omega}_{\text{num}}) \cdot \hat{\mathbf{\Sigma}}^{-1}(\tilde{\omega}_{\text{num}}) \cdot \hat{\mathbf{U}}^{\dagger}(\tilde{\omega}_{\text{num}}) \cdot \hat{\mathbf{A}}_{\text{out}}(\tilde{\omega}_{\text{num}}) \,, \tag{4.83}$$

which we here use to reconstruct the QNM fields. Both the computation of the resonance frequencies and QNM field distributions are of particular interest in Section 7.3 about the HMM cavities, for which we determine the mode structure despite relatively weak peaks in the reflectance spectra.

4.4.1 Surface plasmon polariton dispersion

We close this chapter, with a short, yet important example for the computation of resonances in layered systems. For this, we consider a single dielectric-metal interface and show that SPPs [1, 84] emerge from the pole spectrum of the associated S-matrix. As we assume a planar, infinitely extended interface between two isotropic dielectrics $\epsilon^{(0)}$ and $\epsilon^{(1)}$, the system is effectively one-

dimensional. Therefore, the fields are of the form

$$\boldsymbol{E}(\boldsymbol{r},t) = \mathrm{e}^{\mathrm{i}k_x x}\boldsymbol{E}(z,\omega) \quad \text{and} \quad \boldsymbol{H}(\boldsymbol{r},t) = \mathrm{e}^{\mathrm{i}k_x x}\boldsymbol{H}(z,\omega)\,. \tag{4.84}$$

Here, we introduce the Bloch-phase with the angular wavenumber k_x, which without loss of generality points in the x-direction. Therefore, all derivatives in lateral direction take the form

$$\partial_x \boldsymbol{q}(x,z,\omega) = \mathrm{i}k_x \boldsymbol{q}(x,z,\omega)\,. \tag{4.85}$$

In order to compute the S-matrix, we need to solve the field propagation problem Eq. (4.2) for both TE and TM polarization. As the fields are only x-dependent in the Bloch phase, the matrix operators $\hat{\boldsymbol{L}}$ from Eq. (4.4) simplify to the matrices

$$\hat{\mathbf{L}}_{\mathrm{TE}}(\omega) = \begin{pmatrix} 0 & \omega - \frac{k_x^2}{\omega\epsilon(\omega)} \\ \omega\epsilon(\omega) & 0 \end{pmatrix}\,, \tag{4.86a}$$

$$\hat{\mathbf{L}}_{\mathrm{TM}}(\omega) = \begin{pmatrix} 0 & \omega - \frac{k_x^2}{\omega\epsilon(\omega)} \\ \omega\epsilon(\omega) & 0 \end{pmatrix}\,. \tag{4.86b}$$

With these matrices, we solve the eigenvalue problem Eq. (4.9) to determine the angular propagation wavenumbers k_z as well as the field expansion matrices $\hat{\mathbf{Q}}$ defined in Eqs. (4.44) in both half-spaces. For both polarizations, we find

$$k_z = \pm\sqrt{\omega^2\,\epsilon(\omega) - k_x^2}\,, \tag{4.87}$$

which is equivalent to the standard dispersion relation Eq. (3.32) of a plane wave in an isotropic dielectric. Here, we explicitly restrict the square root to its positive branch. The associated eigenmodes are set by the field expansion coefficient matrices

$$\hat{\mathbf{Q}}_{\mathrm{TE}} = \begin{pmatrix} \frac{\omega}{k_z} & -\frac{\omega}{k_z} \\ 1 & 1 \end{pmatrix} \quad \text{and} \quad \hat{\mathbf{Q}}_{\mathrm{TM}} = \begin{pmatrix} 1 & 1 \\ \frac{\omega\epsilon(\omega)}{k_z} & -\frac{\omega\epsilon(\omega)}{k_z} \end{pmatrix}\,. \tag{4.88}$$

With the help of these matrices, we can directly compute the interface mode matching matrix between the two layers according to Eq. (4.52). For both polarizations, the interface matrix takes the form

$$\hat{\mathbf{I}}(0,1) = \frac{1}{2}\begin{pmatrix} 1+a & 1-a \\ 1-a & 1+a \end{pmatrix}\,, \tag{4.89}$$

with the entries

$$a_{\mathrm{TE}} = \frac{\sqrt{\omega^2\epsilon^{(1)}(\omega) - k_x^2}}{\sqrt{\omega^2\epsilon^{(0)}(\omega) - k_x^2}} \quad \text{and} \quad a_{\mathrm{TM}} = \frac{\epsilon^{(0)}(\omega)}{\epsilon^{(1)}(\omega)}\frac{\sqrt{\omega^2\epsilon^{(1)}(\omega) - k_x^2}}{\sqrt{\omega^2\epsilon^{(0)}(\omega) - k_x^2}}\,. \tag{4.90}$$

To compute the resonances, we calculate the S-matrix according to Eq. (4.54), which results in

$$\hat{\mathbf{S}}(0,1) = \begin{pmatrix} \frac{2a}{1+a} & \frac{1-a}{1+a} \\ \frac{a-1}{1+a} & \frac{2}{1+a} \end{pmatrix}, \tag{4.91}$$

with the same coefficients a from the interface matrix. It is obvious, that the S-matrix has a pole for

$$a \to \tilde{a} = -1. \tag{4.92}$$

However, we note that the determinant

$$\det \hat{\mathbf{S}}(0,1) = \frac{4a + (1-a)^2}{(1+a)^2} = \frac{(1+a)^2}{(1+a)^2} = 1. \tag{4.93}$$

Hence, in this particular case, the larger singular value σ_1 of the S-matrix diverges, while the second singular value σ_2 tends to zero, such that

$$\lim_{a \to -1} \det \hat{\mathbf{S}}(0,1) = \lim_{a \to -1} \sigma_1 \sigma_2 = 1. \tag{4.94}$$

Therefore, the numerical search of resonances should always rely on the singular value decomposition, despite the higher numerical effort compared to simply calculating the determinant.

The resonance condition

$$\tilde{a}_{\mathrm{TE}} = -1 \overset{!}{=} \frac{\sqrt{\omega^2 \epsilon^{(1)}(\omega) - k_x^2}}{\sqrt{\omega^2 \epsilon^{(0)}(\omega) - k_x^2}}, \tag{4.95}$$

cannot be fulfilled in TE polarization, as we are explicitly restricted to the positive branch of the square root. In contrast, the resonance condition in TM polarization

$$\tilde{a}_{\mathrm{TM}} = -1 \overset{!}{=} \frac{\epsilon^{(0)}(\omega)}{\epsilon^{(1)}(\omega)} \frac{\sqrt{\omega^2 \epsilon^{(1)}(\omega) - k_x^2}}{\sqrt{\omega^2 \epsilon^{(0)}(\omega) - k_x^2}}, \tag{4.96}$$

can be matched, if the two layer permittivities have a different sign. This is the case for interfaces between dielectrics and metals as considered here, where we find resonances corresponding to the SPPs with the dispersion relation

$$k_x = \pm \omega \sqrt{\frac{\epsilon^{(0)}(\omega)\epsilon^{(1)}(\omega)}{\epsilon^{(0)}(\omega) + \epsilon^{(1)}(\omega)}}, \tag{4.97}$$

along the interface.

Fig. 4.5 shows this dispersion relation for an interface between vacuum $\epsilon^{(0)} = 1$ and a Drude model describing the metal. Here, we use the permittivity introduced in the material model
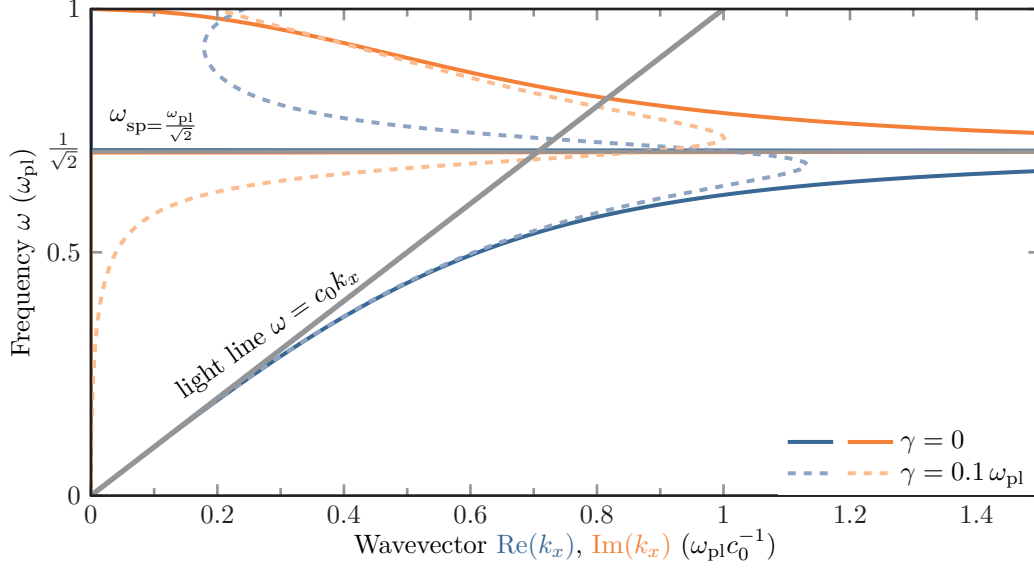
Figure 4.5: SPP dispersion relation Eq. (4.97) for a vacuum and Drude-metal interface. Solid lines mark the dispersion $\mathrm{Re}(k_x)$ and dissipation $\mathrm{Im}(k_x)$ for a Drude metal without damping $\gamma = 0$ and plasma frequency ω_{pl}. Dashed lines show the dispersion for a typical damping of $\gamma = 0.1\,\omega_{\mathrm{pl}}$. Both the light-line as well as the surface plasmon frequency ω_{sp} are marked with grey lines.

Section 3.2 given as

$$\epsilon^{(1)}(\omega) = 1 - \frac{\omega_{\mathrm{pl}}^2}{\omega(\omega + \mathrm{i}\gamma)}\,, \tag{4.98}$$

such that the dispersion relation reduces to

$$k_x = \omega \sqrt{\frac{1 - \frac{\omega_{\mathrm{pl}}^2}{\omega(\omega+\mathrm{i}\gamma)}}{2 - \frac{\omega_{\mathrm{pl}}^2}{\omega(\omega+\mathrm{i}\gamma)}}}\,. \tag{4.99}$$

As the Drude permittivity changes to a positive sign for frequencies $\omega > \omega_{\mathrm{pl}}$, the resonance condition Eq. (4.96) holds for frequencies below the plasma frequency ω_{pl}. Correspondingly, the dispersion relation only applies to SPPs bound and traveling along the surface with frequencies $\omega < \omega_{\mathrm{pl}}$. While the dispersion curve $\mathrm{Re}(k_x)$ follows the light line for very small frequencies, the SPP dispersion approaches the surface plasmon frequency ω_{sp} with increasing $\mathrm{Re}(k_x)$. The surface plasmon frequency can be calculated from the damping-free ($\gamma \to 0$) dispersion

$$k_x = \omega \sqrt{\frac{1 - \frac{\omega_{\mathrm{pl}}^2}{\omega^2}}{2 - \frac{\omega_{\mathrm{pl}}^2}{\omega^2}}} = \omega \sqrt{\frac{\omega^2 - \omega_{\mathrm{pl}}^2}{2\omega^2 - \omega_{\mathrm{pl}}^2}}\,, \tag{4.100}$$

for which $k_x \to \infty$ as

$$\omega \to \omega_{\mathrm{sp}} = \frac{\omega_{\mathrm{pl}}}{\sqrt{2}}.$$ (4.101)

If the frequency is increased beyond the surface plasmon frequency ω_{sp} the SPP modes feature very high losses and the propagation along the surface is strongly inhibited. As the dispersion $\mathrm{Re}(k_x)$ for propagating SPPs lies below the light line, the SPP modes cannot be excited by a plane wave impinging from the far-field onto the metal surface.

We discuss different SPP excitations for various geometries in Chapter 6 for localized SPPs on Drude metal spheres as well as propagating SPP modes on the freestanding perforated gold films and the mode mapping using electron energy loss spectroscopy (EELS) computations. While in Chapter 7 we use the coupling of several SPP modes between the single metal layers forming the investigated HMM cavities, in Chapter 8 the SPPs are used in the metal grating DBR lasing cavities to tailor the lasing modes and reach high confinement of light.

Discontinuous Galerkin time-domain method

After the discussion on how to numerically solve Maxwell's equations in frequency domain in the preceding Chapter 4, we here present a numerical method, which works in the time domain. This method is the discontinuous Galerkin time-domain (DGTD) method. While the latter two words obviously point out, that we solve the equations of motion in time domain, the first words indicate which kind of basis functions and weight functions are used to discretize the fields in the spatial dimensions. In the Fourier modal method (FMM) (cf. Chapter 4), we essentially used a piecewise plane-wave basis expansion for the fields. Here, we use a polynomial basis defined on a finite-element mesh (see Section 5.2). Using this finite-element mesh has an advantage over the commonly used finite difference time domain (FDTD) method [63], which relies on a regular grid for field discretization. The latter makes it more difficult to approximate or sufficiently resolve curved surfaces. Yet, this advantage of the DGTD raises the problem of how to couple the neighboring elements. This is achieved using the so-called numerical flux, which is discussed in Section 5.3. The numerical flux allows for the implementation of both, boundary conditions (BCs) as well as the introduction of field sources (see Section 5.4). Both FDTD and DGTD methods have in common how to handle dispersive material models, which is shown in Section 5.5 about auxiliary differential equations (ADEs). Last but not least, we discuss in Section 5.6 how these time-domain methods accomplish simulating quasi-infinite space using perfectly matched layers (PMLs). These absorb out-going waves while not reflecting them at the interface to the physical domain.

5.1 Maxwell's equations in conservation form

While the aforementioned FDTD method uses the Yee-grid [63, 139], the DGTD method [73, 74] uses a finite element mesh. As the first step of the method, only the spatial discretization of the fields on the single elements is considered. Only then the elements are coupled via their interfaces in a second step using an approximation for the flux of the field. Hence, to apply the DGTD method, it requires the equations of motion to be in a conservation law form, i.e.,

$$\underline{\underline{Q}} \cdot \frac{\partial}{\partial t} q(r,t) + \nabla \cdot \underline{\underline{F}}\left(q(r,t)\right) = S(q(r,t),r,t)\,. \tag{5.1}$$

A closer inspection of Maxwell's equations (2.1) for non-dispersive materials shows that one can cast them into this form [73–77] using

$$\underline{\underline{Q}} = \begin{pmatrix} \underline{\underline{\epsilon}}\,(r) & \underline{\underline{0}} \\ \underline{\underline{0}} & \underline{\underline{\mu}}\,(r) \end{pmatrix}\,, \tag{5.2a}$$

$$q(r,t) = \begin{pmatrix} E(r,t) \\ H(r,t) \end{pmatrix} , \tag{5.2b}$$

$$e_i \cdot \underline{\underline{F}}\left(q(r,t)\right) = \begin{pmatrix} -e_i \times H(r,t) \\ e_i \times E(r,t) \end{pmatrix} \tag{5.2c}$$

$$\text{and} \quad S(q(r,t),r,t) = \begin{pmatrix} -j_{\mathrm{f}}(r,t) \\ 0 \end{pmatrix} . \tag{5.2d}$$

To handle dispersive material models (cf. Chapter 3), we expand the field vector q with auxiliary fields (see Section 5.5), which then couple back either over the flux $\underline{\underline{F}}$ or source term S, e.g., via a polarization current, into the E- and H-field components. Despite the field vector extension, the discretization scheme does not change. Thus, we present it for the basic Maxwell's equations first.

5.2 Discretization and local solutions

For all numerical computations, the electromagnetic fields are captured in a finite volume, the computational domain. It contains all the essential physical features, i.e., regions containing different materials. This domain is decomposed into a tessellation of different sized and potentially different shaped elements. It forms a mesh. Within this thesis, only two-dimensional triangular and three-dimensional tetrahedral meshes are considered. As mesh generation is a research area on its own, we here rely on open-source software. We use both gmsh [140] and Netgen [141] for the mesh generation, in which you can use constructive solid geometry to define different regions and contours to be meshed. Fig. 5.1 shows examples for both a two- and three-dimensional mesh, including a cylindrical or spherical scatterer contained in a finite volume, respectively. Furthermore, this volume is subdivided by contours and regions to apply both field sources and BCs.

First, we consider the solution of Maxwell's equations (5.1) on a single element Δ_k. We assume that the fields can be approximated numerically by expansion into a set of basis functions Ψ_i:

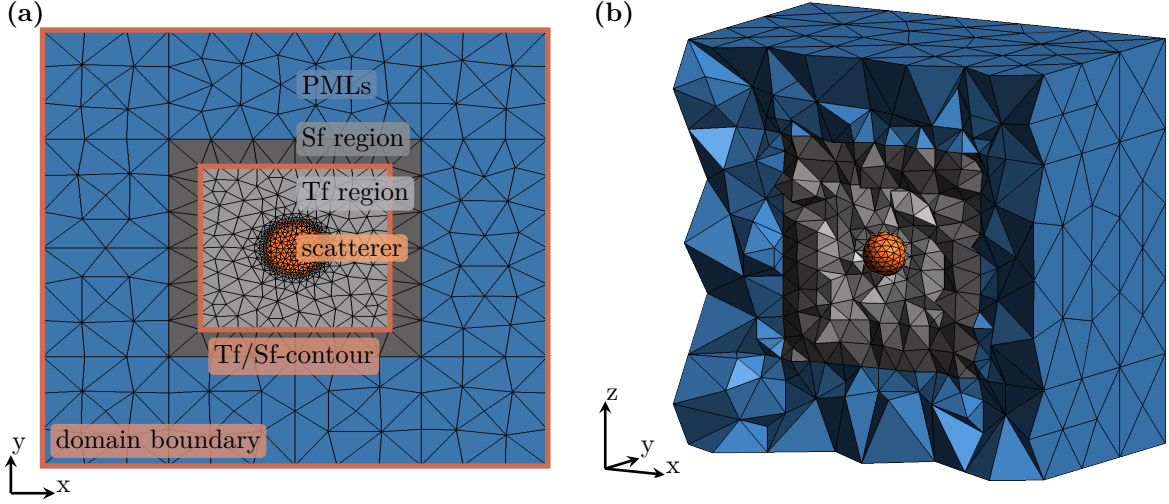$$q\left(r,t\right) \approx q_N\left(r,t\right) = \sum_i \tilde{q}_i^{(k)}\left(t\right) \Psi_i\left(r\right) \quad \text{for} \quad r \in \Delta_k . \tag{5.3}$$

To solve Maxwell's equations (5.1) one then requires that the residual term

$$\underline{\underline{Q}} \cdot \frac{\partial}{\partial t} q_N(r,t) + \nabla \cdot \underline{\underline{F}}\left(q_N(r,t)\right) - S(r,t) = \mathbf{res}\left(r,t\right) \tag{5.4}$$

is orthogonal to a given set of test-functions Φ_j, i.e.,

$$\int_{\Delta_k} \mathrm{d}^d r \, \Phi_j\left(r\right) \cdot \left[\underline{\underline{Q}} \cdot \frac{\partial}{\partial t} q_N(r,t) + \nabla \cdot \underline{\underline{F}}\left(q_N(r,t)\right) - S(r,t) \right] = \int_{\Delta_k} \mathrm{d}^d r \, \Phi_j\left(r\right) \cdot \mathbf{res}\left(r,t\right) \overset{!}{=} 0 . \tag{5.5}$$

Figure 5.1: Example meshes of a **(a)** two-dimensional cylindrical and **(b)** three-dimensional spherical scatterer contained in a box volume. The surrounding volume is subdivided into scattered field (Sf) and total field (Tf) regions and includes PMLs as the outer boundary layer.

Within a Galerkin method, the test functions are chosen to agree with the basis functions $\boldsymbol{\Phi}_i = \boldsymbol{\Psi}_i$. Inserting the field expansion Eq. (5.3), we obtain a set of ordinary differential equations (ODEs) for the time-dependent field expansion coefficients $\tilde{\boldsymbol{q}}^{(k)}(t)$. For the i-th coefficient, the ODE reads

$$\partial_t \tilde{q}_i^{(k)}(t) = -\sum_{j=1}^{6N} \int_{\Delta_k} \mathrm{d}^d r\, \boldsymbol{\Psi}_i \cdot \underline{\underline{\boldsymbol{Q}}}^{-1} \cdot \left[\boldsymbol{\nabla} \cdot \underline{\underline{\boldsymbol{F}}} \left(\tilde{\boldsymbol{q}}^{(k)}(t), \boldsymbol{r}, t \right) \right] \cdot \boldsymbol{\Psi}_j\, \tilde{q}_j^{(k)}(t)$$

$$+ \int_{\Delta_k} \mathrm{d}^d r\, \boldsymbol{\Psi}_i(\boldsymbol{r}) \cdot \underline{\underline{\boldsymbol{Q}}}^{-1} \cdot \boldsymbol{S}(\boldsymbol{r}, t)\,. \tag{5.6}$$

Here, we assume the material tensor $\underline{\underline{\boldsymbol{Q}}}$ to be spatially constant on each element. The resulting set of ODEs is numerically solved by using a Runge-Kutta method [129] for numerical integration. More precisely, for all DGTD computations carried out in this thesis, we use an implementation of a fourth-order 14-stage low-storage Runge-Kutta solver [142]. The default initial condition for the electromagnetic field is $\tilde{\boldsymbol{q}}^{(k)}(t=0) = \boldsymbol{0}$. It ensures that Maxwell's divergence equations (2.1a) and (2.1b) are fulfilled at the beginning and therefore throughout the entire field simulation (s. Section 2.4). Nevertheless, we still need to address how to couple the individual elements across their common boundary and, most importantly, the choice of basis functions used for this spatial discretization.

5.2.1 Lagrange polynomial basis

Within the DGTD implementation, we choose a set of N Lagrange polynomial basis functions $L_i(\boldsymbol{r})$ for each of the six field components. Hence, the basis functions $\boldsymbol{\Psi}$ are of the form

$$\boldsymbol{\Psi}_{i\in[1,N]} = \begin{pmatrix} L_i(\boldsymbol{r}) \\ 0 \\ 0 \\ 0 \\ 0 \\ 0 \end{pmatrix}, \boldsymbol{\Psi}_{i\in[N+1,2N]} = \begin{pmatrix} 0 \\ L_{i-N}(\boldsymbol{r}) \\ 0 \\ 0 \\ 0 \\ 0 \end{pmatrix}, \boldsymbol{\Psi}_{i\in[2N+1,3N]} = \begin{pmatrix} 0 \\ 0 \\ L_{i-2N}(\boldsymbol{r}) \\ 0 \\ 0 \\ 0 \end{pmatrix}, \dots \quad (5.7)$$

and span a $6N$-dimensional polynomial vector space

$$V_{\boldsymbol{\Psi}}^{\Delta_k} = \mathrm{span}\left\{\boldsymbol{\Psi}_i\left(\boldsymbol{r}\in\Delta_k\right) : i \in \left\{1, 6N\right\}\right\} \quad (5.8)$$

on each element Δ_k. The Lagrange polynomials themselves are determined by a set of interpolation points within the element Δ_k by their defining condition

$$L_i(\boldsymbol{r}_j) = \delta_{ij}. \quad (5.9)$$

This gives rise to a *nodal* scheme, in which the field expansion coefficients $\tilde{q}_i^{(k)}$ take the same value as the field at the corresponding interpolation point $\boldsymbol{r}_i$ on the element. The contrary would be a *modal* scheme, for which only the entire sum of expansion coefficients weighted by the basis functions return the corresponding field values.

On one-dimensional elements, i.e., line segments, the Lagrange polynomials of order p are defined by a set of distinct interpolation points $\left\{x_i, i = [0, p]\right\}$ with

$$L_j(x) = \prod_{\substack{i=0 \\ i\neq j}}^{p} \frac{x - x_i}{x_j - x_i}. \quad (5.10)$$

However, there is no easy definition on higher dimensional elements. Hence, one uses a different polynomial basis $\left\{\psi_i, i = [1, N]\right\}$, which would give rise to a modal scheme and then transforms it into the Lagrange polynomial basis. The transformation

$$L_i(\boldsymbol{r}) = \sum_{j=1}^{N} \left(\hat{\mathbf{V}}^{\mathrm{T}}\right)^{-1}_{ij} \psi_j(\boldsymbol{r}) \quad (5.11)$$

is defined by the inverse of the transformation matrix $\hat{\mathbf{V}}$, a generalized Vandermonde matrix [73], with elements

$$\hat{\mathbf{V}}_{ij} = \psi_j(\boldsymbol{r}_i). \quad (5.12)$$

Here, $\boldsymbol{r}_i$ are the interpolation points defining the set of Lagrange polynomials. As this definition
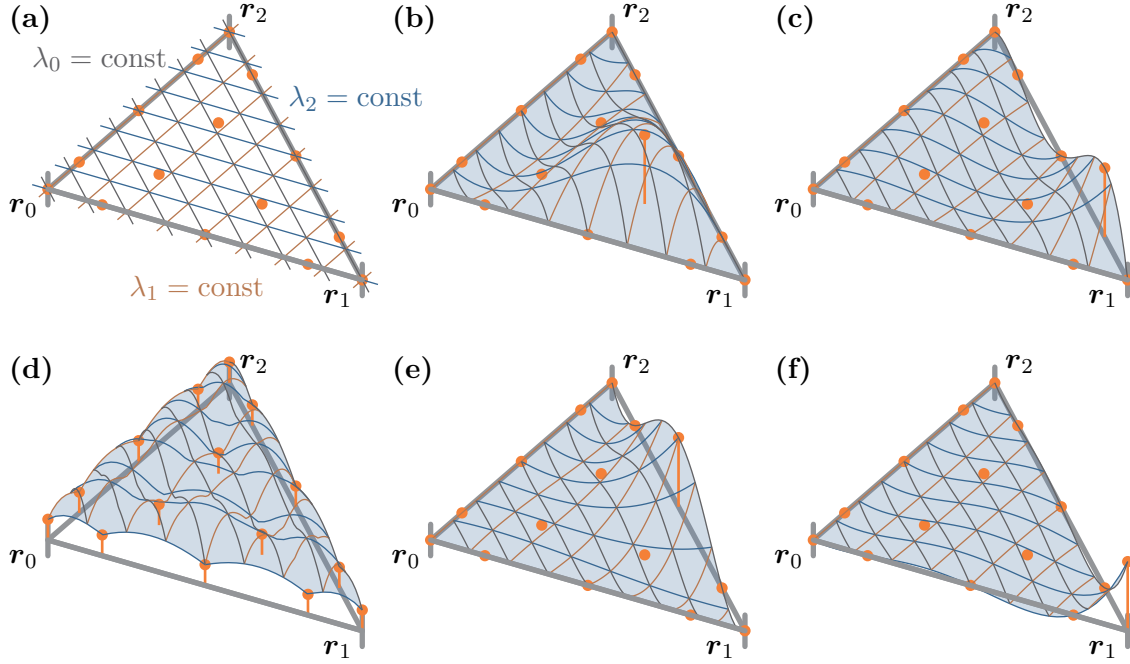
Figure 5.2: (a) Barycentric coordinates $\boldsymbol{\lambda}$ defined on a triangle. Orange dots mark the position of fourth-order Lagrange polynomial *warp & blend* nodes. **(b,c,e,f)** Examples for different fourth-order Lagrange polynomials defined by the node set. Each polynomial is 1 at one and 0 at all other nodes. **(d)** Lebesgue constant $\Lambda(\boldsymbol{\lambda})$ (s. Eq. (5.25)) for the given node set.

involves the inverse of the Vandermonde matrix the natural choice for $\{\psi_i\}$ as monomials up to order p [75], i.e.,

$$\psi_i^{2D}(\boldsymbol{r}) = x^{k_i} y^{l_i} \qquad \text{with} \quad 0 \le k_i + l_i \le p, \qquad i \in \left[1, N = \frac{(p+1)(p+2)}{2}\right], \tag{5.13}$$

$$\psi_i^{3D}(\boldsymbol{r}) = x^{k_i} y^{l_i} z^{m_i} \quad \text{with} \quad 0 \le k_i + l_i + m_i \le p, \quad i \in \left[1, N = \frac{(p+1)(p+2)(p+3)}{6}\right], \tag{5.14}$$

is unsuitable. For high polynomial orders p, the Vandermonde matrix becomes more and more ill-conditioned, as its condition number grows exponentially [143]. Instead of a monomial basis, a set of orthogonal polynomials on triangles and tetrahedra, the Koornwinder-Dubiner polynomials [144, 145] are used. To define the polynomials for each element, we introduce a coordinate transformation

$$\bar{\boldsymbol{r}} = \hat{\mathbf{A}} \cdot (\boldsymbol{r} - \boldsymbol{r}_0) \tag{5.15}$$

onto a reference triangle or tetrahedron. Both in two and three dimensions the element Δ_k can

be mapped onto a reference element with corner vertices

$$\bar{r}_0 = \begin{pmatrix} 0 \\ 0 \end{pmatrix}, \quad \bar{r}_1 = \begin{pmatrix} 1 \\ 0 \end{pmatrix} \quad \text{and} \quad \bar{r}_2 = \begin{pmatrix} 0 \\ 1 \end{pmatrix}, \tag{5.16}$$

for the triangle and

$$\bar{r}_0 = \begin{pmatrix} 0 \\ 0 \\ 0 \end{pmatrix}, \quad \bar{r}_1 = \begin{pmatrix} 1 \\ 0 \\ 0 \end{pmatrix}, \quad \bar{r}_2 = \begin{pmatrix} 0 \\ 1 \\ 0 \end{pmatrix} \quad \text{and} \quad \bar{r}_3 = \begin{pmatrix} 0 \\ 0 \\ 1 \end{pmatrix}, \tag{5.17}$$

for the tetrahedron. Correspondingly, the transformation matrices in two and three dimensions read

$$\hat{\mathbf{A}} = \left(r_1 - r_0, r_2 - r_0 \right)^{-1} \quad \text{and} \quad \hat{\mathbf{A}} = \left(r_1 - r_0, r_2 - r_0, r_3 - r_0 \right)^{-1}. \tag{5.18}$$

Furthermore, we introduce the barycentric coordinates $\boldsymbol{\lambda}$ on the reference element. Given the dimension D of the simplex, one defines

$$r = \sum_{i=0}^{D} \lambda_i r_i, \quad \text{with the normalization} \quad \sum_{i=0}^{D} \lambda_i = 1, \tag{5.19}$$

where r_i are the corner vertices of the triangle (see e.g., Fig. 5.2 (a)) or tetrahedron. Here, the barycentric coordinates vary between zero and one within the simplex. The corner r_i is reached when $\lambda_i = 1$ and the opposite face (line or triangle) is reached by $\lambda_i = 0$.

The aforementioned Koornwinder-Dubiner polynomials [144, 145] are defined with respect to these barycentric coordinates

$$\psi_{kl}^{2D}(r) = \frac{1}{\sqrt{(2l+1)(2l+2k+2)}} P_l^{(0,0)}\left(\frac{2\lambda_1}{1-\lambda_0} - 1\right) (1-\lambda_0)^l P_k^{(2l+1,0)}\left(2\lambda_0 - 1\right), \tag{5.20}$$

$$\psi_{kln}^{3D}(r) = \frac{1}{\sqrt{(2n+1)(2n+2l+2)(2k+2n+2l+3)}} P_n^{(0,0)}\left(2\frac{\lambda_2}{1-\lambda_0-\lambda_1} - 1\right) \left(\frac{1-\lambda_0-\lambda_1}{1-\lambda_0}\right)^n$$

$$\cdot P_l^{(2n+1,0)}\left(2\frac{\lambda_1}{1-\lambda_0} - 1\right) (1-\lambda_0)^{n+l} P_k^{(2n+2l+2,0)}\left(2\lambda_0 - 1\right). \tag{5.21}$$

As the polynomials incorporate the Jacobi polynomials [146], which are orthogonal with respect to the inner product

$$\int_{-1}^{1} \mathrm{d}x\, (1-x)^\alpha (1+x)^\beta P_n^{(\alpha,\beta)} P_m^{(\alpha,\beta)} = \frac{2^{\alpha+\beta+1}}{2n+\alpha+\beta+1} \frac{\Gamma\left(n+\alpha+1\right)\Gamma\left(n+\beta+1\right)}{\Gamma\left(n+\alpha+\beta+1\right)\Gamma\left(n+1\right)} \delta_{nm}, \tag{5.22}$$

the Koornwinder-Dubiner polynomials are orthonormal with respect to the products

$$\int_\Delta \mathrm{d}^2 r \, \psi_{kl}^{\mathrm{2D}}\left(\boldsymbol{r}\right) \psi_{nm}^{\mathrm{2D}}\left(\boldsymbol{r}\right) = \int_0^1 \mathrm{d}\lambda_0 \int_0^{1-\lambda_0} \mathrm{d}\lambda_1 \, \psi_{kl}^{\mathrm{2D}}\left(\boldsymbol{\lambda}\right) \psi_{nm}^{\mathrm{2D}}\left(\boldsymbol{\lambda}\right) = \delta_{kn}\delta_{lm} \tag{5.23}$$

and $\quad \displaystyle\int_\Delta \mathrm{d}^3 r \, \psi_{kln}^{\mathrm{3D}}\left(\boldsymbol{r}\right) \psi_{mop}^{\mathrm{3D}}\left(\boldsymbol{r}\right) = \int_0^1 \mathrm{d}\lambda_0 \int_0^{1-\lambda_0} \mathrm{d}\lambda_1 \int_0^{1-\lambda_0-\lambda_1} \mathrm{d}\lambda_2 \psi_{kln}^{\mathrm{3D}}\left(\boldsymbol{\lambda}\right) \psi_{mop}^{\mathrm{3D}}\left(\boldsymbol{\lambda}\right) = \delta_{km}\delta_{lo}\delta_{np} \,.$

$$\tag{5.24}$$

These polynomials address the problem of the ill-conditioned Vandermonde matrix contained in the transformation into the Lagrange polynomial basis set in Eq. (5.11). However, there is still the freedom to choose the actual interpolation points (nodes) $\boldsymbol{r}_j$ defining the Lagrange polynomial basis set by Eq. (5.9). In the implementation of the DGTD method, we use the *warp & blend* nodes presented by T. Warburton in [147]. They are chosen such that they all lie within the element Δ and minimize the Lebesgue constant

$$\Lambda_p = \max_{\boldsymbol{\lambda}\in\Delta} \sum_{i=1}^{N} \left|L_i\left(\boldsymbol{\lambda}\right)\right| := \max_{\boldsymbol{\lambda}\in\Delta} \Lambda\left(\boldsymbol{\lambda}\right) \,, \tag{5.25}$$

in good approximation. This minimizes the overall spatial discretization error [73, 147]. Fig. 5.2 shows the nodes and example Lagrange basis functions on a triangle for polynomial order $p = 4$. Note that the *warp & blend* nodes follow a D_3 symmetry if the element was transformed into an equilateral triangle. Accordingly, Fig. 5.2 (b)-(f) only show those polynomials which are distinct under affine and symmetry transformation. Fig. 5.2 (d) shows the outline of the Lebesgue constant $\Lambda\left(\boldsymbol{\lambda}\right)$. As on the single nodes, it evaluates to $\Lambda = 1$, the maxima lie in between the *warp & blend* nodes and are located such that all the maxima approximately have the same value.

5.3 Element coupling with the numerical flux

So far only the local solution on a single element Δ_k was outlined in Eq. (5.6). To provide a coupling between two neighboring elements, we employ the flux term within Eq. (5.5). Integration by parts results in an integral over the element surface $\partial\Delta_k$ with normal vector $\boldsymbol{n}(\boldsymbol{r})$ pointing outwards:

$$\int_{\Delta_k} \mathrm{d}^d r \, \boldsymbol{\Psi}_j\left(\boldsymbol{r}\right) \cdot \left[\underline{\underline{\boldsymbol{Q}}} \cdot \frac{\partial}{\partial t} \boldsymbol{q}_N(\boldsymbol{r},t) - \boldsymbol{S}(\boldsymbol{r},t)\right] - \sum_{i=1}^{d} \boldsymbol{e}_i \cdot \underline{\underline{\boldsymbol{F}}}\left(\boldsymbol{q}_N(\boldsymbol{r},t)\right) \cdot \partial_i \boldsymbol{\Psi}_j$$

$$= -\int_{\partial\Delta_k} \mathrm{d}^{d-1} r \, \boldsymbol{\Psi}_j\left(\boldsymbol{r}\right) \cdot \left[\boldsymbol{n}\left(\boldsymbol{r}\right) \cdot \underline{\underline{\boldsymbol{F}}}\left(\boldsymbol{q}_N(\boldsymbol{r},t)\right)\right] \,. \tag{5.26}$$

Within the surface integral the flux is replaced with an approximate flux

$$\underline{\underline{\boldsymbol{F}}}\left(\boldsymbol{q}_N\left(\boldsymbol{r},t\right)\right) \to \underline{\underline{\boldsymbol{F}}}^*\left(\boldsymbol{q}_N\left(\boldsymbol{r},t\right)\right) \,, \tag{5.27}$$

the so-called numerical flux $\underline{\underline{F}}^*$ [73, 74]. Reversing the integration by parts results in the strong form of Maxwell's equations

$$\int_{\Delta_k} \mathrm{d}^d r\, \boldsymbol{\Psi}_j\left(\boldsymbol{r}\right) \cdot \left[\underline{\underline{Q}} \cdot \frac{\partial}{\partial t} \boldsymbol{q}_N(\boldsymbol{r},t) + \boldsymbol{\nabla} \cdot \underline{\underline{F}}\left(\boldsymbol{q}_N(\boldsymbol{r},t)\right) - \boldsymbol{S}(\boldsymbol{r},t)\right]$$
$$= \int_{\partial\Delta_k} \mathrm{d}^{d-1} r\, \boldsymbol{\Psi}_j\left(\boldsymbol{r}\right) \cdot \left[\boldsymbol{n}\left(\boldsymbol{r}\right) \cdot \left(\underline{\underline{F}}\left(\boldsymbol{q}_N(\boldsymbol{r},t)\right) - \underline{\underline{F}}^*\left(\boldsymbol{q}_N(\boldsymbol{r},t)\right)\right)\right]. \tag{5.28}$$

Here, the integral over the element's surface $\partial\Delta_k$ guarantees the coupling to the neighboring element, as the numerical flux $\underline{\underline{F}}^*\left(\boldsymbol{q}_N(\boldsymbol{r},t)\right)$ involves the field expansion also on the neighboring element. Therefore, we extend the numerical approximation of the fields Eq. (5.3) to all N_Δ elements within the computational domain:

$$\boldsymbol{q}\left(\boldsymbol{r},t\right) \approx \boldsymbol{q}_N\left(\boldsymbol{r},t\right) = \sum_{k=1}^{N_\Delta} \sum_{i=1}^{N_p} \tilde{q}_i^{(k)}(t) \boldsymbol{\Psi}_i^{(k)}\left(\boldsymbol{r}\right), \quad \text{where} \quad \boldsymbol{\Psi}_i^{(k)} = \begin{cases} \boldsymbol{\Psi}_i\left(\boldsymbol{r}\right) & \text{for} \quad \boldsymbol{r} \in \Delta_k, \\ \boldsymbol{0} & \text{for} \quad \boldsymbol{r} \notin \Delta_k. \end{cases} \tag{5.29}$$

Correspondingly, Maxwell's equations for non-dissipative media in discretized form are determined by the ODEs

$$\partial_t \tilde{\boldsymbol{q}}(t) = \hat{\mathbf{H}} \cdot \tilde{\boldsymbol{q}}(t) + \tilde{\boldsymbol{S}}(t). \tag{5.30}$$

Here, the $N_p \cdot N_\Delta$ element-wise ordered field expansion coefficients are

$$\tilde{\boldsymbol{q}}_j(t) = \tilde{q}_i^{(k)}(t), \quad \text{with} \quad i = \left(j \bmod N_p\right) + 1, \quad \text{and} \quad k = \left\lceil \frac{j}{N_\Delta} \right\rceil, \tag{5.31}$$

as respective base function and element indices. The field expansion coefficients $\tilde{\boldsymbol{q}}$ describe the field in the entire computational domain. While the source term $\tilde{\boldsymbol{S}}$ is contributing only element-wise (cf. Eq. (5.6)), the matrix $\hat{\mathbf{H}}$ includes both the in-element flux as well as the coupling to the neighboring elements with the numerical flux. Thus the matrix $\hat{\mathbf{H}}$ has a block form, with element self-coupling $\hat{\mathbf{H}}^{(k)}$ on the diagonal and the coupling between the elements $\hat{\mathbf{H}}^{(k,k')}$ in the off-diagonal entries. The on-element matrix takes the form

$$\hat{\mathbf{H}}^{(k)} = \left[\hat{\mathbf{M}}^{(k)}\right]^{-1} \cdot \sum_l \hat{\mathbf{D}}_l^{(k)} \cdot \left[e_l \cdot \underline{\underline{F}}\left(\tilde{\boldsymbol{q}}^{(k)}\right)\right]. \tag{5.32}$$

Here, we define the on-element mass matrix

$$\hat{\mathbf{M}}_{ij}^{(k)} = \int_{\Delta_k} \mathrm{d}^d r\, \boldsymbol{\Psi}_i^{(k)}(\boldsymbol{r}) \cdot \underline{\underline{Q}}^{(k)} \cdot \boldsymbol{\Psi}_j^{(k)}(\boldsymbol{r}). \tag{5.33}$$

It assumes the material tensor $\underline{\underline{Q}}^{(k)}$ to be constant on the single element. Furthermore, we define

the l-th Cartesian component of the differentiation matrix

$$\hat{\mathbf{D}}_{l,ij}^{(k)} = \int_{\Delta_k} \mathrm{d}^d r \, \boldsymbol{\Psi}_i^{(k)}(\boldsymbol{r}) \partial_l \boldsymbol{\Psi}_j^{(k)}(\boldsymbol{r}), \quad \text{with} \quad l \in \{x, y, z\}. \tag{5.34}$$

Here, the flux $\boldsymbol{e}_l \cdot \underline{\underline{\boldsymbol{F}}}$ projected on the l-th Cartesian direction is already interpolated using the same Lagrange polynomial basis. This means, that the vectorial object $\boldsymbol{e}_l \cdot \underline{\underline{\boldsymbol{F}}}$ for the first N entries accounts only for the E_x-field component, the second N entries for the E_y-field component, etc. Due to the nodal scheme, the flux is computed locally for each node and only depends on the field expansion coefficients $\tilde{\boldsymbol{q}}^{(k)}$ on the element itself.

The off-diagonal terms $\hat{\mathbf{H}}^{(k,k')}$ of the overall matrix $\hat{\mathbf{H}}$ are purely defined by the numerical flux. It is

$$\hat{\mathbf{H}}^{(k,k')} = \left[\hat{\mathbf{M}}^{(k)}\right]^{-1} \cdot \hat{\mathbf{I}}^{(k,k')} \cdot \left[\boldsymbol{n}^{(k,k')} \cdot \underline{\underline{\boldsymbol{F}}}\left(\tilde{\boldsymbol{q}}^{(k)}\right) - \boldsymbol{n}^{(k,k')} \cdot \underline{\underline{\boldsymbol{F}}}^*\left(\tilde{\boldsymbol{q}}^{(k)}, \tilde{\boldsymbol{q}}^{(k')}\right)\right]. \tag{5.35}$$

Here, $\hat{\mathbf{M}}^{(k)}$ is the mass matrix of the element Δ_k from above and

$$\hat{\mathbf{I}}_{ij}^{(k,k')} = \int_{\partial\Delta_k \cap \partial\Delta_{k'}} \mathrm{d}^{d-1} r \, \boldsymbol{\Psi}_i^{(k)}(\boldsymbol{r}) \cdot \boldsymbol{\Psi}_j^{(k)}(\boldsymbol{r}), \tag{5.36}$$

is the face mass matrix on the surface between the element Δ_k and its neighboring element $\Delta_{k'}$. Furthermore, $\boldsymbol{n}^{(k,k')}$ is the normal vector of the associated interface and points from the element Δ_k into the neighboring element $\Delta_{k'}$. Moreover, the flux terms $\boldsymbol{n}^{(k,k')} \cdot \underline{\underline{\boldsymbol{F}}}$ and $\boldsymbol{n}^{(k,k')} \cdot \underline{\underline{\boldsymbol{F}}}^*$ have to be understood as already projected onto the element's Lagrange basis functions. Additionally, it is implicitly assumed within the numerical flux, that each element uses the same basis as the neighboring element. This means, that the nodes defining the Lagrange basis on each element coincide on each interface for both elements. Note, that also only the field expansion coefficients on the specific interface do contribute, as the Lagrange basis functions vanish for all nodes which do not lie on the interface (cf. Fig. 5.2 and Eq. (5.9)).

Although the actual form of the numerical flux determines whether we obtain a stable and converging discretization scheme, it is not unique [73]. The easiest form for the numerical flux is given by the central flux. It only includes the average of the local fields on the element's surface ("−"-side) and the same surface shared with the neighboring element ("+"-side). Here, for Maxwell's equations, it has the form

$$\boldsymbol{e}_i \cdot \underline{\underline{\boldsymbol{F}}}^*\left(\boldsymbol{q}\left(\boldsymbol{r},t\right)\right) = \frac{1}{2}\begin{pmatrix} -\boldsymbol{e}_i \times \left(\boldsymbol{H}^-\left(\boldsymbol{r},t\right) + \boldsymbol{H}^+\left(\boldsymbol{r},t\right)\right) \\ \boldsymbol{e}_i \times \left(\boldsymbol{E}^-\left(\boldsymbol{r},t\right) + \boldsymbol{E}^+\left(\boldsymbol{r},t\right)\right) \end{pmatrix}. \tag{5.37}$$

Although this is the easiest form for the numerical flux, it has a disadvantage. For the central flux, the spectrum of $\hat{\mathbf{H}}$ is purely imaginary. Thus, all its modes lie on the stability boundary for the ODE set (cf. Fig. 5.6 (a)).

Therefore, we use another flux within this thesis, which counters this problem. This is the *upwind* flux. For the derivation of the numerical flux following the upwind scheme [73], it is

assumed that the actual fields along the element surface (a line element in two-dimensional and a triangle in three-dimensional setups) only vary slightly along with that interface. However, the fields may be discontinuous from one element to the other. While this behavior is expected on material interfaces, it is not physical at interfaces of elements contained in regions with the same material. Yet, the time-stepping algorithm used to solve the ODE (5.6) may also introduce field discontinuities at such interfaces within the time-scale of a single time-step Δt. The upwind flux takes into account such field discontinuities at the interface by solving the one-dimensional Riemann problem [148, 149] along the normal direction of the interface in question. It remedies unphysical field jumps at every time-step Δt. This is basically achieved by enforcing the correct field BC only for those parts of the fields, which contribute to a flow into the neighboring element. Moreover, the upwind flux damps very high-frequency modes in the field expansion coefficient ODEs (5.30) [73] and stabilizes the DGTD scheme.

5.3.1 The one-dimensional Riemann problem

The one-dimensional Riemann problem solves the time evolution of a field discontinuity across an element interface. Therefore, we introduce the relative interface coordinates as shown in Fig. 5.3.
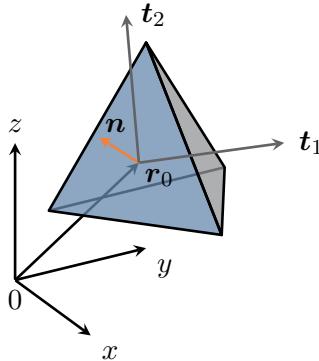
Figure 5.3: Surface triangle of a single tetrahedral element contained in a three-dimensional mesh. The local coordinate system is spanned by the normal vector $\boldsymbol{n}$ and two tangential vectors $\boldsymbol{t}_1$ and $\boldsymbol{t}_2$.

As the numerical flux for a two-dimensional system can be directly inferred from the full three-dimensional one, we only consider triangular interfaces here. Given the normal-vector

$$\boldsymbol{n}\left(\boldsymbol{r}_0\right) = \boldsymbol{n} = n_x \boldsymbol{e}_x + n_y \boldsymbol{e}_y + n_z \boldsymbol{e}_z \,, \tag{5.38}$$

of the surface for a given point $\boldsymbol{r}_0$, we can locally construct two surface tangential vectors $\boldsymbol{t}_1\left(\boldsymbol{r}_0\right)$ and $\boldsymbol{t}_2\left(\boldsymbol{r}_0\right)$, such that

$$\boldsymbol{n} = \boldsymbol{t}_1 \times \boldsymbol{t}_2 \quad \text{and} \quad \boldsymbol{n} \cdot \boldsymbol{t}_1 = \boldsymbol{n} \cdot \boldsymbol{t}_2 = \boldsymbol{t}_1 \cdot \boldsymbol{t}_2 = 0 \,. \tag{5.39}$$

Introducing the local coordinates (n, t_1, t_2) on our triangular surface, we have

$$\boldsymbol{r} = n\,\boldsymbol{n}\,(\boldsymbol{r}_0) + t_1\,\boldsymbol{t}_1\,(\boldsymbol{r}_0) + t_2\,\boldsymbol{t}_2\,(\boldsymbol{r}_0) + \boldsymbol{r}_0\,, \tag{5.40}$$

or for a given point $\boldsymbol{r} = (x, y, z)^{\mathrm{T}}$:

$$n = \boldsymbol{n}\,(\boldsymbol{r}_0)\cdot[\boldsymbol{r}-\boldsymbol{r}_0]\,, \quad t_1 = \boldsymbol{t}_1\,(\boldsymbol{r}_0)\cdot[\boldsymbol{r}-\boldsymbol{r}_0]\,, \quad t_2 = \boldsymbol{t}_2\,(\boldsymbol{r}_0)\cdot[\boldsymbol{r}-\boldsymbol{r}_0]\,. \tag{5.41}$$

Since this coordinate transformation only involves a translation and rotation, the divergence operator acting on a vector-field $\boldsymbol{f}$ is

$$\nabla\cdot\boldsymbol{f} = \nabla_T\cdot\boldsymbol{f} + \boldsymbol{n}\cdot\frac{\partial}{\partial n}\boldsymbol{f}\,, \tag{5.42}$$

where the tangential derivatives are given by

$$\nabla_T\cdot\boldsymbol{f} = \boldsymbol{t}_1\cdot\partial_{t_1}\boldsymbol{f} + \boldsymbol{t}_2\cdot\partial_{t_1}\boldsymbol{f}\,. \tag{5.43}$$

The electromagnetic field $\boldsymbol{q}$ is assumed to vary slowly in tangential direction on the element interface, i.e.,

$$\nabla_T\cdot\underline{\underline{\boldsymbol{F}}}\Big(\boldsymbol{q}\,(\boldsymbol{r},t)\Big) = \boldsymbol{0}\,. \tag{5.44}$$

Hence, Maxwell's equations (5.1) in conservation form turn into

$$\underline{\underline{\boldsymbol{Q}}}\cdot\partial_t\boldsymbol{q}\,(\boldsymbol{r},t) + \boldsymbol{n}\cdot\partial_n\underline{\underline{\boldsymbol{F}}}\Big(\boldsymbol{q}\,(\boldsymbol{r},t)\Big) = \boldsymbol{0}\,, \tag{5.45}$$

on the element interface. For the derivation of the numerical flux, we are neglecting the source terms. While volumetric sources are accounted for within the single element discretization (cf. Eq. (5.6)), there still can be surface currents, which would change the field boundary conditions. As this current sheet technique [87, 117, 150] is not used within this thesis, the entire source term is set to zero here.

For the derivation of the numerical flux, we further assume, that at the beginning of the time-step Δt, the fields $\boldsymbol{q}_0$ near the surface are discontinuous, but are otherwise constant in $\boldsymbol{n}$-direction, i.e.,

$$\boldsymbol{q}_0(n, t_1, t_2, t) = \boldsymbol{q}^-\,(t_1, t_2, t)\,\Theta(-n) + \boldsymbol{q}^+\,(t_1, t_2, t)\,\Theta(n)\,. \tag{5.46}$$

As the conservation form of Eq. (5.45) with parametrically fixed tangential coordinates t_1 and t_2 is a one-dimensional hyperbolic partial differential equation (PDE) of the form

$$\partial_t\boldsymbol{q}\,(n, t) + \hat{\mathbf{A}}\cdot\partial_n\boldsymbol{q}\,(n, t) = \boldsymbol{0}\,, \tag{5.47}$$

the solution for the fields $\boldsymbol{q}\,(\boldsymbol{r}, t + \Delta t)$ is the standard solution of the one-dimensional Riemann

problem [148, 149]. Here, the matrix $\hat{\mathbf{A}}$ is defined by

$$\hat{\mathbf{A}}(n) = \underline{\underline{\boldsymbol{Q}}}^{-1}(n) \cdot \begin{pmatrix} \hat{\mathbf{0}} & -\hat{\mathbf{N}}^\times \\ \hat{\mathbf{N}}^\times & \hat{\mathbf{0}} \end{pmatrix}, \quad \text{where} \quad \hat{\mathbf{N}}^\times = \begin{pmatrix} 0 & n_z & n_y \\ n_z & 0 & -n_x \\ -n_y & n_x & 0 \end{pmatrix}, \tag{5.48}$$

for Maxwell's equations where the matrix $\hat{\mathbf{N}}^\times$ stems from the curl operators. From the Riemann problem solution, we infer the numerical upwind flux.
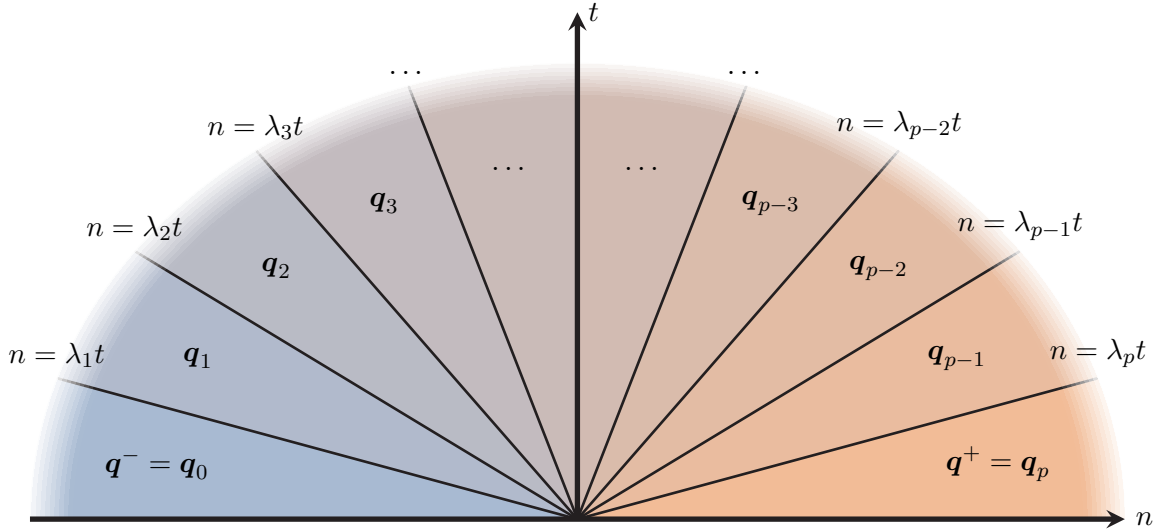
Figure 5.4: Sketched solution of a one-dimensional Riemann problem Eq. (5.47). Initially, the field $\boldsymbol{q}$ is discontinuous on the left $\boldsymbol{q}^-$ and right side $\boldsymbol{q}^+$. The field splits in up to p discontinuities at the characteristics $n = \lambda_i t$.

In the general case, we suppose, that the $p \times p$ matrix

$$\hat{\mathbf{A}} = \hat{\mathbf{V}} \cdot \hat{\mathbf{\Lambda}} \cdot \hat{\mathbf{V}}^{-1}, \tag{5.49}$$

is diagonalizable. Here, $\hat{\mathbf{\Lambda}}$ is a diagonal matrix containing the real-valued, sorted eigenvalues $\lambda_1, \ldots, \lambda_p$. This allows us to define the field

$$\boldsymbol{\alpha}(n, t) = \hat{\mathbf{V}}^{-1} \cdot \boldsymbol{q}(n, t). \tag{5.50}$$

The field components α_i obey

$$\partial_t \alpha_i(n, t) + \lambda_i \partial_n \alpha_i(n, t) = 0, \tag{5.51}$$

which is solved by

$$\alpha_i(n, t) = \alpha_i(n - \lambda_i t). \tag{5.52}$$

Hence, each part of the initial condition projected on the corresponding eigenvector contribution propagates with the characteristic velocity λ_i. Given the initial condition on $\boldsymbol{q}_0(n,t)$, we find $p+1$ distinct regions in the n-t-plane, with different field values as depicted in Fig. 5.4. As the field $\boldsymbol{q}(n,t)$ is expanded into the eigenvectors of $\hat{\mathbf{A}}$ with the amplitudes $\boldsymbol{\alpha}(n,t)$, i.e.,

$$\boldsymbol{q}(n,t) = \alpha_1(n,t)\,\boldsymbol{v}_1 + \cdots + \alpha_p(n,t)\,\boldsymbol{v}_p\,, \tag{5.53}$$

passing the i-th characteristic in the n-t-plane, the corresponding field expansion $\boldsymbol{q}(n,t)$ has a jump from the left to the right value in

$$\alpha_i(n < \lambda_i t, t) = \alpha_i^- \quad \rightarrow \quad \alpha_i(n > \lambda_i t, t) = \alpha_i^+\,, \quad \text{with} \quad \boldsymbol{\alpha}^\pm = \hat{\mathbf{V}}^{-1} \cdot \boldsymbol{q}^\pm\,. \tag{5.54}$$

Therefore, the field values in the m-th sector are

$$\boldsymbol{q}^{(m)}(n,t) = \sum_{i=1}^{m} \alpha_i^+(n,t)\,\boldsymbol{v}_i + \sum_{i=m+1}^{p} \alpha_i^-(n,t)\,\boldsymbol{v}_i\,. \tag{5.55}$$

Note, that for $m=0$ and $m=p$ the first and second sum is zero, respectively. Consequently, the field difference of two adjacent regions is given by

$$\boldsymbol{q}^{(m)}(n,t) - \boldsymbol{q}^{(m+1)}(n,t) = \left(\alpha_{m+1}^- - \alpha_{m+1}^+\right)\boldsymbol{v}_{m+1} := -\delta_{m+1}\boldsymbol{v}_{m+1} \quad \text{for} \quad m \in [0, p-1] \tag{5.56}$$

and directly determined by the amplitude differences $\delta_i = \alpha_i^+ - \alpha_i^-$. Applying the matrix $\hat{\mathbf{A}}$ to these equations leads to the well-known Rankine-Hugoniot-conditions [73, 148]

$$\boldsymbol{n} \cdot \underline{\underline{\boldsymbol{F}}}\left(\boldsymbol{q}^{(m)}(n,t)\right) - \boldsymbol{n} \cdot \underline{\underline{\boldsymbol{F}}}\left(\boldsymbol{q}^{(m+1)}(n,t)\right) = \lambda_{m+1}\left(\boldsymbol{q}^{(m)}(n,t) - \boldsymbol{q}^{(m+1)}(n,t)\right)\,. \tag{5.57}$$

They are relating the change in flux with the characteristic speed and field difference. While these conditions can be used to derive a numerical flux directly (cf. [75, 76]), we present a slightly different but yet equivalent approach here. From Eq. (5.56) it follows, that the initial field difference

$$\boldsymbol{q}^{(p)} - \boldsymbol{q}^{(0)} = \hat{\mathbf{V}} \cdot \boldsymbol{\delta} = \boldsymbol{q}^+ - \boldsymbol{q}^-\,, \tag{5.58}$$

directly fixes the amplitude differences by

$$\boldsymbol{\delta} = \hat{\mathbf{V}}^{-1} \cdot \left(\boldsymbol{q}^+ - \boldsymbol{q}^-\right)\,. \tag{5.59}$$

The formal solution of the Riemann problem is therefore given by

$$\boldsymbol{q}(n,t) = \boldsymbol{q}^- + \sum_{i=1}^{p} \Theta\left(n - \lambda_i t\right)\delta_i\boldsymbol{v}_i \tag{5.60}$$

and solely depends on the field values $\boldsymbol{q}^\pm$. The numerical upwind flux $\underline{\underline{\boldsymbol{F}}}^*$ is defined for the

element ("$-$"-side) as

$$\boldsymbol{n} \cdot \underline{\underline{\boldsymbol{F}}}^{*} \Big(\boldsymbol{q}\left(\boldsymbol{r}, t\right) \Big) := \boldsymbol{n} \cdot \underline{\underline{\boldsymbol{F}}} \Big(\boldsymbol{q} \Big(n = 0^{-}, t_1, t_2, t \Big) \Big) \tag{5.61}$$

and its neighboring element ("$+$"-side) as

$$\boldsymbol{n} \cdot \underline{\underline{\boldsymbol{F}}}^{*} \Big(\boldsymbol{q}\left(\boldsymbol{r}, t\right) \Big) := \boldsymbol{n} \cdot \underline{\underline{\boldsymbol{F}}} \Big(\boldsymbol{q} \Big(n = 0^{+}, t_1, t_2, t \Big) \Big) \, . \tag{5.62}$$

Consequently, the upwind flux only accounts for the directional components of the fields flowing into the neighboring element. It requires evaluating the field solution of the Riemann problem at the different sides of the interface boundary $n = 0^{\pm}$.

We define the interface fields as

$$\boldsymbol{q}^{-*}\left(t_1, t_2\right) := \boldsymbol{q} \Big(n = 0^{-}, t_1, t_2, t \Big) \overset{(5.60)}{=} \boldsymbol{q}^{-} + \sum_{\lambda_i \leq 0} \delta_i\left(t_1, t_2\right) \boldsymbol{v}_i\left(t_1, t_2\right) \tag{5.63a}$$

$$\text{and} \quad \boldsymbol{q}^{+*}\left(t_1, t_2\right) := \boldsymbol{q} \Big(n = 0^{+}, t_1, t_2, t \Big) \overset{(5.60)}{=} \boldsymbol{q}^{+} - \sum_{\lambda_i \geq 0} \delta_i\left(t_1, t_2\right) \boldsymbol{v}_i\left(t_1, t_2\right) \, . \tag{5.63b}$$

As the DGTD scheme requires the difference of the actual and the numerical flux (cf. Eq. (5.28)), we have to compute

$$\boldsymbol{n} \cdot \underline{\underline{\boldsymbol{F}}} \Big(\boldsymbol{q} \Big(n = 0^{\pm}, t_1, t_2, t \Big) \Big) - \boldsymbol{n} \cdot \underline{\underline{\boldsymbol{F}}}^{*} \Big(\boldsymbol{q} \Big(n = 0^{\pm}, t_1, t_2, t \Big) \Big)$$

$$\overset{(5.61),(5.62)}{=} \boldsymbol{n} \cdot \underline{\underline{\boldsymbol{F}}} \Big(\boldsymbol{q}^{\pm}\left(t_1, t_2, t\right) - \boldsymbol{q}^{\pm*}\left(t_1, t_2, t\right) \Big) \, , \tag{5.64}$$

where we exploit the linearity of the flux in the fields $\boldsymbol{q}$ for Maxwell's equations. With this, we can derive the numerical upwind flux for anisotropic non-dispersive materials. We basically follow the presentation of Alvarez *et al.* [77] to compute the field differences

$$\boldsymbol{q}^{\pm}\left(t_1, t_2, t\right) - \boldsymbol{q}^{\pm*}\left(t_1, t_2, t\right) \tag{5.65}$$

in the following section.

5.3.2 Upwind flux for non-dispersive anisotropic materials

For the calculation of the numerical upwind flux, we transform the non-dispersive material tensors $\underline{\underline{\boldsymbol{\epsilon}}}$ and $\underline{\underline{\boldsymbol{\mu}}}$ into the local basis $\{\boldsymbol{n}, \boldsymbol{t}_1, \boldsymbol{t}_2\}$. As an example, the permittivity tensor is given in the Cartesian tensor components by

$$\underline{\underline{\boldsymbol{\epsilon}}} = \sum_{x_i, x_j} \epsilon_{x_i x_j} \boldsymbol{e}_{x_i} \otimes \boldsymbol{e}_{x_j} \, , \quad \text{where} \quad x_i, x_j \in \{x, y, z\} \tag{5.66}$$

are Cartesian coordinates. We introduce the local unit vectors $\boldsymbol{e}_{y_i} \in \{\boldsymbol{n}, \boldsymbol{t}_1, \boldsymbol{t}_2\}$, i.e.,

$$\underline{\underline{\epsilon}} = \sum_{y_i, y_j} \tilde{\epsilon}_{y_i y_j} \boldsymbol{e}_{y_i} \otimes \boldsymbol{e}_{y_j}. \tag{5.67}$$

Thus, the tensor components in the surface aligned coordinate frame are related to the Cartesian entries by

$$\tilde{\epsilon}_{y_i y_j} = \sum_{x_i, x_j} \epsilon_{x_i x_j} \boldsymbol{e}_{y_i} \cdot \boldsymbol{e}_{x_i} \boldsymbol{e}_{x_j} \cdot \boldsymbol{e}_{y_j} \quad \Leftrightarrow \quad \hat{\tilde{\epsilon}} = \hat{\mathbf{R}}^{-1} \cdot \hat{\epsilon} \cdot \hat{\mathbf{R}}, \tag{5.68}$$

with the rotation matrix

$$\hat{\mathbf{R}} = \begin{pmatrix} \boldsymbol{n} & \boldsymbol{t}_1 & \boldsymbol{t}_2 \end{pmatrix}, \text{ i.e., } \hat{\mathbf{R}}_{ij} = \boldsymbol{e}_{y_i} \cdot \boldsymbol{e}_{x_j} \text{ and } \hat{\mathbf{R}}^{-1} = \hat{\mathbf{R}}^{\mathrm{T}}. \tag{5.69}$$

Furthermore, we assume that the fields are constant along the tangential directions according to Eq. (5.44), i.e.,

$$\nabla_T \times \boldsymbol{E}(\boldsymbol{r}, t) = \nabla_T \times \boldsymbol{H}(\boldsymbol{r}, t) = \boldsymbol{0}. \tag{5.70}$$

Hence, Maxwell's curl equations, e.g., Eq. (2.1d), on the element's interface are of the form

$$\begin{pmatrix} \epsilon_{nn} & \epsilon_{nt_1} & \epsilon_{nt_2} \\ \epsilon_{t_1 n} & \epsilon_{t_1 t_1} & \epsilon_{t_1 t_2} \\ \epsilon_{t_2 n} & \epsilon_{t_2 t_1} & \epsilon_{t_2 t_2} \end{pmatrix} \cdot \partial_t \begin{pmatrix} E_n \\ E_{t_1} \\ E_{t_2} \end{pmatrix} = \partial_n (\boldsymbol{n} \times \boldsymbol{H}) = \begin{pmatrix} 0 \\ -\partial_n H_{t_2} \\ \partial_n H_{t_1} \end{pmatrix}. \tag{5.71}$$

Thus the normal component of the $\boldsymbol{E}$-field is set by

$$\partial_t E_n = -\frac{1}{\epsilon_{nn}} \left(\partial_t \epsilon_{nt_1} E_{t_1} + \partial_t \epsilon_{nt_2} E_{t_2} \right), \tag{5.72}$$

with which only the field components tangential to the surface contribute to the flux, i.e.,

$$\begin{pmatrix} \epsilon_{t_1 t_1} - \frac{\epsilon_{t_1 n} \epsilon_{nt_1}}{\epsilon_{nn}} & \epsilon_{t_1 t_2} - \frac{\epsilon_{t_1 n} \epsilon_{nt_2}}{\epsilon_{nn}} \\ \epsilon_{t_2 t_1} - \frac{\epsilon_{t_2 n} \epsilon_{nt_1}}{\epsilon_{nn}} & \epsilon_{t_2 t_2} - \frac{\epsilon_{t_2 n} \epsilon_{nt_2}}{\epsilon_{nn}} \end{pmatrix} \cdot \partial_t \begin{pmatrix} E_{t_1} \\ E_{t_2} \end{pmatrix} = \begin{pmatrix} -\partial_n H_{t_2} \\ \partial_n H_{t_1} \end{pmatrix}. \tag{5.73}$$

In analogy, we find the $\boldsymbol{H}$-field time derivatives related to the $\boldsymbol{E}$-field by

$$\begin{pmatrix} \mu_{t_1 t_1} - \frac{\mu_{t_1 n} \mu_{nt_1}}{\mu_{nn}} & \mu_{t_1 t_2} - \frac{\mu_{t_1 n} \mu_{nt_2}}{\mu_{nn}} \\ \mu_{t_2 t_1} - \frac{\mu_{t_2 n} \mu_{nt_1}}{\mu_{nn}} & \mu_{t_2 t_2} - \frac{\mu_{t_2 n} \mu_{nt_2}}{\mu_{nn}} \end{pmatrix} \cdot \partial_t \begin{pmatrix} H_{t_1} \\ H_{t_2} \end{pmatrix} = \begin{pmatrix} \partial_n E_{t_2} \\ -\partial_n E_{t_1} \end{pmatrix}. \tag{5.74}$$

To derive the numerical upwind flux, we need to solve the Riemann-Problem for the four-dimensional PDE

$$\hat{\mathbf{Q}}(n) \cdot \partial_t \boldsymbol{q}(n, t) + \hat{\mathbf{M}}_r \cdot \partial_n \boldsymbol{q}(n, t) = 0, \tag{5.75}$$

where

$$
\hat{\mathbf{Q}} = \begin{pmatrix} \epsilon_{t_1 t_1} - \frac{\epsilon_{t_1 n} \epsilon_{n t_1}}{\epsilon_{nn}} & \epsilon_{t_1 t_2} - \frac{\epsilon_{t_1 n} \epsilon_{n t_2}}{\epsilon_{nn}} & 0 & 0 \\ \epsilon_{t_2 t_1} - \frac{\epsilon_{t_2 n} \epsilon_{n t_1}}{\epsilon_{nn}} & \epsilon_{t_2 t_2} - \frac{\epsilon_{t_2 n} \epsilon_{n t_2}}{\epsilon_{nn}} & 0 & 0 \\ 0 & 0 & \mu_{t_1 t_1} - \frac{\mu_{t_1 n} \mu_{n t_1}}{\mu_{nn}} & \mu_{t_1 t_2} - \frac{\mu_{t_1 n} \mu_{n t_2}}{\mu_{nn}} \\ 0 & 0 & \mu_{t_2 t_1} - \frac{\mu_{t_2 n} \mu_{n t_1}}{\mu_{nn}} & \mu_{t_2 t_2} - \frac{\mu_{t_2 n} \mu_{n t_2}}{\mu_{nn}} \end{pmatrix}
$$

$$
=: \begin{pmatrix} \epsilon_{11} & \epsilon_{12} & 0 & 0 \\ \epsilon_{21} & \epsilon_{22} & 0 & 0 \\ 0 & 0 & \mu_{11} & \mu_{12} \\ 0 & 0 & \mu_{21} & \mu_{22} \end{pmatrix} = \begin{pmatrix} \hat{\boldsymbol{\epsilon}} & \hat{\mathbf{0}} \\ \hat{\mathbf{0}} & \hat{\boldsymbol{\mu}} \end{pmatrix} , \tag{5.76}
$$

$$
\boldsymbol{q} = \begin{pmatrix} E_{t_1} \\ E_{t_2} \\ H_{t_1} \\ H_{t_2} \end{pmatrix} \quad \text{and} \quad \hat{\mathbf{M}}_r = \begin{pmatrix} \hat{\mathbf{0}} & \hat{\mathbf{D}} \\ \hat{\mathbf{D}}^{-1} & \hat{\mathbf{0}} \end{pmatrix} = \begin{pmatrix} 0 & 0 & 0 & 1 \\ 0 & 0 & -1 & 0 \\ 0 & -1 & 0 & 0 \\ 1 & 0 & 0 & 0 \end{pmatrix} . \tag{5.77}
$$

The solution of the Riemann problem requires the characteristics $n = \lambda_i t$ with speeds λ_i defined by Eq. (5.49) as well as the field amplitude differences $\boldsymbol{\delta}$ defined by Eq. (5.59). Hence, we need to find the eigenvalues and eigenvectors of the matrix

$$
\hat{\mathbf{A}} = \hat{\mathbf{Q}}^{-1} \cdot \hat{\mathbf{M}}_r = \begin{pmatrix} \hat{\mathbf{0}} & \hat{\boldsymbol{\epsilon}}^{-1} \cdot \hat{\mathbf{D}} \\ \hat{\boldsymbol{\mu}}^{-1} \cdot \hat{\mathbf{D}}^{-1} & \hat{\mathbf{0}} \end{pmatrix} . \tag{5.78}
$$

Due to the off-diagonal form, we can simplify the eigenvalue calculation with

$$
0 = \det \left(\hat{\mathbf{A}} - \lambda \hat{\mathbf{1}}_4 \right) = \det \left(-\lambda \hat{\mathbf{1}}_2 \right) \det \left(-\lambda \hat{\mathbf{1}}_2 + \lambda^{-1} \hat{\boldsymbol{\mu}}^{-1} \cdot \hat{\mathbf{D}}^{-1} \cdot \hat{\boldsymbol{\epsilon}}^{-1} \cdot \hat{\mathbf{D}} \right) ,
$$

$$
= \det \left(\underbrace{\hat{\boldsymbol{\mu}}^{-1} \cdot \hat{\mathbf{D}}^{-1} \cdot \hat{\boldsymbol{\epsilon}}^{-1} \cdot \hat{\mathbf{D}}}_{=: \hat{\boldsymbol{\Gamma}}} - \lambda^2 \hat{\mathbf{1}}_2 \right) . \tag{5.79}
$$

The resulting biquadratic characteristic polynomial for the eigenvalues λ can, thus, be reduced to the computation of the eigenvalues of a second-order characteristic polynomial for the matrix $\hat{\boldsymbol{\Gamma}}$. Given the eigenvalues and eigenvectors of this 2×2-matrix $\hat{\boldsymbol{\Gamma}}$ and the diagonalization

$$
\hat{\boldsymbol{\Gamma}} = \hat{\mathbf{R}}_\Gamma \cdot \hat{\boldsymbol{\Lambda}} \cdot \hat{\boldsymbol{\Lambda}} \cdot \hat{\mathbf{R}}_\Gamma^{-1} , \tag{5.80}
$$

we directly find the spectral decomposition of $\hat{\mathbf{A}}$, as

$$
\hat{\mathbf{A}} = \hat{\mathbf{V}} \cdot \begin{pmatrix} -\hat{\boldsymbol{\Lambda}} & \hat{\mathbf{0}} \\ \hat{\mathbf{0}} & \hat{\boldsymbol{\Lambda}} \end{pmatrix} \cdot \hat{\mathbf{V}}^{-1} , \tag{5.81}
$$

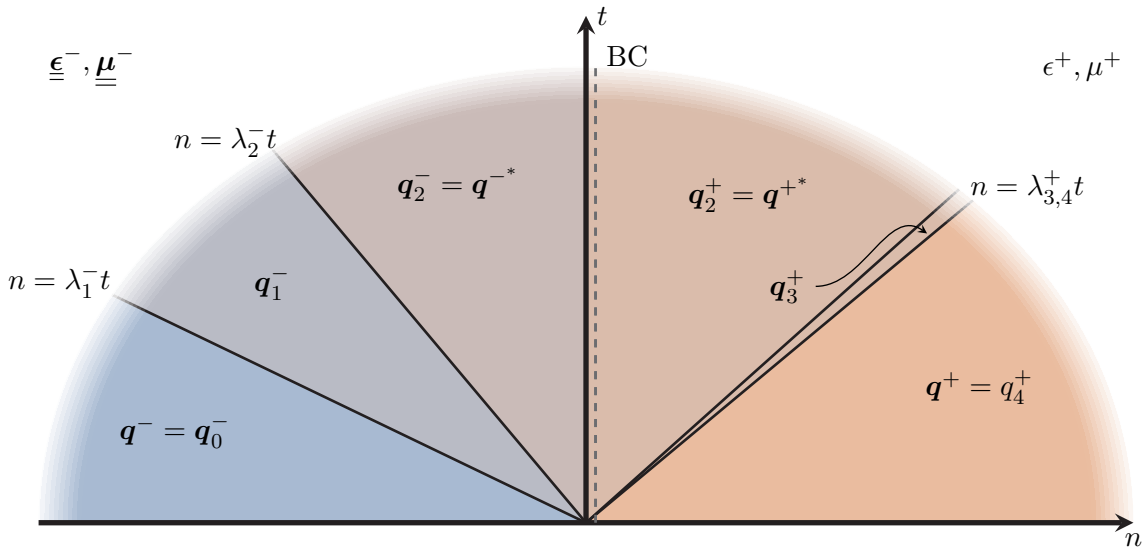where

$$\hat{\mathbf{V}} = \begin{pmatrix} \hat{\boldsymbol{\epsilon}}^{-1} \cdot \hat{\mathbf{D}} \cdot \hat{\mathbf{R}}_\Gamma \cdot \hat{\boldsymbol{\Lambda}}^{-1} & 0 \\ 0 & \hat{\mathbf{R}}_\Gamma \end{pmatrix} \cdot \frac{1}{\sqrt{2}} \begin{pmatrix} -\hat{\mathbf{1}}_2 & \hat{\mathbf{1}}_2 \\ \hat{\mathbf{1}}_2 & \hat{\mathbf{1}}_2 \end{pmatrix} \tag{5.82a}$$

$$\text{and} \quad \hat{\mathbf{V}}^{-1} = \frac{1}{\sqrt{2}} \begin{pmatrix} -\hat{\mathbf{1}}_2 & \hat{\mathbf{1}}_2 \\ \hat{\mathbf{1}}_2 & \hat{\mathbf{1}}_2 \end{pmatrix} \cdot \begin{pmatrix} \hat{\boldsymbol{\Lambda}}^{-1} \cdot \hat{\mathbf{R}}_\Gamma^{-1} \hat{\boldsymbol{\mu}}^{-1} \cdot \hat{\mathbf{D}}^{-1} & 0 \\ 0 & \hat{\mathbf{R}}_\Gamma^{-1} \end{pmatrix} . \tag{5.82b}$$

As a consequence, there are always two positive and two negative characteristic speeds.

Figure 5.5: Sketch of the Riemann problem for a non-dispersive anisotropic material interfacing an isotropic material. Initially, the field $\boldsymbol{q}$ is discontinuous on the left $\boldsymbol{q}^-$ and right side $\boldsymbol{q}^+$. The discontinuities propagate with the characteristic speeds λ_i depending on the polarization components determined in Eq. (5.82) away from the interface at $n = 0$ generating different field value zones. The speed $\lambda_{3,4}^+ = c_0\sqrt{\epsilon^+\mu^+}$ is degenerate. The field BC is enforced on the interface between the fields $\boldsymbol{q}^{-,*}$ and $\boldsymbol{q}^{+,*}$.

So far, we implicitly assumed that the materials do not change when solving the Riemann problem. However within the DGTD method, we allow material interfaces and thus the effective material matrix can jump, i.e.,

$$\hat{\mathbf{Q}}(n) = \hat{\mathbf{Q}}^- \Theta(-n) + \hat{\mathbf{Q}}^+ \Theta(n) . \tag{5.83}$$

In Fig. 5.5 we show an example case for the Riemann problem, in which we couple an anisotropic material on one side to a non-dispersive isotropic one on the other. To obtain the solution to the Riemann problem, we require the fields $\boldsymbol{q}$ to fulfill the correct BC across the element interfaces.

As only the tangential field components

$$\boldsymbol{q} = \begin{pmatrix} E_{t_1} \\ E_{t_2} \\ H_{t_1} \\ H_{t_2} \end{pmatrix}, \tag{5.84}$$

contribute to the flux, the fields

$$\boldsymbol{q}^{+,*} - \boldsymbol{q}^{-,*} \overset{(2.44)}{=} \boldsymbol{0}, \tag{5.85}$$

have to be continuous across the interface. Moreover, there are two characteristics on each side of the interface resulting in two field jumps on each side. For the anisotropic material, these correspond to ordinary and extra-ordinary waves [77]. Consequently, the characteristic velocities are determined by the intersections of the isofrequency contour (IFC) shown in Fig. 3.1 (b) for frequency normalized wave vectors pointing in $\boldsymbol{n}$-direction. For the isotropic case the characteristic velocities $\lambda_{3,4}^+ = \sqrt{\epsilon^+ \mu^+} c_0$, i.e., the in-medium speed of light, are degenerate and the eigenvectors $\boldsymbol{v}_{3,4}^+$ are set by the two allowed polarization directions as in Section 2.7.1. Following the material matrix jump in Eq. (5.83), we obtain the field difference

$$\boldsymbol{q}^+ - \boldsymbol{q}^- = \hat{\mathbf{V}}_\pm \cdot \boldsymbol{\delta}, \tag{5.86}$$

on each side of the interface from the Rankine-Hugoniot conditions Eq. (5.57). Here, the field expansion matrix $\hat{\mathbf{V}}_\pm$ contains the eigenvectors of "$-$"-side and "$+$"-side correspondingly for negative and positive characteristic speeds. It reads

$$\hat{\mathbf{V}}_\pm = \frac{1}{\sqrt{2}} \begin{pmatrix} -\hat{\mathbf{M}}_- & \hat{\mathbf{M}}_+ \\ \hat{\mathbf{1}} & \hat{\mathbf{1}} \end{pmatrix} \cdot \begin{pmatrix} \hat{\mathbf{R}}_{\Gamma,-} & \hat{\mathbf{0}} \\ \hat{\mathbf{0}} & \hat{\mathbf{R}}_{\Gamma,+} \end{pmatrix}, \tag{5.87}$$

where

$$\hat{\mathbf{M}}_\pm \overset{(5.82)}{=} \hat{\boldsymbol{\epsilon}}_\pm^{-1} \cdot \hat{\mathbf{D}} \cdot \hat{\mathbf{R}}_{\Gamma,\pm} \cdot \hat{\mathbf{\Lambda}}_\pm^{-1} \cdot \hat{\mathbf{R}}_{\Gamma,\pm}^{-1}. \tag{5.88}$$

For the numerical flux, we need the fields on the corresponding interface for times $t > 0$, i.e.,

$$\boldsymbol{q}^{-,*} - \boldsymbol{q}_0^- = \delta_1 \boldsymbol{v}_{1,-} + \delta_2 \boldsymbol{v}_{2,-}. \tag{5.89}$$

That means, we need to calculate the Riemann problem amplitudes differences $\boldsymbol{\delta}$ first. The required inverse of the matrix $\hat{\mathbf{V}}_\pm$ is given by

$$\hat{\mathbf{V}}_\pm^{-1} = \sqrt{2} \begin{pmatrix} \hat{\mathbf{R}}_{\Gamma,-}^{-1} & \hat{\mathbf{0}} \\ \hat{\mathbf{0}} & \hat{\mathbf{R}}_{\Gamma,+}^{-1} \end{pmatrix} \cdot \begin{pmatrix} \left(\hat{\mathbf{M}}_+ + \hat{\mathbf{M}}_-\right)^{-1} & \hat{\mathbf{0}} \\ \hat{\mathbf{0}} & \left(\hat{\mathbf{M}}_+ + \hat{\mathbf{M}}_-\right)^{-1} \end{pmatrix} \cdot \begin{pmatrix} -\hat{\mathbf{1}} & \hat{\mathbf{M}}_+ \\ \hat{\mathbf{1}} & \hat{\mathbf{M}}_- \end{pmatrix}. \tag{5.90}$$

We define the tangential field differences at the interface at the beginning of the time step as

$$\Delta \boldsymbol{E}_t := \left(E_{t_1}^+ - E_{t_1}^-\right) \boldsymbol{t}_1 + \left(E_{t_2}^+ - E_{t_2}^-\right) \boldsymbol{t}_2 \, , \tag{5.91a}$$

$$\Delta \boldsymbol{H}_t := \left(H_{t_1}^+ - H_{t_1}^-\right) \boldsymbol{t}_1 + \left(H_{t_2}^+ - H_{t_2}^-\right) \boldsymbol{t}_2 \, , \tag{5.91b}$$

which means

$$\boldsymbol{q}_+ - \boldsymbol{q}_- = \begin{pmatrix} \Delta \boldsymbol{E}_{\mathrm{t}} \\ \Delta \boldsymbol{H}_{\mathrm{t}} \end{pmatrix} . \tag{5.92}$$

Following Eq. (5.59), the amplitude differences of the associated Riemann problem are

$$\boldsymbol{\delta} = \hat{\mathbf{V}}_{\pm}^{-1} \cdot \left(\boldsymbol{q}_+ - \boldsymbol{q}_-\right) = \sqrt{2} \begin{pmatrix} \hat{\mathbf{R}}_{\Gamma,-}^{-1} \cdot \left(\hat{\mathbf{M}}_+ + \hat{\mathbf{M}}_-\right)^{-1} \cdot \left(\hat{\mathbf{M}}_+ \cdot \Delta \boldsymbol{H}_{\mathrm{t}} - \Delta \boldsymbol{E}_{\mathrm{t}}\right) \\ \hat{\mathbf{R}}_{\Gamma,+}^{-1} \cdot \left(\hat{\mathbf{M}}_+ + \hat{\mathbf{M}}_-\right)^{-1} \cdot \left(\hat{\mathbf{M}}_- \cdot \Delta \boldsymbol{H}_{\mathrm{t}} + \Delta \boldsymbol{E}_{\mathrm{t}}\right) \end{pmatrix} . \tag{5.93}$$

The flux difference of actual and numerical flux Eq. (5.64) requires the tangential field difference

$$\boldsymbol{q}^{-,*} - \boldsymbol{q}_0^- = \delta_1 \boldsymbol{v}_{1,-} + \delta_2 \boldsymbol{v}_{2,-} \, . \tag{5.94}$$

This means, we use the first two columns of $\hat{\mathbf{V}}_{\pm}$ and the amplitudes $\boldsymbol{\delta}$. We find

$$
\begin{aligned}
\boldsymbol{q}^{-,*} - \boldsymbol{q}_0^- &= \frac{1}{\sqrt{2}} \begin{pmatrix} -\hat{\mathbf{M}}_- \cdot \hat{\mathbf{R}}_{\Gamma,-} \\ \hat{\mathbf{R}}_{\Gamma,-} \end{pmatrix} \cdot \sqrt{2} \, \hat{\mathbf{R}}_{\Gamma,-}^{-1} \cdot \left(\hat{\mathbf{M}}_+ + \hat{\mathbf{M}}_-\right)^{-1} \cdot \left(\hat{\mathbf{M}}_+ \cdot \Delta \boldsymbol{H}_{\mathrm{t}} - \Delta \boldsymbol{E}_{\mathrm{t}}\right) \\
&= \begin{pmatrix} -\hat{\mathbf{M}}_- \cdot \left(\hat{\mathbf{M}}_+ + \hat{\mathbf{M}}_-\right)^{-1} \cdot \left(\hat{\mathbf{M}}_+ \cdot \Delta \boldsymbol{H}_{\mathrm{t}} - \Delta \boldsymbol{E}_{\mathrm{t}}\right) \\ \left(\hat{\mathbf{M}}_+ + \hat{\mathbf{M}}_-\right)^{-1} \cdot \left(\hat{\mathbf{M}}_+ \cdot \Delta \boldsymbol{H}_{\mathrm{t}} - \Delta \boldsymbol{E}_{\mathrm{t}}\right) \end{pmatrix} .
\end{aligned}
\tag{5.95}
$$

In principle, this sets the flux from the element ("$-$"-side) into its neighboring element ("$+$"-side). The opposite flux term is obtained with a change of sign in the field differences $\Delta \boldsymbol{E}_t$ and $\Delta \boldsymbol{H}_t$ as well as the interchange of the $\pm$-index of the material parameter related matrices. As the DGTD scheme operates not with the tangential but the fully six-dimensional electromagnetic field vector, we cast this flux difference term into a form acting on the entire six-dimensional field vector as assumed in Eq. (5.28). Thus, the flux term is of the form

$$\boldsymbol{n} \cdot \underline{\underline{\boldsymbol{F}}} - \boldsymbol{n} \cdot \underline{\underline{\boldsymbol{F}}}^* = \begin{pmatrix} -\boldsymbol{n} \times \left(\boldsymbol{H}^- - \boldsymbol{H}^{-,*}\right) \\ \boldsymbol{n} \times \left(\boldsymbol{E}^- - \boldsymbol{E}^{-,*}\right) \end{pmatrix} , \tag{5.96}$$

for the given normal vector $\boldsymbol{n}$ of the element interface.

To express the flux in terms of the full initial field differences,

$$\Delta \boldsymbol{E} = \boldsymbol{E}^+ - \boldsymbol{E}^- \quad \text{and} \quad \Delta \boldsymbol{H} = \boldsymbol{H}^+ - \boldsymbol{H}^- \, , \tag{5.97}$$

we perform a coordinate transformation between the Cartesian field components and the interface coordinates with the rotation matrix

$$\hat{\mathbf{R}} = \begin{pmatrix} \boldsymbol{n} & \boldsymbol{t}_1 & \boldsymbol{t}_2 \end{pmatrix}.$$

(5.98)

We use the identities

$$\boldsymbol{n} \times \boldsymbol{E} = \boldsymbol{n} \times \hat{\mathbf{R}} \cdot \begin{pmatrix} E_n \\ E_{t_1} \\ E_{t_2} \end{pmatrix} = \hat{\mathbf{R}} \cdot \begin{pmatrix} 0 & 0 & 0 \\ 0 & 0 & -1 \\ 0 & 1 & 0 \end{pmatrix} \cdot \begin{pmatrix} E_n \\ E_{t_1} \\ E_{t_2} \end{pmatrix} = \hat{\mathbf{R}} \cdot \begin{pmatrix} 0 & \mathbf{0}^{\mathrm{T}} \\ \mathbf{0} & \hat{\mathbf{D}}^{-1} \end{pmatrix} \cdot \boldsymbol{E}, \quad (5.99a)$$

$$\boldsymbol{n} \times \boldsymbol{n} \times \boldsymbol{E} = \hat{\mathbf{R}} \cdot \begin{pmatrix} 0 & 0 & 0 \\ 0 & -1 & 0 \\ 0 & 0 & -1 \end{pmatrix} \cdot \begin{pmatrix} E_n \\ E_{t_1} \\ E_{t_2} \end{pmatrix} = -\hat{\mathbf{R}} \cdot \boldsymbol{E}.$$

(5.99b)

We can transform the numerical flux components as

$$\boldsymbol{n} \times \left(\boldsymbol{E}^- - \boldsymbol{E}^{-,*} \right)$$

$$\overset{(5.95)}{=} -\hat{\mathbf{R}} \cdot \begin{pmatrix} 1 & \mathbf{0}^{\mathrm{T}} \\ \mathbf{0} & \hat{\mathbf{D}}^{-1} \cdot \left[\hat{\mathbf{M}}_+^{-1} + \hat{\mathbf{M}}_-^{-1} \right]^{-1} \cdot \hat{\mathbf{M}}_+^{-1} \hat{\mathbf{D}} \end{pmatrix} \cdot \hat{\mathbf{R}}^{-1} \cdot \hat{\mathbf{R}} \cdot \begin{pmatrix} 0 & \mathbf{0}^{\mathrm{T}} \\ \mathbf{0} & \hat{\mathbf{D}} \cdot \Delta\boldsymbol{E}_t \end{pmatrix}$$

$$- \hat{\mathbf{R}} \cdot \begin{pmatrix} 1 & \mathbf{0}^{\mathrm{T}} \\ \mathbf{0} & \hat{\mathbf{D}}^{-1} \cdot \left[\hat{\mathbf{M}}_+^{-1} + \hat{\mathbf{M}}_-^{-1} \right]^{-1} \end{pmatrix} \cdot \hat{\mathbf{R}}^{-1} \cdot \hat{\mathbf{R}} \cdot \begin{pmatrix} 0 & \mathbf{0}^{\mathrm{T}} \\ \mathbf{0} & -\hat{\mathbf{1}} \cdot \Delta\boldsymbol{H}_t \end{pmatrix},$$

$$= -\left[\hat{\mathbf{Y}}_- + \hat{\mathbf{Y}}_+ \right]^{-1} \cdot \hat{\mathbf{Y}}_+ \cdot \boldsymbol{n} \times \Delta\boldsymbol{E} - \left[\hat{\mathbf{Y}}_- + \hat{\mathbf{Y}}_+ \right]^{-1} \cdot \boldsymbol{n} \times \boldsymbol{n} \times \Delta\boldsymbol{H} \quad (5.100a)$$

and $\quad -\boldsymbol{n} \times \left(\boldsymbol{H}^- - \boldsymbol{H}^{-,*} \right)$

$$\overset{(5.95)}{=} \hat{\mathbf{R}} \cdot \begin{pmatrix} 1 & \mathbf{0}^{\mathrm{T}} \\ \mathbf{0} & \hat{\mathbf{D}}^{-1} \cdot \left[\hat{\mathbf{M}}_+ + \hat{\mathbf{M}}_- \right]^{-1} \cdot \hat{\mathbf{M}}_+ \hat{\mathbf{D}} \end{pmatrix} \cdot \hat{\mathbf{R}}^{-1} \cdot \hat{\mathbf{R}} \cdot \begin{pmatrix} 0 & \mathbf{0}^{\mathrm{T}} \\ \mathbf{0} & \hat{\mathbf{D}} \cdot \Delta\boldsymbol{H}_t \end{pmatrix}$$

$$- \hat{\mathbf{R}} \cdot \begin{pmatrix} 1 & \mathbf{0}^{\mathrm{T}} \\ \mathbf{0} & \hat{\mathbf{D}}^{-1} \cdot \left[\hat{\mathbf{M}}_+ + \hat{\mathbf{M}}_- \right]^{-1} \end{pmatrix} \cdot \hat{\mathbf{R}}^{-1} \cdot \hat{\mathbf{R}} \cdot \begin{pmatrix} 0 & \mathbf{0}^{\mathrm{T}} \\ \mathbf{0} & -\hat{\mathbf{1}} \cdot \Delta\boldsymbol{E}_t \end{pmatrix},$$

$$= \left[\hat{\mathbf{Z}}_- + \hat{\mathbf{Z}}_+ \right]^{-1} \cdot \hat{\mathbf{Z}}_+ \cdot \boldsymbol{n} \times \Delta\boldsymbol{H} - \left[\hat{\mathbf{Z}}_- + \hat{\mathbf{Z}}_+ \right]^{-1} \cdot \boldsymbol{n} \times \boldsymbol{n} \times \Delta\boldsymbol{E}. \quad (5.100b)$$

Here, we defined the generalized admittance and impedance matrices

$$\hat{\mathbf{Y}}_\pm := \hat{\mathbf{R}} \cdot \begin{pmatrix} 1 & \mathbf{0}^{\mathrm{T}} \\ \mathbf{0} & \hat{\mathbf{M}}_\pm^{-1} \cdot \hat{\mathbf{D}} \end{pmatrix} \cdot \hat{\mathbf{R}}^{-1} \overset{(5.82)}{=} \hat{\mathbf{R}} \cdot \begin{pmatrix} 1 & \mathbf{0}^{\mathrm{T}} \\ \mathbf{0} & \hat{\mathbf{R}}_{\Gamma,\pm} \cdot \hat{\mathbf{\Lambda}}_\pm^{-1} \cdot \hat{\mathbf{R}}_{\Gamma,\pm}^{-1} \cdot \hat{\boldsymbol{\mu}}^{-1} \end{pmatrix} \cdot \hat{\mathbf{R}}^{-1}, \quad (5.101a)$$

$$\hat{\mathbf{Z}}_{\pm} := \hat{\mathbf{R}} \cdot \begin{pmatrix} 1 & \mathbf{0}^{\mathrm{T}} \\ \mathbf{0} & \hat{\mathbf{M}}_{\pm} \cdot \hat{\mathbf{D}}^{-1} \end{pmatrix} \cdot \hat{\mathbf{R}}^{-1} \overset{(5.88)}{=} \hat{\mathbf{R}} \cdot \begin{pmatrix} 1 & \mathbf{0}^{\mathrm{T}} \\ \mathbf{0} & \hat{\boldsymbol{\epsilon}}_{\pm}^{-1} \cdot \hat{\mathbf{D}} \cdot \hat{\mathbf{R}}_{\Gamma,\pm} \cdot \hat{\boldsymbol{\Lambda}}_{\pm}^{-1} \cdot \hat{\mathbf{R}}_{\Gamma,\pm}^{-1} \cdot \hat{\mathbf{D}}^{-1} \end{pmatrix} \cdot \hat{\mathbf{R}}^{-1},$$

(5.101b)

where we used $\hat{\mathbf{D}}^{-1} = -\hat{\mathbf{D}}$ for the latter. These matrices contain the field propagation speeds in the diagonal matrix $\hat{\boldsymbol{\Lambda}}$, the corresponding transversal component of the polarization vectors in $\hat{\mathbf{R}}_{\Gamma}$ and the interface projected permittivity $\hat{\boldsymbol{\epsilon}}$ or permeability matrix $\hat{\boldsymbol{\mu}}$ from Eq. (5.76), respectively. Consequently, the numerical upwind flux term used in the DGTD scheme for non-dispersive anisotropic materials reads

$$\boldsymbol{n} \cdot \underline{\underline{\boldsymbol{F}}} - \boldsymbol{n} \cdot \underline{\underline{\boldsymbol{F}}}^* = \begin{pmatrix} \left[\hat{\mathbf{Z}}_+ + \hat{\mathbf{Z}}_-\right]^{-1} \cdot \left[\Delta\boldsymbol{E} - \boldsymbol{n}\left(\boldsymbol{n}\cdot\Delta\boldsymbol{E}\right) + \hat{\mathbf{Z}}_+ \cdot \boldsymbol{n}\times\Delta\boldsymbol{H}\right] \\ \left[\hat{\mathbf{Y}}_+ + \hat{\mathbf{Y}}_-\right]^{-1} \cdot \left[\Delta\boldsymbol{H} - \boldsymbol{n}\left(\boldsymbol{n}\cdot\Delta\boldsymbol{H}\right) - \hat{\mathbf{Y}}_+ \cdot \boldsymbol{n}\times\Delta\boldsymbol{E}\right] \end{pmatrix}. \tag{5.102}$$

With this numerical flux, we achieve a stable DGTD scheme. Fig. 5.6 (b) shows a prototypical spectrum for a spatial discretization matrix $\hat{\mathbf{H}}$, as defined in Eq. (5.30). As an exemplary setup, we use a single unit cube containing five elements with a $p=4$ Lagrange polynomial basis. The cube is filled with a magneto-optic (MO) material

$$\underline{\underline{\boldsymbol{\epsilon}}} = \begin{pmatrix} 1 & -\frac{i}{2} & 0 \\ \frac{i}{2} & 1 & 0 \\ 0 & 0 & 2 \end{pmatrix} \quad \text{and} \quad \underline{\underline{\boldsymbol{\mu}}} = \underline{\underline{\mathbf{1}}}. \tag{5.103}$$

Additionally, we apply perfect electric conductor (PEC) BCs (see Section 5.3.4) at the cube surface.

Here, we only use a small setup with five elements, as the matrix $\hat{\mathbf{H}}$ has already 1050×1050 entries. However, it is very sparse, as only neighboring elements are coupled. The eigenvalues $\lambda_{\hat{\mathbf{H}},i}$ of the discretization matrix $\hat{\mathbf{H}}$ correspond to the complex frequencies $\tilde{\omega}_i = i\lambda_{\hat{\mathbf{H}},i}$ of the modes supported in that computational domain. For low frequencies $\omega_i = \text{Im}(\lambda_{\hat{\mathbf{H}},i})$, the associated damping $-\text{Re}(\lambda_{\hat{\mathbf{H}},i})$ is negligible. These are the physically relevant modes. With increasing frequencies, the complex eigenvalues bend more and more into the negative half-plane, which leads to increased damping. These high-frequency modes are therefore suppressed by the damping introduced by the upwind flux. It indirectly enforces a sufficiently fine discretization that shifts the same high-frequency modes back to the imaginary axis. Furthermore, a line of purely damped modes is supported. These spurious modes emerge from the non-divergence-free basis which also accounts for static fields introduced by charges [74].

Although Fig. 5.6 (b) shows a prototypical stable spectrum, the DGTD scheme using the upwind flux Eq. (5.102) is only conditionally stable. Besides the time-step used in the Runge-Kutta integrator [75, 142], there is a restriction on allowed non-dispersive material tensors used. The main criterion here is, that characteristic propagation speeds $\hat{\boldsymbol{\Lambda}}$ computed in the diagonalization Eq. (5.80) are real-valued. This sets a restriction on the choice of permittivity and permeability tensors. In the most general case, the material tensors are complex-valued. This requires an expansion of the DGTD scheme to complex-valued fields $\boldsymbol{q}$ which is straightforward, as long
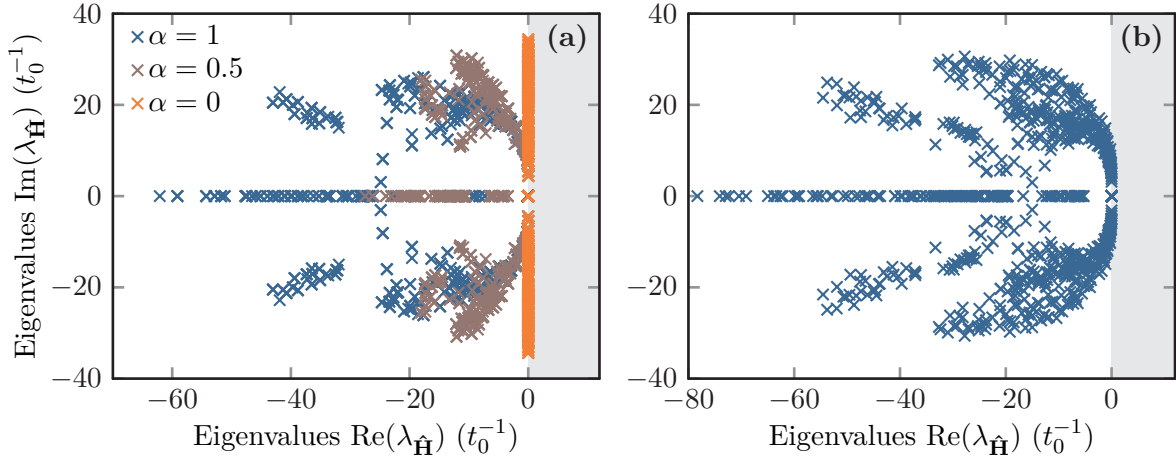
Figure 5.6: Spectrum of a DGTD spatial discretization operator $\hat{\mathbf{H}}$ (see Eq. (5.30)), for a unit cube consisting of five tetrahedral elements including a fourth-order Lagrange polynomial basis with PEC BCs applied at the boundary. The unit cube contains **(a)** vacuum ($\epsilon = \mu = 1$) or **(b)** an MO example material Eq. (5.103). Both examples use the upwind flux **(a)** Eq. (5.107) and **(b)** Eq. (5.102), respectively. **(a)** Gradual variation between upwind and central flux with upwind parameter $\alpha \in [0,1]$. Gray shaded areas mark regions of exponentially growing, i.e., unstable modes.

as only linear materials are involved in the simulation setup. If non-magnetic materials are considered, there is also a sufficient criterion for the dielectric tensor. For isotropic permittivities $\epsilon \in \mathbb{C}$, the spectra in Fig. 5.6 rotate around the origin. This means, that the physically relevant low frequencies modes, either for the negative or positive frequency components shift to positive real eigenvalues, which corresponds to an exponential gain, i.e., a numerical explosion. A non-dispersive complex-valued permittivity ϵ leads to unstable Maxwell's equations. It violates the basic stability criterion for any dispersive permittivity model

$$\epsilon(\omega) = \epsilon^*(-\omega)\,, \tag{5.104}$$

which directly follows from the associated and necessarily real-valued response kernel in Eq. (2.8). In order to obtain a stable set of PDEs, it at least requires a change in the otherwise constant $\mathrm{Im}(\epsilon)$ for switching between positive and negative frequencies. For the anisotropic non-dispersive permittivity tensors this translates to the sufficient stability condition

$$\underline{\underline{\epsilon}} = \underline{\underline{\epsilon}}^{\dagger}\,, \tag{5.105}$$

which is just met for the example with the MO material type used for Fig. 5.6 (b).

5.3.3 Upwind flux for isotropic materials

The numerical upwind flux for the more commonly used non-dispersive isotropic material model in the DGTD method can be directly inferred from the anisotropic case Eq. (5.102). For this,

both the admittance and impedance matrices in Eq. (5.101) simplify to diagonal matrices as

$$\hat{\mathbf{Y}}_{\pm} \to Y_{\pm}\,\hat{\mathbf{1}} = \sqrt{\frac{\epsilon_{\pm}}{\mu_{\pm}}}\,\hat{\mathbf{1}} \quad \text{and} \quad \hat{\mathbf{Z}}_{\pm} \to Z_{\pm}\,\hat{\mathbf{1}} = \sqrt{\frac{\mu_{\pm}}{\epsilon_{\pm}}}\,\hat{\mathbf{1}}\,. \tag{5.106}$$

Here, the material tensors $\hat{\boldsymbol{\epsilon}}_{\pm}$ and $\hat{\boldsymbol{\mu}}_{\pm}$ as well as polarization vectors in $\hat{\mathbf{R}}_{\Gamma,\pm}$ are diagonal and the included interface basis rotations $\hat{\mathbf{R}}$ cancel out. We recover the well-known form [73–75] of the upwind flux

$$\boldsymbol{n}\cdot\underline{\underline{\boldsymbol{F}}} - \boldsymbol{n}\cdot\underline{\underline{\boldsymbol{F}}}^{*} = \begin{pmatrix} \frac{1}{\bar{Z}}\left(\alpha\left[\Delta\boldsymbol{E} - \boldsymbol{n}(\boldsymbol{n}\cdot\Delta\boldsymbol{E})\right] + Z_{+}\boldsymbol{n}\times\Delta\boldsymbol{H}\right) \\ \frac{1}{\bar{Y}}\left(\alpha\left[\Delta\boldsymbol{H} - \boldsymbol{n}(\boldsymbol{n}\cdot\Delta\boldsymbol{H})\right] - Y_{+}\boldsymbol{n}\times\Delta\boldsymbol{E}\right) \end{pmatrix}, \tag{5.107}$$

where

$$\bar{Z} := Z_{+} + Z_{-} \quad \text{and} \quad \bar{Y} := Y_{+} + Y_{-}\,. \tag{5.108}$$

Note, that in this case, the characteristics are degenerate for both polarizations contributing to the flux over the elements interface. This is sketched on the right "+"-side in Fig. 5.5. Furthermore, we introduce a parameter α. It allows to continuously switch between the upwind flux ($\alpha = 1$) and an impedance / admittance weighted form of the central flux ($\alpha = 0$, cf. Eq. (5.37)) [73, 74].

In Fig. 5.6 (a) we show a prototypical spectrum of a DGTD spatial discretization matrix $\hat{\mathbf{H}}$, as defined in Eq. (5.30). Hereby the example setup is a unit cube containing five elements with a $p = 4$ Lagrange polynomial basis. The unit-cube is filled with vacuum, i.e., $\epsilon = \mu = 1$. The spectrum is shown for different upwind parameters α. For a pure upwind flux ($\alpha = 1$), the spectrum has a similar shape as in the anisotropic test case shown in Fig. 5.6 (b). For a decreasing upwind parameter, the spectrum is compressed to the imaginary axis further and further. In the limit of $\alpha = 0$, it reaches a material-weighted form of the central flux, for which both low- and high-frequency modes supported by the discretized field are on the edge of the stability region.

5.3.4 Boundary conditions

Additionally to the flux between elements, we need to specify what happens if an element has no neighboring element, i.e., if the element lies at the boundary of the computational domain. Commonly used BCs at the interface include PEC BCs, perfect magnetic conductor (PMC) BCs as well as radiation conditions, i.e., Silver Müller boundary conditions (SMBCs).

For a PEC the tangential electric field $\boldsymbol{n}\times\boldsymbol{E}\left(\boldsymbol{r}_{\mathrm{BC}}, t\right) = \boldsymbol{0}$ and for the PMC the tangential magnetic field $\boldsymbol{n}\times\boldsymbol{H}\left(\boldsymbol{r}_{\mathrm{BC}}, t\right) = \boldsymbol{0}$ at the boundary [81]. This can, for example, be used to model perfectly conducting metals. In the SMBCs, we assume a first-order approximation to the radiation condition [136–138] in which the electromagnetic field is assumed to be spherical and propagate unhindered out of the domain. Consequently, the SMBCs try to emulate infinite space. As the approximation only holds for sufficiently large computational domains, one can

additionally use PMLs to suppress the back-scattering at the domain boundary while maintaining the domain size. PMLs are introduced in Section 5.6. Besides these BCs fixing the fields dependent on only one boundary element, there also exist periodic boundary conditions (PBCs). These can be implemented very easily, by mapping the interface of the boundary element to that of its periodic partner. In this case, the numerical flux behaves the same as for internal elements of the mesh.

Perfect electric conductor and perfect magnetic conductor boundary conditions

The BCs can be directly implemented using the numerical flux Eq. (5.102). Here, we enforce the field BCs in the solution of the Riemann problem on the fields $\boldsymbol{q}^{-,*}$ as shown in Fig. 5.5. For the PEC BCs, the tangential electric field must be zero at the boundary, i.e., $\boldsymbol{n} \times \boldsymbol{E}^{-,*} = \boldsymbol{0}$. The magnetic field can take any value at the same time, inducing an instantaneous surface current at the boundary. This behavior can be modeled by preventing any flux contribution from the $\boldsymbol{H}$-field. For this, one introduces a fictitious neighboring element, setting the field $\boldsymbol{H}^+ \overset{!}{=} \boldsymbol{H}^-$ for any time t. This sets the magnetic field difference $\Delta \boldsymbol{H} = \boldsymbol{0}$ in the numerical flux Eq. (5.102). The electric field difference is furthermore determined by the electric part of the numerical flux

$$\boldsymbol{n} \times (\boldsymbol{E}^- - \underbrace{\boldsymbol{E}^{-,*}}_{\overset{\mathrm{PEC}}{=} \boldsymbol{0}}) = - \left(\hat{\mathbf{Y}}_- + \hat{\mathbf{Y}}_+ \right)^{-1} \cdot \hat{\mathbf{Y}}_+ \cdot \boldsymbol{n} \times \Delta \boldsymbol{E} \,. \tag{5.109}$$

Assuming the same admittance in the fictitious neighboring element $\hat{\mathbf{Y}}_+ = \hat{\mathbf{Y}}_-$ (mirror condition), determines the electric field difference. Hence, the PEC BCs are determined by

$$\Delta \boldsymbol{E} = -2\boldsymbol{E}^- \quad \text{and} \quad \Delta \boldsymbol{H} = \boldsymbol{0} \,. \tag{5.110}$$

The PMC BCs are determined in analogy by exchanging the role of the $\boldsymbol{E}$- and $\boldsymbol{H}$-field. Thus, the PMC BCs can be enforced with the numerical flux containing the field differences

$$\Delta \boldsymbol{E} = \boldsymbol{0} \quad \text{and} \quad \Delta \boldsymbol{H} = -2\boldsymbol{H}^- \,. \tag{5.111}$$

Silver-Müller boundary conditions

The basis of the SMBCs is a first-order approximation to the frequency domain radiation conditions in an isotropic medium [136–138], given by

$$\lim_{r \to \infty} r \left[(\nabla \times \boldsymbol{E}(\boldsymbol{r}, \omega)) \times \boldsymbol{e}_r - \mathrm{i} k_r \boldsymbol{E}(\boldsymbol{r}, \omega) \right] = 0 \tag{5.112a}$$

$$\text{and} \quad \lim_{r \to \infty} r \left[(\nabla \times \boldsymbol{H}(\boldsymbol{r}, \omega)) \times \boldsymbol{e}_r - \mathrm{i} k_r \boldsymbol{H}(\boldsymbol{r}, \omega) \right] = 0 \,. \tag{5.112b}$$

Here, $r = |\boldsymbol{r}|$ is the distance from any given scatterer, $\boldsymbol{e}_r$ the radial unit vector and $k_r = \sqrt{\epsilon \mu}\,\omega$ the corresponding wave vector in radial direction. The condition assumes that in the far-field of any scatterer the field propagates as a spherical wave into infinity. Hence, SMBCs are absorbing BCs. Following the derivation presented in [76], we approximate this condition at finite positions

$\boldsymbol{r} = \boldsymbol{r}_{\mathrm{BC}}$ for which we replace the spherical boundary with the normal vector $\boldsymbol{e}_r$ by the actual simulation domain boundary with normal vector $\boldsymbol{n}$. This yields

$$\left(\nabla \times \boldsymbol{E}(\boldsymbol{r}_{\mathrm{BC}}, \omega)\right) \times \boldsymbol{n} - \mathrm{i}k_r \boldsymbol{E}(\boldsymbol{r}_{\mathrm{BC}}, \omega) = 0 \tag{5.113a}$$

$$\text{and} \quad \left(\nabla \times \boldsymbol{H}(\boldsymbol{r}_{\mathrm{BC}}, \omega)\right) \times \boldsymbol{n} - \mathrm{i}k_r \boldsymbol{H}(\boldsymbol{r}_{\mathrm{BC}}, \omega) = 0 \,. \tag{5.113b}$$

Inserting Maxwell's curl-equations (2.31c) and (2.31d) in frequency domain sets the conditions as

$$\mathrm{i}\omega\mu\boldsymbol{H} \times \boldsymbol{n} - \mathrm{i}k_r \boldsymbol{E} = 0 \quad \text{and} \quad -\mathrm{i}\omega\epsilon\boldsymbol{E} \times \boldsymbol{n} - \mathrm{i}k_r \boldsymbol{H} = 0 \,. \tag{5.114}$$

Thus, independent of the frequency the SMBCs are set by

$$-\boldsymbol{n} \times \boldsymbol{H}(\boldsymbol{r}, t) = Y\boldsymbol{E}(\boldsymbol{r}, t) \quad \text{and} \quad \boldsymbol{n} \times \boldsymbol{E}(\boldsymbol{r}, t) = Z\boldsymbol{H}(\boldsymbol{r}, t) \,, \tag{5.115}$$

with the impedance $Z = Y^{-1}$ of the isotropic non-dispersive material (cf. Eq. (5.106)). To obtain the numerical flux for the SMBCs, we enforce the condition

$$-\boldsymbol{n} \times \boldsymbol{H}^- \overset{!}{=} Y\boldsymbol{E}^* \quad \text{and} \quad \boldsymbol{n} \times \boldsymbol{E}^- \overset{!}{=} Z\boldsymbol{H}^* \,. \tag{5.116}$$

Thus, we relate the interface fields $\boldsymbol{q}^*$ after the time step with the initial fields $\boldsymbol{q}^-$ at the beginning of the time step. Inserting the SMBCs into the numerical upwind flux Eq. (5.107) results in

$$\frac{1}{Z}\boldsymbol{n} \times \boldsymbol{n} \times \left(\Delta\boldsymbol{E} + 2\boldsymbol{E}^-\right) = \boldsymbol{n} \times \left(\Delta\boldsymbol{H} + 2\boldsymbol{H}^-\right) \,, \tag{5.117a}$$

$$\boldsymbol{n} \times \left(\Delta\boldsymbol{E} + 2\boldsymbol{E}^-\right) = -\frac{1}{Y}\boldsymbol{n} \times \boldsymbol{n} \times \left(\Delta\boldsymbol{H} + 2\boldsymbol{H}^-\right) \,. \tag{5.117b}$$

As there is no unique solution for the field differences determining the flux, one chooses the only solution not mixing the fields, i.e.,

$$\Delta\boldsymbol{E} = -2\boldsymbol{E}^- \quad \text{and} \quad \Delta\boldsymbol{H} = -2\boldsymbol{H}^- \,. \tag{5.118}$$

While these SMBCs work very well for plane waves with normal incidence, the reflections caused by waves impinging with small incidence angles are rather high. To reduce these reflections, there are two possible ways: Increasing the simulation domain size significantly or the use of PMLs, which are introduced in Section 5.6. Increasing the simulation domain size typically also increases the number of elements. Therefore, also the number of degrees of freedom to be computed increases with the power of the setup dimension. Hence, the use of PMLs often requires less computational time to achieve the same numerical accuracy.

5.4 Field sources

So far, we have discussed how to setup a computation to solve Maxwell's curl-equations for non-dispersive material distributions. We showed how to enforce BCs and compute the fields given

the Lagrange polynomial interpolation on the elements. As a typical computation starts with zero-field initial conditions, we introduce source terms for a setup excitation.

For these, we split the fields into a total field, the a priori known incident excitation field as well as the scattered field, i.e.,

$$\boldsymbol{E}_{\text{tot}}(\boldsymbol{r}, t) = \boldsymbol{E}_{\text{inc}}(\boldsymbol{r}, t) + \boldsymbol{E}_{\text{scat}}(\boldsymbol{r}, t) \quad \text{and} \quad \boldsymbol{H}_{\text{tot}}(\boldsymbol{r}, t) = \boldsymbol{H}_{\text{inc}}(\boldsymbol{r}, t) + \boldsymbol{H}_{\text{scat}}(\boldsymbol{r}, t) \,. \tag{5.119}$$

Typically, one wants to solve Maxwell's equations for a non-trivial material distribution. However, the propagation of the incident field shall be analytically known for a simple material setup with permittivity ϵ_{bg} and permeability μ_{bg}. Then, the incident field is a solution to Maxwell's equations (2.1) for that setup, i.e.,

$$(\text{SI}) \qquad\qquad \partial_t \boldsymbol{E}_{\text{inc}}(\boldsymbol{r}, t) = \frac{1}{\epsilon_0 \epsilon_{\text{bg}}(\boldsymbol{r})} \nabla \times \boldsymbol{H}_{\text{inc}}(\boldsymbol{r}, t) \tag{5.120a}$$

$$(\text{SI}) \qquad\qquad \text{and} \quad \partial_t \boldsymbol{H}_{\text{inc}}(\boldsymbol{r}, t) = -\frac{1}{\mu_0 \mu_{\text{bg}}(\boldsymbol{r})} \nabla \times \boldsymbol{E}_{\text{inc}}(\boldsymbol{r}, t) \,. \tag{5.120b}$$

An example widely used in this thesis is a pulsed plane wave in a homogeneous isotropic dielectric with $\epsilon_{\text{bg}}(\boldsymbol{r}) = \epsilon_{\text{bg}}$ and $\mu_{\text{bg}} = 1$. The fields are given by

$$(\text{SI}) \qquad\qquad \boldsymbol{E}_{\text{inc}}(\boldsymbol{r}, t) = \boldsymbol{E}_0 \, \eta \left(t - \sqrt{\epsilon_{\text{bg}}} \frac{\boldsymbol{n} \cdot \boldsymbol{r}}{c_0} \right) \tag{5.121a}$$

$$(\text{SI}) \qquad\qquad \text{and} \quad \boldsymbol{H}_{\text{inc}}(\boldsymbol{r}, t) = \frac{\sqrt{\epsilon_{\text{bg}}}}{Z_0} \, \boldsymbol{n} \times \boldsymbol{E}_0 \, \eta \left(t - \sqrt{\epsilon_{\text{bg}}} \frac{\boldsymbol{n} \cdot \boldsymbol{r}}{c_0} \right) \,, \tag{5.121b}$$

where $\boldsymbol{E}_0$ defines the field strength and polarization (cf. Section 2.7.1) of the plane wave, $\boldsymbol{n} = \frac{\boldsymbol{k}}{|\boldsymbol{k}|}$ defines the propagation direction and $\eta(t)$ is the time dependence of the wave. As exemplary time dependence, we use a Gaussian modulated wave (see Eq. (B.20)), i.e.,

$$\eta(t) = \cos \left(\omega_0 (t - t_0) \right) \mathrm{e}^{-\frac{(t - t_0)^2}{2\sigma^2}} \,, \tag{5.122}$$

with a carrier frequency ω_0, a temporal width σ, and a time off-set t_0. For further details on time dependencies please refer to Appendix B. These plane waves can for example be used to compute the scattering spectra of spherical scatterers or the transmittance and reflectance spectra similar to the FMM in Section 4.3.1.

The main point is to compute the Sf for non-trivial material distributions, which automatically also determines the Tf. To compute the Sf in the DGTD method there are two possibilities. The first is the introduction of a total field / scattered field (Tf/Sf) contour which splits the computational domain into a Tf and Sf region. The incident field is then introduced on that contour into the domain using the numerical flux. In the second method, one only solves for the Sf in the entire domain, for which the incident field acts as a volumetric source term.

5.4.1 Total field / scattered field source

As the Tf/Sf contour (see e.g., Fig. 5.1) splits the domain into a Tf and Sf region, the fields on the contour jump by the incident field. This means, that for the computation of the numerical flux on element interfaces, which are part of that contour, the field BCs have to be altered by that jump. Consequently, we change the BC of the fields in the flux derivation Eq. (5.85) to

$$q^{*,+} - q^{*,-} = q_{\text{inc}} \, , \tag{5.123}$$

with which the overall tangential field component differences Eq. (5.59) change to

$$\hat{\mathbf{V}}_{\pm}^{-1} \cdot \left(q_+ - q_- - q_{\text{inc}} \right) = \delta \, . \tag{5.124}$$

Therefore the Tf/Sf contour source can be applied by exchanging the field differences entering the numerical flux computation for either anisotropic materials Eq. (5.102) or isotropic materials Eq. (5.107) to

$$\Delta \boldsymbol{E} \to \Delta \boldsymbol{E} - \boldsymbol{E}_{\text{inc}} \quad \text{and} \quad \Delta \boldsymbol{H} \to \Delta \boldsymbol{H} - \boldsymbol{H}_{\text{inc}} \, . \tag{5.125}$$

For the plane wave incident field in Eq. (5.121), an isotropic material is assumed. If only a Tf/Sf source shall be applied, the Tf region must contain all deviations in the material parameters from those assumed for the incident field Maxwell's equations. Examples for these are shown in Fig. 5.1, which only contain a cylindrical or spherical scatterer completely surrounded by the Tf/Sf contour. It is also possible to use several closed Tf/Sf contours in a single computational domain, e.g., two spheres or two planes closing at infinity. If one or more Tf/Sf contours do not suffice, one needs to additionally apply Sf sources described in the next section.

Additionally to the introduction of incident fields into the computational domain, the Tf/Sf contours can also be used to obtain important scattering data. Both the Sf $q_{\text{scat}}(\boldsymbol{r}, t)$ and Tf $q_{\text{tot}}(\boldsymbol{r}, t)$ are accessible on either side of the contour. Therefore a recording of the respective fields allows computing the on-the-fly Fourier transform

$$q_{\text{scat/tot}}(\boldsymbol{r}, \omega) \overset{(2.30)}{\approx} \sum_j \Delta t \, q_{\text{scat/tot}} \left(\boldsymbol{r}, j\Delta t \right) \mathrm{e}^{\mathrm{i}\omega j \Delta t} \, . \tag{5.126}$$

Here, after each time-step Δt of the Runge-Kutta solver [129, 142], a new field term is added. These frequency-dependent fields can then be used to compute the time-averaged Poynting vector $\langle \boldsymbol{S} \rangle_\tau (\boldsymbol{r}, \omega)$ on the contour and derived scattering quantities like the scattering, absorption, and extinction cross section (see Section 2.8.2) or reflectance and transmittance spectra (see Section 2.8.3) depending on the choice of the contour and geometry.

5.4.2 Scattered field source

For the Sf source, we insert the field decomposition Eq. (5.119) of the Tf into Maxwell's equations (2.1) and replace the curl of the incident fields [63, 74]. This results in the Sf Maxwell's equations

$$(\text{SI}) \quad \epsilon_0 \underline{\underline{\epsilon}}(\boldsymbol{r}) \cdot \partial_t \boldsymbol{E}_{\text{scat}}(\boldsymbol{r}, t) - \nabla \times \boldsymbol{H}_{\text{scat}}(\boldsymbol{r}, t) \overset{(5.120)}{=} \epsilon_0 \left[\epsilon_{\text{bg}}(\boldsymbol{r}) - \underline{\underline{\epsilon}}(\boldsymbol{r}) \right] \cdot \partial_t \boldsymbol{E}_{\text{inc}}(\boldsymbol{r}, t) , \quad (5.127\text{a})$$

$$(\text{SI}) \quad \mu_0 \underline{\underline{\mu}}(\boldsymbol{r}) \cdot \partial_t \boldsymbol{H}_{\text{scat}}(\boldsymbol{r}, t) + \nabla \times \boldsymbol{E}_{\text{scat}}(\boldsymbol{r}, t) \overset{(5.120)}{=} \mu_0 \left[\mu_{\text{bg}}(\boldsymbol{r}) - \underline{\underline{\mu}}(\boldsymbol{r}) \right] \cdot \partial_t \boldsymbol{H}_{\text{inc}}(\boldsymbol{r}, t) . \quad (5.127\text{b})$$

These can be cast into the same conservation form Eq. (5.1) required for the DGTD method, replacing the fields with the Sf, i.e.,

$$\boldsymbol{q}(\boldsymbol{r}, t) \to \boldsymbol{q}_{\text{scat}}(\boldsymbol{r}, t) . \quad (5.128)$$

Here, the incident fields constitute a volumetric source term

$$\boldsymbol{S}(\boldsymbol{r}, t) = \left[\underline{\underline{\boldsymbol{Q}}}_{\text{bg}}(\boldsymbol{r}) - \underline{\underline{\boldsymbol{Q}}}(\boldsymbol{r}) \right] \cdot \partial_t \boldsymbol{q}_{\text{inc}}(\boldsymbol{r}, t) = \begin{pmatrix} \left(\epsilon_{\text{bg}}(\boldsymbol{r}) - \underline{\underline{\epsilon}}(\boldsymbol{r}) \right) \cdot \partial_t \boldsymbol{E}_{\text{inc}}(\boldsymbol{r}, t) \\ \left(\mu_{\text{bg}}(\boldsymbol{r}) - \underline{\underline{\mu}}(\boldsymbol{r}) \right) \cdot \partial_t \boldsymbol{H}_{\text{inc}}(\boldsymbol{r}, t) \end{pmatrix} , \quad (5.129)$$

which is non-zero everywhere, where the material distributions $\underline{\underline{\boldsymbol{Q}}}_{\text{bg}}(\boldsymbol{r})$ of the incident field and $\underline{\underline{\boldsymbol{Q}}}(\boldsymbol{r})$ differ. This means, in every scatterer, the Sf is generated by the previously specified incident field.

5.5 Auxiliary differential equations

To implement the dispersive and thus also dissipative material models introduced in Chapter 3, we have to cast the field relation

$$(\text{SI}) \quad \boldsymbol{P}(\boldsymbol{r}, \omega) = \epsilon_0 \underline{\underline{\chi}}(\boldsymbol{r}, \omega) \cdot \boldsymbol{E}(\boldsymbol{r}, \omega) , \quad (5.130)$$

with the frequency-dependent susceptibility back into the time domain [63]. Furthermore, the resulting PDEs shall satisfy the conservation form Eq. (5.1) of the DGTD method [74–76]. This is done with the help of ADEs which introduce auxiliary fields, like polarization currents into the DGTD field state vector $\boldsymbol{q}(\boldsymbol{r}, t)$. These ADEs are derived from the frequency-dependent susceptibilities of the different material models, replacing frequency factors to the fields by the corresponding time-derivatives (see Eq. (2.33)). Apart from the four-level system (4LS) material model, all other material models introduced in Chapter 3 are characterized by a susceptibility of the form

$$\underline{\underline{\chi}}(\omega) = \sum_{c \in \{x, y, z\}} \frac{a_{0,c} + a_{1,c}(-\text{i}\omega) + a_{2,c}(-\text{i}\omega)^2}{b_{0,c} + b_{1,c}(-\text{i}\omega) + b_{2,c}(-\text{i}\omega)^2} \boldsymbol{e}_c \boldsymbol{e}_c^{\text{T}} . \quad (5.131)$$

This corresponds to a rational function

$$\chi_{c,c}(\omega) = \frac{p(\omega)}{q(\omega)} \quad (5.132)$$

in the susceptibility tensor components, with second-order polynomials p and q. Note that the presented ADE scheme also works for higher orders [74, 75, 131] as well as susceptibilities rotated into a different coordinate frame. Here, automatically the stability condition of the DGTD method is fulfilled by

$$\underline{\underline{\chi}}^{\dagger}(-\omega) = \underline{\underline{\chi}}(\omega) \,. \tag{5.133}$$

Furthermore, several material model susceptibilities can be added, i.e.,

$$\underline{\underline{\chi}}_{\text{tot}}(\omega) = \epsilon_{\text{bg}} + \sum_i \underline{\underline{\chi}}_i(\omega) \,. \tag{5.134}$$

The coupling to Maxwell's curl equations (2.1d) is mediated by the polarization current

$$\boldsymbol{j}_p(\boldsymbol{r}, t) = \partial_t \boldsymbol{P}(\boldsymbol{r}, t) \,, \tag{5.135}$$

by

$$\epsilon_{\text{bg}} \partial_t \boldsymbol{E}(\boldsymbol{r}, t) = \nabla \times \boldsymbol{H}(\boldsymbol{r}, t) - \boldsymbol{j}_p(\boldsymbol{r}, t) \,. \tag{5.136}$$

For the single polarization and electric field components, the susceptibility Eq. (5.131) implies

$$\left(b_{0,c} + b_{1,c}(-\mathrm{i}\omega) + b_{2,c}(-\mathrm{i}\omega)^2 \right) P_c(\boldsymbol{r}, \omega) = \left(a_{0,c} + a_{1,c}(-\mathrm{i}\omega) + a_{2,c}(-\mathrm{i}\omega)^2 \right) E_c(\boldsymbol{r}, \omega) \,, \tag{5.137}$$

and therefore the ADE

$$\partial_t^2 \left(b_2 P_c(\boldsymbol{r}, t) - a_2 E_c(\boldsymbol{r}, t) \right) = -\partial_t \left(b_1 P_c(\boldsymbol{r}, t) - a_1 E_c(\boldsymbol{r}, t) \right) - b_0 P_c(\boldsymbol{r}, t) + a_0 E_c(\boldsymbol{r}, t) \,. \tag{5.138}$$

One defines an auxiliary field for the highest order time-derivative, in this case an auxiliary current density

$$b_{2,c} \boldsymbol{j}_{\text{aux},c}(\boldsymbol{r}, t) := \partial_t \left(b_{2,c} P_c(\boldsymbol{r}, t) - a_{2,c} E_c(\boldsymbol{r}, t) \right) \,, \tag{5.139}$$

which is directly related to the polarization current $\boldsymbol{j}_p$ reduced by the response at infinite frequencies $\chi_{c,c}(\omega \to \infty) = \frac{a_{2,c}}{b_{2,c}}$ by

$$\boldsymbol{j}_{p,c}(\boldsymbol{r}, t) = \boldsymbol{j}_{\text{aux},c}(\boldsymbol{r}, t) - \frac{a_{2,c}}{b_{2,c}} \partial_t E_c(\boldsymbol{r}, t) \,. \tag{5.140}$$

It couples back to Eq. (5.136) by

$$\left[\epsilon_{\text{bg}} + \underline{\underline{\chi}}_{\infty} \right] \cdot \partial_t \boldsymbol{E}(\boldsymbol{r}, t) = \nabla \times \boldsymbol{H}(\boldsymbol{r}, t) - \boldsymbol{j}_{\text{aux}}(\boldsymbol{r}, t) \,. \tag{5.141}$$

To obtain the full set of ADEs, we furthermore compute the time-derivative of the auxiliary current, i.e.,

$$\partial_t j_{\mathrm{aux},c}(\boldsymbol{r},t) \stackrel{(5.138),(5.140)}{=} -\frac{b_{1,c}}{b_{2,c}} j_{\mathrm{aux},c}(\boldsymbol{r},t) + \left(\frac{a_{1,c}}{b_{2,c}} - \frac{b_{1,c}a_{2,c}}{b_{2,c}^2} \right) \partial_t E_c(\boldsymbol{r},t)$$
$$- \frac{b_{0,c}}{b_{2,c}} P_c(\boldsymbol{r},t) + \frac{a_{0,c}}{b_{2,c}} E_c(\boldsymbol{r},t) \,. \tag{5.142}$$

We replace the $\boldsymbol{E}$-field time derivative with Eq. (5.141) to arrive at the final set of PDEs containing Maxwell's equations as well as the ADEs. Assuming we add N susceptibilities of the form Eq. (5.131), the ADEs take the form

$$\underline{\underline{Q}} \cdot \partial_t \boldsymbol{q}(\boldsymbol{r},t) + \nabla \cdot \underline{\underline{F}}\big(\boldsymbol{q}(\boldsymbol{r},t)\big) = \boldsymbol{S}\big(\boldsymbol{q}(\boldsymbol{r},t)\big) \,, \tag{5.143}$$

with the field vector and material tensor

$$\boldsymbol{q}(\boldsymbol{r},t) = \begin{pmatrix} \boldsymbol{E} \\ \boldsymbol{H} \\ \boldsymbol{P}^{(1)} \\ \boldsymbol{j}_{\mathrm{aux}}^{(1)} \\ \vdots \\ \boldsymbol{P}^{(N)} \\ \boldsymbol{j}_{\mathrm{aux}}^{(N)} \end{pmatrix} \quad \text{and} \quad \underline{\underline{Q}} = \begin{pmatrix} \epsilon_{\mathrm{bg}}\underline{\underline{1}} + \sum_i \underline{\underline{a}}_2^{(i)} \cdot \left[\underline{\underline{b}}_2^{(i)}\right]^{-1} & \underline{\underline{0}} & \underline{\underline{0}} & \cdots & \underline{\underline{0}} \\ \underline{\underline{0}} & \mu_{\mathrm{bg}}\underline{\underline{1}} & \underline{\underline{0}} & \cdots & \underline{\underline{0}} \\ \underline{\underline{0}} & \underline{\underline{0}} & \underline{\underline{1}} & \cdots & \underline{\underline{0}} \\ \vdots & \vdots & \vdots & \ddots & \vdots \\ \underline{\underline{0}} & \underline{\underline{0}} & \underline{\underline{0}} & \cdots & \underline{\underline{1}} \end{pmatrix}. \tag{5.144}$$

Here, we defined the tensors

$$\underline{\underline{a}}_j^{(i)} = \sum_{c \in \{x,y,z\}} a_{j,c}^{(i)} \boldsymbol{e}_c \boldsymbol{e}_c^{\mathrm{T}} \quad \text{and} \quad \underline{\underline{b}}_j^{(i)} = \sum_{c \in \{x,y,z\}} b_{j,c}^{(i)} \boldsymbol{e}_c \boldsymbol{e}_c^{\mathrm{T}} \,, \tag{5.145}$$

for the susceptibilities Eq. (5.131). The flux term has the form

$$\boldsymbol{e}_j \cdot \underline{\underline{F}}(\boldsymbol{r},t) = \begin{pmatrix} -\boldsymbol{e}_j \times \boldsymbol{H}(\boldsymbol{r},t) \\ \boldsymbol{e}_j \times \boldsymbol{E}(\boldsymbol{r},t) \\ \underline{\underline{a}}_2^{(1)} \cdot \left[\underline{\underline{b}}_2^{(1)}\right]^{-1} \cdot \underline{\underline{\epsilon}}_\infty^{-1} \cdot \boldsymbol{e}_j \times \boldsymbol{H}(\boldsymbol{r},t) \\ \left(\underline{\underline{a}}_2^{(1)} \cdot \underline{\underline{b}}_1^{(1)} - \underline{\underline{a}}_1^{(1)} \cdot \underline{\underline{b}}_2^{(1)}\right) \cdot \left[\underline{\underline{b}}_2^{(1)}\right]^{-2} \cdot \underline{\underline{\epsilon}}_\infty^{-1} \cdot \boldsymbol{e}_j \times \boldsymbol{H}(\boldsymbol{r},t) \\ \vdots \\ \underline{\underline{a}}_2^{(N)} \cdot \left[\underline{\underline{b}}_2^{(N)}\right]^{-1} \cdot \underline{\underline{\epsilon}}_\infty^{-1} \cdot \boldsymbol{e}_j \times \boldsymbol{H}(\boldsymbol{r},t) \\ \left(\underline{\underline{a}}_2^{(N)} \cdot \underline{\underline{b}}_1^{(N)} - \underline{\underline{a}}_1^{(N)} \cdot \underline{\underline{b}}_2^{(N)}\right) \cdot \left[\underline{\underline{b}}_2^{(N)}\right]^{-2} \cdot \underline{\underline{\epsilon}}_\infty^{-1} \cdot \boldsymbol{e}_j \times \boldsymbol{H}(\boldsymbol{r},t) \end{pmatrix}, \tag{5.146}$$

while the ADE source term is determined by

$$\boldsymbol{S}(\boldsymbol{r},t) = \begin{pmatrix} \sum_i \boldsymbol{j}_{\mathrm{aux}}^{(i)}(\boldsymbol{r},t) \\ \boldsymbol{0} \\ \boldsymbol{j}_{\mathrm{aux}}^{(1)}(\boldsymbol{r},t) + \underline{\underline{\boldsymbol{a}}}_2^{(1)} \cdot \left[\underline{\underline{\boldsymbol{b}}}_2^{(1)}\right]^{-1} \cdot \underline{\underline{\boldsymbol{\epsilon}}}_\infty^{-1} \cdot \sum_i \boldsymbol{j}_{\mathrm{aux}}^{(i)}(\boldsymbol{r},t) \\ \left(\underline{\underline{\boldsymbol{a}}}_2^{(1)} \cdot \underline{\underline{\boldsymbol{b}}}_1^{(1)} - \underline{\underline{\boldsymbol{a}}}_1^{(1)} \cdot \underline{\underline{\boldsymbol{b}}}_2^{(1)}\right) \cdot \left[\underline{\underline{\boldsymbol{b}}}_2^{(1)}\right]^{-2} \cdot \underline{\underline{\boldsymbol{\epsilon}}}_\infty^{-1} \cdot \sum_i \boldsymbol{j}_{\mathrm{aux}}^{(i)}(\boldsymbol{r},t) + \\ \cdots + \left[\underline{\underline{\boldsymbol{b}}}_2^{(1)}\right]^{-1} \cdot \left[\underline{\underline{\boldsymbol{a}}}_0^{(1)} \cdot \boldsymbol{E}^{(1)}(\boldsymbol{r},t) - \underline{\underline{\boldsymbol{b}}}_1^{(1)} \cdot \boldsymbol{j}_{\mathrm{aux}}^{(1)}(\boldsymbol{r},t) - \underline{\underline{\boldsymbol{b}}}_0^{(1)} \cdot \boldsymbol{P}^{(1)}(\boldsymbol{r},t)\right] \\ \vdots \\ \boldsymbol{j}_{\mathrm{aux}}^{(N)}(\boldsymbol{r},t) + \underline{\underline{\boldsymbol{a}}}_2^{(N)} \cdot \left[\underline{\underline{\boldsymbol{b}}}_2^{(N)}\right]^{-1} \cdot \underline{\underline{\boldsymbol{\epsilon}}}_\infty^{-1} \cdot \sum_i \boldsymbol{j}_{\mathrm{aux}}^{(i)}(\boldsymbol{r},t) \\ \left(\underline{\underline{\boldsymbol{a}}}_2^{(N)} \cdot \underline{\underline{\boldsymbol{b}}}_1^{(N)} - \underline{\underline{\boldsymbol{a}}}_1^{(N)} \cdot \underline{\underline{\boldsymbol{b}}}_2^{(N)}\right) \cdot \left[\underline{\underline{\boldsymbol{b}}}_2^{(N)}\right]^{-2} \cdot \underline{\underline{\boldsymbol{\epsilon}}}_\infty^{-1} \cdot \sum_i \boldsymbol{j}_{\mathrm{aux}}^{(N)}(\boldsymbol{r},t) + \\ \cdots + \left[\underline{\underline{\boldsymbol{b}}}_2^{(N)}\right]^{-1} \cdot \left[\underline{\underline{\boldsymbol{a}}}_0^{(N)} \cdot \boldsymbol{E}^{(N)}(\boldsymbol{r},t) - \underline{\underline{\boldsymbol{b}}}_1^{(N)} \cdot \boldsymbol{j}_{\mathrm{aux}}^{(N)}(\boldsymbol{r},t) - \underline{\underline{\boldsymbol{b}}}_0^{(N)} \cdot \boldsymbol{P}^{(N)}(\boldsymbol{r},t)\right] \end{pmatrix} . \tag{5.147}$$

Here, we defined

$$\underline{\underline{\boldsymbol{\epsilon}}}_\infty := \epsilon_{\mathrm{bg}}\underline{\underline{\boldsymbol{1}}} + \sum_i \underline{\underline{\boldsymbol{a}}}_2^{(i)} \cdot \left[\underline{\underline{\boldsymbol{b}}}_2^{(i)}\right]^{-1} . \tag{5.148}$$

In the full set of ADEs, we notice three important things.

First, when the permittivity $\underline{\underline{\boldsymbol{\epsilon}}}_\infty$ is anisotropic, we require the anisotropic numerical flux Eq. (5.102) in the DGTD scheme. This is the case as soon as the susceptibility numerator polynomial $p(\omega)$ in Eq. (5.131) has the same order as in the denominator polynomial $q(\omega)$, i.e., here $\underline{\underline{\boldsymbol{a}}}_2 \neq \underline{\underline{\boldsymbol{0}}}$.

Second, when any except the zeroth-order numerator term $\underline{\underline{\boldsymbol{a}}}_0$ is non-zero, the entire sum of all auxiliary currents (see source term Eq. (5.147)) drives both the polarization $\boldsymbol{P}$ and auxiliary current $\boldsymbol{j}_{\mathrm{aux}}$ for each term of the total susceptibility $\underline{\underline{\boldsymbol{\chi}}}_{\mathrm{tot}}$ in Eq. (5.134).

Third, for the same case, the flux Eq. (5.146) for the auxiliary fields depends on $\nabla \times \boldsymbol{H}$. This, in principle, requires a derivation of the entire numerical upwind flux for these ADEs.

To calculate the numerical upwind flux for this set of ADEs, we have to solve the one-dimensional Riemann problem at the interface of two elements of the DGTD mesh. Similarly to Section 5.3.2, we switch to the interface coordinate system $\{\boldsymbol{n}, \boldsymbol{t}_1, \boldsymbol{t}_2\}$. With the assumption of no tangential variation of the fields $\boldsymbol{q}(\boldsymbol{r},t) \approx \boldsymbol{q}(n,t)$ on the interface as in Eq. (5.44), only the normal-direction derivative $\nabla \to \boldsymbol{n}\partial_n$ is considered. This allows for a reduction to the tangential field components (cf. Eqs. (5.73) and (5.74)), as the normal field components do not contribute to the numerical flux because of the curl-operation. The flux derivation requires the solution of the source-free Riemann problem Eq. (5.47) with the extension to the ADE fields

$$\boldsymbol{q} = \left(E_{t_1}, E_{t_2}, H_{t_1}, H_{t_2}, P_{t_1}, P_{t_2}, j_{\mathrm{aux},t_1}, j_{\mathrm{aux},t_1}\right)^{\mathrm{T}} . \tag{5.149}$$

For the derivation, we restrict the fields to only one term of the susceptibility defined in Eq. (5.131). The extension to the auxiliary fields also requires an extension of the matrix $\hat{\mathbf{A}} \to \hat{\mathbf{A}}_{\mathrm{ADE}}$ determining the field propagation in the Riemann problem Eq. (5.47). The new matrix takes a block

form

$$
\hat{\mathbf{A}}_{\mathrm{ADE}} = \begin{pmatrix} \hat{\mathbf{A}} & \hat{\mathbf{0}} \\ \hat{\mathbf{B}} & \hat{\mathbf{0}} \end{pmatrix}, \tag{5.150}
$$

where the matrix $\hat{\mathbf{A}}$ is the original 4×4-matrix for the electromagnetic fields, as defined in Eq. (5.78). The second 4×4-matrix $\hat{\mathbf{B}}$ is defined by the coupling tensor entries $\underline{\underline{a}}_i$ and $\underline{\underline{b}}_i$ from the flux in Eq. (5.146). Although the resulting matrix $\hat{\mathbf{A}}_{\mathrm{ADE}}$ is singular, it can be diagonalized by

$$
\hat{\mathbf{A}}_{\mathrm{ADE}} = \hat{\mathbf{W}} \cdot \hat{\mathbf{\Lambda}}_{\mathrm{ADE}} \cdot \hat{\mathbf{W}}^{-1}, \tag{5.151}
$$

where

$$
\hat{\mathbf{W}} = \begin{pmatrix} \hat{\mathbf{V}} & \hat{\mathbf{0}} \\ \hat{\mathbf{B}} \cdot \hat{\mathbf{V}} \cdot \hat{\mathbf{\Lambda}}^{-1} & \hat{\mathbf{1}} \end{pmatrix}, \quad \hat{\mathbf{\Lambda}}_{\mathrm{ADE}} = \begin{pmatrix} \hat{\mathbf{\Lambda}} & \hat{\mathbf{0}} \\ \hat{\mathbf{0}} & \hat{\mathbf{0}} \end{pmatrix} \quad \text{and} \quad \hat{\mathbf{W}}^{-1} = \begin{pmatrix} \hat{\mathbf{V}}^{-1} & \hat{\mathbf{0}} \\ -\hat{\mathbf{B}} \cdot \hat{\mathbf{A}}^{-1} & \hat{\mathbf{1}} \end{pmatrix}. \tag{5.152}
$$

Here, the block entries are determined by the diagonalization in Eq. (5.81) of the original matrix $\hat{\mathbf{A}}$ for the anisotropic Maxwell's equations. Provided the split of the tangential fields

$$
q^+ - q^- = \Delta q = \begin{pmatrix} \Delta q_{\mathrm{em}} \\ \Delta q_{\mathrm{aux}} \end{pmatrix}, \tag{5.153}
$$

into the electromagnetic and auxiliary fields, we can compute the field difference amplitude vector as in Eq. (5.59)

$$
\delta = \hat{\mathbf{W}}_{\pm}^{-1} \cdot \Delta q \overset{(5.152)}{=} \begin{pmatrix} \hat{\mathbf{V}}_{\pm}^{-1} \cdot \Delta q_{\mathrm{em}} \\ -\hat{\mathbf{B}}_{\pm} \cdot \hat{\mathbf{A}}_{\pm}^{-1} \cdot \Delta q_{\mathrm{em}} + \Delta q_{\mathrm{aux}} \end{pmatrix}. \tag{5.154}
$$

To finally compute the field difference $q^- - q^{-,*}$ required for the numerical flux Eq. (5.64), according to Eqs. (5.56) and (5.89), we need to sum up all eigenvectors

$$
\begin{pmatrix} \hat{\mathbf{V}}_- \\ \underline{\underline{\hat{\mathbf{B}}}}_- \cdot \underline{\underline{\hat{\mathbf{V}}}}_- \cdot \underline{\underline{\hat{\mathbf{\Lambda}}}}_-^{-1} \end{pmatrix} \tag{5.155}
$$

in $\hat{\mathbf{W}}_-$ associated with negative characteristic velocities in the matrix $\hat{\mathbf{\Lambda}}_{\mathrm{ADE}}$. The resulting field difference is of the form

$$
q^{-,*} - q^- \overset{(5.56)}{=} \begin{pmatrix} \hat{\mathbf{V}}_- \\ \underline{\underline{\hat{\mathbf{B}}}}_- \cdot \underline{\underline{\hat{\mathbf{V}}}}_- \cdot \underline{\underline{\hat{\mathbf{\Lambda}}}}_-^{-1} \end{pmatrix} \cdot \delta \overset{(5.154)}{=} \begin{pmatrix} \hat{\mathbf{V}}_- \cdot \hat{\mathbf{V}}_{\pm}^{-1} \cdot \Delta q_{\mathrm{em}} \\ \underline{\underline{\hat{\mathbf{B}}}}_- \cdot \underline{\underline{\hat{\mathbf{V}}}}_- \cdot \underline{\underline{\hat{\mathbf{\Lambda}}}}_-^{-1} \cdot \hat{\mathbf{V}}_{\pm}^{-1} \cdot \Delta q_{\mathrm{em}} \end{pmatrix} = \begin{pmatrix} q_{\mathrm{em}}^{-,*} - q_{\mathrm{em}}^- \\ q_{\mathrm{aux}}^{-,*} - q_{\mathrm{aux}}^- \end{pmatrix}. \tag{5.156}
$$

Here, the upper entries for the electromagnetic field correspond one-to-one to these derived in Eq. (5.95). As the flux in Eq. (5.146) only acts on the electromagnetic field part, the correspond-

ing numerical flux is consequently given by

$$n \cdot \underline{\underline{F}} - n \cdot \underline{\underline{F}}^* \tag{5.157}$$

$$= \begin{pmatrix} \left[\hat{\mathbf{Z}}_+ + \hat{\mathbf{Z}}_-\right]^{-1} \cdot \left[\Delta E - n(n \cdot \Delta E) + \hat{\mathbf{Z}}_+ \cdot n \times \Delta H\right] \\ \left[\hat{\mathbf{Y}}_+ + \hat{\mathbf{Y}}_-\right]^{-1} \cdot \left[\Delta H - n(n \cdot \Delta H) - \hat{\mathbf{Y}}_+ \cdot n \times \Delta E\right] \\ -\underline{\underline{a}}_{2,-}^{(1)} \cdot \left[\underline{\underline{b}}_{2,-}^{(1)}\right]^{-1} \cdot \underline{\underline{\epsilon}}_{\infty,-}^{-1} \cdot \left[\hat{\mathbf{Z}}_+ + \hat{\mathbf{Z}}_-\right]^{-1} \cdot \left[\Delta E - n(n \cdot \Delta E) + \hat{\mathbf{Z}}_+ \cdot n \times \Delta H\right] \\ \left(\underline{\underline{a}}_{1,-}^{(1)} \cdot \underline{\underline{b}}_{2,-}^{(1)} - \underline{\underline{a}}_{2,-}^{(1)} \cdot \underline{\underline{b}}_{1,-}^{(1)}\right) \cdot \left[\underline{\underline{b}}_{2,-}^{(1)}\right]^{-2} \cdot \underline{\underline{\epsilon}}_{\infty,-}^{-1} \cdot \left[\hat{\mathbf{Z}}_+ + \hat{\mathbf{Z}}_-\right]^{-1} \cdot \left[\Delta E - n(n \cdot \Delta E) + \hat{\mathbf{Z}}_+ \cdot n \times \Delta H\right] \\ \vdots \\ -\underline{\underline{a}}_{2,-}^{(N)} \cdot \left[\underline{\underline{b}}_{2,-}^{(N)}\right]^{-1} \cdot \underline{\underline{\epsilon}}_{\infty,-}^{-1} \cdot \left[\hat{\mathbf{Z}}_+ + \hat{\mathbf{Z}}_-\right]^{-1} \cdot \left[\Delta E - n(n \cdot \Delta E) + \hat{\mathbf{Z}}_+ \cdot n \times \Delta H\right] \\ \left(\underline{\underline{a}}_{1,-}^{(N)} \cdot \underline{\underline{b}}_{2,-}^{(N)} - \underline{\underline{a}}_{2,-}^{(N)} \cdot \underline{\underline{b}}_{1,-}^{(N)}\right) \cdot \left[\underline{\underline{b}}_{2,-}^{(N)}\right]^{-2} \cdot \underline{\underline{\epsilon}}_{\infty,-}^{-1} \cdot \left[\hat{\mathbf{Z}}_+ + \hat{\mathbf{Z}}_-\right]^{-1} \cdot \left[\Delta E - n(n \cdot \Delta E) + \hat{\mathbf{Z}}_+ \cdot n \times \Delta H\right] \end{pmatrix}.$$

For this, we basically inserted the already known terms for the electric and magnetic field differences from Eqs. (5.100). This numerical flux allows the application of all susceptibilities of the form Eq. (5.131), which covers a wide variety of applications for specific material models.

Based on this general treatment of ADEs, we next discuss the ADEs for the material models introduced in Chapter 3 and used in this thesis.

5.5.1 Lorentz model

First, we start with the Lorentz model, which describes the response of bound charges. From the susceptibility Eq. (3.7) in the isotropic case, i.e.,

$$\chi_{\mathrm{L}}(\omega) = \frac{\Delta_\epsilon \omega_{\mathrm{L}}^2}{\omega_{\mathrm{L}}^2 - \mathrm{i}\gamma_{\mathrm{L}}\omega - \omega^2} \,, \tag{5.158}$$

we can deduce the corresponding tensors

$$\underline{\underline{a}}_0 = \Delta_\epsilon \omega_{\mathrm{L}}^2 \underline{\underline{1}}, \quad \underline{\underline{a}}_1 = \underline{\underline{a}}_2 = \underline{\underline{0}}, \quad \underline{\underline{b}}_0 = \omega_{\mathrm{L}}^2 \underline{\underline{1}}, \quad \underline{\underline{b}}_1 = \gamma_{\mathrm{L}} \underline{\underline{1}}, \quad \text{and} \quad \underline{\underline{b}}_2 = \underline{\underline{1}}\,. \tag{5.159}$$

They are determined by the Lorentz pole strength Δ_ϵ, the pole frequency ω_{L} as well as the damping γ_{L}. Therefore, the ADEs used in the DGTD method for the Lorentz model are

$$\epsilon_{\mathrm{bg}}\partial_t E(r,t) = \nabla \times H(r,t) - j_{\mathrm{p}}(r,t)\,, \tag{5.160a}$$

$$\partial_t P(r,t) = j_{\mathrm{aux}}(r,t) \equiv j_{\mathrm{p}}(r,t)\,, \tag{5.160b}$$

$$\partial_t j_{\mathrm{p}}(r,t) = -\gamma_{\mathrm{L}} j_{\mathrm{p}}(r,t) - \omega_{\mathrm{L}}^2 P(r,t) + \Delta_\epsilon \omega_{\mathrm{L}}^2 E(r,t)\,. \tag{5.160c}$$

Consequently, the model is purely local as it does not involve a flux-term in the auxiliary fields. Furthermore, there is no coupling to currents of other susceptibilities, as only the $\underline{\underline{a}}_0$-term in the susceptibility is non-zero. To compute the influence of a Lorentz model, the DGTD method

requires two auxiliary fields, i.e., the polarization $\boldsymbol{P}$ and current $\boldsymbol{j}_p$. It doubles the degrees of freedom to be computed in each element containing the material model.

5.5.2 Drude model

Second, we discuss the ADEs for the Drude model used to describe the response of a metal. The susceptibility (see Eq. (3.15)) given by

$$\chi(\omega) = -\frac{\omega_{\mathrm{pl}}^2}{\omega^2 + \mathrm{i}\omega\gamma}, \tag{5.161}$$

determines the susceptibility factors by the plasma frequency ω_{pl} and the damping constant γ as

$$\underline{\underline{a}}_0 = \omega_{\mathrm{pl}}^2 \underline{\underline{1}}, \quad \underline{\underline{a}}_1 = \underline{\underline{a}}_2 = \underline{\underline{b}}_0 = \underline{\underline{0}}, \quad \underline{\underline{b}}_1 = \gamma \underline{\underline{1}}, \quad \text{and} \quad \underline{\underline{b}}_2 = \underline{\underline{1}}. \tag{5.162}$$

The corresponding ADEs have the same properties as for the Lorentz model and read

$$\epsilon_{\mathrm{bg}}\partial_t \boldsymbol{E}(\boldsymbol{r}, t) = \nabla \times \boldsymbol{H}(\boldsymbol{r}, t) - \boldsymbol{j}_{\mathrm{p}}(\boldsymbol{r}, t), \tag{5.163a}$$

$$\partial_t \boldsymbol{j}_{\mathrm{p}}(\boldsymbol{r}, t) = -\gamma \boldsymbol{j}_{\mathrm{p}}(\boldsymbol{r}, t) + \omega_{\mathrm{pl}}^2 \boldsymbol{E}(\boldsymbol{r}, t). \tag{5.163b}$$

In contrast to the Lorentz model, only the current, i.e., one auxiliary field is required for the Drude model.

5.5.3 Effective medium approximation HMM

As third and last material compliant with the rational form of the susceptibility Eq. (5.131), we discuss the effective medium approximation (EMA) hyperbolic metamaterial (HMM) introduced in Section 3.4.1. The anisotropic permittivity Eqs. (3.38) and (3.41) of a one-dimensional stack of dielectric and metallic layers is given by

$$\underline{\underline{\epsilon}}(\omega) = \begin{pmatrix} -\frac{(1-f)\omega_{\mathrm{pl}}^2 - \epsilon_{\mathrm{d}}\omega(\omega+\mathrm{i}\gamma)}{\omega(\omega+\mathrm{i}\gamma)} & 0 & 0 \\ 0 & -\frac{(1-f)\omega_{\mathrm{pl}}^2 - \epsilon_{\mathrm{d}}\omega(\omega+\mathrm{i}\gamma)}{\omega(\omega+\mathrm{i}\gamma)} & 0 \\ 0 & 0 & \epsilon_{\mathrm{d}}\frac{\omega_{\mathrm{pl}}^2 - \epsilon_{\mathrm{d}}\omega(\omega+\mathrm{i}\gamma)}{f\omega_{\mathrm{pl}}^2 - \epsilon_{\mathrm{d}}\omega(\omega+\mathrm{i}\gamma)} \end{pmatrix}. \tag{5.164}$$

Here, we assume the layers to be stacked in z-direction. The layers are described by a non-dispersive dielectric ϵ_d as well as the Drude model with plasma frequency ω_{pl} and damping γ. The thickness ratio of the single layers within a unit cell is described by the fill factor $f \in [0, 1]$ from pure metallic to pure dielectric. Thus, the tensor entries in the permittivity similar to

Eq. (5.131), are determined by

$$\underline{\underline{a}}_0 = \begin{pmatrix} (1-f)\omega_{\mathrm{pl}}^2 & 0 & 0 \\ 0 & (1-f)\omega_{\mathrm{pl}}^2 & 0 \\ 0 & 0 & \omega_{\mathrm{pl}}^2 \end{pmatrix}, \quad \underline{\underline{a}}_1 = \epsilon_{\mathrm{d}}\gamma\,\underline{\underline{1}}, \quad \underline{\underline{a}}_2 = \epsilon_{\mathrm{d}}\,\underline{\underline{1}}, \tag{5.165a}$$

$$\underline{\underline{b}}_0 = \begin{pmatrix} 0 & 0 & 0 \\ 0 & 0 & 0 \\ 0 & 0 & f\frac{\omega_{\mathrm{pl}}^2}{\epsilon_d} \end{pmatrix}, \qquad\qquad \underline{\underline{b}}_1 = \gamma\,\underline{\underline{1}}, \quad \underline{\underline{b}}_2 = \underline{\underline{1}}. \tag{5.165b}$$

This results in the set of ADEs describing the EMA HMM given by

$$\epsilon_d\partial_t \boldsymbol{E}(\boldsymbol{r},t) = \nabla \times \boldsymbol{H}(\boldsymbol{r},t) - \boldsymbol{j}_p(\boldsymbol{r},t)\,, \tag{5.166a}$$

$$\partial_t \boldsymbol{D}(\boldsymbol{r},t) = \nabla \times \boldsymbol{H}(\boldsymbol{r},t)\,, \tag{5.166b}$$

$$\partial_t j_{p,x/y}(\boldsymbol{r},t) = -\gamma j_{p,x/y}(\boldsymbol{r},t) + (1-f)\omega_{\mathrm{pl}}^2 E_{x/y}(\boldsymbol{r},t)\,, \tag{5.166c}$$

$$\partial_t j_{p,z}(\boldsymbol{r},t) = -\gamma j_{p,z}(\boldsymbol{r},t) - f\frac{\omega_{\mathrm{pl}}^2}{\epsilon_d} D_z(\boldsymbol{r},t) + \omega_{\mathrm{pl}}^2 E_z(\boldsymbol{r},t)\,. \tag{5.166d}$$

Here, we see that the ADEs are essentially those of the Drude model, but now with anisotropic driving parameters for the currents $\boldsymbol{j}_p$. In the metal limit $f = 0$, the ADEs are identical to those of the Drude model Eq. (5.163). In the dielectric limit $f = 1$, the driving terms of the currents vanish, as in this case $\boldsymbol{D}(\boldsymbol{r},t) = \epsilon_{\mathrm{d}}\boldsymbol{E}(\boldsymbol{r},t)$.

5.5.4 Four-level system

In contrast to the three previous material models, the 4LS material model introduced in Section 3.5 does not comply with the form of the susceptibility Eq. (5.131). However, the equations of motion (3.64) to (3.66) are already in the conservation form required for the DGTD method. We, therefore, expand the DGTD field vector with the polarizations, currents, and occupation densities as auxiliary fields, i.e.,

$$\boldsymbol{q}(\boldsymbol{r},t) = \begin{pmatrix} \boldsymbol{E}(\boldsymbol{r},t) \\ \boldsymbol{H}(\boldsymbol{r},t) \\ \boldsymbol{p}_{03}(\boldsymbol{r},t) \\ \boldsymbol{p}_{12}(\boldsymbol{r},t) \\ \boldsymbol{j}_{03}(\boldsymbol{r},t) \\ \boldsymbol{j}_{12}(\boldsymbol{r},t) \\ N_0(\boldsymbol{r},t) \\ N_1(\boldsymbol{r},t) \\ N_2(\boldsymbol{r},t) \\ N_3(\boldsymbol{r},t) \end{pmatrix}, \quad \text{and set} \quad \underline{\underline{Q}} = \begin{pmatrix} \underline{\underline{\epsilon}}_{\mathrm{bg}} & \underline{\underline{0}} & \underline{\underline{0}} & \cdots & 0 \\ \underline{\underline{0}} & \underline{\underline{\mu}}_{\mathrm{bg}} & \underline{\underline{0}} & \cdots & 0 \\ \underline{\underline{0}} & \underline{\underline{0}} & \underline{\underline{1}} & \cdots & 0 \\ \vdots & \vdots & \vdots & \ddots & \vdots \\ \underline{\underline{0}} & \underline{\underline{0}} & \underline{\underline{0}} & \cdots & 1 \end{pmatrix}. \tag{5.167}$$

The flux term for the auxiliary fields is zero and the source term is equivalent to the right-hand sides of Eqs. (3.64) to (3.66), respectively. Another difference lies in the initial condition of the

auxiliary fields. In contrast to the previous fields, the total occupation must fulfill $N_0 + N_1 + N_2 + N_3 = 1$. Typically, one chooses a fully occupied ground state $N_0 = 1$ as an initial condition, while all other fields are zero.

5.6 Perfectly matched layers

After the discussion on dispersive material models used in the thesis, we close this chapter with a description of PMLs. These are artificial anisotropic absorbing material layers [63, 74, 75, 151] used to prevent back-reflections caused by the BCs discussed in Section 5.3.4. Hereby, the PMLs are perfectly matched to the adjacent material, i.e., the boundary to the material to be terminated does not cause any reflections for an ideal PML. This idea of an absorbing material layer can be implemented with a complex continuation of the coordinates used in the PML regions [63, 151]. Typically, these regions are set as axis-aligned outer boundary layers to the computational domain, i.e., as a surrounding box for either two- or three-dimensional meshes as shown in Fig. 5.1.

As an example of how to introduce such a coordinate transformation, we consider a PML aligned in x-direction. For this, we replace the coordinates by

$$x \to \tilde{x} = x + i\frac{\sigma}{\omega}\left(x - x_{\mathrm{PML}}\right) \Theta\left(x - x_{\mathrm{PML}}\right) . \tag{5.168}$$

An example path for this transformation is shown in Fig. 5.7 (a). This coordinate continuation works in frequency domain and the specific choice of the real-valued prefactor $\frac{\sigma}{\omega}$ guarantees, that for a non-dispersive material all frequency components of a plane wave field

$$\boldsymbol{q}(x,\omega) \propto \mathrm{e}^{ik_x x} \overset{x_{\mathrm{PML}}=0}{\to} \boldsymbol{q}(\tilde{x},\omega) \propto \mathrm{e}^{ik_x x}\mathrm{e}^{-\sigma\frac{k_x}{\omega}x} , \quad \text{with} \quad k_x \leq \sqrt{\epsilon_{\mathrm{bg}}\mu_{\mathrm{bg}}}\,\omega , \tag{5.169}$$

are damped with the same spatial decay length σ^{-1}. The associated damping of a plane wave inside the PML is sketched in Fig. 5.7 (b).

The continuation of the coordinates within the PMLs causes a change of the spatial derivatives

$$\frac{\partial}{\partial x} \to \frac{1}{s_x(\omega)}\frac{\partial}{\partial x} , \quad \frac{\partial}{\partial y} \to \frac{1}{s_y(\omega)}\frac{\partial}{\partial y} \quad \text{and} \quad \frac{\partial}{\partial z} \to \frac{1}{s_z(\omega)}\frac{\partial}{\partial z} , \tag{5.170}$$

in Maxwell's curl-equations (2.31) in frequency domain to

$$-i\omega\epsilon\boldsymbol{E}\left(\omega\right) = \tilde{\nabla}\left(\omega\right) \times \boldsymbol{H}\left(\omega\right) , \tag{5.171a}$$

$$i\omega\mu\left(\omega\right)\boldsymbol{H}\left(\omega\right) = \tilde{\nabla}\left(\omega\right) \times \boldsymbol{E}\left(\omega\right) . \tag{5.171b}$$

Here, we defined

$$\tilde{\nabla}\left(\omega\right) = \left(\frac{1}{s_x\left(\omega\right)}\partial_x, \frac{1}{s_y\left(\omega\right)}\partial_y, \frac{1}{s_z\left(\omega\right)}\partial_z\right)^{\mathrm{T}} , \tag{5.172}$$
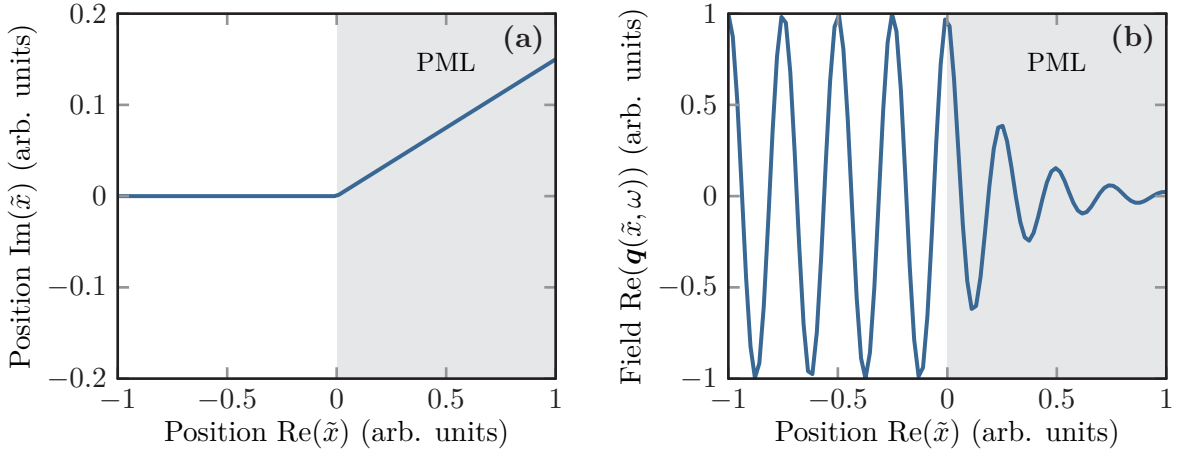
Figure 5.7: (a) Path of a complex continued coordinate $\tilde{x}$ used for the implementation of PMLs. **(b)** Damping of a plane wave, i.e., Fourier component of the field with a fixed frequency, impinging on the PML based on the coordinates shown in **(a)**.

with the stretching factors

$$s_i\left(\omega\right) = 1 - \frac{\sigma_i}{\mathrm{i}\omega}, \quad \text{for} \quad i \in \{x, y, z\}. \tag{5.173}$$

For the implementation of these PMLs, there exist two possibilities.

In the first case of uniaxial perfectly matched layers (uPMLs), the change in the derivatives is cast onto the material parameters, which introduces an anisotropic dispersive permittivity tensor $\underline{\underline{\epsilon}}(\omega)$ and permeability tensor $\underline{\underline{\mu}}(\omega)$. These artificial dispersive materials are described with ADEs as in the previous Section 5.5. This has the advantage of an unchanged numerical flux in the DGTD method and is, therefore, easier to implement. However, a trade-off using uPMLs arises, when dispersive materials shall be terminated. For each dispersive material model, a new set of ADEs has to be derived and implemented.

The second alternative case is to leave the coordinate stretching in place with the spatial derivative operators. This gives rise to stretched coordinate perfectly matched layers (SCPMLs). Due to the frequency-dependence of the stretching factors in Eq. (5.173), these PMLs still require a set of ADEs. Moreover, a new numerical flux has to be introduced for the auxiliary fields. Once implemented, the SCPMLs can be directly used with other ADEs for dispersive material models like those introduced in Section 5.5.

5.6.1 Uniaxial PMLs

Within the thesis, we only use uPMLs to terminate scalar non-dispersive materials defined by parameters ϵ_r for the permittivity and μ_r for the permeability. For the uPMLs, the material parameters are replaced by dispersive tensors [63, 152]

$$\epsilon_r \to \epsilon_r \underline{\underline{\Lambda}}_{\mathrm{tot}}(\omega) \quad \text{and} \quad \mu_r \to \mu_r \underline{\underline{\Lambda}}_{\mathrm{tot}}(\omega). \tag{5.174}$$

Here, the overall tensor

$$\underline{\underline{\Lambda}}_{\text{tot}}(\omega) = \underline{\underline{\Lambda}}_x(\omega) \cdot \underline{\underline{\Lambda}}_y(\omega) \cdot \underline{\underline{\Lambda}}_z(\omega) = \begin{pmatrix} \frac{s_y s_z}{s_x} & 0 & 0 \\ 0 & \frac{s_x s_z}{s_y} & 0 \\ 0 & 0 & \frac{s_x s_y}{s_z} \end{pmatrix}. \tag{5.175}$$

It is composed of the single direction tensors

$$\underline{\underline{\Lambda}}_x(\omega) = \begin{pmatrix} \frac{1}{s_x} & 0 & 0 \\ 0 & s_x & 0 \\ 0 & 0 & s_x \end{pmatrix}, \quad \underline{\underline{\Lambda}}_y(\omega) = \begin{pmatrix} s_y & 0 & 0 \\ 0 & \frac{1}{s_y} & 0 \\ 0 & 0 & s_x \end{pmatrix} \quad \text{and} \quad \underline{\underline{\Lambda}}_z(\omega) = \begin{pmatrix} s_z & 0 & 0 \\ 0 & s_z & 0 \\ 0 & 0 & \frac{1}{s_z} \end{pmatrix}, \tag{5.176}$$

which introduce the wave-damping in the specific directions. Inside the PML regions, the stretching factors $s_i(\omega)$ are defined by Eq. (5.173). The resulting frequency-dependent permittivity and permeability imply another set of ADEs to compute the fields inside the uPMLs. Similar to the previous Section 5.5, one finds the ADEs for the uPMLs [75, 151] given by

$$\epsilon_r \partial_t \boldsymbol{E}(\boldsymbol{r}, t) = \nabla \times \boldsymbol{H}(\boldsymbol{r}, t) + \begin{pmatrix} [+\sigma_x - \sigma_y - \sigma_z] \, \epsilon_r E_x(\boldsymbol{r}, t) \\ [-\sigma_x + \sigma_y - \sigma_z] \, \epsilon_r E_y(\boldsymbol{r}, t) \\ [-\sigma_x - \sigma_y + \sigma_z] \, \epsilon_r E_z(\boldsymbol{r}, t) \end{pmatrix} - \boldsymbol{P}(\boldsymbol{r}, t), \tag{5.177a}$$

$$\partial_t \boldsymbol{P}(\boldsymbol{r}, t) = \begin{pmatrix} [\sigma_x(+\sigma_x - \sigma_y - \sigma_z) + \sigma_y \sigma_z] \, \epsilon_r E_x(\boldsymbol{r}, t) \\ [\sigma_y(-\sigma_x + \sigma_y - \sigma_z) + \sigma_x \sigma_z] \, \epsilon_r E_y(\boldsymbol{r}, t) \\ [\sigma_z(-\sigma_x - \sigma_y + \sigma_z) + \sigma_x \sigma_y] \, \epsilon_r E_z(\boldsymbol{r}, t) \end{pmatrix} - \begin{pmatrix} \sigma_x P_x(\boldsymbol{r}, t) \\ \sigma_y P_y(\boldsymbol{r}, t) \\ \sigma_z P_z(\boldsymbol{r}, t) \end{pmatrix}, \tag{5.177b}$$

$$\mu_r \partial_t \boldsymbol{H}(\boldsymbol{r}, t) = -\nabla \times \boldsymbol{E}(\boldsymbol{r}, t) + \begin{pmatrix} [+\sigma_x - \sigma_y - \sigma_z] \, \epsilon_r H_x(\boldsymbol{r}, t) \\ [-\sigma_x + \sigma_y - \sigma_z] \, \epsilon_r H_y(\boldsymbol{r}, t) \\ [-\sigma_x - \sigma_y + \sigma_z] \, \epsilon_r H_z(\boldsymbol{r}, t) \end{pmatrix} - \boldsymbol{M}(\boldsymbol{r}, t), \tag{5.177c}$$

$$\partial_t \boldsymbol{M}(\boldsymbol{r}, t) = \begin{pmatrix} [\sigma_x(+\sigma_x - \sigma_y - \sigma_z) + \sigma_y \sigma_z] \, \epsilon_r H_x(\boldsymbol{r}, t) \\ [\sigma_y(-\sigma_x + \sigma_y - \sigma_z) + \sigma_x \sigma_z] \, \epsilon_r H_y(\boldsymbol{r}, t) \\ [\sigma_z(-\sigma_x - \sigma_y + \sigma_z) + \sigma_x \sigma_y] \, \epsilon_r H_z(\boldsymbol{r}, t) \end{pmatrix} - \begin{pmatrix} \sigma_x M_x(\boldsymbol{r}, t) \\ \sigma_y M_y(\boldsymbol{r}, t) \\ \sigma_z M_z(\boldsymbol{r}, t) \end{pmatrix}. \tag{5.177d}$$

This clearly shows that the ADEs for the auxiliary fields $\boldsymbol{P}$ and $\boldsymbol{M}$ do not contain a flux term and are therefore local.

For the use within the DGTD method, the choice of the spatial damping parameter $\sigma = \sigma_{x,y,z}$ is important. Inside a single uPML on the boundary of the computational domain in i-th direction, the corresponding value $\sigma_i > 0$ is set. Thus, only in the corners of the computational domain (see Fig. 5.1), the different σ_i-values are non-zero simultaneously. A thorough analysis of the ideal choice of damping parameters σ is provided, e.g., in [75, 151]. As an approximate rule, one sets the parameter to $\sigma \approx \frac{10}{2d}$, where d is the thickness of the PML which should at least cover half the main operation wavelength in the computation. If the values for σ are chosen too small, the uPML is hardly absorbing anything. If the damping σ is set to high, the exponential decay within an element cannot be approximated by the Lagrange polynomial basis functions (see Section 5.2.1). Therefore, in the limit of $\sigma \to \infty$ the PMLs turn into a perfect mirror. To

use the PMLs with dispersive materials, we next discuss the second option of SCPMLs.

5.6.2 Complex frequency-shifted stretched coordinate PMLs

For the SCPMLs, used to terminate dispersive materials, one additionally introduces a frequency filter into the damping [63, 153, 154]. This allows for selective damping of, e.g., high-frequency signals. In contrast to the DGTD method which assumes element-wise constant ADE parameters, the FDTD method uses such spatially dependent frequency filters, which can reduce the necessary PML thickness and partly deal with evanescent fields [63, 154]. One replaces the stretching factors in Eq. (5.173) by

$$s_i(\omega) = 1 - \frac{\sigma_i}{\mathrm{i}\omega - \alpha_i} \,. \tag{5.178}$$

Here, the introduced values α_i correspond to a low-pass filter. As the parameter is a complex shift to the frequencies, these PMLs are referred to as complex frequency-shifted perfectly matched layers (CFSPMLs).

In contrast to the uPMLs, we directly introduce auxiliary fields for the CFSPMLs in the complex continued Maxwell's equations (5.171), i.e.,

$$-\mathrm{i}\omega\epsilon\left(\omega\right)E_i(\boldsymbol{r},\omega) = \sum_{j,k}\epsilon_{ijk}\left[\partial_i H_k(\boldsymbol{r},\omega) + \underbrace{\left(\frac{1}{s_j\left(\omega\right)}-1\right)\partial_j H_k(\boldsymbol{r},\omega)}_{-G^E_{ij}(\boldsymbol{r},\omega)}\right], \tag{5.179a}$$

$$-\mathrm{i}\omega\mu\left(\omega\right)H_i(\boldsymbol{r},\omega) = -\sum_{j,k}\epsilon_{ijk}\left[\partial_j E_k(\boldsymbol{r},\omega) + \underbrace{\left(\frac{1}{s_j\left(\omega\right)}-1\right)\partial_j E_k(\boldsymbol{r},\omega)}_{G^H_{ij}(\boldsymbol{r},\omega)}\right]. \tag{5.179b}$$

Here, we define the auxiliary fields G^E and G^H. These can be cast back into the time domain using

$$\frac{1}{s_i\left(\omega\right)} - 1 = \frac{\sigma_i}{\mathrm{i}\omega - (\sigma_i + \alpha_i)} \,, \tag{5.180}$$

as well as

$$G^E_{ij}(\boldsymbol{r},\omega) = -\sum_{k}\epsilon_{ijk}\frac{\sigma_j}{\mathrm{i}\omega - \left(\sigma_j + \alpha_j\right)}\partial_j H_k(\boldsymbol{r},\omega)\,,$$

$$-\mathrm{i}\omega G^E_{ij}(\boldsymbol{r},\omega) = -\left(\sigma_j + \alpha_j\right)G^E_{ij}(\boldsymbol{r},\omega) + \sum_{k}\epsilon_{ijk}\sigma_j\partial_j H_k(\boldsymbol{r},\omega) \tag{5.181a}$$

$$\text{and} \qquad G^H_{ij}(\boldsymbol{r},\omega) = \sum_{k}\epsilon_{ijk}\frac{\sigma_j}{\mathrm{i}\omega - \left(\sigma_j + \alpha_j\right)}\partial_j E_k(\boldsymbol{r},\omega)\,,$$

$$-\mathrm{i}\omega G_{ij}^{H}(\boldsymbol{r},\omega) = -\left(\sigma_j + \alpha_j\right) G_{ij}^{H}(\boldsymbol{r},\omega) - \sum_k \epsilon_{ijk}\sigma_j\partial_j E_k(\boldsymbol{r},\omega)\,. \tag{5.181b}$$

Replacing the frequency factors according to Eq. (2.33), the ADEs for the auxiliary fields read

$$\partial_t G_{ij}^{E}(\boldsymbol{r},t) = -\left(\sigma_j + \alpha_j\right) G_{ij}^{E}(\boldsymbol{r},t) + \sum_k \epsilon_{ijk}\sigma_j\partial_j H_k(\boldsymbol{r},t) \tag{5.182a}$$

$$\text{and} \qquad \partial_t G_{ij}^{H}(\boldsymbol{r},t) = -\left(\sigma_j + \alpha_j\right) G_{ij}^{H}(\boldsymbol{r},t) - \sum_k \epsilon_{ijk}\sigma_j\partial_j E_k(\boldsymbol{r},t)\,. \tag{5.182b}$$

Besides the damping with the parameter $\sigma_j + \alpha_j$, these contain spatial derivatives of the $\boldsymbol{E}$- and $\boldsymbol{H}$-field as driving terms. Therefore, there is a non-vanishing flux component for the auxiliary fields. Assuming, without loss of generality, non-dispersive materials, we can cast these ADEs into the conservation form Eq. (5.1) for the DGTD method. In contrast to the uPMLs, we have twice as many auxiliary fields and the field vector is given by

$$\boldsymbol{q}(\boldsymbol{r},t) = \left(E_x, E_y, E_z, H_x, H_y, H_z, G_{xy}^{E}, G_{xz}^{E}, G_{yx}^{E}, G_{yz}^{E}, G_{zx}^{E}, G_{zy}^{E}, G_{xy}^{H}, G_{xz}^{H}, G_{yx}^{H}, G_{yz}^{H}, G_{zx}^{H}, G_{zy}^{H}\right)^{\mathrm{T}}\,. \tag{5.183}$$

The material tensor is extended to

$$\underline{\underline{Q}} = \mathrm{diag}\left(\epsilon, \epsilon, \epsilon, \mu, \mu, \mu, \sigma_y^{-1}, \sigma_z^{-1}, \sigma_x^{-1}, \sigma_z^{-1}, \sigma_x^{-1}, \sigma_y^{-1}, \sigma_y^{-1}, \sigma_z^{-1}, \sigma_x^{-1}, \sigma_z^{-1}, \sigma_x^{-1}, \sigma_y^{-1}\right)\,, \tag{5.184}$$

while the source term, neglecting other ADE or free volumetric sources, reads

$$\boldsymbol{S}(\boldsymbol{r},t) = -\Bigg(G_{xy}^{E} + G_{xz}^{E}, G_{yx}^{E} + G_{yz}^{E}, G_{zx}^{E} + G_{zy}^{E}, G_{xy}^{H} + G_{xz}^{H}, G_{yx}^{H} + G_{yz}^{H}, G_{zx}^{H} + G_{zy}^{H},$$

$$\frac{\alpha_y + \sigma_y}{\sigma_y}G_{xy}^{E}, \frac{\alpha_z + \sigma_z}{\sigma_z}G_{xz}^{E}, \frac{\alpha_x + \sigma_x}{\sigma_x}G_{yx}^{E}, \frac{\alpha_z + \sigma_z}{\sigma_z}G_{yz}^{E}, \frac{\alpha_x + \sigma_x}{\sigma_x}G_{zx}^{E}, \frac{\alpha_y + \sigma_y}{\sigma_y}G_{zy}^{E},$$

$$\frac{\alpha_y + \sigma_y}{\sigma_y}G_{xy}^{H}, \frac{\alpha_z + \sigma_z}{\sigma_z}G_{xz}^{H}, \frac{\alpha_x + \sigma_x}{\sigma_x}G_{yx}^{H}, \frac{\alpha_z + \sigma_z}{\sigma_z}G_{yz}^{H}, \frac{\alpha_x + \sigma_x}{\sigma_x}G_{zx}^{H}, \frac{\alpha_y + \sigma_y}{\sigma_y}G_{zy}^{H}, \Bigg)^{\mathrm{T}}\,. \tag{5.185}$$

Finally, the flux entries take the form

$$\boldsymbol{e}_x \cdot \underline{\underline{\boldsymbol{F}}}\left(\boldsymbol{q}\right) = \left(0, H_z, -H_y, 0, -E_z, E_y, \quad 0, 0, H_z, 0, -H_y, 0, \quad 0, 0, -E_z, 0, E_y, 0\right)^{\mathrm{T}}, \tag{5.186a}$$

$$\boldsymbol{e}_y \cdot \underline{\underline{\boldsymbol{F}}}\left(\boldsymbol{q}\right) = \left(-H_z, 0, H_x, E_z, 0, -E_x, \quad -H_z, 0, 0, 0, 0, H_x, \quad E_z, 0, 0, 0, 0, -E_x\right)^{\mathrm{T}}, \tag{5.186b}$$

$$\boldsymbol{e}_z \cdot \underline{\underline{\boldsymbol{F}}}\left(\boldsymbol{q}\right) = \left(H_y, -H_x, 0, -E_y, E_x, 0, \quad 0, H_y, 0, -H_x, 0, 0, \quad 0, -E_y, 0, E_x, 0, 0\right)^{\mathrm{T}}. \tag{5.186c}$$

As the auxiliary fields G^E and G^H contain spatial derivatives of the $\boldsymbol{E}$- and $\boldsymbol{H}$-fields and are determined by non-zero flux terms, we require a derivation of the numerical upwind flux here.

5.6.3 Upwind flux for CFSPMLs

Due to the splitting of the curl-operator in Eqs. (5.179), the derivation of the CFSPML upwind flux for the auxiliary fields becomes more challenging. The simplification to only tangential field components in the Riemann problem Eq. (5.47) used for the upwind flux derivation is no longer possible here. Based on the splitting which is similar to the original split-field PMLs by Bérenger [63, 154, 155] used in the FDTD method, the numerical split-flux

$$\left[\boldsymbol{n}\cdot\boldsymbol{F} - \boldsymbol{n}\cdot\boldsymbol{F}^*\right]_{G^E_{ij}} = \sum_k \epsilon_{ijk}\frac{n_j}{\bar{Z}}\left(Z_+\Delta\boldsymbol{H} - \alpha\boldsymbol{n}\times\Delta\boldsymbol{E}\right)_k, \tag{5.187a}$$

$$\left[\boldsymbol{n}\cdot\boldsymbol{F} - \boldsymbol{n}\cdot\boldsymbol{F}^*\right]_{G^H_{ij}} = \sum_k \epsilon_{ijk}\frac{n_j}{\bar{Y}}\left(Y_+\Delta\boldsymbol{E} + \alpha\boldsymbol{n}\times\Delta\boldsymbol{H}\right)_k, \tag{5.187b}$$

has been suggested in [75, 151]. This split-flux is induced by an analogy consideration from the isotropic numerical upwind flux Eq. (5.107) including the admittances $Y_\pm$ and impedances $Z_\pm$ therein. The original flux, e.g.,

$$\left[\boldsymbol{n}\cdot\boldsymbol{F} - \boldsymbol{n}\cdot\boldsymbol{F}^*\right]_{E_x} = \left[\boldsymbol{n}\cdot\boldsymbol{F} - \boldsymbol{n}\cdot\boldsymbol{F}^*\right]_{G^E_{xy}} + \left[\boldsymbol{n}\cdot\boldsymbol{F} - \boldsymbol{n}\cdot\boldsymbol{F}^*\right]_{G^E_{xz}} \tag{5.188}$$

is split into the two contributions of the auxiliary fields.

Here, we provide a full derivation of this flux and show that it agrees with the upwind flux for the CFSPML set of ADEs (5.182). For the derivation of the upwind flux, we follow the steps presented in Section 5.3.1. For this, we here consider the one-dimensional Riemann problem on an element interface for the entire 18-dimensional field vector Eq. (5.183). To obtain the characteristics and field discontinuities near the interface (see Fig. 5.4), we need to diagonalize the matrix

$$\hat{\mathbf{A}}_{\text{CFSPML}} = \begin{pmatrix} 0 & 0 & 0 & 0 & \frac{n_z}{\epsilon} & -\frac{n_y}{\epsilon} \\ 0 & 0 & 0 & -\frac{n_z}{\epsilon} & 0 & \frac{n_x}{\epsilon} \\ 0 & 0 & 0 & \frac{n_y}{\epsilon} & -\frac{n_x}{\epsilon} & 0 \\ 0 & -\frac{n_z}{\mu} & \frac{n_y}{\mu} & 0 & 0 & 0 \\ \frac{n_z}{\mu} & 0 & -\frac{n_x}{\mu} & 0 & 0 & 0 \\ -\frac{n_y}{\mu} & \frac{n_x}{\mu} & 0 & 0 & 0 & 0 \\ 0 & 0 & 0 & 0 & 0 & -n_y\sigma_y \\ 0 & 0 & 0 & 0 & n_z\sigma_z & 0 \\ 0 & 0 & 0 & 0 & 0 & n_x\sigma_x \\ 0 & 0 & 0 & -n_z\sigma_z & 0 & 0 \\ 0 & 0 & 0 & 0 & -n_x\sigma_x & 0 \\ 0 & 0 & 0 & n_y\sigma_y & 0 & 0 \\ 0 & 0 & n_y\sigma_y & 0 & 0 & 0 \\ 0 & -n_z\sigma_z & 0 & 0 & 0 & 0 \\ 0 & 0 & -n_x\sigma_x & 0 & 0 & 0 \\ n_z\sigma_z & 0 & 0 & 0 & 0 & 0 \\ 0 & n_x\sigma_x & 0 & 0 & 0 & 0 \\ -n_y\sigma_y & 0 & 0 & 0 & 0 & 0 \end{pmatrix} \hat{\mathbf{0}}_{12\times18} \quad . \tag{5.189}$$

It determines the field dynamics in the Riemann problem Eq. (5.47). However, a problem arises here.

First, the upper 6×6-matrix block determined by Maxwell's curl equations is already singular. In the setup deriving the flux for Maxwell's equations without any auxiliary fields in Section 5.3.2, this allowed fixing the normal field components in dependence of the tangential components. Therefore, the Riemann problem Eq. (5.75) only contains the tangential fields. Despite its singularity, this matrix is well diagonalizable, similarly to that of the material ADEs shown in Eq. (5.150).

The second even more important problem arises as the matrix $\hat{\mathbf{A}}_{\mathrm{CFSPML}}$ is not even diagonalizable, which is assumed for the upwind flux derivation in Eq. (5.49). The matrix $\hat{\mathbf{A}}_{\mathrm{CFSPML}}$ can be transformed into a Jordan normal form, i.e.,

$$\hat{\mathbf{A}}_{\mathrm{CFSPML}} = \hat{\mathbf{V}} \cdot \hat{\mathbf{J}} \cdot \hat{\mathbf{V}}^{-1} , \tag{5.190}$$

in which the matrix $\hat{\mathbf{J}}$ is not diagonal. It contains block matrices with entries both on the diagonal and one-entries on the superdiagonal of each block. Here, it takes the form

$$\hat{\mathbf{J}} = \begin{pmatrix} \hat{\mathbf{0}}_{10 \times 10} & & & & & \hat{\mathbf{0}}_{8 \times 10} & & & \\ & 0 & 1 & 0 & 0 & 0 & 0 & 0 & 0 \\ & 0 & 0 & 0 & 0 & 0 & 0 & 0 & 0 \\ & 0 & 0 & 0 & 1 & 0 & 0 & 0 & 0 \\ & 0 & 0 & 0 & 0 & 0 & 0 & 0 & 0 \\ \hat{\mathbf{0}}_{10 \times 8} & 0 & 0 & 0 & 0 & -\frac{1}{\sqrt{\epsilon\mu}} & 0 & 0 & 0 \\ & 0 & 0 & 0 & 0 & 0 & -\frac{1}{\sqrt{\epsilon\mu}} & 0 & 0 \\ & 0 & 0 & 0 & 0 & 0 & 0 & \frac{1}{\sqrt{\epsilon\mu}} & 0 \\ & 0 & 0 & 0 & 0 & 0 & 0 & 0 & \frac{1}{\sqrt{\epsilon\mu}} \end{pmatrix} . \tag{5.191}$$

Hence, within the Riemann problem, we have to account for the two non-diagonal 2×2-blocks

$$\hat{\mathbf{J}}_{11,12} = \hat{\mathbf{J}}_{13,14} = \begin{pmatrix} 0 & 1 \\ 0 & 0 \end{pmatrix} , \tag{5.192}$$

contained in the diagonal of the matrix $\hat{\mathbf{J}}$ for the Jordan normal form of $\hat{\mathbf{A}}_{\mathrm{CFSPML}}$. As the Riemann problem splits apart for every diagonal matrix block, we solve the homogeneous Riemann problem

$$\partial_t \boldsymbol{q}(n,t) + \hat{\mathbf{A}} \partial_n \boldsymbol{q}(n,t) = 0 , \tag{5.193}$$

with two-dimensional fields $\boldsymbol{q}(n,t)$, where

$$\hat{\mathbf{A}} = \hat{\mathbf{V}} \cdot \begin{pmatrix} \lambda & 1 \\ 0 & \lambda \end{pmatrix} \cdot \hat{\mathbf{V}}^{-1} . \tag{5.194}$$

As in the fully diagonalizable case, we expand the fields $\boldsymbol{q}$ in terms of the (associated) eigenvectors

$\boldsymbol{v}$ contained in the matrix $\hat{\mathbf{V}}$ and define

$$\boldsymbol{\alpha}(n,t) = \hat{\mathbf{V}}^{-1} \cdot \boldsymbol{q}(n,t) \,. \tag{5.195}$$

This means we need to solve two equations for the field amplitudes $\boldsymbol{\alpha}$.

Similar to the fully diagonalizable case Eq. (5.51), this is an advection equation for the second amplitude given by

$$\partial_t \alpha_2(n,t) + \lambda \partial_n \alpha_2(n,t) = 0 \,. \tag{5.196}$$

It is solved by

$$\alpha_2(n,t) = \alpha_2(n - \lambda t, t = 0) \,. \tag{5.197}$$

For the first amplitude, we find the inhomogeneous advection equation

$$\partial_t \alpha_1(n,t) + \lambda \partial_n \alpha_1(n,t) = -\partial_n \alpha_2(n,t) \,. \tag{5.198}$$

Note, how the solution of α_2 acts as a source term here. Considering the solution for the Riemann problem with the initial field jump $\Delta\alpha_2 = \alpha_2^+ - \alpha_2^-$, this source term is of the form

$$-\partial_n \alpha_2(n,t) = \left(\alpha_2^+ - \alpha_2^- \right) \delta(n - \lambda t) \,. \tag{5.199}$$

We can use the Green's function

$$G\left(n - n', t - t'\right) = \delta\left(n - n' - \lambda(t - t')\right) \,, \tag{5.200}$$

to calculate the solution of the inhomogeneous advection Eq. (5.198). Thus, the solution contains a δ-distribution. Here, in the relevant case of $\lambda = 0$, it is given by

$$\alpha_1(n,t) = -\partial_n \alpha_2(n)t + \alpha_1(n, t = 0) = \left(\alpha_2^+ - \alpha_2^- \right) t\,\delta(n) + \alpha_1(n, t = 0) \,, \tag{5.201}$$

and contains a δ-discontinuity at the interface $n = 0$, which grows linearly in time. However, in this specific case, this δ-discontinuity poses no serious problem. Although we need to know the field values at the material interface to calculate the flux, the associated eigenvectors only contain entries for the CFSPML auxiliary field components G^E and G^H. Similar to the discussion about the flux derivation for the dispersive material ADEs in Section 5.5, also the CFSPML flux in Eq. (5.186) relies on the evaluation of the electromagnetic field components only. The relevant eigenvectors and associated eigenvectors for the non-zero blocks of the Jordan normal form in

Eq. (5.190) are given by

$$
\begin{pmatrix} \boldsymbol{v}_{11} & \boldsymbol{v}_{12} & \boldsymbol{v}_{13} & \boldsymbol{v}_{14} & \boldsymbol{v}_{15} & \boldsymbol{v}_{16} & \boldsymbol{v}_{17} & \boldsymbol{v}_{18} \end{pmatrix} = \tag{5.202}
$$

$$
\begin{pmatrix}
0 & 0 & 0 & n_x & \frac{n_z}{\sqrt{\epsilon\mu}} & 0 & -\frac{n_z}{\sqrt{\epsilon\mu}} & 0 \\[4pt]
0 & 0 & 0 & n_y & 0 & -\frac{n_z}{\sqrt{\epsilon\mu}} & 0 & \frac{n_z}{\sqrt{\epsilon\mu}} \\[4pt]
0 & 0 & 0 & n_z & -\frac{n_x}{\sqrt{\epsilon\mu}} & \frac{n_y}{\sqrt{\epsilon\mu}} & \frac{n_x}{\sqrt{\epsilon\mu}} & -\frac{n_y}{\sqrt{\epsilon\mu}} \\[4pt]
0 & n_x & 0 & 0 & \frac{n_x n_y}{\mu} & -\frac{n_y^2+n_z^2}{\mu} & \frac{n_x n_y}{\mu} & -\frac{n_y^2+n_z^2}{\mu} \\[4pt]
0 & n_y & 0 & 0 & \frac{n_y^2-1}{\mu} & \frac{n_x n_y}{\mu} & \frac{n_y^2-1}{\mu} & \frac{n_x n_y}{\mu} \\[4pt]
0 & n_z & 0 & 0 & \frac{n_y n_z}{\mu} & \frac{n_x n_z}{\mu} & \frac{n_y n_z}{\mu} & \frac{n_x n_z}{\mu} \\[4pt]
-n_y n_z \sigma_y & 0 & 0 & 0 & \frac{n_y^2 n_z \sigma_y}{Z} & \frac{n_x n_y n_z \sigma_y}{Z} & -\frac{n_y^2 n_z \sigma_y}{Z} & -\frac{n_x n_y n_z \sigma_y}{Z} \\[4pt]
n_y n_z \sigma_z & 0 & 0 & 0 & \frac{n_z\left(n_x^2+n_z^2\right)\sigma_z}{Z} & -\frac{n_x n_y n_z \sigma_z}{Z} & \frac{\left(n_y^2-1\right)n_z \sigma_z}{Z} & \frac{n_x n_y n_z \sigma_z}{Z} \\[4pt]
n_x n_z \sigma_x & 0 & 0 & 0 & -\frac{n_x n_y n_z \sigma_x}{Z} & -\frac{n_x^2 n_z \sigma_x}{Z} & \frac{n_x n_y n_z \sigma_x}{Z} & \frac{n_x^2 n_z \sigma_x}{Z} \\[4pt]
-n_x n_z \sigma_z & 0 & 0 & 0 & \frac{n_x n_y n_z \sigma_z}{Z} & -\frac{n_z\left(n_y^2+n_z^2\right)\sigma_z}{Z} & -\frac{n_x n_y n_z \sigma_z}{Z} & \frac{n_z\left(n_y^2+n_z^2\right)\sigma_z}{Z} \\[4pt]
-n_x n_y \sigma_x & 0 & 0 & 0 & \frac{n_x\left(n_y^2-1\right)\sigma_x}{Z} & \frac{n_x^2 n_y \sigma_x \sqrt{\epsilon}}{\sqrt{\mu}} & \frac{n_x\left(n_x^2+n_z^2\right)\sigma_x}{Z} & -\frac{n_x^2 n_y \sigma_x}{Z} \\[4pt]
n_x n_y \sigma_y & 0 & 0 & 0 & -\frac{n_x n_y^2 \sigma_y}{Z} & \frac{n_y\left(n_y^2+n_z^2\right)\sigma_y}{Z} & \frac{n_x n_y^2 \sigma_y}{Z} & -\frac{n_y\left(n_y^2+n_z^2\right)\sigma_y \sqrt{\epsilon}}{\sqrt{\mu}} \\[4pt]
0 & 0 & n_y n_z \sigma_y & 0 & n_x n_y \sigma_y & -n_y^2 \sigma_y & n_x n_y \sigma_y & -n_y^2 \sigma_y \\[4pt]
0 & 0 & -n_y n_z \sigma_z & 0 & 0 & -n_z^2 \sigma_z & 0 & -n_z^2 \sigma_z \\[4pt]
0 & 0 & -n_x n_z \sigma_x & 0 & -n_x^2 \sigma_x & n_x n_y \sigma_x & -n_x^2 \sigma_x & n_x n_y \sigma_x \\[4pt]
0 & 0 & n_x n_z \sigma_z & 0 & -n_z^2 \sigma_z & 0 & -n_z^2 \sigma_z & 0 \\[4pt]
0 & 0 & n_x n_y \sigma_x & 0 & 0 & n_x n_z \sigma_x & 0 & n_x n_z \sigma_x \\[4pt]
0 & 0 & -n_x n_y \sigma_y & 0 & n_y n_z \sigma_y & 0 & n_y n_z \sigma_y & 0
\end{pmatrix}.
$$

These are calculated with the help of Mathematica [156] for the case in which the element's interface normal component $|n_y| < 1$. The vectors $\boldsymbol{v}_{11}$ and $\boldsymbol{v}_{13}$ associated with the inhomogeneous advection equations are zero for the first six electromagnetic field entries and are therefore not contributing to the numerical flux. The same holds for the first ten vectors $\boldsymbol{v}_1$ to $\boldsymbol{v}_{10}$ not shown here.

The calculation of the numerical upwind flux defined in Eq. (5.64) requires the field differences on the element interface, i.e.,

$$
\boldsymbol{q}^{-,*} - \boldsymbol{q}^- = \delta_1 \boldsymbol{v}_{-,15} + \delta_2 \boldsymbol{v}_{-,16} + \delta_3 \boldsymbol{v}_{12} + \delta_4 \boldsymbol{v}_{14} + \sum_j \delta_{-,j}^{(\mathrm{nc})} \boldsymbol{v}_{\mathrm{L}j}^{(\mathrm{nc})} \tag{5.203a}
$$

$$
\text{and} \quad \boldsymbol{q}^+ - \boldsymbol{q}^{+,*} = \delta_5 \boldsymbol{v}_{+,17} + \delta_6 \boldsymbol{v}_{+,18} + \delta_7 \boldsymbol{v}_{12} + \delta_8 \boldsymbol{v}_{14} + \sum_k \delta_{+,k}^{(\mathrm{nc})} \boldsymbol{v}_{+,j}^{(\mathrm{nc})}. \tag{5.203b}
$$

These differences between the fields $\boldsymbol{q}^\pm$ at the beginning of a DGTD time step and the interface fields $\boldsymbol{q}^{\pm,*}$ at the end of the time step, contain the amplitude differences $\boldsymbol{\delta}$ as defined in Eq. (5.59). Additionally, the eigenvectors, i.e., field polarization states, with either zero and negative or zero and positive characteristic speeds are included. The characteristic speeds are obtained from the diagonal of the matrix $\hat{\boldsymbol{J}}$ shown in Eq. (5.191). Note, that field eigenvectors $\boldsymbol{v}_{12}$ and $\boldsymbol{v}_{14}$ with zero speed are accounted for twice on each side of the interface. Accordingly, the field amplitude differences δ_j are introduced twice on each element side and are fixed by the field BCs. In

contrast to the defining Eq. (5.59) which shall hold on either element interface side individually, a new set of indices is introduced here. All eigenvectors without entries in the electromagnetic fields are labeled as non-contributing (nc), as they do not contribute to the numerical flux, which is calculated by applying the flux Eq. (5.186) to the interface field differences.

To impose the field BCs, we rely on the interface coordinate system $\{\boldsymbol{n}, \boldsymbol{t}_1, \boldsymbol{t}_2\}$ defined in Section 5.3.1. The continuity of the tangential $\boldsymbol{E}$- and $\boldsymbol{H}$-field components (see Eqs. (2.44)) are imposed by

$$\begin{pmatrix} \boldsymbol{t}_1 \\ \boldsymbol{0}_{(15)} \end{pmatrix} \cdot \left(\boldsymbol{q}^{+,*} - \boldsymbol{q}^{-,*} \right) = 0 \quad \text{and} \quad \begin{pmatrix} \boldsymbol{0}_{(3)} \\ \boldsymbol{t}_1 \\ \boldsymbol{0}_{(12)} \end{pmatrix} \cdot \left(\boldsymbol{q}^{+,*} - \boldsymbol{q}^{-,*} \right) = 0 \,, \tag{5.204a}$$

$$\begin{pmatrix} \boldsymbol{t}_2 \\ \boldsymbol{0}_{(15)} \end{pmatrix} \cdot \left(\boldsymbol{q}^{+,*} - \boldsymbol{q}^{-,*} \right) = 0 \quad \text{and} \quad \begin{pmatrix} \boldsymbol{0}_{(3)} \\ \boldsymbol{t}_2 \\ \boldsymbol{0}_{(12)} \end{pmatrix} \cdot \left(\boldsymbol{q}^{+,*} - \boldsymbol{q}^{-,*} \right) = 0 \,. \tag{5.204b}$$

The continuity of the $\boldsymbol{D}$- and $\boldsymbol{B}$-fields normal component (see Eqs. (2.43)) is equivalent to

$$\begin{pmatrix} \boldsymbol{n} \\ \boldsymbol{0}_{(15)} \end{pmatrix} \cdot \left(\hat{\mathbf{Q}}_+ \cdot \boldsymbol{q}^{+,*} - \hat{\mathbf{Q}}_- \cdot \boldsymbol{q}^{-,*} \right) = 0 \quad \text{and} \quad \begin{pmatrix} \boldsymbol{0}_{(3)} \\ \boldsymbol{n} \\ \boldsymbol{0}_{(12)} \end{pmatrix} \cdot \left(\hat{\mathbf{Q}}_+ \cdot \boldsymbol{q}^{+,*} - \hat{\mathbf{Q}}_- \cdot \boldsymbol{q}^{-,*} \right) = 0 \,.$$
$$\tag{5.205}$$

All non-contributing eigenvectors $\boldsymbol{v}_{\pm}^{(\mathrm{nc})}$ are normal to the vectors used for the BC definition, such that the specification of the amplitudes δ_1 to δ_8 suffices to determine the numerical upwind flux. Since the vectors $\boldsymbol{v}_{12}$ and $\boldsymbol{v}_{14}$ correspond to the normal vectors for either the $\boldsymbol{E}$- or $\boldsymbol{H}$-field components, we can not determine the amplitude pairs δ_3, δ_7 and δ_4, δ_8 completely. We find, that

$$\boldsymbol{n} \cdot \Delta \boldsymbol{D} = \epsilon_- \delta_3 + \epsilon_+ \delta_7 \quad \text{and} \quad \boldsymbol{n} \cdot \Delta \boldsymbol{B} = \mu_- \delta_4 + \mu_+ \delta_8 \,. \tag{5.206}$$

A possible choice to equal out the amplitudes is

$$\delta_3 = \delta_7 = \frac{\boldsymbol{n} \cdot \Delta \boldsymbol{D}}{\epsilon_- + \epsilon_+} \quad \text{and} \quad \delta_4 = \delta_8 = \frac{\boldsymbol{n} \cdot \Delta \boldsymbol{B}}{\mu_- + \mu_+} \,. \tag{5.207}$$

This equally distributes the field contribution to either side of the interface. The remaining four contributing field difference amplitudes δ_j defined in Eqs. (5.203) are fixed by the other four tangential BCs as well as the initial field differences by

$$\begin{pmatrix} \boldsymbol{t}_1 \cdot \Delta \boldsymbol{E} \\ \boldsymbol{t}_1 \cdot \Delta \boldsymbol{H} \\ \boldsymbol{t}_2 \cdot \Delta \boldsymbol{E} \\ \boldsymbol{t}_2 \cdot \Delta \boldsymbol{H} \end{pmatrix} = \begin{pmatrix} \boldsymbol{t}_1 \cdot (\boldsymbol{E}^+ - \boldsymbol{E}^-) \\ \boldsymbol{t}_1 \cdot (\boldsymbol{H}^+ - \boldsymbol{H}^-) \\ \boldsymbol{t}_2 \cdot (\boldsymbol{E}^+ - \boldsymbol{E}^-) \\ \boldsymbol{t}_2 \cdot (\boldsymbol{H}^+ - \boldsymbol{H}^-) \end{pmatrix} = \hat{\mathbf{V}}_{\pm} \cdot \begin{pmatrix} \delta_1 \\ \delta_2 \\ \delta_5 \\ \delta_6 \end{pmatrix} \,. \tag{5.208}$$

Here, the coupling matrix

$$
\hat{\mathbf{V}}_\pm = \begin{pmatrix}
\frac{n_y^2-1}{\sqrt{\epsilon-\mu_-}} & \frac{n_x n_y}{\sqrt{\epsilon-\mu_-}} & \frac{1-n_y^2}{\sqrt{\epsilon+\mu_+}} & -\frac{n_x n_y}{\sqrt{\epsilon+\mu_+}} \\
0 & \frac{n_z}{\mu_-} & 0 & \frac{n_z}{\mu_+} \\
0 & \frac{n_z}{\sqrt{\epsilon-\mu_-}} & 0 & -\frac{n_z}{\sqrt{\epsilon+\mu_+}} \\
\frac{1-n_y^2}{\mu_-} & -\frac{n_x n_y}{\mu_-} & \frac{1-n_y^2}{\mu_+} & -\frac{n_x n_y}{\mu_+}
\end{pmatrix} ,
\tag{5.209}
$$

is obtained by projection of the vectors $\boldsymbol{v}_{15}$ to $\boldsymbol{v}_{18}$ on the respective tangential interface vectors

$$
\boldsymbol{t}_1 = \begin{pmatrix} -n_z & 0 & n_x \end{pmatrix}^{\mathrm{T}} \quad \text{and} \quad \boldsymbol{t}_2 = \begin{pmatrix} n_x n_y & 1 - n_y^2 & n_y n_z \end{pmatrix}^{\mathrm{T}}
\tag{5.210}
$$

used for the BC definitions in Eqs. (5.204). Consequently, the field difference amplitudes are

$$
\begin{pmatrix} \delta_1 \\ \delta_2 \\ \delta_5 \\ \delta_6 \end{pmatrix} = \begin{pmatrix}
\frac{\left(-\Delta E_y n_x n_y + \Delta H_z Z_+ n_y - \Delta E_z n_x n_z + \Delta E_x \left(n_y^2 + n_z^2\right) - \Delta H_y n_z Z_+\right)\mu_-}{n_z(Z_- + Z_+)} \\
\frac{\left(\Delta E_x n_x n_y + \Delta E_z n_z n_y + \Delta E_y \left(n_y^2 - 1\right) + \Delta H_z n_x Z_+ - \Delta H_x n_z Z_+\right)\mu_-}{n_z(Z_- + Z_+)} \\
\frac{\left(\Delta E_y n_x n_y + \Delta H_z Z_- n_y + \Delta E_z n_x n_z - \Delta E_x \left(n_y^2 + n_z^2\right) - \Delta H_y n_z Z_-\right)\mu_+}{n_z(Z_- + Z_+)} \\
-\frac{\left(\Delta E_x n_x n_y + \Delta E_z n_z n_y + \Delta E_y \left(n_y^2 - 1\right) - \Delta H_z n_x Z_- + \Delta H_x n_z Z_-\right)\mu_+}{n_z(Z_- + Z_+)}
\end{pmatrix} .
\tag{5.211}
$$

With these amplitudes, we obtain the numerical upwind flux for the CFSPML ADEs as

$$
\boldsymbol{n} \cdot \boldsymbol{F}\left(\boldsymbol{q}^{-}\right) - \boldsymbol{n} \cdot \boldsymbol{F}\left(\boldsymbol{q}^{-,*}\right) \overset{(5.203),(5.186)}{=}
$$

$$
\begin{pmatrix}
\frac{1}{Z}\left(\left[\Delta\boldsymbol{E} - n(\boldsymbol{n}\cdot\Delta\boldsymbol{E})\right] + Z_+\boldsymbol{n}\times\Delta\boldsymbol{H}\right) \\[4pt]
\frac{1}{Y}\left(\left[\Delta\boldsymbol{H} - n(\boldsymbol{n}\cdot\Delta\boldsymbol{H})\right] - Y_+\boldsymbol{n}\times\Delta\boldsymbol{E}\right) \\[4pt]
\frac{1}{Z}n_y\left[Z_+\left[\Delta\boldsymbol{H} - \boldsymbol{n}\left(\boldsymbol{n}\cdot\Delta\boldsymbol{H}\right)\right] - \boldsymbol{n}\times\Delta\boldsymbol{E}\right]_z + n_y\frac{\boldsymbol{n}\cdot\Delta\boldsymbol{B}}{\mu_++\mu_-}n_z \\[4pt]
-\frac{1}{Z}n_z\left[Z_+\left[\Delta\boldsymbol{H} - \boldsymbol{n}\left(\boldsymbol{n}\cdot\Delta\boldsymbol{H}\right)\right] - \boldsymbol{n}\times\Delta\boldsymbol{E}\right]_y - n_z\frac{\boldsymbol{n}\cdot\Delta\boldsymbol{B}}{\mu_++\mu_-}n_y \\[4pt]
-\frac{1}{Z}n_x\left[Z_+\left[\Delta\boldsymbol{H} - \boldsymbol{n}\left(\boldsymbol{n}\cdot\Delta\boldsymbol{H}\right)\right] - \boldsymbol{n}\times\Delta\boldsymbol{E}\right]_z - n_x\frac{\boldsymbol{n}\cdot\Delta\boldsymbol{B}}{\mu_++\mu_-}n_z \\[4pt]
\frac{1}{Z}n_z\left[Z_+\left[\Delta\boldsymbol{H} - \boldsymbol{n}\left(\boldsymbol{n}\cdot\Delta\boldsymbol{H}\right)\right] - \boldsymbol{n}\times\Delta\boldsymbol{E}\right]_x + n_z\frac{\boldsymbol{n}\cdot\Delta\boldsymbol{B}}{\mu_++\mu_-}n_x \\[4pt]
\frac{1}{Z}n_x\left[Z_+\left[\Delta\boldsymbol{H} - \boldsymbol{n}\left(\boldsymbol{n}\cdot\Delta\boldsymbol{H}\right)\right] - \boldsymbol{n}\times\Delta\boldsymbol{E}\right]_y + n_x\frac{\boldsymbol{n}\cdot\Delta\boldsymbol{B}}{\mu_++\mu_-}n_y \\[4pt]
-\frac{1}{Z}n_y\left[Z_+\left[\Delta\boldsymbol{H} - \boldsymbol{n}\left(\boldsymbol{n}\cdot\Delta\boldsymbol{H}\right)\right] - \boldsymbol{n}\times\Delta\boldsymbol{E}\right]_x - n_y\frac{\boldsymbol{n}\cdot\Delta\boldsymbol{B}}{\mu_++\mu_-}n_x \\[4pt]
-\frac{1}{Y}n_y\left[Y_+\left[\Delta\boldsymbol{E} - \boldsymbol{n}\left(\boldsymbol{n}\cdot\Delta\boldsymbol{E}\right)\right] + \boldsymbol{n}\times\Delta\boldsymbol{H}\right]_z - n_y\frac{\boldsymbol{n}\cdot\Delta\boldsymbol{D}}{\epsilon_++\epsilon_-}n_z \\[4pt]
\frac{1}{Y}n_z\left[Y_+\left[\Delta\boldsymbol{E} - \boldsymbol{n}\left(\boldsymbol{n}\cdot\Delta\boldsymbol{E}\right)\right] + \boldsymbol{n}\times\Delta\boldsymbol{H}\right]_y + n_z\frac{\boldsymbol{n}\cdot\Delta\boldsymbol{D}}{\epsilon_++\epsilon_-}n_y \\[4pt]
\frac{1}{Y}n_x\left[Y_+\left[\Delta\boldsymbol{E} - \boldsymbol{n}\left(\boldsymbol{n}\cdot\Delta\boldsymbol{E}\right)\right] + \boldsymbol{n}\times\Delta\boldsymbol{H}\right]_z + n_x\frac{\boldsymbol{n}\cdot\Delta\boldsymbol{D}}{\epsilon_++\epsilon_-}n_z \\[4pt]
-\frac{1}{Y}n_z\left[Y_+\left[\Delta\boldsymbol{E} - \boldsymbol{n}\left(\boldsymbol{n}\cdot\Delta\boldsymbol{E}\right)\right] + \boldsymbol{n}\times\Delta\boldsymbol{H}\right]_x - n_z\frac{\boldsymbol{n}\cdot\Delta\boldsymbol{D}}{\epsilon_++\epsilon_-}n_x \\[4pt]
-\frac{1}{Y}n_x\left[Y_+\left[\Delta\boldsymbol{E} - \boldsymbol{n}\left(\boldsymbol{n}\cdot\Delta\boldsymbol{E}\right)\right] + \boldsymbol{n}\times\Delta\boldsymbol{H}\right]_y - n_x\frac{\boldsymbol{n}\cdot\Delta\boldsymbol{D}}{\epsilon_++\epsilon_-}n_y \\[4pt]
\frac{1}{Y}n_y\left[Y_+\left[\Delta\boldsymbol{E} - \boldsymbol{n}\left(\boldsymbol{n}\cdot\Delta\boldsymbol{E}\right)\right] + \boldsymbol{n}\times\Delta\boldsymbol{H}\right]_x + n_y\frac{\boldsymbol{n}\cdot\Delta\boldsymbol{D}}{\epsilon_++\epsilon_-}n_x
\end{pmatrix} . \tag{5.212}
$$

Within this numerical flux, we recover the same numerical upwind flux for the electromagnetic field components as in Eq. (5.107). In contrast, to the first six field entries, the upwind flux for the CFSPML auxiliary fields G^E and G^H contain a projection of the same terms onto the corresponding normal vector components and an additional term depending on either the field difference $\Delta\boldsymbol{D}$ or $\Delta\boldsymbol{B}$, respectively. These terms stem from the imposed normal-component BC in Eq. (5.207). In the case of identical background permittivities and permeabilities, we find

$$
\frac{\boldsymbol{n}\cdot\Delta\boldsymbol{D}}{\epsilon_+ + \epsilon_-} \overset{\epsilon_+=\epsilon_-}{\longrightarrow} \frac{\boldsymbol{n}\cdot\Delta\boldsymbol{E}}{2} \quad \text{and} \quad \frac{\boldsymbol{n}\cdot\Delta\boldsymbol{B}}{\mu_+ + \mu_-} \overset{\mu_+=\mu_-}{\longrightarrow} \frac{\boldsymbol{n}\cdot\Delta\boldsymbol{H}}{2} , \tag{5.213}
$$

and the numerical upwind flux Eq. (5.212) reduces to the split-flux presented in Eq. (5.187). This split-flux is used in the subsequent chapter to terminate a single dispersive gold layer. Within the thesis, we only use the CFSPMLs with the damping parameters σ chosen as described in Section 5.6.1 about the uPMLs. The complex frequency shift is set to $\alpha = 0$ here, as for typical DGTD setups the computational accuracy depends much stronger on the actual damping σ than the frequency shift α. This is, e.g., shown in a full parameter screening presented in [151].

CHAPTER 6

Electron energy loss spectroscopy

Electron energy loss spectroscopy (EELS) is a well-established method for the characterization of materials using a transmission electron microscope (TEM) [4, 157]. While often used for atomic resolution imaging, it also provides a versatile tool for the characterization of plasmonic nanostructures [5]. EELS relies on the measurement of the electron energy loss of a nearly monoenergetic electron beam interacting with a given sample. Typically the electrons in the TEM used are accelerated to energies in the range of $E \in [50\,\text{keV}, 400\,\text{keV}]$ [5]. The energy loss experienced by the electrons interacting with a sample structure reaches from the meV to keV regime depending on the different interactions, i.e., from plasmon excitations to the ionization of inner atomic shells [157].

Here, we concentrate on the excitation of surface plasmon polaritons (SPPs) in metallic nanostructures, which lead to electron energy losses in the regime of a few electronvolts, i.e., $\Delta E_{\text{loss}} \in [0.5\,\text{eV}, 10\,\text{eV}]$. This electron energy loss is determined in a scanning transmission electron microscope (STEM), in which the electron beam is focused to the vicinity or directly at the metallic nanostructure. Typically the STEM current is reduced so far that the electron beam becomes so diluted, such that statistically, the interaction with the plasmonic sample happens single electron by electron. For the relativistically moving electrons, the interaction time lies in the regime of a few hundred femtoseconds.

In this chapter, we discuss how to compute the electron energy loss probability (EELP) spectra for swift electrons interacting with spherical plasmonic nanoparticles as well as a thin periodically perforated gold film. In Section 6.1 we summarize a short derivation of the EELP which relies on the perturbative interaction of a single electron charge and its self-induced electromagnetic field. Normally the EELP computations rely on the induced field of a single electron point-charge [5, 158]. However, we here introduce an approximate computation utilizing smoothed electron charge distributions, presented in Appendix A. This heuristic treatment allows for the computation of the EELP not only in the direct vicinity of a plasmonic scatterer, i.e., in the exponential fall-off region of the SPP modes supported but also for a numerically reliable evaluation of the EELP for electron trajectories intersecting the metallic sample. A thorough test of this smoothed charge implementation is carried out in Section 6.2 for a metallic sphere with a Drude model permittivity. In the final Section 6.3, we compute the transmittance spectra of the periodically perforated gold films with extraordinary optical transmission (EOT) presented in the introductory Chapter 1. We close this last section with discontinuous Galerkin time-domain (DGTD) computations of the EELP mapping, which is related but not identical to the projected photonic local density of states (LDOS) [159] determined by the SPP modes supported on the gold film. Both transmittance spectra and EELP maps are compared with experimental data [K7].

6.1 Basics of EELS

In order to derive the EELP one has in principle to solve both the Dirac equation of the single electron moving at relativistic speeds simultaneously with quantized electromagnetic field [160]. However, the main focus of this chapter lies in the numerical computation of the EELP. Hence, we outline the short historical and semiclassical derivation by Ritchie [6] following the presentation in [5, 161].

The EELP $\Gamma(\omega)$ is defined by the electron energy loss

(SI) $$\Delta E_{\mathrm{loss}} = \int_0^\infty \mathrm{d}E\, E\, \Gamma(E/\hbar) = \int_0^\infty \mathrm{d}(\hbar\omega)\, \hbar\omega\, \Gamma(\omega)\,, \tag{6.1}$$

which a single electron experiences during the interaction with a sample. The change in energy

(SI) $$\Delta E = e \int_{-\infty}^\infty \mathrm{d}t\, \dot{\boldsymbol{r}}_e(t) \cdot \boldsymbol{E}_{\mathrm{scat}}\left(\boldsymbol{r}_e(t), t\right)\,, \tag{6.2}$$

of a classical electron is determined by the scattered field (Sf). The Sf is a response of the material induced by the electron. It acts back on the electron itself, which follows the (center of charge) trajectory $\boldsymbol{r}_e(t)$. Within the derivation [5, 6, 161] both energy losses are equated. For this, we apply the Fourier transform of the scattered, real-valued $\boldsymbol{E}$-field and find

(SI) $$\Delta E = \frac{e}{2\pi} \int_{-\infty}^\infty \mathrm{d}\omega \int_{-\infty}^\infty \mathrm{d}t\, \dot{\boldsymbol{r}}_e(t) \cdot \boldsymbol{E}_{\mathrm{scat}}\left(\boldsymbol{r}_e(t), \omega\right) \mathrm{e}^{-\mathrm{i}\omega t}\,,$$
$$= \frac{e}{\pi} \int_0^\infty \mathrm{d}\omega \int_{-\infty}^\infty \mathrm{d}t\, \mathrm{Re}\left[\dot{\boldsymbol{r}}_e(t) \cdot \boldsymbol{E}_{\mathrm{scat}}\left(\boldsymbol{r}_e(t), \omega\right) \mathrm{e}^{-\mathrm{i}\omega t}\right]\,. \tag{6.3}$$

Here the electron trajectory $\boldsymbol{r}_e(t)$ is still parameterized by the time t. As the single electrons are accelerated to high kinetic energies, they carry a high momentum. Within the no-recoil approximation (NRA) it is assumed that each electron loses energy but hardly changes its trajectory. For the interaction region, we assume a straight-line trajectory

$$\boldsymbol{r}_e(t) = \boldsymbol{v}\,t + \boldsymbol{r}_0\,, \quad \text{where} \quad \boldsymbol{v} = v\boldsymbol{e}_z\,. \tag{6.4}$$

Within the thesis and without loss of generality, we set the electron movement into z-direction. Consequently, the electron trajectory is also parameterized by the coordinates x_0 and y_0, the fixed velocity v, and the position z. We can infer the EELP by direct comparison of Eq. (6.1) and the classical energy loss Eq. (6.3) to be

(SI) $$\Gamma(\omega) = \frac{e}{\pi\hbar^2\omega} \int_{-\infty}^\infty \mathrm{d}t\, \mathrm{Re}\left[\dot{\boldsymbol{r}}_e(t) \cdot \boldsymbol{E}_{\mathrm{scat}}\left(\boldsymbol{r}_e(t), \omega\right) \mathrm{e}^{-\mathrm{i}\omega t}\right]\,,$$
$$\overset{(6.4)}{=} \frac{e}{\pi\hbar^2\omega} \int_{-\infty}^\infty \mathrm{d}z\, \mathrm{Re}\left[\boldsymbol{E}_{\mathrm{scat},z}\left(x_0, y_0, z, \omega\right) \mathrm{e}^{-\mathrm{i}\omega\frac{z-z_0}{v}}\right]\,. \tag{6.5}$$

As the EELP spectrum contains the scattered electric field $\boldsymbol{E}_{\mathrm{scat}}$ induced by the electron point

charge with charge density

$$\text{(SI)} \qquad \rho(\boldsymbol{r}) = -e\,\delta(\boldsymbol{r} - \boldsymbol{r}_e(t))\,, \qquad (6.6)$$

it is also closely related to electric scattered field Green's tensor $\underline{\underline{\boldsymbol{G}}}_{\text{scat}}$. The dyadic Green's tensor can itself be expanded into the resonances, i.e., quasinormal mode (QNM) of the system [122]. This allows for a mapping of these modes, especially SPPs by scanning the impact position of the electron beam with respect to the lateral coordinates x and y. As the electric scattered field Green's tensor $\underline{\underline{\boldsymbol{G}}}_{\text{scat}}$ solves the inhomogeneous version of the Helmholtz equation (2.55), i.e.,

$$\text{(SI)} \qquad \nabla \times \nabla \times \underline{\underline{\boldsymbol{G}}}_{\text{scat}}(\boldsymbol{r}, \boldsymbol{r}', \omega) - \frac{\omega^2}{c_0^2}\left(\epsilon_r(\boldsymbol{r}, \omega) - 1\right)\underline{\underline{\boldsymbol{G}}}_{\text{scat}}(\boldsymbol{r}, \boldsymbol{r}', \omega) = \underline{\underline{\boldsymbol{1}}}\,\delta(\boldsymbol{r} - \boldsymbol{r}')\,, \qquad (6.7)$$

it is directly related to the scattered electric field of the electron by

$$\text{(SI)} \qquad \boldsymbol{E}_{\text{scat}}(\boldsymbol{r}, \omega) = \mathrm{i}\omega\mu_0 \int \mathrm{d}^3 r'\, \underline{\underline{\boldsymbol{G}}}_{\text{scat}}(\boldsymbol{r}, \boldsymbol{r}', \omega) \cdot \boldsymbol{j}(\boldsymbol{r}, \omega)\,. \qquad (6.8)$$

The connection between EELP and the electric Green's tensor follows directly given the current density associated with the electron passing the sample. By charge conservation Eq. (2.2) it is determined from the electron's point charge density Eq. (6.6) by

$$\text{(SI)} \qquad \boldsymbol{j}(\boldsymbol{r}, \omega) = -e\,\boldsymbol{v}\int \mathrm{d}t\, \mathrm{e}^{\mathrm{i}\omega t}\delta(\boldsymbol{r} - \boldsymbol{r}_e(t)) \overset{(6.4)}{=} -e\,\delta(x - x_0)\delta(y - y_0)\mathrm{e}^{\mathrm{i}\omega\frac{z-z_0}{v}}\boldsymbol{e}_z\,. \qquad (6.9)$$

Consequently, the EELP is related to the scattered field Green's tensor and thus the material response of the electron by

$$\text{(SI)} \qquad \Gamma(\omega) = -\frac{e^2\mu_0}{\pi\hbar^2}\int \mathrm{d}z \int \mathrm{d}z'\, \mathrm{Im}\left[\boldsymbol{e}_z \cdot \underline{\underline{\boldsymbol{G}}}_{\text{scat}}(x_0, y_0, z, x_0, y_0, z, \omega) \cdot \boldsymbol{e}_z, \mathrm{e}^{\mathrm{i}\omega\frac{z'-z}{v}}\right]\,. \qquad (6.10)$$

This involves the imaginary part of the Green's tensor projected to the z-direction, in which the electron passes. This term is very similar to the photonic LDOS [84] given by

$$\text{(SI)} \qquad \mathcal{N}_{\boldsymbol{z}}(\boldsymbol{r}, \omega) = \frac{2\omega}{\pi c_0^2}\mathrm{Im}\left[\boldsymbol{e}_z \cdot \underline{\underline{\boldsymbol{G}}}(\boldsymbol{r}, \boldsymbol{r}, \omega) \cdot \boldsymbol{e}_z\right]\,. \qquad (6.11)$$

The LDOS is, e.g., important for the calculation of Purcell factors [54, 84] describing the change in decay times of fluorescent molecules as are used in Chapter 8. For metallic nanostructures, the supported SPP modes can lead to a high photonic LDOS as well as EELS signal. Both do not necessarily generate the same signal [162]. However, it should be noted, that the LDOS projected on the electron trajectory and the EELP spectrum are proportional for structures, which are homogeneous in the electron beam direction [159].

As the EELP depends on the Green's tensor, we essentially reconstruct its z, z-entry within the DGTD computations. The required imaginary part of the full Green's tensor in vacuum takes a

finite value (see e.g., [84])

$$\text{(SI)} \qquad \text{Im} \underline{\underline{\boldsymbol{G}}}_{\text{tot}}\left(\boldsymbol{r}, \boldsymbol{r}, \omega\right) = \frac{\omega}{6\pi c_0} \underline{\underline{\mathbf{1}}}, \qquad (6.12)$$

at the point charge positions, while the real part diverges. As the EELP spectrum only involves the scattered Green's tensor, the divergence only poses a problem, when the electron hits a dielectric or metallic material. If the permittivity $\epsilon_r \neq 1$ somewhere in the electron beam also the imaginary part of the scattered field Green's tensor $\underline{\underline{\boldsymbol{G}}}_{\text{scat}}$ diverges. However, an electron passing through a material normally experiences a screening on atomic length scales and its charge distribution is not point-like. Therefore, it is possible to also obtain EELP spectra within DGTD computations, for which the electron beam hits the material, see e.g., [161, 163, 164]. This relies on the implicit smoothing by the discretization with Lagrange polynomials on the elements describing the setup geometry (cf. Section 5.2.1). Consequently, the numerical results are dependent on the specific discretization. Especially in cases in which the electron hits a discretization node of the Lagrange polynomial basis, the evaluation of close to divergent fields can lead to an exponential increase in the numerical error and thus incorrect EELP spectra.

To circumvent this deficiency, we introduce smoothed charge distributions into the DGTD method. This enables a reliable computation of the scattered electric field and EELP for beam positions within a material. Here, we choose a Gaussian charge distribution

$$\text{(SI)} \qquad \rho(\boldsymbol{r}') = -\frac{e}{\sqrt{\pi}^3 \sigma_e^3} \mathrm{e}^{-r'^2/\sigma_e^2}, \qquad (6.13)$$

in the electrons rest-frame coordinates $\boldsymbol{r}'$. The smoothing radius σ_e determines the width of the distribution. The computation of the scattered field in the DGTD method requires prior knowledge of the incident electromagnetic fields to be used as a source term in either an Sf or total field / scattered field (Tf/Sf) excitation scheme (cf. Section 5.4). A full derivation of these fields in Appendix A yields

$$\text{(SI)} \qquad \boldsymbol{E}(\boldsymbol{r}, t) = -\frac{\gamma e}{4\pi\epsilon_0} \frac{\boldsymbol{r} - \boldsymbol{r}_e(t)}{\varrho^3} \left[\text{erf}\left(\frac{\varrho}{\sigma_e}\right) - \frac{2}{\sqrt{\pi}} \frac{\varrho}{\sigma_e} \mathrm{e}^{-\varrho^2/\sigma_e^2} \right], \qquad (6.14a)$$

$$\text{(SI)} \qquad \boldsymbol{B}(\boldsymbol{r}, t) = \frac{\boldsymbol{v}}{c_0^2} \times \boldsymbol{E}(\boldsymbol{r}, t), \qquad (6.14b)$$

in the reference frame of the sample. Here

$$\text{(SI)} \qquad \varrho = \varrho(\boldsymbol{r}, t) = \sqrt{\left[\boldsymbol{r} - \boldsymbol{r}_e(t)\right]^2 + \frac{\gamma^2}{c_0^2} \left[\boldsymbol{v} \cdot \left(\boldsymbol{r} - \boldsymbol{r}_e(t)\right)\right]^2}, \qquad (6.15)$$

is the transformed radial coordinate from the rest-frame. To test and validate the implementation of these fields used as a source term, we first apply it for DGTD EELP computations of a Drude metal sphere. The results can be directly compared to Mie calculations [8, 9, 165].

6.2 EELP of a single metallic sphere

The test setup for the smoothed charge distribution EELS computations relies on a metal sphere with radius $R = 50\,\text{nm}$. For the Drude material model

$$\epsilon_{\text{Au}}(\omega) = 1 - \frac{\omega_{\text{pl}}^2}{\omega\left(\omega + \mathrm{i}\gamma\right)}\,, \tag{6.16}$$

we use the parameters

(SI) $$\hbar\omega_{\text{pl}} = 8.75\,\text{eV} \quad \text{and} \quad \hbar\gamma = 0.058\,\text{eV}\,, \tag{6.17}$$

which are obtained from Johnson and Christy [166] with a fit to the measured gold permittivity. However, using only the Drude model neglects the gold interband transitions, which can and will be accounted for by additional Lorentz model susceptibilities for the final perforated gold film computations covered in Section 6.3. For the swift electron, we use the same kinetic energy

(SI) $$E_{\text{kin}} = 300\,\text{keV}\,, \tag{6.18}$$

as in the experiments for the gold films [K7]. This corresponds to an electron velocity [167, 168] of

(SI) $$v = \sqrt{1 - \left(\frac{E_{\text{kin}}}{m_e c_0^2} + 1\right)^{-2}}\, c_0 \approx 0.77\,c_0\,. \tag{6.19}$$

For the DGTD computations, we use a mesh similar to that in Fig. 5.1 (b) and apply an Sf source in order to compute the scattered field in the entire computational domain. For the initialization of the computations, we set the center of charge of the Gaussian electron charge distribution to be $z_0 = -4.5\,\mu\text{m}$ away from the sphere. Fig. 6.1 shows a sketch of the setup.
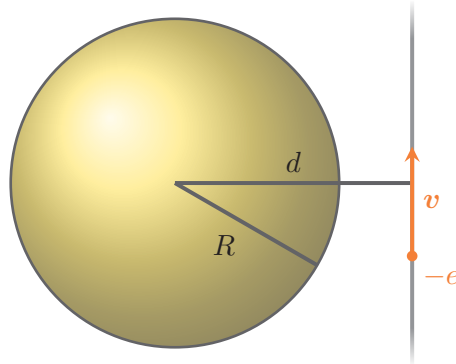
Figure 6.1: EELS computation setup sketch of a gold sphere with radius R passed by an electron with velocity v at an impact distance d from the sphere's center.

Setting the electron start point far away from the scatterer ensures sufficiently small electromagnetic fields at the start of the computation approximately fulfilling the zero-field initial conditions for the DGTD method. Additionally, we tune the charge adiabatically both at the start and end

of the computation. We replace

$$q = -e \quad \rightarrow \quad q(t) = -e\,\eta(t)\,, \tag{6.20}$$

where we use a polynomial ramped-up and ramped-down time dependence $\eta(t)$ like the continuous wave introduced in Appendix B.2.2, Eq. (B.23), while setting the carrier frequency to $\omega_0 = 0$. This allows to numerically only evaluate the DGTD source term of the incident field Eq. (6.14) for a finite time of flight. Here, the charge moves $L_z = 9\,\mu\text{m}$ from below to above the sphere. This corresponds to a flight time of

$$T = \frac{L_z}{v} = 39\,\text{fs}\,, \tag{6.21}$$

while the ramp-up and ramp-down times of the charge are set to $t_{\text{up}} = t_{\text{down}} = 5\,\text{fs}$ each. This adiabatic ramp-up of the electron charge suppresses high-frequency numeric errors occurring for a sudden switch-on of the electrons incident field at the beginning of the DGTD computations. The ramp-down process allows stopping the numerical evaluation of the incident field if the electron is sufficiently far away from the scatterer. This saves numerical simulation time.

6.2.1 Single EELP spectrum computation
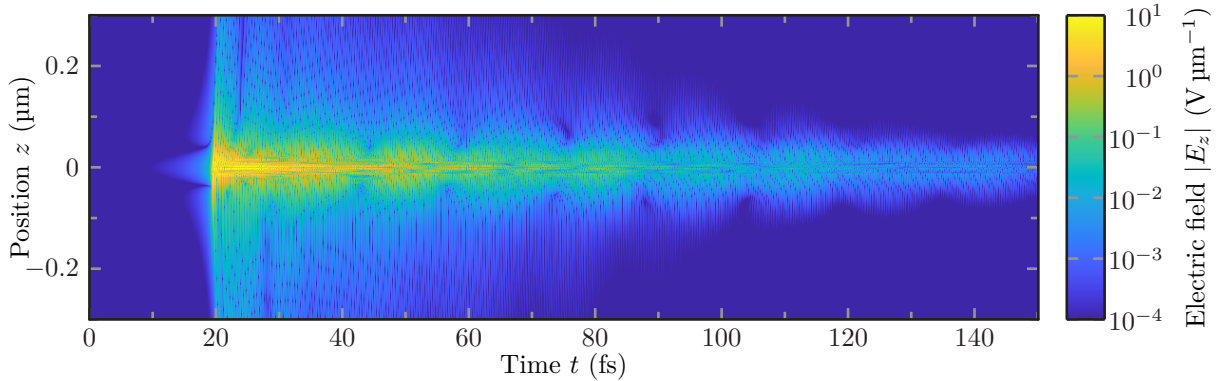
Figure 6.2: Induced electric field strength $|E_z|(z,t)$ for an electron passing the gold sphere at a distance of $d = 51\,\text{nm}$ from the sphere's center. The sphere radius is $R = 50\,\text{nm}$ and the electron reaches the closest proximity at $t \approx 19.5\,\text{fs}$.

Before we investigate the influence of the charge smoothing and the impact distance, we start with a single exemplary EELP computation. For this computation, the electron passes just outside the sphere at a distance $d = 51\,\text{nm}$ from the center. The smoothing radius is set to $\sigma_e \approx 2\,\text{nm}$. Fig. 6.2 shows the recorded scattered electric field $E_z(z,t)$ on the trajectory of the electron for the entire simulation time. The scattered electric field, which is generated by the Sf source from within the gold sphere slowly increases until the electron comes into close proximity of the sphere around $t \approx 19.5\,\text{fs}$. As a consequence, the electron excites the localized SPP modes supported by the gold sphere. These SPPs decay relatively slowly compared to the time the

electron needs to pass. It leaves the recorded z-interval after just another $1.3\,\text{fs}$. This restriction to $z \in [-0.3\,\mu\text{m}, 0.3\,\mu\text{m}]$ is sufficient to compute the EELP spectrum according to the integral in Eq. (6.5), as the scattered field decreased exponentially from the sphere's surface. The main numerical uncertainty is generated by the finite simulation time, which causes windowing [169] in the fast Fourier transform (FFT) [170, 171] into the frequency-dependent scattered field $E_z(z, \omega)$ required for the EELP computation.
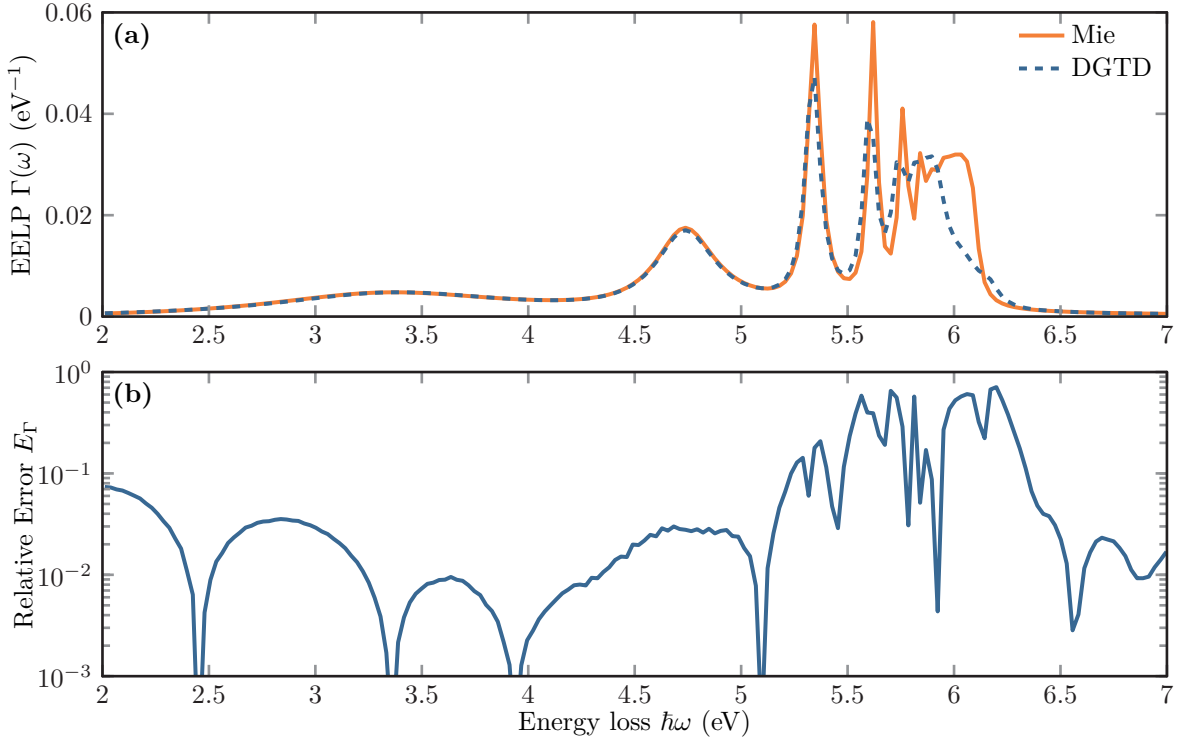
Figure 6.3: **(a)** EELP spectrum for a single $R = 50\,\text{nm}$ gold sphere for a swift electron passing at $d = 51\,\text{nm}$ from the sphere's center. Both spectra are computed with the DGTD method as well as a Mie solver by García de Abajo [8, 9, 165]. **(b)** Relative error Eq. (6.22) between the spectra obtained from the DGTD and Mie calculations.

Fig. 6.3 (a) shows the EELP spectrum computed from the recorded scattered field. The spectrum is compared to a Mie calculation [8, 9, 165] for the same setup. Here, we observe several peaks, which correspond with increasing energy to the dipole, quadrupole, and high-order SPP resonances of the sphere, respectively. As the SPP dispersion flattens (see Fig. 4.5) at the surface plasmon frequency $\omega_{\text{sp}} = \frac{\omega_{\text{pl}}}{\sqrt{2}}$ for the ideally lossless Drude metal, the resonances show an accumulation at this energy $\hbar\omega_{\text{sp}} \approx 6.2\,\text{eV}$. Here, we observe a limiting factor by the mesh and Lagrange polynomial discretization of the sphere used for the DGTD computations. The higher the mode order is, the shorter the SPP wavelength on the surface becomes, which cannot be resolved any longer for a given discretization. For the DGTD, we use a third-order polynomial basis, while the sphere elements' characteristic side length [140] lies below $h_{\text{sph}} = 40\,\text{nm}$. The Mie calculations have been performed including spherical harmonics up to the order $l = 20$.

Fig. 6.3 (b) shows an increased relative error

$$E_\Gamma(\omega) = \left| 1 - \frac{\Gamma^{(\text{DGTD})}(\omega)}{\Gamma^{(\text{Mie})}(\omega)} \right|, \tag{6.22}$$

between the methods for these higher-order mode peaks. For the dipole ($\hbar\omega \approx 3.3\,\text{eV}$) and quadrupole ($\hbar\omega \approx 4.7\,\text{eV}$), the relative error lies below five percent for this test setup. As the higher-order modes are suppressed by the damping of interband transitions accounting for a more realistic gold permittivity model (see Eq. (6.25)), the chosen coarse discretization used for the DGTD is reasonably accurate for a quantitative comparison.

6.2.2 Electron smoothing radius influence and EELP map
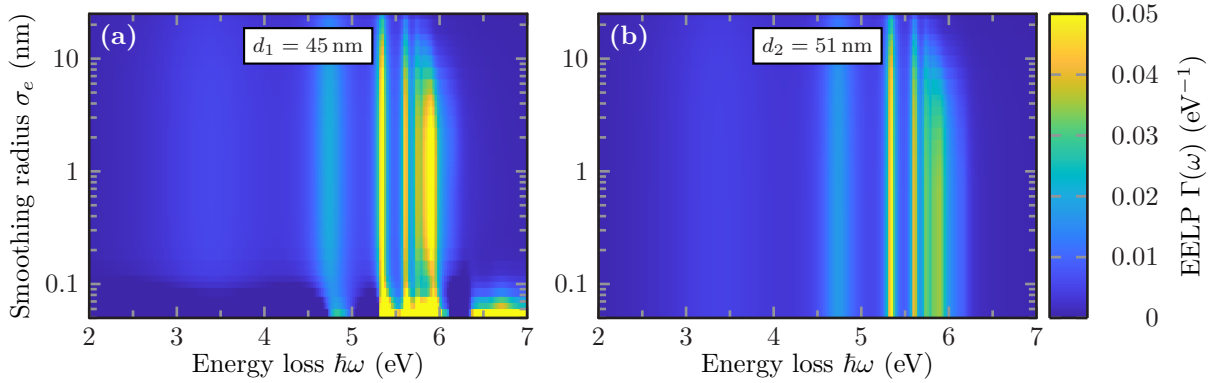
Figure 6.4: EELP for a single $R = 50\,\text{nm}$ gold sphere in dependence of the rest-frame smoothing radius σ_e of the swift electron charge distribution for two different excitation positions: merely inside **(a)** and outside **(b)** the gold sphere.

Given the relatively accurate computation of the gold sphere EELP spectra, we investigate the dependence on the electron charge distribution rest-frame smoothing radius σ_e as defined in Eq. (6.13). For this, we perform a scan of computations similar to those of the previous section and systematically vary the smoothing radius $\sigma_e \in [0.5\,\text{nm}, 25\,\text{nm}]$.

We analyze two different cases for the impact distance d of the electron beam. In the first case, the electron hits the sphere at a distance $d_1 = 45\,\text{nm} < R = 50\,\text{nm}$ from the sphere's center. In the second case, the electron passes just outside the sphere with $d_2 = 51\,\text{nm}$. Fig. 6.4 shows the corresponding EELP spectra in relation to the smoothing radius σ_e. In both cases, the same resonances as in Fig. 6.3 (a) are observed. The EELP is stronger, however, when the electron hits the gold sphere. For increasing smoothing radii $\sigma_e \gtrsim 10\,\text{nm}$ the EELP fades out starting at the higher-order modes. This is caused by the averaged excitation of the higher-order modes. Furthermore, the scattered field E_z is only evaluated on the center of charge trajectory in Eq. (6.5) instead of a weighted integral over the entire charge distribution cross section. The main difference between the two cases occurs for small charge smoothing radii σ_e. For trajectories outside the gold sphere as in Fig. 6.4 (b), the EELP spectrum converges with decreasing σ_e. For

electron trajectories hitting the sphere, the EELP spectra show a significant change at small values of σ_e and can even diverge, if the electron hits a single interpolation node of the Lagrange basis functions used in the DGTD method. In Fig. 6.4 (a) this change happens for $\sigma_e < 0.1\,\mathrm{nm}$ for the chosen sphere discretization. For the following computations, we use a radius $\sigma_e \approx 2\,\mathrm{nm}$ providing reliable spectra for both trajectories inside and outside the gold material.
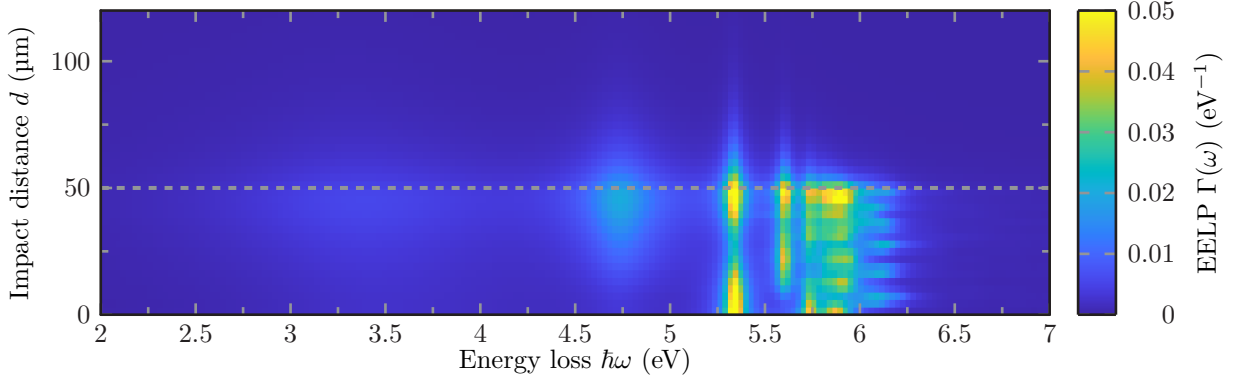
Figure 6.5: EELP map for a single gold sphere with radius $R = 50\,\mathrm{nm}$ (dashed line) computed with an electron density smoothing radius $\sigma_e \approx 2\,\mathrm{nm}$.

Nevertheless, it should be noted that this choice for σ_e restricts the resolution for the variation of the electron trajectory with respect to the impact distance d. Fig. 6.5 shows such an EELP map, in which we record the spectra for different impact distances d. For distances $d > R = 50\,\mathrm{nm}$, we observe how the resonances in the EELP spectra fade away exponentially as does the probed E_z-field component of the excited SPPs. For the two lowest order modes, the EELP peaks at the surface, while the higher-order modes show an increasing number of maxima for trajectories hitting the sphere. These originate from the SPP fields on the top and bottom as well as sides of the spheres for increasing mode order causing a constructive interference at these distances d.
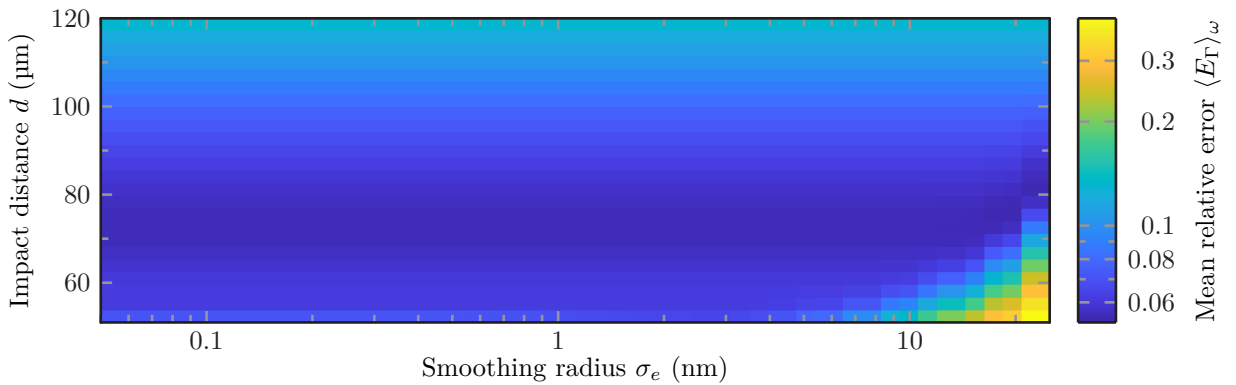
Figure 6.6: Energy-averaged error $\langle E_\Gamma \rangle_\omega$ between DGTD and Mie calculations of the EELP for a $R = 50\,\mathrm{nm}$ gold sphere with respect to both the impact distance d and electron charge distribution smoothing radius σ_e.

Finally, we study the relative error with respect to the electron charge distribution smoothing radius σ_e as well as the distance d between the DGTD EELP computations and the Mie calculations [8, 9, 165]. For this, we define a frequency-averaged relative error for the EELP spectra, i.e.,

$$\langle E_\Gamma(d, \sigma_e)\rangle_\omega := \frac{1}{\Delta\omega} \int d\omega \left| 1 - \frac{\Gamma^{(\text{DGTD})}(\omega; d, \sigma_e)}{\Gamma^{(\text{Mie})}(\omega; d, \sigma_e)} \right|, \tag{6.23}$$

where we integrate over the recorded energy window $\hbar\omega \in [2\,\text{eV}, 7\,\text{eV}]$ containing the SPP resonances. This mean relative error is depicted in Fig. 6.6. We see that for distances $d > R$ outside the sphere the error is roughly independent of the smoothing radius. Only for large smoothing radii $\sigma_e \gtrsim 10\,\text{nm}$ and small impact distances $d \lesssim 70\,\text{nm}$, the difference between the Gaussian and point charge distributions become noticeable, as the incident electric field changes significantly from the r^{-2} dependence typical for a point charge. The variation in the mean relative error with respect to the distance d is caused by the discretization and simulation time. For small distances, the higher-order modes have a large contribution and are not sufficiently resolved. The higher-order modes have a stronger spatial exponential decay, therefore the error first decreases. With further increased distance, the fields of all SPP modes are rather weak. Hence, the error increases again due to the numerical errors of the FFT of the electric field relying on a finite simulation time.

In summary, it was shown that the introduction of a smoothed charge distribution into the DGTD EELS computations can reproduce the spectra obtained by Mie calculations using a point charge distribution. However, there is a strong dependence on the mesh refinement for high energies near the surface plasmon frequency ω_{sp}. Furthermore, the smoothed charge distributions open the possibility to numerically reliable compute spectra for the electron trajectory hitting the metallic material.

6.3 EELS on thin periodically perforated gold films

In the introduction Chapter 1, we have discussed the effect of EOT on periodically perforated metallic thin films and potential applications. Although there exists a wide variety of far-field studies for rectangular gratings with cylindrical holes, only a few near-field studies of comparable structures can be found. These include scanning near-field optical microscopy (SNOM) [172–176] and energy-filtered STEM on structures with a few holes or slits [177–179]. Here, we investigate a free-standing periodically perforated gold film [K7]. This gold film includes a rectangular hole grating with periods $p_x = 800\,\text{nm}$ and $p_y = 600\,\text{nm}$. Each of the 100×100 unit cells contains a hole with radius $R \approx 100\,\text{nm}$ and is produced by focused ion beam milling [K7, 180]. The gold film thickness is $d = 22\,\text{nm}$. To characterize the gold film, we investigate both the far-field response by the computation of transmittance spectra as well as the near-field characterization with EELS. All the spectra and EELP maps obtained from the DGTD method are then compared to experimental measurements [K7].

For the DGTD method, we use two similar simulation domains both for the EELP and transmittance spectra computation, which are shown in Fig. 6.7 (a) and (b), respectively. These

(a)

(b)

Air, PML

Air, Tf region

Tf/Sf contour

Air, Sf region

Au, Sf region

Au, Tf region

Au, PML

Air, PML

Air, Sf region

Tf/Sf contour

Au, Tf region

Trans. contour

Air, Tf region

Air, PML
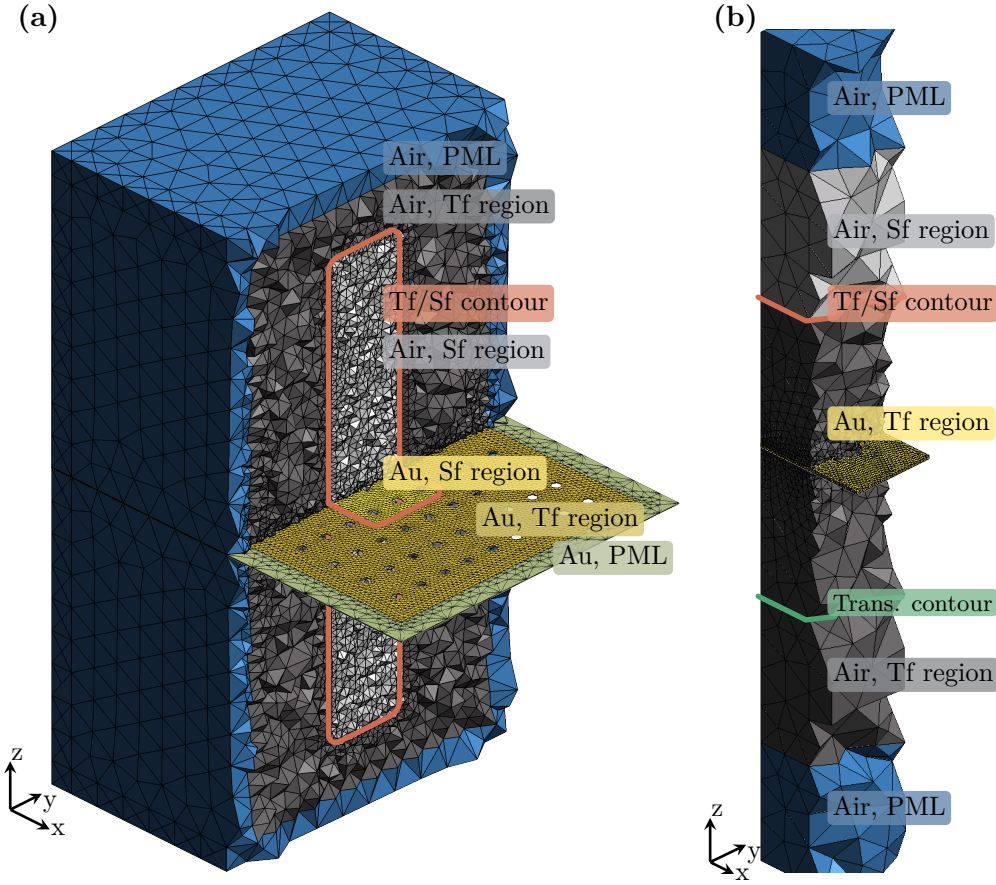
Figure 6.7: Meshes used for the DGTD computations of the **(a)** EELP spectra and **(b)** transmittance spectra of a periodically perforated $d = 22$ nm thick gold film. Different computational regions are marked by name. The EELS setup **(a)** includes complex frequency-shifted perfectly matched layers (CFSPMLs) on the outside of the total field (Tf) region and includes the gold layer. The transmittance setup **(b)** contains uniaxial perfectly matched layers (uPMLs) and periodic boundary conditions (PBCs).

meshes are generated using gmsh [140]. For the EELS computations, we use a 9×9 rectangular hole array for the perforated gold film as the electron beam excitation breaks the transversal symmetry. This film is extruded by $0.8\,\mu$m both in the x- and y-direction to the boundary of the computational domain on which we impose Silver Müller boundary conditions (SMBCs). As the gold film implicitly extends to infinity, we use CFSPMLs as introduced in Section 5.6.2 to terminate the gold material layer. Both below and above the gold film we add an air region with height $d_{\mathrm{air}} = 6\,\mu$m each, which are also terminated by the $d_{\mathrm{PML}} = 0.5\,\mu$m of CFSPMLs. In contrast to the gold sphere EELS computations, we cannot use a pure Sf source here. As the CFSPMLs rely on a complex continuation of the spatial coordinates, this would require the incident field Eq. (6.14), which acts as an Sf source term Eq. (5.129) in the DGTD method, also to be continued in the complex coordinate plane. Hence, all the PMLs have to be located in a Tf

region. Consequently, we introduce a Tf/Sf contour including a 3×3 array in the center of the gold film as shown in Fig. 6.7 (a). This means we extend the DGTD implementation to apply a Tf/Sf source on the contour and an Sf source in the inner part of the gold film simultaneously.

For the transmittance computations, we use a pulsed plane wave source Eq. (5.121) with straight incidence and Gaussian time dependence $\eta(t)$ according to Eq. (B.20). For the computations, we only use a single unit cell. The mesh is shown in Fig. 6.7 (b). Both in x- and y-direction, we apply PBCs. Above and below the gold grating's unit cell, we arrange two $1\,\mu m$ thick air layers ($\epsilon_r = 1$) each. Between the layers, we define specific contours. On the upper contour, the Tf/Sf source is applied. It splits the simulation domain into the Sf and Tf region. On the lower contour, we record the power flux and consequently the transmittance spectrum Eq. (2.109). Additionally, the simulation domain is terminated with SMBCs and $0.8\,\mu m$ thick uPMLs.

As the transmittance and EELP spectra are compared to measured data [K7], we extend the material model for the gold film to also account for interband transitions. We add three additional Lorentz poles Eq. (3.7) to the Drude model permittivity, i.e.,

$$\epsilon_{Au}(\omega) = \epsilon_{bg} - \frac{\omega_{pl}^2}{\omega(\omega + i\gamma)} + \sum_{i=1}^{3} \frac{\Delta_{\epsilon,i}\omega_{L,i}^2}{\omega_{L,i}^2 - i\gamma_{L,i}\omega - \omega^2} \,. \tag{6.24}$$

Here, the parameters are fitted [K1] to the permittivity data by Johnson and Christy [166] and take the values

(SI) $\qquad\qquad \Delta_{\epsilon,1} = 1.51 \,, \quad \hbar\omega_{L,1} = 2.91\,eV \quad \text{and} \quad \hbar\gamma_{L,1} = 1.02\,eV \,, \tag{6.25a}$

(SI) $\qquad\qquad \Delta_{\epsilon,2} = 1.02 \,, \quad \hbar\omega_{L,2} = 3.66\,eV \quad \text{and} \quad \hbar\gamma_{L,2} = 1.20\,eV \,, \tag{6.25b}$

(SI) $\qquad\qquad \Delta_{\epsilon,3} = 0.80 \,, \quad \hbar\omega_{L,3} = 4.42\,eV \quad \text{and} \quad \hbar\gamma_{L,3} = 1.18\,eV \,, \tag{6.25c}$

for the Lorentz poles and

(SI) $\qquad\qquad \epsilon_{bg} = 6.39 \,, \quad \hbar\omega_{pl} = 9.03\,eV \quad \text{and} \quad \hbar\gamma = 76\,meV \,, \tag{6.26}$

for the background permittivity and Drude model.

Before we numerically determine the EELP spectra, we compute the transmittance of the periodically perforated gold film. We use two different polarizations

$$\boldsymbol{E}_0^{(1)} = \boldsymbol{e}_x \quad \text{and} \quad \boldsymbol{E}_0^{(2)} = \boldsymbol{e}_y \,, \tag{6.27}$$

along the short and long period axes for the plane wave excitation Eq. (5.121) with straight incidence $\boldsymbol{k}||\boldsymbol{e}_z$. For the Gaussian time dependence, we set the carrier frequency to $\hbar\omega_0 = 1.653\,eV$. We set the temporal width to $\sigma = 2.5\,fs$ with a sufficiently broad spectrum (cf. Eq. (B.22)) to excite the film within the recording frequency window $\hbar\omega \in [1\,eV, 2.2\,eV]$.

Fig. 6.8 shows both measured [K7] as well as the computed transmittance spectra of the freestanding gold film. For both polarization directions, the spectra show a very good agreement. The resonances indicated by the EOT maxima lie at lower frequencies for the excitation polarization aligned along the long period p_x and are blue-shifted for the polarization along the
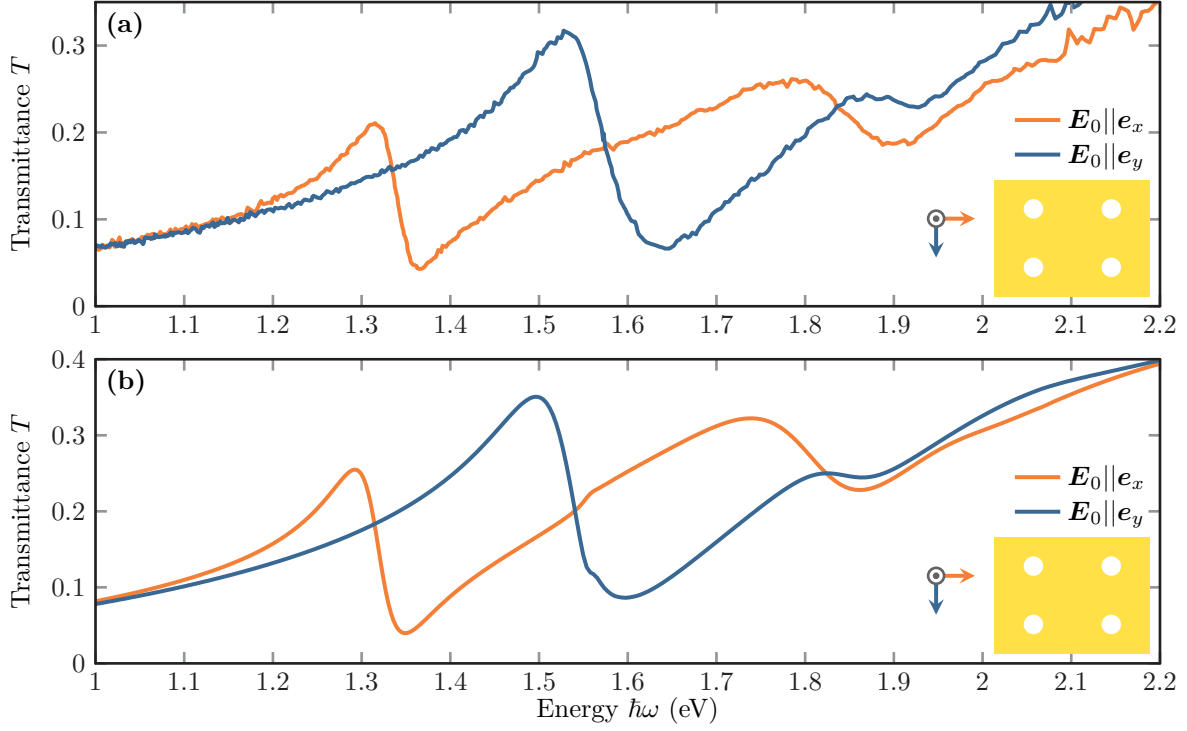
Figure 6.8: Transmittance spectra $T(\omega)$ for excitation under straight incident plane wave pulses both along the longer x-direction and shorter y-direction axis of the periodically perforated gold film. **(a)** Experimentally obtained spectra with data graciously provided by M. Prämassing [K7]. **(b)** Spectra computed by the DGTD method.

short period y-axis. The corresponding mode order can be estimated from the SPP dispersion Eq. (4.97) and the reciprocal grid vectors $\boldsymbol{G}_{x/y} = \frac{2\pi n_{x/y}}{p_{x/y}} \boldsymbol{e}_{x/y}$ [181]. For this, we neglect the holes and also only account for a single metal-dielectric interface as the symmetric and antisymmetric dispersion nearly agrees for frequencies far below the metal plasma frequency ω_{pl} [57]. Given the grating periods $p_{x/y}$, for straight incidence, the SPP resonances approximately occur at

$$\text{(SI)} \qquad \omega = 2\pi c_0 \sqrt{\frac{n_x^2}{p_x^2} + \frac{n_y^2}{p_y^2}} \sqrt{\frac{\epsilon_{\mathrm{Au}} + \epsilon_{\mathrm{air}}}{\epsilon_{\mathrm{Au}} \, \epsilon_{\mathrm{air}}}} \,, \qquad (6.28)$$

where $n_x, n_y \in \mathbb{N}$ determine the corresponding SPP mode order [181]. The lower energy peaks in the transmittance spectra thereby correspond to the $(1,0)$-mode ($\hbar\omega \approx 1.29\,\mathrm{eV}$) for x-polarization and $(0,1)$-mode ($\hbar\omega \approx 1.5\,\mathrm{eV}$) for y-polarization. The higher frequency $\hbar\omega \approx 1.74\,\mathrm{eV}$ in x-polarization and $\hbar\omega \approx 1.83\,\mathrm{eV}$ in y-polarization transmittance peaks correspond to the $(1,1)$-mode excitation but are split in frequency due to the holes and finite film thickness. To spatially map the underlying SPP resonances we next perform EELS computations.
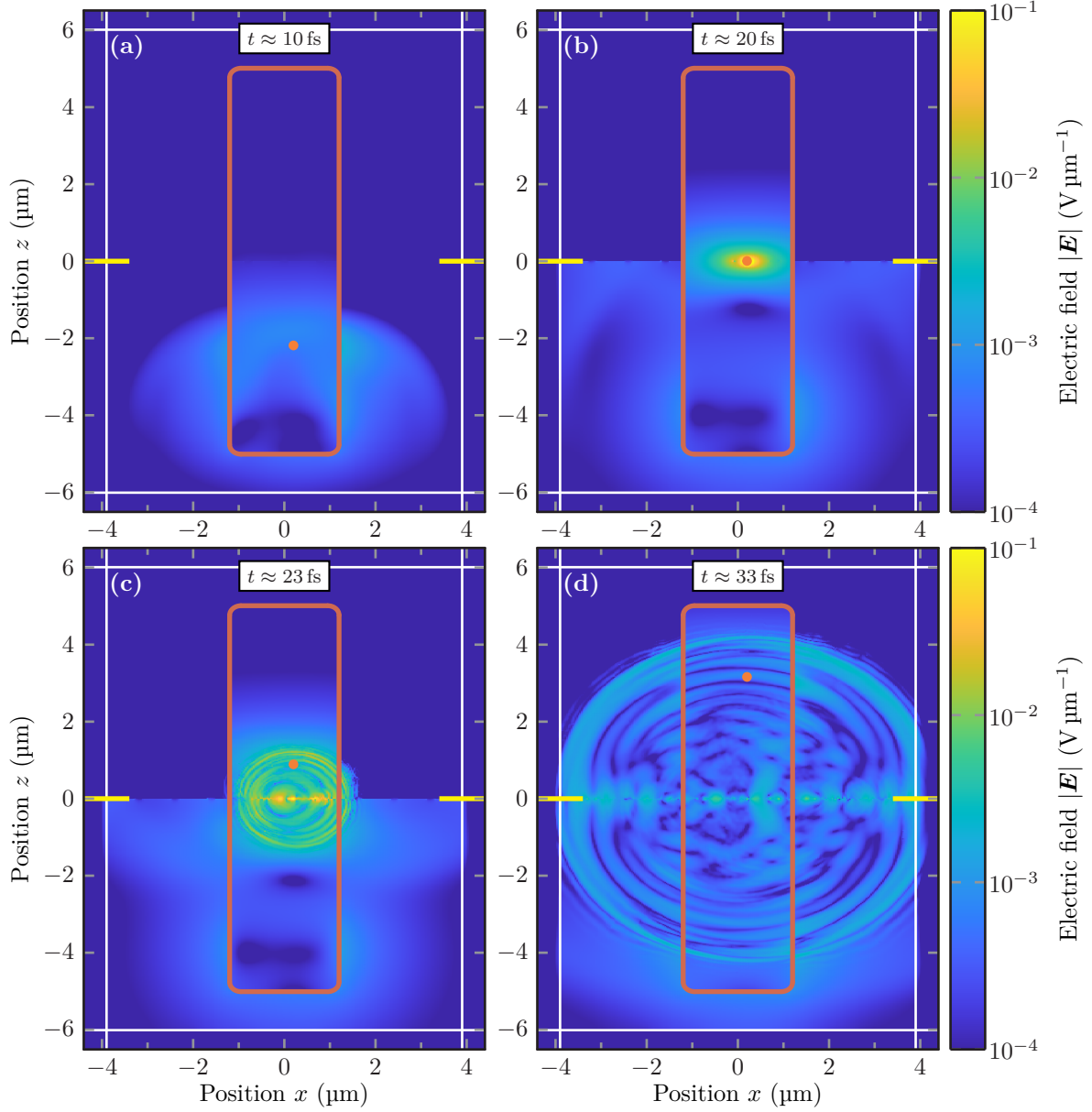
Figure 6.9: Induced and total field $|\boldsymbol{E}|(x, z, t)$ of an electron passing the periodically perforated gold film with $\boldsymbol{v} = 0.77\,c_0\,\boldsymbol{e}_z$ at $x_0 = 120\,\text{nm}$ from the center hole. The Tf/Sf contour is marked in red. White lines indicate the PML boundaries and the yellow lines indicate the position of the gold film. The orange dot marks the electron position. **(a)** The electron charge was adiabatically ramped up, but the electron does not hit the film yet. **(b)** The electron impacts the gold film. **(c)** Generated spherical waves and SPPs along the perforated gold film are launched. **(d)** The induced electric field is absorbed in the PMLs.

6.3.1 Single EELP spectrum computations

We start with a single DGTD computation of an EELP spectrum. Here, we set the electron trajectory intersection point within the gold film close to the edge of the central hole ($R = 100\,\text{nm}$) in the simulation domain shown in Fig. 6.7 (a). The intersection point lies at

$$\boldsymbol{r}_{\perp,0} = \left(x_0, y_0\right)^{\text{T}} = \left(120\,\text{nm}, 0\,\text{nm}\right)^{\text{T}} . \tag{6.29}$$

Similar to Section 6.2, we use a Gaussian charge distribution Eq. (6.13) for the electron with a smoothing radius $\sigma_e = 2\,\text{nm}$. The electron starts at $z_0 = -4.5\,\text{µm}$ below the gold film and moves upwards with $\boldsymbol{v} = 0.77\,c_0\,\boldsymbol{e}_z$. Additionally, the charge is ramped-up and -down as in the gold sphere example Eq. (6.20). We use a ramp-up and ramp-down time of $t_{\text{up}} = t_{\text{down}} = 5\,\text{fs}$. Given the parameter setup, we can compute the electromagnetic fields in the entire simulation domain.

Fig. 6.9 shows different snapshots of the scattered and total field $|\boldsymbol{E}|$ computed with the DGTD. It shows the x-z-coordinate cross section at $y = 0\,\text{µm}$ for different times t. In Fig. 6.9 (a) the electron charge was just ramp-up. Outside the Tf/Sf contour (red line) we see a combination of the electron's incident field and a static field component, which is introduced by the charge ramp-up. In the Sf region inside the red line, a small and relatively smoothly extended field is observed. This low-frequency field is also generated from the Tf/Sf contour due to the ramp-up process as a numerical artifact. At time $t \approx 19.5\,\text{fs}$ the electron hits the gold film which is shown in Fig. 6.9 (b). In the gold film, we see a strong scattered field, which is generated by the incident field Eq. (6.14) used in the Sf source. The small low-frequency fields get reflected on the gold layer. Consequently, there is no field in the upper half-plane Tf region. A few femtoseconds later the electron has passed the material layer as shown in Fig. 6.9 (c). Besides a spherical field pulse propagating outwards also the SPP modes on the gold film are excited and well visible by the field enhancement on the gold layer. After $t \approx 33\,\text{fs}$, both the wavefront and SPPs have reached the CFSPMLs and get absorbed. The fields decay exponentially in the PML layers, which can be seen on the white lines in Fig. 6.9 (d).
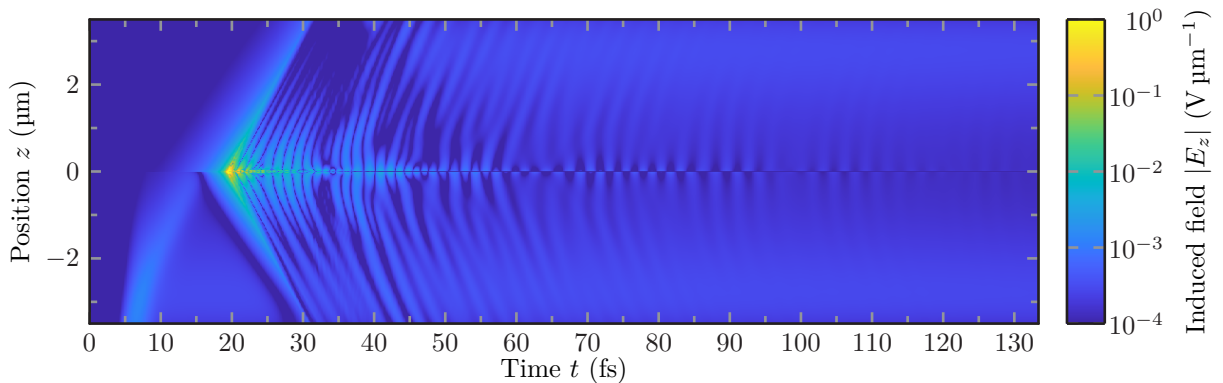
Figure 6.10: Induced electric field $|E_z|$ along the electron trajectory used to compute the EELP Eq. (6.5) for an electron hitting the perforated gold film at $x_0 = 120\,\text{nm}$ and $y_0 = 0\,\text{nm}$.

In addition to the cross section through the computational domain, which provides a good overview of the excitation behavior, we also record the scattered E_z-field on the electron trajectory. This field is shown in Fig. 6.10 for the entire simulation time $T = 135\,\text{fs}$. With $z \in [-2.5\,\mu\text{m}, 2.5\,\mu\text{m}]$ the recording trajectory lies completely in the Sf region. Besides the initial pulse propagating to the far-field also the SPP field oscillations on the gold film around $z = 0\,\mu\text{m}$ are well observable. While the field of the SPP modes decays by several orders of magnitudes during the simulated time, there remains a small quasi-static field both far below and above the gold film. This static field stems from the ramp-up and -down process, which induces implicit charges in the mesh. However, as the main interest in the EELP computation lies at frequencies well above zero, this poses a minor problem. The influence of the low-frequency contribution can be systematically controlled by using longer ramping times as well as setting the electron's initial position further away from the gold film.
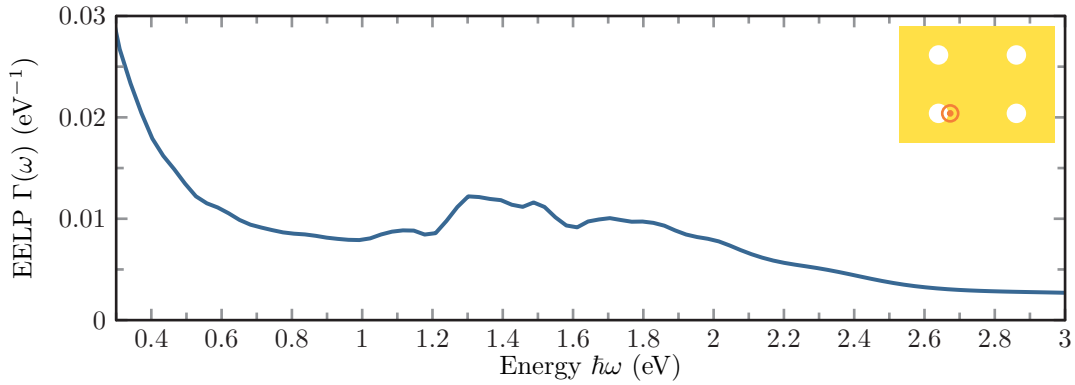
Figure 6.11: EELP spectrum $\Gamma(\omega)$ for an electron hitting the periodically perforated gold film. The impact position $x_0 = 120\,\text{nm}$ and $y_0 = 0\,\text{nm}$ lies in the vicinity of the $R = 100\,\text{nm}$ hole. The orange out-of-plane arrow marks the impact position and velocity vector $\boldsymbol{v} = 0.77\,c_0\,\boldsymbol{e}_z$ on the sketch of the perforated gold film.

In Fig. 6.11 we show the EELP spectrum resulting from the recorded field according to Eq. (6.5). The EELP spectrum shows maxima at the same spectral positions as the transmittance spectra in Fig. 6.8. Especially the SPP (1,0)-mode at 1.29 eV and (0,1)-mode at 1.5 eV are well visible. Furthermore, we observe an increase at small frequencies which stems from the static fields in the scattered electric field E_z observed in Fig. 6.10.

6.3.2 Comparison of experimental and numerical EELP maps

To obtain a complete picture of the SPP modes excited in the EELS, we scan the position $\boldsymbol{r}_{\perp,0}$ of the electron beam over the length of the unit cell. For each position, we compute the corresponding EELP spectrum. In Fig. 6.12 we show both experimental [K7] as well as numerically computed EELP spectra directly compared to the respective transmittance spectra from Fig. 6.8. For the computation of this EELP scan, the position x_0 of the electron beam is varied between the hole center at $x_0 = 0\,\mu\text{m}$ and the right boundary of the gold grating's unit cell at $x_0 = 0.4\,\mu\text{m}$. Simultaneously the beam position $y_0 = 0\,\mu\text{m}$ remains fixed. For the comparison with the measured EELP x-position map, the computed map is mirrored and

periodically continued. The computed and measured EELP spectra show a qualitatively good agreement both for beam positions inside ($|x_0| < R = 100\,\mathrm{nm}$) and outside the holes. For each of the maxima in the transmittance spectra Fig. 6.12 (a,c), we find corresponding maxima in the EELP maps Fig. 6.12 (b,d). The EELP is especially strong on the edges of the holes, as here the field enhancement of the captured E_z-field component is strongest. Inside the holes, the EELP decreases significantly, as the SPP modes fall off exponentially towards the center. Additionally to the transmittance maxima energies marked in Fig. 6.12 (c), we find two more maxima in the EELP spectra (dashed lines). These correspond to the excitation of dark modes not coupling to the far-field. Thus, the modes cannot be excited by the straight incident plane wave used in the transmittance computations.
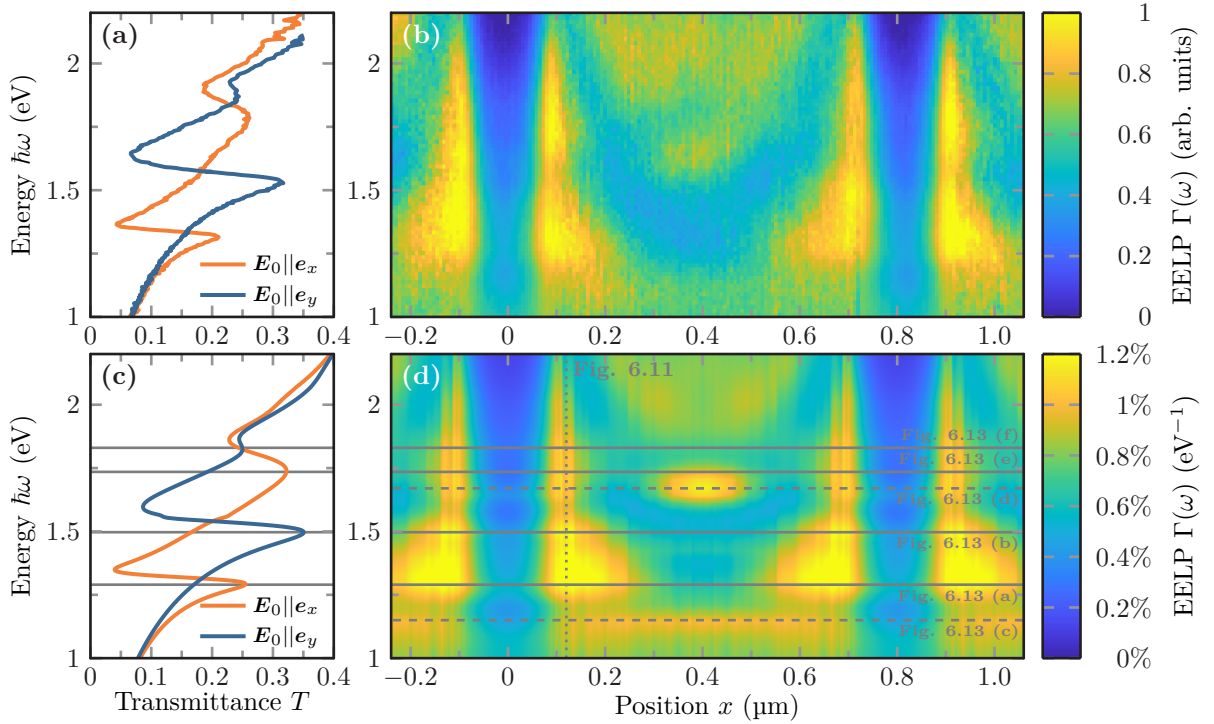
Figure 6.12: **(b)** Experimental and **(d)** computational EELP maps $\Gamma(x,\omega)$ along the x-direction mayor axis of the perforated gold film and transmittance spectra **(a,c)** from Fig. 6.8. **(a,b)** Experimental data was graciously provided by M. Prämassing [K7]. Gray lines indicate the transmittance **(c)** as well as EELP **(d)** maxima. Dashed lines mark dark modes.

The computation of the full x_0 and y_0 dependent EELP maps at the resonances energies marked in Fig. 6.12 (c.d) allows an indirect mapping of the excited SPP modes. This mapping depends on the E_z-field distribution of the specific modes excited by the electron. These EELP maps are shown in Fig. 6.13 for two unit cells in each direction. Due to symmetry, the computation relies on a scan of the first quadrant of the unit cell only.

For the $(1,0)$-mode and $(0,1)$-mode, we observe an expected dipolar pattern with orientation in x- and y-direction shown Fig. 6.13 (a) and (b), respectively. Note, however, that the phase

information of the scattered field obtained from the computation is lost by the computation of the EELP spectrum. Hence, we infer the mode order from the number of EELP maxima. This can also be directly done from the experimental observation [K7]. Correspondingly, the EELP maps in Fig. 6.13 (c) and Fig. 6.13 (d) correspond to dark modes, with orders $(0.5, 0.5)$ as well as $(1.5, 0)$ according to the number of EELP maxima. These modes are dark as the field pattern repeats over two instead of one unit cell and can thus not be coupled to a straight incident plane wave. In contrast, the EELP maps in Fig. 6.13 (e,f) show a superposition of the $(1,1)$-modes traversing in both diagonal directions. This supports the findings for transmittance spectra.
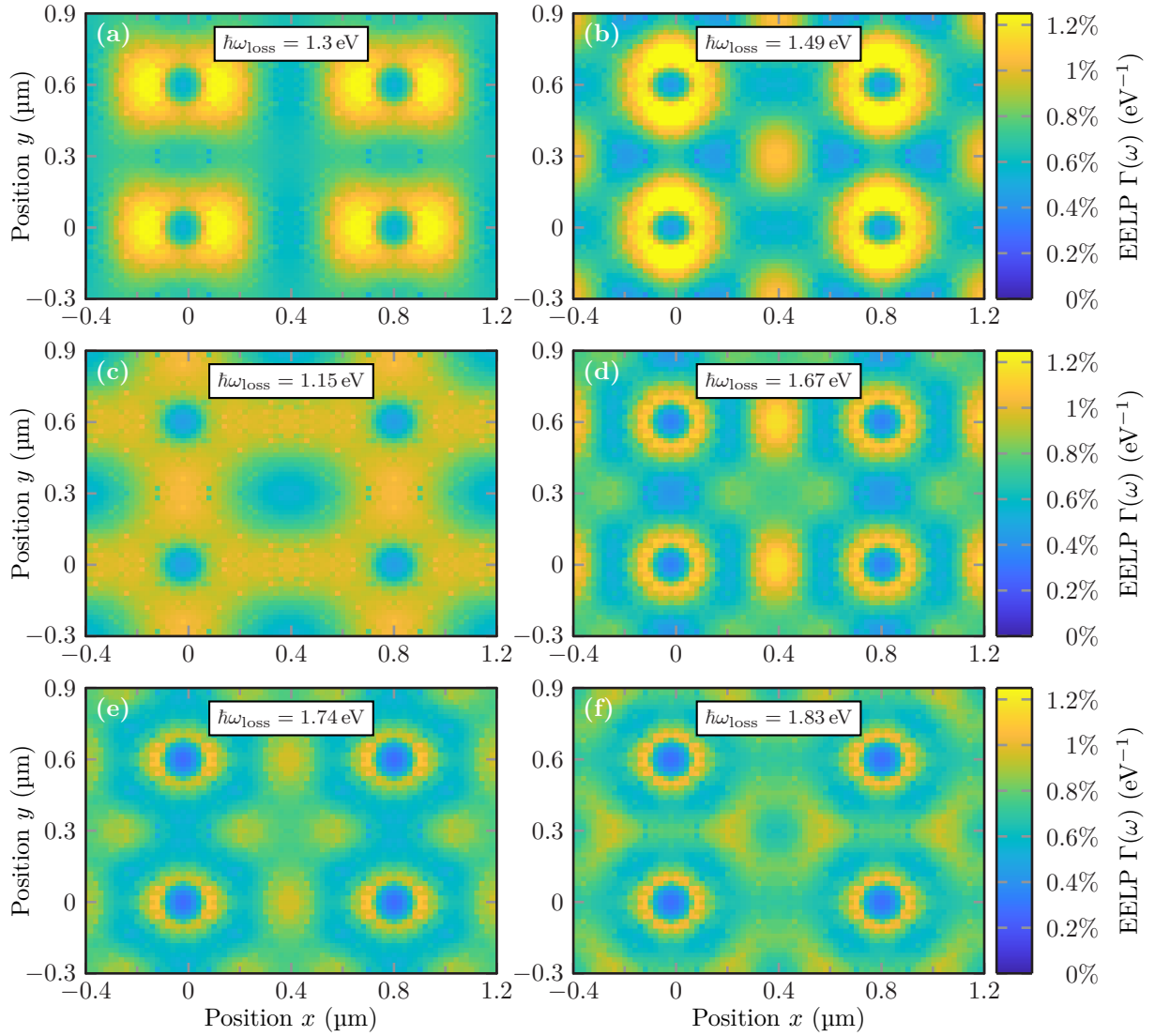
Figure 6.13: EELP maps plotted for two unit cells in both directions for the loss energies marked in Figure 6.12 (d).

Overall, the EELP maps provide an insight into the field distributions of the free-standing gold film, which can be directly compared to the experiment. Furthermore, the introduction of

the smoothed charge distribution for the EELP spectra computation delivers reliable numerical results, which withstand a qualitative comparison to the experiment, especially for electron trajectories traversing the gold film.

Magneto-optic metasurfaces and hyperbolic metamaterial cavities

This chapter focuses on resonances in systems containing anisotropic materials, namely magneto-optic (MO) and hyperbolic metamaterials (HMMs).

Within the optical domain, the MO response is typically rather weak. However, associated effects like the Faraday rotation [29] are essential for photonic applications like miniaturized non-reciprocal devices, e.g., optical isolators [182, 183]. Therefore, we discuss in Section 7.2 how to use a system of MO scatterers forming a metasurface [44] to generate a large Faraday rotation accompanied by a high transmittance. We outline a shape optimization approach [K8] of the constituting scatterers to even further enhance the Faraday rotation maintaining the high transmittance. As the numerical computations require the non-dispersive anisotropic material model for the discontinuous Galerkin time-domain (DGTD) method (cf. Sections 5.1), a full convergence study on the implementation is provided within the first Section 7.1 of this chapter.

Following the results about the MO metasurfaces, we discuss cavities built of thin, stacked layers of metallic and dielectric materials forming an HMM cavity. As we show in Section 7.3, these cavities provide subwavelength resonances as well as a high density of states, which both are well tuneable with respect to material and geometry parameters determining the HMM properties.

7.1 Convergence behavior for anisotropic materials comparing DGTD and Mie calculations

In Section 5.3.2 we presented the numerical upwind flux for non-dispersive anisotropic materials as used in the DGTD method. Both the numerical flux, as well as the on-element operations (cf. Section 5.2) have been implemented within the C++ code of the research group *Theoretical Optics & Photonics (TO&P* group). As so far only the implementation for two-dimensional anisotropic materials [75, 184] was included, we perform a full extensive convergence study. For the tests, we compute the scattering efficiencies of spheres filled with a given anisotropic material. Here, we investigate both the internal DGTD convergence behavior as well as a direct comparison against the analytical Mie calculations [78, 79] which all have been graciously provided by P. Varytis.

In the following four sections, we consider four distinct test cases, all of which are sketched in Fig. 7.1. First, we compare the scattering efficiencies of an isotropic dielectric sphere using the new anisotropic material implementation against the already existing isotropic one. Secondly, diagonal anisotropic dielectric tensors are considered, for which it is still possible to obtain
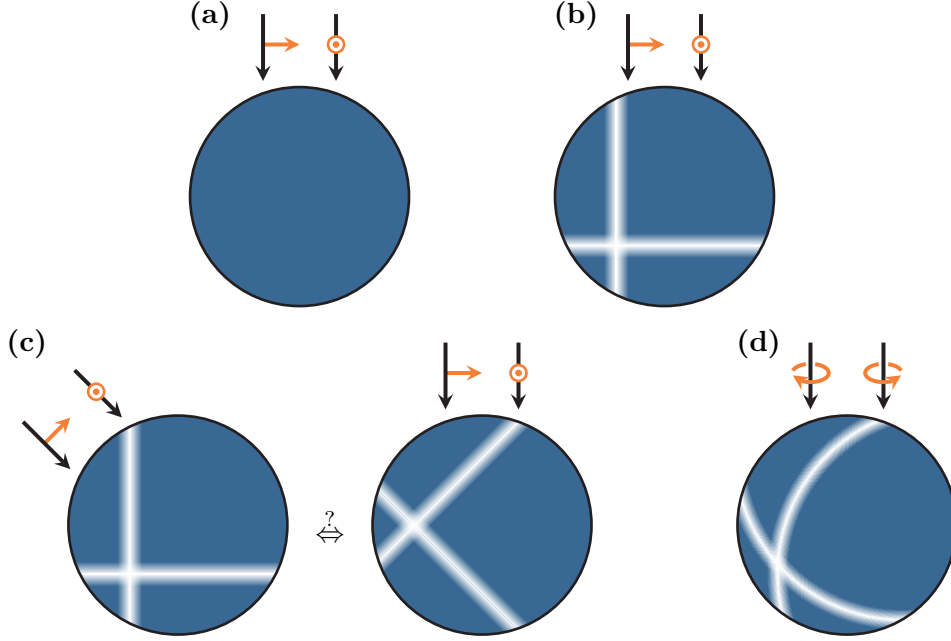
Figure 7.1: Scattering efficiency test cases for the DGTD implementation of non-dispersive anisotropic materials with different excitation polarizations. Black arrows indicate the propagation direction of the exciting plane wave, while orange arrows indicate the polarization of the electric field. **(a)** Comparison of an isotropic dielectric material between Mie computations, the existing isotropic and the new anisotropic DGTD material implementation. **(b)** Comparison of a diagonal anisotropic dielectric material with Mie and DGTD computations. **(c)** Comparison of a rotated excitation on a diagonal dielectric tensor against the corresponding full anisotropic dielectric tensor under *straight* excitation. **(d)** Scattering efficiency computations comparing Mie and DGTD computations for a complex-valued MO dielectric tensor.

the scattering efficiency within the Mie-scattering implementation [78]. Thirdly, we compare the scattering efficiencies of a *fully* anisotropic dielectric sphere against the scattering efficiency obtained in the principal axis frame of the dielectric tensor, in which it is diagonal again. Finally, we investigate the scattering on an MO dielectric material, which in contrast to the other cases requires the DGTD to operate with complex-valued, rather than real-valued fields.

7.1.1 Isotropic material tensors

First, we investigate the plane wave scattering on a sphere with a given radius R. We perform DGTD computations using the mesh already shown Fig. 5.1 (b). Within the DGTD computations, we use a sphere with a test radius of $R = 250\,\mathrm{nm}$ which is excited by a Gaussian modulated plane wave

$$(\text{SI}) \quad \boldsymbol{E}_{\mathrm{inc}}\left(\boldsymbol{r}, t\right) = \boldsymbol{E}_0^{(1)} \eta\left(t - c_0^{-1} \boldsymbol{e}_z \cdot \boldsymbol{r}\right), \quad \text{with} \quad \eta\left(t\right) \overset{(\text{B.20})}{=} \cos\left(\omega_0(t - t_0)\right) \mathrm{e}^{-\frac{(t-t_0)^2}{2\sigma^2}}, \quad (7.1)$$
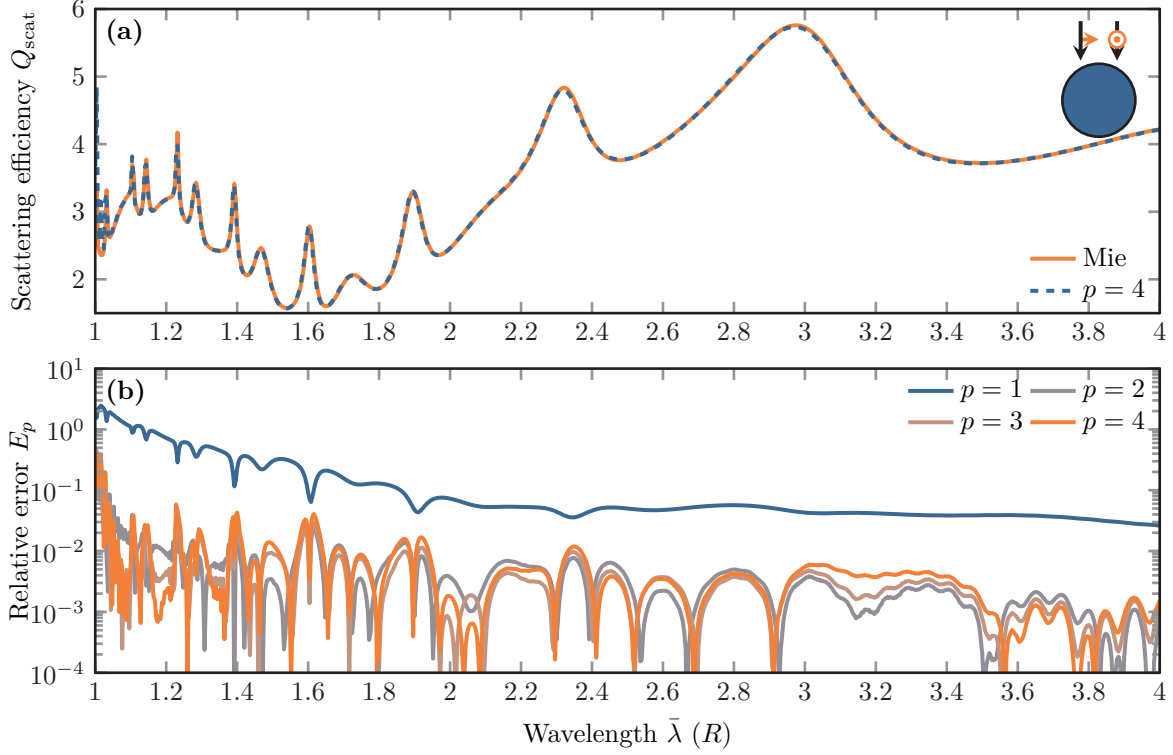
Figure 7.2: **(a)** Scattering efficiency of a dielectric sphere with permittivity $\epsilon = 4$ computed both with a Mie scattering implementation [78] and the DGTD method using a $p = 4$ Lagrange polynomial basis. **(b)** Relative errors (7.5) between the Mie calculations and DGTD computations with varying polynomial order p for the finest mesh of the convergence scan.

using the total field / scattered field (Tf/Sf) formalism from Section 5.4.1. Here, we use a pulse width of $\sigma \approx 1.334\,\text{fs}$ in order to cover a spectral excitation range of $\lambda \in [R, 4R] = [250\,\text{nm}, 1\,\mu\text{m}]$ containing both low- and high-order resonances. The central carrier wavelength is chosen as $\lambda_0 = \frac{2\pi c_0}{\omega_0} = 1.8R = 450\,\text{nm}$. Accordingly, we set the time offset $t_0 = 10\sigma \approx 13.34\,\text{fs}$ in order to guarantee vanishing fields at computation start. Here, we consider only the first of the two different excitation polarizations

$$\boldsymbol{E}_0^{(1)} || \boldsymbol{e}_x \quad \text{and} \quad \boldsymbol{E}_0^{(1)} || \boldsymbol{e}_y \,, \tag{7.2}$$

which are suggested by the arrows used in Figure 7.1 (a), as the scattering spectrum is polarization independent. Within the computation, we record the power flux on the aforementioned Tf/Sf-contour in order to compute the scattering cross section spectrum C_{scat} of the sphere. Thereafter, we compute the scattering efficiency [90] from the scattering cross section and the sphere radius R:

$$Q_{\text{scat}} = \frac{C_{\text{scat}}}{\pi R^2} \,. \tag{7.3}$$

As we use a non-dispersive permittivity for the spherical scatterer and due to the scale invariance of Maxwell's equations, we use the rescaled wavelength

$$\bar{\lambda} = \frac{\lambda}{R} \tag{7.4}$$

instead of the wavelength λ to characterize the scattering spectrum.

In Figure 7.2 (a) we show the resulting scattering efficiency spectrum for a sphere with a permittivity of $\epsilon = 4$ and using the mesh with the finest resolution for the DGTD convergence study using fourth-order ($p = 4$) Lagrange polynomial basis functions. Both computations very well resemble each other, showing the typical Mie resonances. There are only stronger, yet still, relatively small deviations for small wavelengths, as can be expected by the finite resolution imposed by the mesh element sizes h and the used polynomial order p. Figure 7.2 (b) shows the relative error

$$E_p(\tilde{h}) = \left| 1 - \frac{Q^p_{\text{scat}}(\tilde{h})}{Q^{\text{Mie}}_{\text{scat}}} \right| \tag{7.5}$$

for the finest mesh ($\tilde{h} = \tilde{h}_{\min}$) considered in this convergence study. Here, we define a dimensionless mesh refinement factor $\tilde{h} = h/h_0$, with which we scale the characteristic element length [140] $h_0 = 100\,\text{nm}$ over an entire order of magnitude. The error for the $p = 1$ Lagrange polynomial computations is significantly different from the $p = 2, 3, 4$ computations. While one expects a convergence behavior to be of the type [73]

$$E \propto \tilde{h}^{p+1} \tag{7.6}$$

for the DGTD method, we here see a clear deviation from the exponential convergence with respect to the polynomial basis function order. This indicates a different source for the numerical error.

Thus, we next check how much the newly implemented anisotropic material integration kernel deviates from the already existing isotropic one. We perform the scattering computations with the same computation parameters and evaluate the kernel difference error

$$E^\Delta_p(\tilde{h}) = \left| Q^p_{\text{scat,iso}}(\tilde{h}) - Q^p_{\text{scat,aniso}}(\tilde{h}) \right| \tag{7.7}$$

between both material models point-wise for each characteristic mesh element side length scaling factor $\tilde{h}$ and basis function polynomial order p. Figure 7.3 shows the kernel difference error for four different polynomial orders and different mesh sizes. We observe that for all the computations the scattering spectra obtained with either implementation agree down to machine accuracy. However, for small wavelengths $\lambda \approx 1R$ the error increases. This can be attributed to the strong decay in the excitation spectrum (cf. Fig. B.2 (b)) which the scattered flux is normalized to. Hence, the errors on the machine accuracy level get enhanced.

Since the implementations provide consistent results, we have a look into the convergence behavior of the scattering spectra with respect to the mesh element size refinement factor $\tilde{h}$. In Figure 7.4 we show the wavelength-resolved convergence for four polynomial orders. We again
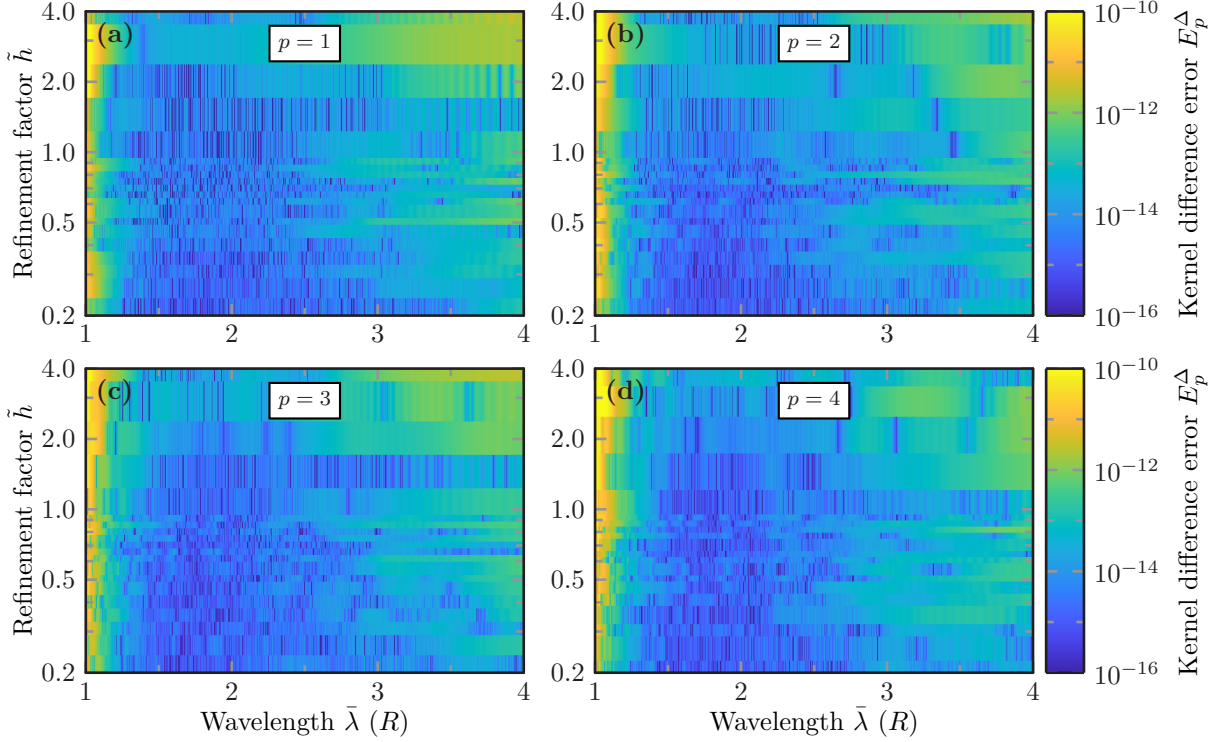
Figure 7.3: Wavelength-resolved kernel difference error $E_p^\Delta(\tilde{h})$, Eq. (7.7), determined by the scattering efficiencies computed within the isotropic and anisotropic material implementation for different basis polynomial orders p and mesh refinements $\tilde{h}$.

observe, that the $p = 1$ computations strongly deviate from the remaining polynomial order computations. Especially the $p = 3$ and $p = 4$ convergence behavior is very similar.

To get a fast assessment of the convergence, we also show the wavelength-averaged relative error $\left\langle E_p(\tilde{h}) \right\rangle_\lambda$ in Fig. 7.5 (a), where we average for all recorded wavelengths $\lambda \in [R, 4R]$. Additionally, we introduce the relative error between DGTD computations comparing against the finest mesh computation for each polynomial order p:

$$E_p^{\mathrm{DG}}(\tilde{h}) = \left| 1 - \frac{Q_{\mathrm{scat}}^p(\tilde{h})}{Q_{\mathrm{scat}}^p(\tilde{h}_{\min})} \right| . \tag{7.8}$$

The corresponding wavelength-averaged error $\left\langle E_p^{\mathrm{DG}}(\tilde{h}) \right\rangle_\lambda$ is shown in Figure 7.5 (b). For all the errors, we find an expected polynomial $\tilde{h}^\gamma$ convergence. For coarse meshes, i.e., large $\tilde{h}$, the change in error gets more and more noisy, as we do not track the actual (minimal) element mesh size, but only the parameter for the maximally allowed element mesh size provided for the meshing software *gmsh* [140]. To find the actual convergence order we perform a fit to the $p = 1$ and $p = 4$ mesh size scans, as the $p = 2, 3, 4$ convergence roughly share the same slope. For the $p = 1$ computations we find a convergence exponent of $\gamma_1 = 1.26$ for the Mie
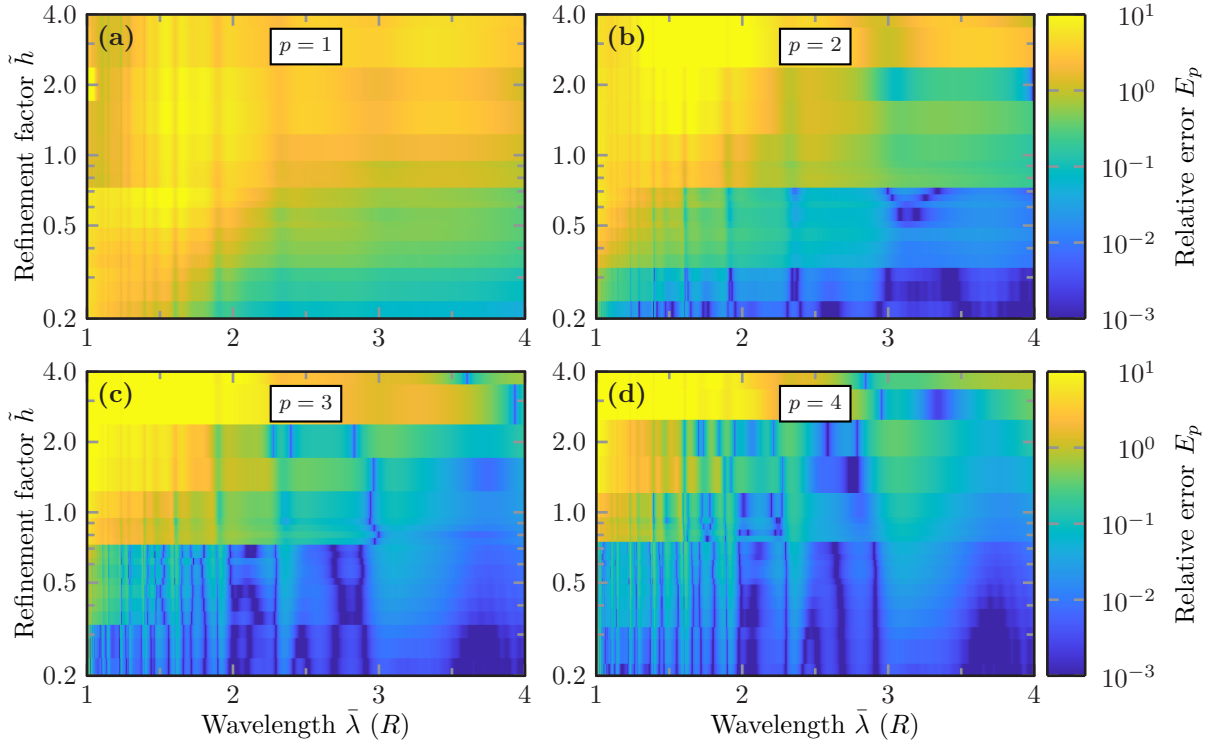
Figure 7.4: Wavelength-resolved relative error $E_p(\tilde{h})$, Eq. (7.5), between DGTD and Mie computations for different basis polynomial order p and mesh refinements $\tilde{h}$.
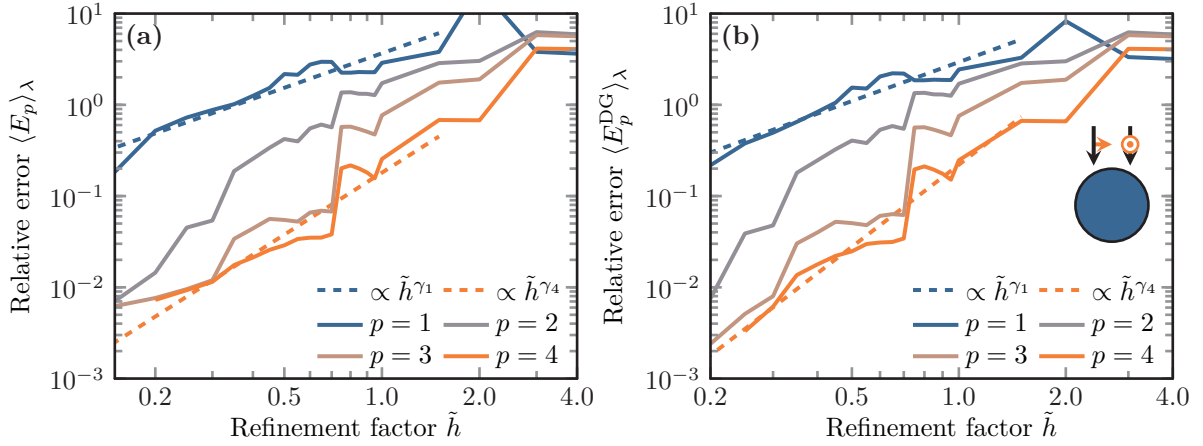
Figure 7.5: Wavelength-averaged relative errors, **(a)** $\langle E_p \rangle_\lambda(\tilde{h})$ comparing Mie against DGTD computations and **(b)** $\langle E_p^{\mathrm{DG}} \rangle_\lambda(\tilde{h})$ comparing DGTD computations against results with finest mesh parameter $\tilde{h}_{\mathrm{min}}$, for four different basis polynomial orders p. Dashed lines show polynomial fits $\tilde{h}^\gamma$ for the convergence behavior for first and fourth-order basis sets, with parameters **(a)** $\gamma_1 \approx 1.26$ and $\gamma_4 \approx 2.26$, as well as **(b)** $\gamma_1 \approx 1.42$ and $\gamma_4 \approx 2.99$.

and $\gamma_1 = 1.42$ for the DGTD computations, which clearly lies below the expected value of two ($\gamma_p = p + 1$). We attribute this deviation to a still insufficient discretization using these low order basis functions, as the difficulty of resolving highly oscillating fields over the entire wavelength range arises. For the $p = 4$ computations, we find exponents $\gamma_4 = 2.26$ for the Mie and $\gamma_4 = 2.99$ for the DGTD computations. While the internal DGTD error is very close to the expected convergence behavior for an order $p = 2$ polynomial basis, the deviation for the error comparing to the Mie computations might be attributed to both mesh size noise as well as spectral leakage [169] and aliasing [129] in the DGTD spectra. The latter arise due to the on-the-fly Fourier transform Eq. (5.126), which is used to obtain the scattering spectra. As the time-dependent fields are artificially cut at the maximal simulation time, this leads to oscillations in the resulting spectra, which can be systematically decreased with an increasing simulation time. This oscillatory behavior can be well observed for small wavelengths λ and mesh refinement factors $\tilde{h}$ in Fig. 7.4 (c,d), as the error is not improving in the same systematic way as for larger wavelengths. The reason that both the $p = 3$ and $p = 4$ computations only provide a convergence behavior as for a $p = 2$ polynomial basis lies within the surface discretization of the sphere. Here, we only use linear tetrahedral elements. Thus, also the surface of the sphere is only linearly approximated and therefore limiting the convergence order. To circumvent this problem, one can use curvilinear elements on the surface [185, 186], which utilizes element faces defined by higher-order (two-dimensional) polynomials. However, with curved element surfaces also the normal vector of an elements' surface varies across that surface. Hence, the implementation of the numerical flux (5.102) becomes much more challenging, especially for anisotropic materials with their surface normal dependent impedance and admittance matrices (5.101). We therefore only use linear elements performing $p = 4$ computations, which still provide smaller errors, while simultaneously relinquishing the exponential convergence advantage compared to the $p = 2$ computations.

7.1.2 Diagonal material tensors

In the second setup, we replace the material permittivity of the scattering sphere with a diagonal anisotropic tensor, while maintaining all other computation parameters from the isotropic case. Similarly to [77], we choose a dielectric material tensor

$$\underline{\boldsymbol{\epsilon}} = \begin{pmatrix} 2 & 0 & 0 \\ 0 & 2 & 0 \\ 0 & 0 & 4 \end{pmatrix} . \tag{7.9}$$

Since the scattering with an anisotropic material is no longer polarization-independent, we have to consider both polarizations: We choose

$$\boldsymbol{k}||\boldsymbol{e}_x \quad \text{with} \quad \boldsymbol{E}_0^{(1)}||\boldsymbol{e}_y \quad \text{or} \quad \boldsymbol{E}_0^{(2)}||\boldsymbol{e}_z , \tag{7.10}$$

i.e., the Gaussian modulated plane wave (7.1) propagates in x-direction and is either linearly y- or z-polarized. The corresponding scattering efficiency spectra are shown in Figure 7.6 (a,c). In contrast to the z-polarized excitation, the y-polarized excitation does not cause strong resonances in the scattering spectrum. Since the permittivity tensor values are set with $\epsilon_{xx} = \epsilon_{yy}$, the
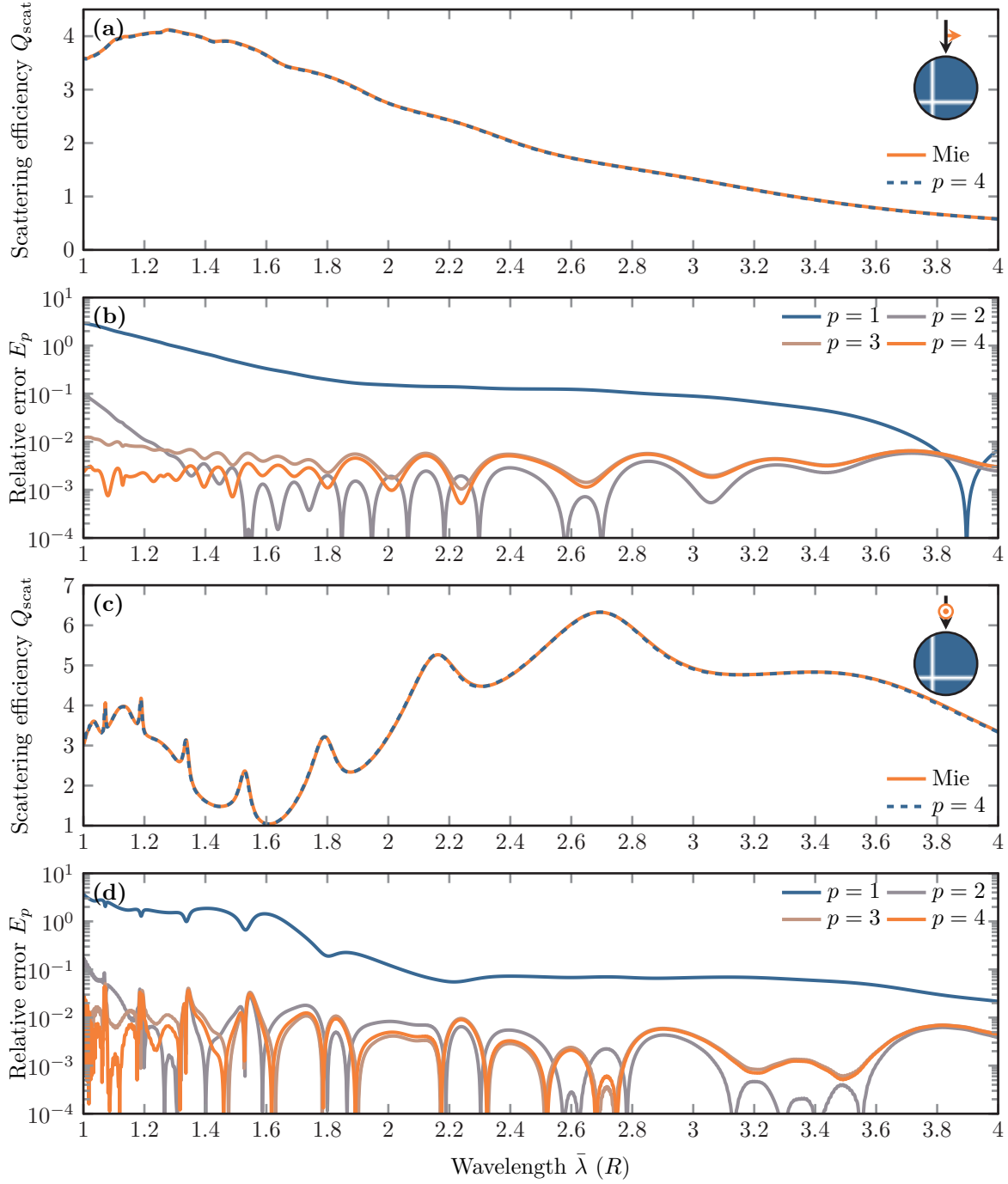
Figure 7.6: Scattering efficiencies of a dielectric sphere with diagonal permittivity tensor (7.9), for y-polarization **(a)** and z-polarization **(c)** from both a Mie calculation [78] and the DGTD method with a $p = 4$ polynomial basis. Corresponding relative errors (7.5) **(b,d)** between the Mie calculations and DGTD computations for the finest mesh of the convergence scan and different polynomial orders p.

strong resonances shift to wavelengths that are smaller than the ones computed here, for this polarization. We again observe that the relative errors Eq. (7.5) for both polarization directions and the most finely resolved meshes only differ significantly for the polynomial basis order $p = 1$ and higher orders $p = 2, 3, 4$, as the surface discretization does not change within the DGTD method (see Figure 7.6 (b,d)).
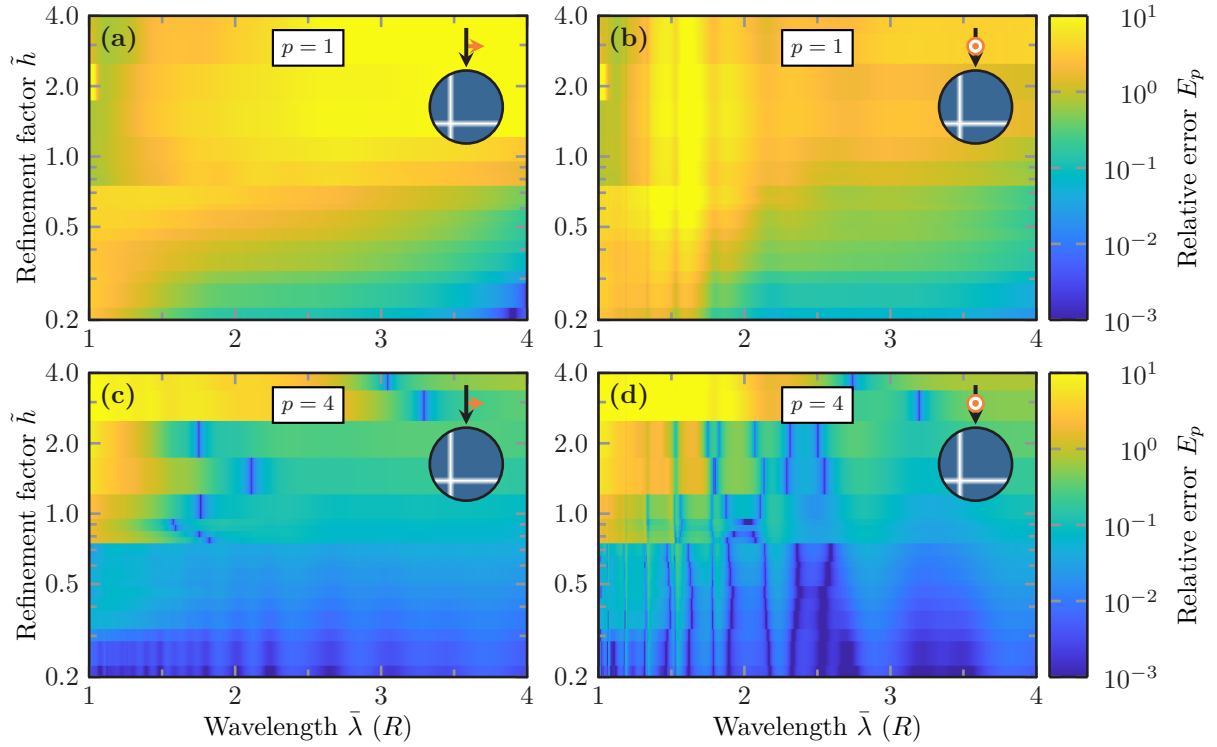
Figure 7.7: Wavelength-resolved relative error $E_p(\tilde{h})$, Eq. (7.5), between DGTD and Mie scattering efficiency computations with the diagonal anisotropic permittivity (7.9) and for different basis polynomial order p and mesh refinements $\tilde{h}$.

Upon closer inspection of the convergence behavior for the wavelength-resolved h-refinement of the relative error in Figure 7.7, we observe the same behavior. Despite the higher resonances in the z-polarization spectrum (see Figure 7.7 (b,d)), the error is more prone to aliasing and the actual mesh discretization. However, all computations show a systematic improvement with increasing h-refinement, which also transfers to the wavelength-averaged convergence plots in Figure 7.8 (a,b). For both polarizations, the convergence is similar to that observed for the isotropic scatterer. We again notice that the convergence exponents γ are higher for the wavelength-averaged DGTD relative internal error (see Figure 7.8 (c,d)) than for those of the relative error comparing the results to the Mie computations. As the Mie computations converge exponentially with increasing angular degree l of the underlying vector spherical harmonic basis functions [78, 90], the errors from the DGTD computations are orders of magnitudes larger. Therefore, the effect of the apparent faster convergence within the DGTD results indicates, that the computations systematically improve towards the Mie results from one direction. Due to the
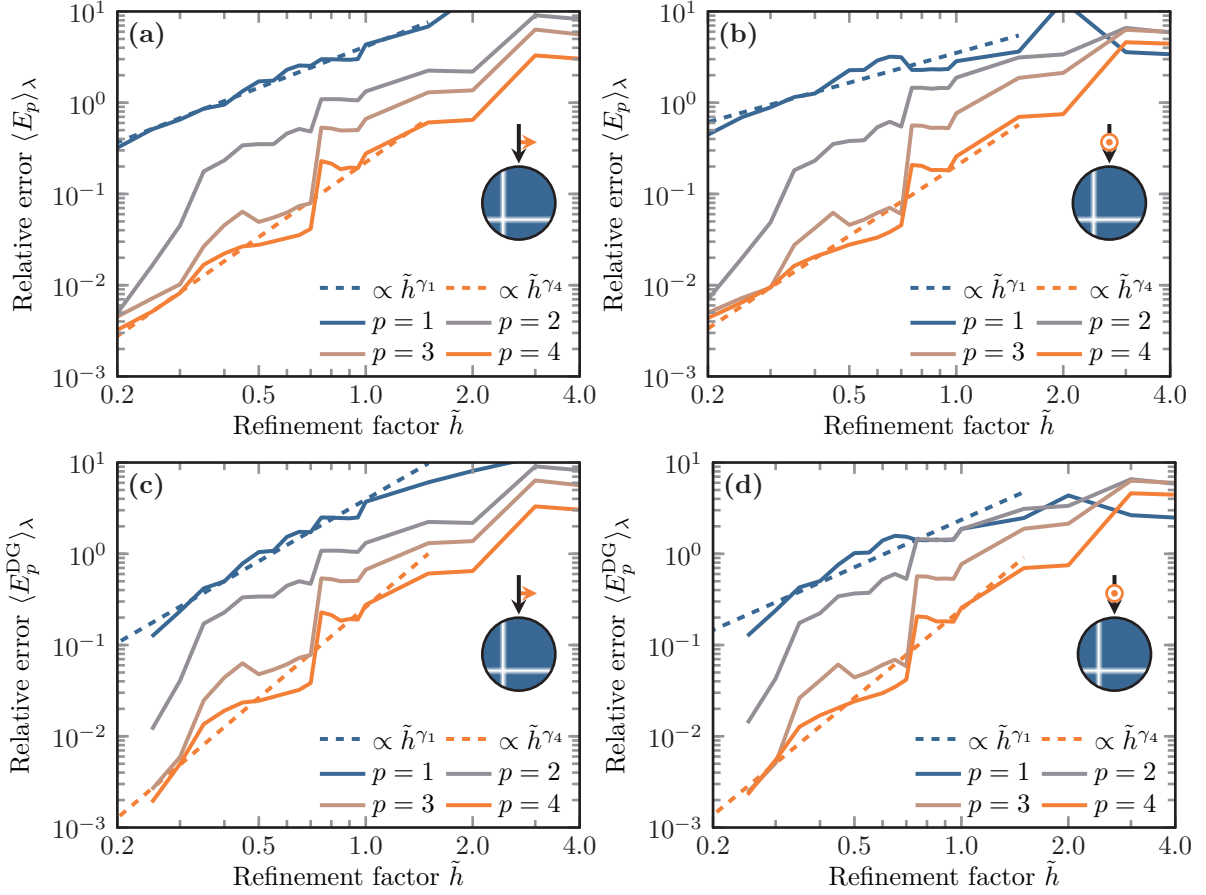
Figure 7.8: Wavelength-averaged relative errors, **(a,b)** $\langle E_p \rangle_\lambda(\tilde{h})$ comparing Mie against DGTD computations and **(c,d)** $\langle E_p^{\mathrm{DG}} \rangle_\lambda(\tilde{h})$ comparing DGTD computations against results with finest mesh parameter, each for different basis polynomial order p. Dashed lines show polynomial fits $\tilde{h}^\gamma$ for the convergence behavior for first- and fourth-order basis sets. Fit parameters for the y-polarization are **(a)** $\gamma_1 \approx 1.50$ and $\gamma_4 \approx 2.72$, as well as **(c)** $\gamma_1 \approx 2.25$ and $\gamma_4 \approx 3.31$. Fit parameters for the z-polarization are **(b)** $\gamma_1 \approx 1.09$ and $\gamma_4 \approx 2.55$, as well as **(d)** $\gamma_1 \approx 1.73$ and $\gamma_4 \approx 3.23$.

discretization of the sphere within the meshing software, the polyhedral approximation always only is inscribed to that sphere. Therefore the actual scatterer simulation volume approaches the real sphere volume from below and the computed resonances shift from smaller wavelengths to the actual resonance spectral position with improved h-refinement. Overall it shall be noted, that within this convergence study we are able to obtain errors as low as 0.5% for a relatively strongly anisotropic material.

7.1.3 Fully anisotropic material tensors

In the third test, we investigate the convergence behavior for a fully anisotropic dielectric tensor, i.e., all off-diagonal entries are non-zero. We, therefore, prepare two different setups for the DGTD computations, as shown in Figure 7.1 (c). The first setup includes a diagonal $\underline{\underline{\epsilon}}$-tensor as tested in the previous section and an excitation of the scattering sphere, with both the $\boldsymbol{k}$-vector and polarization vector $\boldsymbol{E}_0$ rotated against the main coordinate axis. In the second setup, we rotate the parameters of the exciting plane wave into the coordinate frame and also rotate the dielectric tensor, such that all off-diagonal entries are non-zero. The scattering efficiency spectra are then compared to each other.

For the diagonal material tensor, we again use

$$\underline{\underline{\epsilon}}_{\mathrm{d}} = \begin{pmatrix} 2 & 0 & 0 \\ 0 & 2 & 0 \\ 0 & 0 & 4 \end{pmatrix} . \tag{7.11}$$

Introducing a rotation matrix

$$\hat{\mathbf{R}}\left(\alpha,\beta,\gamma\right) = \begin{pmatrix} \cos\alpha\cos\gamma - \sin\alpha\cos\beta\sin\gamma & \sin\alpha\cos\gamma + \cos\alpha\cos\beta\sin\gamma & \sin\beta\sin\gamma \\ -\cos\alpha\sin\gamma - \sin\alpha\cos\beta\cos\gamma & -\sin\alpha\sin\gamma + \cos\alpha\cos\beta\cos\gamma & \sin\beta\cos\gamma \\ \sin\alpha\sin\beta & -\cos\alpha\sin\beta & \cos\beta \end{pmatrix} , \tag{7.12}$$

using the three Euler angles [187, 188] α, β and γ, we can set the excitation direction and polarization vectors for the first "diagonal" setup as

$$\boldsymbol{k}_{\mathrm{d}} = \hat{\mathbf{R}}\left(\alpha,\beta,\gamma\right) \cdot \boldsymbol{e}_x , \quad \boldsymbol{E}_{0,\mathrm{d}}^{(1)} = \hat{\mathbf{R}}\left(\alpha,\beta,\gamma\right) \cdot \boldsymbol{e}_y \quad \text{and} \quad \boldsymbol{E}_{0,\mathrm{d}}^{(2)} = \hat{\mathbf{R}}\left(\alpha,\beta,\gamma\right) \cdot \boldsymbol{e}_z . \tag{7.13}$$

For the second "rotated" setup we consequently rotate the permittivity tensor

$$\underline{\underline{\epsilon}}_{\mathrm{r}} = \hat{\mathbf{R}}^{\mathrm{T}}\left(\alpha,\beta,\gamma\right) \cdot \underline{\underline{\epsilon}}_{\mathrm{d}} \cdot \hat{\mathbf{R}}\left(\alpha,\beta,\gamma\right) , \tag{7.14}$$

such that the excitation directions and polarization vectors are aligned with the coordinate axes, i.e.,

$$\boldsymbol{k}_{\mathrm{r}} = \boldsymbol{e}_x , \quad \boldsymbol{E}_{0,\mathrm{r}}^{(1)} = \boldsymbol{e}_y \quad \text{and} \quad \boldsymbol{E}_{0,\mathrm{r}}^{(2)} = \boldsymbol{e}_z . \tag{7.15}$$

We choose

$$\alpha = 1 , \quad \beta = 2 , \quad \text{and} \quad \gamma = \frac{1}{2} , \tag{7.16}$$
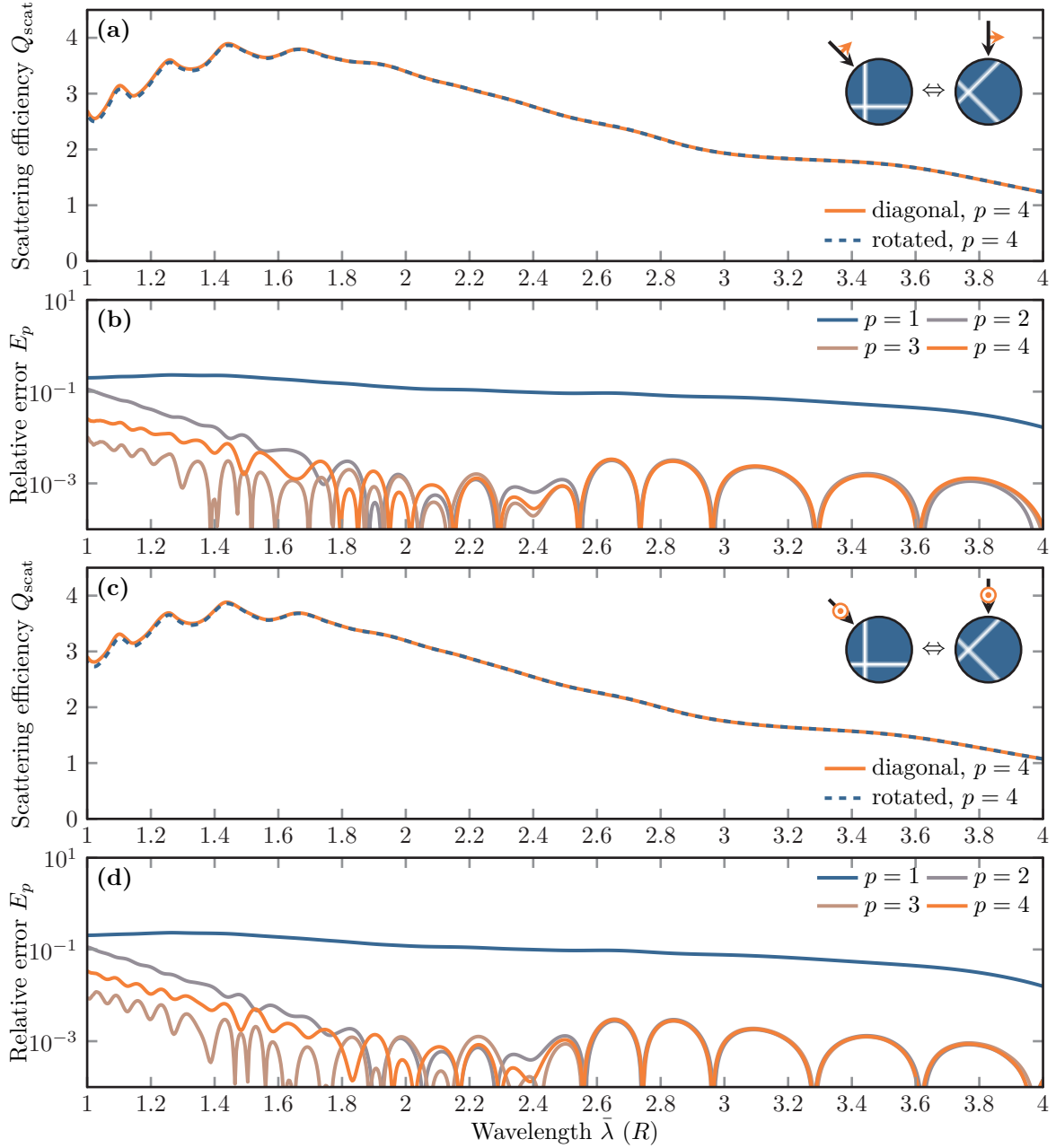
Figure 7.9: Scattering efficiencies of a dielectric sphere with diagonal permittivity tensor (7.11) upon excitation with rotated polarization vectors (7.18), **(a)** $\boldsymbol{E}_{0,d}^{(1)}$ and **(c)** $\boldsymbol{E}_{0,d}^{(2)}$ compared to the rotated *fully* anisotropic permittivity tensor (7.17) upon excitation in y-polarization **(a)** and z-polarization **(c)**. All spectra are computed with the DGTD method using a $p = 4$ polynomial basis. **(b,d)** Corresponding relative errors (7.5) between the different DGTD computations for the finest mesh of the convergence scan and different polynomial orders p.

such that the fully occupied tensor is

$$\underline{\underline{\boldsymbol{\epsilon}}}_{\mathrm{r}} \approx \begin{pmatrix} 3.17 & -0.75 & -0.64 \\ -0.75 & 2.48 & 0.41 \\ -0.64 & 0.41 & 2.23 \end{pmatrix}, \tag{7.17}$$

while the excitation vectors for the diagonal tensor turn to

$$\boldsymbol{k}_{\mathrm{d}} \approx \begin{pmatrix} 0.64 \\ 0.05 \\ 0.77 \end{pmatrix}, \quad \boldsymbol{E}_{0,\mathrm{d}}^{(1)} \approx \begin{pmatrix} 0.63 \\ -0.60 \\ -0.49 \end{pmatrix} \quad \text{and} \quad \boldsymbol{E}_{0,\mathrm{d}}^{(2)} \approx \begin{pmatrix} 0.43 \\ 0.79 \\ -0.41 \end{pmatrix}. \tag{7.18}$$

All other simulation parameters of the Gaussian modulated plane wave (see Equation (7.1)) remain the same.
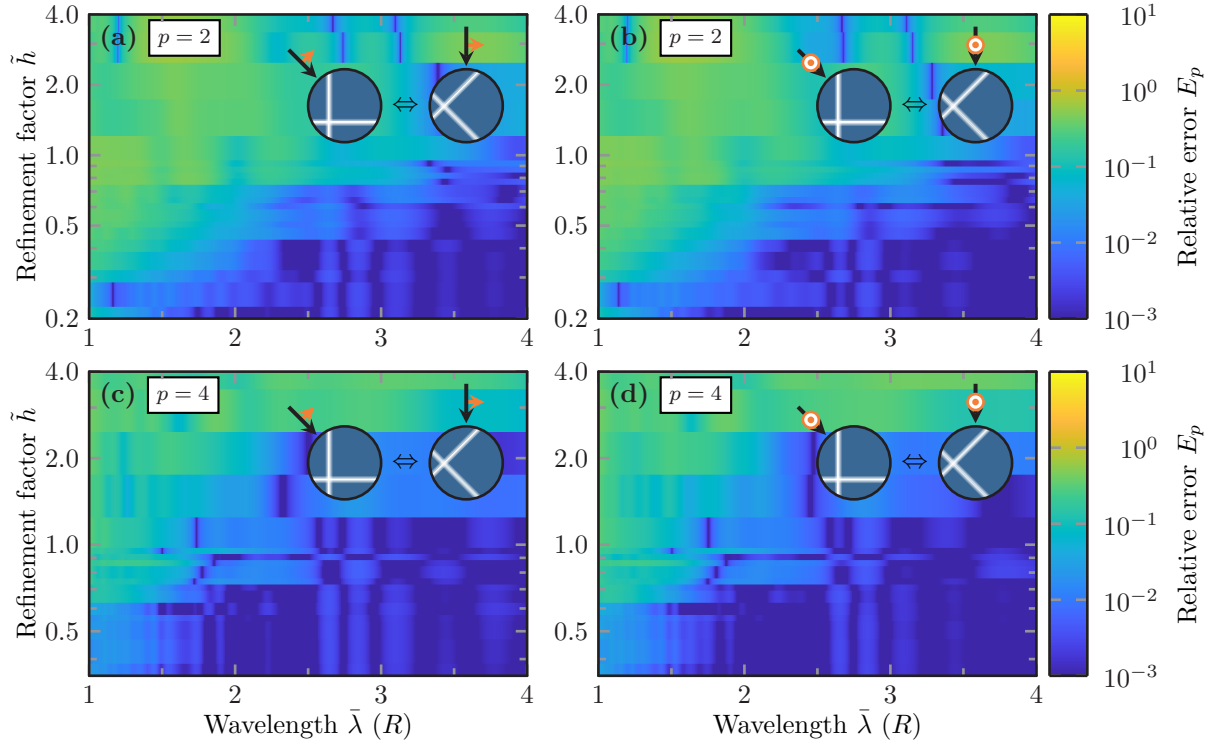
Figure 7.10: Wavelength-resolved relative error $E_p(\tilde{h})$, Eq. (7.5), between the DGTD scattering efficiency computations for the diagonal permittivity tensor with rotated excitation and the counter-rotated system. Both are computed for different basis polynomial order **(a,b)** $p = 2$ and **(c,d)** $p = 4$, different mesh refinements $\tilde{h}$ and the two different polarizations (7.18) used for the excitation with a plane wave.

In Figure 7.9 (a,c) we show the scattering efficiencies for both polarizations. While both spectra agree well, the deviation is highest in the low wavelength region, in which the resonances become more pronounced. However, the relative errors in Figure 7.9 (b,d) show the same behavior as

in the isotropic and diagonal anisotropic case, namely, the $p = 1$ errors are significantly higher than the $p = 2, 3, 4$ computation errors of the scattering efficiencies.
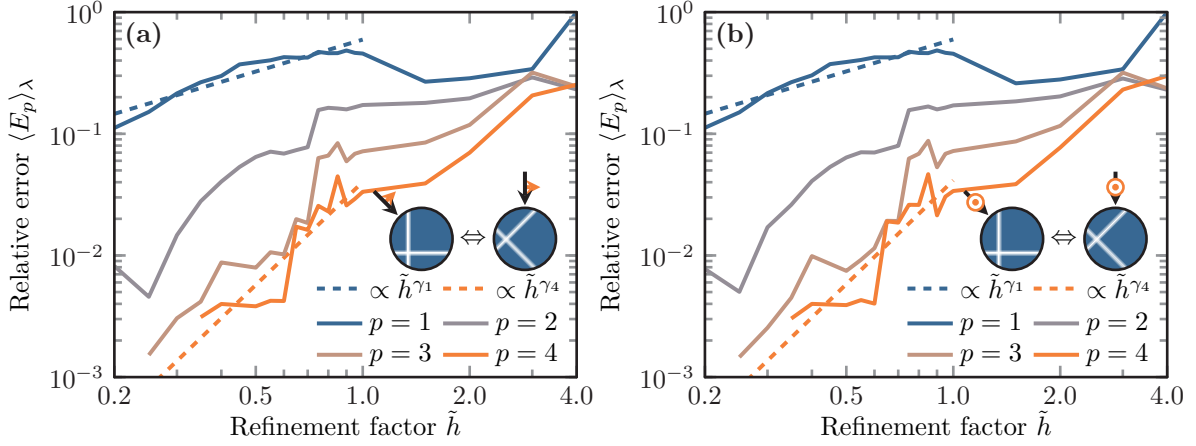
Figure 7.11: Wavelength-averaged relative errors, $\langle E_p \rangle_\lambda(\tilde{h})$ comparing DGTD computations with diagonal (7.11) and rotated permittivity tensor (7.17) for two different linear excitation polarizations (7.18), **(a,b)**. Dashed lines show polynomial fits $\tilde{h}^\gamma$ for the convergence behavior for first- and fourth-order basis sets, with parameters **(a)** $\gamma_1^{(1)} \approx 0.87$ and $\gamma_4^{(1)} \approx 2.81$, as well as **(b)** $\gamma_1^{(2)} \approx 0.87$ and $\gamma_4^{(2)} \approx 2.83$.

In Figure 7.10 we show the wavelength-resolved relative error convergence with respect to the mesh refinement factor $\tilde{h}$. For both polarizations, the error in the small wavelength region $\lambda \lesssim 2R$ is significantly higher for the $p = 2$ computations (see Figure 7.10 (a,c)) than compared to that of the $p = 4$ computations (see Figure 7.10 (a,c)). But since the convergence of the wavelength-averaged relative error $\langle E_p \rangle_\lambda$ shows roughly the same slope in Figure 7.11 for both polynomial orders, the relative offset factor can be attributed to the lower number of discretization points used for the lower polynomial order computations. Again the slopes of the $p = 2, 3, 4$ convergence behaviors agree and $\gamma_4^{(1)} = 2.81$ as well as $\gamma_4^{(2)} = 2.83$ have the expected value for a second-order convergence behavior induced by the use of a linearly approximated sphere surface. The $p = 1$ computations, again provide slopes of $\gamma_1^{(1)} = 0.87$ as well as $\gamma_1^{(2)} = 0.87$, in the same manner as already seen for the diagonal test case of the previous section. For the chosen mesh sizes we again obtain relative errors as low as 0.5%, such that the real-valued, three-dimensional, non-dispersive anisotropic material tensor implementation for the DGTD method can be considered reliably operating.

7.1.4 Magneto-optic material tensors

In the fourth and final test setup (see Figure 7.1 (d)), we use a complex-valued anisotropic material tensor, as derived in Section 3.3 about the MO materials. We use the tensor

$$\underline{\underline{\epsilon}} = \begin{pmatrix} \epsilon_r & \mathrm{i}g & 0 \\ -\mathrm{i}g & \epsilon_r & 0 \\ 0 & 0 & \mathrm{i}\epsilon_r \end{pmatrix} = \begin{pmatrix} 6.25 & 0.1\mathrm{i} & 0 \\ -0.1\mathrm{i} & 6.25 & 0 \\ 0 & 0 & \mathrm{i}6.25 \end{pmatrix}. \tag{7.19}$$

With the increased value of $\epsilon_r = 6.25$, a sphere with a radius as large as in the previous examples would lead to a lot of resonances and requires an even finer mesh resolution. Hence, we here investigate the scattering of a

(SI) $$R = 50\,\mathrm{nm} \tag{7.20}$$

sphere and record spectra for wavelengths

(SI) $$\lambda \in [3R, 8R] = [150\,\mathrm{nm}, 400\,\mathrm{nm}]. \tag{7.21}$$

As excitation, we use a Gaussian modulated plane wave with left circular polarization (LCP) and right circular polarization (RCP). Since both the polarization vectors (2.82) for LCP and RCP as well as the permittivity tensor (7.19) are complex-valued, we also need to perform the DGTD computations with complex fields. Here, one exploits the linearity of Maxwell's equations and only takes the real values of the fields to compute the final observables. This means the time-dependent incident field has to be real-valued in the end as well. This means, that given a real-valued incident field time dependence

$$\eta(t) = \frac{1}{2\pi} \int_{-\infty}^{\infty} \mathrm{d}\omega\, \eta(\omega)\, \mathrm{e}^{-\mathrm{i}\omega t}, \tag{7.22}$$

with its spectral components $\eta(\omega) = \eta^*(-\omega)$, for each positive frequency ω, the incident plane wave field in circular polarization has to take the form [189]

$$\boldsymbol{E}_{\mathrm{inc}}^{\pm}(\boldsymbol{r}, t) = 2\mathrm{Re}\left[\frac{1}{2\pi} \int_0^{\infty} \mathrm{d}\omega\, \boldsymbol{E}_0^{\pm}\eta(\omega)\mathrm{e}^{\mathrm{i}\frac{\omega}{c}\left(\boldsymbol{e}_k \cdot \boldsymbol{r} - ct\right)} \right]. \tag{7.23}$$

Here $E_0^{\pm}$ are the LCP $(+)$ and RCP $(-)$ polarization vectors, as introduced in Eq. (2.82). While maintaining the spectrum of the time dependence guarantees the same time-dependent behavior of the field, we have to restrict ourselves to a positive frequency integral within the Fourier transform for any elliptically and therefore also circularly polarized incident field. Otherwise, the rotation direction of the field changes for negative frequencies, as there is a change in the sign of the complex phase. The factor two has to be introduced in order to recover the incident field of the form (7.1) for linear polarization, i.e., $\boldsymbol{E}_0^{\pm} \to \boldsymbol{E}_0 = \boldsymbol{E}_0^*$. In order to simplify the source term computation, we introduce a complex-valued time dependence $\eta_c(t)$, such that for

any complex-valued polarization vector $\boldsymbol{E}_0$

$$\boldsymbol{E}_{\text{inc}}(\boldsymbol{r}, t) = \text{Re} \left(\boldsymbol{E}_0 \eta_c \left(t - c_0^{-1} \boldsymbol{e}_k \cdot \boldsymbol{r} \right) \right) . \tag{7.24}$$

Consequently, we require that

$$\eta(t) = 2\text{Re} \left(\frac{1}{2\pi} \int_0^\infty \mathrm{d}\omega \, \eta(\omega) \mathrm{e}^{-\mathrm{i}\omega t} \right) \overset{!}{=} \text{Re} \left(\eta_c(t) \right) , \tag{7.25}$$

for the real- and complex-valued time dependence. Therefore, we can compute the complex-valued time dependence as

$$\eta_c(t) = \frac{2}{2\pi} \int_{-\infty}^\infty \mathrm{d}\omega \, \eta(\omega) \Theta(\omega) \mathrm{e}^{-\mathrm{i}\omega t} = 2\eta(t) * \underbrace{\mathcal{F}^{-1} \left[\Theta(\omega) \right] (t)}_{\frac{1}{2}\delta(t) - \frac{\mathrm{i}}{2\pi} \text{P} \frac{1}{t}}$$

$$= \eta(t) - \frac{\mathrm{i}}{\pi} \text{P} \int_{-\infty}^\infty \mathrm{d}t' \, \frac{\eta(t')}{t - t'} = \eta(t) + \mathrm{i}\mathcal{H} \left[\eta(t') \right] (t) , \tag{7.26}$$

where the real part per design is the original real-valued time dependence and the imaginary part is the Hilbert-transformation $\mathcal{H}$ [189, 190] of the time dependence $\eta(t)$. Here P $\int$ is the Cauchy principal value integral. Typical time dependencies used within the DGTD computations take the form of a slowly modulated carrier wave, i.e.,

$$\eta(t) = \cos \left(\omega_0(t - t_0) + \phi_0 \right) f \left(t - t_0 \right) . \tag{7.27}$$

As the envelope function $f(t)$ is assumed to be slowly varying, both Fourier transform of the carrier wave and $f(\omega)$ have negligible spectral overlap. Thus, one can apply the Bedrosian theorem [191] and the Hilbert transformation is

$$\mathcal{H} \left[\eta(t') \right] (t) = f \left(t - t_0 \right) \mathcal{H} \left[\cos \left(\omega_0(t - t_0) + \phi_0 \right) \right] (t)$$

$$= -\sin \left(\omega_0(t - t_0) + \phi_0 \right) f \left(t - t_0 \right) . \tag{7.28}$$

For the complex-valued field DGTD computations, we use the complex-valued Gaussian modulated plane wave incident field

$$\boldsymbol{E}_{\text{inc}}^\pm(\boldsymbol{r}, t) = \boldsymbol{E}_0^\pm \eta_c \left(t - c_0^{-1} \boldsymbol{e}_z \cdot \boldsymbol{r} \right) = \boldsymbol{E}_0^\pm \mathrm{e}^{-\mathrm{i}\omega_0(t - t_0)} \mathrm{e}^{-\frac{(t - t_0)^2}{2\sigma^2}} . \tag{7.29}$$

Here, we set the polarization vectors to

$$\boldsymbol{E}_0^+ = \frac{1}{\sqrt{2}} \left(\boldsymbol{e}_x + \mathrm{i}\boldsymbol{e}_y \right) \text{ for LCP} \quad \text{and} \quad \boldsymbol{E}_0^- = \frac{1}{\sqrt{2}} \left(\boldsymbol{e}_x - \mathrm{i}\boldsymbol{e}_y \right) \text{ for RCP.} \tag{7.30}$$

Because of the adjusted spectral observation range, also the pulse modulation parameters are changed to

(SI) $$\lambda_0 = \frac{2\pi c_0}{\omega_0} = 300\,\text{nm}\,, \quad \sigma \approx 1.167\,\text{fs} \quad \text{and} \quad t_0 = 10\,\sigma \approx 11.67\,\text{fs}\,. \tag{7.31}$$

With the choice of the temporal width σ of the Gaussian envelope determining also the spectral width (B.22), the Bedrosian theorem (7.28) holds to a sufficient level, as

(SI) $$1 \lessapprox \frac{c_0\sigma}{\lambda_0} = \frac{7}{6}\,. \tag{7.32}$$

From the Fourier transformed fields, we again compute the time-averaged Poynting vector (2.93), the scattering cross section C_{scat} (2.104) and finally the scattering efficiency $Q_{\text{scat}}^{\pm}$ for both LCP and RCP. Since the MO material provides different refractive indices for LCP and RCP waves, we also compute the difference

$$\Delta Q = Q_{\text{scat}}^{+} - Q_{\text{scat}}^{-}\,. \tag{7.33}$$

For the non-absorptive permittivity chosen here, Eq. (7.33) gives a measure for the strength of the Faraday effect of the material [29], while it also provides a measure for the analog of circular dichroism [86]. As the spherical particles scatter LCP and RCP light differently, light passing through such particle dust would appear dichroic, as the overall extinction is solely determined by the scattering cross sections of the single constituting particles.

In Figure 7.12 (a) we show the scattering efficiencies for both polarizations. We again compare the DGTD spectra against Mie calculations performed by P. Varytis [78]. The spectra show a good agreement for both Mie resonances captured in the spectrum. However, a deviation for small wavelengths $\lambda \approx 3R$ can still be observed. In Figure 7.12 (b) we show the left-right difference signal ΔQ for both the $p = 4$ DGTD computation as well as the Mie calculations. As there is no strong deviation, we additionally investigate the relative error

$$E_p^{\Delta Q} = \frac{|\Delta Q^{(\text{DG})} - \Delta Q^{(\text{Mie})}|}{\max\left(|\Delta Q^{(\text{DG})}|, |\Delta Q^{(\text{Mie})}|\right)}\,, \tag{7.34}$$

which is constructed to maximally get to one, if either of the left-right difference spectra becomes zero. This relative error is shown in Figure 7.12 (c). We again observe that the error for the $p = 1$ computations is significantly higher than that for the $p = 2, 3, 4$ computations which show a similar behavior. However, the error is an order of magnitude higher than in the previous sections, as the left-right difference ΔQ is an order of magnitude smaller than the scattering efficiency spectra it is obtained from.

In Figure 7.13 we show the wavelength-resolved convergence behavior of the left-right scattering efficiency difference for different polynomial basis function orders p. For the first-order polynomial basis, the relative error does not show a systematic improvement (see Figure 7.13 (a)), as
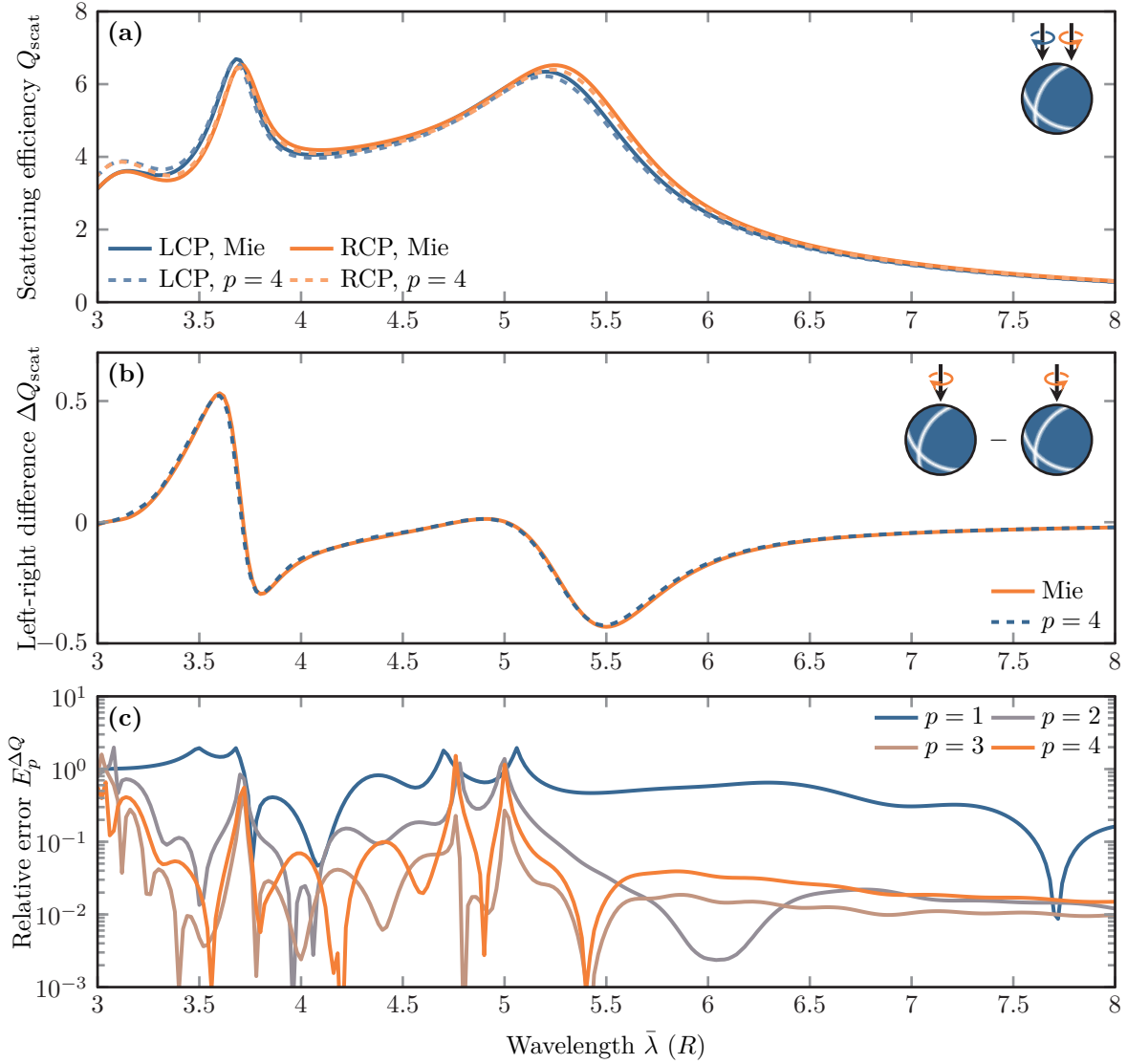
Figure 7.12: **(a)** Comparison of scattering efficiencies of a full-dielectric MO sphere excited in LCP and RCP, computed with both the complex-valued DGTD method and Mie calculations [78]. The DGTD computations stem from the finest mesh of the convergence scan and utilize a polynomial Lagrange basis of order $p = 4$. **(b)** Left-right difference signal (7.33) computed for either method using the spectra above. **(c)** Relative error (7.34) between the DGTD computations and the Mie calculations, for different polynomial basis orders p and the finest mesh used in the convergence scan.

the mesh element size

$$h = \tilde{h}\, h_0 \,, \tag{7.35}$$

is not small enough, even for the lowest mesh refinement factor $\tilde{h}_{\min}$. Here the mesh element
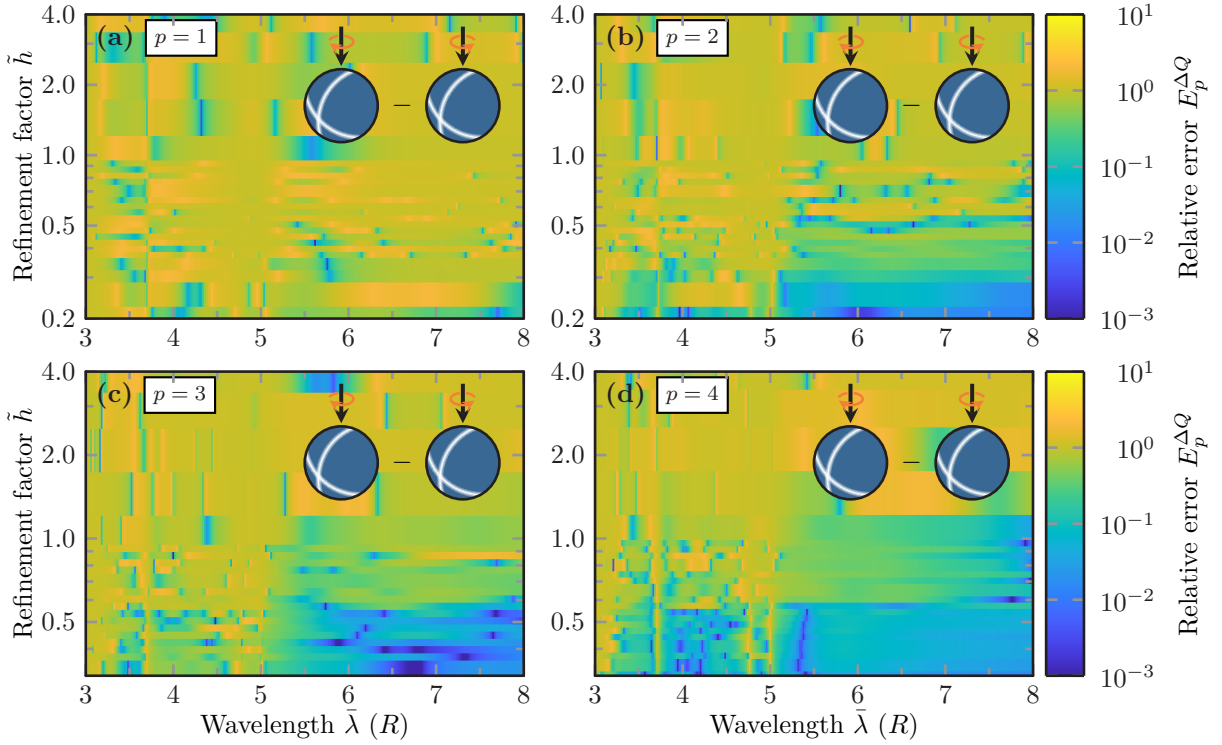
Figure 7.13: Wavelength-resolved relative error (7.34) of the MO left-right scattering efficiency difference between the Mie calculations and DGTD computations determined for different mesh refinements $\tilde{h}$ (see Eq. (7.35)) and polynomial orders p.

size was changed to $h_0 = 20\,\text{nm}$ as also the sphere radius was decreased compared to the previous sections. However, for the other polynomial orders, we can clearly observe a systematic improvement with increasing $\tilde{h}$-refinement. The same can also be observed for the wavelength-averaged relative error $\langle E_p^{\Delta Q}\rangle_\lambda$, shown in Figure 7.14. This holds both for a comparison between DGTD computations against Mie calculations (a) as well as DGTD with the finest mesh DGTD computation performed in the convergence scan (b). Since we compare the difference between the LCP and RCP scattering efficiency spectra, the resulting convergence behavior seems to be effectively lowered by one degree, i.e., the error decreases with $\gamma_4 \approx 1.63$ for the Mie calculations and $\gamma_4 \approx 1.78$ for the DGTD computations respectively. However, with the given mesh size, it is still possible to obtain relative errors as small as 5%.

Summarizing the convergence study for the anisotropic material implementation, we have shown that for all viable non-dispersive anisotropic permittivity tensors resulting in a stable DGTD scheme, we can perform reliable and systematically improvable computations. While the results from Mie calculations clearly perform better for the spherical scattering problems converging exponentially with angular momenta l, the DGTD method's main application lies in the computation for material distributions with more sophisticated geometries.
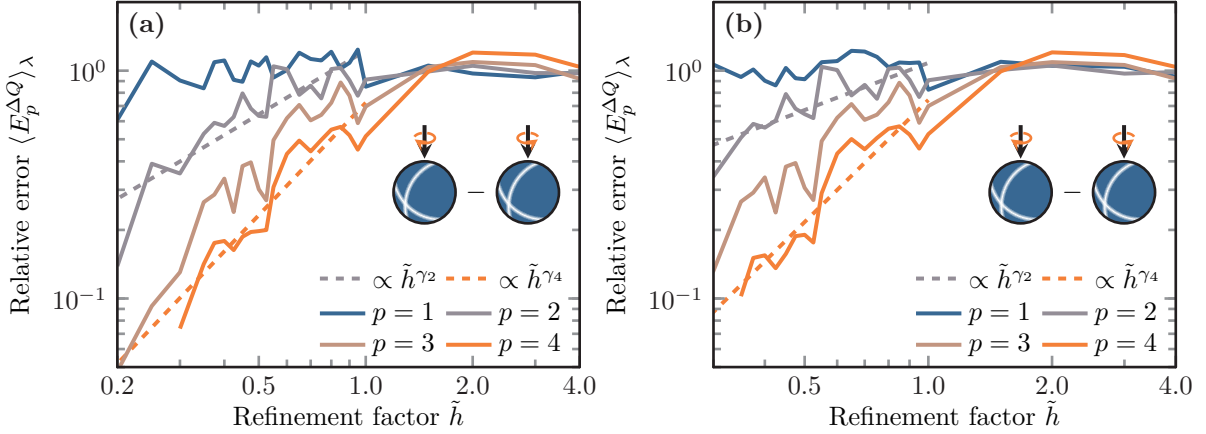
Figure 7.14: Wavelength-averaged relative errors, $\langle E_p^{\Delta Q}\rangle_\lambda(\tilde{h})$ of the left-right scattering efficiency difference comparing **(a)** DGTD computations against Mie computations and **(b)** DGTD computations with the finest mesh of the convergence study, each for different basis polynomial order p. Dashed lines show polynomial fits $\tilde{h}^\gamma$ for the convergence behavior for second- and fourth-order basis sets, with parameters **(a)** $\gamma_1 \approx 0.93$ and $\gamma_4 \approx 1.6$, as well as **(b)** $\gamma_1 \approx 0.68$ and $\gamma_4 \approx 1.78$.

7.2 Shape-optimization for enhanced Faraday rotation

Ensured of the correct operation of the DGTD's anisotropic material implementation, we apply the method to an MO shape-optimization problem. MO nanostructures provide unique opportunities to control the light-matter interaction at the nanoscale. MO materials offer a wide variety of effects, like the MO Kerr effect and Faraday rotation [29]. While MO effects are typically rather weak in the optical domain, the main goal often is to provide a resonant enhancement of the related effects.

Here, we want to concentrate on a specific application to enhance the Faraday rotation of a Huygens' metasurface [192] consisting of MO nanoscale scatterers. This work is based on a setup by A. Christofi *et al.* [44] and was collaboratively worked on with P. Varytis [K8, 193]. The original setup is a metasurface of cylindrical bismuth iron garnet (BIG) scatterers embedded in a silicon dioxide (SiO$_2$) matrix. Upon excitation with linearly polarized light, the polarization direction is rotated due to the Faraday effect in the MO material. The Faraday rotation angle, i.e., the rotation angle of the field polarization of the transmitted light compared to the incident polarization direction, is rather low for a homogeneous layer of MO material. Introducing a periodical array of cylinder scatterers with adjusted height and radius not only leads to a significant increase in the Faraday rotation angle but also allows for near-unity transmittance due to the interference of an electric and magnetic dipole resonance [44].

In this thesis, we do not only reproduce the results [44] of the cylindrical scatterer metasurface with the DGTD method but also outline how to use an algorithm for shape optimization to obtain both a high Faraday rotation as well as maintaining a high transmittance of the metasurface. For that purpose, we introduce a shape modification of the scatterers' surface using spline curves and

perform a random search test, which in future works can be replaced with more sophisticated optimization algorithms, like a Bayesian optimization [194].

7.2.1 Cylindrical scatterer metasurface

First, we consider a periodical square lattice with periods $p_x = p_y = 850\,\text{nm}$ composed of MO cylinders with varying radius R and a height of $H = 260\,\text{nm}$, as shown in Figure 7.15 (a). As MO example material we use BIG, which in the near-infrared (NIR) can be modeled with a relative permeability of $\mu_r = 1$ and a relative permittivity tensor

$$\underline{\underline{\epsilon}} = \begin{pmatrix} \epsilon_r & -\mathrm{i}g & 0 \\ \mathrm{i}g & \epsilon_r & 0 \\ 0 & 0 & \epsilon_r \end{pmatrix} , \tag{7.36}$$

where the gyration vector is set along the z-direction (by setting a static external magnetic field) and $\epsilon_r = 6.25$ as well as $g = 0.06$ [195]. The surrounding SiO$_2$ host medium is modeled as an isotropic non-dispersive medium with $\epsilon_\text{h} = 2.1$ and $\mu_\text{h} = 1$. In order to compute both the transmittance spectrum as well as the Faraday rotation angle, we use the DGTD method. For this purpose, we prepare a computational domain with its lower part depicted in Figure 7.15 (a). It consists of the unit cell containing a single scatterer in the center ($z = 0$) and is surrounded by two $1.5\,\mu\text{m}$ thick layers of SiO$_2$ each. On the bottom, we introduce a Tf/Sf-contour between the two SiO$_2$ layers to excite the metasurface with a Gaussian modulated plane wave

(SI)
$$\boldsymbol{E}_\text{inc}(\boldsymbol{r}, t) = \boldsymbol{e}_x \eta_c \left(t - \frac{\sqrt{\epsilon_\text{h}}}{c_0} \boldsymbol{e}_z \cdot \boldsymbol{r} \right) , \tag{7.37}$$

where $\eta_c(t)$ is the complex version (cf. Eq. (7.26)) of the Gaussian time dependence (B.20) and the plane wave is originally polarized in x-direction. On top of the metasurface, we use a similar contour to the Tf/Sf-contour in order to record both the transmittance spectra Eq. (2.109) and also the frequency-dependent electric fields $\boldsymbol{E}\left(x, y, z = z_\text{trans}, \omega\right)$, from which we can compute the Faraday rotation angle as well as the ellipticity. The parameters of the Gaussian pulse are chosen as $\sigma = 4.8\,\text{fs}$, $t_0 = 46.7\,\text{fs}$ and $\lambda_0 = \frac{2\pi c_0}{\omega_0} = 1.4\,\mu\text{m}$ in order to have a sufficiently broad excitation spectrum, to record the transmittance and Faraday rotation spectra in the wavelength range

(SI)
$$\lambda \in \left[1.2\,\mu\text{m}, 1.45\,\mu\text{m} \right] . \tag{7.38}$$

We use periodic boundary conditions (PBCs) both in x- and y-direction, while the computational domain is terminated with a $500\,\text{nm}$ thick perfectly matched layer (PML) both on the top and bottom, additionally to the Silver Müller boundary conditions (SMBCs) used.

Given the permittivity of the host medium and wavelength range of excitation (7.38), the excitation of the metasurface almost completely lies within the zeroth diffraction order

(SI)
$$\lambda > \lambda^{(1)} = p_{x/y} \sqrt{\epsilon_h} \approx 1.231\,\mu\text{m} , \tag{7.39}$$
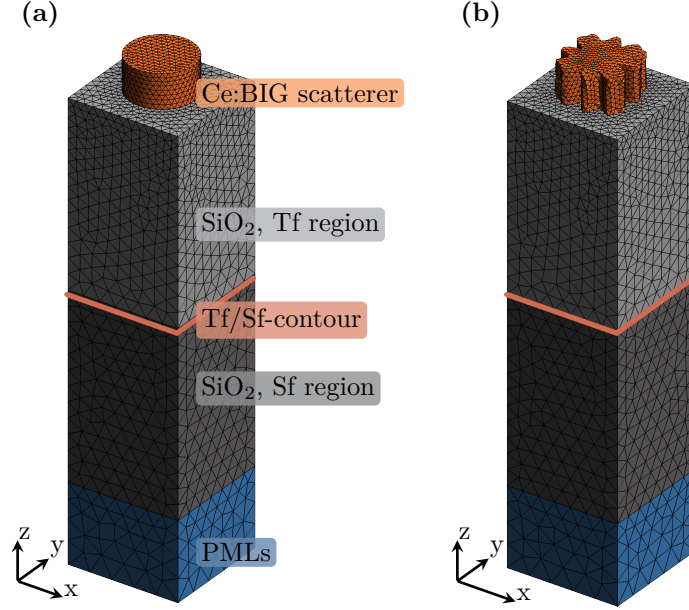
Figure 7.15: Example meshes for the lower part of the computational domain for the MO metasurfaces, containing **(a)** a cylindrical scatterer with radius $R = 250\,\mathrm{nm}$ and **(b)** the best shape-modified scatterer found in a random search. The upper parts of the mirror-symmetric meshes are not shown.

of the grating created. While the transmittance spectrum $T(\omega)$ by construction accounts only for the energy leaving into the far-field, a far-field transformation has to be performed for the transmitted electric fields recorded at a finite distance z_{trans} of the metasurface to obtain the far-field polarization state. Given the computed frequency-dependent field $\boldsymbol{E}_{\mathrm{trans}}(\boldsymbol{r}, \omega)$ on the transmission contour, this far-field transformation simply reduces to a field average over the unit cell (uc)

$$\boldsymbol{E}_{\mathrm{trans}}^{(0)}(\omega) = \frac{1}{A_{\mathrm{uc}}} \int_{\mathrm{uc}} \mathrm{d}x\,\mathrm{d}y\,\boldsymbol{E}_{\mathrm{trans}}\left(x, y, z = z_{\mathrm{trans}}, \omega\right)\,, \tag{7.40}$$

as the only contribution to the far-field radiation stems from the zeroth diffraction order. Given the incident polarization axis $\boldsymbol{c} = \boldsymbol{e}_x$ as well as the incident wave vector $\boldsymbol{e}_k = \boldsymbol{e}_z$, we can compute both the Faraday rotation angle $\theta(\omega)$ and ellipticity angle $\chi(\omega)$ as described in Section 2.7.1, specifically Equations (2.78). To quantify the demand for a high transmittance as well as a large Faraday rotation angle, we define a figure of merit (FoM) as

$$\Theta(\omega) := \begin{cases} |\theta(\omega)| \sqrt{T(\omega)} & \text{for} \quad T(\omega) > 0.3\,, \\ 0 & \text{else}\,. \end{cases} \tag{7.41}$$

Thereby, we introduced a cut-off filter condition for low transmittances.
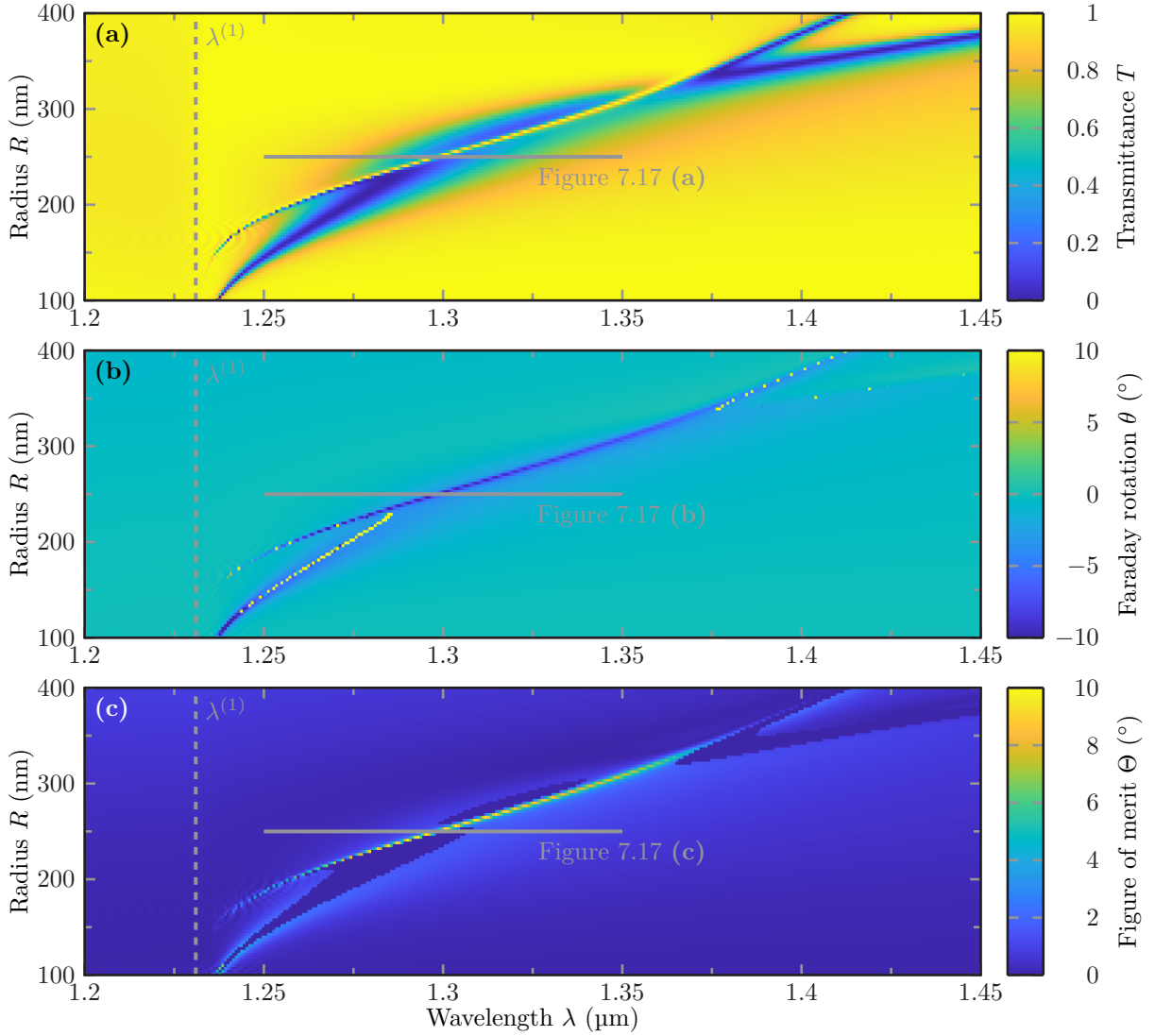
Figure 7.16: Transmittance **(a)**, Faraday rotation **(b)** and FoM **(c)** spectra for an MO metasurface consisting of periodically arranged cylindrical scatterers with varying radius R.

While Christofi *et al.* [44] were able to demonstrate a maximal FoM

$$\Theta^+ := \max_{\lambda > \lambda^{(1)}} \Theta(\lambda) \tag{7.42}$$

as high as $\Theta^+ \approx 7.5°$ for a relatively large radius of $R = 310 \, \text{nm}$, we can achieve an even higher FoM decreasing the radius R of the cylinder scatterers further. However, it already is a huge improvement to increase the Faraday rotation angle to $\theta^+ = -7.5°$ compared to a homogeneous layer of the same material only providing angles of $\theta = -0.75°$ [44]. In Figure 7.16, we show the transmittance (a), the Faraday angle (b) as well as the resulting FoM (c) for cylinder radii varying between $R \in [100 \, \text{nm}, 400 \, \text{nm}]$. For large radii $R > 350 \, \text{nm}$, we observe two distinct
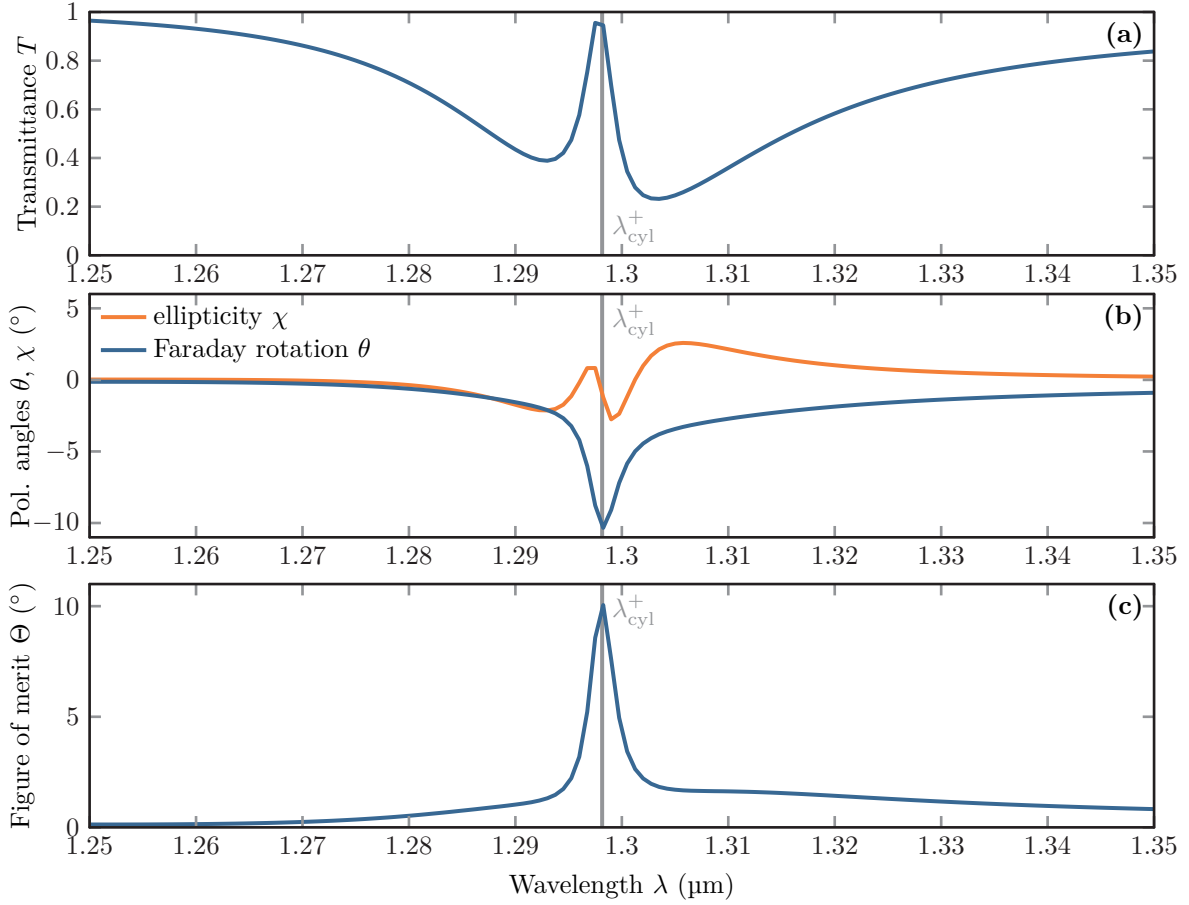
Figure 7.17: Transmittance **(a)**, Faraday rotation and ellipticity **(b)** as well as FoM **(c)** spectrum for an MO metasurface consisting of cylindrical scatterers with a radius $R = 250\,\mathrm{nm}$. The FoM peaks at the wavelength $\lambda_{\mathrm{cyl}}^{+} = 1.2982\,\mu\mathrm{m}$.

resonances in the transmittance spectra, as also already shown in [44]. With decreasing radius R these resonances both shift to lower wavelength and interfere. Due to the interference the resulting setup forms a Huygens' metasurface and provides a spectrally narrow resonance with peak transmittance one. This interference again vanishes for further decreased radii $R < 200\,\mathrm{nm}$ as the resonances shift towards the edge of the first diffraction order $\lambda^{(1)}$ (see Eq. (7.39)). At the same time the Faraday rotation (see Fig. 7.16 (b)), follows the resonance of the transmittance spectrum and reaches a deep minimum at $R \approx 250\,\mathrm{nm}$. We also notice, that the Faraday rotation angle reaches very high values (yellow clipped pixels in panel (b)), when the corresponding transmittance reaches zero value (cf. panel (a)). This is caused by the method used here: In comparison to a frequency-domain method, the DGTD method is more susceptible to numerical errors in the transmitted fields. Hence, also the Faraday rotation angle can take arbitrarily high values as it is essentially computed from random noise. This is the reason to introduce the transmittance cut-off filter in Eq. (7.41), which was also used in Fig. 7.16 (c). Consequently, the highest FoM is reached for a radius of $R = 250\,\mathrm{nm}$.

The corresponding spectra for this specific radius are shown in Fig. 7.17 (a-c). For the $R = 250\,\text{nm}$ radius, we reach both a peak transmittance of $T(\lambda_{\text{cyl}}^+) \approx 1$ and a Faraday rotation angle as low as $\theta(\lambda_{\text{cyl}}^+) = -\Theta(\lambda_{\text{cyl}}^+) \approx -10.1°$. The corresponding mesh used for the computation is shown in Fig. 7.15 (a) and the spectra are shown in Fig. 7.17 (a-c). However, we here omitted the transmittance filter, as the transmittance is well above zero for the computed wavelength range. Additionally, we also show the corresponding ellipticity spectrum $\chi(\lambda)$. As transmittance is one at the resonance, the ellipticity is equal to zero, as expected. Thus, the polarization is completely rotated but remains linear. Therefore, we show that a decreased radius R of the cylinders can already lead to a further enhancement of the Faraday rotation, up to a maximum FoM of $\Theta^+ = 10.1°$ compared to the results reproduced by us and originally presented in [44]. However, we can achieve an even higher FoM using a shape-optimization of the scatterers, which is outlined in the following section.

7.2.2 Shape-modified scatterer metasurface

The idea of varying the scatterer radius is now extended to varying the entire cross section, by adjusting radial points of the scatterer which then are connected by spline interpolation. We, therefore, introduce a set of $4N$ control points

$$\boldsymbol{r}_i = \begin{pmatrix} r_i \cos(i\Delta\phi) \\ r_i \sin(i\Delta\phi) \end{pmatrix}, \quad \text{with} \quad i \in [1, 4N], \tag{7.43}$$

which are equiangularly distributed by $\Delta\phi = \frac{2\pi}{4N}$ in the unit cell. The radial positions r_i are chosen such, that they lie between a minimal radius $r_{\min} = 75\,\text{nm}$ and a minimal distance to the unit cell boundary of $d = 60\,\text{nm}$, which is shown in Fig. 7.18 (a). To avoid self-intersecting splines of the scatterer boundary curve, we additionally introduce a Gaussian smoothing for the control point positions

$$\bar{\boldsymbol{r}}_i = \frac{\sum_{j=1}^{4N} w_{ij} \boldsymbol{r}_j}{\sum_{j=1}^{4N} w_{ij}}. \tag{7.44}$$

The Gaussian weights are

$$w_{ij} = \exp\left(-|\phi_i - \phi_j|^2 \langle|\boldsymbol{r}|\rangle^2 / L^2\right), \tag{7.45}$$

where $L = 5 r_{\min} \Delta\phi$ is the correlation length of neighboring points and $\phi_i = i\Delta\phi$. This correlation length on the one hand prevents self-intersections of the shape defining spline interpolation by introducing a correlation for (at least) five consecutive neighboring points. On the other hand, it also guarantees that there are no sharp edges on the scatterer contour, such that it also accounts for natural smoothing in a potential experimental structure. To preserve the independence with respect to excitations with x- or y-polarization we enforce a four-fold symmetry, thus only varying N of the $4N$ points. A corresponding smoothed scatterer cross section is shown in Fig. 7.18 (b), where we use $4N = 60$ control points. For the final three-dimensional scatterers, we keep the height at $H = 260\,\text{nm}$.
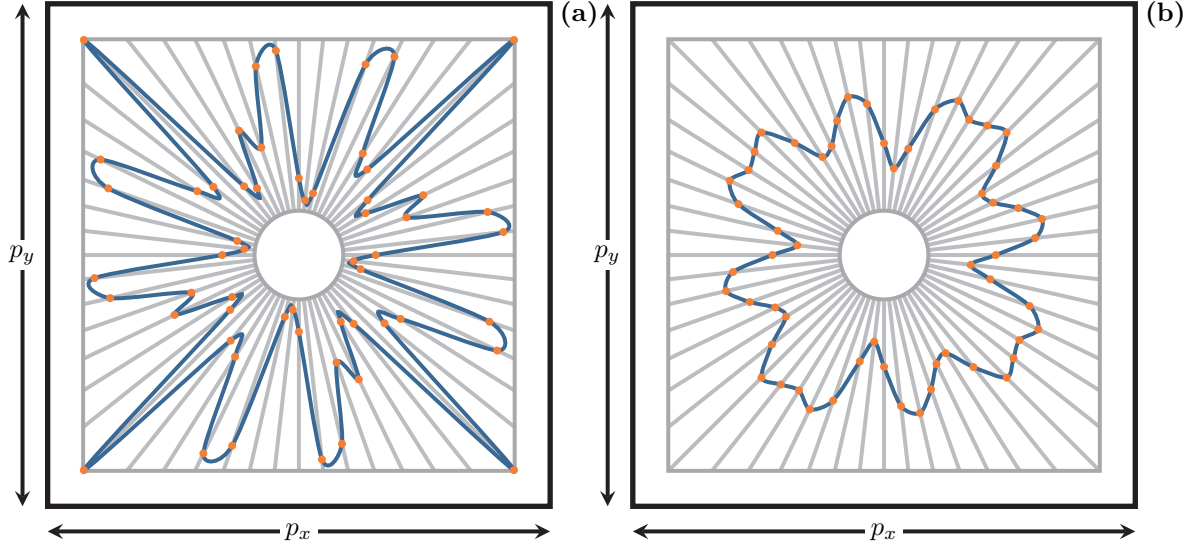
Figure 7.18: Two-dimensional scatterer cross sections created with a spline interpolation without **(a)** and with **(b)** Gaussian smoothing (7.44) for a given set of control points set within the random search algorithm.

To find an even further enhanced FoM than that for the cylindrical scatterers, we perform a simple random search of the radii spanning the search space of shape configurations, i.e., we provide randomly generated [196, 197] sets of the control points $\bar{r}_i$. For each of the 300 configurations, we use the resulting mesh, e.g., the mesh in Fig. 7.15 (b), to compute the transmittance and Faraday rotation spectra, as outlined in the previous section. Here, the number of control points per quadrant is set to $N = 15$ in order to provide a sufficient angular resolution for the possible structures spanning the search space. Within the DGTD computations, we keep the same parameters as in the case of cylindrical scatterers.

In Fig. 7.19, we show the spectra for the scatterer with the highest FoM found in the random search. For comparison also the spectra of the $R = 250\,\mathrm{nm}$ cylindrical scatterer are shown. While the resonance shifts from $\lambda_{\mathrm{cyl}}^+ = 1.2982\,\mu\mathrm{m}$ for the cylinder scatterer to $\lambda_{\mathrm{sm}}^+ = 1.295\,\mu\mathrm{m}$ for the shape-modified scatterer, the transmittance only slightly decreases to $T(\lambda_{\mathrm{sm}}^+) = 0.98$. At the same time the chirality of the structure, which is rotated against the unit cell frame (cf. Fig. 7.15 (b)), supports an even stronger Faraday rotation and the angle decreases to $\theta(\lambda_{\mathrm{sm}}^+) = -12.1°$, such that the FoM is even further increased to $\Theta(\lambda_{\mathrm{sm}}^+) \approx 12.0°$. At the same wavelength the ellipticity also consistently is close to $\chi(\lambda_{\mathrm{sm}}^+) \approx 0$. We thus have shown, that it is possible to already find a further enhanced FoM by only performing a random search. However, a random search is merely the first step for a more elaborate and efficient optimization scheme. As the computations per sample structure require several days of computation time (on an Intel Xeon E5-2670 using 8 cores), a Bayesian optimization algorithm [194] is a more suitable choice for a real optimization algorithm. In [K8], we show that with the same structural setup but the usage of Catmull-Rom splines instead of the Gaussian filter FoMs as high as $\Theta = 15°$ can be achieved.
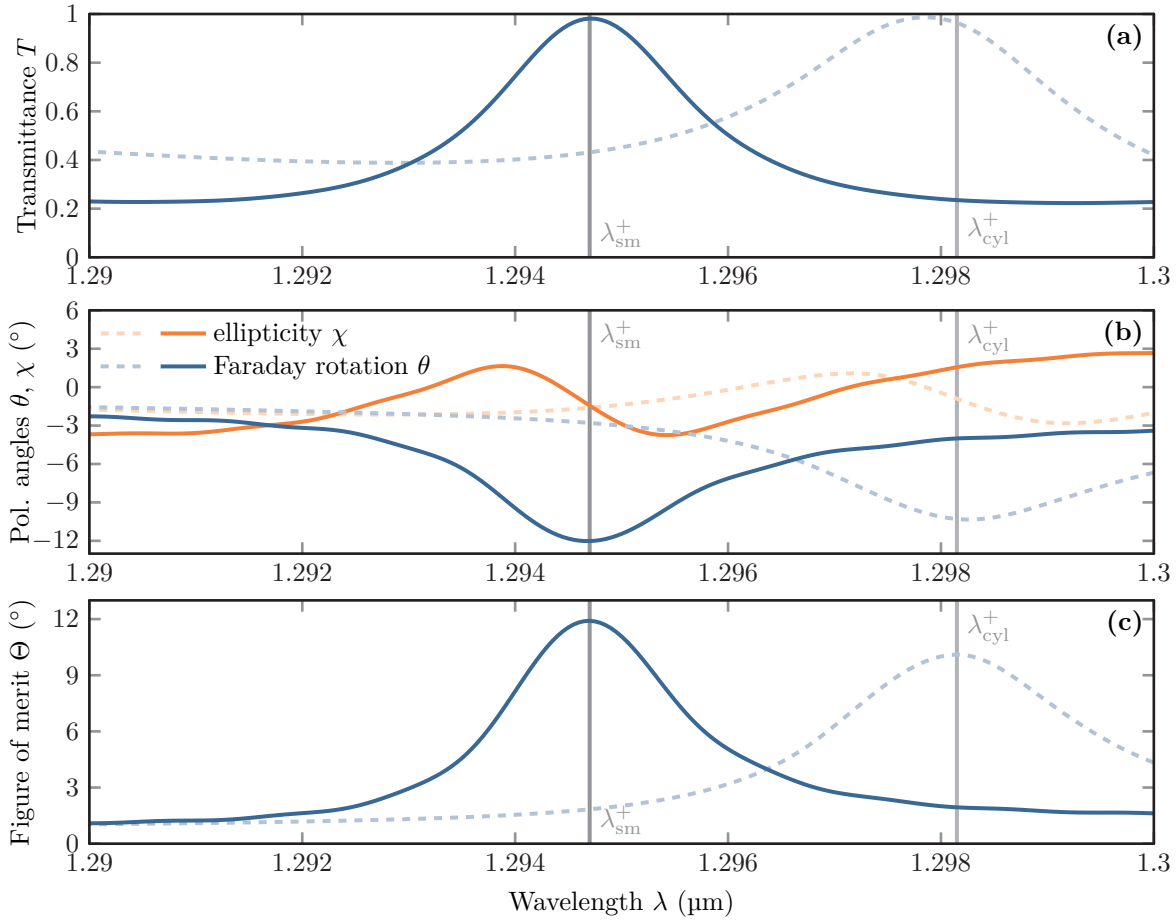
Figure 7.19: Transmittance **(a)**, Faraday rotation and ellipticity **(b)** as well as FoM **(c)** spectrum for the best shape-modified scatterer structure found in the random search (solid lines) as well as the spectra for the optimally scaled cylindrical disks for comparison (dashed lines). The FoM for the metasurface with shape-modified scatterers peaks at the wavelength $\lambda_{sm}^+ = 1.295\,\mu m$.

7.2.3 Convergence of spectra

Although the results presented in the previous Section 7.2.2 show a significant improvement compared to the non-optimized structures, we need to address the bounds of the numerical uncertainties of the underlying computations. In Section 7.1.4 about the scattering cross sections of the MO spheres, we observed uncertainties as small as five percent. Therefore, we perform both a mesh refinement as well as simulation time convergence study in order to assess the uncertainties tied to the computations presented.

In Figure 7.20 we show the convergence behavior of the transmittance (a), the Faraday angle (b) as well as the FoM (c) for all recorded wavelengths. Here, we vary the maximally allowed element side length h [140]. Therefore, we again introduce a dimensionless scaling factor $\tilde{h} = \frac{h}{h_0}$, where the element characteristic side length of the scatterers is set to $h_0 = 80\,\text{nm}$. The mesh is
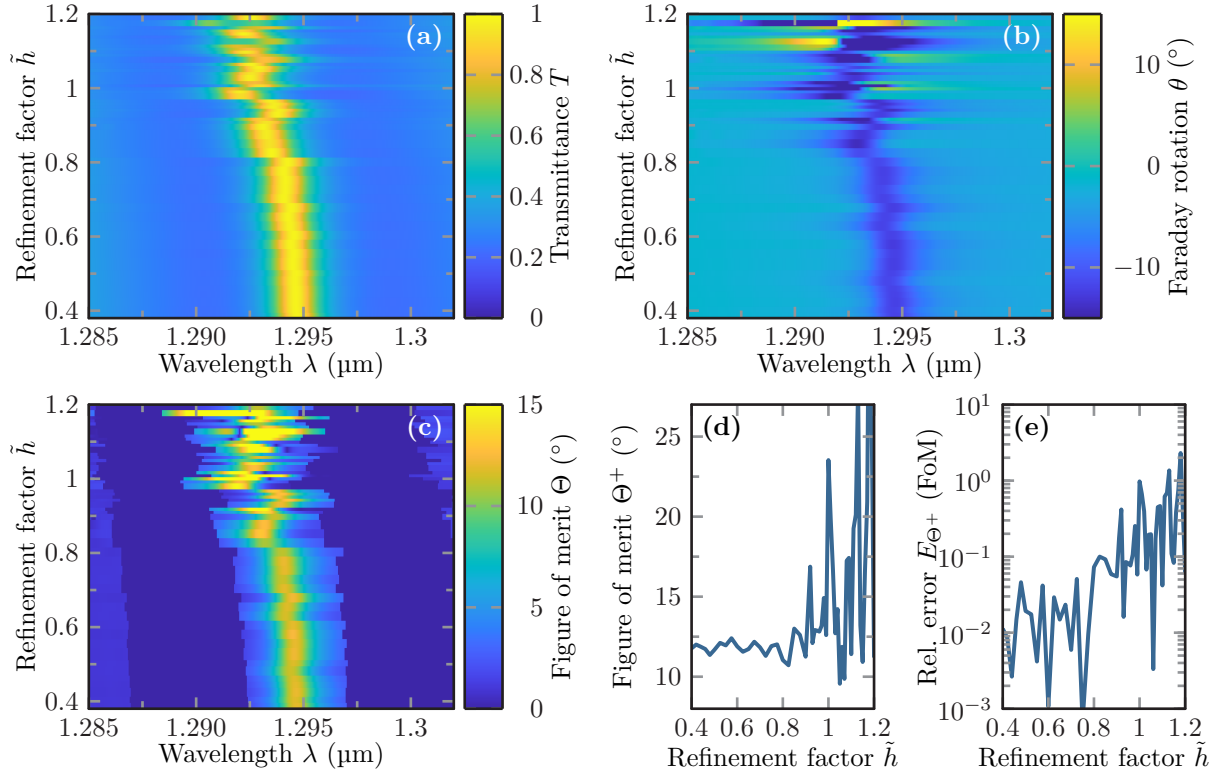
Figure 7.20: Convergence with respect to the mesh refinement $\tilde{h}$ of the transmittance **(a)**, Faraday rotation **(b)** as well as FoM **(c)** spectra for the best metasurface found in the random search. Panel **(d)** shows the peak FoM Θ^+ in dependence of the mesh refinement factor. **(e)** Corresponding relative error E_Θ^+ comparing the FoM with respect to the finest mesh used in the convergence scan.

uniformly refined with decreasing $\tilde{h}$. Figure 7.15 (b) shows the best example mesh found in the random search with a refinement factor of $\tilde{h} = 0.5$. For both the transmittance as well as the Faraday rotation angle and thus also the FoM we observe that for coarse meshes the spectra show erratic jumps in the spectral position of the resonance. This can be attributed to the strongly varying surface geometries of the meshes created. Moreover, we also observe a systematic shift of the resonances to larger wavelengths, as the actual meshed volume of the scatterer converges to its boundary from the inside. Thus the effective (meshed) volume increases systematically with the decreasing $\tilde{h}$, which leads to the systematic shift because of the scale invariance of Maxwell's equations. The finer the mesh, the smaller are the deviations in the spectral positions. Despite the small changes in the spectral position, the maximal value of the FoM-spectrum, i.e., the actual FoM Θ^+ , systematically converges to a fixed value (see Figure 7.20 (d)). In Figure 7.20 (e) we show the relative error

$$E_{\Theta^+}(\tilde{h}) = \left| 1 - \frac{\Theta^+(\tilde{h})}{\Theta^+(\tilde{h}^*)} \right| , \tag{7.46}$$

where $\tilde{h}^* = 0.38$ defines the finest mesh of the convergence scan. For this relative error, we observe a polynomial convergence behavior, comparing the single DGTD computations to that with the finest mesh provided in the scan. This is expected for these third-order Lagrange polynomial basis computations, as already seen in Section 7.1.4. We again observe a numerical error on the order of five percent.
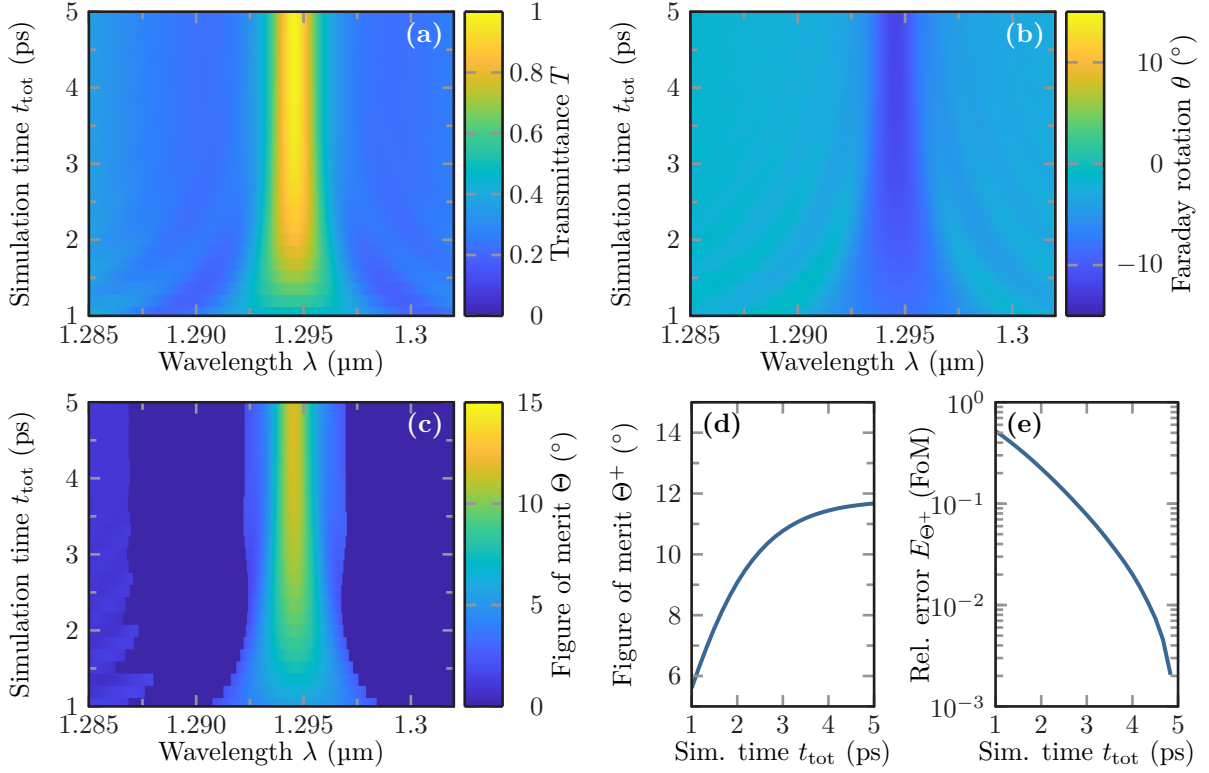
Figure 7.21: Convergence with respect to the total simulation time t_{tot} of the transmittance **(a)**, Faraday rotation **(b)** as well as FoM **(c)** spectra for the best metasurface found in the random search. Panel **(d)** shows the peak FoM Θ^+ in dependence of the mesh refinement factor. **(e)** Corresponding relative error E_{Θ^+} comparing the FoM with respect to the finest mesh used in the convergence scan.

Another important factor for the convergence of the numerical computations is the simulation time. Narrow resonances indicate modes with a high quality factor and thus a long lifetime of the fields, once they are excited. As the underlying spectra are computed within a time-domain method, we use an on-the-fly Fourier transform (see Eq. (5.126)) in order to recover the frequency-dependent fields and Poynting vectors. As the computations are initialized with zero fields, the fields also need to be sufficiently small at the end of the computation in order to prevent spectral leakage [169] and aliasing [129]: If the fields have a relatively high amplitude at the end of the simulation at time t_{tot} the resulting frequency-dependent fields get convoluted

with the Fourier transform of a box function, i.e.,

$$\boldsymbol{E}(\omega) \rightarrow t_{\text{tot}} e^{i\omega t_{\text{tot}}/2} \text{sinc}\left(\frac{\omega t_{\text{tot}}}{2}\right) * \boldsymbol{E}(\omega)\,. \tag{7.47}$$

In Fig. 7.21, we show the convergence behavior of the transmittance (a), Faraday rotation (b) as well as the FoM (c) for different total simulation times t_{tot}. In all three panels, we can clearly see, the influence of the sinc-function on the spectra for small times $t_{\text{tot}} < 3\,\text{ps}$: left and right of the main resonance we observe oscillations, which are closing in to the resonance peak and fade away with increasing t_{tot}. The corresponding simulations have been performed with a mesh refinement of $\tilde{h} = 0.5$. Both in Figure 7.21 (c) and (d), we can clearly see how the FoM Θ increases as also the total simulation time t_{tot} grows. As the fields of the resonance radiate from the metasurface with a temporal exponential decay, also the recorded fields contributing to the on-the-fly Fourier transform first add up quickly and then less and less with increasing time t_{tot}. Figure 7.21 (e) shows that the numerical error of the simulation can be well suppressed below the level of the mesh-refinement error, as we reach errors as low as 0.2% within the simulation time convergence scan. Overall the relative numerical errors are much smaller than the computed Faraday rotation enhancement ratio between the cylindrical and shape-modified scatterers.

7.3 Designing mid-IR HMM cavities

Optical microcavities are an integral component in applied and fundamental physics. They enable a strong light confinement accompanied with large field enhancement and control of light [46, 47], as well as a high density of states and thus also a strong interaction with emitters, leading to an enhanced Purcell effect [52, 53, T3]. Further applications include subwavelength imaging [49–51], increased optical nonlinearities [198, 199] and reach as far as increased fluctuation induced phenomena, like quantum friction [55].

Here, we present an HMM microcavity and how to determine the resonances and field distributions of the cavity. This cavity is a quasi-one-dimensional setup of a ZnO and heavily doped ZnO:Ga material stack acting as an HMM microcavity. The work presented was partly published in [K3] and builds the foundation for a detailed study of the HMM defining parameters, like the number of unit cells, as well as the fill factor f (see Section 3.4.1), shown in [K9]. The striking point of the HMM clearly is its dispersion, which allows for (in principal) indefinitely large $\boldsymbol{k}$-vectors at finite frequencies. Finite $\boldsymbol{k}$-vectors are one of the limiting factors of conventional material cavity sizes at given frequencies, as with decreasing size no resonances can be supported any longer. While typical setups using noble metals like gold and silver work with an HMM type II material both up to the visible regime [200, 201], the use of the highly doped ZnO:Ga enables to also utilize and investigate cavity resonances with an HMM type I material due to the low plasma frequency. In contrast to an HMM type II material which only couples evanescently to free-space, the cavity modes originating in the HMM type I frequency region can be directly excited from the far-field. It is shown how the HMM type I upper-frequency threshold introduces an accumulation point of cavity resonance frequencies for cavities relatively small compared to the operating wavelength.
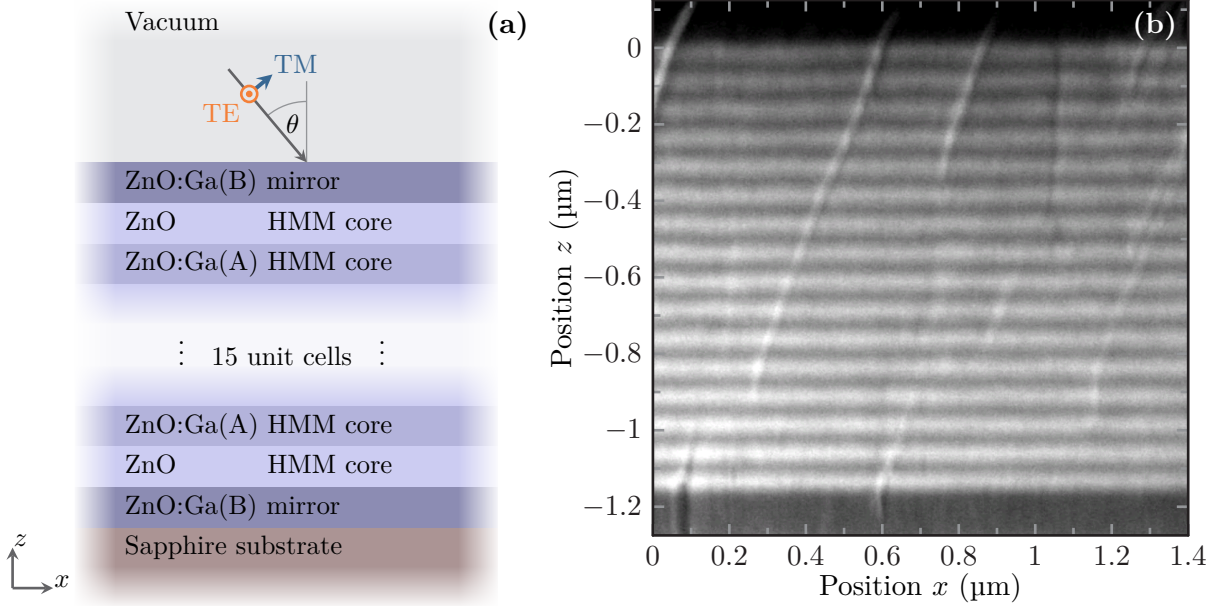
Figure 7.22: (a) Sketch of the HMM cavity design consisting of 31 interlaced layers of ZnO and doped ZnO:Ga. **(b)** Scanning electron microscope (SEM) image of the cavity cross section provided by E. Travkin [K3]. Darker areas indicate a higher free-electron concentration.

The geometrical setup of the quasi-one-dimensional ZnO / ZnO:Ga cavities is shown in Figure 7.22 (a). In the experimental realization, the microcavity samples are grown by molecular beam epitaxy [K3] on a sapphire substrate. The actual HMM core, consisting of 31 alternating layers of ZnO and doped ZnO:Ga(A) is embedded in two highly doped ZnO:Ga(B) layers acting as cavity mirrors. Here the ZnO act as dielectric layers, while the doped ZnO:Ga layers are the metallic counter-part for the HMM material. Figure 7.22 (b) shows an SEM image of a cavity cross section. The reflectance spectra of the micro-cavities are measured to experimentally determine the resonances structure for both transverse electric (TE) and transverse magnetic (TM) polarization. Additionally, a variation of the incident angle θ provides insight into the mode dispersion. Figure 7.23 shows the reflectance spectra for both polarizations and different incident angles. In Section 3.4 it was pointed out, that the HMM type I material dispersion is hyperbolic for only one polarization, here the TM polarization. Therefore we only observe ordinary Fabry-Pérot resonances in TE polarization. In TM polarization, however, we observe a broad shoulder as well as additional resonance peaks at around 0.5 eV. These stem from the hyperbolic dispersion of the system.

In order to numerically assess the resonance structure of the system, the involved materials, namely the ZnO, doped ZnO:Ga as well as the sapphire substrate need to be modeled with relative permittivities. It was demonstrated in [56] that it is sufficient to model the ZnO as
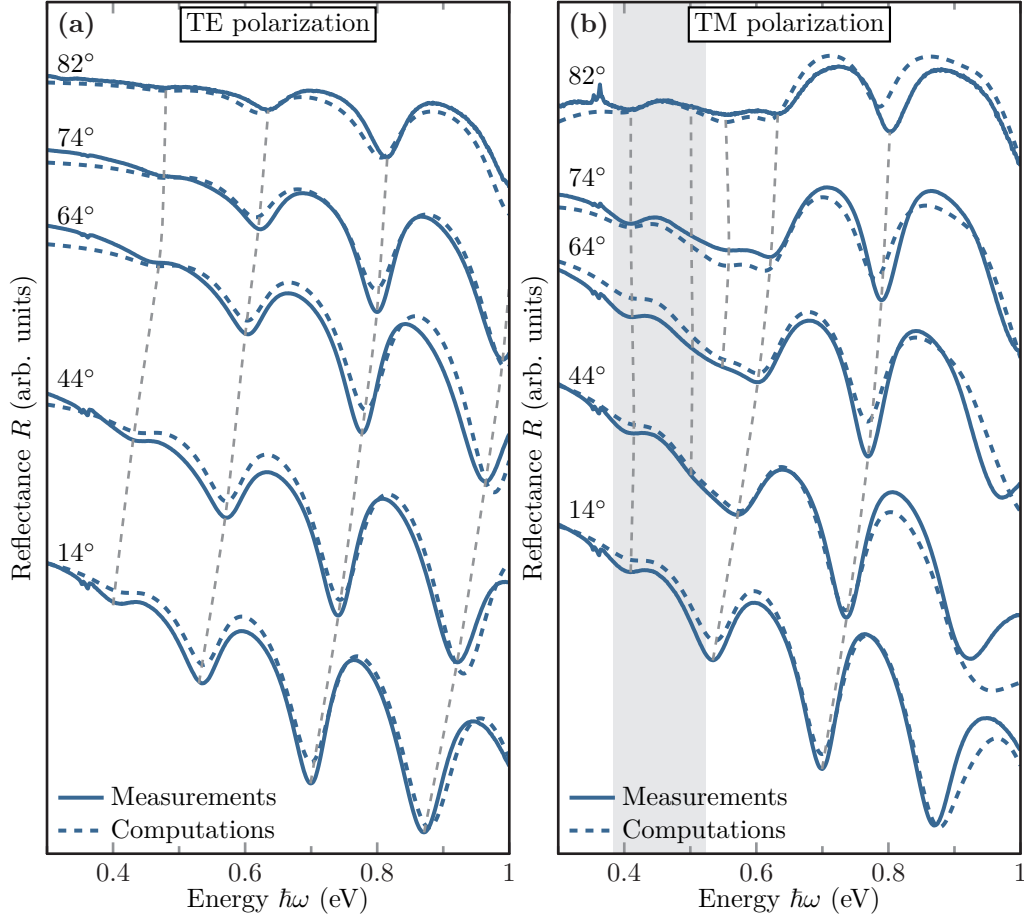
Figure 7.23: Experimental and computational reflectance spectra for a 31 layer HMM ZnO / ZnO:Ga microcavity both for TE **(a)** and TM **(b)** polarization. The incident angle θ of the excitation wave is varied in both measurements and scattering matrix (S-matrix) computations. Dashed lines mark the peaks indicating the underlying resonances. The shaded area in panel **(b)** marks the HMM type I frequency region. Experimental spectra are graciously provided by E. Travkin [K3].

effectively non-dispersive dielectric and the doped ZnO:Ga as a Drude metal, i.e.,

$$\epsilon_{\text{ZnO:Ga(A,B)}}(\omega) = \epsilon_{\text{ZnO}} - \frac{\omega_{\text{pl,A,B}}^2}{\omega\left(\omega + \mathrm{i}\gamma_{\text{A,B}}\right)} \, . \tag{7.48}$$

Thereby, the doping level, which is controlled in the growth process, determines the plasma frequency in the model. Thus, we can compute the reflectance spectra of the cavity for both polarizations using the S-matrix algorithm from Chapter 4 and fit the material parameters for both the ZnO and ZnO:Ga(A,B) with the two different doping levels. For the ZnO as well as the background permittivity for the doped ZnO:Ga layers, one finds $\epsilon_{\text{ZnO}} = 3.7$. The material parameters for both the internal doped layers, as well as the highly doped mirroring layers are

determined as

$$\hbar\omega_{\text{pl,A}} = 1.01\,\text{eV} \quad \text{and} \quad \hbar\gamma_{\text{A}} = 0.11\,\text{eV}\,, \tag{7.49a}$$

$$\hbar\omega_{\text{pl,B}} = 1.76\,\text{eV} \quad \text{and} \quad \hbar\gamma_{\text{B}} = 0.11\,\text{eV}\,. \tag{7.49b}$$

Furthermore, the sapphire permittivity is approximated as $\epsilon_{\alpha\text{-Al}_2\text{O}_3} \approx 2.89$ [202] in the frequency region of interest. Additionally, the thicknesses of the different layers are determined by the sample growth process and are

$$d_{\text{ZnO}} = 44\,\text{nm}\,, \quad d_{\text{ZnO:Ga(A)}} = 42\,\text{nm}\,, \tag{7.50}$$

for the internal and

$$d_{\text{ZnO:Ga(B)}} = 145\,\text{nm}\,, \tag{7.51}$$

for the mirror layers. Given the material parameters and layer thicknesses, this also sets the fill factor of the HMM-core as

$$f = \frac{d_{\text{ZnO}}}{d_{\text{ZnO}} + d_{\text{ZnO:Ga(A)}}} \approx 0.51\,, \tag{7.52}$$

and therefore also the HMM type I frequency boundaries Eq. (3.44) shown by the shaded area in Figure 7.23 (b), which lies between $\hbar\omega \in \big[0.38\,\text{eV}, 0.52\,\text{eV}\big]$.

Based on these parameters, the resonances of the microcavities can be determined numerically in two different ways. The easier but less accurate method is to recompute the reflectance spectra of the cavity with a reduced material damping γ. This assumes, that the resonance frequency is barely shifting with a reduced damping constant. In Figure 7.24 (a) we show the reflectance spectrum for an incident angle of $\theta = 74°$ computed using the S-matrix method. Reducing the damping of the HMM doped ZnO:Ga(A) core material to a percent of the original value, the peaks just below the upper HMM type I frequency become more and more distinct, i.e., spectrally narrower and thus better to distinguish.

The second option to determine the resonances is to compute the poles of the S-matrix. To this end, we numerically compute the inverse of the maximal singular value $\bar{\sigma}^{-1}(\omega)$ of the microcavities S-matrix as explained in Section 4.4. In Figure 7.24 (b) we show the corresponding logarithmic map of this inverse singular value for complex frequencies ω. The inverse maximal singular value $\bar{\sigma}^{-1}(\omega)$ is zero if the S-matrix has a pole and thus reaches a resonance. We can compute the resonance frequencies of the S-matrix with numerical minimization [171] of $\log_{10}\bar{\sigma}^{-1}(\omega)$. This is numerically favorable over a direct root search, as the singular values are always positive and can also include branch cuts in the frequency.

The resonance frequencies for the S-matrix with an effective medium approximation (EMA) HMM-core are marked with circles in Figure 7.24 (b). Both the reflectance spectra in the low-loss regime as well as the thorough computation of the S-matrix poles reveal the same resonance structure. Above the HMM type I frequencies ($\hbar\omega > 0.523\,\text{eV}$) we again observe ordinary Fabry-Pérot resonances of the finite size cavity. Below the threshold, however, we find an accumulation point of resonances, which get weaker and weaker in amplitude when approaching the HMM
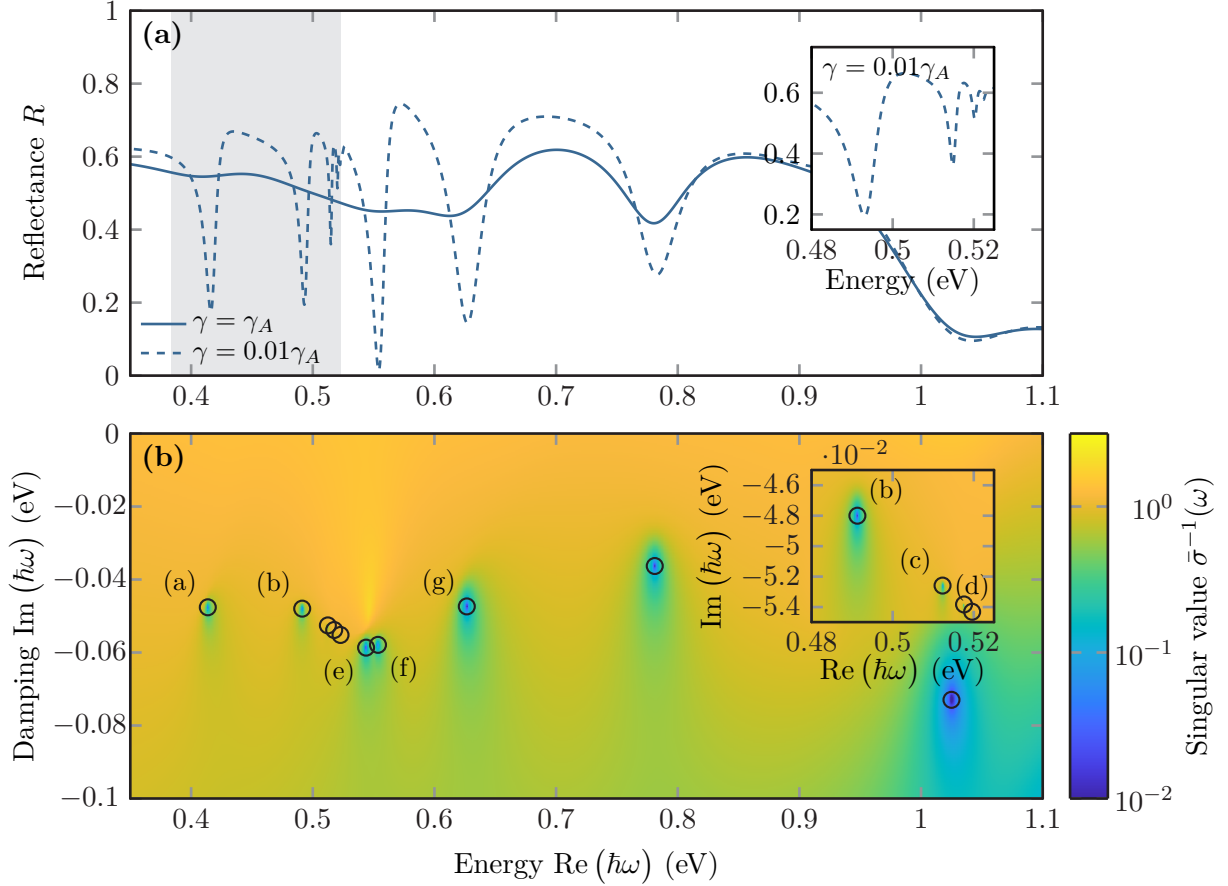
Figure 7.24: (a) Computed scattering spectra of the HMM-cavity for an incident angle of $\theta = 74°$ for both the fitted ZnO:Ga material damping $\gamma = \gamma_A$ as well as in the low-loss regime $\gamma = 0.01\gamma_A$. **(b)** Compute inverse maximal singular values of the S-matrix for the full material damping $\gamma = \gamma_A$ and same incident angle. Insets show the upper spectral boundary of the HMM type I region including the resonance accumulation point. Circles mark the resonance frequencies. The corresponding resonance field distributions are shown in Fig. 7.25 according to the labels.

type I upper frequency. While in the low-loss reflectance spectra the minima in the spectrum get weaker approaching $\hbar\omega \approx 0.523\,\text{eV}$, also the poles of the S-matrix get less and less pronounced. This poses a challenge for the numerical minimization algorithm, as the starting value for the minimization needs to be sufficiently close to the actual pole. It is remarkable, however, that the S-matrix containing the fully damped ZnO:Ga(A) material model shows all the poles, which are responsible for the long "shoulder" in the reflectance spectra. As both the reflectance spectra and computed S-matrix poles agree very well for the EMA HMM as well as the full 31 layer system, we here only show the EMA results.

Additionally to the resonances, we can also compute the associated field distributions of the QNMs (see Section 4.4). However, we here compare both the EMA and full layer setup, as
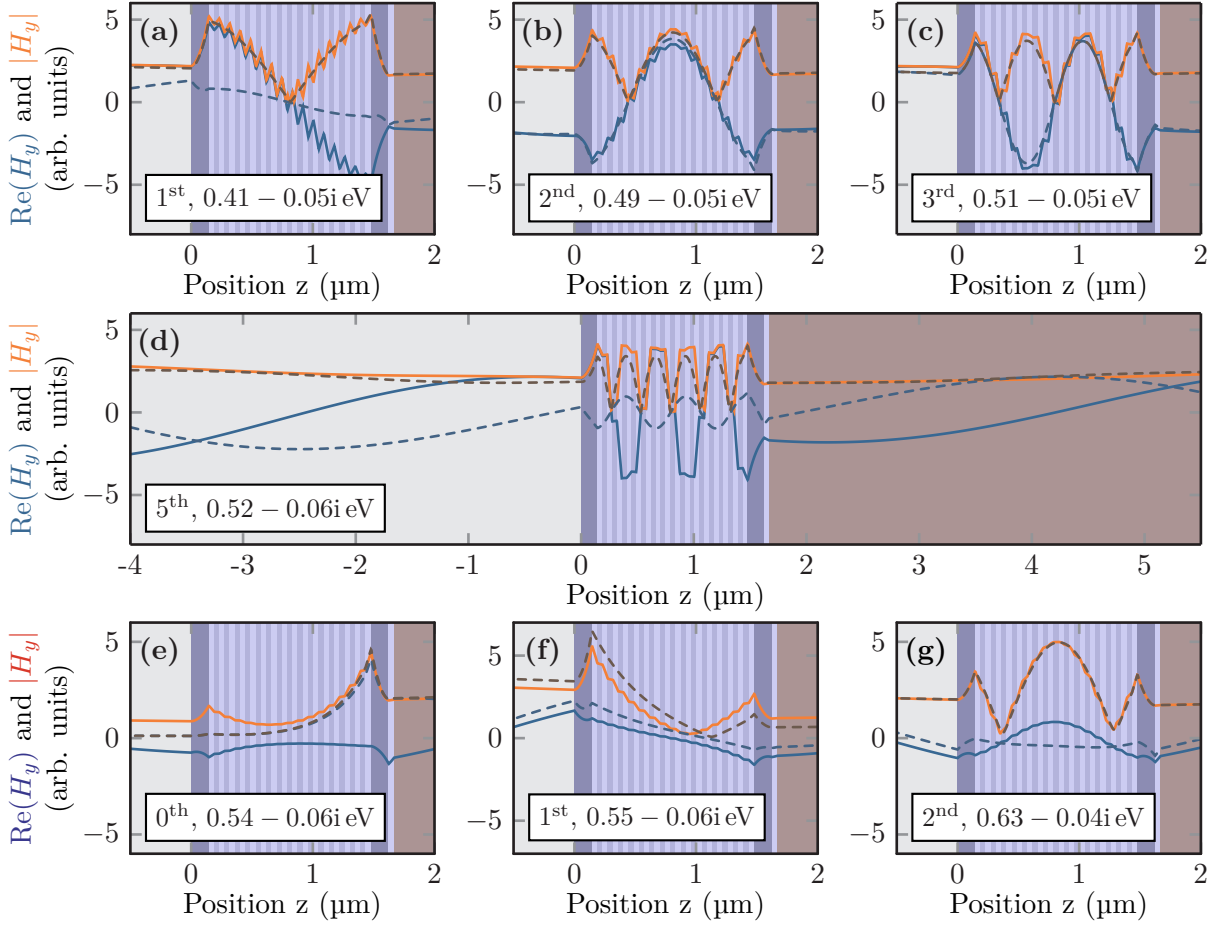
Figure 7.25: Field distributions of the quasinormal modes (QNMs) at the resonance frequencies shown in Fig. 7.24 both for the full layer system (solid) as well as EMA HMM model (dashed lines) compute for an incident angle of $\theta = 74°$.

it indicates the boundaries of the EMA for the HMM model. The field distributions for the resonances in Fig. 7.24 (b) are shown in Fig. 7.25. For the resonances in the HMM type I frequency region, we observe that the mode order, determined by the number of in-cavity field nodes, increases with increasing frequency (see Fig. 7.25 (a) to (d)). This can be explained by the hyperbolic dispersion of the material providing the relatively high k_z-values at finite frequency. We also notice that the HMM is realized by the internal coupling of surface plasmon polaritons (SPPs): the field distributions computed within the EMA material model are smooth and the field distributions for the fully layered material including the isotropic dielectric and Drude metal show strong cusps at the material interfaces. We also notice, that with increasing mode order the number of material layers becomes more and more important, as the field oscillation needs to be realized by the coupling of the single interface SPPs. This effect is already very prominent for the fifth-order mode shown in Fig. 7.25 (d). This also indicates that in comparison to the EMA S-matrix the fully layered system can only provide a finite set of resonances below the accumulation frequency and therefore the EMA as well as the hyperbolic dispersion breaks down. The EMA

assumption of the internal wavelength being shorter than the material layers does not hold any longer.

Additionally, to the high order modes of the HMM core, with its high density of states, there are also two resonances originating from the coupling of the external mirror SPP coupling. These are the zeroth- and first-order modes (Fig. 7.25 (e) and (f) respectively) coupling in a symmetric and antisymmetric manner. Here, the zeroth-order mode is frequency-stable regarding changes of the cavity size, potentially enabling applications with subwavelength cavities. The modes at even higher frequencies are ordinary Fabry-Pérot resonances, as the ZnO:Ga(A) material in the HMM core acts as a dielectric. Accordingly also the field distributions (see Fig. 7.25 (g)) show a normal smooth behavior for both the EMA and fully layered systems. As the computed resonances have a complex frequency the fields also show the QNM typical divergence outside the cavity [122] well seen in Fig. 7.25 (d).
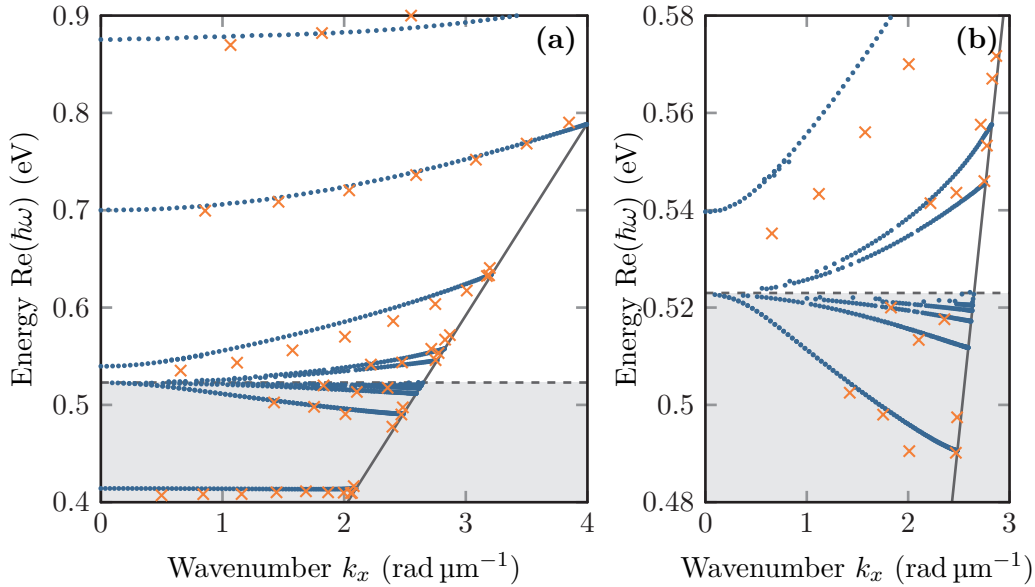
Figure 7.26: Dispersion relation of the resonance frequencies computed for different transversal wave vector components k_x, i.e., different incident angles θ. Blue dots mark the numerically found poles for the EMA S-matrix. Orange crosses show the minima positions of the experimental spectra from Fig. 7.23. Panel **(b)** shows a close-up from **(a)** on the accumulation point of resonance frequencies. The gray shaded area shows the HMM type I region. The light line is marked in solid gray.

A variation of the incident angle θ in the computations of the S-matrix poles yields the dispersion relation of the single resonances with respect to the lateral wave-vector component k_x. The dispersion relation is shown in Fig. 7.26 comparing the computed resonance frequencies with those obtained from the experimental spectra. For $k_x = 0$ the resonances in TE and TM polarization are naturally degenerate and show a normal ascending mode order. This, however, changes with increasing k_x and therefore an increasing incident angle θ. Here, the mode continuum below the HMM type I upper frequency shows a negative dispersion indicating negative group velocities. Further, both the zeroth- and first-order modes emerge showing a positive curvature in the

dispersion. We observe that the resonances found in the measured spectra agree well with the computed spectra over the entire range of incident angles. However, the relatively high damping in the doped ZnO:Ga materials leads to less pronounced signals in reflectance spectra for the additional modes emerging from the HMM. This is the limiting factor for this setup, which in principle could be overcome using another material, e.g., indium tin oxide (ITO) [200, 201].

Furthermore, we observe, that this HMM microcavity provides a high number of modes at the HMM type I upper limit frequency, which can be tuned by the doping level of the ZnO:Ga. The mode structure can be tailored in the growth process by changes of the cavity geometry, i.e., a change in the fill factor f as well as the overall cavity size L and number of layers [K9]. This outlines a variety of applications like the tuneability of the high density of states, which may allow for a tailored emission control of dye molecules or quantum dots included into or above the microcavity. Moreover, the plasma frequency of the ZnO:Ga HMM core material can be dynamically tuned through optical pumping on the picosecond scale [203]. Therefore, the mode continuum of the HMM type I region can be actively controlled and outlines a way for a subwavelength-sized dynamical optical switching.

Lasing cavities with distributed Bragg reflectors and plasmonic silver grating

In this chapter, we combine both the knowledge about periodic structures from the Fourier modal method (FMM) and the advantages of the discontinuous Galerkin time-domain (DGTD) method to understand and describe the lasing cavity setup outlined in the introduction Chapter 1. First, we analyze how to construct the cavity using a titanium dioxide (TiO_2) / silicon dioxide (SiO_2) distributed Bragg reflector (DBR) and how to choose its geometrical parameters to obtain a well-defined lasing mode. Furthermore, we introduce a silver metal grating and investigate the influence on the *cold* cavity spectrum as well as the field distribution under resonant excitation. As a next step, we include the dye material, for which we use the four-level system (4LS) material model derived in Section 3.5. There, we provide the concrete material parameters for the guest:host material with Tris(8-hydroxyquinoline)aluminum (Alq_3) as matrix and 4-(dicyanomethylene)-2-methyl-6-[p-(dimethylamino)-styryl]-4H-pyran (DCM) as emitter (Alq_3:DCM) used and show how to obtain a lasing threshold from the DGTD computations within the simple, metal-free DBR cavity design. Finally, we conclude the chapter analyzing the full system, containing the DBR cavity, the 4LS material model as well as the metallic grating.
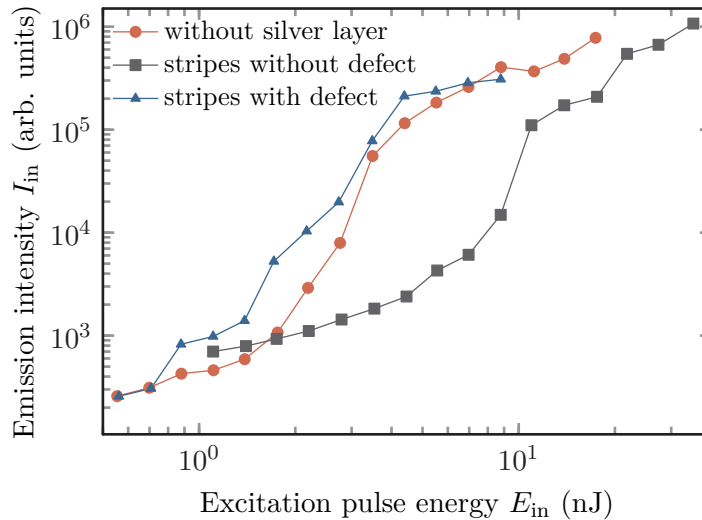
Figure 8.1: Measured lasing thresholds of Alq_3:DCM filled DBR cavities with and without silver grating upon different excitations with a focused beam. The focal positions, as well as the silver grating defect system, are sketched in Figure 8.2, with the same color-coding. Experimental data was graciously provided by M. Kliem [K4].
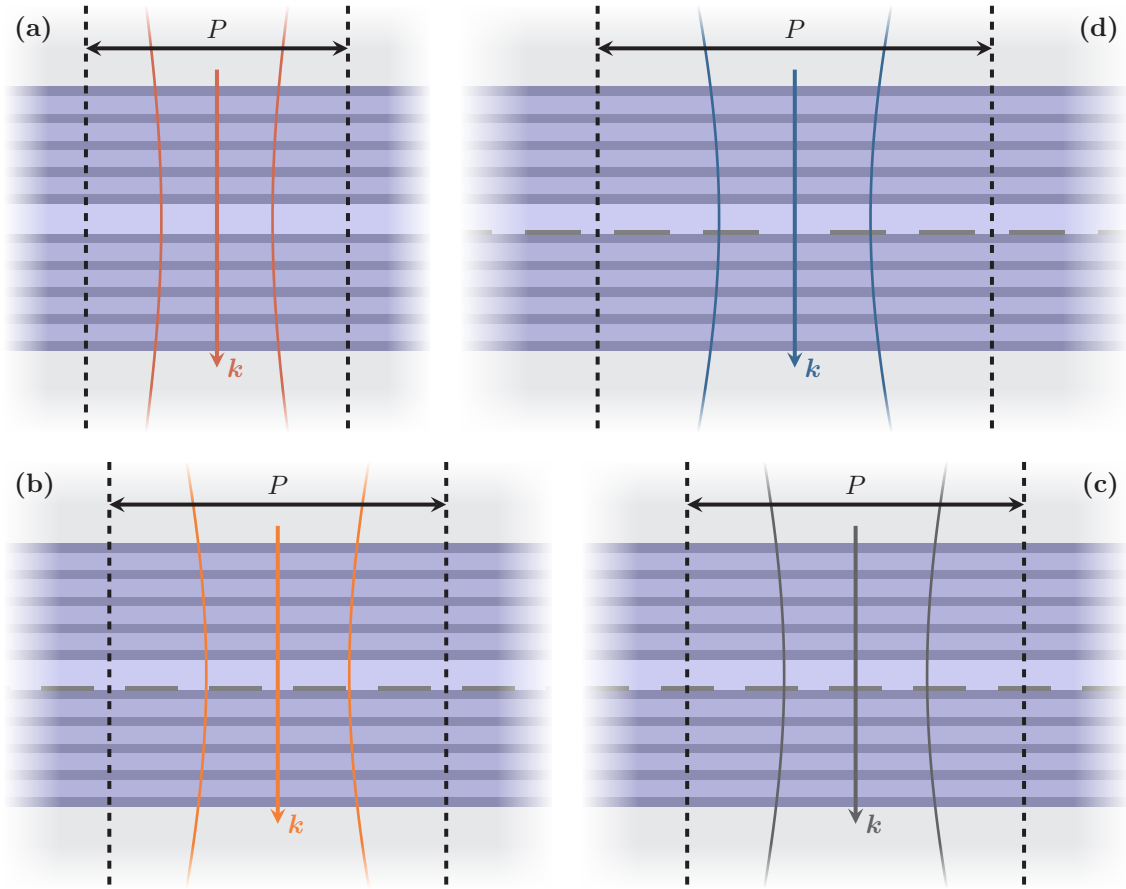
Figure 8.2: Four different focused beam excitation modes of an Alq₃:DCM filled DBR microcavity containing a silver grating. Computations include a grating supercell with period P. Focused beam excitation of a **(a)** bare cavity, i.e., without silver grating, as well as **(b)** and **(c)** a regular silver grating with the focus on a gap and stripe of the grating (on-stripe excitation (OSE)), respectively. **(d)** Focused beam excitation of a silver grating including a defect.

The main goal of the numerical investigation is to explain and reproduce the experimentally obtained lasing thresholds presented in Figure 8.1. In the experiment, we distinguish between three different excitation modes of the DBR cavity including the silver grating. These are shown in Figure 8.2. For completeness of the numerical study, we additionally consider a fourth excitation mode. Thereby the cavity is excited with the pump beam focused into a regular grating gap, instead of the defect, a silver stripe of the grating or the bare cavity. The experimental microcavities are constituted by a pair of 21-layer DBRs and contain a dissipative silver grating. The remarkable result of the measured lasing thresholds is that the defect system (blue line), despite the dissipative grating, shows the lowest overall threshold. It lies not only below the threshold for OSE (gray line) of the regular silver grating without defect but also below the lasing threshold of the bare cavity (red line). To explain this finding, we investigate the underlying lasing modes provided by the cavities and their influence on the lasing thresholds in the following sections.

8.1 Design of the DBR

In principle, a DBR is a quasi-one-dimensional photonic-crystal [204, 205], which consists of two different dielectric material layers. In the experimental setup presented above and in the introduction Chapter 1 the DBR consists of alternating layers of SiO$_2$ and TiO$_2$. The photonic band structure of a DBR contains photonic stop bands [205]. Within that frequency region, the DBR acts as a perfect mirror for plane waves impinging on the layer system, as no wave propagation is supported. Thus, DBRs can be utilized as frequency selective mirrors. To obtain a photonic stop band at a given operation frequency, the alternating dielectric layers of the DBR have to be designed such that both layers have a thickness of approximately a quarter of the in-medium operation wavelength ($\frac{\lambda}{4}$-thickness). This causes destructive interference in the material [60].

The main purpose of the DBRs used here is to act as a mirror for the lasing cavity filled with the Alq$_3$:DCM organic molecules. Hence, the thicknesses are designed such, that the photonic stop band lies around the $\lambda_{\mathrm{em}} = 640\,\mathrm{nm}$ emission wavelength of the dye. The DBR setup is not only investigated with the frequency-domain FMM (see Chapter 4) but also the DGTD method (see Chapter 5). Therefore, we use a Lorentz model (see Section 3.1) to describe the dispersive TiO$_2$ material, i.e.,

$$\epsilon_{\mathrm{TiO_2}}(\omega) = \epsilon_{\mathrm{bg}} + \frac{\Delta_{\mathrm{L}}\omega_{\mathrm{L}}^2}{\omega_{\mathrm{L}}^2 - \omega^2 - \mathrm{i}\gamma_{\mathrm{L}}\omega}\,, \tag{8.1}$$

where we take the model parameters

(SI) $\quad \epsilon_{\mathrm{bg}} = 3.32\,, \quad \Delta_{\mathrm{L}} = 3.18\,, \quad \omega_{\mathrm{L}} = 6.2 \times 10^{15}\,\mathrm{rad\,s^{-1}} \quad \text{and} \quad \gamma_{\mathrm{L}} = 1.98 \times 10^{14}\,\mathrm{rad\,s^{-1}}\,, \tag{8.2}$

which have been used and fitted in [80, K10]. On contrary, the SiO$_2$ is modeled as a non-dispersive dielectric with $\epsilon_{\mathrm{SiO_2}} = 2.165$ [206, 207] as its permittivity is nearly constant for the operation wavelengths $\lambda \in [350\,\mathrm{nm}, 850\,\mathrm{nm}]$. Consequently, the thicknesses of the DBR constituting layers are set to

(SI) $\quad\quad\quad\quad\quad\quad\quad d_{\mathrm{TiO_2}} = 57.4\,\mathrm{nm} \quad \text{and} \quad d_{\mathrm{SiO_2}} = 108.3\,\mathrm{nm}\,, \tag{8.3}$

to center the DBR stop band around the operation wavelength $\lambda \approx 640\,\mathrm{nm}$. Given the setup parameters, we can compute the scattering spectra of the DBR with the scattering matrix (S-matrix) algorithm presented in Section 4.3.

In Fig. 8.3 we show the resulting transmittance, reflectance, and absorbance spectra of a DBR for an increasing number of DBR unit cells, i.e., pairs of TiO$_2$ / SiO$_2$ layers. Both in the experiment and the computations, an odd number of layers is used. For each DBR the first and last layer is made out of SiO$_2$. We observe, that with the increasing number of unit cells the reflectance nearly approaches unity in the first DBR stop band frequency window, which acts as a mirror for the microcavity. The stopband is formed for wavelengths between $\lambda_{\mathrm{sb,min}} \approx 540\,\mathrm{nm}$ and $\lambda_{\mathrm{sb,max}} \approx 780\,\mathrm{nm}$ and becomes more and more pronounced with an increasing number of DBR layers, as can be seen in Fig. 8.3 (a) to (d). In this wavelength interval, the transmittance drops to almost zero. As the TiO$_2$ is modeled with a spectrally broad single Lorentz pole in Eq. (8.1),
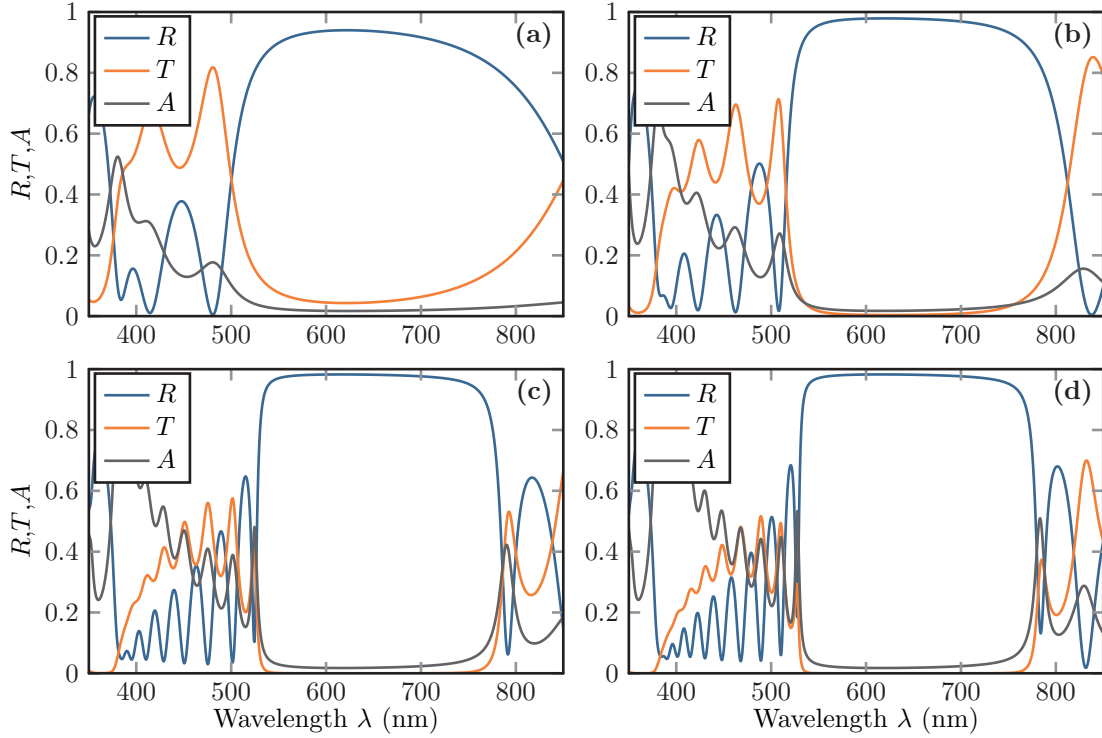
Figure 8.3: DBR reflectance R, transmittance T, and absorbance A spectra for different numbers of TiO_2 and SiO_2 layers: **(a)** 5 layers, **(b)** 9 layers, **(c)** 17 layers, and **(d)** 21 layers.

a slight over-estimation of the absorption leads to a non-zero absorbance within the stopband. This results in a reflectance slightly lower than one. Below the minimal wavelength $\lambda_{\mathrm{sb,min}}$ of the first DBR stop band reflection minima and maxima are observed, the number of which increases proportionally with the number of layers used to set up the DBR [60]. Due to the increased absorption in the TiO_2 material model also the overall absorbance spectra significantly increase for wavelength $\lambda \lesssim 450\,\mathrm{nm}$. This behavior is qualitatively independent of the number of DBR layers.

8.2 Introduction of an active material

Given the DBR design, which ensures reflectivity in the photoluminescence window of the Alq_3:DCM dye, the next step is to characterize the entire lasing cavity. We, therefore, model the active material by a 4LS using the material model introduced in Section 3.5. Here, we present all material parameters of the 4LS used in the final DGTD lasing threshold computations.

8.2.1 Material parameters

The material parameters of the 4LS modeling the Alq_3:DCM are obtained from different experimental observations. From the absorption spectra [58, 59, 208] we can obtain the central

absorption wavelength

$$\lambda_{03} = 470\,\text{nm}\,. \tag{8.4}$$

To determine the dephasing constant γ_{03} as well as coupling constant ζ_{03} of the 0–3-transition of the 4LS we can use the Lorentzian susceptibility, which we obtain from the Fourier transform Eq. (2.33) of Eq. (3.65) in the limit of a weak excitation, i.e., $N_0 \approx 1$ and $N_3 \approx 0$:

$$(-\mathrm{i}\omega)^2\,\boldsymbol{p}_{03}(\omega) - \mathrm{i}\omega\gamma_{03}\boldsymbol{p}_{03}(\omega) + \omega_{03}^2\boldsymbol{p}_{03}(\omega) = \underbrace{(N_0 - N_3)}_{\approx 1}\zeta_{03}\boldsymbol{E}(\omega)\,. \tag{8.5}$$

With

$$\boldsymbol{D}(\omega) \overset{(3.63)}{=} \epsilon_{\text{bg}}\boldsymbol{E}(\omega) + N_{\text{dye}}\boldsymbol{p}_{03}(\omega) \overset{!}{=} \epsilon_{\text{bg}}\boldsymbol{E}(\omega) + \chi_{03}(\omega)\boldsymbol{E}(\omega)\,, \tag{8.6}$$

we recover the Lorentz model susceptibility

$$\chi_{03}(\omega) = \frac{N_{\text{dye}}N_0\zeta_{03}}{\omega_{03}^2 - \mathrm{i}\omega\gamma_{03} - \omega^2} \overset{(3.7)}{\equiv} \frac{\Delta_\epsilon\omega_L^2}{\omega_L^2 - \mathrm{i}\gamma_L\omega - \omega^2}\,. \tag{8.7}$$

While the molecule concentration can be estimated as

$$N_{\text{dye}} \approx 2.5 \times 10^{20}\,\text{cm}^{-3} = 0.25\,\text{nm}^{-3} \tag{8.8}$$

from the experimental sample preparation [K4], the remaining parameters of the susceptibility can be fitted to a complex-valued index of refraction obtained, by e.g., ellipsometry [209], for a single molecule layer [K4, 210]. This delivers the material parameters

$$\omega_{03} \approx 4.01 \times 10^{15}\,\text{rad s}^{-1}\,,\ \ \gamma_{03} \approx 4.8 \times 10^{15}\,\text{rad s}^{-1}\,,\ \ \Delta_{03} \approx 0.1\ \text{and}\ \epsilon_{\text{bg}} \approx 2.8\,, \tag{8.9}$$

for the absorption transition of the Alq$_3$:DCM material. Thus, also the level coupling constant for the 0–3-transition is determined as

$$\zeta_{03} = \frac{\Delta_{03}\omega_{03}^2}{N_{\text{dye}}} \approx 3.63 \times 10^{-7}\,\text{A}\,\text{m}^2\,\text{V}^{-1}\,\text{s}\,. \tag{8.10}$$

Similarly, the parameters for the 1–2-transition are obtained from the photoluminescence spectra [58]. The main emission peak lies at

$$\lambda_{12} = 640\,\text{nm}\,. \tag{8.11}$$

Although the photoluminescence spectrum is normally broadened by vibrational transitions [113], here, it is only modeled by a single broadened Lorentz peak, which leads to a dephasing rate of

$$\gamma_{12} \approx 4.8 \times 10^{14}\,\text{rad s}^{-1}\,. \tag{8.12}$$

Even if the radiative contribution of the spontaneous emission to the electromagnetic field is neglected in the 4LS material model, we use the spontaneous emission time $\tilde{\tau}_{12} = 4\,\text{ns}$ [211] to

determine the coupling constant defined in Eq. (3.68) as

$$\text{(SI)} \qquad \zeta_{12} = \frac{6\pi\epsilon_{\text{bg}}\epsilon_0 c_0^2}{\omega_{12}^2 \tilde{\tau}_{12}} = 5.68 \times 10^{-8}\,\text{A}\,\text{m}^2\,\text{V}^{-1}\,\text{s}^{-1}\,. \qquad (8.13)$$

Here, we use the transition frequency

$$\text{(SI)} \qquad \omega_{12} \approx 2.94 \times 10^{15}\,\text{rad}\,\text{s}^{-1}\,. \qquad (8.14)$$

Finally, we set the non-radiative decay times τ_{ij} between the different levels of the 4LS. These can be accessed experimentally by, e.g., pump-probe experiments [118] and typically lie on the picosecond time scale. They are orders of magnitudes smaller than the spontaneous emissions times of the dipole transitions, which enables lasing in the first place. Any occupation of the third level must be transferred sufficiently fast into the second level in order to achieve a population inversion $\Delta N_{12} = N_2 - N_1 > 0$ for the emission transition. For the actual computations of the lasing thresholds, it is only important, that these decay times are sufficiently larger than the field time periods $\tau_{ij} \gg T_{ij} = \frac{2\pi}{\omega_{ij}}$, which reside in the single femtosecond scale. We thus set

$$\text{(SI)} \qquad \tau_{01} = 50\,\text{fs} \quad \text{and} \quad \tau_{23} = 100\,\text{fs}\,. \qquad (8.15)$$

The non-radiative decay times of the dipole transitions are assumed to be much larger $\tau_{03}, \tau_{12} \gg \tau_{01}, \tau_{23}$. Consequently, we only allow a radiative coupling on the dipole transitions by setting

$$\tau_{03}, \tau_{12} \to \infty\,. \qquad (8.16)$$

With all the parameters set for the 4LS model, we can now compute the properties of both the lasing cavities for both weak and strong pump fields. We first start with the *cold*, i.e., weakly excited cavity without silver grating, for which we only need the Lorentz model Eq. (8.7) of the 0–3-transition.

8.2.2 Lasing cavity

In the preceding Section 8.1, we have seen, that the given DBR has a photonic stop band at the emission frequency of the Alq$_3$:DCM dye. To obtain a lasing cavity we use two DBRs as mirrors and introduce an active material layer in between. Here the layer thickness is chosen to be (approximately) half the in-material emission wavelength, i.e.,

$$\text{(SI)} \qquad d_{\text{Alq}_3:\text{DCM}} = 190\,\text{nm}\,. \qquad (8.17)$$

Introducing this material layer leads to the formation of a defect resonance within the DBR cavity. Fig. 8.4 shows the resulting peak in the reflectance spectrum. Here, we again vary the number of layers for each of the DBRs constituting the cavity. The spectra are computed under plane wave excitation with the S-matrix algorithm presented in Chapter 4. Increasing the number of DBR layers leads to an increase of the quality factor of the defect resonance. This can also be well observed by the relative field enhancement shown in Fig. 8.5. It shows the **E**-field distribution in the same cavities as in Fig. 8.4 for a resonantly tuned plane wave excitation at
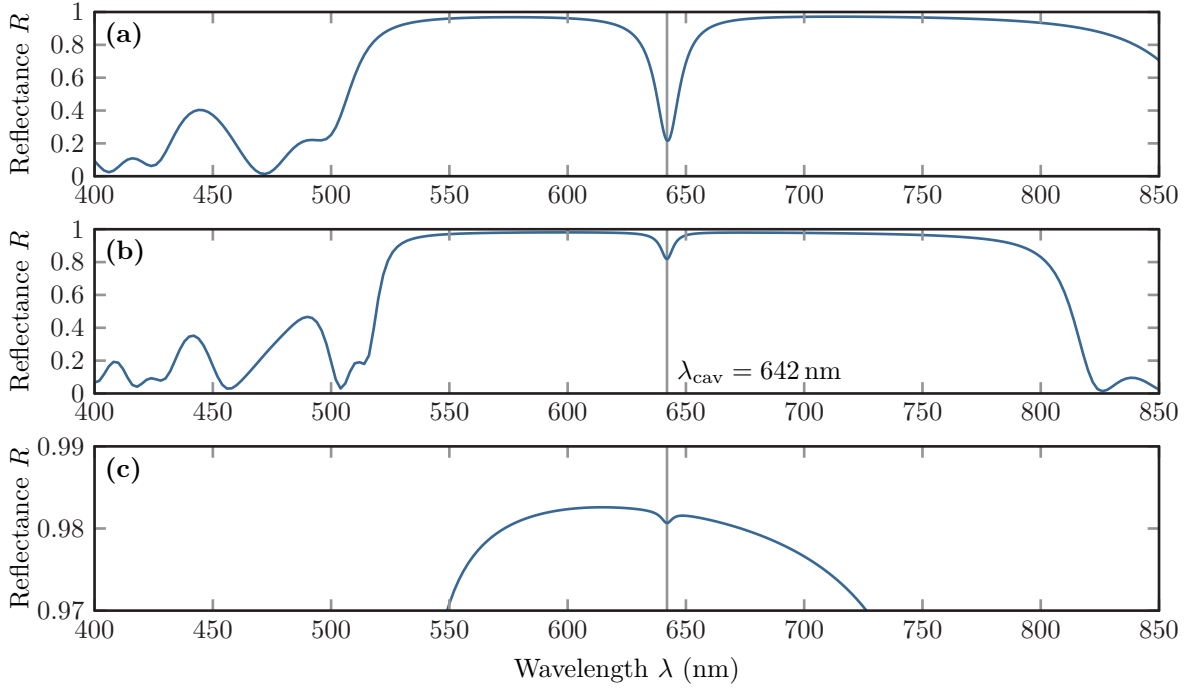
Figure 8.4: Reflectance spectra R for a microcavity with two DBRs including a 190 nm Alq$_3$:DCM material layer. Each DBR consist of **(a)** 5, **(b)** 9 or 17 **(c)** SiO$_2$ / TiO$_2$ layers, respectively.

the cavity wavelength $\lambda_{\mathrm{cav}} = 642$ nm. Furthermore, it is well visible that within the DBR two adjacent SiO$_2$ / TiO$_2$ layers have a $\frac{\lambda}{2}$-length, as the nodal points of the field occur at every second interface.

This simple cavity with its single resonance can already act as a microlaser. However, before we investigate the behavior upon strong field focused beam excitation, we also study the *cold* cavities including the whole silver grating used in the experimental realization [K4]. The *cold* cavity mode structure is essential to explain the different laser thresholds onset observed in the experiment (cf. Fig. 8.1).

8.2.3 Introduction of the metal grating into the cavity

In Fig. 8.2 (b,c) the metal stripe grating is sketched. These silver stripes, which experimentally are produced with a photolithographic lift-off process [K4], have a thickness of

(SI)
$$d_{\mathrm{Ag}} = 25\,\mathrm{nm}\,. \tag{8.18}$$

While in the experiment also different grating periods with lateral unit cell lengths of $p = 6\,\mu\mathrm{m}$ and $p = 7\,\mu\mathrm{m}$ have been investigated, we here focus on the smallest and numerically least
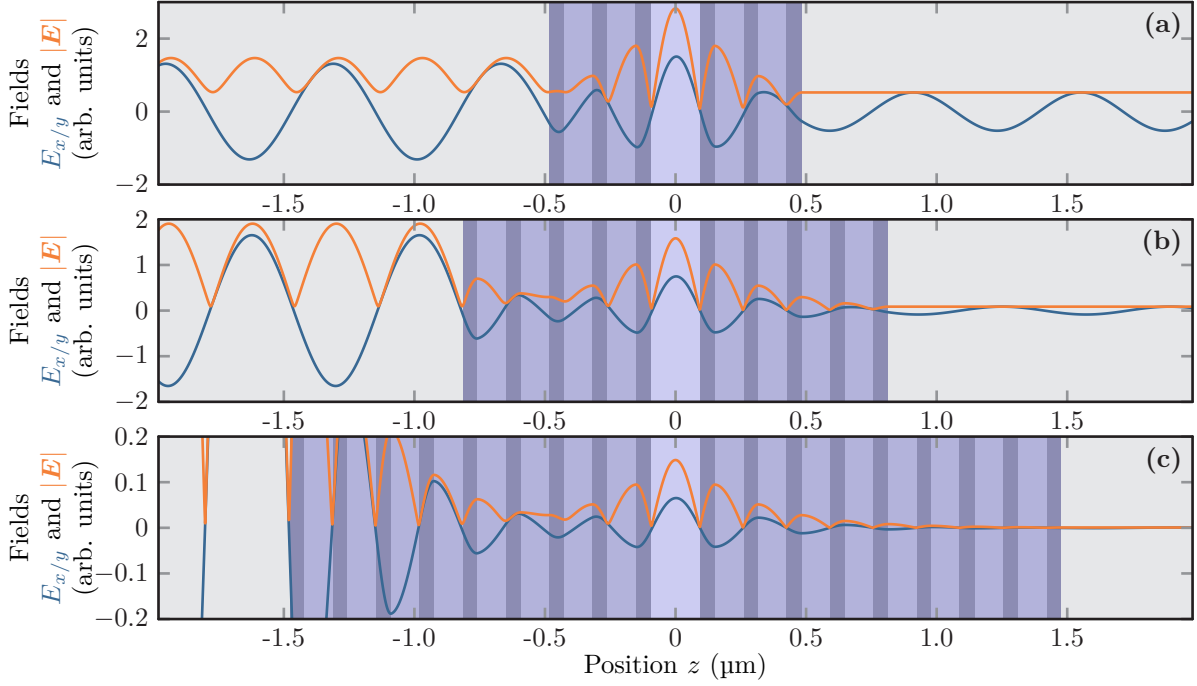
Figure 8.5: Electric field distribution and field strength in the bare cavity upon excitation with a plane wave impinging from the left half-space resonantly tuned to the cavity mode at $\lambda_{\text{cav}} = 642\,\text{nm}$. Panels **(a)** - **(c)** show fields for different numbers of DBR layers (cf. Fig. 8.4).

demanding, yet computationally still very challenging silver grating with a period of

$$p = 5\,\mu\text{m}\,. \tag{8.19}$$

(SI)

Within that single grating unit cell, the stripes and gaps have the widths

$$w_{\text{stripe}} = 3.1\,\mu\text{m} \quad \text{and} \quad w_{\text{gap}} = 1.9\,\mu\text{m}\,. \tag{8.20}$$

(SI)

To model the relative permittivity of the silver stripes we use the Drude model presented in Section 3.2, i.e.,

$$\epsilon_{\text{Ag}} = \epsilon_{\text{bg}} - \frac{\omega_{\text{pl,Ag}}^2}{\omega(\omega + \mathrm{i}\gamma_{\text{Ag}})}\,. \tag{8.21}$$

Here, we use the fit to permittivity data by Johnson and Christy [166], which sets

$$\epsilon_{\text{bg}} = 1\,, \quad \omega_{\text{pl,Ag}} = 13.89 \times 10^{15}\,\text{rad}\,\text{s}^{-1} \quad \text{and} \quad \gamma_{\text{Ag}} = 3.23 \times 10^{13}\,\text{rad}\,\text{s}^{-1}\,, \tag{8.22}$$

(SI)

as the silver material parameters.

For this quasi-two-dimensional system, we compute the reflectance spectra for cavities with different numbers of DBR layers. Fig. 8.6 shows the spectra for 5, 9, and 17 layers, respectively.
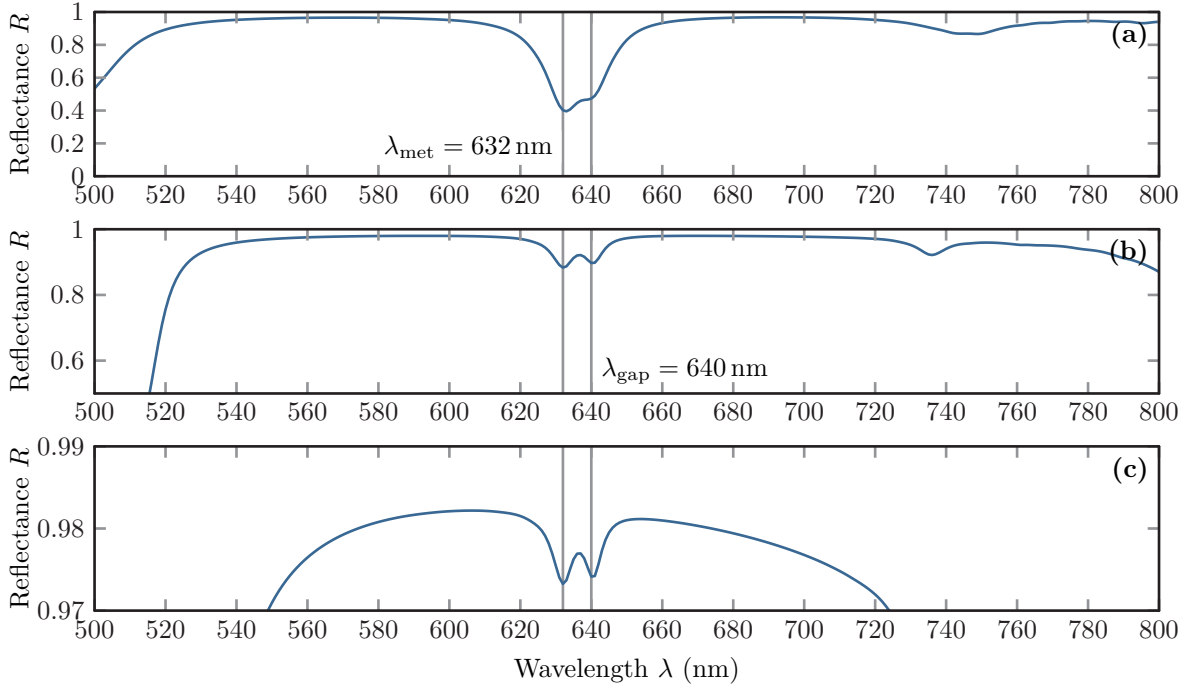
Figure 8.6: Reflectance spectra R for a microcavity with two DBRs including a 190 nm Alq$_3$:DCM material layer and a patterned silver grating with period $p = 5\,\mu m$. Each setup with 5 **(a)**, 9 **(b)**, and 17 **(c)** layer DBRs shows two resonance peaks at $\lambda_{met} = 632\,nm$ and $\lambda_{gap} = 640\,nm$ marked by solid lines.

Compared to the bare cavity spectra from Fig. 8.4, these spectra now contain two instead of one peak (cf. Fig. 8.4) in the DBR stop band wavelength window. Thus, adding a silver stripe not only introduces a small spectral shift $\lambda_{cav} \rightarrow \lambda_{gap} = 640\,nm$ but also creates a second distinct mode in the system.

To further characterize the resonances, we compute the $\boldsymbol{E}$-field distributions of the grating for a plane wave excitation using the FMM as described in Section 4.3. Here, we use a plane wave with straight incidence, i.e., $\boldsymbol{k}\|\boldsymbol{e}_z$, which excites a superposition of the modes supported for each unit cell. The $\boldsymbol{E}$-field distributions for the specific excitation frequencies and DBR layer numbers are shown in Fig. 8.7. The first mode at $\lambda_{met} = 632\,nm$ has field maxima on the single silver metal stripes (see Fig. 8.7 (a,c,e)). On the contrary, the second mode at $\lambda_{gap} = 640\,nm$ shows a field confinement in the gaps of the silver grating (see Fig. 8.7 (b,d,f)). The *gap* mode is more symmetric in DBR stacking direction than the *metal* mode and it has a significantly higher field contribution in the transmission channel. Thus, the silver stripes essentially work as small mirroring layers. This also explains the slight blue shift of the *metal* mode as the essential cavity size is reduced compared to the *gap* mode. Additionally, we observe an increase in the effective field enhancement of both cavity modes with an increasing number of DBR layers, which indicates a systematic increase in the quality factor.
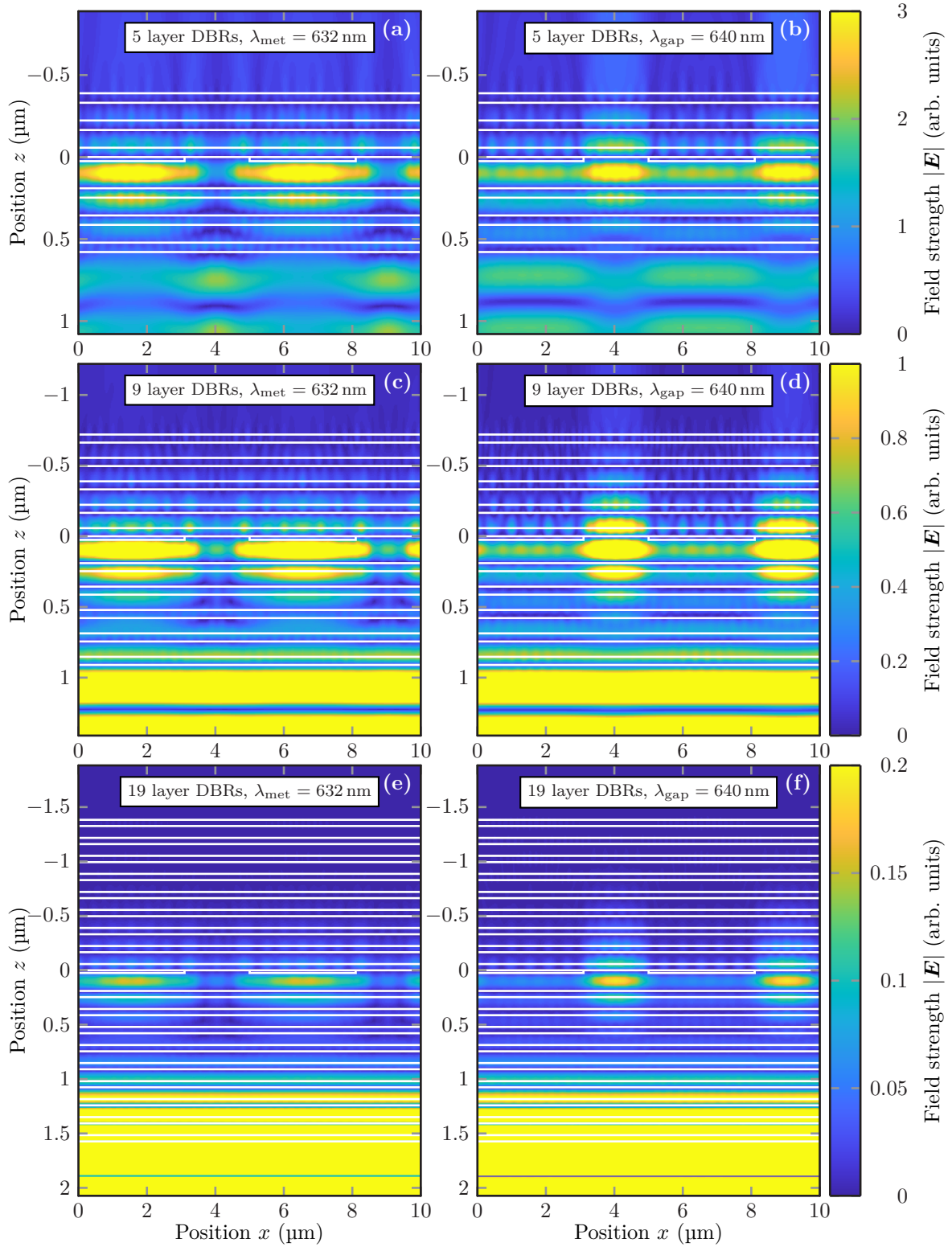
Figure 8.7: Electric field distributions of the DBR cavities including the silver grating in the $d = 190\,\mathrm{nm}$ thick Alq$_3$:DCM layer for different plane wave excitation resonance wavelengths as seen in Fig 8.6 and number of constituting DBR layers, i.e., **(a,b)** 5, **(c,d)** 9 and **(e,f)** 17 layers per DBR.

8.3 Lasing thresholds

After the characterization of the passive DBR microcavity, i.e., excitation below the lasing threshold, we discuss the computation of the lasing thresholds using the fully nonlinear 4LS material model (cf. Section 3.5) to describe the Alq₃:DCM material model. In contrast to the plane wave excitation used in the previous section, we here use a focused beam excitation as sketched in Figure 8.2. The excitation with a focused pump beam enables a direct addressability of the different modes supported by the DBR microcavity including the grating. Before we compare the different excitation modes for the metal grating DBR cavities, we step by step present how to compute the lasing thresholds for the bare cavity, i.e., the DBR cavity without silver grating.

8.3.1 Lasing threshold computation for the bare cavity

To compute the lasing threshold of the DBR microcavity without silver grating as sketched in Figure 8.2 (a) we use the DGTD method. Although, the structure without silver grating is an effectively one-dimensional setup the excitation with a focused Gaussian beam breaks the symmetry in lateral direction. This in principle suggests a fully three-dimensional computation. However, we restrict the computational setup to an essentially two-dimensional one, which suffices for a qualitative explanation of the experimentally observed lasing thresholds from Fig. 8.1. We thus assume a two-dimensional Gaussian-shaped pump beam as presented in Appendix B, which is assumed to have a homogeneous field in y-direction. Additionally, we assume periodic boundary conditions in lateral x-direction. For the exemplary computations presented here, we use an overall setup period of $P = 20\,\mu\text{m}$. The DBRs used in the example consist of only five layers each, as an increase in the number of DBR layers significantly increases the computational run time, as also the number of elements in the DGTD method increases. Hence, a smaller system is better suited for in-depth investigations.

To launch the focused Gaussian pump beam Eq. (B.8) into the computational domain, we use a total field / scattered field (Tf/Sf) setup for the DGTD method as explained in Section 5.4.1. We, therefore, introduce a Tf/Sf contour $2\,\mu\text{m}$ above the DBR microcavity (cf. Figure 8.9 (a)). Above this Tf/Sf contour another $2\,\mu\text{m}$ air layer ($\epsilon_r \approx 1$) is introduced. Below the DBR cavity, this setup is mirrored with two air layers, containing another contour to compute the transmission signal below the cavity. The computational domain is terminated with Silver Müller boundary conditions (SMBCs) (cf. Section 5.3.4), which prevents any transmitted, reflected, and emitted radiation to be reflected at the boundary, as the outermost boundaries are sufficiently far away. We do not use perfectly matched layers (PMLs) here, due to a stability problem for long simulation times, emerging from spurious guided modes in the DBR system, which leads to slowly diverging fields in the implementation used. The computational domain is tessellated using *gmsh* [140] with element sizes down to the $h_{\min} \approx d_{\text{Ag}} = 22\,\text{nm}$. The element size here is chosen such, that there are at least four elements per in-medium wavelengths. Furthermore, we use a third-order Lagrange polynomial basis (cf. Section 5.2.1).

The pump beam is focused on the center of the Alq₃:DCM layer, i.e., at

$$\boldsymbol{r}_0 = \left(x_0, z_0\right)^{\text{T}} = \boldsymbol{0}\,. \tag{8.23}$$

The beam half-width is set to $\sigma_x = 3\,\mu\text{m}$ comparable to the experimental circular focus with a full width half maximum (FWHM) of approximately $7\,\mu\text{m}$ [K4]. The pump pulse propagates in negative z-direction, i.e., $\boldsymbol{n} = -\boldsymbol{e}_z$. We use a time-modulated focused excitation to comply with the zero-field initial condition for the DGTD method, ensuring that Maxwell's divergence equations (2.1a) and (2.1b) are fulfilled for all times up to numerical accuracy. Instead of a Gaussian modulated time dependence Eq. (B.20), we use a polynomial ramped continuous-wave time dependence (see Appendix B.2.2, Eq. (B.23)) for the pump pulse. This ensures a short overall pulse duration T_{pulse} to obtain a high pulse energy E_{in} for given maximal field amplitude $|\boldsymbol{E}_0|$ and thus saves some computation time. The beam carrier frequency

$$\text{(SI)} \qquad\qquad \omega_{\text{exc}} = \frac{2\pi c_0}{\lambda_{\text{exc}}} \qquad\qquad (8.24)$$

is set according to the vacuum carrier wavelength

$$\text{(SI)} \qquad\qquad \lambda_{\text{exc}} = 532\,\text{nm}\,, \qquad\qquad (8.25)$$

to resonantly drive the 0–3 transition of the 4LS modeling the Alq$_3$:DCM. The entire excitation pulse lasts $T_{\text{pulse}} \approx 4\,\text{ps}$, which contains a ramp-up of $t_{\text{up}} = 0.33\,\text{ps}$ and ramp-down time of $t_{\text{down}} = 0.67\,\text{ps}$. The variation of the focused beam amplitude $|\boldsymbol{E}_0|$ sets the incident beam energy. It can be recorded from the incident beam power flux on the Tf/Sf contour. To compute this input energy we numerically integrate both over the entire Tf/Sf contour length (area) as well as over the recorded frequency window in the computation according to Eq. (2.95). The initial 4LS occupations are prepared in the ground state, i.e.,

$$N_0(t=0) = 1 \quad \text{and} \quad N_{1,2,3}(t=0) = 0\,, \qquad\qquad (8.26)$$

as the system operates at room temperature. Given an input field amplitude and the initial conditions, we can then compute the entire system dynamics. As an example, we present a computation for which the excitation field strength lies above the lasing threshold.

In Figure 8.8 (a), we show the electric field strength along the centerline $x = x_0 = 0$ of the DBR cavity. Due to the above threshold excitation, we not only observe the field on the excitation time-period of the pump beam ($t \le T_{\text{pulse}} = 4\,\text{ps}$) but also field emission at later times. During the excitation time with the pump pulse, we observe out-going wavefronts both above the Tf/Sf contour and below the DBR cavity. These correspond to the reflected and transmitted pump field respectively. The reflection of the pump beam also leads to the interference pattern between to upper boundary of the top DBR and the Tf/Sf contour, as this region is part of the total field (Tf) domain. After a partial absorption of the pump pulse, there are several field emission bursts for $t > T_{\text{pulse}} = 4\,\text{ps}$. These pulses originate from the stimulated emission of the excited Alq$_3$:DCM.

In Figure 8.8 (b), we show the spatially averaged occupation numbers of the 4LS. Here, we average the occupation numbers over the thickness of the Alq$_3$:DCM layer, i.e.,

$$\langle N_i \rangle_z (x,t) = \frac{1}{d_{\text{Alq}_3:\text{DCM}}} \int_0^{d_{\text{Alq}_3:\text{DCM}}} \mathrm{d}z\, N_i(x,z,t)\,. \qquad\qquad (8.27)$$
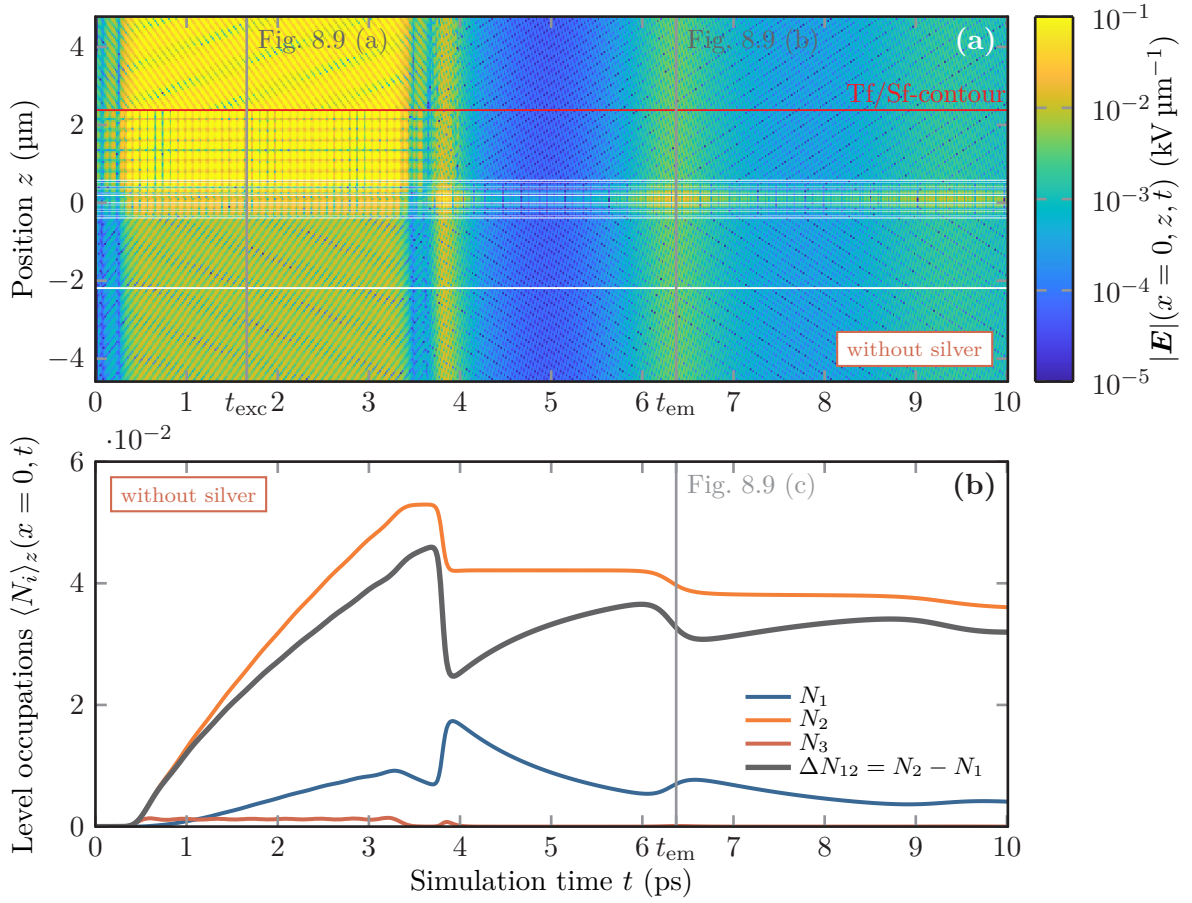
Figure 8.8: (a) Electric field strength for a grating-free DBR cavity upon a focused beam excitation above lasing threshold. The field is shown along the focus line $x = 0\,\mu m$. The full spatial field patterns at times t_{exc} during excitation and t_{em} during the second emission pulse are shown in Fig. 8.9. **(b)** Time dependence of the thickness-averaged occupation densities $\langle N_i \rangle_z$ defined in Eq. (8.27) as well as population inversion $\Delta N_{12} = N_2 - N_1$ along the focus line.

During the excitation with the pump beam, we observe how the occupation N_2 of the second level systematically increases. At the same time, the occupation N_3 of the third level remains at a small nearly constant value, as the non-radiative decay to the second level empties the third level relatively fast. Although we neglect the non-radiative coupling between the first and second level, we also observe an increase in the occupation N_1 of the first level. As the emission transition is modeled with a broad Lorentzian line shape, this increase can be explained by the off-resonant interaction with the pump-beam itself. However, we observe a clear increase in the population inversion $\Delta N_{12} = N_2 - N_1$, which is responsible for the lasing. In contrast to the continuous-wave operation of a laser with $\Delta N_{12} \geq 0$ [93], we here require to exceed a positive finite population inversion threshold, due to the finite excitation duration and finite quality factor of the cavity mode. For the pump energy and thus excitation field strength chosen here, the first

stimulated emission pulse occurs at the end of the pump beam excitation at $t \approx 3.9\,\text{ps}$. This is accompanied by symmetrically emitted fields (Figure 8.8 (a)) as well as a drop in the population inversion (Figure 8.8 (b)). While the occupation of the second level remains nearly constant, the occupation of the first level increases during the emission and then decays non-radiatively into the ground state. Hence, the population inversion increases over the threshold for the stimulated emission and a second emission pulse occurs at $t = t_{\text{em}} \approx 6.4\,\text{ps}$. With increasing time, this pattern repeats with an increase in the time between the emission pulses and a simultaneous decrease in the emission pulse field strength and thus also energy. Consequently, the population inversion reaches a finite, non-zero value in the simulation. While this transient emission behavior is well known in the switch-off process [211], the finite population inversion actually decays due to spontaneous emission, which we here neglected. However, the numerical method is still well suited, as the emission pattern occurs on a picosecond time scale, while the spontaneous emission of the Alq$_3$:DCM lies at $\tilde{\tau} \approx 4\,\text{ns}$ [211].
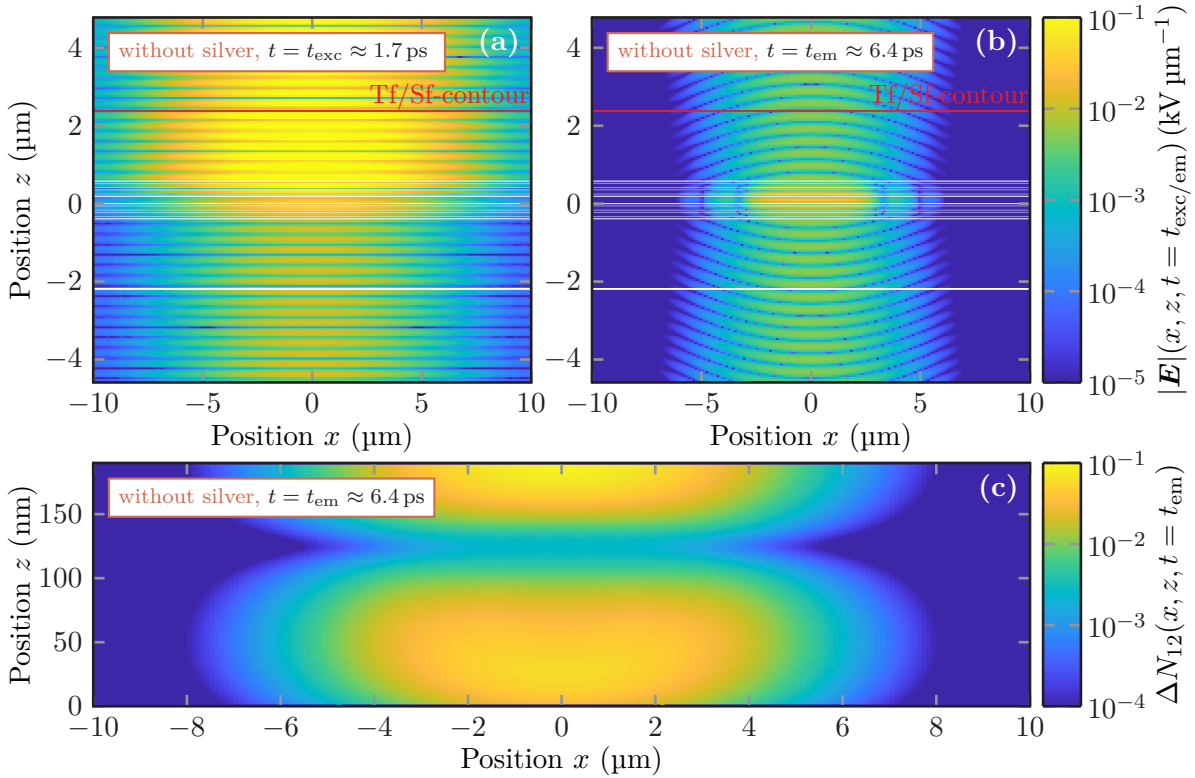
Figure 8.9: Electric field strength distributions of a DBR microcavity upon above threshold excitation during the time-modulated pumping **(a)** as well as the second emission peak **(b)**. Panel **(c)** shows the population inversion ΔN_{12} of the emission transition after the cavity excitation.

Besides the emission dynamics also the field distributions in the entire DBR microcavity are important for a complete characterization. In Figure 8.9 (a,b) we show the electric field distribution in the entire simulation unit cell both during the pump beam excitation $t = t_{\text{exc}} \approx 1.7\,\text{ps}$

and the second emission pulse at $t = t_{em} \approx 6.4\,\mathrm{ps}$. In Figure 8.9 (a), we observe the transversal Gaussian fall-off of the excitation pulse in the upper half-space, as well as the superposition of the reflected and incident field in the Tf domain between the top DBR and the Tf/Sf contour. Below the cavity, we see an order of magnitudes smaller transmitted field. Most of the electric field is absorbed by the Alq$_3$:DCM. The emission pulses also resemble a Gaussian beam as depicted in Figure 8.9 (b). For these bare DBR cavities, the emission is also symmetric into the upper and lower half-space. Further, the increase in the emission wavelength compared to that of the pump pulse can be seen. This change in wavelength also explains the spatial distribution shape of the population inversion ΔN_{12} build-up during the excitation, which is depicted in Figure 8.9 (c). The distribution is governed by the Gaussian shape and the wavelength of the excitation beam. We, therefore, find a nodal line in the active material, as the cavity is designed at half of the longer emission (in-medium) wavelength. Although the spatial overlap with the electric field distribution of the lasing mode is not ideal, it is sufficiently strong to enable a good coupling.
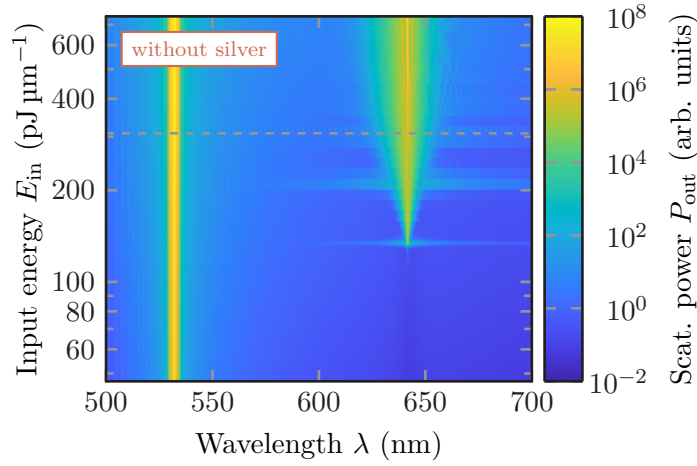
Figure 8.10: Wavelength-resolved scattered power of the bare cavity in dependence of the focused pump beam input energy E_{in}. The dashed line marks the input energy used for the computation results of Fig. 8.8 and Fig. 8.9.

For a comparison with the experimentally determined lasing thresholds, we need to compute the energy balance of the microcavities. For this, we compute the frequency-resolved power flux both on the Tf/Sf contour above and transmission contour below the DBR cavity. With a variation of the pump beam field amplitude $|\boldsymbol{E}_0|$, we can directly set the input energy of the pump pulse, which is also computed on the Tf/Sf contour according to Eq. (2.95). However, we numerically integrate here only over the recorded frequency window with $\lambda \in [500\,\mathrm{nm}, 700\,\mathrm{nm}]$ instead of all frequencies. Figure 8.10 shows the power balance of the scattered, i.e., reflected, transmitted and emitted radiation in dependence of the pump pulse input energy for the wavelengths recorded. The peak line at the pump pulse carrier wavelength $\lambda_0 = 532\,\mathrm{nm}$ originates from the reflected and transmitted field. This peak also systematically increases with increasing pump pulse input energy. Furthermore, we observe the lasing threshold at the cavity resonance wavelength $\lambda_{cav} = 640\,\mathrm{nm}$. The onset of the threshold lies at a pump pulse input energy of $E_{in} \approx 130\,\mathrm{pJ\,\mu m^{-1}}$. Upon the lasing threshold and also at higher input energy, e.g., $E_{in} \approx 200\,\mathrm{pJ\,\mu m^{-1}}$, we observe a spectral broadening of the output power signal. This broadening is due to the windowing [169]

in the on-the-fly Fourier transform used to compute the frequency-dependent Poynting vector on the respective contours. This occurs due to the finite simulation time as the emission pulses observed in Figure 8.8 move non-linearly into the finite simulation window from infinite times with increasing pump input energy E_{in}. However, this poses a minor problem as the emission pulses are not only delayed with decreasing input energy but also significantly fade in strength. Thus, it is sufficient to set a finite simulation time to obtain a finite accuracy level within the computations.

Influence of the unit cell period

While the spectrally resolved energy balance clearly indicates the lasing threshold already, we can also compute the input pulse energy by frequency integration as well as the emitted energy. Hence, we obtain a single lasing threshold that can be compared to the experiment. We compute the output energy similar to Eq. (2.95), i.e.,

$$
\begin{aligned}
E_{out} &= -\frac{2}{\pi} \int_{\omega_1}^{\omega_2} d\omega \, P_{out}(\omega) \\
&= -\frac{2}{\pi} \int_{\omega_1}^{\omega_2} d\omega \int_{-P/2}^{P/2} dx \left[\langle \boldsymbol{S}_z \rangle_\tau \left(x, z_{Tf/Sf}, \omega \right) - \langle \boldsymbol{S}_z \rangle_\tau \left(x, z_{trans}, \omega \right) \right] .
\end{aligned}
\tag{8.28}
$$

Here, the boundary frequencies $\omega_{1/2} = \frac{2\pi c_0}{\lambda_{1/2}}$ for the numerical integration are set by choosing the wavelength window $\lambda \in [\lambda_1, \lambda_2] = [630\,\text{nm}, 650\,\text{nm}]$ around the main emission peak. The time-averaged Poynting vector component for the output power computation is evaluated both on the Tf/Sf-contour position $z_{Tf/Sf}$ above the cavity and on the transmission contour position z_{trans} below the cavity. As the output power P_{out} depends on the computational domain period P, it has to be ensured that this period is sufficiently large. In Figure 8.9 (b) we have seen that the emitted beam slowly diverges with increasing distance to the cavity. Hence, the width P of the computational domain must ensure a sufficient fall-off of the lateral field and Poynting vector on the integration contours in Eq. (8.28). The same criterion also applies to the incident pump beam.
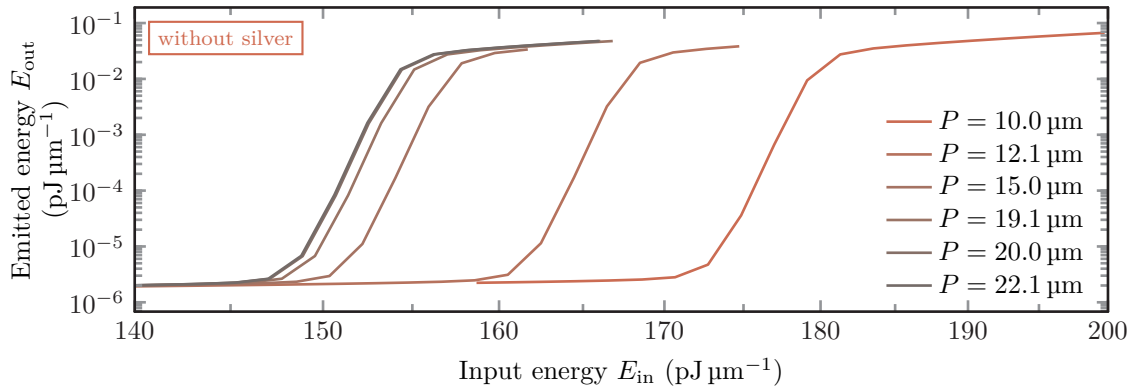
Figure 8.11: Lasing thresholds of the bare cavity with 5 layer DBRs for different overall computational domain periods P.

Consequently, we compute the lasing thresholds for different fixed domain widths P to find a lower bound value for numerically reliable thresholds, which can also be used in the supercell computations used for the cavities including the silver grating. Fig. 8.11 shows these thresholds. The overall lasing threshold shape is independent of the computational domain widths P. This indicates that already the $P = 10\,\mu m$ domain suffices to accommodate the emission pulse width. However, the thresholds shift to lower input energies with increasing widths P. The main reason for this shift lies in the width of the incident beam, which is systematically wider than the emission beam (cf. Fig. 8.9 (a) vs. (b)). For small widths P, the incident pump beam is artificially cut in lateral direction, thus it requires a higher field strength and input energy to achieve the same excitation level in the active material. From Fig. 8.11 we conclude, that for the given input beam width $\sigma_x = 3\,\mu m$ the computational domains should at least have a width of $P = 20\,\mu m$, as the lasing threshold on-set hardly changes for larger widths.

8.3.2 Lasing threshold comparison for the different grating realizations

We finally investigate the lasing of the cavities filled with the silver stripe grating. Here, we distinguish three excitation modes as sketched in Fig. 8.2 (b,c,d). For the regular grating, the focus of the pump beam is either located in a gap $x_0 = 0\,\mu m$ or on a single silver stripe $x_{\text{OSE}} = -2.5\,\mu m$ in OSE. For the defect setup, a single gap in the grating is increased to a width of $w_{\text{defect}} = 4\,\mu m$. Upon defect excitation, the focus is centered on this defect at $x_0 = 0\,\mu m$. We can compute both the lasing thresholds as well as the field distributions for a scan of different pump beam input energies

Similar to the bare cavity investigation of the previous Section 8.3.1 we first consider the field distributions for the different excitation modes, for which the pump beam energies lie just above the lasing threshold. Here, we investigate cavities with DBRs with 17 SiO_2 / TiO_2 layers. Fig. 8.12 shows the time dependence of the electric field distributions at the focus position for each excitation mode. For all three excitation modes, the pump beam has the same field strength. The focused beam duration is the same as for the bare cavity case, namely $T_{\text{pulse}} \approx 4\,ps$. As the excitation pulse energy is set just above the lasing threshold, we only observe a single emission burst for the OSE at $t_{\text{OSE}} \approx 5.3\,ps$ and defect excitation at $t_{\text{def}} \approx 5.8\,ps$ in Fig. 8.12 (a,c). For the gap excitation in Fig 8.12 (b), we observe two emission peaks at different times $t_{\text{gap},1} \approx 5.8\,ps$ and $t_{\text{gap},2} \approx 8\,ps$. In between, the pulses interfere and show a beating pattern, which indicates different emission wavelengths. In all three cases, the remaining emitted field is guided inside the DBR cavity and dissipates due to the silver grating after the main emission into the lower and upper half-space.

Figure 8.13 shows the full two-dimensional emission field patterns corresponding to the emission times presented in Fig. 8.12. For the OSE and the second gap excitation emission pulse the field distributions in Fig. 8.13 (a,c) are mainly determined by the *metal* modes observed in the *cold* cavity characterization from Section 8.2.3. In contrast, the first gap excitation emission pulse, as well as the emission upon defect excitation are supported by the *gap* mode. The latter modes have a Gaussian emission shape and symmetrically emit fields into the upper and lower half-space. The *metal* modes on the contrary show a directional emission into the upper-half space and also show several maxima in lateral direction, which indicate emission into several
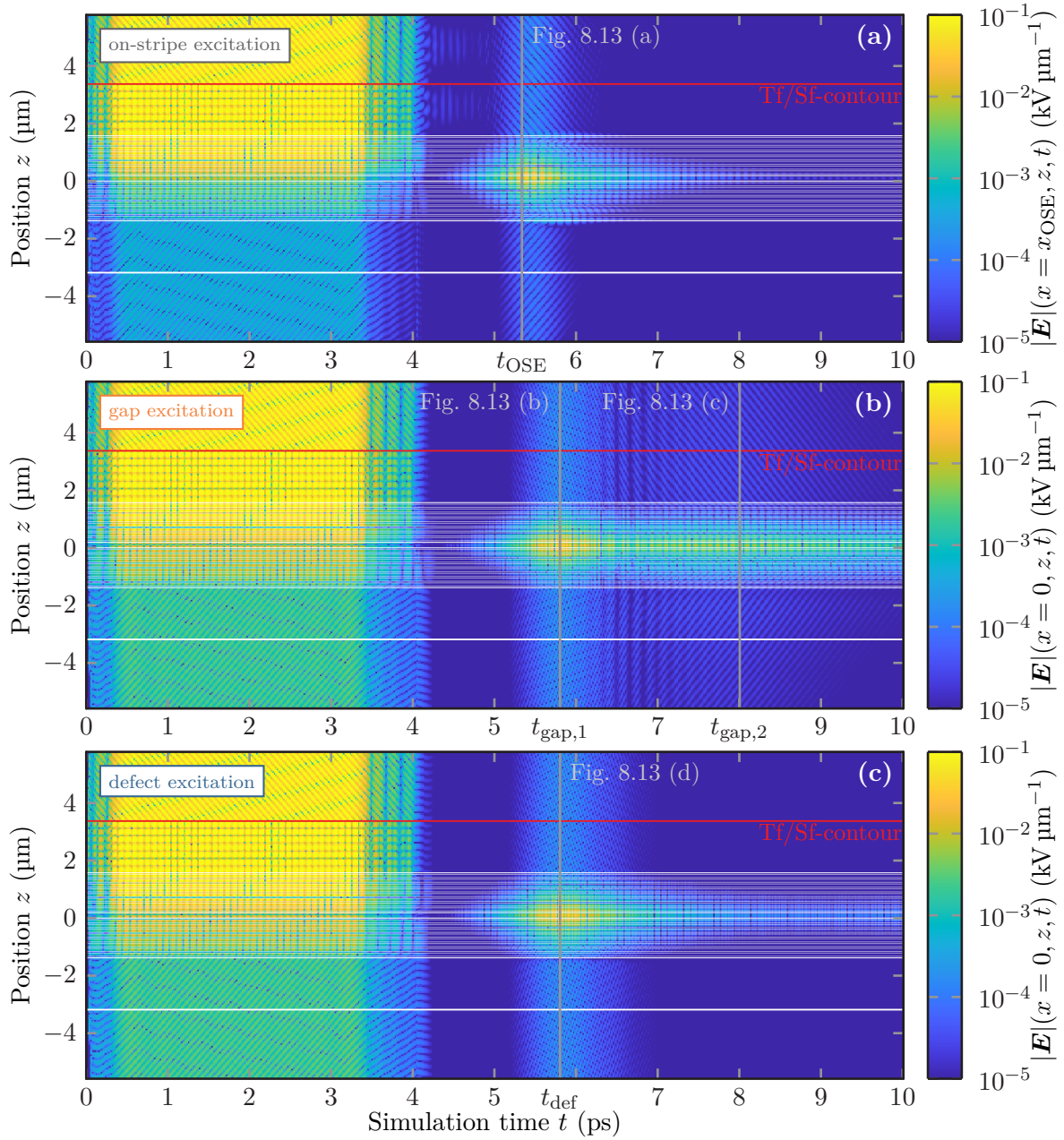
Figure 8.12: Time dependence of the electric field strength at the centerline of the focused beam excitation for three different grating excitation modes according to Fig. 8.2 (b) - (d).

diffraction orders. As both the *gap* as well as *metal* mode are excited upon gap excitation with the focused pump beam, this indeed explains the beating pattern observed in Fig. 8.12 (b) due to the small spectral separation of these two modes (see Fig. 8.6 (c)).

The excitation of both modes clearly depends on the focal position as well as the width of the
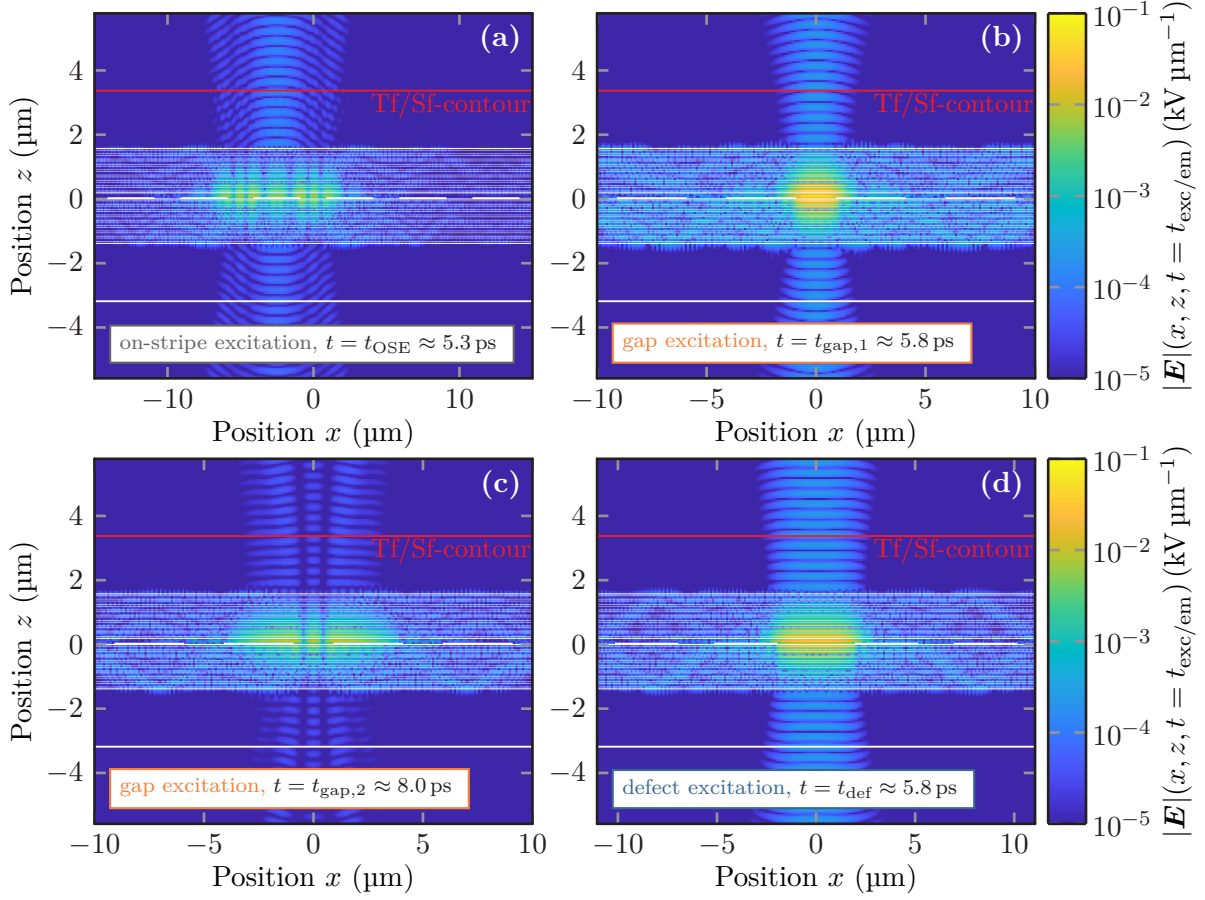
Figure 8.13: Distribution of the electric field strength at the emission times from Fig. 8.2 for the three different excitation modes for the DBR microcavities including the silver grating.

pump beam relative to the gap sizes inside the grating. For the OSE the field distribution is largest upon the stripe focused by the pump beam as well as its two adjacent stripes. For the gap excitation, the pump beam with the focal width $\sigma_x = 3\,\mu m$ is much wider than the actual gap width of $w_{\text{gap}} = 1.9\,\mu m$. Thus, it nearly equally supports the lasing of both modes. The *metal* mode is excited for the two adjacent stripes to the gap. The *gap* mode is highly confined and shows a large beam divergence of the emitted fields. The overall field confinement is even larger than in the defect case, as the defect width $w_{\text{defect}} = 4\,\mu m$ leads to predominant coupling to the corresponding defect mode only. Additionally, these findings are supported by the population inversion distributions ΔN_{12} presented in Fig. 8.14. For the OSE the population inversion Fig. 8.14 (a) is highest on the stripes and also shows the Gaussian shape of the pump beam as before. Yet the nodal lines are shifted according to the reflective silver patterning. For the defect excitation in Fig. 8.14 (b) it is highest in the defect gap of the silver grating. The oscillations in both population inversion distributions originate from the emission into fields guided in the DBR microcavity. These guided fields are also visible in all the field distributions in Fig. 8.13. While most of these field contributions dissipate due to the silver's absorption,
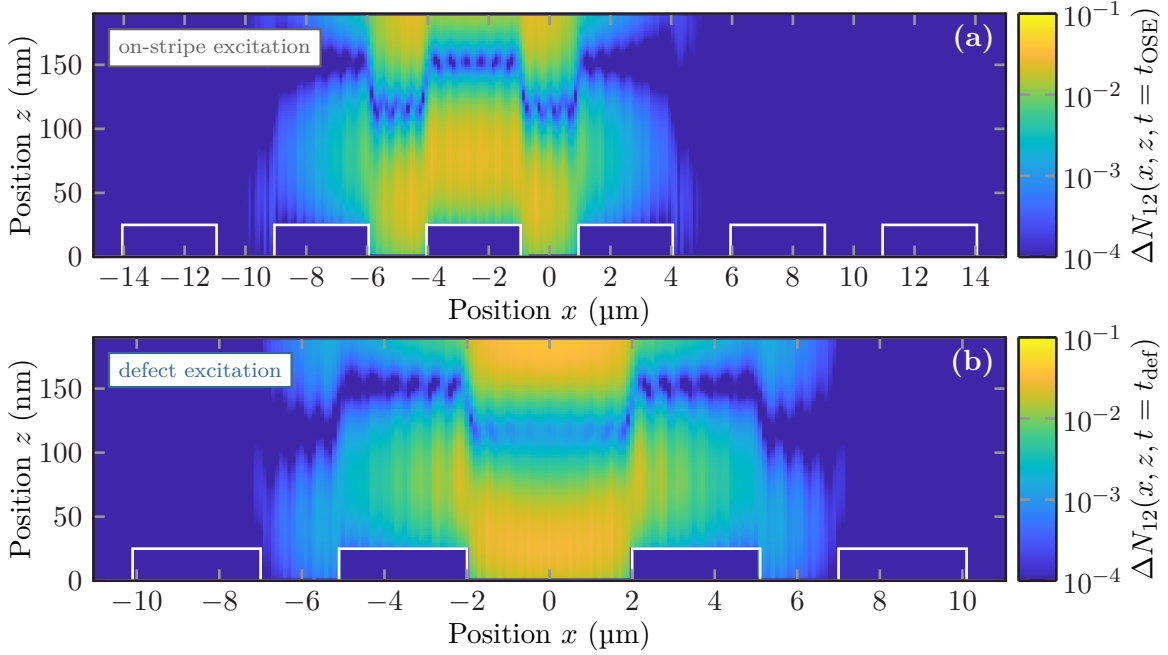
Figure 8.14: Spatial distribution of the population inversion ΔN_{12} both for the OSE **(a)** as well as the defect excitation **(b)**. The distributions are shown for the times of emission according to Fig. 8.12 (a) and (c).

the sufficiently large supercell width $P \geq 20\,\mu\text{m}$ ensures a minute contribution to the lasing thresholds from the guided field scattered from the silver grating.

Understanding the basic contributions of the lasing modes, we next investigate the energy balance of the cavity. It is shown in Fig. 8.15 for all four excitation modes and microcavities with 17 layer DBRs. For all excitation modes the reflection and transmission peak at the driving wavelength $\lambda_{\text{exc}} = 532\,\text{nm}$ is equally pronounced. However, the lasing threshold onsets strongly depend on the focal position of the excitation beam. As already indicated in the field distribution discussion, the position allows for a laser mode switching. For the bare cavity, the system is lasing at the cavity mode wavelength $\lambda_{\text{cav}} = 642\,\text{nm}$. For the OSE only the *metal* mode at $\lambda_{\text{met}} = 632\,\text{nm}$ starts lasing for the scanned input energies. For the excitation of the regular-sized gap, both the *metal* and *gap* mode with $\lambda_{\text{gap}} = 640\,\text{nm}$ start lasing nearly at the same input energy. Widening the gap to the defect leads to a suppression of the *metal* mode lasing and the corresponding defect mode shows the strongest signal.

For comparison to the experimental lasing thresholds, we integrate the output power P_{out} according to Eq. (8.28) for wavelengths $\lambda \in [630\,\text{nm}, 650\,\text{nm}]$. Additionally, we also investigate the dependence on the number of DBR layers, which are set lower than the 21 layers used in the experiment for the lasing threshold DGTD computations. The main reason is, that including a higher number of layers requires more elements to discretize the computational domain. Hence, also the computational effort increases nearly linearly with the number of DBR layers. To achieve comparability between the setups with a different number of DBR layers, we normalize the lasing thresholds to the onset energy of the OSE lasing threshold for each DBR realization.
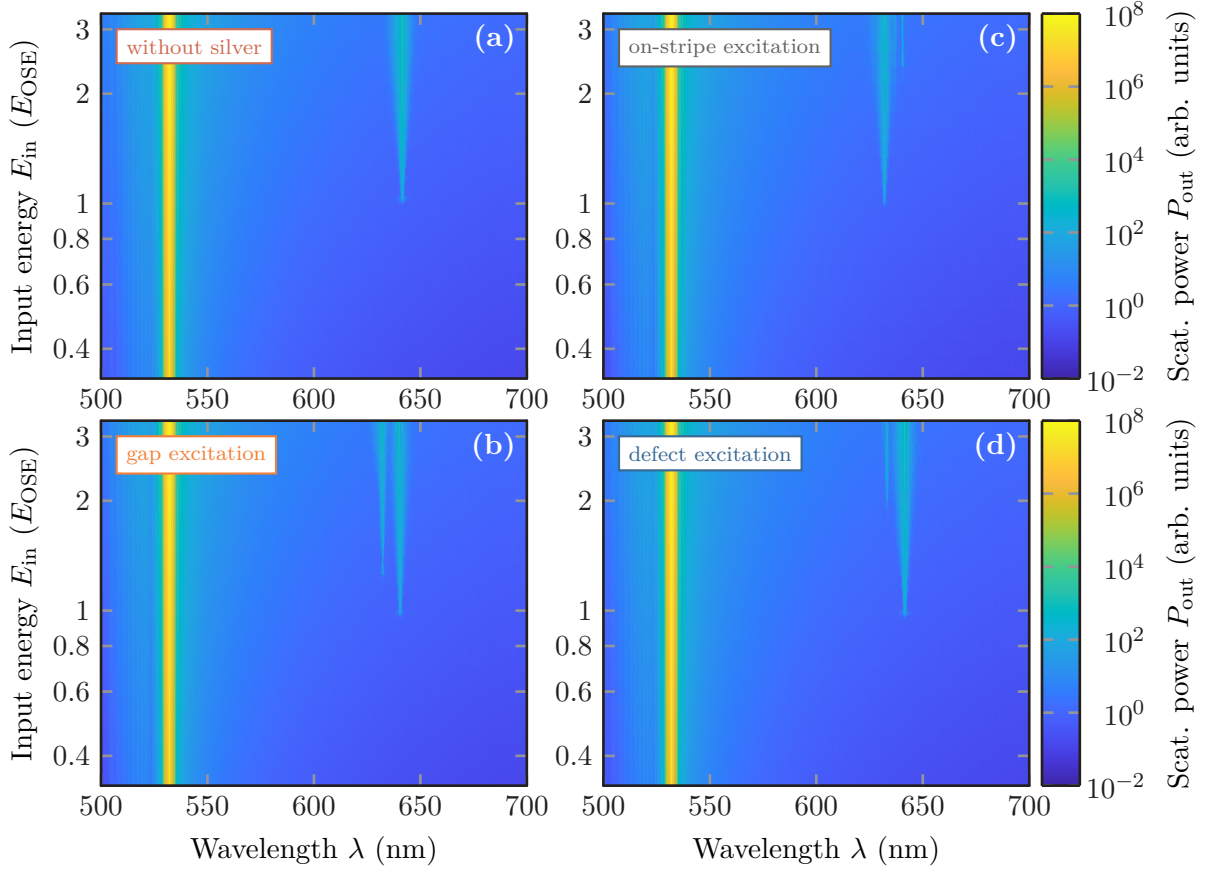
Figure 8.15: Wavelength-resolved scattered power of the DBR cavities in dependence of the focused pump beam input energy E_{in}. The excitation modes for the different panels correspond to those of Fig. 8.2. The input energy is normalized to the lasing threshold onset of the OSE.

The number directly influences the coupling of the pump beam into the cavity, as the spectral position of the transmittance minima near the stopband strongly depends on the layer number (cf. Fig. 8.3).

The lasing thresholds computed for all four excitation modes and an increasing number of DBR layers used for the microcavities are shown in Fig 8.16. In contrast to the experimental observation (see Fig. 8.1), the lasing threshold for the OSE lies significantly lower for small numbers of DBR layers used. This however changes with an increasing number of DBR layers used in the microcavity, such that already for the 17 SiO_2 / TiO_2 DBR layers, the lasing threshold for OSE nearly coincides with the lasing threshold of the bare cavity in Fig. 8.16 (c). The OSE lasing threshold shows a relative shift to higher and higher energies, as the cavity quality factor becomes more and more reliant on the DBR mirroring properties instead of the silver grating. The overall cavity quality factor shifts with an increasing number of DBR layers and the variation in the number of DBR layers shows the trend towards the 21 layers experimental configuration. In
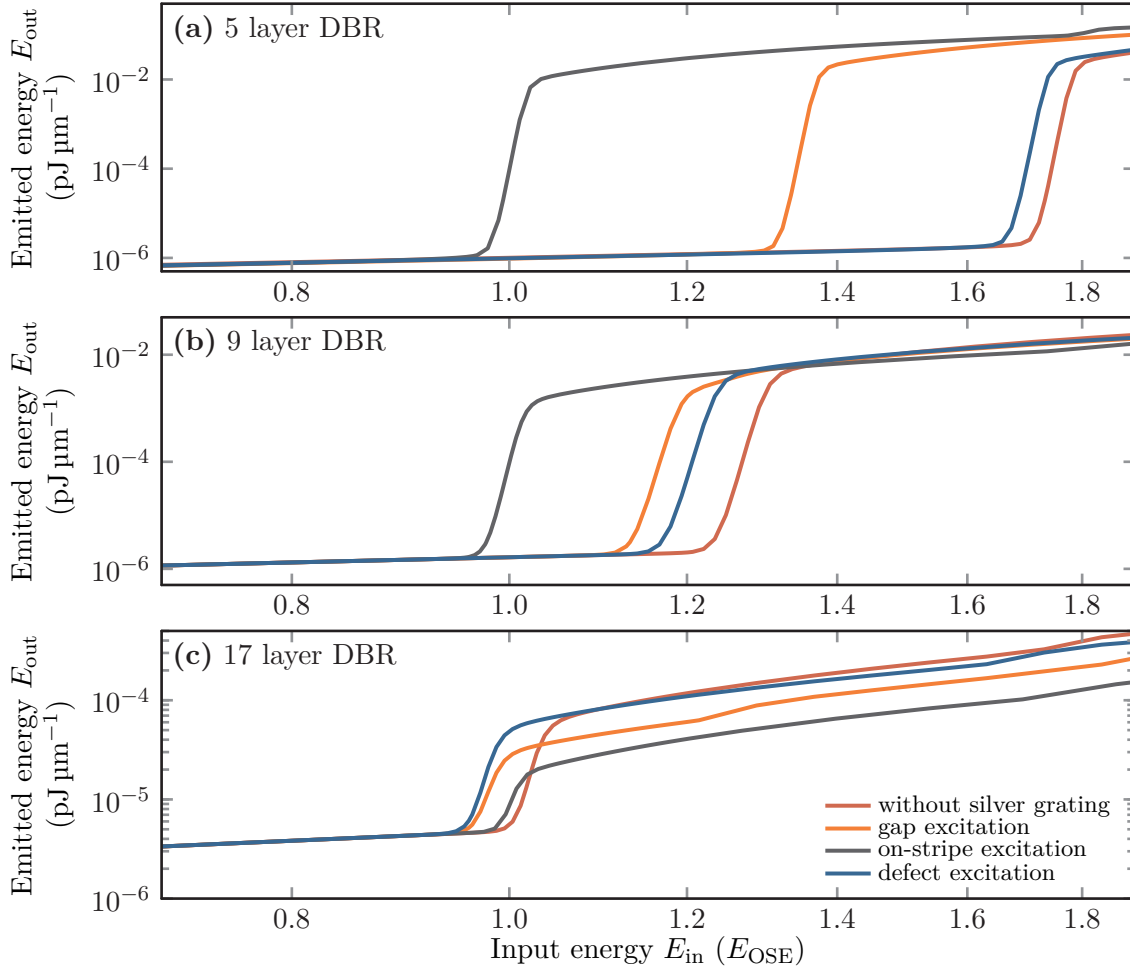
Figure 8.16: Lasing thresholds computed for four different excitation modes with an increasing number of DBR layers used for the microcavities sketched in Fig. 8.2 including a silver grating. The focused beam input energies are normalized to the OSE lasing threshold onset for better comparability of the **(a)** 5, **(b)** 9, and 17 **(c)** layer DBRs used for the microcavities.

all three cases, we notice that the defect excitation threshold always lies below that of the bare cavity, which agrees well with the experiment. This is due to the additional field confinement and plasmonic enhancement of the defect lasing mode. The gap excitation lasing thresholds always lie in between the OSE and the defect lasing thresholds. Here the main reason is that the pump beam width is significantly wider than the gap width itself. Hence, both the *metal* and *gap* modes are excited.

In summary, we qualitatively explained the experimentally obtained lasing threshold. The implementation of the 4LS material model into the DGTD method allows for a wide variety of applications with different geometries. However, the main challenges remain in the long simulation run times required to cover the full non-linear dynamics as well as the determination of all the involved material parameters. Uncertainties in the material parameters normally restrict

the method to qualitative predictions, which still can be very useful for finding a new device design.

CHAPTER 9

Conclusion and outlook

In this thesis, we provided an extension of the discontinuous Galerkin time-domain (DGTD) method for different material models to investigate different nanophotonic setups. We summarize and discuss the results and point out the implications for future works and open challenges.

The investigated systems include a periodically perforated gold film, which supports extraordinary optical transmission (EOT). We provided numerical computations of the transmittance as well as electron energy loss probability (EELP) spectra to characterize the surface plasmon polariton (SPP) modes of the system. These spectra show a good agreement with the ones obtained in the experiment [K7]. This, in principle, allows an in-depth study of the geometry parameters of the gold film to tailor the response and SPPs supported even before manufacturing the actual physical samples.

On the technical level, these electron energy loss spectroscopy (EELS) computations require the implementation of complex frequency-shifted perfectly matched layers (CFSPMLs) to terminate the quasi-infinite gold layer within the finite size computational domain. Although the gold film itself is described with an already implemented Drude and Lorentz model [74], the implementation of the DGTD method in the research group *Theoretical Optics & Photonics (TO&P group)* code required a fix of the CFSPML numerical flux. For this implementation of the split flux [75, 151], we explicitly have shown that it agrees directly with the upwind flux for the CFSPML auxiliary differential equations (ADEs) in conjunction with Maxwell's equations. Furthermore, we expanded the DGTD implementation to allow for simultaneous use of both, total field / scattered field (Tf/Sf) and pure scattered field (Sf) sources. This is required as the electron input field for the EELS computations cannot be directly evaluated as an Sf source within the CFSPMLs, i.e., in the terminated dispersive material.

For the source term itself, we introduced the fields of relativistically moving finite-size charge distributions. The EELS computations require reconstructing the scattered field Green's tensor entries, which actually rely on point charges as source terms. However, the smoothing enables controlled approximate computations of the EELP spectra for electron beam trajectories traversing and also penetrating the sample, e.g., the perforated gold film considered here. In previous studies [163, 212] the smoothing was implicitly mediated by the finite resolution of the Lagrange polynomial basis used in the DGTD scheme. Here, we performed a full smoothing radius analysis comparing the DGTD results to Mie calculations [8, 9, 213] of a Drude metal sphere. We found that the smoothing radius should be set around $\sigma \approx 2\,\mathrm{nm}$ for EELP spectra computations, which rely on the SPPs modes of metallic nanostructures. This proves to be a good choice for the gold film setup. We observed that for all the electron trajectories, in particular those passing through the material, the resulting EELP spectra show a very good qualitative agreement with the experiment.

However, it should be remembered, that these results rely on substantial approximations, i.e., first-order perturbation in the electron energy as well as the no-recoil approximation (NRA). As our implementation lacks a full quantum mechanical description of the electron beam as well as the screening experienced by the electron passing through the material, both approximations should be assessed in future investigations.

Furthermore, the smoothing length used for the excitation electron suggests using a refined material model beyond the simple Drude model. To investigate a potential non-local response as well as plasmon excitations in the material, an extension to a hydrodynamic Drude model description [100, 214, 215] of the conduction electrons can be used with the TO&P group implementation of the DGTD method [216–218].

For the optimization of the magneto-optic (MO) metasurface setup, we implemented the non-dispersive anisotropic material model [77] into the DGTD method. For this, we not only derived the full numerical upwind flux but also performed a complete convergence study in comparison to Mie calculations [78, 79]. Moreover, we implemented a new import function for meshes generated with the help of *gmsh* [140]. Similar to previously used *Netgen* [141] meshing software, the newer *gmsh* versions also support constructive solid geometry [140]. Additionally, *gmsh* offers a wider variety in shape operations, like edge fillets used for the EELS setup or spline curved surfaces extruded into volumes, on which the MO metasurface scatterers rely. The *gmsh* mesher even enables to generate volumes for surfaces with customized roughness [K11] and can even handle intricate topologies like metallic nanosponges [219, 220].

With the use of extruded spline curve shapes for the MO metasurface scatterer lattice, we have been able to outline a shape optimization. It significantly increases the polarization rotation angle. Within a random search, we achieved a 50% enhancement in Faraday rotation compared to the best, same height cylindrical scatterer array [44] maintaining a near-unity transmittance. However, the performed random search should only be understood as the first step of a more sophisticated optimization scheme. As the Faraday rotation angle shows a relatively strong dependence on the scatterer surface shape, it also requires a relatively fine mesh resolution to obtain a decent numerical accuracy. As the stable time-step of the utilized Runge-Kutta solver is restricted by the smallest element in the mesh [76, 142, 164], this requires relatively long simulation run-times up to two days per example structure. Therefore, one should use an optimization algorithm suited for costly objective functions, i.e., figures of merit like the Faraday rotation here. Possible choices can include genetic algorithms [221] or Bayesian optimization schemes [194, 222, 223].

Another method to increase the convergence of strongly surface-dependent quantities, like the Faraday rotation in this specific example, is the use of higher-order, curvilinear elements [185, 186]. However, their implementation is especially cumbersome for non-dispersive anisotropic materials. As the curved surfaces have spatially dependent normal vectors, the impedance and admittance matrices required for the numerical flux need to be evaluated at every single Lagrange interpolation node of the element's surface instead of only once per element face.

As a second anisotropic material, we considered near-infrared (NIR) hyperbolic metamaterial (HMM) cavities. Here, we analyzed the cavity mode structure both for the fully layered material as well as the effective medium approximation (EMA) and compared the results to the experiment

[K3]. We reproduced the mode structure for the tunable ZnO:Ga HMM cavity, which includes a mode accumulation point at the HMM type II upper frequency bound. Due to the doped ZnO:Ga, the cavities cannot only be tailored [K9] with regards to the geometry, i.e., the fill factor of the stacked layers, but also the effective plasma frequency used in the Drude model describing the ZnO:Ga [56] can be changed. Furthermore, we indicated the breakdown of the EMA and showed the persistence of the coupled SPP modes which remain even for subwavelength sized cavities. We computed the full resonances and their dispersion by analytic continuation of the scattering matrix (S-matrix) algorithm. This directly allows for a comparison with the reflectance spectra maxima.

Besides the investigation of differently tuned HMM cavities with different fill factors, layer and overall cavity sizes [K9], such HMM cavities can also be used to tailor the emission characteristics of included emitters, e.g., dye molecules or quantum dots. For the numerical characterization and computation of Purcell factors, future investigations should also focus on the computation of the corresponding Green's tensors in stratified media [224], but can also include the application of the DGTD method both with complete layer stacks [T3] as well as the introduced EMA material model.

Finally, we discussed and investigated a lasing microcavity consisting of two titanium dioxide (TiO$_2$) / silicon dioxide (SiO$_2$) distributed Bragg reflectors (DBRs) and guest:host material with Tris(8-hydroxyquinoline)aluminum (Alq$_3$) as matrix and 4-(dicyanomethylene)-2-methyl-6-[p-(dimethylamino)-styryl]-4H-pyran (DCM) as emitter (Alq$_3$:DCM) as an active material layer. We computed the lasing thresholds for this cavity and compared the lasing thresholds to cavities including a silver grating with and without defect. Here, we qualitatively reproduced the experimentally measured lasing thresholds and could show how the field confinement of the defect state leads to a lasing threshold at lower onset energies as in the case of the metal-free bare cavity [K4]. While the characterization of the cavity modes is obtained from the Fourier modal method (FMM), the computation of the lasing thresholds is based on two-dimensional DGTD computations for transverse magnetic (TM) polarization. For these, we implemented a four-level system (4LS) material model as well as two-dimensional focused beams for the DGTD method.

The evaluation of such focused beams is computationally demanding as it involves two Fourier transforms, which, especially for strongly focused broad-band beams, contain a lot of Fourier components to be added. Here, an improvement can be made in the future by eliminating the frequency-domain Fourier transform exploiting the dispersion relation of the contributing plane waves. This comes at the cost of losing the frequency-independent focal width of the beam. While for the two-dimensional beams used here the numerical effort remains comparably low, it is imperative to exploit the plane wave dispersion for three-dimensional focused beam implementations. While Ref. [225] concentrates on the derivation for such three-dimensional focused beams motivated by geometrical optics, we follow the derivation of the two-dimensional beams in Appendix B, which allows a full characterization of the beam field distribution in the focal plane. A corresponding three-dimensional Gaussian beam has been implemented into the DGTD method code of the *TO&P* group and can be readily used for further application.

One potential example is a recently studied hybrid system of SiO$_2$ and dye-coated silver nanowires to which small gold nanospheres can be attached [19, 226]. The nanowires experience a directional excitation of SPPs upon circular polarized focused beam excitation due to the spin-momentum

locking of light [226, 227]. These systems can act as sensors for chiral, i.e., bi-isotropic materials [86] disturbing the coupling between the nanowires and gold spheres excited with right circular polarization (RCP) or left circular polarization (LCP) beams. The same effect can also be investigated by replacing the gold spheres with MO materials, which would also alter the RCP and LCP coupling to the nanowires.

Besides the extension of the focused beam excitation, also the 4LS used in the two-dimensional case here can be directly extended to the full three-dimensional model. However, one should be careful with the system size and required simulation time. The thin silver grating inside the lasing cavity contains very small mesh elements. This leads to small integration time-steps in the Runge-Kutta solver used for the DGTD method. Thus, the simulation run-time for a single computation takes up to ten days. The same holds for the thin perforated gold layer in the EELS computations which also require up to seven days of simulation run time. To remedy this problem, an extension of the DGTD method into separate regions with different element sizes can be beneficial. It is achieved by a mesh partitioning algorithm and allows for a different time-integration method [228] which uses different time steps for regions with different mesh resolutions. However, the potential decrease in run-time comes at the cost of the need to synchronize the fields at the mesh partition boundaries. Also, the long simulation times of several ten picoseconds in the nonlinear 4LS setups are inconvenient for three-dimensional systems. A potential, yet approximate solution is to describe the dynamics with only a few quasinormal modes (QNMs) [122, 229] and expansion coefficients modeling the full system dynamics.

Overall, we have been able to implement useful material model extensions for the DGTD and FMM. These have been successfully used to describe and characterize the presented experimental setups. Additionally, this opens new applications for the computational characterization as well as optimization of nanophotonic and nanoplasmonic systems.

Electromagnetic field of relativistically moving smoothed charge distributions

Within this appendix, we provide an in-depth derivation of the electromagnetic fields caused by an electron with a smooth charge distribution, which moves at relativistic speeds. Therefore, we make assumptions about the charge distribution in the electron's rest frame in Section A.1. In the following Section A.2, we derive the electromagnetic field in the reference frame, as needed in the EELS computations presented in Chapter 6. These calculated fields act as the incident field (cf. Section 5.4) for the used DGTD method.

A.1 Charge distributions and fields in the rest frame

Normally the computation of EELP spectra or more precisely the components of the scattered field Green's tensor (cf. Section 6.1), requires the electromagnetic field of a constantly moving point charge (electron) with a fixed velocity $\boldsymbol{v}$. Although, a closed-form derivation of the point charge fields is given by evaluation of the Línert-Wichert potentials [81, 167], it is more challenging to calculate the electromagnetic fields in the reference frame for finite-sized charge distributions. An easier way is to first calculate the static electric field in the particle's rest frame and then apply a relativistic boost into the frame of reference needed for the EELS computations. Hence, we first introduce three different rest frame charge distributions and then calculate the corresponding electric fields in the following sections.

As we restrict the charge distributions $\rho = \rho(\varrho)$ to a spherical symmetry, also the electric field has the same symmetry, i.e.,

$$\boldsymbol{E}\left(\boldsymbol{r} - \boldsymbol{r}_0\right) = E_\varrho\left(\varrho\right)\boldsymbol{e}_\varrho . \tag{A.1}$$

Here, the center of the charge distribution lies at $\boldsymbol{r}_0$. In the chosen spherical coordinates $(\varrho, \vartheta, \varphi)$ the radius is defined by $\varrho = |\boldsymbol{r} - \boldsymbol{r}_0|$ and $\boldsymbol{e}_\varrho$ is the corresponding radial unit-vector [230]. To calculate the field, we use the integral formulation [81] of Gauss' law Eq. (2.1a), i.e.,

(SI) $$\int_V \mathrm{d}^3 r\, \nabla \cdot \boldsymbol{E} = \frac{1}{\epsilon_0}\int_V \mathrm{d}^3 r\, \rho\left(\varrho\right) = \int_{\partial V} \boldsymbol{E}\cdot \mathrm{d}\boldsymbol{f} . \tag{A.2}$$

Here, we consider spherical volumes V centered around $\boldsymbol{r}_0$ together with the spherical symmetry assumptions

$$\boldsymbol{E}\left(\boldsymbol{r} - \boldsymbol{r}_0\right) = E_\varrho\left(\varrho\right)\boldsymbol{e}_\varrho \quad \text{and} \quad \mathrm{d}\boldsymbol{f} = \left(\partial_\vartheta \boldsymbol{r} \times \partial_\varphi \boldsymbol{r}\right)\mathrm{d}\vartheta\,\mathrm{d}\varphi = \varrho^2 \sin\vartheta\,\boldsymbol{e}_\varrho\,\mathrm{d}\vartheta\,\mathrm{d}\varphi . \tag{A.3}$$

Hence, for the spherical test volumes with radius ϱ, it follows that

$$
\text{(SI)} \qquad \varrho^2 E_\varrho \left(\varrho \right) 4\pi = \frac{4\pi}{\epsilon_0} \int_0^\varrho \mathrm{d}\varrho' \, \varrho'^2 \rho(\varrho') \,. \qquad \text{(A.4)}
$$

For a given radial charge distribution $\rho \left(\varrho \right)$, we can compute the electric field $\boldsymbol{E}(\boldsymbol{r} - \boldsymbol{r}_0) = E_\varrho(\varrho) \boldsymbol{e}_\varrho$, which is determined by the radial component

$$
\text{(SI)} \qquad E_\varrho \left(\varrho \right) = \frac{1}{\epsilon_0} \frac{1}{\varrho^2} \int_0^\varrho \mathrm{d}\varrho' \, \varrho'^2 \rho(\varrho') \,. \qquad \text{(A.5)}
$$

This rest frame radial electric field component is calculated for three different charge distributions.

A.1.1 Point charge

For completeness, we start with a point charge, i.e.,

$$
\rho \left(\boldsymbol{r} \right) = q \, \delta^{(3)} \left(\boldsymbol{r} - \boldsymbol{r}_0 \right) = \frac{q}{4\pi \varrho^2} \delta(\varrho) \,. \qquad \text{(A.6)}
$$

Consequently, the radial part of the electric field is given by

$$
\text{(SI)} \qquad E_\varrho \left(\varrho \right) \overset{\text{(A.5)}}{=} \frac{q}{4\pi\epsilon_0} \frac{1}{\varrho^2} \,. \qquad \text{(A.7)}
$$

With the radial unit-vector

$$
\boldsymbol{e}_\varrho = \frac{\boldsymbol{r} - \boldsymbol{r}_0}{|\boldsymbol{r} - \boldsymbol{r}_0|} \,, \qquad \text{(A.8)}
$$

the fields in the rest frame take the well-known form (see e.g., [81, 83]):

$$
\text{(SI)} \qquad \boldsymbol{E} \left(\boldsymbol{r}; \boldsymbol{r}_0 \right) = E_\varrho \left(\varrho \right) \boldsymbol{e}_\varrho = \frac{q}{4\pi\epsilon_0} \frac{\boldsymbol{r} - \boldsymbol{r}_0}{|\boldsymbol{r} - \boldsymbol{r}_0|^3} \,. \qquad \text{(A.9)}
$$

As the point charge is at rest the magnetic induction $\boldsymbol{B}(\boldsymbol{r}) = \boldsymbol{0}$ vanishes in the rest frame.

A.1.2 Gaussian charge distribution

As the electron beam used in a scanning transmission electron microscope (STEM) is focused on a finite spot size, we next consider a Gaussian distribution to model the finite expansion of the electron wave function. Given the characteristic width σ_e, the charge distribution takes the form

$$
\rho \left(\varrho \right) = A \, \mathrm{e}^{-\varrho^2/\sigma_e^2} \quad \text{with} \quad A \overset{\text{(A.12)}}{=} \frac{q}{(\sqrt{\pi}\sigma_e)^3} \,. \qquad \text{(A.10)}
$$

Here, the normalization constant A is restricted by the total charge

$$q = \int_V \mathrm{d}^3 r \, \rho(\boldsymbol{r}) \,, \tag{A.11}$$

of the charge distribution and is calculated by

$$
\begin{aligned}
q &= \int_0^{2\pi} \mathrm{d}\varphi \int_{-1}^1 \mathrm{d}\cos\vartheta \int_0^\infty \mathrm{d}\varrho \, \varrho^2 A e^{-\varrho^2/\sigma_e^2} \\
&= 4\pi A \int_0^\infty \mathrm{d}\varrho \, \varrho^2 e^{-\varrho^2/\sigma_e^2} \\
&= -4\pi A \frac{1}{2} \sigma_e \frac{\partial}{\partial \sigma_e^{-1}} \int_0^\infty e^{-\varrho^2/\sigma_e^2} \mathrm{d}\varrho \\
&= -2\pi A \sigma_e \frac{\partial}{\partial \sigma_e^{-1}} \left[\sqrt{\pi} \frac{\sigma_e}{2} \operatorname{erf}\left(\frac{\varrho}{\sigma_e}\right) \right] \Bigg|_{\varrho=0}^{\infty} \\
&= -2\pi A \sigma_e \sqrt{\pi} \frac{1}{2} \left[\left(\frac{\partial}{\partial \sigma_e^{-1}} \sigma_e\right) \operatorname{erf}\left(\frac{\varrho}{\sigma_e}\right) + \sigma_e \left(\frac{\partial}{\partial \sigma_e^{-1}} \operatorname{erf}\left(\frac{\varrho}{\sigma_e}\right)\right) \right] \Bigg|_{\varrho=0}^{\infty} \\
&= -2\pi A \sigma_e \sqrt{\pi} \frac{1}{2} \left[-\sigma_e^2 \operatorname{erf}\left(\frac{\varrho}{\sigma_e}\right) + \sigma_e \varrho \frac{2}{\sqrt{\pi}} e^{-\frac{\varrho^2}{\sigma_e^2}} \right] \Bigg|_{\varrho=0}^{\infty} \\
&= A \sigma_e^3 \sqrt{\pi^3} \,. \tag{A.12}
\end{aligned}
$$

To compute the radial electric field component Eq. (A.5), we need to solve the same radial integral for varying radii ϱ,

$$\int_0^\varrho \mathrm{d}x \, x^2 \rho(x) = A \int_0^\varrho \mathrm{d}x \, x^2 e^{-x^2/\sigma_e^2} \tag{A.13}$$

$$= \frac{A \sigma_e \sqrt{\pi}}{4} \left[\sigma_e^2 \operatorname{erf}\left(\frac{x}{\sigma_e}\right) - \frac{2\sigma_e x}{\sqrt{\pi}} e^{-x^2/\sigma_e^2} \right] \Bigg|_{x=0}^{\varrho} \tag{A.14}$$

$$= \frac{q}{\left(\sqrt{\pi}\sigma_e\right)^3} \frac{\sigma_e \sqrt{\pi}}{4} \left[\sigma_e^2 \operatorname{erf}\left(\frac{\varrho}{\sigma_e}\right) - \frac{2\sigma_e \varrho}{\sqrt{\pi}} e^{-\varrho^2/\sigma_e^2} \right] \tag{A.15}$$

$$= q \left[\frac{1}{4\pi} \operatorname{erf}\left(\frac{\varrho}{\sigma_e}\right) - \frac{\varrho}{\sqrt{4\pi^3}\sigma_e} e^{-\varrho^2/\sigma_e^2} \right] \,. \tag{A.16}$$

Consequently, the radial part of the electric field reads

(SI) $$E_\varrho(\varrho) = \frac{q}{4\pi\epsilon_0} \frac{1}{\varrho^2} \left[\operatorname{erf}\left(\frac{\varrho}{\sigma_e}\right) - \frac{2}{\sqrt{\pi}} \frac{\varrho}{\sigma_e} e^{-\varrho^2/\sigma_e^2} \right] \,. \tag{A.17}$$

A.1.3 Cosine-squared charge distribution

While the Gaussian charge distribution has an infinite fall-off, we also consider a second model, which goes to zero at a finite smoothing radius σ_e. This cosine-squared charge distribution takes the form

$$\rho\left(\varrho\right) = A\cos^2\left(\frac{\pi\varrho}{2\sigma_e}\right)\Theta\left(a-\varrho\right)\quad\text{with}\quad A\overset{\text{(A.25)}}{=}\frac{3\pi}{2(\pi^2-6)}\frac{q}{\sigma_e^3}.\tag{A.18}$$

Both for the normalization of the charge distribution as well as the calculation of the radial part of the electric field, we need to solve the radial integral

$$\int_0^\varrho \mathrm{d}x x^2 \rho\left(x\right) = A\int_0^\varrho \mathrm{d}x x^2 \cos^2\left(\frac{\pi x}{2a}\right)\Theta\left(a-x\right).\tag{A.19}$$

Due to the Heaviside-Theta-function, we only need to consider

$$\int \mathrm{d}x x^2\,\cos^2\left(\frac{\pi x}{2a}\right),\tag{A.20}$$

which can be integrated by parts twice. Here, we require several integrals of the $\cos^2$-function, such as

$$\int \cos^2\left(bx\right)\mathrm{d}x = \frac{1}{b}\int\cos^2\left(y\right)\mathrm{d}y = \frac{1}{2b}\left[bx+\cos\left(bx\right)\sin\left(bx\right)\right],\tag{A.21}$$

and

$$\begin{aligned}\frac{1}{2b}\int\left[bx+\cos\left(bx\right)\sin\left(bx\right)\right]\mathrm{d}x &= \frac{1}{4}x^2 + \frac{1}{2b^2}\int\cos\left(y\right)\sin\left(y\right)\mathrm{d}y\\ &= \frac{1}{4}x^2 - \frac{1}{4b^2}\cos^2\left(bx\right),\end{aligned}\tag{A.22}$$

as well as

$$\int\left[\frac{1}{4}x^2 - \frac{1}{4b^2}\cos^2\left(bx\right)\right]\mathrm{d}x = \frac{1}{12}x^3 - \frac{1}{8b^3}\left[bx+\cos\left(bx\right)\sin\left(bx\right)\right],\tag{A.23}$$

for the integration by parts. As a result, we find with $b=\frac{\pi}{2\sigma_e}$ for the total integral:

$$\begin{aligned}\int\mathrm{d}x x^2\cos^2\left(\frac{\pi x}{2\sigma_e}\right) =&x^2\frac{1}{2b}\left[bx+\cos\left(bx\right)\sin\left(bx\right)\right] - \int 2x\frac{1}{2b}\left[bx+\cos\left(bx\right)\sin\left(bx\right)\right]\mathrm{d}x\\ =&x^2\frac{1}{2b}\left[bx+\cos\left(bx\right)\sin\left(bx\right)\right] - 2x\left[\frac{1}{4}x^2 - \frac{1}{4b^2}\cos^2\left(bx\right)\right]\\ &+2\int\left[\frac{1}{4}x^2 - \frac{1}{4b^2}\cos^2\left(bx\right)\right]\mathrm{d}x\end{aligned}$$

$$
= \frac{1}{6}x^3 + \frac{1}{2b}x^2 \cos{(bx)} \sin{(bx)}
$$

$$
+ \frac{1}{4b^2}x \left[2\cos^2{(bx)} - 1 \right] - \frac{1}{4b^3}\cos{(bx)}\sin{(bx)} \ . \tag{A.24}
$$

Consequently, the charge distribution normalization is given by

$$
q = \int_0^{2\pi} \mathrm{d}\varphi \int_{-1}^{1} \mathrm{d}\cos\vartheta \int_0^{\infty} \mathrm{d}\varrho\, \varrho^2 A \cos\left(\frac{\pi\varrho}{2a}\right) \Theta\left(\sigma_e - \varrho\right)
$$

$$
= 4\pi A \left[\frac{\varrho^3}{6} + \frac{\varrho^2}{2b}\cos{(b\varrho)}\sin{(b\varrho)} + \frac{\varrho}{4b^2}\left[2\cos^2{(b\varrho)} - 1\right] - \frac{1}{4b^3}\cos{(b\varrho)}\sin{(b\varrho)} \right]\Bigg|_{\varrho=0,b=\frac{\pi}{2\sigma_e}}^{\varrho=\sigma_e}
$$

$$
= 4\pi A \left(\frac{\sigma_e^3}{6} - \frac{\sigma_e}{4b^2} \right)\Bigg|_{b=\frac{\pi}{2\sigma_e}}
$$

$$
= 4\pi A \sigma_e^3 \left(\frac{1}{6} - \frac{1}{\pi^2} \right) = A\sigma_e^3 \frac{2(\pi^2 - 6)}{3\pi} \ . \tag{A.25}
$$

Correspondingly, the radial electric field takes the form

$$
E_\varrho(\varrho) = \frac{3q}{8(\pi^2 - 6)\epsilon_0 \sigma_e^3} \frac{1}{\varrho^2} \left[\frac{\varrho^3}{6} + \left(\frac{\varrho^2}{2b} - \frac{1}{4b^3} \right)\cos{(b\varrho)}\sin{(b\varrho)} + \frac{\varrho}{4b^2}\left[2\cos^2{(b\varrho)} - 1\right] \right] \Theta\left(\sigma_e - \varrho\right)
$$

$$
+ \frac{q}{4\pi\epsilon_0 \varrho^2} \Theta\left(\varrho - \sigma_e\right) \ . \tag{A.26}
$$

As expected, the electric field outside the charge distribution's finite radius resembles that of the point charge in Eq. (A.7).

A.2 Fields in the frame of reference

In this section, we apply the Lorentz transformation of the electrostatic fields obtained for the previously discussed charge distributions. For the EELS computations presented in Chapter 6, the charge distributions move at a relativistic speed ($v \approx 0.77c_0$). Apart from the NRA, it is also assumed, that upon interaction with the plasmonic scatterers the shape of the charge distributions is hardly altered. To change into the reference frame Σ' of the plasmonic scatterers we need to consider a boost [81, 167, 168] with the velocity vector $\boldsymbol{v}$ of the electron's center of charge motion, i.e.,

$$
\hat{\boldsymbol{\Lambda}}\left(\boldsymbol{v}\right) = \hat{\boldsymbol{1}} - \gamma\boldsymbol{\beta}\cdot\underline{\underline{\boldsymbol{K}}} + \frac{\gamma - 1}{\beta^2}\left(\boldsymbol{\beta}\cdot\underline{\underline{\boldsymbol{K}}}\right)^2 \ , \tag{A.27}
$$

with

$$\boldsymbol{\beta} = \frac{\boldsymbol{v}}{c_0} \quad \text{and} \quad \gamma = \frac{1}{\sqrt{1 - \beta^2}} \quad \text{and} \quad \underline{\underline{\boldsymbol{K}}} = \left(\hat{\mathbf{K}}_x, \hat{\mathbf{K}}_y, \hat{\mathbf{K}}_z \right)^{\mathrm{T}}$$ (A.28)

where

$$\hat{\mathbf{K}}_x = \begin{pmatrix} 0 & 1 & 0 & 0 \\ 1 & 0 & 0 & 0 \\ 0 & 0 & 0 & 0 \\ 0 & 0 & 0 & 0 \end{pmatrix} \quad \text{and} \quad \hat{\mathbf{K}}_y = \begin{pmatrix} 0 & 0 & 1 & 0 \\ 0 & 0 & 0 & 0 \\ 1 & 0 & 0 & 0 \\ 0 & 0 & 0 & 0 \end{pmatrix} \quad \text{and} \quad \hat{\mathbf{K}}_z = \begin{pmatrix} 0 & 0 & 0 & 1 \\ 0 & 0 & 0 & 0 \\ 0 & 0 & 0 & 0 \\ 1 & 0 & 0 & 0 \end{pmatrix}.$$ (A.29)

Both the fields and the coordinates need to be transformed, to obtain the fields of a constantly moving charge distribution. The boost matrix is equivalent to

$$\hat{\boldsymbol{\Lambda}} \left(\boldsymbol{v} \right) = \begin{pmatrix} \gamma & -\gamma \boldsymbol{\beta}^{\mathrm{T}} \\ -\gamma \boldsymbol{\beta} & \hat{\mathbf{1}}_3 + \frac{\gamma - 1}{\beta^2} \boldsymbol{\beta} \otimes \boldsymbol{\beta} \end{pmatrix}.$$ (A.30)

Accordingly, the Minkowski-space four-vector transforms as

$$\begin{pmatrix} c_0 t' \\ x' \\ y' \\ z' \end{pmatrix} = x'^{\mu} = \hat{\boldsymbol{\Lambda}}^{\mu}{}_{\nu} \left(\boldsymbol{v} \right) x^{\nu} = \begin{pmatrix} \gamma & -\gamma \boldsymbol{\beta}^{\mathrm{T}} \\ -\gamma \boldsymbol{\beta} & \hat{\mathbf{1}}_3 + \frac{\gamma - 1}{\beta^2} \boldsymbol{\beta} \otimes \boldsymbol{\beta} \end{pmatrix} \cdot \begin{pmatrix} c_0 t \\ x \\ y \\ z \end{pmatrix},$$ (A.31)

such that

$$t' = \gamma \left(t - \frac{\boldsymbol{\beta} \cdot \boldsymbol{r}}{c_0} \right),$$ (A.32a)

$$\boldsymbol{r}' = \gamma \left(\frac{1}{\gamma} \boldsymbol{r} - \boldsymbol{v} t + \frac{\gamma - 1}{\gamma} \frac{\boldsymbol{\beta}}{\beta^2} \left(\boldsymbol{\beta} \cdot \boldsymbol{r} \right) \right).$$ (A.32b)

Furthermore, we can determine the electric and magnetic field from the transformation behavior of the field-tensor:

$$F^{\mu\nu} = \begin{pmatrix} 0 & -E_x & -E_y & -E_z \\ E_x & 0 & -c_0 B_z & c_0 B_y \\ E_y & c_0 B_z & 0 & -c_0 B_x \\ E_z & -c_0 B_y & c_0 B_x & 0 \end{pmatrix} =: \begin{pmatrix} 0 & -\boldsymbol{E}^{\mathrm{T}} \\ \boldsymbol{E} & c_0 \hat{\mathbf{B}}^{\times} \end{pmatrix}.$$ (A.33)

The tensor transforms as

$$F'^{\mu\nu} = \Lambda^{\mu}{}_{\rho} \Lambda^{\nu}{}_{\sigma} F^{\rho\sigma},$$ (A.34)

which can also be formulated using matrix notation as the multiplication

$$\hat{\mathbf{F}}' = \hat{\mathbf{\Lambda}} \cdot \hat{\mathbf{F}} \cdot \hat{\mathbf{\Lambda}}^{\mathrm{T}} \, . \tag{A.35}$$

Using

$$\beta^2 = 1 - \frac{1}{\gamma^2} = \frac{\gamma^2 - 1}{\gamma^2} = \frac{(\gamma+1)(\gamma-1)}{\gamma^2} \, , \tag{A.36}$$

we calculate the tensor components

$$
\begin{aligned}
\hat{\mathbf{F}}'^{00} =& -\gamma^2 \boldsymbol{\beta} \cdot \boldsymbol{E} + \gamma^2 \boldsymbol{E} \cdot \boldsymbol{\beta} + \gamma^2 c_0 \left(\boldsymbol{\beta} \times \boldsymbol{B} \right) \cdot \boldsymbol{\beta} \\
=& 0 \, ,
\end{aligned} \tag{A.37a}
$$

$$
\begin{aligned}
\hat{\mathbf{F}}'^{0i} =& \gamma^2 \boldsymbol{\beta}^{\mathrm{T}} \left(\boldsymbol{\beta} \cdot \boldsymbol{E} \right) - \gamma \boldsymbol{E}^{\mathrm{T}} - \gamma c_0 \left(\boldsymbol{\beta} \times \boldsymbol{B} \right)^{\mathrm{T}} \\
& - \gamma \frac{\gamma-1}{\beta^2} \left(\boldsymbol{E} \cdot \boldsymbol{\beta} \right) \boldsymbol{\beta}^{\mathrm{T}} - \gamma \frac{\gamma-1}{\beta^2} c_0 \left[\left(\boldsymbol{\beta} \times \boldsymbol{B} \right) \cdot \boldsymbol{\beta} \right] \boldsymbol{\beta}^{\mathrm{T}} \\
=& -\gamma \left[\boldsymbol{E}^{\mathrm{T}} + c_0 \left(\boldsymbol{\beta} \times \boldsymbol{B} \right)^{\mathrm{T}} \right] + \frac{\gamma^2}{\gamma+1} \left(\boldsymbol{\beta} \cdot \boldsymbol{E} \right) \boldsymbol{\beta}^{\mathrm{T}} \, ,
\end{aligned} \tag{A.37b}
$$

$$
\begin{aligned}
\hat{\mathbf{F}}'^{i0} =& \gamma \boldsymbol{E} + \gamma \frac{\gamma-1}{\beta^2} \left(\boldsymbol{E} \cdot \boldsymbol{\beta} \right) \boldsymbol{\beta} - \gamma^2 \boldsymbol{\beta} \left(\boldsymbol{E} \cdot \boldsymbol{\beta} \right) - \gamma c_0 \boldsymbol{B} \times \boldsymbol{\beta} - \gamma \frac{\gamma-1}{\beta^2} c_0 \left[\left(\boldsymbol{\beta} \times \boldsymbol{B} \right) \cdot \boldsymbol{\beta} \right] \boldsymbol{\beta} \\
=& \gamma \left[\boldsymbol{E}^{\mathrm{T}} + c_0 \left(\boldsymbol{\beta} \times \boldsymbol{B} \right)^{\mathrm{T}} \right] - \frac{\gamma^2}{\gamma+1} \left(\boldsymbol{\beta} \cdot \boldsymbol{E} \right) \boldsymbol{\beta}^{\mathrm{T}} \, ,
\end{aligned} \tag{A.37c}
$$

$$
\begin{aligned}
\hat{\mathbf{F}}'^{ij} =& -\gamma \boldsymbol{E} \boldsymbol{\beta} \otimes \boldsymbol{\beta} - \gamma \frac{\gamma-1}{\beta^2} \boldsymbol{\beta} \otimes \boldsymbol{\beta} \left(\boldsymbol{\beta} \cdot \boldsymbol{E} \right) + \gamma \boldsymbol{\beta} \otimes \boldsymbol{E} + c_0 \hat{\mathbf{B}}^{\times} + \frac{\gamma-1}{\beta^2} c_0 \boldsymbol{\beta} \otimes \left(\boldsymbol{\beta} \times \boldsymbol{B} \right) \\
& + \gamma \frac{\gamma-1}{\beta^2} \boldsymbol{\beta} \otimes \boldsymbol{\beta} \left(\boldsymbol{\beta} \cdot \boldsymbol{E} \right) + \frac{\gamma-1}{\beta^2} c_0 \left(\boldsymbol{B} \times \boldsymbol{\beta} \right) \otimes \boldsymbol{\beta} + \left(\frac{\gamma-1}{\beta^2} \right)^2 c_0 \boldsymbol{\beta} \otimes \boldsymbol{\beta} \left[\left(\boldsymbol{\beta} \times \boldsymbol{B} \right) \cdot \boldsymbol{\beta} \right] \\
=& c_0 \hat{\mathbf{B}}^{\times} + \gamma \left(\boldsymbol{\beta} \otimes \boldsymbol{E} - \boldsymbol{E} \otimes \boldsymbol{\beta} \right) + c_0 \frac{\gamma^2}{\gamma+1} \left[\boldsymbol{\beta} \otimes \left(\boldsymbol{\beta} \times \boldsymbol{B} \right) - \left(\boldsymbol{\beta} \times \boldsymbol{B} \right) \otimes \boldsymbol{\beta} \right] \, .
\end{aligned} \tag{A.37d}
$$

From here, one can directly derive the transformation behavior of the field vectors. It is obvious that the transformed field tensor is antisymmetric, as is the original field tensor. We next show how to obtain the transformed $\boldsymbol{B}$-field components, since they cannot be directly inferred from the equations. We consider the B_z-component entry of $\hat{\mathbf{F}}'$, which demonstrates how to obtain all transformed $\boldsymbol{B}$-field components:

$$
\begin{aligned}
\text{(SI)} \qquad c_0 B_z' =& c_0 B_z + \gamma \left(\beta_y E_x - E_y \beta_x \right) + c_0 \frac{\gamma-1}{\beta^2} \left[\beta_y \left(\boldsymbol{\beta} \times \boldsymbol{B} \right)_x - \left(\boldsymbol{\beta} \times \boldsymbol{B} \right)_y \beta_x \right] \\
=& c_0 B_z - \gamma \left(\boldsymbol{\beta} \times \boldsymbol{E} \right)_z + c_0 \frac{\gamma-1}{\beta^2} \left[\beta_y \left(\beta_y B_z - \beta_z B_y \right) - \left(\beta_z B_x - \beta_x B_z \right) \beta_x \right] \\
=& c_0 B_z - \gamma \left(\boldsymbol{\beta} \times \boldsymbol{E} \right)_z + c_0 \frac{\gamma-1}{\beta^2} \left[\beta^2 B_z - \beta_z \left(\boldsymbol{\beta} \cdot \boldsymbol{B} \right) \right] \\
=& c_0 \gamma B_z - \gamma \left(\boldsymbol{\beta} \times \boldsymbol{E} \right)_z - c_0 \beta_z \frac{\gamma^2}{\gamma+1} \left(\boldsymbol{\beta} \cdot \boldsymbol{B} \right) \, .
\end{aligned} \tag{A.38}
$$

Hence, the electromagnetic fields transform as

(SI)
$$\boldsymbol{E}' = \gamma \left[\boldsymbol{E} + c_0 \left(\boldsymbol{\beta} \times \boldsymbol{B} \right) \right] - \frac{\gamma^2}{\gamma + 1} \boldsymbol{\beta} \left(\boldsymbol{\beta} \cdot \boldsymbol{E} \right) , \tag{A.39a}$$

(SI)
$$\boldsymbol{B}' = \gamma \left[\boldsymbol{B} + \frac{1}{c_0} \left(\boldsymbol{\beta} \times \boldsymbol{E} \right) \right] - \frac{\gamma^2}{\gamma + 1} \boldsymbol{\beta} \left(\boldsymbol{\beta} \cdot \boldsymbol{B} \right) . \tag{A.39b}$$

Both with the field transformation as well as the transformation of space and time Eq. (A.31) we calculate the field distributions in the reference frame Σ'.

The electric field in the rest frame solely depends on the difference between the position $\boldsymbol{r}$ of field evaluation and the position of the charge's center of mass $\boldsymbol{r}_0$. We, therefore, first consider the transformation of this difference vector associating it with the offset $\boldsymbol{r}_0'$ in the reference frame. That means we perform a translation, a boost, and a backward translation in the reference frame, i.e.,

$$
\begin{aligned}
\boldsymbol{r} - \boldsymbol{r}_0 \overset{(A.32)}{=} & \; \boldsymbol{r}' - \boldsymbol{r}_0' - \gamma \boldsymbol{\beta} c_0 t' + \frac{\gamma - 1}{\beta^2} \boldsymbol{\beta} \left[\boldsymbol{\beta} \cdot \left(\boldsymbol{r}' - \boldsymbol{r}_0' \right) \right] \\
= & \; \boldsymbol{r}' \underbrace{- \boldsymbol{r}_0' - \boldsymbol{\beta} c_0 t'}_{-\boldsymbol{R}'(t')} - \left(\gamma - 1 \right) \boldsymbol{\beta} c_0 t' + \frac{\gamma - 1}{\beta^2} \boldsymbol{\beta} \left(\boldsymbol{\beta} \cdot \left(\boldsymbol{r}' - \boldsymbol{r}_0' \right) \right) \\
= & \; \boldsymbol{r}' - \boldsymbol{R}'(t') + \frac{\gamma - 1}{\beta^2} \boldsymbol{\beta} \left[\boldsymbol{\beta} \cdot \left(\boldsymbol{r}' - \boldsymbol{r}' - \boldsymbol{\beta} c_0 t' \right) \right] \\
= & \; \boldsymbol{r}' - \boldsymbol{R}'(t') + \frac{\gamma - 1}{\beta^2} \boldsymbol{\beta} \left[\boldsymbol{\beta} \cdot \left(\boldsymbol{r}' - \boldsymbol{R}'(t') \right) \right] , \\
= & \; \Delta \boldsymbol{R}'(t') + \frac{\gamma - 1}{\beta^2} \boldsymbol{\beta} \left[\boldsymbol{\beta} \cdot \Delta \boldsymbol{R}'(t') \right] .
\end{aligned}
\tag{A.40}
$$

Here,

(SI)
$$\boldsymbol{R}'(t') = \boldsymbol{r}_0' + \boldsymbol{\beta} c_0 t' = \boldsymbol{r}_0' + \boldsymbol{v} t' \tag{A.41}$$

is the center of charge motion trajectory of the charge distribution and $\Delta \boldsymbol{R}'(t') = \boldsymbol{r}' - \boldsymbol{R}'(t')$ is the time-dependent position difference vector to the current charge position. As the electric fields Eq. (A.5) of the charge distribution also depend on the radius ϱ, we also calculate the transformation of

$$
\begin{aligned}
\varrho^2 = (\boldsymbol{r} - \boldsymbol{r}_0)^2 &= \Delta \boldsymbol{R}'^2(t') + 2 \frac{\gamma - 1}{\beta^2} \left[\boldsymbol{\beta} \cdot \Delta \boldsymbol{R}'(t') \right]^2 + \frac{(\gamma - 1)^2}{\beta^4} \beta^2 \left[\boldsymbol{\beta} \cdot \Delta \boldsymbol{R}'(t') \right]^2 \\
&= \Delta \boldsymbol{R}'^2(t') + \frac{2\gamma - 2 + \gamma^2 - 2\gamma + 1}{\beta^2} \left[\boldsymbol{\beta} \cdot \Delta \boldsymbol{R}'(t') \right]^2 \\
&= \Delta \boldsymbol{R}'^2(t') + \frac{\gamma^2 - 1}{\beta^2} \left[\boldsymbol{\beta} \cdot \Delta \boldsymbol{R}'(t') \right]^2 \\
&= \Delta \boldsymbol{R}'^2(t') + \gamma^2 \left[\boldsymbol{\beta} \cdot \Delta \boldsymbol{R}'(t') \right]^2 .
\end{aligned}
\tag{A.42}
$$

This leaves open the transformation of the electric and magnetic fields into the reference frame. For this, we consider the rest frame field distributions

$$\boldsymbol{E}\left(\boldsymbol{r};\boldsymbol{r}_0\right) = E_\varrho\left(\boldsymbol{r};\boldsymbol{r}_0\right)\boldsymbol{e}_\varrho\left(\boldsymbol{r};\boldsymbol{r}_0\right) \quad \text{and} \quad \boldsymbol{B}\left(\boldsymbol{r}\right) = 0\,. \tag{A.43}$$

Here, we exploit the radial charge distribution and the therefore centrosymmetric electric field around $\boldsymbol{r}_0$ in the rest frame. It is

$$E_\varrho\left(\boldsymbol{r};\boldsymbol{r}_0\right) = E_\varrho\left(|\boldsymbol{r}_0 - \boldsymbol{r}|\right) \quad \text{and} \quad \boldsymbol{e}_\varrho\left(\boldsymbol{r};\boldsymbol{r}_0\right) = \frac{\boldsymbol{r} - \boldsymbol{r}_0}{|\boldsymbol{r} - \boldsymbol{r}_0|}\,. \tag{A.44}$$

Consequently, the transformed electric field which still depends on the rest frame coordinates is given by

$$\boldsymbol{E}'\left(\boldsymbol{r};\boldsymbol{r}_0\right) \overset{(A.39)}{=} \gamma\frac{E_\varrho\left(|\boldsymbol{r} - \boldsymbol{r}_0|\right)}{|\boldsymbol{r} - \boldsymbol{r}_0|}\left[\boldsymbol{r} - \boldsymbol{r}_0 - \frac{\gamma - 1}{\gamma\beta^2}\boldsymbol{\beta}\left(\boldsymbol{\beta}\cdot(\boldsymbol{r} - \boldsymbol{r}_0)\right)\right]\,, \tag{A.45}$$

where we used

$$\frac{\gamma}{\gamma + 1} = \frac{\gamma - 1}{\gamma\beta^2}\,. \tag{A.46}$$

Yet, it still requires a change in the reference frame coordinates. The last factor in the transformed electric field is equal to the inverse coordinate transformation of Eq. (A.40) and the remaining factors only depend on the radial component transformed in Eq. (A.42). Consequently, the transformed electric field reads

$$\boldsymbol{E}'(\boldsymbol{r}',t') = \gamma\frac{E_\varrho(\varrho(\boldsymbol{r}',t'))}{\varrho(\boldsymbol{r}',t')}\Delta\boldsymbol{R}'(\boldsymbol{r}',t')\,. \tag{A.47}$$

The corresponding magnetic induction is directly given by Eq. (A.39) as

$$\text{(SI)} \qquad \boldsymbol{B}'(\boldsymbol{r}',t') \overset{(A.39)}{=} \frac{\gamma}{c_0}\boldsymbol{\beta}\times\boldsymbol{E}(\boldsymbol{r},\boldsymbol{r_0}) = \frac{\gamma}{c_0}\frac{E_\varrho(\varrho)}{\varrho}\underbrace{\boldsymbol{\beta}\times(\boldsymbol{r} - \boldsymbol{r}_0)}_{\overset{(A.40)}{=}\boldsymbol{\beta}\times\Delta\boldsymbol{R}'(t')} = \frac{1}{c_0}\boldsymbol{\beta}\times\boldsymbol{E}'(\boldsymbol{r}',t')\,. \tag{A.48}$$

The radial fields for the charge distributions considered in the previous Section A.1 suffice to numerical evaluate the fields as needed in the DGTD method. However, the Sf sources (see Section 5.4.2) used within the DGTD method also require the time-derivatives of these fields. For the magnetic induction, the time-derivative is directly related to that of the electric field by

$$\text{(SI)} \qquad \partial_{t'}\boldsymbol{B}'(\boldsymbol{r}',t') = \frac{1}{c_0}\boldsymbol{\beta}\times\partial_{t'}\boldsymbol{E}'(\boldsymbol{r}',t')\,. \tag{A.49}$$

The time-derivative of the electric field simplifies to

$$\partial_{t'} \boldsymbol{E}'(\boldsymbol{r}',t') \quad = \quad \gamma \partial_{t'} \left[\frac{E_\rho(\varrho)}{\varrho} \left(\boldsymbol{r}' - \boldsymbol{R}'(t') \right) \right]$$

$$\overset{(\text{A.41})}{=} -\gamma \boldsymbol{v} \frac{E_\rho(\varrho)}{\varrho} + \gamma \left(\boldsymbol{r}' - \boldsymbol{R}'(t') - \right) \partial_{t'} \varrho \, \partial_\varrho \frac{E_\rho(\varrho)}{\varrho} \, , \qquad (\text{A.50})$$

where

$$\partial_{t'} \varrho(\boldsymbol{r}',\boldsymbol{t}') = \partial_{t'} \left[\Delta \boldsymbol{R}'^2(\boldsymbol{r}',t) + \gamma^2 \left[\boldsymbol{\beta} \cdot \Delta \boldsymbol{R}'(\boldsymbol{r}',t) \right]^2 \right]^{1/2}$$

$$= -\boldsymbol{v} \cdot \nabla_{\Delta \boldsymbol{R}'} \left[\left| \Delta \boldsymbol{R}' \right|^2 + \gamma^2 \left(\boldsymbol{\beta} \cdot \Delta \boldsymbol{R}' \right)^2 \right]^{1/2}$$

$$= -\frac{\boldsymbol{v} \cdot \left[2\Delta \boldsymbol{R}' + 2\gamma^2 \boldsymbol{\beta} \left(\boldsymbol{\beta} \cdot \Delta \boldsymbol{R}' \right) \right]}{2 \left[\left| \Delta \boldsymbol{R}' \right|^2 + \gamma^2 \left(\boldsymbol{\beta} \cdot \Delta \boldsymbol{R}' \right)^2 \right]^{1/2}}$$

$$= -\frac{\gamma^2 \boldsymbol{v} \cdot \Delta \boldsymbol{R}'(\boldsymbol{r}',\boldsymbol{t}')}{\varrho(\boldsymbol{r},t)} \, . \qquad (\text{A.51})$$

This means that for any given radial charge distribution in the rest frame also the field

$$\frac{1}{\varrho} \partial_\varrho \frac{E_\varrho(\varrho)}{\varrho} \qquad (\text{A.52})$$

has to be calculated in order to numerically evaluate the time-derivated electromagnetic fields.

Before we discuss the smooth charge distributions, we provide the fields for the case of a point charge as presented in Section A.1.1. With the radial part of the electric field in the rest frame according to Eq. A.7, the electromagnetic fields in the reference frame take the well-known form [81, 167]:

$$(\text{SI}) \qquad \boldsymbol{E}'(\boldsymbol{r}',t') = \frac{\gamma q}{4\pi\epsilon_0} \frac{\boldsymbol{r}' - \boldsymbol{r}'_0 - \boldsymbol{v}t'}{\left[(\boldsymbol{r}' - \boldsymbol{r}'_0 - \boldsymbol{v}t')^2 + \gamma^2 [\boldsymbol{\beta} \cdot (\boldsymbol{r}' - \boldsymbol{r}'_0 - \boldsymbol{v}t')]^2 \right]^{\frac{3}{2}}} \, , \qquad (\text{A.53a})$$

$$(\text{SI}) \qquad \boldsymbol{B}'(\boldsymbol{r}',t') = \frac{\gamma q}{4\pi\epsilon_0 c_0} \frac{\boldsymbol{\beta} \times (\boldsymbol{r}' - \boldsymbol{r}'_0 - \boldsymbol{v}t')}{\left[(\boldsymbol{r}' - \boldsymbol{r}'_0 - \boldsymbol{v}t')^2 + \gamma^2 [\boldsymbol{\beta} \cdot (\boldsymbol{r}' - \boldsymbol{r}'_0 - \boldsymbol{v}t')]^2 \right]^{\frac{3}{2}}} \, . \qquad (\text{A.53b})$$

A.2.1 Numerically stable evaluation of the electromagnetic fields

For any finite-sized, i.e., not point-like, charge distribution the electric field takes finite values in the center of the distribution. This raises the problem of accurate numerical evaluation of the electric field formulas derived in the preceding section. Specifically, a problem arises in the

denominators, if

$$\boldsymbol{r}' \to \boldsymbol{R}'(t') \quad \text{and therefore} \quad \varrho \to 0 \, . \tag{A.54}$$

For this, we consider the examples derived in Section A.1. These are the radial field components $E_\varrho(\varrho)/\varrho$ related to the Gaussian charge distribution, i.e.,

$$\text{(SI)} \qquad \frac{E_{\rho,\text{Guass}}(\varrho)}{\varrho} = \frac{q}{4\pi\epsilon_0} \frac{1}{\varrho^3} \left[\text{erf}\left(\frac{\varrho}{\sigma_e}\right) - \frac{2}{\sqrt{\pi}} \frac{\varrho}{\sigma_e} e^{-\varrho^2/\sigma_e^2} \right] \, , \tag{A.55}$$

and the cosine-squared charge distribution, i.e.,

$$\frac{E_{\rho,\cos^2}(\varrho)}{\varrho} = \frac{q}{4\pi\epsilon_0} \frac{1}{\varrho^3} \Theta\left(\varrho - \sigma_e\right) + \frac{3\pi}{8\left(\pi^2 - 6\right)} \frac{q}{\epsilon_0} \frac{1}{\varrho^3} \Theta\left(\sigma_e - \varrho\right) \cdot \tag{A.56}$$

$$\left[\frac{1}{6} \frac{\varrho^3}{\sigma_e^3} + \left(\frac{1}{\pi} \frac{\varrho^2}{\sigma_e^2} - \frac{2}{\pi^3}\right) \cos\left(\frac{\pi}{2} \frac{\varrho}{\sigma_e}\right) \sin\left(\frac{\pi}{2} \frac{\varrho}{\sigma_e}\right) + \frac{1}{\pi^2} \frac{\varrho}{\sigma_e} \left(2\cos^2\left(\frac{\pi}{2} \frac{\varrho}{\sigma_e}\right) - 1\right) \right] \, ,$$

respectively. The field evaluation close to the charge requires a numerically accurate evaluation in the limit

$$\lim_{\varrho \to 0} \frac{E_\rho(\varrho)}{\varrho} \, . \tag{A.57}$$

A Taylor expansion using Mathematica [156] results in the small distance behavior for the Gaussian charge distribution

$$\frac{E_{\rho,\text{Guass}}(\varrho)}{\varrho} = \frac{q}{4\pi\epsilon_0} \frac{1}{\sqrt{\pi}\sigma_e^3} \left(\frac{4}{3} - \frac{4}{5} \frac{\varrho^2}{\sigma_e^2} + \frac{2}{7} \frac{\varrho^4}{\sigma_e^4} - \frac{2}{27} \frac{\varrho^6}{\sigma_e^6} + \mathcal{O}\left(\varrho^8/\sigma_e^8\right)\right) \tag{A.58}$$

and

$$\frac{E_{\rho,\cos^2}(\varrho)}{\varrho} = \frac{q}{4\pi\epsilon_0} \frac{\pi^2}{\left(\pi^2 - 6\right)\sigma_e^3} \left(2 - \frac{6}{5} \left(\frac{\pi}{2} \frac{\varrho}{\sigma_e}\right)^2 + \frac{2}{7} \left(\frac{\pi}{2} \frac{\varrho}{\sigma_e}\right)^4 - \frac{4}{135} \left(\frac{\pi}{2} \frac{\varrho}{\sigma_e}\right)^6 + \mathcal{O}\left(\varrho^8/\sigma_e^8\right)\right) \tag{A.59}$$

for the cosine-squared charge distribution. As both field evaluations contain denominators in the third power of ϱ, the implementation should at least contain the fourth power approximation in order to maintain a numerical field evaluation down to machine accuracy.

For the time-derivatives of the electromagnetic fields in Eq. (A.50), we furthermore need to evaluate the field

$$\text{(SI)} \qquad \frac{1}{\varrho} \partial_\varrho \frac{E_\rho(\varrho)}{\varrho} \overset{\text{(A.5)}}{=} \frac{1}{\epsilon_0} \frac{1}{\varrho} \partial_\varrho \frac{1}{\varrho^3} \int_0^\varrho \text{d}x x^2 \rho(x) = \frac{1}{\epsilon_0} \left(\frac{\rho(\varrho)}{\varrho^2} - 3\frac{E_\rho(\varrho)}{\varrho^3}\right) \, . \tag{A.60}$$

For the Gaussian charge distribution, this is given by

$$\text{(SI)} \quad \frac{1}{\varrho}\partial_\varrho \frac{E_{\rho,\text{Gauss}}(\varrho)}{\varrho} = \frac{q}{\epsilon_0}\left[\frac{1}{(\sigma_e\sqrt{\pi})^3}\frac{e^{-\varrho^2/\sigma_e^2}}{\varrho^2} - \frac{3}{4\pi}\frac{1}{\varrho^5}\left[\text{erf}\left(\frac{\varrho}{\sigma_e}\right) - \frac{2}{\sqrt{\pi}}\frac{\varrho}{\sigma_e}e^{-\varrho^2/\sigma_e^2}\right]\right], \quad \text{(A.61)}$$

and for $\varrho \ll \sigma_e$, we find

$$\text{(SI)} \quad \frac{1}{\varrho}\partial_\varrho \frac{E_{\rho,\text{Gauss}}(\varrho)}{\varrho} = \frac{q}{\epsilon_0}\frac{1}{\sigma_e^5\sqrt{\pi}^3}\left(-\frac{2}{5} + \frac{2}{7}\frac{\varrho^2}{\sigma_e^2} - \frac{1}{9}\frac{\varrho^4}{\sigma_e^4} + \frac{1}{33}\frac{\varrho^6}{\sigma_e^6} + \mathcal{O}\left(\varrho^8/\sigma_e^8\right)\right). \quad \text{(A.62)}$$

Analogously, we find

$$\frac{1}{\varrho}\partial_\varrho \frac{E_{\rho,\cos^2}(\varrho)}{\varrho}$$

$$= \frac{q}{\epsilon_0}\frac{3\pi}{2(\pi^2-6)}\left[\frac{1}{\sigma_e^3\varrho^2}\cos^2\left(\frac{\pi}{2}\frac{\varrho}{\sigma_e}\right)\Theta(\sigma_e - \varrho) - \frac{3}{\varrho^5}\cdot\right.$$

$$\left.\left(\frac{1}{6}\frac{\varrho^3}{\sigma_e^3} + \left(\frac{1}{\pi}\frac{\varrho^2}{\sigma_e^2} - \frac{2}{\pi^3}\right)\cos\left(\frac{\pi}{2}\frac{\varrho}{\sigma_e}\right)\sin\left(\frac{\pi}{2}\frac{\varrho}{\sigma_e}\right) + \frac{1}{\pi^2}\frac{\varrho}{\sigma_e}\left(2\cos^2\left(\frac{\pi}{2}\frac{\varrho}{\sigma_e}\right) - 1\right)\right)\Theta(\sigma_e - \varrho)\right]$$

$$- \frac{3q}{4\pi\epsilon_0}\frac{1}{\varrho^5}\Theta(\varrho - \sigma_e) \quad \text{(A.63)}$$

for the cosine-squared distribution, which for small $\varrho \ll \sigma_e$ is approximated by

$$\frac{1}{\varrho}\partial_\varrho \frac{E_{\rho,\cos^2}(\varrho)}{\varrho} \quad \text{(A.64)}$$

$$= \frac{q}{\epsilon_0}\frac{3\pi^3}{2(\pi^2-6)}\frac{1}{\sigma_e^5}\left(-\frac{1}{10} + \frac{1}{21}\left(\frac{\pi}{2}\frac{\varrho}{\sigma_e}\right)^2 - \frac{1}{135}\left(\frac{\pi}{2}\frac{\varrho}{\sigma_e}\right)^4 + \frac{2}{3465}\left(\frac{\pi}{2}\frac{\varrho}{\sigma_e}\right)^6 + \mathcal{O}\left(\varrho^8/\sigma_e^8\right)\right).$$

The latter also contains the field values

$$\text{(SI)} \quad \frac{1}{\varrho}\partial_\varrho \frac{E_\rho(\varrho)}{\varrho} = \frac{3q}{4\pi\epsilon_0}\frac{1}{\varrho^5} \quad \text{(A.65)}$$

to compute the time-derivatives of the electromagnetic fields Eq. (A.50) for a point charge.

2D-focused beams in the DGTD method

In this appendix, we present a short derivation of the two-dimensional focused beam sources, as used for the computations in the 4LS lasing setup presented in Chapter 8. Moreover, we present the different time dependencies used either for the focused beam source or the plane wave sources used in the computations employing the DGTD method.

B.1 Pulse construction with Fourier transforms

While there is an implementation for a three-dimensional focused beam source available in the *TO&P* group's code source of the DGTD method used, it lacks a two-dimensional version. The three-dimensional version was implemented in the scope of a bachelor's thesis [231] and is basically following [225]. This implementation makes use of the Debye-Wolf diffraction integral [232] and the integration kernel is obtained in a geometrical optics limit in order to avoid one Fourier transform from the frequency into the time domain. While this reduces the numerical evaluation effort, it yet poses some restrictions on the choice of (analytically) known combinations of focal field distributions and the pulse time dependence. For a Gaussian pulse, this, e.g., requires the focal width to vary proportionally to the wavelength of the corresponding frequency component. Therefore, we here perform a complete pulse reconstruction using both one spatial and one temporal Fourier transform. The fields $\boldsymbol{q} = (\boldsymbol{E}, \boldsymbol{H})^{\mathrm{T}}$ are of the form

$$\boldsymbol{q}\left(\boldsymbol{r}, t\right) = \frac{1}{(2\pi)^3} \int \mathrm{d}^2 k \int \mathrm{d}\omega \, \boldsymbol{q}\left(\boldsymbol{k}, \omega\right) \mathrm{e}^{\mathrm{i}\boldsymbol{k}\cdot\boldsymbol{r} - \mathrm{i}\omega t} \,. \tag{B.1}$$

For the derivation of the pulsed source, we assume that the electromagnetic field propagates in the direction $\boldsymbol{n} = (n_x, 0, n_z)^{\mathrm{T}}$, in the effectively two-dimensional simulation domain (cf. Section 2.6.1). As we have seen in Section 2.7 about the field propagation in homogeneous, isotropic material layers the single plane waves obey the dispersion relation

$$k_n = \pm\sqrt{\omega^2 \, \epsilon\mu - k_t^2} \,, \tag{B.2}$$

for both transverse electric (TE) and TM polarization. Here

$$k_n = \boldsymbol{k} \cdot \boldsymbol{n} \quad \text{and} \quad k_t = \boldsymbol{k} \cdot \boldsymbol{t} \tag{B.3}$$

are the in-plane components of the $\boldsymbol{k}$-vector both in respect to the propagation direction $\boldsymbol{n}$ and the transverse direction $\boldsymbol{t} = \boldsymbol{n} \times \boldsymbol{e}_y = (-n_z, 0, n_x)^{\mathrm{T}}$. For a forward propagating focused beam

pulse, we only take wave contributions traveling into positive $\boldsymbol{n}$-direction into account and find

$$E_{y,t}(\boldsymbol{r},t) = \frac{1}{(2\pi)^2} \int \mathrm{d}k_t \int \mathrm{d}\omega \, E_{y,t}\left(k_t,\omega\right) \mathrm{e}^{\mathrm{i}k_t\,\boldsymbol{t}\cdot\boldsymbol{r} - \mathrm{i}k_n(k_t,\omega)\,\boldsymbol{n}\cdot(\boldsymbol{r}-\boldsymbol{r}_0) - \mathrm{i}\omega t} \,, \tag{B.4}$$

for TE polarization (E_y field) and TM polarization (E_t field), respectively. The other field components are then fixed by the two-dimensional Maxwell's equations (2.49). Thus, for TE polarization with

$$H_n\left(k_t,\omega\right) = -\frac{k_t}{\omega\mu} E_y\left(k_t,\omega\right) \quad \text{and} \quad H_t\left(k_t,\omega\right) = \frac{k_n(k_t,\omega)}{\omega\mu} E_y\left(k_t,\omega\right) \,, \tag{B.5}$$

we have

$$H_n(\boldsymbol{r},t) = -\frac{1}{(2\pi)^2} \int \mathrm{d}k_t \int \mathrm{d}\omega \, \frac{k_t}{\omega\mu} E_y\left(k_t,\omega\right) \mathrm{e}^{\mathrm{i}k_t\,\boldsymbol{t}\cdot\boldsymbol{r} - \mathrm{i}k_n(k_t,\omega)\,\boldsymbol{n}\cdot(\boldsymbol{r}-\boldsymbol{r}_0) - \mathrm{i}\omega t} \,, \tag{B.6a}$$

$$H_t(\boldsymbol{r},t) = \frac{1}{(2\pi)^2} \int \mathrm{d}k_t \int \mathrm{d}\omega \, \frac{k_n(k_t,\omega)}{\omega\mu} E_y\left(k_t,\omega\right) \mathrm{e}^{\mathrm{i}k_t\,\boldsymbol{t}\cdot\boldsymbol{r} - \mathrm{i}k_n(k_t,\omega)\,\boldsymbol{n}\cdot(\boldsymbol{r}-\boldsymbol{r}_0) - \mathrm{i}\omega t} \,. \tag{B.6b}$$

Analogously, in TM polarization with

$$E_n\left(k_t,\omega\right) = -\frac{k_t}{k_n(k_t,\omega)} E_t\left(k_t,\omega\right) \quad \text{and} \quad H_y\left(k_t,\omega\right) = -\frac{\omega\epsilon}{k_n(k_t,\omega)} E_t\left(k_t,\omega\right) \,, \tag{B.7}$$

we find that

$$E_n(\boldsymbol{r},t) = -\frac{1}{(2\pi)^2} \int \mathrm{d}k_t \int \mathrm{d}\omega \, \frac{k_t}{k_n(k_t,\omega)} E_t\left(k_t,\omega\right) \mathrm{e}^{\mathrm{i}k_t\,\boldsymbol{t}\cdot\boldsymbol{r} - \mathrm{i}k_n(k_t,\omega)\,\boldsymbol{n}\cdot(\boldsymbol{r}-\boldsymbol{r}_0) - \mathrm{i}\omega t} \,, \tag{B.8a}$$

$$H_y(\boldsymbol{r},t) = \frac{1}{(2\pi)^2} \int \mathrm{d}k_t \int \mathrm{d}\omega \, \frac{\omega\epsilon}{k_n(k_t,\omega)} E_t\left(k_t,\omega\right) \mathrm{e}^{\mathrm{i}k_t\,\boldsymbol{t}\cdot\boldsymbol{r} - \mathrm{i}k_n(k_t,\omega)\,\boldsymbol{n}\cdot(\boldsymbol{r}-\boldsymbol{r}_0) - \mathrm{i}\omega t} \,. \tag{B.8b}$$

Consequently, the fields are solely determined by the transverse $E_{y,t}$-field components of the respective polarization.

Assuming, we do know the field distribution in the focal plane, in two dimensions it actually is a line, being

$$E_{y,t}\left(\boldsymbol{r} = \tilde{t}\,\boldsymbol{t} + \tilde{n}_0\,\boldsymbol{n}, t\right) = E_{0y,0t}\, f(\tilde{t})\, \eta(t) \,, \tag{B.9}$$

we can already fix the Fourier expansion coefficients in equation (B.4). Here, we defined the transverse and normal coordinates

$$\tilde{t} := \boldsymbol{t} \cdot \boldsymbol{r} \quad \text{and} \quad \tilde{n} := \boldsymbol{n} \cdot \boldsymbol{r} \,. \tag{B.10}$$

Moreover, the focus shall lie at

$$\boldsymbol{r}_0 = \tilde{n}_0\boldsymbol{n} + \tilde{t}_0\boldsymbol{t} = \left(x_0, 0, z_0\right)^{\mathrm{T}} \,. \tag{B.11}$$

Given the focal plane's field, the integrals (B.4) decouple and we can determine the Fourier

coefficients directly by two independent Fourier transforms both for the spatial pulse profile $f(\tilde{t})$ and the time dependence $\eta(t)$ of the pulse:

$$E_{y,t}\left(k_t,\omega\right) = E_{0y,0t} \underbrace{\int \mathrm{d}\tilde{t}\, f(\tilde{t}) \mathrm{e}^{-\mathrm{i}k_t\tilde{t}}}_{f(k_t)} \underbrace{\int \mathrm{d}t\, \eta(t) \mathrm{e}^{\mathrm{i}\omega t}}_{\eta(\omega)} .$$

$(\mathrm{B}.12)$

For the spatial profile, we here want to model a two-dimensional Gaussian pulse, hence

$$f(\tilde{t}) = \mathrm{e}^{-\frac{(\tilde{t}-\tilde{t}_0)^2}{2\sigma^2}} .$$

$(\mathrm{B}.13)$

Here, σ is the pulses' transverse width around the focus point coordinate $\tilde{t}_0$. For the numerical reconstruction of the field, we also need the Fourier transformed function being

$$
\begin{aligned}
f(k) &= \int_{-\infty}^{\infty} \mathrm{d}x\, f(x) \mathrm{e}^{\mathrm{i}kx} \\
&= \int_{-\infty}^{\infty} \mathrm{d}x\, \exp\left(-\frac{1}{2\sigma^2}\left((x-x_0)^2 + \mathrm{i}2\sigma^2 kx\right)\right) \\
&= \exp\left(-\frac{k^2\sigma^2}{2} - \mathrm{i}kx_0\right) \underbrace{\int_{-\infty}^{\infty} \mathrm{d}x\, \exp\left(-\frac{(x+\mathrm{i}k\sigma^2-x_0)^2}{2\sigma^2}\right)}_{\sqrt{2\pi}\sigma} \\
&= \sqrt{2\pi}\sigma \exp\left(-\frac{k^2\sigma^2}{2} - \mathrm{i}kx_0\right) .
\end{aligned}
$$

$(\mathrm{B}.14)$

For the time dependence $\eta(t)$, we use two different functional dependencies, both using a modulated carrier with frequency ω_0 but different envelope functions. In the following sections, we present both once a Gaussian modulated pulse (see Section B.2.1) and a polynomial ramped constant envelope (see Section B.2.2). For both, we also derive the spectrum $\eta(\omega)$ required to numerically reconstruct the pulse.

For the actual numerical evaluation of the integrals (B.4), (B.6), and (B.8) we approximate both the k_t-space as well as the ω-integral by finite sums, i.e., we perform a discrete Fourier transform. Both k_t and ω are sampled equidistantly. Introducing the transversal spatial repetition length L_{rep} and temporal repetition time T_{rep}, the sampling intervals (Nyquist frequencies) can be determined as

$$\Delta k_t = \frac{\pi}{L_{\mathrm{rep}}} \quad \text{and} \quad \Delta\omega = \frac{\pi}{T_{\mathrm{rep}}} ,$$

$(\mathrm{B}.15)$

using the sampling theorem (see e.g., [130, 131]). Consequently, the fields are computed as

$$E_{y,t}(\boldsymbol{r},t) \approx \sum_{i=-N_k}^{N_k} \sum_{j=-N_{\omega,\mathrm{l}}}^{N_{\omega,\mathrm{u}}} \frac{\Delta k_t \Delta\omega}{(2\pi)^2} \mathrm{Re}\left[E_{y,t}(i\Delta k_t, \omega_0 + j\Delta\omega)\mathrm{e}^{\mathrm{i}(k_i\boldsymbol{t}\cdot\boldsymbol{r} - k_n(k_i,\omega_j)\boldsymbol{n}\cdot(\boldsymbol{r}-\boldsymbol{r}_0) - \omega_j t)}\right] .$$

$(\mathrm{B}.16)$
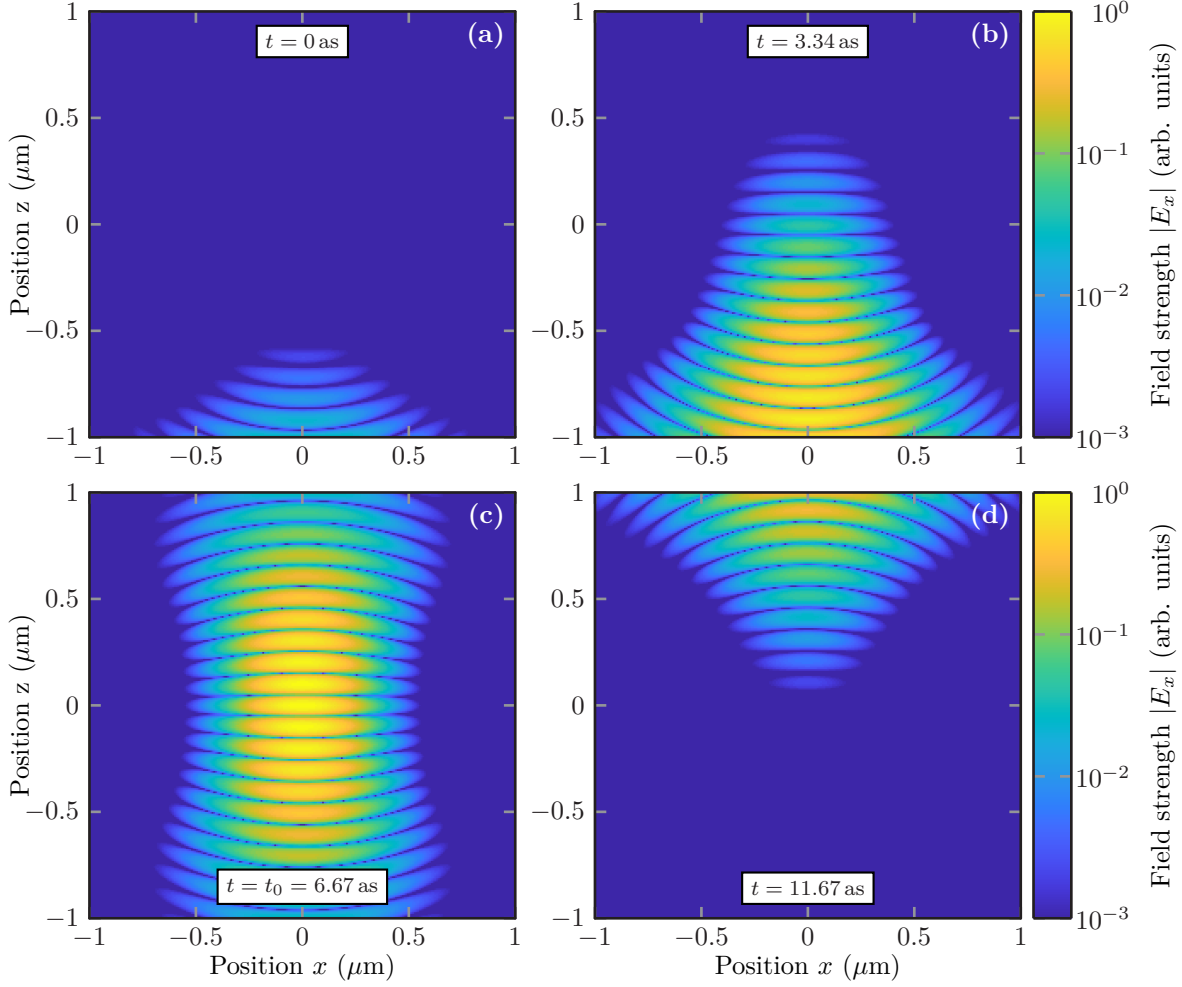
Figure B.1: Field distribution of an exemplary Gaussian beam pulse in TE polarization propagating in positive z-direction for different times t.

Here, we defined

$$k_i = i\Delta k_t \quad \text{and} \quad \omega_j = \omega_0 + j\Delta\omega \,, \tag{B.17}$$

where in k-space we take a symmetric sampling around $k_t = 0$, as the spectrum (B.14) peaks around that value. For the ω-integration, we sample around the carrier frequency ω_0, as all spectra of the time dependencies in question peak around that value. At the same time, we only include terms with positive frequencies ω and afterward compute the real part, as the fields themselves are supposed to be real-valued. Furthermore, we restrict the summation range, i.e., integration boundaries, by setting the N_k and N_ω values. We use the knowledge of the spectral widths of the $f(k)$ and $\eta(\omega)$ functions. For the k-space integral we set

$$N_k = \left\lceil \frac{f_k}{\sigma \Delta k_t} \right\rceil \,, \tag{B.18}$$

with a default factor $f_k = 4.5$ spectral widths. Analogously, given the (Gaussian) spectral width σ_ω of the spectrum $\eta(\omega)$, we set

$$N_{\omega,\mathrm{u}} = \left\lceil \frac{f_\omega}{\sigma_\omega \Delta\omega} \right\rceil \quad \text{and} \quad N_{\omega,\mathrm{l}} = \begin{cases} \left\lceil \frac{\omega_0}{\Delta\omega} - 1 \right\rceil & \text{if} \quad \omega_0 - \frac{f_\omega}{\sigma_\omega \Delta\omega} < \frac{\Delta\omega}{2}, \\ \left\lceil \frac{f_\omega}{\sigma_\omega \Delta\omega} \right\rceil & \text{else}. \end{cases} \tag{B.19}$$

For the lower boundary, the additional restriction is applied in order to only sum over positive values of ω. Again with a default factor of $f_\omega = 4.5$ spectral widths. These factors have been chosen empirically in order to restore at least a relative evaluation accuracy of 10^{-3}, which normally is also the accuracy achieved by the DGTD computations (cf. Section 7.1). Increasing these factors leads to a higher integration accuracy. The integrals for the Gaussian spectra even converge exponentially. However, simultaneously the evaluation time of the field values increases, as more and more k- and ω-components need to be summed up. These fields need to be evaluated as source terms (cf. Section 5.4) for each and every time step in the DGTD method. Note that the fields evaluated outside the first repetition length and repetition time are set to zero in order to achieve a faster evaluation.

In Figure B.1 we present a typical pulse, as it propagates through vacuum. For this example, we use a Gaussian modulated time dependence width a temporal width of $\sigma = 1.34\,\mathrm{as}$ and a carrier wavelength of $\lambda = \frac{2\pi c_0}{\omega_0} = 0.2\,\mathrm{\mu m}$. The pulse reaches its field maximum at $t_0 = 6.67\,\mathrm{as}$ in the focus. This TE-polarized example pulse is focused at $\boldsymbol{r}_0 = \left(0\,\mathrm{\mu m}, 0\,\mathrm{\mu m}\right)^{\mathrm{T}}$ and has a beamwidth of $\sigma_x = 0.15\,\mathrm{\mu m}$. The exact form of the time dependencies used is presented in the following section.

B.2 Pulse time dependencies and spectra

Time-domain computations normally start with an overall zero-field initial condition. The sources relying on the Tf/Sf source (see Section 5.4.1) or scattered field source scheme (see Section 5.4.2) need also to be zero at the start time of the computation. This is necessary to avoid immediate field jumps at the computation start with a broad frequency spectrum and high-frequency components as the main cause for numerical errors. Hence, normally pulsed sources are used. This includes plane wave sources (see Section 5.4 or e.g., [75]), dipole sources (see e.g., [117]), or the focused beam source discussed above for the two-dimensional case and in [225, 231] for the three-dimensional case.

In this section, we discuss two time dependencies used in the computations presented in the thesis. Both time dependencies feature a modulated carrier wave with an angular frequency ω_0. In Section B.2.1 we present a Gaussian modulated time dependence, while in Section B.2.2 we present a constant envelope pulse, which is ramped up and down with polynomial functions.
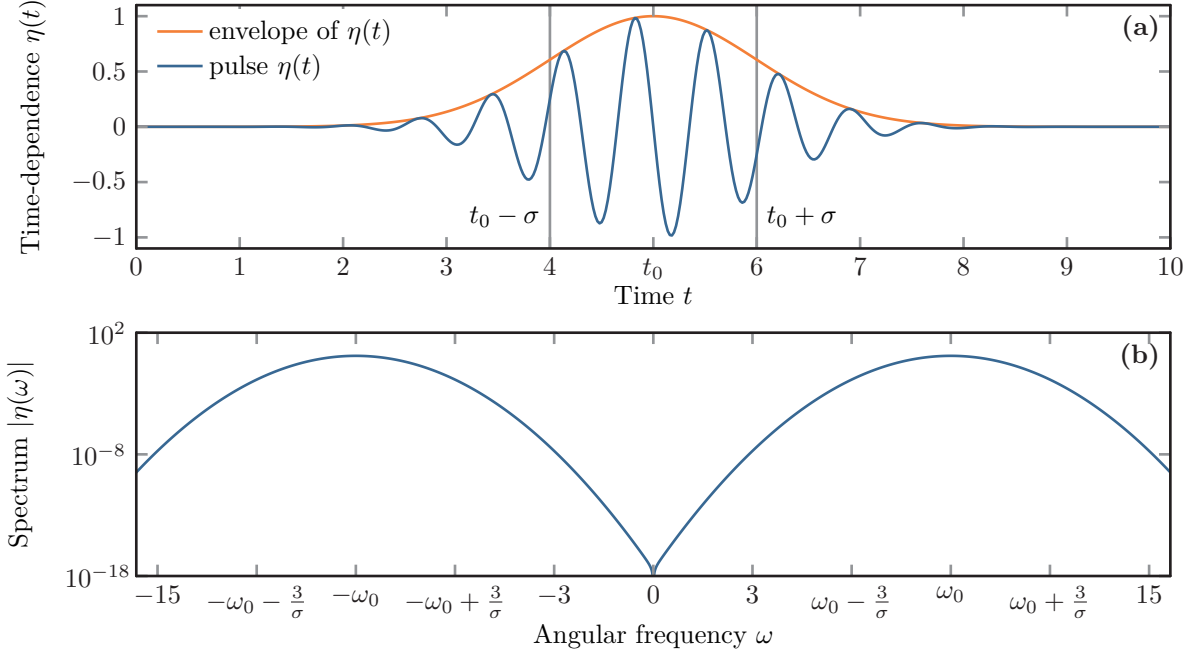
Figure B.2: Gaussian time dependence $\eta(t)$) **(a)** as well as the associated spectrum $|\eta(\omega)|$ **(b)** in dependence of the temporal width σ and time-offset t_0 for example parameters.

B.2.1 Gaussian modulated pulse

For the Gaussian pulse, we take a Gaussian envelope with width σ and amplitude A. It modulates the carrier wave with frequency ω_0 and constant phase-shift ϕ_0. The entire pulse is shifted to a center time t_0 at which the pulse reaches its maximum:

$$\eta(t) = A \cos\left(\omega_0(t - t_0) + \phi_0\right) e^{-\frac{(t-t_0)^2}{2\sigma^2}} \,. \tag{B.20}$$

For the reconstruction of the two-dimensional focused beam source, we need the Fourier transform

$$\eta(\omega) = \int_{-\infty}^{\infty} dt \, \eta(t) e^{i\omega t} \,. \tag{B.21}$$

Splitting the cosine function into two exponential functions, the derivation works analogously as shown in Eq. (B.14), which results in

$$\eta(\omega) = \sqrt{\frac{2}{\pi}} A \sigma e^{i\omega t_0} \left(e^{i\phi_0} e^{-\frac{\sigma^2(\omega+\omega_0)^2}{2}} + e^{-i\phi_0} e^{-\frac{\sigma^2(\omega-\omega_0)^2}{2}} \right) \,. \tag{B.22}$$

This spectrum basically consists of two Gaussian functions centered around $\pm\omega_0$, with a spectral width of σ^{-1}. Figure B.2 shows both the time dependence $\eta(t)$ as well as the spectrum $|\eta(\omega)|$. Here, the amplitude is set to $A = 1$, the time offset to $t_0 = 5$, and the temporal width to $\sigma = 1$.

The carrier frequency is set to $\omega_0 = 2\pi$ in this example.

B.2.2 Ramped continuous wave

For the continuous wave pulse, we use a constant amplitude A to modulate the carrier wave with angular frequencies ω_0 and phase ϕ_0. For the ramping, we design the envelope function such, that we use polynomials, which are ramped up and down between zero and one, while its first and second derivatives are zero both at the start and end times of the ramps. We demand this behavior, as different kinds of sources also require the evaluation of the first and second derivatives of the time dependence, which should not abruptly jump in order to be compatible with the numerical DGTD solver. We define

$$\eta\left(t-t_0\right) = \eta\left(\tau\right) = A \begin{cases} \left(10x_1^3 - 15x_1^4 + 6x_1^5\right)\cos\left(\omega_0\tau - \phi_0\right) & \text{for } \tau \in \left[0, t_1\right]\,, \\ \cos\left(\omega_0\tau - \phi_0\right) & \text{for } \tau \in \left[t_1, t_2\right]\,, \\ \left(1 - 10x_2^3 + 15x_2^4 - 6x_2^5\right)\cos\left(\omega_0\tau - \phi_0\right) & \text{for } \tau \in \left[t_2, t_3\right]\,, \\ 0 & \text{else}\,, \end{cases} \tag{B.23}$$

where

$$\tau = t - t_0\,, \quad x_1 = x(\tau, 0, t_1) = \frac{\tau - 0}{t_1 - 0} \quad \text{and} \quad x_2 = x(\tau, t_2, t_3) = \frac{\tau - t_2}{t_3 - t_2}\,. \tag{B.24}$$

The entire pulse is shifted by the time t_0. Furthermore, the times $t_{\text{up}} = t_1 - t_0$ and $t_{\text{down}} = t_3 - t_2$ are the ramp-up and ramp-down time spans, respectively. The entire pulse duration is $T_{\text{pulse}} = t_3 - t_0$. The prefactors of the ramping polynomial are set by the restrictions on its derivatives both at start times t_0 and t_2 as well as end times t_1 and t_3.

As the computation of the two-dimensional focused beam requires the spectrum of the time dependence, we calculate the Fourier transform:

$$\eta\left(\omega\right) = \int_{-\infty}^{\infty} \mathrm{d}t\, \eta\left(t\right) \mathrm{e}^{\mathrm{i}\omega t} = \int_{-\infty}^{\infty} \mathrm{d}\tau\, \eta\left(\tau\right) \mathrm{e}^{\mathrm{i}\omega(\tau + t_0)}\,. \tag{B.25}$$

For this, we split the integral into three different parts, namely

$$\eta\left(\omega\right) = A\mathrm{e}^{\mathrm{i}\omega t_0} \underbrace{\int_0^{t_1} \mathrm{d}\tau\, \left(10x_1^3 - 15x_1^4 + 6x_1^5\right)\cos\left(\omega_0\tau - \phi_0\right)\mathrm{e}^{\mathrm{i}\omega\tau}}_{I_1\left(\omega, 0, t_1\right)}$$

$$+ A\mathrm{e}^{\mathrm{i}\omega t_0} \underbrace{\int_{t_1}^{t_3} \mathrm{d}\tau\, \cos\left(\omega_0\tau - \phi_0\right)\mathrm{e}^{\mathrm{i}\omega\tau}}_{I_2\left(\omega, t_1, t_3\right)}$$

$$- A\mathrm{e}^{\mathrm{i}\omega t_0} \underbrace{\int_{t_2}^{t_3} \mathrm{d}\tau \left(10x_2^3 - 15x_2^4 + 6x_2^5\right) \cos\left(\omega_0\tau - \phi_0\right) \mathrm{e}^{\mathrm{i}\omega\tau}}_{I_1\left(\omega, t_2, t_3\right)}. \tag{B.26}$$

First, we calculate the Fourier transform of the constant envelope part of the pulse, i.e.,

$$
\begin{aligned}
I_2\left(\omega, t_1, t_3\right) &= \int_{t_1}^{t_3} \mathrm{d}\tau \, \cos\left(\omega_0\tau - \phi_0\right) \mathrm{e}^{\mathrm{i}\omega\tau} \\
&= \frac{1}{2} \int_{t_1}^{t_3} \mathrm{d}\tau \left(\mathrm{e}^{\mathrm{i}(\omega_0\tau - \phi_0)} + \mathrm{e}^{-\mathrm{i}(\omega_0\tau - \phi_0)}\right) \mathrm{e}^{\mathrm{i}\omega\tau}, \\
&= I_2^+\left(\omega, t_1, t_3\right) + I_2^-\left(\omega, t_1, t_3\right),
\end{aligned} \tag{B.27}
$$

where the two split integrals are

$$
\begin{aligned}
I_2^{\pm}\left(\omega, t_1, t_3\right) &= \frac{1}{2} \int_{t_1}^{t_3} \mathrm{d}\tau \, \mathrm{e}^{\mathrm{i}(\omega \pm \omega_0)\tau \mp \mathrm{i}\phi_0}, \\
&= \frac{1}{2}\mathrm{e}^{\mp\mathrm{i}\phi_0}
\begin{cases}
\frac{1}{\mathrm{i}(\omega \pm \omega_0)} \left[\mathrm{e}^{\mathrm{i}(\omega \pm \omega_0)t_3} - \mathrm{e}^{\mathrm{i}(\omega \pm \omega_0)t_1}\right] & \text{for } \omega \neq \mp\omega_0, \\
t_3 - t_1 & \text{for } \omega = \mp\omega_0.
\end{cases}
\end{aligned} \tag{B.28}
$$

As the numerical evaluation of $I_2^{\pm}$ with the frequency difference in the denominator is prone to rounding errors for $\omega \approx \pm\omega_0$, we use the Taylor expansion around this point:

$$I_2^{\pm}\left(\omega = \mp\omega_0 + \delta_\omega, t_1, t_3\right) = \frac{1}{2}\mathrm{e}^{\mathrm{i}\delta_\omega \mp \mathrm{i}\phi_0}(t_3 - t_1)\left[1 + \frac{i}{2}\delta_\omega(t_3 - t_1) + \mathcal{O}\left(\left[\delta_\omega(t_3 - t_1)\right]^2\right)\right]. \tag{B.29}$$

Next, we calculate the Fourier transform of the ramping integrals, i.e.,

$$
\begin{aligned}
I_1\left(\omega, t_1, t_2\right) &= \int_{t_1}^{t_2} \mathrm{d}\tilde{\tau} \left[10\left(\frac{\tilde{\tau} - t_1}{t_2 - t_1}\right)^3 - 15\left(\frac{\tilde{\tau} - t_1}{t_2 - t_1}\right)^4 + 6\left(\frac{\tilde{\tau} - t_1}{t_2 - t_1}\right)^5\right] \cos\left(\omega_0\tilde{\tau} - \phi_0\right) \mathrm{e}^{\mathrm{i}\omega\tilde{\tau}}, \\
&\overset{\tau = \tilde{\tau} - t_1}{=} \int_0^{\Delta t} \mathrm{d}\tau \left[10\left(\frac{\tau}{\Delta t}\right)^3 - 15\left(\frac{\tau}{\Delta t}\right)^4 + 6\left(\frac{\tau}{\Delta t}\right)^5\right] \cos\left(\omega_0\tau - \phi_0 + \omega_0 t_1\right) \mathrm{e}^{\mathrm{i}\omega(\tau + t_1)},
\end{aligned} \tag{B.30}
$$

where $\Delta t = t_2 - t_1$. Splitting the cosine-term into two exponential terms and omitting the constant prefactors, we have to solve sub-integrals of the type

$$I_{1,n}^{\pm}(\omega, \omega_0, \Delta t) = \int_0^{\Delta t} \mathrm{d}\tau \left(\frac{\tau}{\Delta t}\right)^n \mathrm{e}^{\mathrm{i}\left(\omega \pm \omega_0\right)\tau}. \tag{B.31}$$

Additionally, we need to consider the special case in which $\omega = \mp\omega_0$. We then get

$$I_{1,n}^{\pm}(\omega = \mp\omega_0, \omega_0, \Delta t) = \frac{1}{n+1} \left.\frac{\tau^{n+1}}{\Delta t^n}\right|_0^{\Delta t} = \frac{\Delta t}{n+1}. \tag{B.32}$$

In all other cases, the integrals can be solved using the substitution

$$\beta = i\left(\omega \pm \omega_0\right)\Delta t\,, \tag{B.33}$$

where $|\beta| \neq 0$ and replacing $\tau/\Delta t \to \tau$, via

$$I_{1,n}^{\pm}(\omega,\omega_0,\Delta t) = \Delta t \int_0^1 d\tau\, \tau^n e^{\beta\tau} = \Delta t \frac{\partial^n}{\partial \beta^n} \int_0^1 d\tau\, e^{\beta\tau}\,,$$

$$= \Delta t \frac{\partial^n}{\partial \beta^n} \frac{1}{\beta} \left. e^{\beta\tau}\right|_0^1 = \Delta t \frac{\partial^n}{\partial \beta^n} \frac{1}{\beta} \left[e^{\beta} - 1\right]\,. \tag{B.34}$$

For the calculation of $I_{1,n}^{\pm}$, we need these integrals for $n = 3, 4, 5$. Using induction, we can show that

$$\frac{\partial^n}{\partial \beta^n} \frac{1}{\beta} \left[e^{\beta} - 1\right] = (-1)^n n! \frac{e^{\beta} - 1}{\beta^{n+1}} + \sum_{i=0}^{n-1}(-1)^i \frac{n!}{(n-i)!} \frac{e^{\beta}}{\beta^{i+1}}\,. \tag{B.35}$$

The induction base is trivially fulfilled, as the entire sum vanishes for $n = 0$. The induction step is

$$\frac{\partial}{\partial \beta} \frac{\partial^n}{\partial \beta^n} \frac{1}{\beta} \left[e^{\beta} - 1\right] \overset{\text{(B.35)}}{=} \frac{\partial}{\partial \beta}(-1)^n n! \frac{1}{\beta^{n+1}} \left[e^{\beta} - 1\right] + \frac{\partial}{\partial \beta}\sum_{i=0}^{n-1}(-1)^i \frac{n!}{(n-i)!} \frac{e^{\beta}}{\beta^{i+1}}\,,$$

$$= -(-1)^n n!(n+1)\beta^{-(n+2)}\left[e^{\beta}-1\right] + (-1)^n n! e^{\beta}\beta^{-(n+1)}$$

$$+ \sum_{i=0}^{n-1}(-1)^i \frac{n!}{(n-i)!}e^{\beta}\left[-(i+1)]\beta^{-(i+2)} + \beta^{-(i+1)}\right]\,,$$

$$\overset{i'=i+1}{=}(-1)^{n+1}(n+1)!\beta^{-(n+2)}\left[e^{\beta}-1\right]$$

$$+ (-1)^n n! e^{\beta}\beta^{-(n+1)} + (-1)^{(n-1)}\frac{n!}{1!}(-n)e^{\beta}\beta^{-(n+1)}$$

$$+ \sum_{i'=1}^{n-1}(-1)^{i'-1}e^{\beta}\frac{n!}{(n-i'+1)!}(-i')\beta^{-(i'+1)}$$

$$+ e^{\beta}\beta^{-1} + \sum_{i=1}^{n-1}(-1)^i \frac{n!}{(n-i)!}e^{\beta}\beta^{-(i+1)}\,,$$

$$= (-1)^{n+1}(n+1)!\beta^{-(n+2)}\left[e^{\beta}-1\right] + (-1)^n(n+1)!e^{\beta}\beta^{-(n+1)}$$

$$+ e^{\beta}\beta^{-1} + \sum_{i=1}^{n-1}(-1)^i \underbrace{\left[\frac{n!\,i}{(n-i+1)!} + \frac{n!}{(n-i)!}\right]}_{\frac{(n+1)!}{(n-i+1)!}}e^{\beta}\beta^{-(i+1)}\,,$$

$$= (-1)^{n+1}(n+1)!\frac{e^{\beta}-1}{\beta^{n+2}} + \sum_{i=0}^{n}(-1)^i \frac{(n+1)!}{(n+1-i)!}\frac{e^{\beta}}{\beta^{i+1}}\,. \qquad \blacksquare \tag{B.36}$$

Finally, we obtain

$$
\begin{aligned}
I_1\left(\omega, t_1, t_2\right) = {} & \frac{1}{2} e^{i(\omega+\omega_0)t_1 - i\phi_0} \left(10 I_{1,3}^{+}(\omega, \omega_0, \Delta t) - 15 I_{1,4}^{+}(\omega, \omega_0, \Delta t) + 6 I_{1,5}^{+}(\omega, \omega_0, \Delta t)\right) \\
& - \frac{1}{2} e^{i(\omega-\omega_0)t_1 + i\phi_0} \left(10 I_{1,3}^{-}(\omega, \omega_0, \Delta t) - 15 I_{1,4}^{-}(\omega, \omega_0, \Delta t) + 6 I_{1,5}^{-}(\omega, \omega_0, \Delta t)\right) . \quad \text{(B.37)}
\end{aligned}
$$

When evaluating these integrals associated with the signal ramp-up and -down, the rounding error for $|\beta| \to 0$, i.e., $\omega \to \mp\omega_0$, is even further increased by division with a high power of β in the leading term of Eq. (B.35). Consequently, we calculate the Taylor-expansion of Eq. (B.34) to achieve a sufficient numerical evaluation accuracy for $|\beta| \approx 0$. We find that

$$
I_{1,n}^{\pm}(\omega \approx \mp\omega_0, \omega_0, \Delta t) = \Delta t \sum_{k=n+1}^{\infty} \frac{1}{k} \frac{1}{(k-(n+1))!} \beta^{k-(n+1)} \quad \text{(B.38)}
$$

and can stop the series expansion as required by the requested evaluation accuracy.
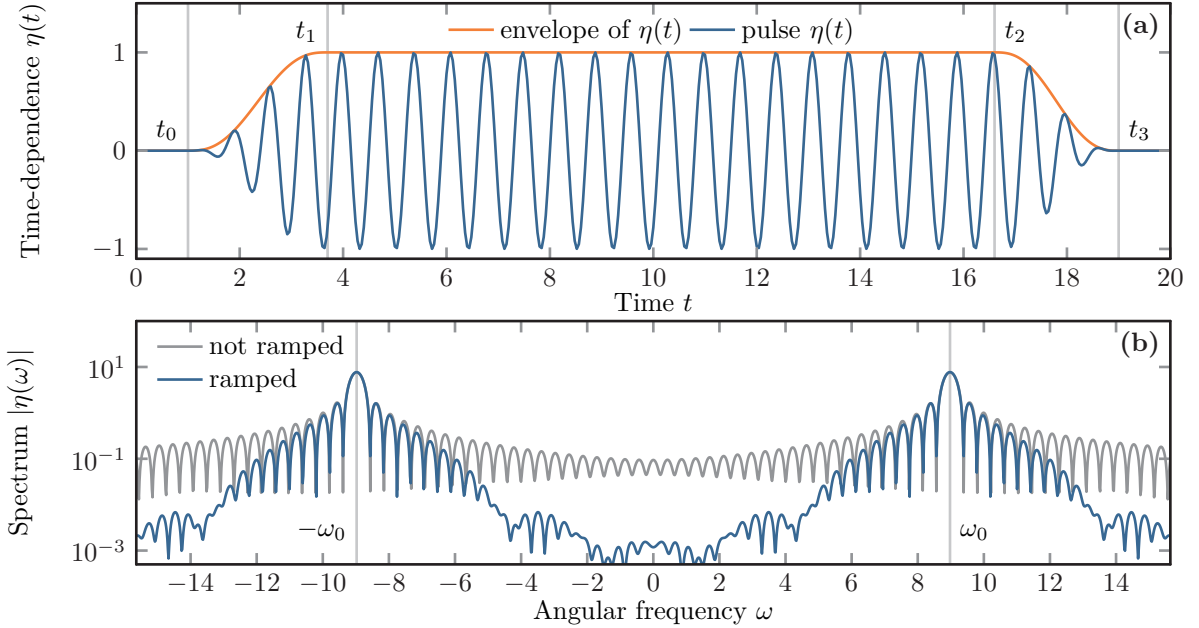
Figure B.3: Example for a continuous wave time dependence **(a)** $\eta(t)$ and the corresponding envelope function. **(b)** Spectrum $|\eta(\omega)|$ of the same continuous wave example with and without the polynomial ramping of the envelope.

In Fig. B.3 we present an example of a continuous wave time dependence $\eta(t)$ and the corresponding spectrum $|\eta(\omega)|$. The time dependence starts at $t_0 = 1.0$ and is ramped up for $t_{\text{up}} = 2.7$ and ramped down for $t_{\text{down}} = 2.4$. The overall duration is set to $T_{\text{pulse}} = 18$ and the carrier frequency is chosen as $\omega_0 = \frac{20\pi}{7}$. The corresponding spectrum shown in Fig. B.3 (b) peaks at $\omega = \pm\omega_0$. Besides the spectrum $|\eta(\omega)|$ of the ramped time dependence also the spectrum of the corresponding rectangular pulse is shown, which resembles a superposition of two sinc-functions as derived in Eq. (B.28). It is well visible, that the ramping of the pulse envelope reduces the bandwidth,

as frequency components far from the carrier frequency ω_0 are suppressed. In consequence, also fewer frequency components are required to compute the two-dimensional Gaussian beam source for nearly the same time dependence. This can drastically reduce the computational time, as the sum in Eq. (B.16) needs to be evaluated at every time step of the DGTD time integration (cf. Section 5.2).

Acronyms

Acknowledgments

Bibliography

1. H. Raether, *Surface Plasmons on Smooth and Rough Surfaces and on Gratings* (Springer-Verlag Berlin Heidelberg New York, 1988) (cit. on pp. 1, 60).

2. S. Kawata, *Near field optics and surface plasmon polaritons* (Springer-Verlag Berlin Heidelberg New York, 2001) (cit. on p. 1).

3. W. L. Barnes, A. Dereux and T. W. Ebbesen, "Surface plasmon subwavelength optics", Nature **424,** 824 (2003) (cit. on p. 1).

4. R. F. Egerton, "Electron energy-loss spectroscopy in the TEM", Reports on Progress in Physics **72,** 016502 (2008) (cit. on pp. 1, 113).

5. F. J. García de Abajo, "Optical excitations in electron microscopy", Rev. Mod. Phys. **82,** 209 (2010) (cit. on pp. 1, 113, 114).

6. R. H. Ritchie, "Plasma Losses by Fast Electrons in Thin Films", Phys. Rev. **106,** 874 (1957) (cit. on pp. 1, 114).

7. M. I. Stockman *et al.,* "Roadmap on plasmonics", Journal of Optics **20,** 043001 (2018) (cit. on p. 1).

8. F. J. García de Abajo and A. Howie, "Relativistic Electron Energy Loss and Electron-Induced Photon Emission in Inhomogeneous Dielectrics", Phys. Rev. Lett. **80,** 5180 (1998) (cit. on pp. 1, 4, 116, 119, 122, 195).

9. F. J. García de Abajo, "Relativistic energy loss and induced photon emission in the interaction of a dielectric sphere with an external electron beam", Phys. Rev. B **59,** 3095 (1999) (cit. on pp. 1, 4, 116, 119, 122, 195).

10. M. I. Stockman, "Nanofocusing of Optical Energy in Tapered Plasmonic Waveguides", Phys. Rev. Lett. **93,** 137404 (2004) (cit. on p. 1).

11. N. Talebi *et al.,* "Excitation of Mesoscopic Plasmonic Tapers by Relativistic Electrons: Phase Matching versus Eigenmode Resonances", ACS Nano **9,** 7641 (2015) (cit. on p. 1).

12. S. Guo *et al.,* "Reflection and Phase Matching in Plasmonic Gold Tapers", Nano Letters **16,** 6137 (2016) (cit. on p. 1).

13. A. Hartschuh, E. J. Sánchez, X. S. Xie and L. Novotny, "High-Resolution Near-Field Raman Microscopy of Single-Walled Carbon Nanotubes", Phys. Rev. Lett. **90,** 095503 (2003) (cit. on p. 1).

14. D. Richards, A. Zayats, F. Keilmann and R. Hillenbrand, "Near-field microscopy by elastic light scattering from a tip", Philosophical Transactions of the Royal Society of London. Series A: Mathematical, Physical and Engineering Sciences **362,** 787 (2004) (cit. on p. 1).

15. C. C. Neacsu *et al.,* "Near-Field Localization in Plasmonic Superfocusing: A Nanoemitter on a Tip", Nano Letters **10,** 592 (2010) (cit. on p. 1).

16. S. Schmidt *et al.,* "Adiabatic Nanofocusing on Ultrasmooth Single-Crystalline Gold Tapers Creates a 10-nm-Sized Light Source with Few-Cycle Time Resolution", ACS Nano **6,** 6040 (2012) (cit. on p. 1).

17. D. Rossouw and G. A. Botton, "Plasmonic Response of Bent Silver Nanowires for Nanophotonic Subwavelength Waveguiding", Phys. Rev. Lett. **110,** 066801 (2013) (cit. on p. 1).

18. A. W. Schell, A. Kuhlicke, G. Kewes and O. Benson, "Flying Plasmons: Fabry-Pérot Resonances in Levitated Silver Nanowires", ACS Photonics **4,** 2719 (2017) (cit. on p. 1).

19. M. Rothe *et al.,* "Silver nanowires with optimized silica coating as versatile plasmonic resonators", Scientific Reports **9,** 3859 (2019) (cit. on pp. 1, 197).

20. M. I. Dyakonov, "New Type of Electromagnetic Wave Propagating at an Interface.", JETP **94,** 119 (1988) (cit. on p. 1).

21. N. Talebi *et al.,* "Wedge Dyakonov Waves and Dyakonov Plasmons in Topological Insulator Bi2Se3 Probed by Electron Beams", ACS Nano **10,** 6988 (2016) (cit. on p. 1).

22. T. W. Ebbesen, H. J. Lezec, H. F. Ghaemi, T. Thio and P. A. Wolff, "Extraordinary optical transmission through sub-wavelength hole arrays", Nature **391,** 667 (1998) (cit. on p. 1).

23. S. Fiedler *et al.,* "Importance of substrates for the visibility of dark plasmonic modes", Opt. Express **28,** 13938 (2020) (cit. on p. 1).

24. J. Grant, I. J. H. McCrindle and D. R. S. Cumming, "Multi-spectral materials: hybridisation of optical plasmonic filters, a mid infrared metamaterial absorber and a terahertz metamaterial absorber", Opt. Express **24,** 3451 (2016) (cit. on p. 2).

25. I. J. H. McCrindle, J. Grant, T. D. Drysdale and D. R. S. Cumming, "Hybridization of optical plasmonics with terahertz metamaterials to create multi-spectral filters", Opt. Express **21,** 19142 (2013) (cit. on p. 2).

26. F. Cheng, J. Gao, T. S. Luk and X. Yang, "Structural color printing based on plasmonic metasurfaces of perfect light absorption", en. Scientific Reports **5,** 11045 (2015) (cit. on p. 2).

27. R. Gordon, D. Sinton, K. L. Kavanagh and A. G. Brolo, "A New Generation of Sensors Based on Extraordinary Optical Transmission", Accounts of Chemical Research **41,** 1049 (2008) (cit. on p. 2).

28. F. Eftekhari *et al.,* "Nanoholes As Nanochannels: Flow-through Plasmonic Sensing", Analytical Chemistry **81,** 4308 (2009) (cit. on p. 2).

29. A. K. Zvezdin and V. A. Kotov, *Modern magnetooptics and magnetooptical materials* (CRC Press, 1997) (cit. on pp. 2, 29, 31, 133, 149, 152).

30. G. Armelles *et al.,* "Localized surface plasmon resonance effects on the magneto-optical activity of continuous Au/Co/Au trilayers", Opt. Express **16,** 16104 (2008) (cit. on p. 2).

31. A. V. Baryshev, H. Uchida and M. Inoue, "Peculiarities of plasmon-modified magneto-optical response of gold-garnet structures", J. Opt. Soc. Am. B **30,** 2371 (2013) (cit. on p. 2).

32. E. Almpanis, P.-A. Pantazopoulos, N. Papanikolaou, V. Yannopapas and N. Stefanou, "Metal-nanoparticle arrays on a magnetic garnet film for tunable plasmon-enhanced Faraday rotation", J. Opt. Soc. Am. B **33,** 2609 (2016) (cit. on p. 2).

33. A. V. Baryshev and A. M. Merzlikin, "Tunable plasmonic thin magneto-optical wave plate", J. Opt. Soc. Am. B **33,** 1399 (2016) (cit. on p. 2).

34. L. Wang *et al.,* "Plasmonics and enhanced magneto-optics in core-shell Co-Ag nanoparticles", Nano letters **11,** 1237 (2011) (cit. on p. 2).

35. G. Armelles *et al.,* "Magneto-optical Properties of Core–Shell Magneto-plasmonic Au–Co x Fe3–x O4 Nanowires", Langmuir **28,** 9127 (2012) (cit. on p. 2).

36. P. Varytis, P. A. Pantazopoulos and N. Stefanou, "Enhanced Faraday rotation by crystals of core-shell magnetoplasmonic nanoparticles", Phys. Rev. B **93,** 214423 (2016) (cit. on p. 2).

37. J. B. González-Díaz *et al.,* "Surface-magnetoplasmon nonreciprocity effects in noble-metal/ferromagnetic heterostructures", Phys. Rev. B **76,** 153402 (2007) (cit. on p. 2).

38. C. Clavero, K. Yang, J. R. Skuza and R. A. Lukaszew, "Magnetic field modulation of intense surface plasmon polaritons", Opt. Express **18,** 7743 (2010) (cit. on p. 2).

39. C. Clavero, K. Yang, J. R. Skuza and R. A. Lukaszew, "Magnetic-field modulation of surface plasmon polaritons on gratings", Opt. Lett. **35,** 1557 (2010) (cit. on p. 2).

40. V. I. Belotelov, L. L. Doskolovich and A. K. Zvezdin, "Extraordinary Magneto-Optical Effects and Transmission through Metal-Dielectric Plasmonic Systems", Phys. Rev. Lett. **98,** 077401 (2007) (cit. on p. 2).

41. A. B. Khanikaev, A. V. Baryshev, A. A. Fedyanin, A. B. Granovsky and M. Inoue, "Anomalous Faraday Effect of a system with extraordinary optical transmittance", Opt. Express **15,** 6612 (2007) (cit. on p. 2).

42. D. Li *et al.,* "Plasmon-enhanced magneto-optical activity in a nanostructure with circle annular arrays", J. Opt. Soc. Am. B **33,** 922 (2016) (cit. on p. 2).

43. M. G. Barsukova *et al.,* "Magneto-Optical Response Enhanced by Mie Resonances in Nanoantennas", ACS Photonics **4,** 2390 (2017) (cit. on p. 2).

44. A. Christofi, Y. Kawaguchi, A. Alù and A. B. Khanikaev, "Giant enhancement of Faraday rotation due to electromagnetically induced transparency in all-dielectric magneto-optical metasurfaces", Optics letters **43,** 1838 (2018) (cit. on pp. 2, 133, 152, 155, 156, 157, 196).

45. M. Decker *et al.,* "High-Efficiency Dielectric Huygens' Surfaces", Advanced Optical Materials **3,** 813 (2015) (cit. on p. 2).

46. A. Poddubny, I. Iorsh, P. Belov and Y. Kivshar, "Hyperbolic metamaterials", Nature photonics **7,** 948 (2013) (cit. on pp. 2, 31, 32, 33, 162).

47. L. Ferrari, C. Wu, D. Lepage, X. Zhang and Z. Liu, "Hyperbolic metamaterials and their applications", Progress in Quantum Electronics **40,** 1 (2015) (cit. on pp. 2, 32, 162).

48. O. Takayama and A. V. Lavrinenko, "Optics with hyperbolic materials [Invited]", J. Opt. Soc. Am. B **36,** F38 (2019) (cit. on p. 2).

49. M. A. Noginov *et al.,* "Controlling spontaneous emission with metamaterials", Opt. Lett. **35,** 1863 (2010) (cit. on pp. 2, 162).

50. P. A. Belov and Y. Hao, "Subwavelength imaging at optical frequencies using a transmission device formed by a periodic layered metal-dielectric structure operating in the canalization regime", Phys. Rev. B **73,** 113110 (2006) (cit. on pp. 2, 162).

51. Z. Jacob, L. V. Alekseyev and E. Narimanov, "Optical Hyperlens: Far-field imaging beyond the diffraction limit", Opt. Express **14,** 8247 (2006) (cit. on pp. 2, 162).

52. Z. Jacob, I. I. Smolyaninov and E. E. Narimanov, "Broadband Purcell effect: Radiative decay engineering with metamaterials", Applied Physics Letters **100,** 181105 (2012) (cit. on pp. 2, 162).

53. J. Kim *et al.,* "Improving the radiative decay rate for dye molecules with hyperbolic metamaterials", Opt. Express **20,** 8100 (2012) (cit. on pp. 2, 162).

54. E. M. Purcell, "Spontaneous emission probabilities at radio frequencies", Phys. Rev. **69,** 681 (1946) (cit. on pp. 2, 115).

55. M. Oelschläger, K. Busch and F. Intravaia, "Nonequilibrium atom-surface interaction with lossy multilayer structures", Phys. Rev. A **97,** 062507 (2018) (cit. on pp. 2, 162).

56. S. Sadofev, S. Kalusniak, P. Schäfer, H. Kirmse and F. Henneberger, "Free-electron concentration and polarity inversion domains in plasmonic (Zn,Ga)O", Physica Status Solidi (B) **252,** 607 (2015) (cit. on pp. 3, 163, 197).

57. E. N. Economou, "Surface Plasmons in Thin Films", Phys. Rev. **182,** 539 (1969) (cit. on pp. 3, 125).

58. V. G. Kozlov *et al.,* "Study of lasing action based on Förster energy transfer in optically pumped organic semiconductor thin films", Journal of Applied Physics **84,** 4096 (1998) (cit. on pp. 3, 174, 175).

59. U. Brackmann, *Lambdachrome® Laser Dyes* tech. rep. (Lambda Physik AG, D-37079 Goettingen · Germany, 2000) (cit. on pp. 3, 174).

60. A. Kavokin, J. J. Baumberg, G. Malpuech and F. P. Laussy, *Microcavities*, 2nd revised edition (Oxford University Press, 2017) (cit. on pp. 3, 173, 174).

61. M. Kaliteevski *et al.,* "Tamm plasmon-polaritons: Possible electromagnetic states at the interface of a metal and a dielectric Bragg mirror", Phys. Rev. B **76,** 165415 (2007) (cit. on p. 3).

62. J. B. Pendry, L. Martín-Moreno and F. J. Garcia-Vidal, "Mimicking Surface Plasmons with Structured Surfaces", Science **305,** 847 (2004) (cit. on p. 3).

63. A. Taflove and S. C. Hagness, *Computation Electrodynamics - The Finite-Difference Time-Domain Method*, 3rd ed. (Artech House, London, 2005) (cit. on pp. 3, 27, 36, 65, 91, 92, 100, 101, 103, 105).

64. S.-H. Chang and A. Taflove, "Finite-difference time-domain model of lasing action in a four-level two-electron atomic system", Opt. Express **12,** 3827 (2004) (cit. on pp. 3, 27, 36, 40).

65. M. G. Moharam and T. K. Gaylord, "Diffraction analysis of dielectric surface-relief gratings", J. Opt. Soc. Am. **72,** 1385 (1982) (cit. on pp. 3, 41).

66. L. Li. *Mathematical Modeling in Optical Science* 111 () (cit. on p. 3).

67. L. Li, "New formulation of the Fourier modal method for crossed surface-relief gratings", J. Opt. Soc. Am. A **14,** 2758 (1997) (cit. on pp. 3, 41).

68. M. G. Moharam, E. B. Grann, D. A. Pommet and T. K. Gaylord, "Formulation for stable and efficient implementation of the rigorous coupled-wave analysis of binary gratings", J. Opt. Soc. Am. A **12,** 1068 (1995) (cit. on p. 3).

69. S. Essig and K. Busch, "Generation of adaptive coordinates and their use in the Fourier Modal Method", Opt. Express **18,** 23258 (2010) (cit. on pp. 3, 41).

70. S. Essig, *Advanced Numerical Methods in Diffractive Optics and Applications to Periodic Photonic Nanostructures*, PhD thesis (2011) (cit. on pp. 3, 41).

71. T. Zebrowski, *The Full Anisotropic Adaptive Fourier Modal Method and its Application to Periodic and Aperiodic Photonic Nanostructures*, PhD thesis (Karlsruhe, 2012) (cit. on pp. 3, 41, 49).

72. L. Li, "Formulation and comparison of two recursive matrix algorithms for modeling layered diffraction gratings", J. Opt. Soc. Am. A **13,** 1024 (1996) (cit. on pp. 3, 53, 54).

73. J. S. Hesthaven and T. Warburton, *Nodal Discontinuous Galerkin Methods* , 1st ed. (Springer Science+Business Media, LCC, 2008) (cit. on pp. 4, 65, 68, 71, 72, 73, 74, 77, 87, 136).

74. K. Busch, M. König and J. Niegemann, "Discontinuous Galerkin methods in nanophotonics", Laser & Photonics Reviews **5,** 773 (2011) (cit. on pp. 4, 65, 72, 85, 87, 91, 92, 93, 100, 195).

75. M. C. König, *Discontinuous Galerkin Methods in Nanophotonics*, PhD thesis (Karlsruhe Insitute of Technology, 2011) (cit. on pp. 4, 24, 65, 69, 77, 85, 87, 92, 93, 100, 102, 105, 133, 195, 215).

76. J. Niegemann, *Higher-Order Methods for Solving Maxwell's Equations in the Time-Domain*, PhD thesis (Universität (TH) Karlsruhe, 2009) (cit. on pp. 4, 65, 77, 88, 92, 196).

77. J. Alvarez, L. D. Angulo, A. R. Bretones and S. G. Garcia, "3-D Discontinuous Galerkin Time-Domain Method for Anisotropic Materials", IEEE Antennas and Wireless Propagation Letters **11,** 1182 (2012) (cit. on pp. 4, 65, 78, 82, 139, 196).

78. P. Varytis, N. Stefanou, A. Christofi and N. Papanikolaou, "Strong circular dichroism of core-shell magnetoplasmonic nanoparticles", J. Opt. Soc. Am. B **32,** 1063 (2015) (cit. on pp. 4, 133, 134, 135, 140, 141, 149, 150, 196).

79. Z. Lin and S. T. Chui, "Electromagnetic scattering by optically anisotropic magnetic particle", Phys. Rev. E **69,** 056614 (2004) (cit. on pp. 4, 133, 196).

80. T. Kiel, *Modenanpassung in photonischen Kristallstrukturen / Eine Erweiterung der B-Spline-Moden-Methode*, Master's thesis (Humboldt-Universität zu Berlin, 2015) (cit. on pp. 5, 47, 55, 173).

81. J. D. Jackson, *Classical Electrodynamics*, 3rd ed. (John Wiley & Sons, Inc., 1999) (cit. on pp. 6, 11, 20, 27, 28, 29, 87, 199, 200, 203, 208).

82. L. D. Landau and E. M. Lifshitz, *Course of theoretical physics. 8, Electrodynamics of continuous media*, 2nd ed. (Pergamon Press, 1996) (cit. on pp. 6, 32).

83. W. Nolting, *Grundkurs theoretische Physik 3 - Elektrodynamik*, 8. Auflage (Springer-Verlag Berlin Heidelberg New York, 2007) (cit. on pp. 6, 11, 20, 48, 200).

84. L. Novotny and B. Hecht, *Principles of Nano-Optics*, 1st ed. (Cambridge University Press, 2006) (cit. on pp. 6, 36, 40, 60, 115, 116).

85. B. I. des Poids et Mesures, "The International System of Units (SI)", 2006 (cit. on pp. 6, 9).

86. M. Schäferling, *Chiral Nanophotonics: Chiral Optical Properties of Plasmonic Systems*, 1st ed. (Springer, 2017) (cit. on pp. 7, 149, 198).

87. J. F. M. Werra, C. Wolff, C. Matyssek and K. Busch, *Current sheets in the Discontinuous Galerkin Time-Domain method: an application to graphene Metamaterials X* (eds V. Kuzmiak, P. Markos and T. Szoplik) **9502** (SPIE, 2015), 33 (cit. on pp. 13, 75).

88. M. Born and E. Wolf, *Principles of Optics, Electromagnetic Theory of Propagation, Interference and Diffraction of Light*, 4th ed. (Pergamon Press, 1970) (cit. on p. 18).

89. J. F. Nye and J. V. Hajnal, "The wave structure of monochromatic electromagnetic radiation", Proceedings of the Royal Society of London. A. Mathematical and Physical Sciences **409,** 21 (1987) (cit. on p. 18).

90. H. C. van de Hulst, *Light Scattering by Small Particles* (Dover Publication, Inc., 1981) (cit. on pp. 24, 135, 141).

91. C. F. Bohren and D. R. Huffman, *Absorption and Scattering of Light by Small Particles* (John Wiley & Sons, Inc., 1970) (cit. on p. 24).

92. L. W. Davis, "Semiclassical treatment of the optical maser", Proceedings of the IEEE **51,** 76 (1963) (cit. on pp. 27, 36).

93. A. E. Siegman, *Lasers* (University Science Books,U.S., 1986) (cit. on pp. 27, 36, 183).

94. Y. Huang and S.-T. Ho, "Computational model of solid-state, molecular, or atomic media for FDTD simulation based on a multi-level multi-electron system governed by Pauli exclusion and Fermi-Dirac thermalization with application to semiconductor photonics", Opt. Express **14,** 3569 (2006) (cit. on p. 27).

95. C. Kittel, *Introduction to Solid State Physics*, 8th Edition (John Wiley and Sons, Inc., 2005) (cit. on pp. 27, 29, 45, 46).

96. R. W. Boyd, *Nonlinear optics*, 3rd ed. (Academic Press, 2008) (cit. on pp. 28, 36).

97. G. Czycholl, *Theoretische Festkörperphysik: von den klassischen Modellen zu modernen Forschungsthemen*, 3rd edition (Springer-Verlag, 2008) (cit. on p. 29).

98. P. R. Berman, "Optical Faraday rotation", American Journal of Physics **78,** 270 (2010) (cit. on p. 29).

99. C. Wolff, R. Rodríguez-Oliveros and K. Busch, "Simple magneto–optic transition metal models for time–domain simulations", Opt. Express **21,** 12022 (2013) (cit. on pp. 29, 31).

100. J. E. Sipe, V. C. Y. So, M. Fukui and G. I. Stegeman, "Analysis of second-harmonic generation at metal surfaces", Phys. Rev. B **21,** 4389 (1980) (cit. on pp. 30, 196).

101. Z. Yu, Z. Wang and S. Fan, "One-way total reflection with one-dimensional magneto-optical photonic crystals", Applied Physics Letters **90,** 121133 (2007) (cit. on p. 31).

102. A. Sihvola, "Metamaterials in electromagnetics", Metamaterials **1,** 2 (2007) (cit. on p. 31).

103. V. G. Veselago, "The Electrodynamics of Substances with Simultaneously Negative Values of ϵ and μ", Soviet Physics Uspekhi **10,** 509 (1968) (cit. on p. 31).

104. J. B. Pendry, "Negative Refraction Makes a Perfect Lens", Phys. Rev. Lett. **85,** 3966 (2000) (cit. on p. 31).

105. O. Takayama and A. V. Lavrinenko, "Optics with hyperbolic materials", J. Opt. Soc. Am. B **36,** F38 (2019) (cit. on p. 32).

106. N. Vasilantonakis, M. E. Nasir, W. Dickson, G. A. Wurtz and A. V. Zayats, "Bulk plasmon-polaritons in hyperbolic nanorod metamaterial waveguides", Laser & Photonics Reviews **9,** 345 (2015) (cit. on p. 33).

107. C. R. Simovski, P. A. Belov, A. V. Atrashchenko and Y. S. Kivshar, "Wire Metamaterials: Physics and Applications", Advanced Materials **24,** 4229 (2012) (cit. on p. 33).

108. P. Guo, R. P. H. Chang and R. D. Schaller, "Tunable infrared hyperbolic metamaterials with periodic indium-tin-oxide nanorods", Applied Physics Letters **111,** 021108 (2017) (cit. on p. 33).

109. V. Agranovich and V. Kravtsov, "Notes on crystal optics of superlattices", Solid State Communications **55,** 85 (1985) (cit. on p. 33).

110. C. Gardiner and P. Zoller, *Quantum noise: A handbook of Markovian and non-Markovian quantum stochastic methods with applications to quantum optics* (Springer Science & Business Media, 2010) (cit. on pp. 36, 38).

111. M. O. Scully and M. S. Zubairy, "Quantum optics", 1999 (cit. on p. 36).

112. B. Valeur and M. N. Berberan-Santos, "Molecular fluorescence", (2012) (cit. on p. 36).

113. M. Weissbluth, *Atoms and molecules* (Academic Press, 1978) (cit. on pp. 36, 175).

114. A. Jablonski, "Efficiency of anti-Stokes fluorescence in dyes", Nature **131,** 839 (1933) (cit. on p. 36).

115. W. P. Schleich, *Quantum optics in phase space*, 1st ed. (John Wiley & Sons, 2001) (cit. on p. 36).

116. J. Sakurai and J. Napolitano, *Modern Quantum Mechanics*, 2nd edition (Addison-Wesley, 2010) (cit. on p. 37).

117. J. F. M. Werra, *Probing plasmonic nanostructures: A theoretical study of light-matter interaction in graphene-based and metallic systems*, PhD thesis (Humboldt-Universität zu Berlin, 2016) (cit. on pp. 40, 75, 215).

118. J. Trieschmann, S. Xiao, L. J. Prokopeva, V. P. Drachev and A. V. Kildishev, "Experimental retrieval of the kinetic parameters of a dye in a solid film", Opt. Express **19,** 18253 (2011) (cit. on pp. 40, 176).

119. L. Li, "Multilayer modal method for diffraction gratings of arbitrary profile, depth, and permittivity", J. Opt. Soc. Am. A **10,** 2581 (1993) (cit. on pp. 41, 51).

120. T. Weiss and E. A. Muljarov, "How to calculate the pole expansion of the optical scattering matrix from the resonant states", Phys. Rev. B **98,** 085433 (2018) (cit. on pp. 41, 59).

121. F. Alpeggiani, N. Parappurath, E. Verhagen and L. Kuipers, "Quasinormal-Mode Expansion of the Scattering Matrix", Phys. Rev. X **7,** 021035 (2017) (cit. on pp. 41, 59).

122. P. T. Kristensen, K. Herrmann, F. Intravaia and K. Busch, "Modeling electromagnetic resonators using quasinormal modes", Adv. Opt. Photon. **12,** 612 (2020) (cit. on pp. 41, 59, 115, 168, 198).

123. L. Li, "Fourier modal method for crossed anisotropic gratings with arbitrary permittivity and permeability tensors", Journal of Optics A: Pure and Applied Optics **5,** 345 (2003) (cit. on p. 41).

124. C. S. Lam, "Decomposition of time-ordered products and path-ordered exponentials", Journal of Mathematical Physics **39,** 5543 (1998) (cit. on p. 43).

125. S. Blanes, F. Casas, J. Oteo and J. Ros, "The Magnus expansion and some of its applications", Physics Reports **470,** 151 (2009) (cit. on p. 43).

126. W. Magnus, "On the exponential solution of differential equations for a linear operator", Communications on Pure and Applied Mathematics **7,** 649 (1954) (cit. on p. 43).

127. N. W. Ashcroft and D. N. Mermin, *Festkörperphysik*, 3. Auflage (Oldenburg Wissenschaftsverlag GmbH, 2007) (cit. on pp. 45, 46).

128. M. Frigo and S. G. Johnson, "The Design and Implementation of FFTW3", Proceedings of the IEEE **93,** 216 (2005) (cit. on p. 46).

129. W. H. Press, S. A. Teukolsky, W. T. Vetterling and B. P. Flannery, *Numerical Recipes 3rd Edition: The Art of Scientific Computing*, 3 (Cambridge University Press, New York, NY, USA, 2007) (cit. on pp. 46, 47, 48, 59, 60, 67, 91, 139, 161).

130. C. E. Shannon, "Communication in the Presence of Noise", Proceedings of the IRE **37,** 10 (1949) (cit. on pp. 46, 213).

131. K. Busch, *Computational Photonics*, Lecture notes (Humboldt-Universität zu Berlin, 2019) (cit. on pp. 46, 93, 213).

132. E. Hewitt and R. E. Hewitt, "The Gibbs-Wilbraham phenomenon: An episode in fourier analysis", English. Archive for History of Exact Sciences **21,** 129 (1979) (cit. on p. 47).

133. P. Bouchon, F. Pardo, R. Haïdar and J.-L. Pelouard, "Fast modal method for subwavelength gratings based on B-spline formulation", J. Opt. Soc. Am. A **27,** 696 (2010) (cit. on p. 47).

134. M. Walz, T. Zebrowski, J. Küchenmeister and K. Busch, "B-spline modal method: A polynomial approach compared to the Fourier modal method", Opt. Express **21,** 14683 (2013) (cit. on p. 47).

135. L. Li, "Use of Fourier series in the analysis of discontinuous periodic structures", J. Opt. Soc. Am. A **13,** 1870 (1996) (cit. on p. 49).

136. S. H. Schot, "Eighty years of Sommerfeld's radiation condition", Historia Mathematica **19,** 385 (1992) (cit. on pp. 59, 87, 88).

137. S. Silver, *Microwave Antenna Theory and Design*, 1st (McGraw-Hill Book Company, Inc., 1949) (cit. on pp. 59, 87, 88).

138. C. Müller, *Grundprobleme der mathematischen Theorie elektromagnetischer Schwingungen* (Springer-Verlag Berlin Heidelberg New York, 1957) (cit. on pp. 59, 87, 88).

139. K. Yee, "Numerical solution of initial boundary value problems involving Maxwell's equations in isotropic media", IEEE Transactions on Antennas and Propagation **14,** 302 (1966) (cit. on p. 65).

140. C. Geuzaine and J.-F. Remacle, "Gmsh: A 3-D finite element mesh generator with built-in pre- and post-processing facilities", International Journal for Numerical Methods in Engineering **79,** 1309 (2009) (cit. on pp. 66, 119, 123, 136, 137, 159, 181, 196).

141. J. Schöberl, "NETGEN An advancing front 2D/3D-mesh generator based on abstract rules", Computing and Visualization in Science **1,** 41 (1997) (cit. on pp. 66, 196).

142. J. Niegemann, R. Diehl and K. Busch, "Efficient low-storage Runge–Kutta schemes with optimized stability regions", Journal of Computational Physics **231,** 364 (2012) (cit. on pp. 67, 85, 91, 196).

143. J. Hesthaven and T. Warburton, "Nodal High-Order Methods on Unstructured Grids: I. Time-Domain Solution of Maxwell's Equations", Journal of Computational Physics **181,** 186 (2002) (cit. on p. 69).

144. T. Koornwinder. *Theory and Application of Special Functions* (ed R. A. Askey) 435 (Academic Press, 1975) (cit. on pp. 69, 70).

145. M. Dubiner, "Spectral methods on triangles and other domains", Journal of Scientific Computing **6,** 345 (1991) (cit. on pp. 69, 70).

146. M. Abramowitz and I. A. Stegun, *Handbook of Mathematical Functions with Formulas, Graphs and Mathematical Tables* (Dover Publications, Inc., New York, 1965) (cit. on p. 70).

147. T. Warburton, "An explicit construction of interpolation nodes on the simplex", Journal of Engineering Mathematics **56,** 247 (2006) (cit. on p. 71).

148. R. J. LeVeque, *Finite volume methods for hyperbolic problems*, Repr. eng (Cambridge [u.a.], 2004) (cit. on pp. 74, 76, 77).

149. E. F. Toro, *Riemann solvers and numerical methods for fluid dynamics : a practical introduction*, 3. ed. eng (Berlin [u.a.], 2009) (cit. on pp. 74, 76).

150. A. H. Mohammadian, V. Shankar and W. F. Hall, "Computation of electromagnetic scattering and radiation using a time-domain finite-volume discretization procedure", Computer Physics Communications **68,** 175 (1991) (cit. on p. 75).

151. M. König, C. Prohm, K. Busch and J. Niegemann, "Stretched-coordinate PMLs for Maxwell's equations in the discontinuous Galerkin time-domain method", Opt. Express **19,** 4618 (2011) (cit. on pp. 100, 102, 105, 111, 195).

152. Z. Sacks, D. Kingsland, R. Lee and J.-F. Lee, "A perfectly matched anisotropic absorber for use as an absorbing boundary condition", IEEE Transactions on Antennas and Propagation **43,** 1460 (1995) (cit. on p. 101).

153. M. Kuzuoglu and R. Mittra, "Frequency dependence of the constitutive parameters of causal perfectly matched anisotropic absorbers", IEEE Microwave and Guided Wave Letters **6,** 447 (1996) (cit. on p. 103).

154. J.-P. Bérenger, "Perfectly matched layer (PML) for computational electromagnetics", Synthesis Lectures on Computational Electromagnetics **2,** 1 (2007) (cit. on pp. 103, 105).

155. J.-P. Bérenger, "A perfectly matched layer for the absorption of electromagnetic waves", Journal of Computational Physics **114,** 185 (1994) (cit. on p. 105).

156. Wolfram Research Inc., "Mathematica, Version 12.0", (cit. on pp. 108, 209).

157. B. Fultz and J. Howe, *Transmission Electron Microscopy and Diffractometry of Materials*, 4th ed. (Springer-Verlag Berlin Heidelberg, 2013) (cit. on p. 113).

158. N. Zabala and A. Rivacoba, "Electron energy loss near supported particles", Phys. Rev. B **48,** 14534 (1993) (cit. on p. 113).

159. F. J. García de Abajo and M. Kociak, "Probing the Photonic Local Density of States with Electron Energy Loss Spectroscopy", Phys. Rev. Lett. **100,** 106804 (2008) (cit. on pp. 113, 115).

160. F. J. García de Abajo and M. Kociak, "Electron energy-gain spectroscopy", New Journal of Physics **10,** 073035 (2008) (cit. on p. 114).

161. C. Matyssek, *Investigation of plasmonic structures by light and electron microscopy*, PhD thesis (Universität Halle-Wittenberg, 2012) (cit. on pp. 114, 116).

162. U. Hohenester, H. Ditlbacher and J. R. Krenn, "Electron-Energy-Loss Spectra of Plasmonic Nanoparticles", Phys. Rev. Lett. **103,** 106801 (2009) (cit. on p. 115).

163. F. von Cube *et al.,* "From Isolated Metaatoms to Photonic Metamaterials: Evolution of the Plasmonic Near-Field", Nano Letters **13,** 703 (2013) (cit. on pp. 116, 195).

164. R. T. H. Diehl, *Analysis of Metallic Nanostructures by a Discontinuous Galerkin Time-Domain Maxwell Solver on Graphics Processing Units*, PhD thesis (Karlsruhe Insitute of Technology, 2012) (cit. on pp. 116, 196).

165. F. J. García de Abajo, "Electron energy loss and cathodoluminescence in spheres", `http://widgets.nanophotonics.es/sphere/index.html`, last accessed on 2020-11-10, (cit. on pp. 116, 119, 122).

166. P. B. Johnson and R. W. Christy, "Optical Constants of the Noble Metals", Phys. Rev. B **6,** 4370 (1972) (cit. on pp. 117, 124, 178).

167. L. D. Landau and E. M. Lifshitz, *Course of theoretical physics. 2, The classical theory of fields*, 3rd ed. (Pergamon Press, 1971) (cit. on pp. 117, 199, 203, 208).

168. W. Nolting, *Grundkurs theoretische Physik 4 - Spezielle Relativitätstheorie, Thermodynamik*, 7. Auflage (Springer-Verlag Berlin Heidelberg New York, 2010) (cit. on pp. 117, 203).

169. F. J. Harris, "On the use of windows for harmonic analysis with the discrete Fourier transform", Proceedings of the IEEE **66,** 51 (1978) (cit. on pp. 119, 139, 161, 185).

170. M. Frigo and S. G. Johnson, "The Design and Implementation of FFTW3", Proceedings of the IEEE **93,** 216 (2005) (cit. on p. 119).

171. MATLAB, *9.6.0.1072779 (R2019a)* (The MathWorks Inc., Natick, Massachusetts, 2019) (cit. on pp. 119, 165).

172. C. Sönnichsen *et al.,* "Launching surface plasmons into nanoholes in metal films", Applied Physics Letters **76,** 140 (2000) (cit. on p. 122).

173. J.-Y. Li, Z.-Y. Li, H.-F. Yang and A.-Z. Jin, "Scanning near-field optical microscopy study of metallic square hole array nanostructures", Journal of Applied Physics **104,** 114303 (2008) (cit. on p. 122).

174. G. Ctistis, P. Patoka, X. Wang, K. Kempa and M. Giersig, "Optical Transmission through Hexagonal Arrays of Subwavelength Holes in Thin Metal Films", Nano Letters **7,** 2926 (2007) (cit. on p. 122).

175. J.-Y. Li, L. Gan and Z.-Y. Li, "Near-field optical observations of surface plasmon wave interference at subwavelength hole arrays perforated in Au film", Chinese Physics B **22,** 117302 (2013) (cit. on p. 122).

176. R. Dhama *et al.,* "Extraordinary Effects in Quasi-Periodic Gold Nanocavities: Enhanced Transmission and Polarization Control of Cavity Modes", ACS Nano **12,** 504 (2018) (cit. on p. 122).

177. W. Sigle *et al.,* "EFTEM study of surface plasmon resonances in silver nanoholes", Ultramicroscopy **110,** 1094 (2010) (cit. on p. 122).

178. N. Talebi, B. Ögüt, W. Sigle, R. Vogelgesang and P. A. van Aken, "On the symmetry and topology of plasmonic eigenmodes in heptamer and hexamer nanocavities", Applied Physics A **116,** 947 (2014) (cit. on p. 122).

179. R. Walther *et al.,* "Interslit Coupling via Ultrafast Dynamics across Gold-Film Hole Arrays", The Journal of Physical Chemistry C **118,** 11043 (2014) (cit. on p. 122).

180. L. Giannuzzi and F. Stevie, "A review of focused ion beam milling techniques for TEM specimen preparation", Micron **30,** 197 (1999) (cit. on p. 122).

181. H. F. Ghaemi, T. Thio, D. E. Grupp, T. W. Ebbesen and H. J. Lezec, "Surface plasmons enhance optical transmission through subwavelength holes", Phys. Rev. B **58,** 6779 (1998) (cit. on p. 125).

182. D. Jalas *et al.,* "What is—and what is not—an optical isolator", Nature Photonics **7,** 579 (2013) (cit. on p. 133).

183. Y. Shoji and T. Mizumoto, "Magneto-optical non-reciprocal devices in silicon photonics", Science and Technology of Advanced Materials **15,** 014602 (2014) (cit. on p. 133).

184. M. König, K. Busch and J. Niegemann, "The Discontinuous Galerkin Time-Domain method for Maxwell's equations with anisotropic materials", Photonics and Nanostructures - Fundamentals and Applications **8,** 303 (2010) (cit. on p. 133).

185. J. Viquerat, *Simulation of electromagnetic waves propagation in nano-optics with a high-order discontinuous Galerkin time-domain method*, PhD thesis (Université Nice Sophia Antipolis, 2015) (cit. on pp. 139, 196).

186. M. Plock, *Numerical analysis of plasmonic nano-structures using the discontinuous Galerkin time-domain method on curvilinear elements*, Master's thesis (Humboldt-Universität zu Berlin, 2020) (cit. on pp. 139, 196).

187. L. D. Landau and E. M. Lifshitz, *Course of theoretical physics. 1, Mechanics*, 2nd ed. (Pergamon Press, 1969) (cit. on p. 143).

188. H. Cheng and K. C. Gupta, "An Historical Note on Finite Rotations", Journal of Applied Mechanics **56,** 139 (1989) (cit. on p. 143).

189. J. Shan, J. I. Dadap and T. F. Heinz, "Circularly polarized light in the single-cycle limit: the nature of highly polychromatic radiation of defined polarization", Opt. Express **17,** 7431 (2009) (cit. on pp. 147, 148).

190. R. N. Bracewell, *The Fourier transform and its applications*, 3rd edition (McGraw-Hill New York, 2000) (cit. on p. 148).

191. E. Bedrosian, "A Product Theorem for Hilbert Transforms", RAND Corporation, RM-3439 (1962) (cit. on p. 148).

192. C. L. Holloway *et al.,* "An Overview of the Theory and Applications of Metasurfaces: The Two-Dimensional Equivalents of Metamaterials", IEEE Antennas and Propagation Magazine **54,** 10 (2012) (cit. on p. 152).

193. P. Varytis, *Tailored disorder and anisotropic scattering in photonic nanostructures*, PhD thesis (Humboldt-Universität zu Berlin, 2019) (cit. on p. 152).

194. E. Brochu, V. M. Cora and N. De Freitas, "A tutorial on Bayesian optimization of expensive cost functions, with application to active user modeling and hierarchical reinforcement learning", arXiv preprint arXiv:1012.2599 (2010) (cit. on pp. 153, 158, 196).

195. Z. Yu, Z. Wang and S. Fan, "One-way total reflection with one-dimensional magneto-optical photonic crystals", Applied physics letters **90,** 121133 (2007) (cit. on p. 153).

196. T. E. Oliphant, *A guide to NumPy* (Trelgol Publishing USA, 2006) (cit. on p. 158).

197. S. Van Der Walt, S. C. Colbert and G. Varoquaux, "The NumPy array: a structure for efficient numerical computation", Computing in Science & Engineering **13,** 22 (2011) (cit. on p. 158).

198. D. de Ceglia *et al.,* "Second-harmonic double-resonance cones in dispersive hyperbolic metamaterials", Phys. Rev. B **89,** 075123 (2014) (cit. on p. 162).

199. G. Marino *et al.,* "Second-Harmonic Generation from Hyperbolic Plasmonic Nanorod Metamaterial Slab", Laser & Photonics Reviews **12,** 1700189 (2018) (cit. on p. 162).

200. G. V. Naik, V. M. Shalaev and A. Boltasseva, "Alternative Plasmonic Materials: Beyond Gold and Silver", Advanced Materials **25,** 3264 (2013) (cit. on pp. 162, 169).

201. H. Khamh, E. Sachet, K. Kelly, J.-P. Maria and S. Franzen, "As good as gold and better: conducting metal oxide materials for mid-infrared plasmonic applications", J. Mater. Chem. C **6,** 8326 (2018) (cit. on pp. 162, 169).

202. I. H. Malitson, F. V. Murphy and W. S. Rodney, "Refractive Index of Synthetic Sapphire", J. Opt. Soc. Am. **48,** 72 (1958) (cit. on p. 165).

203. T. Tyborski *et al.,* "Ultrafast Nonlinear Response of Bulk Plasmons in Highly Doped ZnO Layers", Phys. Rev. Lett. **115,** 147401 (2015) (cit. on p. 169).

204. E. Yablonovitch, "Photonic band-gap structures", JOSA B **10,** 283 (1993) (cit. on p. 173).

205. J. D. Joannopoulos, S. G. Johnson, J. N. Winn and R. D. Meade, *Photonic Crystals – Molding the Flow of Light*, 2nd edition (Princeton Univ. Press, 2008) (cit. on p. 173).

206. L. V. R.-d. Marcos, J. I. Larruquert, J. A. Méndez and J. A. Aznárez, "Self-consistent optical constants of SiO2 and Ta2O5 films", Opt. Mater. Express **6,** 3622 (2016) (cit. on p. 173).

207. I. H. Malitson, "Interspecimen Comparison of the Refractive Index of Fused Silica∗,†", J. Opt. Soc. Am. **55,** 1205 (1965) (cit. on p. 173).

208. C. W. Tang, S. A. VanSlyke and C. H. Chen, "Electroluminescence of doped organic thin films", Journal of Applied Physics **65,** 3610 (1989) (cit. on p. 174).

209. H. G. Tompkins and W. A. MacGahan, *Spectroscopic ellipsometry and reflectometry : A user's guide*, 1st Edition (John Wiley and Sons, Inc., 1999) (cit. on p. 175).

210. S. I. Hintschich *et al., Oblique angle lasing in a periodically pumped organic microcavity Organic Photonics IV* (eds P. L. Heremans, R. Coehoorn and C. Adachi) **7722** (SPIE, 2010), 29 (cit. on p. 175).

211. C. Kallinger *et al.,* "Picosecond amplified spontaneous emission bursts from a molecularly doped organic semiconductor", Journal of Applied Physics **91,** 6367 (2002) (cit. on pp. 175, 184).

212. F. von Cube *et al.,* "Spatio-spectral characterization of photonic meta-atoms with electron energy-loss spectroscopy", Opt. Mater. Express **1,** 1009 (2011) (cit. on p. 195).

213. S. Raza, G. Toscano, A.-P. Jauho, M. Wubs and N. A. Mortensen, "Unusual resonances in nanoplasmonic structures due to nonlocal response", Phys. Rev. B **84,** 121412 (2011) (cit. on p. 195).

214. P. Halevi, "Hydrodynamic model for the degenerate free-electron gas: Generalization to arbitrary frequencies", Phys. Rev. B **51,** 7497 (1995) (cit. on p. 196).

215. F. Haas, "A magnetohydrodynamic model for quantum plasmas", Physics of Plasmas **12,** 062117 (2005) (cit. on p. 196).

216. M. Moeferdt, *Nonlocal and Nonlinear Properties of Plasmonic Nanostructures Within the Hydrodynamic Drude Model*, PhD thesis (Humboldt-Universität zu Berlin, 2017) (cit. on p. 196).

217. D.-N. Huynh, *Nonlinear optical phenomena within the discontinuous Galerkin time-domain method*, PhD thesis (Humboldt-Universität zu Berlin, 2018) (cit. on p. 196).

218. C. Prohm, *Modellierung der linearen und nichtlinearen optischen Eigenschaften metallischer Nanostrukturen mit Hilfe unstetiger Galerkin Verfahren*, Diploma thesis (Karlsruhe Insitute of Technology, 2010) (cit. on p. 196).

219. F. Schwarz and E. Runge, "Towards Optimal Disorder in Gold Nanosponges for Long-Lived Localized Plasmonic Modes", Annalen der Physik **529,** 1600234 (2017) (cit. on p. 196).

220. J. Zhong *et al.,* "Strong Spatial and Spectral Localization of Surface Plasmons in Individual Randomly Disordered Gold Nanosponges", Nano Letters **18,** 4957 (2018) (cit. on p. 196).

221.   R. L. Haupt and S. E. Haupt, *Practical genetic algorithms*, 2nd ed. (John Wiley & Sons, Inc., Hoboken, N.J., 2004) (cit. on p. 196).

222.   J. Wang, S. C. Clark, E. Liu and P. I. Frazier, "Parallel bayesian global optimization of expensive functions", Operations Research **68,** 1850 (2016) (cit. on p. 196).

223.   D. Ginsbourger, R. Le Riche and L. Carraro, *A Multi-points Criterion for Deterministic Parallel Global Optimization based on Kriging NCP07* (Rouen, France, 2007) (cit. on p. 196).

224.   M. Paulus, P. Gay-Balmaz and O. J. F. Martin, "Accurate and efficient computation of the Green's tensor for stratified media", Phys. Rev. E **62,** 5797 (2000) (cit. on p. 197).

225.   İ. R. Çapoğlu, A. Taflove and V. Backman, "Computation of tightly-focused laser beams in the FDTD method", Opt. Express **21,** 87 (2013) (cit. on pp. 197, 211, 215).

226.   M. Rothe *et al.,* "Self-Assembly of Plasmonic Nanoantenna–Waveguide Structures for Subdiffractional Chiral Sensing", ACS Nano (2020) (cit. on pp. 197, 198).

227.   J. Petersen, J. Volz and A. Rauschenbeutel, "Chiral nanophotonic waveguide interface based on spin-orbit interaction of light", Science **346,** 67 (2014) (cit. on p. 198).

228.   A. Demirel, J. Niegemann, K. Busch and M. Hochbruck, "Efficient multiple time-stepping algorithms of higher order", Journal of Computational Physics **285,** 133 (2015) (cit. on p. 198).

229.   S. Franke *et al.,* "Quantization of Quasinormal Modes for Open Cavities and Plasmonic Cavity Quantum Electrodynamics", Phys. Rev. Lett. **122,** 213901 (2019) (cit. on p. 198).

230.   W. Nolting, *Grundkurs theoretische Physik 1 - klassische Mechanik*, 8. Auflage (Springer-Verlag Berlin Heidelberg New York, 2006) (cit. on p. 199).

231.   C. Gryzik, *Fokussierte Strahlen und metallische Nano-Teilchen: Berechnung optischer Kräfte im Rahmen unstetiger Galerkin-Verfahren*, Bachelor's thesis (Humboldt-Universität zu Berlin, 2014) (cit. on pp. 211, 215).

232.   E. Wolf and D. Gabor, "Electromagnetic diffraction in optical systems - I. An integral representation of the image field", Proceedings of the Royal Society of London. Series A. Mathematical and Physical Sciences **253,** 349 (1959) (cit. on p. 211).

Co-supervised theses

T1. P. Ledwon, *Numerik photonischer Kristalle, eine Erweiterung des S-Matrix-Algorithmus in der Fourier-Moden-Methode mit Hilfe der Magnus-Entwicklung*, Bachelor's thesis (Humboldt-Universität zu Berlin, 2017) (cit. on p. 43).

T2. M. Kück, *Implementierung der B-Spline-Moden-Methode zur Anwendung auf photonische Nanostrukturen*, Bachelor's thesis (Humboldt-Universität zu Berlin, 2017) (cit. on p. 47).

T3. R. H. Kieschke, *Optische Eigenschaften von Rhodamin 6G in einem hyperbolischen Metamaterial aus Siliziumdioxid und Silber*, Master's thesis (Humboldt-Universität zu Berlin, 2019) (cit. on pp. 162, 197).

Publication List

K1. B. Schröder *et al.,* "Real-space imaging of nanotip plasmons using electron energy loss spectroscopy", Phys. Rev. B **92,** 085411 (2015) (cit. on pp. 1, 124).

K2. T. Weber, T. Kiel, S. Irsen, K. Busch and S. Linden, "Near-field study on the transition from localized to propagating plasmons on 2D nano-triangles", Opt. Express **25,** 16947 (2017) (cit. on p. 1).

K3. E. Travkin *et al.,* "Anomalous resonances of an optical microcavity with a hyperbolic metamaterial core", Phys. Rev. B **97,** 195133 (2018) (cit. on pp. 3, 162, 163, 164, 197).

K4. M. Kliem *et al.,* "Defect-State Lasing in Photonic Lattices of Metal-Organic Microcavities", Advanced Photonics Research, 2000116 (cit. on pp. 3, 4, 171, 175, 177, 182, 197).

K5. C. Somma *et al.,* "Mid-infrared beam splitter for ultrashort pulses", Opt. Lett. **42,** 2918 (2017) (cit. on p. 3).

K6. M. Moeferdt, T. Kiel, T. Sproll, F. Intravaia and K. Busch, "Plasmonic modes in nanowire dimers: A study based on the hydrodynamic Drude model including nonlocal and nonlinear effects", Phys. Rev. B **97,** 075431 (2018) (cit. on p. 30).

K7. M. Prämassing, S. Irsen, T. Kiel, K. Busch and S. Linden, "Electron energy-loss spectroscopy on thin freestanding perforated gold films", (*submitted* to Phys. Rev. B) (2021) (cit. on pp. 113, 117, 122, 124, 125, 128, 129, 130, 195).

K8. T. Kiel, P. Varytis, B. Beverungen, P. T. Kristensen and K. Busch, "Enhanced Faraday rotation in all-dielectric magneto-optical metasurfaces with Bayesian algorithm shape-optimized scatterers", (*submitted* to Opt. Lett.) (2021) (cit. on pp. 133, 152, 158).

K9. E. Travkin *et al.,* "Dispersion control in a near-infrared subwavelength resonator with a tailored hyperbolic metamaterial", Opt. Lett. **45,** 3665 (2020) (cit. on pp. 162, 169, 197).

K10. T. Pfadler *et al.,* "Structure-induced resonant tail-state regime absorption in polymer: fullerene bulk-heterojunction solar cells", Phys. Rev. B **93,** 205305 (2016) (cit. on p. 173).

K11. F. Loth, T. Kiel, K. Busch and P. T. Kristensen, "Surface roughness in finite element meshes", arXiv preprint arXiv:2002.00894 (2020) (cit. on p. 196).